9 May 2014 | $10

Science

Cultivated Minds

How Rice Farming Has Shaped Psychology

AAAS

EDITORIAL

557 Young Brains on Drugs
Robert L. DuPont and Jeffrey A. Lieberman

NEWS OF THE WEEK

562 A roundup of the week's top stories

NEWS & ANALYSIS

566 Fresh Misconduct Charges Hit Dutch Social Psychology

567 New Sites Bring the Earliest Americans Out of the Shadows

569 'Sea Butterflies' Are a Canary for Ocean Acidification

570 'Rejuvenation Factor' in Blood Turns Back the Clock in Old Mice
>> Reports pp. 630 and 649

571 Designer Microbes Expand Life's Genetic Alphabet

NEWS FOCUS

572 Maritime Ambitions
>> Science *Podcast*

LETTERS

577 Breast Cancer and Environmental Research
J. G. Brody et al.

Copper Limits: Opportunity Costs
J. E. Tilton

Copper Limits: Recycling Potential
G. Lagos

Copper Limits: Human Agency
A. J. Cavallo

578 TECHNICAL COMMENT ABSTRACTS

578 NextGenVOICES

BOOKS *ET AL.*

579 Beauty, Challenges, Ingenuity, and Horrors

EDUCATION FORUM

583 Convergence Between Science and Environmental Education
A. E. J. Wals et al.

PERSPECTIVES

585 A SWELL Channel Indeed
J. A. Mindell
>> Report p. 634

586 Next Steps for Cosmology
J. Silk and J. Chluba

588 Host Controls of HIV Neutralizing Antibodies
B. F. Haynes and L. Verkoczy

590 Trigger Factor Flexibility
M. Gamerdinger and E. Deuerling
>> Research Article p. 597

591 An Internal Cure for Damaged Polymers
Z. Zhao and E. M. Arruda
>> Report p. 620

593 Rice, Psychology, and Innovation
J. Henrich
>> Research Article p. 603

594 A Price to Pay for Adult Neurogenesis
L. A. Mongiat and A. F. Schinder
>> Research Article p. 598

REVIEW

596 Sound Strategies for Hearing Restoration
G. S. G. Géléoc and J. R. Holt
Review Summary; for full text: http://dx.doi.org/10.1126/science.1241062

CONTENTS continued >>

page 572

page 579

ON THE WEB THIS WEEK

>> *Science* Podcast
On this week's show: marine archaeology digs up political complexities and a roundup of stories from our daily news site.

>> Find More Online
Check out *Science* Express, the weekly podcast, videos, daily news, our research journals, and *Science* Careers at **www.sciencemag.org**.

COVER

Farmers drying grains of rice in the sun in China's Anhui province. New psychological tests suggest that China's history of rice farming has given the south more markers of traditional East Asian culture, such as interdependence, holistic thought style, and low divorce rates. In comparison, people in wheat-growing northern China are more independent. See pages 593 and 603.

Photo: Getty Images

DEPARTMENTS

555 This Week in *Science*
558 Editors' Choice
560 *Science* Staff
653 New Products
654 *Science* Careers

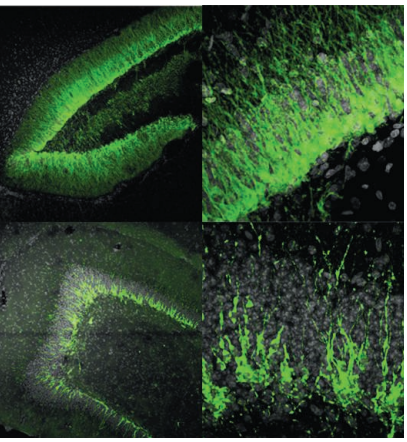

pages 594 & 598

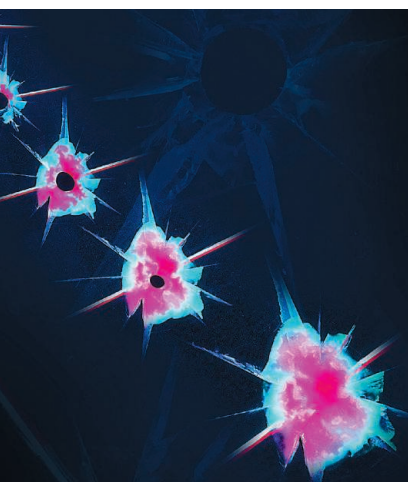

pages 591 & 620

RESEARCH ARTICLES

597 Structural Basis for Protein Antiaggregation Activity of the Trigger Factor Chaperone
T. Saio et al.
Nuclear magnetic resonance data show how molecular chaperones recognize and prevent aggregation and misfolding of unfolded proteins.
Research Article Summary; for full text: http://dx.doi.org/10.1126/science.1250494
>> Perspective p. 590

598 Hippocampal Neurogenesis Regulates Forgetting During Adulthood and Infancy
K. G. Akers et al.
Addition of new neurons leads to remodeling of hippocampal circuitry and memory degradation.
>> Perspective p. 594

603 Large-Scale Psychological Differences Within China Explained by Rice Versus Wheat Agriculture
T. Talhelm et al.
A history of growing rice contributed to an interdependent mode of thought.
>> Perspective p. 593

REPORTS

608 Fermi Surface and Pseudogap Evolution in a Cuprate Superconductor
Y. He et al.

612 Simultaneous Transitions in Cuprate Momentum-Space Topology and Electronic Symmetry Breaking
K. Fujita et al.
Scanning tunneling microscopy is used to provide evidence for a quantum critical point beneath the superconducting dome.

616 Direct, Nonoxidative Conversion of Methane to Ethylene, Aromatics, and Hydrogen
X. Guo et al.
Methyl radicals that form at isolated iron sites in a silica matrix form gas-phase products and do not deposit solid carbon.

620 Restoration of Large Damage Volumes in Polymers
S. R. White et al.
A sequential set of gelation and polymerization reactions are used for patching large gaps in a polymer sample.
>> Perspective p. 591

623 In Situ TEM Observation of a Microcrucible Mechanism of Nanowire Growth
R. Boston et al.
Nanowire growth from a microcrucible catalyst particle at the bottom of the wire is observed in situ.

626 Spatially Distributed Local Fields in the Hippocampus Encode Rat Position
G. Agarwal et al.
Electrical fields within the hippocampus can now be decoded to reveal a rat's location.

630 Vascular and Neurogenic Rejuvenation of the Aging Mouse Brain by Young Systemic Factors
L. Katsimpardi et al.
A circulating growth factor promotes youthful muscles and brains in aged mice.
>> News story p. 570; Report p. 649

634 Identification of LRRC8 Heteromers as an Essential Component of the Volume-Regulated Anion Channel VRAC
F. K. Voss et al.
Components of an elusive swelling-activated anion channel are identified and form a structurally new class of channel.
>> Perspective p. 585

638 Gibberellin Acts Positively Then Negatively to Control Onset of Flower Formation in *Arabidopsis*
N. Yamaguchi et al.
Inflorescence architecture is shaped by a biphasic signaling network involving the plant hormone gibberellin.

641 Cancer Immunotherapy Based on Mutation-Specific CD4+ T Cells in a Patient with Epithelial Cancer
E. Tran et al.
T cells specific for a mutation expressed by tumor cells show antitumor activity in a patient with an epithelial cancer.

645 The Transcription Factor Gata6 Links Tissue Macrophage Phenotype and Proliferative Renewal
M. Rosas et al.
The major self-renewing population of peritoneal macrophages is under discrete tissue-selective transcriptional control.

649 Restoring Systemic GDF11 Levels Reverses Age-Related Dysfunction in Mouse Skeletal Muscle
M. Sinha et al.
A circulating growth factor promotes youthful muscles and brains in aged mice.
>> News story p. 570; Report p. 630

CREDIT: (BOTTOM) AUTONOMOUS MATERIALS SYSTEMS GROUP/BECKHAM INSTITUTE, UNIVERSITY OF ILLINOIS

SCIENCE (ISSN 0036-8075) is published weekly on Friday, except the last week in December, by the American Association for the Advancement of Science, 1200 New York Avenue, NW, Washington, DC 20005. Periodicals Mail postage (publication No. 484460) paid at Washington, DC, and additional mailing offices. Copyright © 2014 by the American Association for the Advancement of Science. The title SCIENCE is a registered trademark of the AAAS. Domestic individual membership and subscription (51 issues): $153 ($74 allocated to subscription). Domestic institutional subscription (51 issues): 1282; Foreign postage extra: Mexico, Caribbean (surface mail) $55; other countries (air assist delivery) $85. First class, airmail, student, and emeritus rates on request. Canadian rates with GST available upon request, GST #1254 88122. Publications Mail Agreement Number 1069624. **Printed in the U.S.A.**

Change of address: Allow 4 weeks, giving old and new addresses and 8-digit account number. **Postmaster:** Send change of address to AAAS, P.O. Box 96178, Washington, DC 20090–6178. **Single-copy sales:** $10.00 current issue, $15.00 back issue prepaid includes surface postage; bulk rates on request. **Authorization to photocopy** material for internal or personal use under circumstances not falling within the fair use provisions of the Copyright Act is granted by AAAS to libraries and other users registered with the Copyright Clearance Center (CCC) Transactional Reporting Service, provided that $30.00 per article is paid directly to CCC, 222 Rosewood Drive, Danvers, MA 01923. The identification code for *Science* is 0036-8075. *Science* is indexed in the *Reader's Guide to Periodical Literature* and in several specialized indexes.

Under the Dome

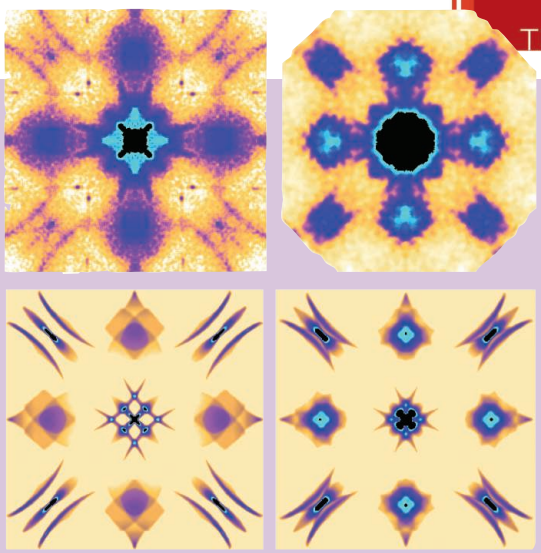

The superconducting transition temperature T_c of copper oxides has a dome-shaped dependence on chemical doping. Whether there is a quantum critical point (QCP) beneath the dome, and whether it is related to the enigmatic pseudogap, has been heavily debated. Two papers address this question in two different families of Bi-based cuprates. In $(Bi,Pb)_2(Sr,La)_2CuO_{6+\delta}$, **He *et al.*** (p. 608) found that the Fermi surface (FS) undergoes a topological change as doping is increased, which points to the existence of a QCP at a doping close to the maximum in T_c, seemingly uncorrelated with the pseudogap. **Fujita *et al.*** (p. 612) studied a range of dopings in $Bi_2Sr_2CaCu_2O_{8+\delta}$ to find an FS reconstruction simultaneous with the disappearance of both rotational and translational symmetry breaking, the latter of which has been associated with the pseudogap. These findings point to a concealed QCP.

One Hormone, Two Phases

The switch from vegetative growth to flowering in the plant *Arabidopsis* involves two phases—inflorescence branching and flowering. **Yamaguchi *et al.*** (p. 638) examined how the phytohormone gibberellin regulates each phase differently. First, gibberellin levels increase and stimulate production of key flowering factors, one of which degrades gibberellin. As gibberellin levels then fall, the next phase of flowering factors is released from gibberellin repression. By regulating inflorescence branching separately from flowering, this system determines overall seed yield.

Individualism Rules?

On a diverse and large set of cognitive tests, subjects in East Asian countries are more inclined to display collectivist choices, whereas subjects in the United States are more inclined to score as individualists. **Talhelm *et al.*** (p. 603; see the Perspective by **Henrich**) suggest that one historical source of influence was societal patterns of farming rice versus wheat, based on three cognitive measures of individualism and collectivism in 1000 subjects from rice- and wheat-growing regions in China.

Upgrading Methane Sans Oxygen

Direct routes to converting methane to higher hydrocarbons can allow natural gas to be used to provide chemical feedstocks. However, the reaction conditions needed to activate the strong C-H bond tend to overoxidize the products. **Guo *et al.*** (p. 616) report a high-temperature nonoxidative route that exposes methane to isolated iron sites on a silica catalyst. Methyl radicals were generated and coupled in the gas phase to form ethylene and aromatics along with hydrogen. The isolation of the active sites avoided surface reactions between the radicals that would deposit solid carbon.

Forget It!

When examining the relationship between the production of new neurons in the hippocampus and memory, studies have generally first manipulated hippocampal neurogenesis and afterward investigated memory formation and found that new neurons help to encode new memories. However, when investigating how similar manipulations of neurogenesis impact established hippocampus-dependent memories, **Akers *et al.*** (p. 598; see the Perspective by **Mongiat and Schinder**) uncovered a role for neurogenesis in memory clearance. Thus, the continuous addition of new neurons both degrades existing information stored in hippocampal circuits and simultaneously provides substrates for new learning.

Self-Healing Larger Wounds

By loading a polymer with pockets of monomer, it is possible to heal small cracks in a sample through the polymerization of the monomer following the formation of a crack. However, large holes are much harder to repair. **White *et al.*** (p. 620; see the Perspective by **Zhao and Arruda**) developed a vascular-like repair system involving a dual-stage strategy to self-heal epoxy thermosets. After injecting a damaged site with precursors, a gel with reversible cross-links rapidly formed, so the material stayed in place that then solidified further upon cross-linking. The approach successfully patched holes larger than 3 centimeters in diameter.

Nanowire Growth Observed

In the hypothetical microcrucible growth mechanism for nanowires, a molten catalytic particle located in a pore on a substrate continually feeds the outward growth of the wire. To observe such a mechanism requires the ability to examine nanowire growth in situ. **Boston *et al.*** (p. 623) studied various stages of Y_2BaCuO_5 nanowire growth using transmission electron microscopy and were able to observe a microcrucible growth mechanism directly.

Help the Aged

Muscle function declines with age, as does neurogenesis in certain brain regions. Two teams analyzed the effects of heterochronic parabiosis in mice. **Sinha *et al.*** (p. 649) found that when an aged mouse shares a circulatory system with a youthful mouse, the aged mouse sees improved muscle function, and **Katsimpardi *et al.*** (p. 630) observed increased generation of olfactory neurons. In both cases, Growth Differentiation Factor 11 appeared to be one of the key components of the young blood.

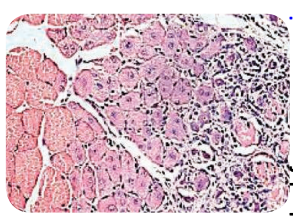

T Cells for Epithelial Tumors

Malignant tumors harbor genetic alterations. Recently, adoptive T cell therapies have taken advantage of this: T cells specific for mutations in tumors are infused into patients to generate an antitumor immune response. Although therapeutic benefit has been seen for melanomas, effectiveness against more common epithelial tumors is unclear. Using whole-exome sequencing, **Tran *et al.*** (p. 641) identified tumor-infiltrating CD4+ T cells specific for a mutated antigen expressed by a tumor from a patient with metastatic cholangiocarcinoma. Infusion of this patient with an expanded-population, mutation-specific T cell resulted in tumor regression and stabilization of disease.

CREDITS (TOP TO BOTTOM): HE *ET AL.*; SINHA *ET AL.*

Downloaded from www.sciencemag.org on May 8, 2014

Additional summaries

Hearing Aid

Many millions of people across the globe are subject to hearing loss. **Géléoc and Holt** (p. 596) review recent developments in potential therapeutic strategies to restore inner-ear function in patients with acquired or genetic forms of deafness. While challenges remain, fundamental research in molecular, gene, and stem-cell therapies has enabled progress toward developing alternatives to conventional, sound amplification–based prostheses.

Extracting Spatial Information

The location of a rat can be deciphered from hippocampal activity by detecting the firing of individual place-selective neurons. In contrast, the local field potential (LFP), which arises from the coherent voltage fluctuations of large hippocampal cell populations, has been hard to decode. **Agarwal *et al.*** (p. 626) worked out how to recover positional information exclusively from multiple-site LFP measurements in the rat hippocampus. The information was as precise as that derived from spiking place cells. The approach might also be applicable more generally for deciphering information from coherent population activity anywhere in the brain.

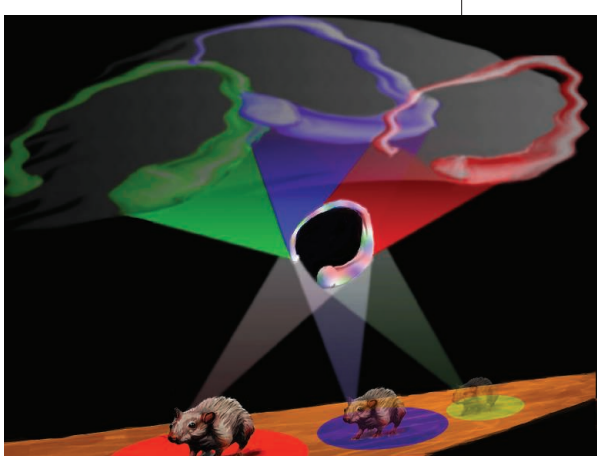

Recognize and Protect

Molecular chaperones play a key role in maintaining protein homeostasis in the cell by preventing protein aggregation and misfolding. Chaperone-substrate complexes tend to be large and dynamic, making structure determination challenging. **Saio *et al.*** (p. 597; see the Perspective by **Gamerdinger and Deuerling**) used advanced NMR spectroscopy techniques to determine the structure of three trigger factor (TF) chaperone molecules in complex with the unfolded substrate, alkaline phosphatase (PhoA), and of each of the TFs in complex with the relevant region of PhoA. TF binds at multiple sites on PhoA through hydrophobic contacts, thus shielding these residues from solvent and preventing aggregation. The stability of the complex increases as longer PhoA regions are engaged by TF, and the multivalent binding keeps the substrate in an extended conformation.

One Swell Ion Channel

When mammalian cells are faced with osmotic challenges, they need to swell or shrink. The molecular characterization of the volume-regulated anion channel (VRAC) remains unknown, although many candidate proteins have been proposed. **Voss *et al.*** (p. 634, published online 10 April; see the Perspective by **Mindell**) used a genome-wide screen to identify a group of leucine-rich repeat–containing (LRRC) proteins necessary for forming VRAC. Suppression of LRRC8A nearly eliminated the presence of VRAC in mammalian cells. A hetero-oligomer of LRRC proteins appears to form VRAC. Identification of VRAC components is an essential step forward in the understanding of swelling-activated ion channels and provides opportunities for understanding both the mechanism of the channel and its role in physiology.

Gata6 Controls Peritoneal Macs

Macrophages seed tissues throughout the body and are shaped both phenotypically and functionally by the microenvironment they inhabit. Despite such heterogeneity, most tissue macrophages self-renew by local proliferation. How this is regulated, however, is unclear. **Rosas *et al.*** (p. 645, published online 24 April) used gene expression analysis to show that the transcription factor Gata6 is specifically expressed in peritoneal macrophages. Gata6 was critical for maintaining the transcriptional signature of peritoneal macrophages and for their proliferative renewal during homeostasis and under inflammatory conditions.

CREDIT: DORUK GOLCU

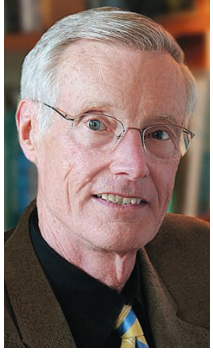

Robert L. DuPont was the first director of the U.S. National Institute on Drug Abuse (1973–1978) and is president of the Institute for Behavior and Health, Rockville, MD.

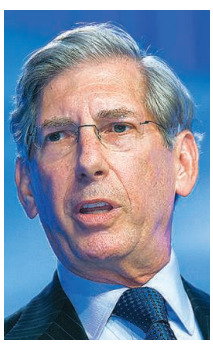

Jeffrey A. Lieberman is president of the American Psychiatric Association and chair of the Department of Psychiatry at Columbia University, New York. E-mail: jlieberman@columbia.edu

Young Brains on Drugs

THE DEBATES OVER LEGALIZATION, DECRIMINALIZATION, AND MEDICAL USES OF MARIJUANA IN THE United States are missing an essential piece of information: scientific evidence about the effects of marijuana on the adolescent brain. Much is known about the effects of recreational drugs on the mature adult brain, but there has been no serious investigation of the risks of marijuana use in younger users. In April 2014, a controversial study* suggested that "casual" use of marijuana is associated with structural abnormalities in the brains of young people (aged 18 to 25), particularly in regions vital to emotion, motivation, and decision-making. The fact that the findings are preliminary and disputed indicates that rigorous research is needed to inform discussions about the public health benefits and risks of legalized marijuana.

Although marijuana remains illegal for people under the age of 21 in the United States (including in the two states that have legalized it for adults), young people will almost certainly have greater exposure to, and likely more ways to access, the drug (as they already do with alcohol and tobacco), as new initiatives to change marijuana laws in many states come to fruition. Proponents of legalization argue that the medically harmful effects of marijuana are "no worse" than those of alcohol and tobacco. But even if that is true, it does not mean that the risks are the same. Over the decades, the United States has funded research to study the long-term health effects of alcohol and tobacco, but not marijuana. Yet many of the most worrisome brain pathologies from drug use are seen in mental health (as opposed to pulmonary disease and cancer with smoking, and gastric and liver disease with alcohol), where marijuana use is associated with, among other conditions, anxiety and psychotic disorders.† Research suggests that early marijuana use is linked to these problems, but their biological underpinnings are a mystery.

The National Survey on Drug Use and Health has repeatedly found that children who began alcohol or marijuana use before age 15 had a fivefold-increased prevalence of substance use disorders later in life.‡ This may be due to effects of early drug use on the trajectory of the brain's subsequent development, but we don't know for sure. What is needed are large longitudinal cohort studies to examine whether marijuana use causes changes in brain function and behavior in young people. The Framingham Heart Study, still ongoing after its initiation 65 years ago, revolutionized our understanding of what causes cardiovascular disease, producing completely unanticipated findings that have led to improved health care and public policy.

The U.S. National Institutes of Health should launch a similar long-term study of preadolescent children and follow them through adolescence into young adulthood, when their brains are most plastic, rapidly developing, reorganizing, and forming enduring neural connections and circuits. The rapid growth of brain science in the past two decades has generated new methods to measure the effects of drugs on brain structure and mental processes. With "big brain" research projects now under way in the United States and Europe, including the BRAIN Initiative announced by President Obama in 2013, to deduce how brain function is linked to behavior and disease, the time is right to rigorously pursue a long-term study of drug effects. Without more scientific evidence to inform policies, we are gambling with the health and safety of our youth in making decisions about psychoactive substances such as marijuana when their real risks are unknown.

– Robert L. DuPont and Jeffrey A. Lieberman

10.1126/science.1254989

*]. M. Gilman *et al., J. Neurosci.* **34**, 5529 (2014). †M. Large *et al., Arch. Gen. Psychiatry* **68**, 555 (2011); L. Degenhardt *et al., Addiction* **108**, 124 (2013). ‡Substance Abuse and Mental Health Services Administration, *Results from the 2012 National Survey on Drug Use and Health: Summary of National Findings*, NSDUH Series H-46, HHS Publication No. (SMA) 13-4795 (Substance Abuse and Mental Health Services Administration, Rockville, MD, 2013).

CREDITS: (TOP LEFT) INSTITUTE FOR BEHAVIOR AND HEALTH, INC.; (BOTTOM LEFT) COLUMBIA UNIVERSITY; (RIGHT) ROBOTBOOT/ISTOCKPHOTO.COM

Downloaded from www.sciencemag.org on May 9, 2014

Published by AAAS

EDITORS' CHOICE

EDITED BY KRISTEN MUELLER AND JESSE SMITH

ECOLOGY

Productive Trees

Forests in tropical Asia may capture carbon and produce wood half as fast again as South American forests. Banin *et al*. compared the growth rates of trees (as above-ground woody production) in permanent forest plots in northwest Amazonia and northern Borneo and found that Bornean forests produced wood at a 49% faster rate than their Amazonian counterparts. The differences remained even when soil conditions and rainfall were controlled for. The greater production in Borneo may partly reflect higher solar radiation, but another important factor appears to be the different tree species composition: Species of the dominant Southeast Asian tree family Dipterocarpaceae exhibit significantly higher production than other tree species in the sampled plots. These results suggest a potential for a key role for dipterocarp forest conservation and restoration to maintain and enhance carbon sequestration. — AMS

J. Ecol. 1111/1365-2745.12263 (2014).

EVOLUTION

Rock Soup

The fossil record of ancient microorganisms is difficult to disentangle, but the consensus is that complex life on Earth emerged during the Archean Eon, between 2.5 and 4 billion years ago. However, several biochemical processes, including the prebiotic synthesis of proteins and nucleic acids, must already have been established to form the structural and genetic basis of even the simplest life forms. The evolution of metabolic pathways is equally perplexing, yet was essential to allow life to develop autotrophy and adapt to different environments. Keller *et al.* exposed phosphorylated sugar intermediates—metabolites that form abiotically—to the harsh temperatures and chemical environment that were probably present in Earth's earliest oceans. With metals such as iron acting as catalysts instead of enzymes, they observed 29 interconversion reactions, including the formation of ribose 5-phosphate: the molecule that forms the backbone of RNA. Additionally, the formation of triose-, tetrose-, pentose-, hexose-, and sedoheptulose phosphates, which are components of modern central carbon metabolism, is consistent with the idea that metabolic reaction networks are of primordial origin and developed as a result of the specific geochemical environments present on early Earth. — NW

Mol. Syst. Biol. **10**, *725* (2014).

CHEMISTRY

Guiding Polymers with DNA

Insights into how a DNA template can guide the formation of conducting polymer nanowires have been obtained from atomic force microscopy (AFM), and molecular dynamics (MD), and coarse-grained simulations. Watson *et al.* prepared polypyrrole [poly(Py)] and poly-2,5-bis(2-thienyl)pyrrole [poly(TPT)] nanowires by mixing the oxidized monomers with $FeCl_3$ and bacteriophage lambda DNA templates in solution. The formation process was followed by removing solution at various times and depositing it on trimethylsilane-modified silica for AFM analysis. For poly(TPT), after 10 min, a low density of spherical polymer particles nucleated on the DNA; at 1 hour, the density and size of the particles increased and developed a beads-on-a-string morphology. By 4 hours, polymer particles began to merge and cover all of the DNA, and by 24 hours, a uniform wire with no distinct particles was seen. The process is similar for poly(Py) but is more rapid, and displays eariler elongation. The MD modeling studies show that DNA rotation promotes polymer binding in the initial stage, and the coarse-grained simulation shows that the smooth-wire formation is driven by a balance between adhesion to the DNA template and lowering the surface tension of the polymer. — PDS

J. Am. Chem. Soc. 10.1021/ja500439v (2014).

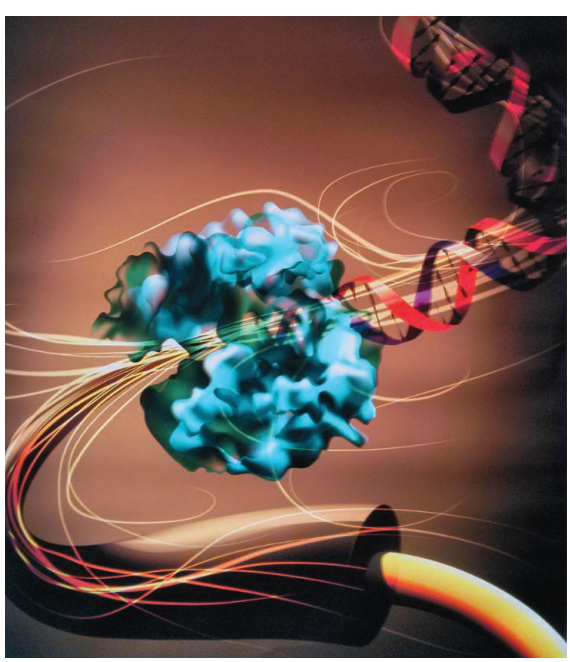

STEM CELLS

The Mechanics of Change

As embryonic stem cells differentiate toward specific cell fates, shifts in the gene regulatory network accompany progression through the different states: from pluripotency, where cells are competent to differentiate into any somatic cell; to a transition state; and finally to a differentiated state where cells are irreversibly committed to a particular cell fate. Pagliara *et al.* used atomic force microscopy to compare the elastic stiffness of mouse cells in each of these different fates. When compressing the cytoplasm of cells in all of these states, a 5 to 10% increase in the cytoplasmic area was observed. However, only nuclei of cells in the transition state became smaller upon compression. When materials become denser with such mechanical stress, they are termed auxetic. Differences in chromatin condensation were observed by electron microscopy of the three cell states with considerably less-condensed nuclei during transition relative to the pluripotent or differentiated state. This work shows that the nucleus undergoes dynamic changes in mechanical properties and chromatin structure as cells transition toward a differentiated state. It is proposed that this auxeticity may be important for cell mechanotransduction. — BAP

Nat. Mater. 10.1038/NMAT3943 (2014).

CREDITS (TOP TO BOTTOM): ANDREA PISTOLESI/GETTY IMAGES; CHEMICAL NANOSCIENCE LABS/NEWCASTLE UNIVERSITY

Downloaded from www.sciencemag.org on May 8, 2014

Published by AAAS

CELL SIGNALING

Sensing Cellular Chloride

Control of the concentration of chloride ions is critical for the proper function of neurons, control of blood pressure, regulation of cell volume, and other physiological functions. Piala *et al*. reveal the molecular basis of a cellular calcium sensor that enables such regulation. Chloride ions are moved across cell membranes by transporters, and the activities of several of such transporters are regulated by phosphorylation though a cascade of protein kinases, the first of which is known as WnK1 [with no lysine (K) 1]. This protein kinase, the authors show, is itself a sensor for chloride concentration. In crystal structures of WnK1 bound by chloride ions, the ion was bound to the catalytic site of the enzyme. This inhibited autophosporylation of the enzyme and thus would lead to activation of appropriate transporters when the concentration of chloride ions dipped below normal. This regulation mechanism is distinct from well-known examples in which calcium ions, for example, regulate kinase activity by binding to a separate regulatory subunit. Furthermore, it helps explain the unusual displacement of the catalytic lysine residue in WnK1, as the chloride binding site occupies the usual position of this essential lysine residue. — LBR

Sci. Signal. **7**, ra41 (2014).

CREDIT: DENIS BALIBOUSE/REUTERS/NEWSCOM

PHYSICS

A Sign-Changing Gap

Superconductors owe some of their fascinating properties to the formation of so-called Cooper pairs of electrons that (loosely) bind to each other thanks to a mediating interaction. The finite energy needed to break them apart is set by a function called "gap," which, for unconventional superconductors, may have a complicated dependence on the momenta of the participating electrons. Much effort has been expended to elucidate the gap function in iron-based superconductors, many of which have multiband electronic structures that favor antiferromagnetism. A compatible gap function that changes sign going from an electron to a hole band was proposed and observed in some of those compounds, but the question remains whether this so-called symmetry is universal among the iron-based superconductors, and in particular whether it holds for the material LiFeAs, which lacks a static magnetic phase. Chi *et al.* use scanning tunneling and photoemission spectroscopy measurements coupled with calculations to analyze the scattering from impurities in LiFeAs. This scattering is sensitive to the change in sign of the gap function, leading to simple selection rules, and the authors find that their data support the gap scenario, and by implication, a magnetism-mediated superconductivity. — JS

Phys. Rev. B **89**, 104522 (2014).

PSYCHOLOGY

Our Moral Vocabulary

Situational factors can exert ephemeral influence on cognitive processes. These effects are not short-lived in the sense of being refuted by the next paper; rather, they can be observed only when stronger or mainline factors fail to dominate the neural pathways underpinning our thoughts. Gantman and Van Bavel nicely illustrate how this works by measuring the extent to which a briefly visible morality-related word is more likely to be detected than an unrelated word. They presented people with words and nonwords for durations ranging from 20 to 100 ms. At the longest durations, words and nonwords were accurately categorized, and there were no differences in accuracy between moral and nonmoral words. At the shortest durations, all words and nonwords were equally difficult to identify. In the middle, where the perceptual awareness for words was near threshold, those words semantically related to morality were slightly—and significantly—more readily identified correctly, so that a 40-ms peek was sufficient, whereas nonmoral words needed an extra 10 ms of exposure. — GJC

Cognition **132**, 22 (2014).

Published by AAAS

AROUND THE WORLD

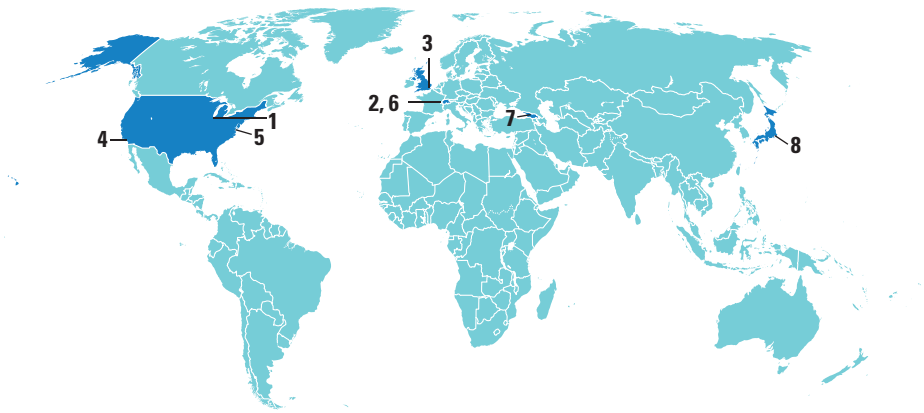

Munster, Indiana **1**

MERS Reaches United States

A deadly new virus that emerged on the Arabian peninsula in 2012 has reached the United States. The Centers for Disease Control and Prevention announced on 2 May that an infection with Middle East respiratory syndrome (MERS) virus had been confirmed in a patient in Community Hospital in Munster, Indiana. The man is a health care worker and had been in Riyadh days before he started experiencing fever, coughing, and shortness of breath. He is in stable condition, according to hospital officials.

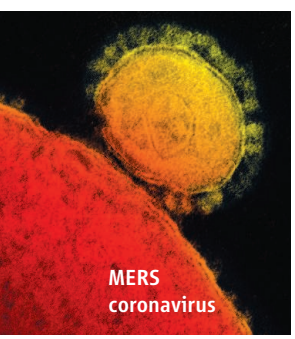
MERS coronavirus

Health authorities are tracing any people who may have had contact with the patient. The man took a flight from Riyadh to London on 24 April and then on to Chicago. From Chicago he traveled to Indiana by bus. Hospital staff members who cared for the patient before the MERS infection was identified have been quarantined at home as a precaution, but the virus does not transmit easily from one person to the next. Travelers have exported MERS to nine other countries, including Germany, the United Kingdom, France, and Malaysia. Most of these patients did not infect anyone else.

Geneva, Switzerland **2**

WHO: Polio an International Emergency

The World Health Organization (WHO) on 5 May declared the spread of wild poliovirus a public health emergency of international concern, saying the recent export of polio from three countries to adjoining areas could threaten global efforts to eradicate the disease. This is just the second time that such an emergency has been declared under the International Health Regulations adopted in 2005; the first was during the H1N1 swine flu pandemic in April 2009.

WHO issued recommendations for travel—which are not legally binding but carry tremendous weight—for the three countries deemed to pose the greatest risk of further spread: Pakistan, Cameroon, and Syria. These countries must ensure that all residents and long-term visitors have proof of recent polio vaccination before leaving the country. WHO is encouraging seven other nations where polio is circulating to implement similar measures. These measures should continue until at least 6 months after any reported case of wild poliovirus.

The Emergency Committee of the International Health Regulations will meet again in 3 months to reassess the situation and decide whether tougher measures are needed. **http://scim.ag/WHOpolio**

London **3**

Ax for Animal Research 'Secrecy Clause'?

The United Kingdom has proposed lifting outdated confidentiality rules that ban the release of information about animal research in the country, including about people or places applying for animal testing licenses and inspection visit reports. Section 24 of the 1986 Animals (Scientific Procedures) Act is "out of step with [government] policy on openness and transparency," said Home Office Minister Norman Baker in a public consultation launched on 1 May.

No secrets here. The U.K. is reconsidering its animal research confidentiality rules.

Animal rights groups and researchers using animals have praised the proposal. Chris Magee, head of policy at the pressure group Understanding Animal Research in London, says that withholding information does not help scientists, because it leaves a "vacuum that activists can fill in with misleading information."

The public consultation closes on 13 June; the government says it will then "work quickly" to analyze the comments and propose a final option. **http://scim.ag/_secclause**

Los Angeles, California **4**

UCLA Returns Sterling Foundation Gift

Sterling

The University of California, Los Angeles (UCLA), has rejected a $3 million, 7-year pledge to support basic kidney research from a foundation founded by Donald Sterling, the disgraced owner of the Los Angeles Clippers basketball team. The university also returned Sterling's initial $425,000 gift.

The university's 29 April decision came the same day the National Basketball Association banned Sterling for life for making "deeply offensive" remarks about African-Americans.

"Mr. Sterling's divisive and hurtful comments demonstrate that he does not share UCLA's core values as a public university that fosters diversity, inclusion and respect," said UCLA spokeswoman Carol Stogsdill in a statement.

CREDITS (TOP TO BOTTOM): AARON LOGAN/WIKIMEDIA COMMONS, FROM HTTP://WWW.LIGHTMATTER.NET/GALLERY/ALBUMS.PHP; NIAID; DANNY MOLOSHOK/AP PHOTO

Published by AAAS

Washington, D.C. **5**

Climate Change Impacts Widespread in U.S.

The impacts of climate change are appearing from sea to shining sea, says a major new report from the U.S. Global Change Research Program. The third official National Climate Assessment (NCA), released 6 May, says that Americans face "wide-ranging impacts in every region of our country and throughout our economy."

The report's 30 chapters cover a variety of regions, sectors, and industries. On adapting to a changing climate, the report says:

Dry heat. New report documents climate impacts.

"[P]lanning is occurring in the public and private sectors and at all levels of government; however, few measures have been implemented." Previous iterations of the NCA have received little fanfare in Washington, but the White House has embraced this report, including giving a series of television interviews with President Barack Obama to TV meteorologists in hopes of advancing his climate agenda.

Geneva, Switzerland **6**

Drug Resistance Overview Paints Grim Picture

The World Health Organization (WHO) presented its first-ever global attempt to assess the spread of drug resistance on 30 April—and the results are sobering. "Without urgent, coordinated action by many stakeholders, the world is headed for a post-antibiotic era, in which common infections and minor injuries which have been treatable for decades can once again kill," wrote Keiji Fukuda, WHO's assistant director-general for health security, in a press statement.

The study presents some data on drugs against influenza, HIV, tuberculosis, and malaria, but it focuses on seven common bacteria and nine classes of drugs used to treat them—for instance, fluoroquinolones to treat *Escherichia coli*, which can cause urinary tract or bloodstream infections. The report finds high rates of resistance for some of the bacteria almost everywhere.

The new report confirms what doctors around the world are experiencing daily. "We see horrendous rates of antibiotic resistance wherever we look in our field operations," said Jennifer Cohn, medical director of the Access Campaign at Doctors Without Borders, in a written statement issued on 30 April. "Ultimately, WHO's report should be a wake-up call to governments to introduce incentives for industry to develop new, affordable antibiotics." **http://scim.ag/drugres**

Nosing Out a Long-Snouted Tyrannosaur

In the 1970s, a relatively small, long-nosed dinosaur was discovered in Mongolia. Some paleontologists claimed it was an unusual member of the tyrannosaurid family (which includes the mighty *Tyrannosaurus rex*). Others were skeptical.

Then, in 2009, paleontologists published details of a similar specimen, also found in Mongolia. As both specimens were juveniles, researchers speculated that the long noses might just be a growth phase the animals passed through on their way to becoming typical tyrannosaurids, with tall, deep skulls and crushing jaws and teeth.

Now, a newly discovered adult specimen, described this week in *Nature Communications* (artist's reconstruction above), might quiet the skeptics. Long-nosed *Qianzhousaurus sinensis* lived about 66 million years ago, at the same time as the much larger *T. rex*. Because the new dino was found in China's Jiangxi province—more than 3000 kilometers from the Mongolian specimens—the team concludes that long-nosed tyrannosaurids were not a fluke, but a major group of dinosaurs with a wide geographical distribution.

Georgia **7**

New Orthopoxvirus Discovered

Scientists at the Centers for Disease Control and Prevention (CDC) in Atlanta have found a distant cousin of the smallpox virus in two cattle herdsmen in northeast Georgia. The new pathogen—which hasn't been named yet—was presented on 1 May at a conference of the CDC's Epidemic Intelligence Service.

The men had appeared at a local clinic with skin lesions and were initially suspected to have a cowpox infection. But researchers at CDC—which has a country office in Georgia—found a new virus in a skin swab from one of the patients, says disease ecologist Darin Carroll, who led the study. Blood tests later showed that >>

CREDITS (TOP TO BOTTOM): CHUANG ZHAO; GETTY IMAGES/ISTOCKPHOTO

Published by AAAS

>>AROUND THE WORLD

several other herdsmen had antibodies to an orthopoxvirus—presumably the same one. Wood mice and voles are the virus's most likely animal hosts, Carroll says.

The smallpox vaccine offers protection against related viruses as well, and researchers have long thought they might see an uptick in human orthopoxvirus infections after smallpox was eradicated and vaccination worldwide was halted in 1980; so far, there is little evidence of that happening.

Emerging. Cattle herdsmen in Georgia were infected with a yet-unnamed orthopoxvirus.

Tokyo **8**

RIKEN Pushes For Plagiarism Checks

Shock waves emanating from allegations of image manipulation and plagiarism in two stem cell papers published in *Nature* this past January continue to ripple through RIKEN, the Japanese institute at the center of the ongoing controversy. Last week, local media reported that questions have arisen about images in research papers published by three more members of a RIKEN committee charged with investigating the *Nature* papers. The news came a week after RIKEN announced it would investigate allegations of image manipulation in papers published by Shunsuke Ishii, who resigned as chair of the investigating committee on 25 April (*Science*, 2 May, p. 454).

Now, the *Yomiuri Shimbun* newspaper is reporting that RIKEN President Ryoji Noyori has asked all laboratory and research group leaders to check all of their previous publications for doctored images and plagiarism. The newspaper quotes an unnamed RIKEN official as saying the directive covers at least 20,000 publications. There was no indication of a deadline for completing the reviews. **http://scim.ag/RIKENcheck**

NIH Funding for Major Causes of Death in the United States

	Condition	Deaths in 2011	Funding in 2013 ($ millions)
1	Heart disease	596,339	1964
2	Cancer	575,313	5274
3	Chronic respiratory diseases	143,382	333
4	Stroke	128,931	282
5	Accidents	122,777	367
6	Alzheimer's disease	84,691	504
7	Diabetes	73,282	1007
8	Pneumonia and influenza	53,667	407
9	Kidney disease	45,731	551
10	Suicide	38,285	37

NIH Disease Funding Scrutinized

How the National Institutes of Health (NIH) sets priorities is getting new attention from Senate and House of Representatives appropriations committees—and a new report requested by the chair of the House panel that funds NIH is providing fodder for the claims of many patient advocacy groups that their disease is being shortchanged. For example, Alzheimer's disease killed more Americans than diabetes in 2011, but received only half the level of NIH funding.

NIH officials defend their current practices by saying the funding levels reflect scientific opportunity, the burden of disease, and global as well as national public health needs. That is particularly illustrated by funding for AIDS, the sixth biggest cause of death globally but not in the top 10 domestically. Its NIH budget is nearly $3 billion, six times that of Alzheimer's even though Alzheimer's claims 10 times more lives in the United States.

NEWSMAKERS

Three Q's

The immensely popular CBS sitcom *The Big Bang Theory* revolves around a gang of physicists and an engineer who work at the California Institute of Technology. *Science* caught up with University of California, Los Angeles, astrophysicist **David Saltzberg**, who's been the show's one and only science consultant since it premiered, at last week's USA Science & Engineering Festival in Washington, D.C. **http://scim.ag/_TBBT**

Saltzberg

Q: *Science* last spoke with you in 2008 (*Science*, 9 May 2008, p. 740). What's changed about the show's portrayal of science since you started?

D.S.: The writers and I used to have to go back and forth a lot more for me to converge on what they wanted. But now … we're a little bit like an old married couple.

The whiteboards the characters use for equations have changed into something where real scientists pitch me their latest results and ask if they can appear on them. It's sort of become a thing to get on the whiteboards. … The big discovery of gravitational waves, which indicated cosmological inflation, got a special place. It appeared on Stephen Hawking's board, which of course is a much higher level than our main characters' boards.

Q: Why do you think it's important to throw in recent events?

D.S.: It's the creative call of the writers. But these physicists live in our universe, so this would be something they would talk about.

Q: Do you plan to see *The Big Bang Theory* through to the end?

D.S.: Yup. Maybe like the universe, there will be no end though.

CREDITS (CLOCKWISE FROM LEFT): © ZURAB KURTSIKIDZE/EPA/CORBIS; PHOTO BY SONJA FLEMMING/CBS VIA GETTY IMAGES; DAVID LIVINGSTON/GETTY IMAGES; TABLE SOURCE: U.S. GOVERNMENT ACCOUNTABILITY OFFICE GAO-14-490R

Published by AAAS

Biotech Industry Vet Tapped To Head Stem Cell Institute

The California Institute for Regenerative Medicine (CIRM) has revealed its choice for president: former biotech CEO **Randy Mills**. The 30 April announcement confirmed predictions that the $3 billion agency would turn to someone from the private sector as it tries to move research to the clinic and faces an uncertain financial future.

Mills

During his 10 years at Columbia, Maryland–based Osiris Therapeutics, Mills oversaw a historic first: drug approval (from Canadian regulators) for a stem cell treatment for complications from bone marrow transplants. "We need something like that to happen with some of our projects," says Jeff Sheehy, a CIRM board member and HIV patient advocate.

CIRM was created through a 2004 California ballot initiative and is funded through bond sales, but that funding is set to run out in 2017. Mills may help cultivate partnerships with potential industry funders, says Michael May, CEO of the Centre for Commercialization and Regenerative Medicine in Toronto, Canada, who served on a 2012 panel reviewing CIRM's structure and policies. Mills will replace Alan Trounson, who announced last October that he would step down to be closer to his family in Australia. **http://scim.ag/_Mills**

Random Sample

Wanted: A Bug Spit Robot

A new malaria vaccine candidate looks promising in trials, but producing it is a nightmare because it grows in mosquito saliva. Now, the company behind it is crowd funding the development of a robot that can tease apart the insects and harvest their tiny salivary glands.

The vaccine, named PfSPZ and produced by Sanaria in Rockville, Maryland, consists of sporozoites, a type of parasitic cell that develops in infected mosquitoes. Skilled humans can dissect the salivary glands of about 150 bugs an hour—not nearly enough for mass production (*Science*, 9 August 2013, p. 605). Now, Sanaria, working with Harvard University's Biorobotics Lab, is developing a "SporoBot" to automate the tedious task; it's asking for $250,000 on Indiegogo.com to assemble a prototype from several already working parts (shown). Rewards include mugs, T-shirts, lab tours, and—if you chip in $50,000—a trip to a trial site in Africa.

FINDINGS

Stellar Explosion Illuminates Cosmic Dark Ages

A rare ultra–high-energy stellar explosion called a gamma ray burst (GRB) offers evidence that the "cosmic dark ages"—when no galaxies or stars illuminated the heavens—lasted at least a billion years after the big bang.

Post–big bang, the universe was filled primarily with neutral hydrogen gas. Light from the first stars and galaxies broke apart, or reionized, the hydrogen atoms. To find out when that happened, researchers look for abundances of neutral hydrogen in the universe's past.

One way to do this is to study GRBs, which occur when a large, rapidly rotating star collapses. The explosion shoots a beam of radiation into space; if pointed toward Earth, it appears as a flash of gamma rays, followed by an afterglow. Astronomers study this radiation to search for the absorption of telltale wavelengths of light by nearby neutral hydrogen.

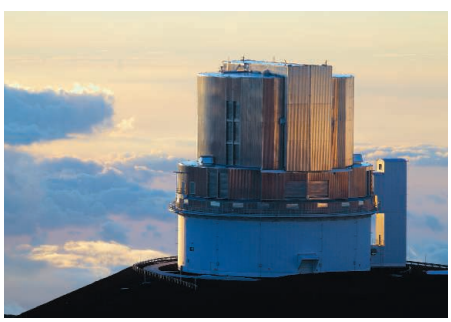
Lit up. Hawaii's Subaru Telescope saw GRB 130606A.

Tomonori Totani, an astronomer at the University of Tokyo, and colleagues measured the spectrum of the afterglow from GRB 130606A, a very distant object that exploded when the universe was just 1 billion years old. Neutral hydrogen made up 10% of the intergalactic gas around the burst—suggesting that the reionization process that ended the dark ages was not yet complete, they report in a paper to be published in June in the *Publications of the Astronomical Society of Japan*. **http://scim.ag/reionized**

Polar Bear Evolution—Fast and Furious

Polar bears split from the brown bear, their closest relative, less than 500,000 years ago—far more recently than the several million years previously estimated, according to a new genomic study published this week in *Cell*.

Researchers from Denmark, China, and the United States sequenced the genomes of 80 polar bears from Greenland and 10 brown bears from a variety of locations. The team also examined the effects of Arctic living on the bears by comparing the species' genomes. Although little more than a blink in time from an evolutionary perspective, 500,000 years was long enough for key genetic differences to evolve between the two species, they found. In polar bears, the most strongly selected genes included several related to lipid processing and to the development of the heart and circulatory system, adaptations that may help polar bears cope with an extremely high-fat diet. One that stood out was a gene called *APOB*, which helps transfer fat from blood into cells.

"The work helps us understand what makes a polar bear a polar bear and how fast this evolution occurred," comments Charlotte Lindqvist, an evolutionary biologist at the University at Buffalo in New York. **http://scim.ag/pbgenome**

CREDITS (TOP TO BOTTOM): SANARIA INC.; CIRM; ED DUNENS/FLICKR/CREATIVE COMMONS; GETTY IMAGES/ISTOCKPHOTO

Published by AAAS

Accused. Jens Förster said he's the victim of "an incredible witch hunt."

SCIENTIFIC INTEGRITY

Fresh Misconduct Charges Hit Dutch Social Psychology

AMSTERDAM—"Oh no," one Dutch psychologist tweeted last week. "Here we go again," another lamented. Scientists here are still searching their souls about two previous scandals—involving Diederik Stapel of Tilburg University in 2011 and Dirk Smeesters of Erasmus University in Rotterdam a year later. Now they have learned that a national research integrity panel has found evidence of data manipulation in the work of Jens Förster, a social psychologist at the University of Amsterdam (UvA). The university has already announced that it will request the retraction of one of Förster's articles.

The case is drawing widespread international attention as well, in part because Förster, who's German and came to Amsterdam in 2007, enjoys a sterling reputation. "He is among the most creative and influential social psychologists of his generation," says Jeffrey Sherman of the University of California, Davis. In 2011, Förster received the Kurt Lewin Award, a major European social psychology prize, for his "pioneering research in the domains of self regulation, creativity, novelty, embodiment and social cognition." Adding to the interest is the nature of the evidence. The panel found no smoking gun; as in the Smeesters case, it based its conclusion entirely on statistical and methodological evidence.

Förster did not respond to multiple requests for comment from *Science*, but in a long open e-mail to colleagues, published on the blog Retraction Watch last week, he called the verdict a "terrible misjudgment" and blamed it on a climate of "hysteria" in the wake of the Stapel affair. "I do feel like the victim of an incredible witch hunt," he wrote.

The case started in September 2012, when a whistleblower sent UvA a 35-page complaint about three of Förster's studies. The complainant had been puzzled by the unusually large effects seen in one study, published in *Social Psychological and Personality Science* (*SPPS*) in 2012. After participants had been "primed" by subtle stimulations—such as smelling scents or hearing poems—their scores on a cognitive ability test went up dramatically.

Intrigued, the researcher asked Förster to send him raw data from the experiments. Förster responded with a limited data set, containing numbers of participants and standard deviations, but not the raw data. The whistleblower also analyzed two papers describing similar experiments, published by Förster in the *Journal of Experimental Psychology: General* in 2009 and 2011. Together, the three papers contained 42 experiments; the means reported were "unusually close to a linear trend" in the vast majority of the experiments, the whistleblower wrote. The chances of this happening were one in 508,000,000,000,000,000,000, he claimed.

A UvA committee that first looked into the allegations agreed that the linearity was "statistically speaking virtually impossible" but said this might have been the result of "sloppy science" or "questionable research practices," such as leaving out odd data points. The panel said it could not ascertain whether the data had been manipulated.

Unsatisfied, the whistleblower appealed to the Netherlands' National Board for Research Integrity (LOWI), which launched its own investigation. The board obtained processed data files from Förster and asked a mathematical stochastics professor to investigate them, which the UvA committee had not done. Its much harsher report, issued on 6 May, says that the "conclusion that research data must have been manipulated is considered unavoidable," and that this constituted a violation of academic integrity. LOWI blames the authors, in particular Förster.

The report addresses only the 2012 paper, which UvA is seeking to retract; the university says it does not justify retracting the other two papers. UvA declined to say whether disciplinary action might be taken. Förster resigned from UvA before the release of the report; on 1 June, he was slated to start a new, 5-year research project at Ruhr University Bochum in Germany, supported by a prestigious €5 million grant from the Alexander von Humboldt Foundation. In a press release last week, the foundation announced that it's postponing the grant—and Förster's participation in an 8 May award ceremony—"until the matter has been clarified."

In his e-mail defense, Förster denied ever manipulating data and vowed to fight to get his case reconsidered. "The conclusion that I manipulated data has never been proved," he wrote. "It remains a conclusion based on likelihoods." Förster also wrote that his co-author on the 2012 paper, Markus Denzler of the Federal University of Applied Administrative Sciences in Brühl, Germany, had "nothing to do with the data collection or the data analysis" for the study. Denzler did not respond to *Science*'s requests for comment.

Although the whistleblower is known to UvA and LOWI, they have not revealed his identity. He answered e-mailed questions from *Science,* but insisted that his name not be used. "It really doesn't matter who filed the complaint," he says. He emphasizes that he knew Förster only by name and holds "no grudges" against him.

The calculations in the complaint, hard to follow for an average reader, have already triggered a lively debate among statisticians

CREDIT: HUMBOLDT-STIFTUNG/SVEN MÜLLER

Published by AAAS

and psychologists. Gregory Francis, a cognitive psychologist at Purdue University in West Lafayette, Indiana, who has investigated several cases of misconduct, says he finds them "very convincing." The complaint "made plain that the reported data are too good to be true. There is little doubt of that," adds social psychologist Brian Nosek of the University of Virginia in Charlottesville. Francis and Nosek say more of Förster's papers should be put under the microscope, as happened with Stapel and Smeesters after the first evidence of fabrication surfaced.

But Sherman says he's giving Förster the benefit of the doubt. "Even if we all agree that the data are unlikely, that does not necessarily indicate fraud," he says. "It is not clear exactly why the data turned out the way that they did. We may understand later what we cannot understand now." Förster's Ph.D. adviser, social psychologist Fritz Strack of the University of Würzburg in Germany, also cautions against a rush to judgment. "Jens Förster was an outstanding doctoral student about whose integrity I have never had any doubts," he says. *SPPS* editor Allen McConnell says UvA has not yet contacted him about the disputed paper.

Dutch scientists, meanwhile, are left to wonder if the string of misconduct cases—there have been several more in fields other than psychology—means there is something rotten in their science system. LOWI, which handles only appeals, has seen its caseload triple since the Stapel affair, with a record 19 cases in 2013. But LOWI Chair Kees Schuyt, a professor emeritus of sociology at UvA, says the increase just shows that whistleblowers in the Netherlands now know what to do. In a recent interview in *NRC Handelsblad*, Schuyt said: "Because of all the publicity about scientific misconduct, people know better how to lodge a complaint within a university and how to appeal to LOWI."

–FRANK VAN KOLFSCHOOTEN

Frank van Kolfschooten is a freelance science writer in Amsterdam and the author of two books about scientific misconduct in the Netherlands.

ARCHAEOLOGY

New Sites Bring the Earliest Americans Out of the Shadows

AUSTIN—The sun was setting as archaeologist Kurt Rademaker climbed past 4500 meters in the Andes Mountains of Peru. His goal was to find the source of the obsidian that ancient people on the coast of Peru had used to make stone tools. But right then, "I was looking for someplace to spend the night," Rademaker says. "I popped over a ridge, right into a rock shelter"—a natural shelter that promised to be a good campsite. That evening he noticed hundreds of black obsidian and red and gray jasper tools littering the area. He'd unknowingly set up his tent right atop the ancient people's camp.

Several more trips up the mountain revealed something even better: a piece of human skull buried near the bones of wild vicuña, guanaco, and deer—the remnants of prehistoric barbecues in the rock shelter. At the meeting of the Society for American Archaeology* here, Rademaker announced that the animal bones date between 12,000 and 12,500 years ago, meaning that the people feasting high in the mountains were among the early inhabitants of the New World. "We have the highest Ice Age site in the Americas with a really successful human occupation," says Rademaker, an archaeologist at the University of Maine, Orono.

Rademaker is one of a new generation of archaeologists searching high and low for new evidence of early Americans—and finding it. Now that most of the field has accepted that humans settled in America before the famous Clovis hunters (*Science*, 25 March 2011, p. 1512), young researchers are staking their careers on a new set of questions. Who were these pre-Clovis people, how quickly did they fan out after arriving from Asia, and how did they adapt to new terrains? Clovis hunters were people of the plains of North America, but researchers are now finding traces of Paleoindians atop mountains in the Sierra Madre and Andes and at the bottom of sinkholes in Florida. They are fleshing out the ghostly outlines of these nomadic people, who spread through North and South America 12,000 to 15,000 years ago.

Ancient footsteps. The earliest Americans left tools and bones at multiple new sites (dates in years).

As a procession of young researchers took the podium at the meeting, several older advocates of pre-Clovis settlement stood back and beamed. "This symposium with so many young South American scholars presenting such good interdisciplinary data would have been impossible 10 years ago," says archaeologist Tom Dillehay of Vanderbilt University in Nashville, who excavated Monte Verde, a crucial pre-Clovis site in Chile. "It's nice to get beyond the Clovis versus pre-Clovis debate." Geoarchaeologist Michael Waters of Texas A&M University, College Station, agrees: "There's definitely a sense of change in the air."

A generation ago, most researchers thought that the first Americans were the Clovis big-game hunters, who left their distinctive fluted spear points in the open basins and ranges of North America starting about 13,000 years ago (*Science*, 23 February 2007, p. 1067). Few believed the scattered claims for Paleoindians before Clovis, and the doubts squelched funding for research that might have sped the acceptance of older sites.

But over time, the evidence for pre-Clovis sites became incontrovertible. The first to be widely accepted was the ancient campsite at Monte Verde. Now reliably dated by radiocarbon to 14,800 years ago, it is the oldest accepted human site in the Americas. Today almost a dozen sites "provide credible

*79th Annual Meeting of the Society for American Archaeology, 23–27 April, Austin.

Downloaded from www.sciencemag.org on May 8, 2014

Published by AAAS

evidence" for pre-Clovis settlement, Waters says. "At a minimum, people were here 15,000 years ago, and probably before that."

Some new evidence is coming from reanalysis of sites where pre-Clovis claims were initially challenged, such as the Page-Ladson sinkhole beneath the Aucilla River in Florida. At this site an hour east of Tallahassee, archaeologists found stone flakes and a mastodon tusk with cut marks in the 1980s and 1990s. Dates of 14,000 years ago seemed too early to be credible. But geoarchaeologist Jessi Halligan of the University of Wisconsin, La Crosse, has returned to the sinkhole. In 2012 and 2013, she and her team dove nearly 8 meters through murky water to excavate the oldest layer of sediment. In 2012, they found bones from a mastodon, bisons, and horses. Then, last summer, "we got lucky," she says.

Two divers were digging in the muck when graduate student Morgan Smith of Texas A&M hit the edge of something hard with his trowel. "Morgan comes boiling up to the surface, shouting 'I have a biface; I have a biface!' " recalls Waters, co-organizer of the expedition, who was safely dry on a boat. A biface is a stone blade unquestionably modified on two sides by humans.

Halligan immediately descended herself, took photos of the biface, and gathered samples of the strawlike layer of mastodon dung (called digesta) where it was found for dating. The radiocarbon dates confirmed that Paleoindians were there about 14,500 years ago, Halligan says. The dates also raise new questions: "If we start to accept that there are sites on the east coast at 14,500 and in South America at 14,800, what does that mean for when people first got here?" she says. "Were they on a superfast march across the country or did they get here 15,000 or 16,000 years ago?"

Judging from the talks at the meeting, the earliest explorers spread rapidly into all sorts of terrain, ranging from the desert of Zacatecas, Mexico, to the rainforests of the Amazon. By the time they left tools at Rademaker's site about 12,000 to 12,500 years ago, these ancient Americans were even able to survive in the extreme high altitude of the Andes. Rademaker thinks they moved seasonally between the mountains and the sea, because obsidian from near the shelter was used to make tools 150 kilometers away at Quebrada Jaguay on the coast of Peru, home to an ancient maritime culture 12,500 to 13,000 years ago (*Science*, 18 September 1998, p. 1775).

More signs that the first Americans rapidly colonized many different environments come from Mexico, where archaeologist Ciprian Ardelean of the Autonomous University of Zacatecas surveyed the unexplored Zacatecas desert for traces of Paleoindians. At Chiquihuite Cave, almost 3000 meters up in the Sierra Madre, he and a small team found a bifacial point. Inside the cave, they dug test trenches that exposed the bones of animals and traces of ash including burned phytoliths, or plant minerals. Two dating methods (radiocarbon on animal bone and an optical date on the sediments) both suggest the site predates Clovis, although Ardelean is cautious: "Two dates are not enough to establish reliable antiquity."

Far to the south in the Aisén region of Patagonia in Chile, archaeologist César Méndez of the University of Chile in Santiago and his colleagues are also surveying a large area, where they are correlating local climate and environmental data from the past 19,000 years with ancient campsites. On a tip from a rancher, they explored one cave—Cueva de la Vieja (Old Lady's Cave)—where they found hearths and stone tools that date to 11,870 years ago. By analyzing seeds and tools at that site and others, Méndez's team has found that in Patagonia, the early people sought places where they could gather berries as well as hunt foxes, armadillos, and other small animals, so they weren't entirely dependent on big game. "It gives us a pretty good idea of the kind of environment human beings preferred," Méndez says.

No longer seen as the first Americans, the Clovis people are also looking less distinctive. At the meeting, archaeologists reported finding three different types of projectile points at sites in Tierra del Fuego and Uruguay. Among them: stemmed, fluted "fishtail" points reminiscent of Clovis points in appearance and age, dating as far back as 13,000 years ago in Uruguay. Finding similar points 10,000 kilometers apart led some researchers to suggest that the Clovis and South American traditions both arose from an earlier culture that already made bifacial points—an ethereal group whose traces are now being detected in North and South America.

"I think it's irrefutable that by 13,000 years ago, South America was occupied by people with their own cultural and technological tradition," Waters says. "It was not Clovis people marching south." Adds Rademaker: "What we have is these ancient people emerging everywhere." **–ANN GIBBONS**

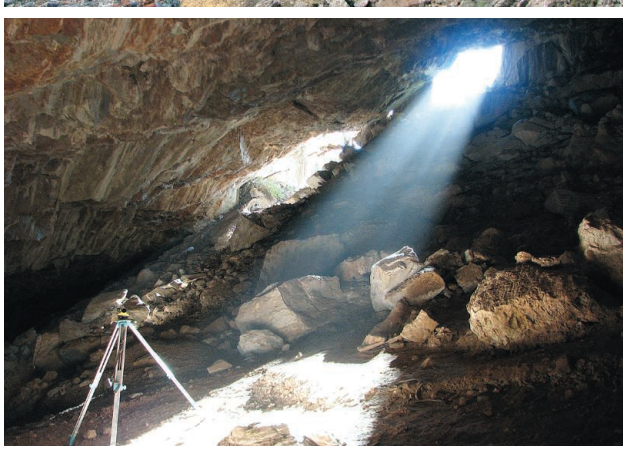

Gimme shelter. Paleoindians camped at Cuncaicha rock shelter in the Andes of Peru (*top*), Cueva de la Vieja in Patagonia, and Chiquihuite Cave in the desert of Mexico.

CREDITS (TOP TO BOTTOM): KURT RADEMAKER; PABLO GONZÁLES; CIPRIAN ARDELEAN

Published by AAAS

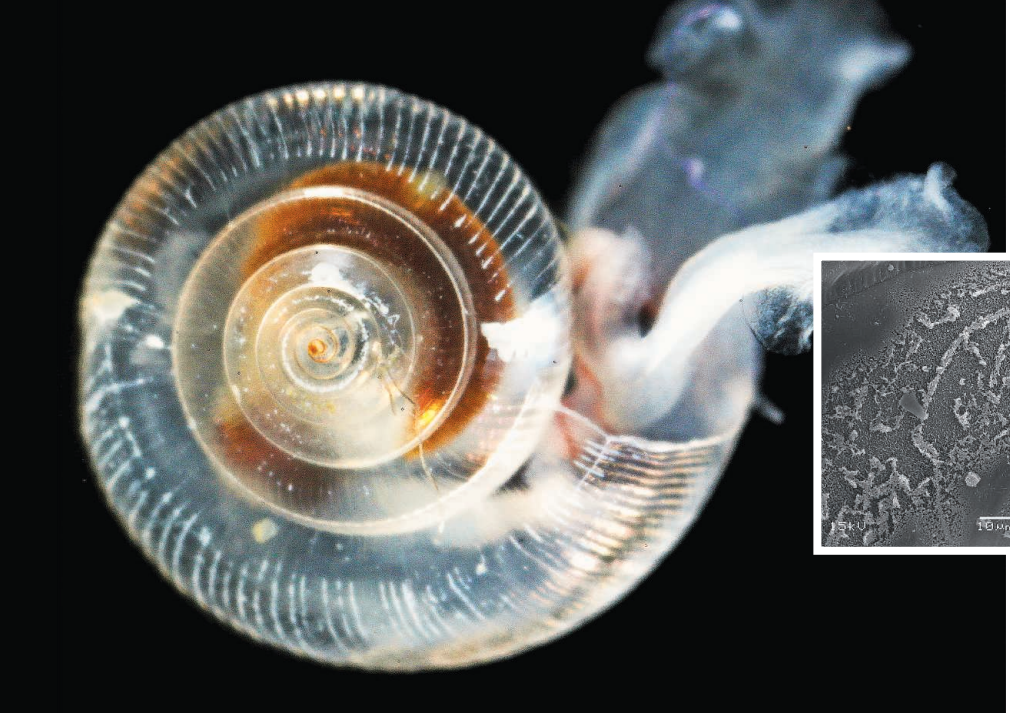

Vulnerable. Acidic waters are pitting and dissolving the shells (*inset*) of pteropod snails along North America's Pacific coast.

CREDITS: NOAA (2)

GLOBAL CHANGE

'Sea Butterflies' Are a Canary for Ocean Acidification

Marine scientists have long warned that rising CO_2 emissions are making the world's oceans more acidic, with worrisome implications for marine life. In the open ocean, the fears seemed largely theoretical—until last week. Along a 1500-kilometer swath of the U.S. Pacific coast, researchers found that acidifying waters are dissolving the shells of tiny sea snails. At least one-half of the damage appears to be linked to human-caused emissions, the scientists estimate.

"I was surprised by the sheer spatial extent" of the damage, says biological oceanographer Nina Bednaršek of the National Oceanic and Atmospheric Administration (NOAA) in Seattle, Washington, the study's lead author. Researchers figured the snails would show some resistance to corrosive waters, so "this is something we [had] not predicted before." The picture is likely to worsen as emissions continue, and it bodes ill for the marine food webs that depend on pteropods, the authors say.

The oceans have absorbed an estimated one-third of the carbon dioxide that humans have pumped into the atmosphere. That's helped slow global warming, but it has also triggered chemical reactions that are lowering the ocean's pH. Average pH in surface waters is now about 8.1—a 30% increase in acidity since the start of the Industrial Revolution—and researchers predict it could drop to 7.8 by 2100 if carbon emissions continue at current rates.

More corrosive water can harm the eggs and larvae of marine creatures, laboratory experiments have shown, and even dissolve the shells built by many invertebrates. Whether such dissolution was already occurring in the open ocean, however, has been unclear. To find out, Bednaršek and colleagues studied pteropods, marine snails nicknamed sea butterflies for their winglike body parts. They focused on the pteropod-rich California Current ecosystem, which stretches from British Columbia to Baja California.

The researchers collected more than 1000 samples of *Limacina helicina* from the top 100 meters of the ocean, at 17 sites along the current. Under the electron microscope, 38% of the normally smooth shells showed signs of severe dissolution, they reported online last week in the *Proceedings of the Royal Society B*. Damaged shells were etched or pitted, and their calcium crystals resembled "cauliflower," Bednaršek says.

The California Current is a known acidification hot spot. Winds along the grand southern flow drive extensive coastal upwelling of deeper, cooler water, which is naturally more acidic than surface waters. But many organisms are well adapted to the challenging conditions, so few researchers expected such a high proportion of damaged shells. "I'm a bit surprised by the severity of [the damage], but maybe I shouldn't be," says biological oceanographer David Mackas, now retired from Fisheries and Oceans Canada.

Human-caused acidification appears to explain the unexpected result, the NOAA team says, based on a model that allowed them to estimate shell damage in the past and future. The researchers found that the number of damaged shells was directly related to the corrosiveness of the water, which varies along the coast today. Based on data on past ocean conditions, they extrapolated that relationship to the preindustrial ocean. The result: Preindustrial acidification probably damaged some 18% of California Current pteropods living at the studied sites—suggesting that human-caused acidification has more than doubled the impact. It will get worse in the future, the analysis suggests. Damage rates at relatively shallow sites with particularly corrosive waters are forecast to rise from 53% today to 71% by 2050.

Although such models can be fraught with assumptions, this one appears "valid" to biological oceanographer Geraint Tarling of the British Antarctic Survey in Cambridge, U.K. Major questions remain, however. One is how the shell damage is affecting pteropod populations—and whether the creatures can ultimately adapt. Previous work has suggested that a damaged shell can make it harder for a pteropod to fight infection, maintain metabolic activity, defend itself against predators, and control buoyancy. But Tarling says experiments in his lab show that the snails can sometimes "patch up their shells from the inside," and he says more work is needed to understand the link between dissolution and mortality. The NOAA team didn't study such mechanisms, but the paper reports no evidence of evolved "resilience" among their pteropods, which are a major food source for West Coast fisheries.

More insight is expected soon. Researchers are busy studying the fates of pteropods in other areas, including the Gulf of Maine in the Atlantic Ocean, to understand how these marine butterflies are coping with an increasingly inhospitable habitat.

–ELI KINTISCH

Downloaded from www.sciencemag.org on May 8, 2014

Published by AAAS

AGING

'Rejuvenation Factor' in Blood Turns Back the Clock in Old Mice

Could the elixir of youth be as simple as a protein found in young blood? In recent years, researchers studying mice found that giving old animals blood from young ones can reverse some signs of aging, and last year one team identified a growth factor in the blood that they think is partly responsible for the antiaging effect on a specific tissue—the heart. Now, that group has shown this same factor can also rejuvenate muscle and the brain.

"This is the first demonstration of a rejuvenation factor" that is naturally produced, declines with age, and reverses aging in multiple tissues, says Harvard University stem cell researcher Amy Wagers, who led efforts to isolate and study the protein. Independently, another team has found that simply injecting plasma from young mice into old mice can boost learning.

The results build on a wave of studies in the last decade in which investigators sewed together the skins of two mice, joining their circulation systems, and studied the effects on various tissues. "It's still a bit creepy for many people. At meetings, people talk about vampires," says neuroscientist Tony Wyss-Coray of Stanford University in California, who led the study of learning. But he, Wagers, and others think unease will give way to excitement. The new work, he says, "opens the possibility that we can try to isolate additional factors" from blood, "and they have effects on the whole body."

Hope and hype are high in the antiaging research arena, and other researchers caution that the work is preliminary. "These are exciting papers," but "it's a starting point," says neuroscientist Sally Temple of the Neural Stem Cell Institute in Rensselaer, New York. Adds Matt Kaeberlein, a biologist who studies aging at the University of Washington, Seattle, "The therapeutic implications are profound if this mechanism holds true in people." But that "is the million-dollar question here, and that may take some time to figure out."

The experimental technique of joining mice's circulatory systems dates back 150 years. Around 2000, then-postdoc Wagers and other researchers in Irving Weissman's and Thomas Rando's labs at Stanford revived the method, known as parabiosis, to study the fate of blood stem cells and muscle cells. To their surprise, they found that when old and young mice were joined, the muscle stem cells in old mice were revitalized. Since then, Stanford researchers and others, including Wagers, have published about a half-dozen papers showing that old-young parabiosis can also improve the health of an aging mouse's liver, spinal cord, and brain.

More recently, Wagers's lab, together with cardiologist Richard Lee's lab at Brigham and Women's Hospital in Boston, isolated a specific protein from mouse blood that they think can explain some of the effects. The protein, growth differentiation factor 11 (GDF11), was known to regulate stem cell activity; it is abundant in young mice but its level drops as the animals age. Last year in *Cell*, Wagers's and Lee's labs reported that injections of GDF11 can reduce the thickening of the heart that typically comes with aging in mice. In a paper in this week's issue of *Science* (p. 649), Wagers's lab shows that 4 weeks of daily GDF11 injections works nearly as well as parabiosis in helping elderly mice recover from a muscle injury and boosts their performance on running and grip strength tests.

In another study of mice injected with GDF11, postdoc Lida Katsimpardi and others in the lab of Harvard neuroscientist Lee Rubin found that GDF11 also encourages growth of new blood vessels and olfactory neurons in the mouse brain. As they report in a second paper in this issue (p. 630), the animals gained a keener sense of smell. In both muscle and the brain, GDF11 appears to work in part by restoring the function of aging stem cells so that they can differentiate into adult tissues.

So far only two other interventions—the drug rapamycin and caloric restriction—have been shown convincingly to slow or reverse aging in multiple tissues, Kaeberlein says. Wagers points out that GDF11 could be safer than a drug because it's found naturally in human blood. Harvard has filed for patents on GDF11, and Wagers says she and her colleagues are "in the process of talking with people" about commercializing it to treat diseases such as Alzheimer's and heart disease. Giving GDF11 itself "would require huge amounts of protein," Wagers says, so it may be better to use a modified form or to target the GDF11 pathway with a different molecule. "These are tractable problems," Wagers says. "The most important hurdle was figuring out a pathway to go after."

Temple agrees that GDF11 has therapeutic promise, but she says she will remain cautious until more is known about GDF11's mechanism. She also notes that some of the "old" mice in the Harvard brain studies were only middle-aged, and whether the effects would hold up in elderly people is unclear. "It's a matter of where you can step in," she says. Nor have any studies yet shown that the treated mice live longer. Neurologist

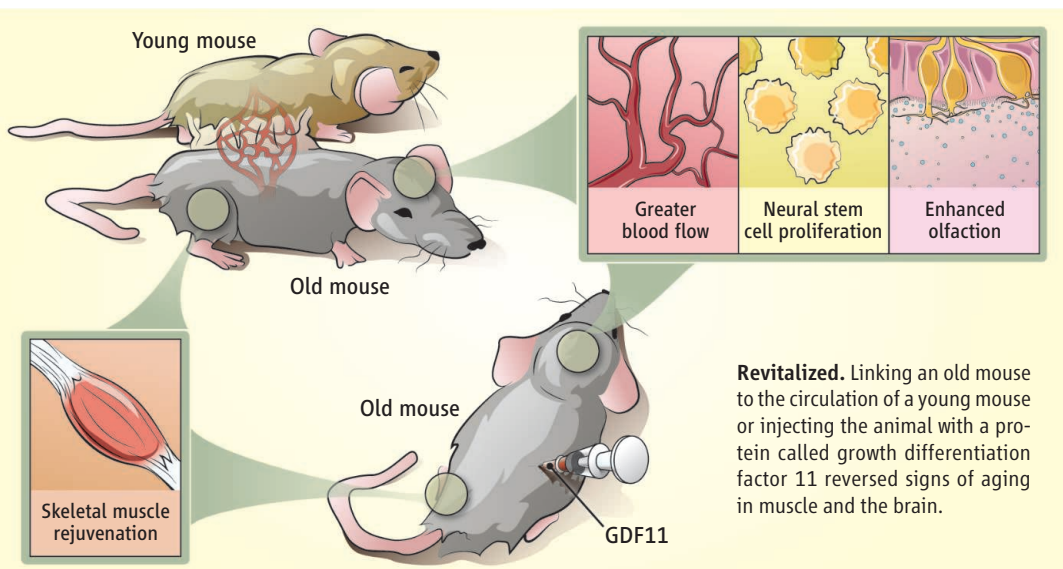

Revitalized. Linking an old mouse to the circulation of a young mouse or injecting the animal with a protein called growth differentiation factor 11 reversed signs of aging in muscle and the brain.

CREDIT: V. ALTOUNIAN/*SCIENCE*

Published by AAAS

Scott Small of Columbia University cautions that GDF11 might restore some memory in Alzheimer's patients, but that the underlying pathology "is still going to grind away." The factor might be more effective for countering the cognitive decline of normal aging, he says.

Already, GDF11 has a potential rival treatment. In *Nature Medicine* this week, Wyss-Coray's lab at Stanford and Saul Villeda and co-workers at the University of California, San Francisco, reported that parabiosis can rejuvenate another part of the mouse brain, the hippocampus, where memories are made and stored. Old mice that underwent parabiosis formed more new connections between nerve cells there. Although Wyss-Coray's group has not yet isolated any rejuvenation factors from the young blood, they have found what might be an alternative. When the team tried a simpler experiment than parabiosis—giving old mice injections of young mouse plasma, or blood from which red and white cells have been removed—they saw similar effects on the hippocampal neurons. The old mice also performed significantly better than untreated animals on tests of learning and memory.

Plasma is given routinely to patients, so trials of this approach, unlike those testing a new protein, would not require U.S. Food and Drug Administration approval, Wyss-Coray says. His group has started a company that is planning a small clinical trial that would give Alzheimer's patients a series of injections of plasma from young donors. In mouse models of Alzheimer's, they have already seen positive effects, he says.

Let a new wave of hope—and hype—begin.

–JOCELYN KAISER

SYNTHETIC BIOLOGY

Designer Microbes Expand Life's Genetic Alphabet

From bacteria to basketball players, all life as we know it encodes genetic information using two pairs of DNA letters. Not anymore. Now, along with the double helix's two natural pairs—A bound to T and G bound to C—a bacterium growing in a California lab can incorporate and copy a third, artificial pair of letters. For now, the artificial bases—call them X and Y—don't code for anything, unlike natural DNA base pairs, which in various combinations code for the 20 different amino acids that make up proteins. But the newly expanded genetic code opens the door for synthetic biologists to create microbes capable of building their proteins out of as many as 172 different amino acids, both natural and artificial—a potential boon to drug and materials developers.

"This is an amazing enabling technology," says Ross Thyer, a molecular biologist at the University of Texas, Austin, who was not involved in the work, reported in this week's issue of *Nature*. Not only does the feat open the way to a universe of new proteins, but it also gives researchers a new platform for investigating how DNA evolved and why all life is limited to just five bases. (In RNA, T is replaced with U.)

Creating synthetic superbacteria might sound ominous. But Eric Kool, a biological chemist at Stanford University in California, says the risks are low. "These organisms cannot survive outside the laboratory," Kool says. In fact, they can't even build X and Y (more formally known as d5SICS and dNaM) themselves: Researchers synthesize the bases and feed them to the bacteria. "Personally, I think it's a less dangerous way to modify DNA" than existing genetic engineering, Kool says.

Over the decades, synthetic biologists trying to expand life's genetic alphabet have come up with a handful of alternative genetic letters. A few teams, including one led by Floyd Romesberg, a biological chemist at the Scripps Research Institute in San Diego, California, have even managed to get DNA replication proteins called DNA polymerases to copy DNA strands incorporating alternative letters. But that was achieved in test tubes, not inside living cells.

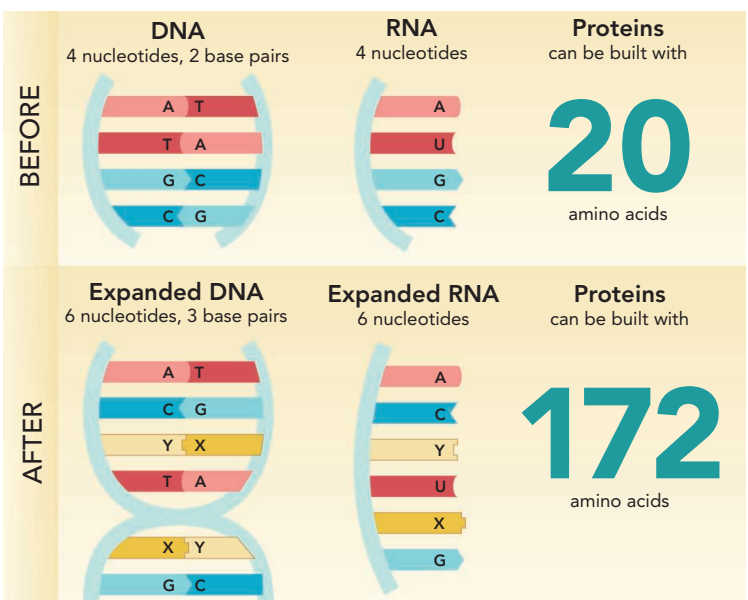

DNA 2.0. By adding a new base pair, X and Y, to DNA's A-T and G-C pairs, researchers will enable organisms to build proteins from as many as 172 different amino acids.

CREDIT: ADAPTED FROM SYNTHORX

Getting live bacteria to replicate altered DNA was another challenge entirely. The bacteria would need either to synthesize the new genetic letters themselves or to import them from the surrounding culture medium. In algae, Romesberg and his colleagues identified a protein that grabs nucleotide bases and pulls them into the cell. They spliced the gene for this transporter protein into *Escherichia coli* bacteria and found it enabled the bacteria to pull in presynthesized X and Y bases as well. The team had also engineered their *E. coli* to harbor small rings of DNA called plasmids carrying X-Y pairs. When the bacteria copied those plasmids, they used the newly imported X and Y bases—yet the engineered cells grew just as well as their native cousins.

Next, Romesberg says he hopes to use his expanded genetic alphabet to create designer proteins. Scripps biochemist Peter Schultz and others have already engineered bacteria to build proteins with dozens of amino acids beyond nature's standard 20. But those experiments use natural DNA to code for unnatural amino acids. The newly expanded genetic alphabet, Thyer says, should yield a vastly more diverse menu of proteins with a wide variety of new chemical functions, such as medicines better able to survive in the body and protein-based materials that assemble themselves. Romesberg says forays into that new world of proteins are already under way.

–ROBERT F. SERVICE

Published by AAAS

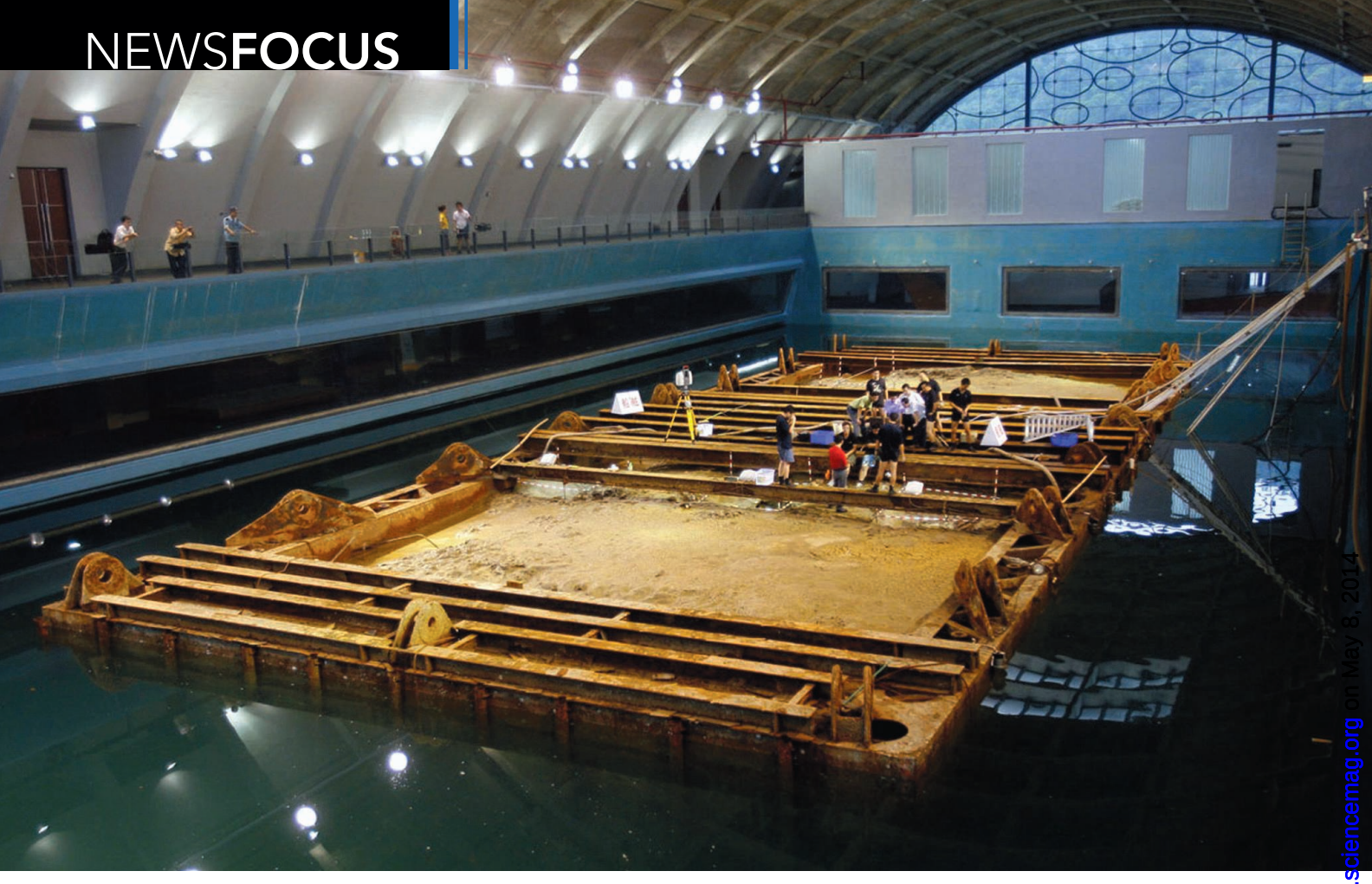

Downloaded from www.sciencemag.org on May 8, 2014

Maritime Ambitions

As China builds a modern armada, it is pouring money into underwater archaeology and rewriting the history of its early exploits on the high seas

HAILING ISLAND, CHINA—Even as Marco Polo was making his epic journey to the Far East in the late 13th century, Chinese seafarers were striking out in the opposite direction along seaways that extended as far as the Middle East. China was entering a period of trade and naval power that culminated with the 15th century voyages of Zheng He, a eunuch admiral who sailed as far as Africa in a 250-ship armada featuring massive *baochuan*, or treasure ships, that dwarfed European vessels.

Five hundred years later, China is again a naval power, building a modern armada while pressing territorial claims in the South China Sea and nearby waters. China casts its reemergence on the high seas as part and parcel of its "peaceful rise," and memories of the past—buttressed by archaeology—are a key element of that storyline. Government officials and scholars have resurrected the once-forgotten Zheng He, for example, as a symbol of benevolent engagement, asserting contrary to many scholars' views that the admiral's voyages were goodwill missions.

And China is showering money on underwater archaeology, hoping to recover vestiges of its glorious maritime past. At a time when looting threatens many sites in the region, the outlay "is a question of protecting our heritage," says Cui Yong, an underwater archaeologist at the Guangdong Provincial Institute of Cultural Relics and Archaeology's Research Center of Underwater Archaeology in Guangzhou. Next month, the government will unveil a $60 million exploratory ship—China's first dedicated to archaeological research. It is lavishing money on countries in Africa and elsewhere that are eager to work with China to excavate submerged riches. China's program also stands out among those in Asia for not profiteering from artifacts.

But critics contend that China has ulterior motives. The burgeoning underwater archaeology program is "related to [Chinese leaders'] view of themselves, and to their power projections in places," says Mark Staniforth, an archaeologist at Monash University, Clayton, in Australia. Several of the areas now targeted for research are the sites of international territorial disputes, and some archaeologists fear that China intends to use reclaimed patrimony to bolster its claims to disputed territories, Staniforth says: "The more cynical view would say that it is about territorial expansion." As China uncovers archaeological treasures that promise to illuminate a key period of history, how much will the political uses of the findings distort the science?

CREDIT: IMAGECHINA/AP

Published by AAAS

Rock the boat. China raised the Song dynasty–era *Nanhai 1* from the sea floor intact. A lavish new museum houses the wreck.

Diving in

In a hangarlike building here on Hailing Island, just off the coast of southern China's Guangdong province, *Nanhai 1*, or *South China Sea 1*, lies encased in silt and bathed in carefully calibrated water. The sea is a few hundred meters away, just visible through an enormous glass wall.

The Song dynasty (960 to 1279 C.E.) merchant ship foundered 56 kilometers offshore, along what was once the Maritime Silk Road. From the 10th to the 15th century, Chinese ships plied routes pioneered by Arab, South Asian, and Southeast Asian traders. Sailing west across the South China Sea and Indian Ocean to the Persian Gulf, they carried porcelain, silk, and tea to the west and spices, ivory, and coral in the other direction—sometimes meeting their end in choppy waters or in one of Southeast Asia's narrow straits. Thanks to a thick blanket of silt, *Nanhai 1* is one of the better preserved wrecks from the era.

In what many consider the most ambitious foray into underwater archaeology yet, a Chinese team in 2007 lifted *Nanhai 1* from the sea floor intact. The $16 million operation involved easing the vessel into a specially designed 530-ton steel container and then using Asia's largest marine salvage engineering ship to raise it to the surface (*Science*, 23 April 2010, p. 424). The endeavor coincided with the construction of the $24 million Guangdong Maritime Silk Road Museum, where the boat now rests, and a $1 million replica. Throw in at least $7.4 million more for excavations and infrastructure, and "the amount of money that [China] put in there is astronomical," Staniforth says.

China has made big strides in underwater archaeology since dredgers off the coast of Quanzhou in Fujian province—once China's largest port—discovered a 13th century junk in 1973. The remains of the first Chinese shipwreck ever excavated promised to shed light on Song-era shipbuilding techniques. Technicians disassembled the ship, which lay under only a few meters of mud, and raised it piece by piece, along with coins, chunks of aromatic wood destined for incense production, and other bits of cargo. But China, then in the throes of the Cultural Revolution, didn't have a single underwater archaeologist to study the relics.

Online
sciencemag.org
Podcast interview with author Mara Hvistendahl (http://scim.ag/pod_6184).

They sat largely untouched for 10 years until the Quanzhou Museum of Overseas Communication (now the Quanzhou Maritime Museum) invited Jeremy Green, a maritime archaeologist at the Western Australian Maritime Museum in Fremantle, to help determine the shape and dimensions of the hull. As far as Green knows, he was the first Westerner to lay eyes on the ship, which hinted at a wealth of wrecks from China's maritime Golden Age awaiting discovery. But China still lacked the knowledge and funds to dive in.

Things began to change a few years later, when a British salvor in 1986 illegally exported $20 million of Ming dynasty porcelain found in the wreck of a 1752 Dutch East India Trading Company ship off Indonesia. The next year, another British salvor—this time with a legal concession—stumbled upon *Nanhai 1*. The back-to-back incidents were a wake-up call. Chinese authorities canceled the salvor's concession, and soon thereafter the National Museum of China (NMC) launched an Underwater Archaeological Research Center.

The research center invited Green back to China in 1989 to lead an intensive underwater training program for Cui, then 27, and seven other curators and land archaeologists. The fledgling underwater archaeologists lacked the expertise to recover *Nanhai 1*, which lay buried under the sea floor beneath 23 meters of water. But 15 years later they finally had the expertise and funding for the risky operation.

China's program "went very rapidly into overdrive because they discovered that they had sites all over the place," Staniforth says. In 2007, researchers from NMC began salvaging *Huaguangjiao 1*, a Song dynasty merchant ship discovered by fishers in 1996. Then in 2009, Cui and colleagues began work on *Nan'ao 1*, a late Ming-era smuggling ship excavated at a depth of 27 meters—a rare find from a period in the 16th and 17th centuries when the Chinese emperor banned maritime trade.

Archaeologists weren't the only ones discovering those sites. The sophisticated remote-sensing equipment that has helped scientists uncover new and deeper wrecks has aided looters as well (*Science*, 17 May 2013, p. 802). Nowhere in the world is the pressure as intense as in Asia, says Jeffrey Adams, an independent heritage management specialist in Minneapolis: "The gold rush, such as it is, is in the South China Sea."

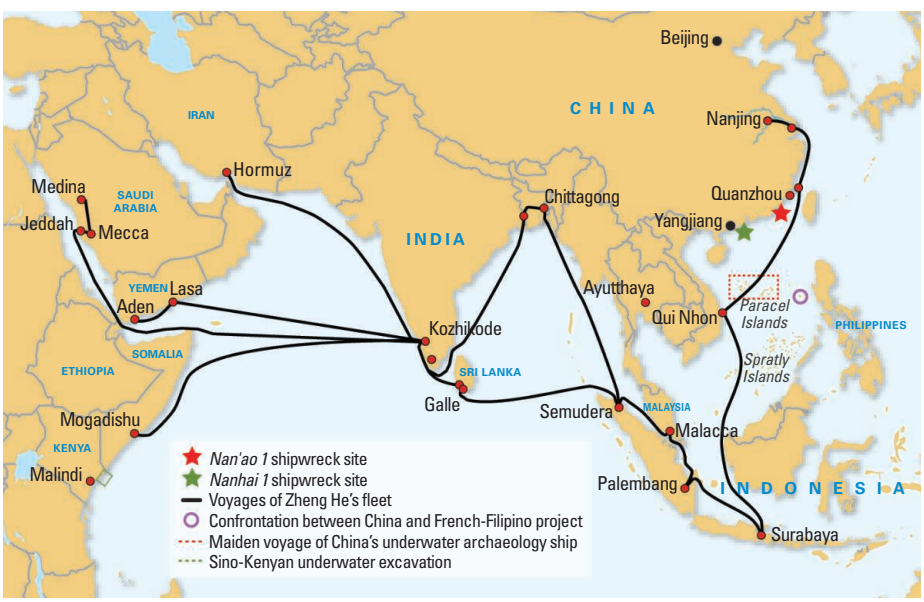

Oceans to explore. China's underwater archaeology projects extend from the South China Sea to East African waters reached by Adm. Zheng He's 15th century fleet.

Some of China's neighbors conduct underwater excavations in collaboration with commercial salvors, with duplicate relics from the expeditions then sold to fill government coffers. In cash-strapped countries like Indonesia and the Philippines, Green says, underwater archaeology programs are largely "run by the finance department." Many archaeologists respect China for embarking on a program focused on research and conservation, avoiding—as far as observers can tell—for-profit archaeology. But some say that the country has goals beyond rediscovering its heritage.

MAP SOURCE: ZHENG-HE-7TH-EXPEDITION-MAPSVG; VMENKOV, BASED ON THE BLANK MAP FILE: ASIE.SVG (VER. 1) BY USER:HISTORICAIR DERIVATIVE WORK: JANN/VIA WIKIMEDIA COMMONS

Published by AAAS

Soft power on the high seas

One pillar of China's program is research that sheds light on the Zheng He era. Roughly a decade ago, China marked the 600-year anniversary of Zheng He's first voyage with a slew of cultural events, including conferences, commemorative stamps, comics, and a musical stage show. Scientists took part as well. In 2003, archaeologists in Nanjing excavated the shipyard where Zheng He's boats were built. They unearthed two rudders that have shed light on Ming-era shipbuilding techniques. The knowledge is now being used to create a replica of one of the admiral's treasure ships, which later this year will set sail along an old Maritime Silk Road route.

The holy grail would be the discovery of a wreck from Zheng He's fleet. To that end, China is looking farther afield and brokering partnerships with countries whose coastal waters the admiral's fleet reached. In 2012, researchers from the Chinese Academy of Sciences' Institute of Acoustics spent 2 weeks using side-scan sonar on a mostly fruitless search for wrecks in the Gulf of Oman. The first round of an even more ambitious project recently concluded in Kenya, where archaeologists from NMC and Peking University in Beijing worked with counterparts from the National Museums of Kenya (NMK) in Nairobi to excavate sites near the route traversed by Zheng He's fleet in 1418, some 80 years before Vasco da Gama rounded the Cape of Good Hope. The $3.2 million, 3-year project searched both underwater and on land. "We have found a lot of areas that have potential," says NMK's Caesar Bita, one of two underwater archaeologists in the country.

The effort in Kenya has its roots in unsubstantiated reports published by Western journalists in the 1990s, says Qin Dashu, who headed up the project's land excavations. Reporters visiting islands in the Lamu Archipelago, off the coast of Kenya, met locals who claimed to have Chinese heritage. One of Zheng He's ships had sunk nearby, the theory went, and sailors swam ashore, eventually marrying local women. Ming dynasty texts state that the admiral's fleet reached the kingdom of Malindi, in what is now Kenya, but they do not mention a shipwreck. In 2005, however, the Chinese government sponsored a young woman from Lamu claiming to be of Chinese descent to study in Nanjing. (Her DNA has not been tested to prove this claim, Qin notes.) The prospect of finding concrete evidence of Zheng He's voyages to Africa intrigued the wife of a member of China's vaunted State Council, Qin says, and the government greenlighted the archaeological project.

The team uncovered intriguing material—though not entirely what officials had in mind. Searching the waters around Lamu, the archaeologists found a local shipwreck laden with pottery. Based on a preliminary analysis of a single shard of Chinese porcelain, the archaeologists believe the wreck to be from the 14th century, too early to say anything about the Zheng He era. At a second underwater site about 40 kilometers from Malindi, they unearthed another red herring: a remnant of a vessel with the telltale triangular sail shape common to local ships.

The notion of a Zheng He shipwreck remains "just a tale," Qin says. But excavating onshore in Mambrui, a coastal site north of Malindi, his team found other evidence of China's influence in Africa: coins from the time of the Yongle Emperor Zhu Di, who was Zheng He's patron, along with shards of porcelain bearing the mark of Zhu Di's imperial kiln. Alone, the coins might simply have meant that smugglers had reached Malindi. But the porcelain suggested something more, Qin says: "It's very unusual to find an [imperial] shard in an African site. It proves that there was some official relationship" between the kingdom and China at the time.

China hopes to broker a similar project with Sri Lanka, the site of the only known inscription referring to Zheng He outside of China. Several years ago, Sri Lanka's culture minister met with administrators from the Chinese Academy of Social Sciences' Institute of Archaeology to discuss collaborating in underwater archaeology. But the talks have apparently stalled. Officials on both sides may be wary of exploring a dark period for Sri Lanka. In 1411, Zheng He's armada invaded Sri Lanka and hauled a local ruler back to the Ming court, replacing him with a puppet ruler.

Geoffrey Wade, a maritime historian at Australian National University in Canberra, notes that Chinese officials cast Zheng He's exploits as "nonexpansionist and nonaggressive, completely unlike the European colonialists." He and others demur, citing historical accounts of Zheng He's fleet using military force, meddling in civil wars, and imposing unequal trading terms. The armada's intervention in Sri Lanka, Wade says, is "one of the most obvious examples of nonpeace and nonfriendship" from the era.

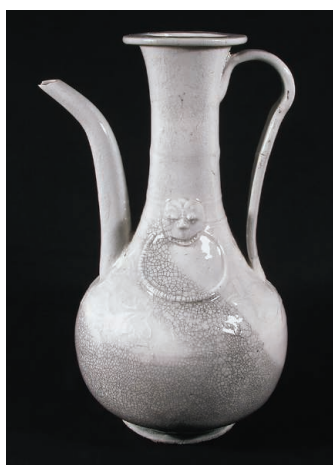

Wealth of a nation. Among the relics from the *Nanhai 1* wreck uncovered by archaeologist Cui Yong's team are a pitcher and a celadon bowl from an imperial kiln.

Political aims?

At the Indo-Pacific Prehistory Association Congress in Hanoi in 2009, Staniforth attended several presentations by Chinese researchers affiliated with mainland government institutions and museums. Some researchers reported on archaeological efforts in the Paracel and Spratly islands, contested archipelagos in the South China Sea. The Paracels are separately claimed by China, Taiwan, and Vietnam, and the Spratlys by Brunei, China, Malaysia, the Philippines, Taiwan, and Vietnam. Chinese underwater archaeologists are now searching for wrecks in both areas—and the tone of their

CREDITS: (LEFT) MARA HVISTENDAHL; (RIGHT) COURTESY OF CUI YONG (2)

Published by AAAS

reports bothered Staniforth. The thrust of the argument in Hanoi, he says, was that "these are Chinese ships, therefore this is Chinese territory."

China is open about that agenda. Archaeological research in the South China Sea, an area rich not just in wrecks but also in oil, gas, and fishing grounds, can aim to further "national territorial sovereignty and maritime rights and interests," according to materials published online by China's Center for Underwater Cultural Heritage, a division of the State Administration of Cultural Heritage set up in 2012. No less a figure than China's vice minister of culture, Li Xiaojie, has echoed that claim in comments published by state media. And at NMC, text for a display of artifacts from *Huaguangjiao 1*, discovered near the Paracel Islands, declared: "China's sovereignty over the islands of the South China Sea has been formed over a long period of historical development."

To beat that drum even harder, a new $160 million National Museum of the South China Sea recently opened on Hainan Island. Nearby is a planned $48 million National Underwater Cultural Heritage South China Sea Protection Base. It will be used for research and restoration of damaged relics and will "strengthen South China Sea underwater heritage protection and law enforcement," according to the Center for Underwater Cultural Heritage's website.

Arguments basing national sovereignty on the discovery of shipwrecks and artifacts baffle international scholars. "If the presence of Chinese ceramics were any indication of sovereignty, then the Victoria and Albert Museum in London would be part of China," Wade says.

And they have irked China's neighbors, who increasingly see the country as an archaeological bully. On 30 March, the Philippines filed a 4000-page arbitration brief with the United Nations, claiming that China's so-called nine-dash line, a territorial claim that encompasses nearly all of the South China Sea, is forbidden by the U.N. Convention on the Law of the Sea. "China's maritime territory policy is not conducive to interactions or cooperation on underwater cultural heritage between China and Southeast Asia as a whole," says Rujaya Abhakorn, director of the Southeast Asian Ministers of Education Organization's Regional Centre for Archaeology and Fine Arts in Bangkok. Countries in the region, he says, are now worried by rumors that "China would claim ownership of all Chinese vessels and artifacts found in Southeast Asia."

China's program "went very rapidly into overdrive because they discovered that they had sites all over the place."

—MARK STANIFORTH, MONASH UNIVERSITY

In 2012, a Chinese marine surveillance vessel reportedly confronted archaeologists in the Scarborough Shoal, a hotly contested area of the Spratly Islands off the coast of the Philippines. Franck Goddio, an underwater archaeologist and the founder of the European Institute for Underwater Archaeology in Paris, had been exploring a 13th century Chinese wreck with a team from the National Museum of the Philippines when the ship pulled up alongside the scientists and ordered them to vacate the area, according to *The Wall Street Journal*. Goddio declined to comment, citing political sensitivities.

Dove or hawk? Officials have portrayed the 15th century admiral Zheng He as an ambassador of peace and a model for China's current policies.

"Archaeology, especially maritime archaeology, is a common heritage of all of us," says Sheldon Clyde Jago-on, an underwater archaeologist with the National Museum of the Philippines in Manila. "Whether Filipino archaeologists discover it, or Vietnamese archaeologists discover it, or Chinese archaeologists discover it, it's part of a whole complex pattern of trade from so many years ago." While he declined to comment on the Scarborough Shoal incident, Jago-on says that "doing archaeology for the benefit of bolstering claims" is "not really science if you ask me." (China's cultural heritage administration did not reply to faxed questions before *Science* went to press.)

Others defend China's program, saying the investment in underwater archaeology makes sense given the rampant looting in the region. It also comes at a time when interest in heritage is growing among the Chinese public. "I don't feel that there's anything sinister happening," says Adams, the independent heritage management specialist. "It's just happening."

In rare cases, foreign archaeologists are getting in on the action. For example, Damien Leloup, an archaeologist with the Explorers Club based in Beijing, spearheaded an exploration last October in and around a river near the city of Jingdezhen, the site of China's most famous imperial kilns. Near where the river emptied into the Yangtze, he and colleagues found a wealth of well-preserved ceramics from the Song dynasty. "I am convinced there are several shipwrecks to be found within the area," he says.

Cui, for one, has tried to insulate himself from the politics buffeting his work. Over dinner, younger archaeologists working on the *Nanhai 1* excavation start a heated discussion about China's recent clashes with the Philippines. Cui quickly silences them. Instead, he prefers to talk about the payoff for archaeology.

Just a short walk away, in 9000 square meters of pristine exhibition space, artifacts from preliminary excavations of *Nanhai 1* rest in glass cases: anchors, bronze coins, and delicate ceramic pieces that were once precious cargo. Cui gestures to a paper-thin bowl impressed with an intricate floral design. "It's rare to find ceramics in this condition" from that era, he says. So far a total of 5000 relics have been removed from the ship. Thousands more are believed to be hidden in the silt.

Nanhai 1 may be a teaser for even more splendid and illuminating relics waiting to be unearthed. Next month, China's dedicated underwater archaeology ship will set sail in search of other wrecks. The 56-meter, 500-ton vessel contains 20 sleeping berths and can store a month's worth of food. Cui can't wait: "I have dreamed of using a ship like that," he says.

The vessel's maiden voyage: the disputed waters of the Paracel Islands.

–MARA HVISTENDAHL

Published by AAAS

LETTERS

edited by Jennifer Sills

Breast Cancer and Environmental Research

CHRISTOPHER WILD, DIRECTOR OF THE INTERNATIONAL AGENCY FOR RESEARCH ON CANCER, introduced the concept of the "exposome," encompassing a person's environmental exposures across a lifetime, with an image of a fiddler crab, warning against science walking sideways with one powerful "genome" claw and a second, radically smaller body of knowledge about environmental exposure (*1*). In this regard, the special section on Breast Cancer (28 March, p. 1451) suffers from a grave imbalance. Discoveries of the BRCA gene are important science and interesting history, and additional low-penetrance breast cancer genes are noteworthy, too. However, given that "most cases of breast cancer have no inherited component" (p. 1462), it's troubling to see a special section on breast cancer that ignores substantial discoveries in environmental breast cancer studies over the same 20 years.

Is cancer research walking sideways?

Three compelling themes have emerged from studies of environmental factors. First, breast cancer is now recognized as a developmental disease, with windows of susceptibility across the life course, beginning in the womb, during puberty and the early reproductive years, and up to the 5 years before diagnosis (*2*). Second, laboratory studies reveal hundreds of common chemicals that activate relevant biological pathways, including genotoxic chemicals that cause mammary gland tumors in rodents (*3*), hormone disruptors that interact with the estrogen receptor and promote tumor proliferation (*4*), and developmental toxicants that alter mammary gland development in rodents in ways that later affect lactation and cancer susceptibility (*5*). Third, the U.S. National Report on Human Exposure to Environmental Chemicals and other exposure studies show that these suspect chemicals are widespread in air and water pollution (*6*), consumer products (*7*), house dust and air (*8*, *9*), and human tissues (*10*).

Three authoritative reports—by the President's Cancer Panel (*6*), Institute of Medicine (*2*), and Interagency Breast Cancer and Environmental Research Coordinating Committee (*11*)—highlight the importance of such research. Because the exposures are so widespread and breast cancer is so common, addressing environmental factors has the potential to save thousands of women each year, even though the relative risks are vastly smaller than for the BRCA genes.

JULIA GREEN BRODY,[1] MARGARET L. KRIPKE,[2] MARION H. KAVANAUGH-LYNCH,[3] JEANNE RIZZO,[4] MICHELE R. FORMAN[5]

[1]Silent Spring Institute, Newton, MA 02458, USA. [2]President's Cancer Panel 2003–2011, Houston, TX 77030, USA. [3]California Breast Cancer Research Program, Oakland, CA 94612, USA. [4]Breast Cancer Fund, San Francisco, CA 94109, USA. [5]School of Human Ecology, University of Texas at Austin, Austin, TX 78712, USA.

*Corresponding author. E-mail: brody@silentspring.org

References

1. C. P. Wild, *Cancer Epidemiol. Biomarkers Prev*. **14**, 1847 (2005).
2. Institute of Medicine, "Breast cancer and the environment: A life course approach" (National Academies Press, Washington, DC, 2012).
3. R. Rudel, K. Attfield, J. Schifano, J. G. Brody, *Cancer* **109**, 2635 (2007).
4. J. Shen *et al.*, *Toxicol. Sci*. **135**, 277 (2013).
5. R. Rudel, S. E. Fenton, J. M. Ackerman, S. Y. Euling, S. L. Makris, *Environ. Health Perspect*. **119**, 1053 (2011).
6. President's Cancer Panel, "Reducing environmental cancer risk: What we can do now" (U.S. Department of Health and Human Services, National Institutes of Health, National Cancer Institute, Washington, DC, 2010).
7. R. E. Dodson *et al.*, *Environ. Health Perspect*. **120**, 935 (2012).
8. R. A. Rudel, L. J. Perovich, *Atmos. Environ*. **43**, 170 (2009).
9. R. A. Rudel *et al.*, *Environ. Sci. Technol.* **44**, 17 (2010).
10. CDC, "Fourth National Report on Human Exposure to Environmental Chemicals" (Centers for Disease Control and Prevention National Center for Environmental Health, Atlanta, GA, 2009).
11. Interagency Breast Cancer and Environmental Research Coordinating Committee, "Breast Cancer and the Environment: Prioritizing Prevention" (IBCERCC, 2013).

Copper Limits: Opportunity Costs

IN THE NEWS FOCUS STORY "THE COMING copper peak" (14 February, p. 722), R. A. Kerr describes the public debate over the long-run availability of copper and other mineral commodities. What is troubling is that despite all we have learned since the publication of *Limits to Growth* (*1*) over four decades ago, we still focus on the fact that Earth contains a fixed stock of copper. Estimates of this stock are always a very tiny fraction of the total copper in Earth, for the logical reason that long before the last copper atoms are mined, costs become prohibitive. The fatal flaw of the fixed stock paradigm is that the amount of copper humans can ultimately produce—what the U.S. Geological Survey (USGS) refers to as resources—

Letters to the Editor

Letters (~300 words) discuss material published in *Science* in the past 3 months or matters of general interest. Letters are not acknowledged upon receipt. Whether published in full or in part, Letters are subject to editing for clarity and space. Letters submitted, published, or posted elsewhere, in print or online, will be disqualified. To submit a Letter, go to www.submit2science.org.

CREDIT: THOMAS BROWN/WIKIMEDIA COMMONS

Chile's copper mines.

changes over time with new technology. For example, USGS in the early 1970s estimated global copper resources at 1.6 billion tons. Its latest figure—5.6 billions tons—has more than tripled (*2*).

More useful is the opportunity cost paradigm, which assesses long-run availability by what society has to give up for another ton of copper (*3*, *4*). It focuses on real prices, and the race between the cost-increasing effects of depletion and the cost-reducing effects of new technology. Over the past century, new technology has kept depletion at bay (*5*). Will this continue over the 21st century? Given the erratic course of technological change, no one knows for certain. What we do know is that global population and copper consumption grew very rapidly during the 20th century; both will grow more slowly over the coming century. We also know that a lot of copper remains in marginal porphyry deposits with 0.4 to 0.5% copper equivalent. This should make it easier than in the past for new technology to keep copper readily available at reasonable costs.

JOHN E. TILTON

Colorado School of Mines, Golden, CO 80401, USA; Catholic University of Chile, Santiago, Chile; and Resources for the Future, Washington, DC 20036, USA. E-mail: jtilton@mines.edu

References

1. D. H. Meadows, D. L. Meadows, J. Randers, W. W. Behrens, *The Limits to Growth* (Universe Books, New York, 1972).
2. K. M. Johnson, J. M. Hammarstrom, M. L. Zientek, C. L. Dicken, "Estimate of undiscovered copper resources of the world, 2013" (U.S. Geological Survey Fact Sheet 2014–3004, 2014); http://dx.doi.org/10.3133/fs20143004.
3. J. E. Tilton, *On Borrowed Time? Assessing the Threat of Mineral Depletion* (Resources for the Future, Washington, DC, 2003).
4. A. Yaksic, J. E. Tilton, *Res. Pol.* **34**, 185 (2009).
5. P. Svedberg, J. E. Tilton, *World Dev.* **34**, 501 (2006).

Copper Limits: Recycling Potential

R. A. KERR'S NEWS FOCUS STORY "THE COMING copper peak" (14 February, p. 722) draws conclusions based on analyses that equate the exploitation of copper to forecasts for other commodities. The concept of peak copper is not valid because copper is used but not consumed (as is oil). As such, the quantity of copper on Earth remains constant throughout civilization.

The peak copper theory is not valid because of the physical and economic effects of recycling. Were copper to become scarcer, its price would rise, but only to some upper limit because more recycled copper would become available. Because of rising global economic per capita income by the end of this century (*1*, *2*), the global rate of economic growth will become slower, and with it the use of copper and of other metals. Reduced growth in copper use implies that the availability of secondary recycled copper will increase, and therefore its competition with primary copper will strengthen.

GUSTAVO LAGOS

Departamento de Ingeniería de Minería, Centro de Minería, Pontificia Universidad Católica de Chile, Macul, Santiago, 7820436, Chile. E-mail: glagos@ing.puc.cl

References

1. IPCC, *Emissions Scenarios*, N. Nakicenovic, R. Swart, Eds. (Cambridge Univ. Press, Cambridge, 2000).
2. A. Calzadilla, "Global income distribution and poverty: Implications from the IPCC SRES scenarios" (Kiel Institute for the World Economy, working paper no. 1664, Germany, 2010).

Copper Limits: Human Agency

THE NEWS FOCUS STORY "THE COMING COPper peak" (R. A. Kerr, 14 February, p. 722) points out that the timing of any production peak depends on a dynamic interplay of geology, economics, and technology. Another crucial factor is human agency. Resource owners and producers are not automatons, but shrewd businesspeople who can usually avoid an abrupt and catastrophic decline in production. For example, at some point in the near future, Chile—the dominant copper producer—might decide that it makes sense not to increase production by more than a factor of 50% by 2030, but to allow prices to increase, thus rationing a scarce commodity. This is one of many reasons to expect that the peak in copper production would not be nearly as disruptive as the News story indicates.

ALFRED J. CAVALLO

Princeton, NJ 08540, USA. E-mail: cavallo-harper@verizon.net

TECHNICAL COMMENT ABSTRACTS

Comment on "Revealing Nature's Cellulase Diversity: The Digestion Mechanism of *Caldicellulosiruptor bescii* CelA"

Alexander V. Gusakov

Brunecky *et al*. (Reports, 20 December 2013, p. 1513) compared the cellulolytic activity of bacterial multimodular cellulase CelA with fungal Cel7A (cellobiohydrolase I from *Trichoderma reesei*). If more active Cel7A from another fungus were used as a reference enzyme under optimal conditions with β-glucosidase added, the reported difference between bacterial and fungal enzymes would be less dramatic.

Full text at http://dx.doi.org/10.1126/science.1251248

Response to Comment on "Revealing Nature's Cellulase Diversity: The Digestion Mechanism of *Caldicellulosiruptor bescii* CelA"

Roman Brunecky, Markus Alahuhta, Qi Xu, Bryon S. Donohoe, Michael F. Crowley, Irina A. Kataeva, Sung-Jae Yang, Michael G. Resch, Michael W. W. Adams, Vladimir V. Lunin, Michael E. Himmel, Yannick J. Bomble

Gusakov critiques our methodology for comparing the cellulolytic activity of the bacterial cellulase CelA with the fungal cellulase Cel7A. We address his concerns by clarifying some misconceptions, carefully referencing the literature, and justifying our approach to point out that the results from our study still stand.

Full text at http://dx.doi.org/10.1126/science.1251701

NextGenVOICES

Science Ethics: Last Call

You have one more week to respond to the NextGen VOICES survey! Share your thoughts about this question:

What is the most challenging ethical question facing young investigators in your field? How should it be addressed?

To submit, go to http://scim.ag/NextGen11

Deadline for submissions is 16 May. A selection of the best responses will be published in the 4 July issue of *Science*. Submissions should be 250 words or less. Anonymous submissions will not be considered. Please submit only once.

CREDIT: SEBASTIAN KAWA, TOMASZ KAWA/WIKIMEDIA COMMONS

Published by AAAS

FILM: ENVIRONMENT

Beauty, Challenges, Ingenuity, and Horrors

For the past two decades, the Environmental Film Festival in the Nation's Capital has spotlighted works that advance "environmental understanding through the power of film." This March, viewers in Washington, DC, were treated to 200 documentaries, dramas, animations, and children's films from 38 countries. Showings included classics (such as Fritz Lang's *Metropolis* from 1927), recent releases (e.g., *Once Upon a Forest* and *Damnation*), and world premieres (e.g., *Your Inner Fish* and *The Hazda*: *The Last of the First*). Several films focused on sustainable urban development; another group explored people's impacts on Earth's ecosystems. The festival's website (www.dcenvironmentalfilmfest.org) includes short descriptions of all; here our reviewers reflect on ten that drew their interest.

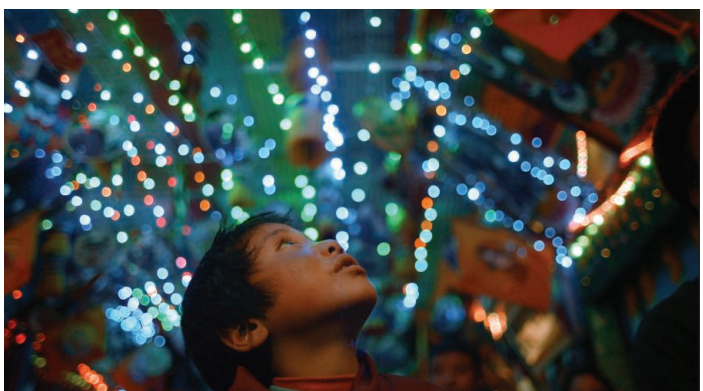

Happiness. Thomas Balmès and Nina Bernfeld, directors. Quark, France/Finland. 2013. 80 minutes. www.quarkprod.com

Happiness opens with the 1999 event that would ultimately cascade into the remote Bhutan village of Laya: King Jigme Wangchuck's announcement that his people will thereafter enjoy the benefit of television throughout the country. The king notes that his proclamation is the first to be received with applause, so it seems the people share his expectation that this technology will bring joy. Still, we find more basic needs left unfulfilled in a family home.

As Peyangki's widowed mother spins yak wool into yarn, she explains to the eight-year-old that school is too costly and suggests that he instead join the monastery. Although he dissents, preferring to stay with the family, they settle without raised voices. Peyangki soon performs the monastic rituals under his lama's direction, but his frequent escapes to converse with schoolchildren and family reveal an inquisitive nature. It's no surprise when he seizes on an invitation from his uncle for a trip to the capital city to buy a television set.

The three-day journey is full of firsts for him (e.g., car ride, city visit) but likely none so alien as standing before a shop window full of TVs airing professional wrestling. The directors make no heavy-handed conclusion, leaving viewers to form their own uneasy questions. For one, does what inspires wonder always bring happiness? And what next? Trucks bearing logs and cable soon clutter the mountain scenery, and the film ends focused on vacant faces lit by a World Wrestling Foundation broadcast. With this close, we're left to wonder how much happiness can be delivered by wire.

– Margaret Moerchen

Food Savers (Die Essensretter). Valentin Thurn, director. Schnittstelle & Thurn, Germany. 2013. 53 minutes. www.thurnfilm.de/de_doku_die_essensretter.php

Waste is interesting. Humans have always produced large volumes of it, and there have been many people who have been ingenious with waste and many who have made a lot of money from it. Valentin Thurn's *Food Savers* is about food waste but, unfortunately, is not interesting. This is a great shame just when Europe has uneasily recognized the immorality of discarding 30 to 50% of the food produced—indeed, the European Parliament considered proclaiming 2014 the Year Against Food Waste. It's not just a moral issue though. Trashing edible food causes major environmental and economic problems, not only because food in landfill rots to generate methane (a greenhouse gas) but also because profit margins are eroded by overfull plates and garbage bins. Although the film is a bit hazy on the economics of food waste, a sense of outrage clearly motivated many of the food producers' and sellers' stories it presents. There are several reasons Europeans waste so much food, including modern ignorance about food preparation, misplaced ideals of perfection, arbitrary "best before" dates, and imprecision of the legally abiding "sell by" dates on perishable items. Steps are being taken to improve matters. Political pressures from escalating prices and weather-induced shortages have led to a multitude of small-scale responses that address problems such as misshapen vegetables or pricing policy. The chain of Ecodestock supermarkets in France features warehouse stock close to sell-by dates. Encouragingly, Ukraine is

pioneering temperature-sensitive "smart" labels for meat, and some Dutch and UK supermarkets are prototyping ready meals made from "best before" discards. These are just a few approaches, but none has yet been implemented on a scale that makes much of a dent in the mountain of European waste food.

A catalog of examples with little in-depth analysis and few statistics, the film seems unlikely to inspire or motivate viewers. And it deals solely with Europe despite our tightly connected world. Wasteful eating in Europe now affects producers and their soil in countries as far apart as Guatemala and Indonesia, not just carrot farmers in Germany.

– Caroline Ash

CREDITS: *HAPPINESS*, © TBC; *FOOD SAVERS*, © SCHNITTSTELLE GMBH THURN-GBR, MARSILIUSSTRASSE 36, 50937 KÖLN, GERMANY

Downloaded from www.sciencemag.org on May 8, 2014

Published by AAAS

The Ginger Ninjas Ride Mexico (Los Ginger Ninjas Rodando Mexico). Sergio Morkin, director. Mexico, 2012. 78 minutes. http://gingerninjas.com/the-film

Touring Mexico on bicycle from Baja California to Chiapas, covering 5000 miles over seven months, sounds like a dream vacation. Yet for the rock band the Ginger Ninjas, such a trip made a statement on the ability to travel and perform without the use of fossil fuels. Favoring scenic roads with little traffic, the band cycled south, arranging shows as they went. They also pedaled to generate power for the digital amplifiers they used at their 100 performances. Filmmaker Sergio Morkin encountered the band at a concert early in the trip and then spent five months following them. He intersperses gorgeous shots of Mexican countryside and nature (such as wintering monarch butterflies) with harrowing events such as navigating freeway traffic and traversing bicycle lanes that are ignored by motorists and police. One senses that some of the group's interpersonal difficulties stem from the complexity, and effort, of traveling by bicycle. Unfortunately, many episodes remain unexplored—including the band's turning down an offer to be sponsored by the Mexican oil company Pemex and a concert in Mexico City at which the heavy regulation by the police substantially affects the group and their performance. Although Morkin effectively documents the band's travels, the band members' individual stories remain fragmented and incomplete. Nonetheless, he shows a slice of life of a group of persevering individuals willing to break their addictions to oil.

– Laura Zahn

Gringo Trails. Pegi Vail, director. Zebra/Icarus, USA, 2013. 80 minutes. http://gringotrails.com

Throughout history, people have been driven by a lust for adventure. In earlier times, such desires could lead to the "discovery" or exploration of landscapes that were relatively untouched by outside influence. As the human population, not to mention the availability of intercontinental transport, has increased, such places have become hard to find. Still, a large group of adventure travelers, commonly referred to as "backpackers," actively continue to search.

In *Gringo Trails*, anthropologist-director Pegi Vail and producer Melvin Estrella reveal processes by which honest travelers' lust for adventure can lead to the destruction of the very magical places they seek. Through stories of several "discovered" places and the voices of those involved, we see how travelers seeking adventure, self-edification, or authenticity can rapidly reduce an "untouched" environment to a highly modified tourist attraction. Across locations from Bolivia to Thailand, these stories demonstrate that our searches for personal transformation through contact with pure nature, cultures different from our own, or "real" dangers—successful or not—often transform the sites we seek such that they become more similar to what we had hoped to escape.

Although aspects of the film are heartbreaking, tales of local communities that both control and benefit from thoughtful management of tourism are encouraging, as are the accounts of those who have learned to reflect on their own impact as travelers. The human desire for adventure is unlikely to disappear as our numbers grow. *Gringo Trails* persuasively encourages those of us who continue to seek to look beyond our own personal searches for transformation.

– Sacha Vignieri

Edward Hopper and the Blank Canvas (La Toile blanche d'Edward Hopper). Jean-Pierre Devilliers, director. Idéale Audience/ARTE France, France, 2012. 52 minutes. www.arte.tv/fr/la-toile-blanche-d-edward-hopper/6955298.html

In some ways, Jean-Pierre Devilliers' documentary offers a conventional biography of a famous artist. It features insights from artists and art historians and notes milestones in Edward Hopper's life (1882–1967) and career. Devilliers examines paintings in relation to contemporaneous events and the artist's evolving style. His coverage extends to some of Hopper's early works, which included watercolors and commercial illustrations. Hopper appears on some of the canvases and in photographs and videos, with most of the latter excerpted from a 1964 interview by friend and fellow artist Brian O'Doherty.

Devillers' film also offers something different, a chance to view Hopper's art in diverse settings, from city benches to empty beaches. Sometimes pieces are shown where they were created: scenes capture Hopper's studios in New York City and on Cape Cod in changing light, with relevant paintings digitally superimposed onto blank canvases. Other times, the original paintings were removed from storage racks and propped on an easel for close-up views of brush strokes.

CREDITS: *GINGER NINJAS*, © SERGIO MORKIN, 2012; *GRINGO TRAIL*, COURTESY OF ICARUS FILMS; *EDWARD HOPPER*, © ARTE FRANCE

It may not be possible to explain the power of Hopper's most famous images, but Devilliers presents an appropriate tribute to them and their creator. O'Doherty remarked that he always had a sense of time slowing down when he was with Hopper, a sense that infuses Hopper's paintings as well. The film allows viewers to linger in front of those paintings long after the museums close. **– Trista Wagoner**

Sand Wars. Denis Delestrac, director. Rappi & La Compagnie des Taxi-Brousse, France, 2013. 80 minutes.
http://sand-wars.com

This summer, when you go to the beach and feel the soft, warm sand between your wiggling toes, savor the sensation, knowing that in future you might be walking on rocks. *Sand Wars* presents a sobering look at how economic, ecologic, and social forces are combining to put a serious dent in the underappreciated resource that is sand. Although sand is renewable over geologic time scales, as mountains grind down and their remains run into the ocean, dams (whether used for hydroelectric power, water supply, or flood control) block this flow of sediment. Sand might be renewable in human time scales through recapture of recycled glass, but that process is expensive. Easily

accessible surface sources of sand in the bulk quantities needed have largely been exhausted. Sand, on the other hand, seems to be everywhere in the ocean. Unfortunately, sand taken from ocean or lake floors leaves trenches that then receive material drifting down from nearby beaches. In Indonesia, entire islands have disappeared through this process.

Why do we need so much sand? We use the material to produce computer chips, cosmetics, detergents, and all sorts of other conveniences of modern life. But by far the greatest consumption of sand lies in producing concrete—an enormous amount of which is absorbed yearly in the construction of new roads and expanding cities, not to mention beach-side retreats. (And modern buildings often use a great deal of glass, the principal constituent of which is quartz sand.) As the film effectively argues, sand from the ocean floors may be free for the taking but is costly in its absence. **– Pamela J. Hines**

Tiny: A Story About Living Small. Merete Mueller and Christopher Smith, directors. Speak Thunder, USA, 2013. 62 minutes.
http://tiny-themovie.com

It's a movement. Across the United States, people are building small houses—dwellings of 200 square feet or less—for themselves and their families. *Tiny* chronicles the adventures of one such person. At age 30, Christopher Smith decided to build a small cabin in the mountains outside of Boulder, Colorado. Lacking any construction experience, he found instructions through blogs, YouTube videos, and trips to the hardware store. Despite intermittently running out of money, he and his partner Merete Mueller completed a 130-square-foot abode from scratch in two years for $25,000. They built the house on wheels, not for mobility but to ensure that it was classified as a temporary dwelling and thus not bound by the building and zoning codes (which,

as is common, required a minimum size of 600 square feet). The home contains a solar generator, a composting toilet, and a propane sailboat-fireplace. Mueller and Smith also plunged into filming their construction project in order to explore questions around how we define and value homes. They eventually expanded the film's scope to include tours of a half dozen other tiny homes and interviewers with builders and activists in the tiny house movement. Following in their footsteps requires ingenuity, a desire to leave a smaller footprint, the will to simplify, and a willingness to ask, "what really makes us feel at home?" However, as one interviewee remarks, "We don't all have to give up all our material possessions and live in 89 square feet. But let's think about maybe giving up our McMansions and … living a little smarter." **– Barbara R. Jasny**

Z'Alp. Thomas Rickenmann, director. ExtraMileFilms, Switzerland, 2013. 100 minutes. www.alpfilm.ch

In *z'Alp*, Thomas Rickenmann interweaves majestic landscapes of the Swiss alps, overland travel as animals and their minders move together uphill, and the intimate spaces of family life. He shifts seamlessly among these elements to impart an experience of annual treks from valley to mountain that have been playing out for centuries in Switzerland. Each year, farmers shift their livestock to fields at higher elevations, following the spring as it rolls up mountainsides and thus allowing the lower fields to regrow in time for the livestock's autumn return.

The film features three families, who live in three regions of Switzerland. Rickenmann intercuts their separate journeys to highlight common connections with the environment and the many struggles occasioned by the livestock and terrain. Reflections of the distinctive traditions of the families and their regions occur throughout the film. For instance, a cappella performances of local indigenous folk music accompany many of the landscape sequences. Aside from the bouts of song and discordant but joyful ringing of cowbells, *z'Alp* is a very quiet film, which gives the viewer space to relax and take in the scenery.

CREDITS: *SAND WARS*, © SAND WARS; *TINY*, © KEVIN HOTH/COURTESY MERETE MUELLER AND CHRISTOPHER SMITH; *Z'ALP*, © EXTRAMILEFILMS 2013

Rickenmann effectively conveys the feel of these alpine climbs: capturing the closed-in feeling of mounting a narrow, rough staircase with a file of stumbling cows and the humbling sensation of walking along as one of a few humans among a swarm of leaping sheep. He neatly accomplishes the latter through the use of a drone-mounted camera that, soaring above the assembled creatures, removes the slight height difference between people and sheep and forces them all into one abstract traveling mass.

Inside the family farmhouses and shared dwellings along the path, we hear the farmers' stories of past treks and changes over the years (such as the occasional addition of a truck or helicopter to complement the long days of walking). Many of these interior scenes are warmly lit and accompanied by a meal, providing a contrast to the feeling of exposure encountered on the slopes. Perhaps most important, *z'Alp* presents its subject not like a relic of a bygone era but as a living experience. We see small children and young adults growing up with the mountains and the trek as vital parts of their lives.

– Sarah Crespi

Africa: Kalahari. Katrina Bartlam, director. BBC Natural History Unit, UK, 2013. 59 minutes. www.bbc.co.uk/programmes/p010jc6r

From its opening breathtaking scenes of the sweeping Namib sand dunes to the closing moments of the Sun setting over the Etosha Salt Lake, ***Kalahari*** garnered oohs and aahs from the younger members of its audience. Responses ranged from squeals of joy at the perennial crowd-pleasing meerkats to ouches as a cheeky "teenage" leopard trying to snag his mother's prey out of its arboreal hiding place fails and lands with a thump on the ground below.

The Kalahari ("land of great thirst") encompasses 900,000 km^2 of desert and semidesert savannah in Botswana, Namibia, and South Africa. Shot in some of the most inhospitable territory on Earth, this stunning episode from a BBC series on African natural history narrated by David Attenborough boasts several cinematographic firsts. Using special starlight cameras and tiny micro-

phones hidden around a rare water hole, the dedicated film team recorded a veritable throng of endangered black rhinos out for a nightly drink. The team also obtained unique footage of two black rhinos attempting to mate. Given that every day, on average, poachers kill a black rhino for its horns (sadly worth their weight in gold), Attenborough suggests that we may never witness such a sight again.

In another extraordinary clip, an old and a young bull giraffe battle for the rights to a tiny patch of oasis and a young female. Striking slow-motion shots capture the neck-to-neck combat as the males strive to bring one another down. A third eye-popping scene takes viewers into Namibia's subterranean Dragon's Breath Lake, whose ancient water is home to the endemic blind golden catfish.

Like so much of Attenborough's incomparable natural history work, the film will contribute greatly to conservation by educating the public about the fragility of Earth's ecosystems and its threatened wildlife treasures.

– Orla M. Smith

Blood Glacier (Blutgletscher) [or **The Station].** Marvin Kren, director. Allegro, Austria, 2013. 93 minutes. www.allegrofilm.at/filme/blutgletscher

Not an environmental disaster movie nor even a movie about the environment, *Blood Glacier* is an old-fashioned horror movie. A low-budget creature feature in the grand B movie tradition, it borrows liberally from the horror movie canon and relies on a positive overabundance of genre clichés. Its presence at an environmental film festival is surely an indication of the organizers' sense of humor.

A rather tenuous plot device links the retreat of glaciers to the appearance of a ghoulish horde of animal chimeras. A nondescript red microbe locked in the ice of a glacier high in the Alps is exposed as the ice melts, coloring the glacier. A small team of scientists working in a nearby climate-monitoring station discovers the microbe and then learns that local animals exposed to the

microbe hybridize with their prey. A rift develops among the researchers about the significance of the discovery—does its scientific value outweigh the danger to society?—and how it might influence their future in the light of an imminent assessment visit by a government minister. Needless to say, their inaction leads to disaster. The monsters (which include a beetle-fox, an insect-ibex, and a bee-crow) begin to menace the scientists as well as the visiting government delegation.

Clearly made on the cheap, the movie has few computer-graphics effects. Most of the monsters are physical (and not always plausible) models. The plot is predictable, and the director falls back on "jump scares" and poorly lit scenes to draw out the horror. But for all its many failings, the film is not a failure. Gerhard Liebmann (the renegade scientist Janek) gives a performance far beyond the material's merit. Brigitte Kren (Minister Bodicek) is a delight to watch in her role as an older woman, taking control of the disastrous situation, saving those that she can, and marshaling the little eccentric band of survivors. The show's real star, though, is the location. Set high up among the mountains, the research station is surrounded by great piles of scree, rubble chewed up by the glaciers and laid bare by their retreat. It's a rugged, bony, and mostly lifeless place—unfriendly and unforgiving, a threat in and of itself to those that stray into it.

Perhaps the landscape is a metaphor for our effects on the world: It sometimes seems we are hell-bent on making our home a hostile, alien place, where monsters might well rise up out of the ground. In the final scene, our heroes fly to safety over one of the glaciers, stained red by the microbe, and just for a moment it looks like a vast and livid wound, as if Earth has been stabbed and its flesh laid open. This fleeting image is more disturbing, and more fittingly horrifying, than any other in the film.

– Guy Riddihough

10.1126/science.1253377

CREDITS: *AFRICA: KALAHARI*, © AFRICA: KALAHARI; *BLOOD GLACIER*, © ALLEGRO FILM

Published by AAAS

SCIENCE EDUCATION

Convergence Between Science and Environmental Education

Citizen science and concerns about sustainability can catalyze much-needed synergy between environmental education and science education.

Arjen E. J. Wals,[1]* Michael Brody,[2] Justin Dillon,[3] Robert B. Stevenson[4]

Urgent issues such as climate change, food scarcity, malnutrition, and loss of biodiversity are highly complex and contested in both science and society (*1*). To address them, environmental educators and science educators seek to engage people in what are commonly referred to as sustainability challenges. Regrettably, science education (SE), which focuses primarily on teaching knowledge and skills, and environmental education (EE), which also stresses the incorporation of values and changing behaviors, have become increasingly distant. The relationship between SE and EE has been characterized as "distant, competitive, predator-prey and host-parasite" (*2*). We examine the potential for a convergence of EE and SE that might engage people in addressing fundamental socioecological challenges.

Since the end of World War II, SE has been driven primarily by a need to develop a sufficient pool of science and engineering talent to accelerate innovation and to remain competitive. EE emerged in the early 1960s out of a need to respond to emergent environmental crises. It tried to do so by developing the ecological and environmental literacy required to understand the sociopolitical, value-laden, place-based, and emotional contexts in which environmental issues arise and need to be resolved. An example of the difference between early SE and EE is that, while the former might teach students how to monitor water quality, identify pollutants, and understand technologies that can reduce pollution, EE would involve an analysis of circumstances and behaviors that caused the pollution, as well as identifying ways to clean up a river involving the local community, policy-makers, and industry.

The complex nature of current sustainability challenges, and the need for competent citizens who can adequately respond to them, is such that EE and SE need to develop a mature symbiotic relationship. The recent *International Handbook of Research on Environmental Education* (*3*) describes a trend in favor of such convergence, which, in combination with increased interest in citizen science supported by information and communications technology (ICT), may make education more responsive to current global challenges.

Science education and environmental education do not have to clash. The Harlem Success Garden in New York City is a living classroom where students grow their own produce.

CREDIT: RICHARD B. LEVINE/NEWSCOM

Research in Environmental Education

Initially, much research in EE (especially in the United States) focused on the effectiveness of EE activities in changing individual environmental behaviors. This approach contributed to the persistent but ill-founded assumption that there is a simple linear relationship between knowledge, awareness, attitude, and environmental behavior. Research, most notably from social psychology, has long revealed that this is far too simplistic an explanation of what affects people's actions (*4*).

Today much EE research focuses on investigating the conditions and learning processes that enable citizens, young and old, to (i) develop their own capacity to think critically, ethically, and creatively in appraising environmental situations; (ii) make informed decisions about those situations; and (iii) develop the capacity and commitment to act individually and collectively in ways that sustain and enhance the environment (*3*).

This new focus implies less emphasis on establishing linkages between educational interventions and behavioral outcomes. More attention is now being given to an understanding of the learning processes and the capacities of individuals and communities needed to help resolve complex socioecological issues. This focus also calls for a better understanding of people's cognitive and emotional responses to environmental issues. These responses are influenced by their worldviews and belief systems, which in turn are linked to identity (*5*). For example, recent research has rendered problematic a focus solely on better comprehension of the science of climate change owing to "identity-protective cognition theory," which indicates that many people's positions on climate change are largely shaped by their political and religious affiliations and identities (*6*).

EE research currently offers insights into how to engage the public with environmental issues through participatory action,

[1]Wageningen University, 6708PB Wageningen, Netherlands. [2]Montana State University, Bozeman, MT 59717, USA. [3]King's College London, London SE1 9NH, UK. [4]James Cook University, Cairns, Qld 4870, Australia. *Corresponding author. E-mail: arjen.wals@wur.nl

Downloaded from www.sciencemag.org on May 8, 2014

Published by AAAS

whereas SE research has traditionally provided insights into learners' understanding of the natural systems and processes that are at the heart of these issues (*7*). The necessity of connecting the two has been recognized by the North American Association for Environmental Education (NAAEE) in a joint initiative with Underwriters Laboratories to link environmental education with science, technology, engineering, and mathematics (E-STEM) (*8*). Recently, a number of prominent SE researchers have stressed the importance of science educators engaging with sustainability issues by complementing disciplinary understanding with more integrative thinking and linking scientific knowledge with other forms of knowledge such as indigenous knowledge and local (place-based) understanding (*9*). So, although SE may have evolved separately from EE, recent research and developments in both EE and SE converge toward generating an interdisciplinary and contextual approach to integrating research in science, education, and the environment (*3*).

Citizen Science

At the same time, the rise of citizen science (CS) also enables for people to engage with science on relevant environmental issues in collaboration with scientists working in local contexts (*10*, *11*). In a recent review, Dickinson *et al*. reported that the primary impacts of CS are seen in biological studies of global climate change (*12*). The authors conclude that CS and the resulting ecological data can be viewed as a public good that is generated through increasingly collaborative tools and resources. They consider public participation in science a critical component of what they call Earth stewardship.

Citizen science most often refers to community-based local monitoring of changes in the environment using simple data acquisition devices and communication tools. More recently, CS has taken advantage of the Internet, social media, and mobile applications in crowd-sourcing scientific data (*13*)—resulting in what we refer to as ICT-supported CS. This trend connects well with recent EE research that identifies the use of social media as well as technology-enhanced citizen data acquisition as a way to enhance the interaction between research in science, education, and the environment (*3*).

Linking EE, SE, and CS

Creating synergy between EE and SE through ICT-supported CS provides opportunities for new forms of education that can lead to the engagement of seemingly unrelated actors and organizations in making new knowledge and in taking the actions necessary to address socioecological challenges. An example of such synergy emerges from so-called "whole-school approaches" to sustainability and the creation of eco-schools, where different forms of learning (e.g., inquiry-based, disciplinary, and social learning) blend with the use of ICT, citizen science, and community engagement (*14*). Such approaches may involve redesigning school grounds using knowledge from SE—to give such spaces a more central place in teaching about health, food, and ecology—as well as using EE to strengthen community involvement and develop a sense of place.

For instance, by creating "edible gardens" (see the photo), schools can, with the involvement of a wide range of societal actors (e.g., a local garden center, a restaurant, a community organization, and the local government), simultaneously improve the quality and relevance of their education and transform their relationship with the local community (*15*). Soil preparation, seed selection, planting, maintaining, harvesting, and preparing a meal require basic scientific knowledge that connects with the SE curriculum while also creating other benefits, such as community engagement, learner empowerment, improved personal health, and a better connection with food and place (*16*).

Recent EE research indicates that the use of CS in these blended or hybrid learning configurations helps learners contribute to the quality of their local environment (*3*). This process can be enhanced by projects such as YardMap, an ICT-supported CS project, funded by the U.S. National Science Foundation, which enables members of the public not only to increase their appreciation of their local "yard" through the use of mapping software but also to take action for improving the habitats of birds.

Place and Identity

The examples of SE and EE converging, supported by CS, emphasize the importance of place and place-based identity in determining our relations with the planet. The focus on identity is timely: The complexity and uncertainty brought on by globalization and the rapid pace of technological and social change result in substantial cultural shifts, including a search for meaning and affiliation in locally defined identities (*5*). The reasons for the recently established disconnect between people and place that results from a preoccupation with and dependency on ICT (*17*) are underresearched, but there is some evidence that such technologies can actually reconnect people and places (*18*). Numerous examples exist of citizens monitoring changes in the environment (e.g., bird migration patterns and quality of water, soil, and air) using geographic information systems, cell phones, and specially designed monitoring applications (*11*). As such, ICT devices actually get people to go outdoors, even those who normally are not inclined to do so. Participation in scientific studies through ICT-supported CS offers the potential to deepen the experience of the physical place of which people are part and to develop their understanding of how science works.

Society has to learn how to address sustainability challenges. Creating synergy between EE and SE mediated by ICT-supported CS provides an opportunity for such learning. We advocate support for collaborative research efforts among scientists, educators, and the public, linking science and society with place and identity, through more effective processes of public engagement and learning that can result in meaningful socioecological outcomes. The data gathered and shared using ICT can provide useful input to environmental scientists while simultaneously empowering citizens to engage in ongoing debates about local and global sustainability issues and what needs to be done to address them.

References and Notes

1. M. C. Nisbet, *Env. Sci. and Pol. for Sust. Dev.* **51**, 12 (2009).
2. A. Gough, *Int. J. Sci. Educ.* **24**, 1201 (2002).
3. R. B. Stevenson, M. Brody, J. Dillon, A. E. J. Wals, Eds., *International Handbook of Research on Environmental Education* (Routledge, New York, 2013).
4. A. Kollmuss, J. Agyeman, *Environ. Educ. Res.* **8**, 239 (2002).
5. R. B. Stevenson, C. Stirling, in *Engaging Environmental Education: Learning, Culture and Agency*, R. B. Stevenson, J. Dillon, Eds. (Sense Publishers, Rotterdam, 2010), pp. 219–238.
6. D. M. Kahan, H. Jenkins-Smith, D. Braman, *J. Risk Res.* **14**, 147 (2011).
7. R. W. Bybee, *Science* **329**, 996 (2010).
8. NAAEE, E-STEM (2013); www.naaee.net/sites/default/files/E-STEM/ESTEM_NAAEE2013TearSheet.pdf
9. R. Tytler, *Res. Sci. Educ.* **42**, 155 (2012).
10. J. L. Shirk *et al.*, *Ecol. Society* **17**, 29 (2012).
11. R. Bonney, *et al.*, *Science* **343**, 1436 (2014).
12. J. L. Dickinson *et al.*, *Front. Ecol. Environ* **10**, 291 (2012).
13. J. Silvertown, *Trends Ecol. Evol.* **24**, 467 (2009).
14. L. G. Hargreaves, *Educ. Rev.* **6**, 69 (2008); www.developmenteducationreview.com/issue6-perspectives2.
15. J. R. Ruiz-Gallardo, A. Verde, A. Valdes, *J. Environ. Educ.* **44**, 252 (2013).
16. A. C. Bell, J. E. Dyment, *Environ. Educ. Res.* **14**, 77 (2008).
17. P. Zaradic, *Sci. Am.* **18**, 24 (2008).
18. J. L. Dickinson, R. L. Crain, H. K. Reeve, J. P. Schuldt, *Trends Ecol. Evol.* **28**, 561 (2013).

10.1126/science.1250515

Published by AAAS

CELL BIOLOGY

A SWELL Channel Indeed

A constituent of an elusive anion channel that maintains cellular water balance is identified.

Joseph A. Mindell

Water constitutes about two-thirds of the mass of most living organisms. It serves as a solvent in the cell cytoplasm and exterior, and like other molecules, it moves down its concentration gradient by osmosis. Indeed, the diffusion of water is responsible for the dilemma in *The Rime of the Ancient Mariner*, Samuel Taylor Coleridge's epic poem: "Water, water, everywhere, Nor any drop to drink." If the mariner were to drink seawater, with its high concentration of dissolved salts, the water in his cells would diffuse out (down its concentration gradient), dehydrating the cells and killing the seafarer. Two recent studies, by Qiu *et al*. (*1*) and by Voss *et al*. on page 634 in this issue (*2*), advance our understanding of how animal cells deal with such osmotic challenges.

Because their plasma membranes are fluid, flexible, and permeable to water, animal cells tend to swell, even to the point of bursting, when exposed to dilute environments. Some mammalian cells face daily osmotic challenges, such as intestinal cells in response to drinking spring water or kidney cells involved in concentrating and diluting urine. Pathological conditions, such as low concentration of sodium in blood (hyponatremia), also cause large fluxes of water into cells and lead to swelling, with potentially fatal consequences. To mitigate these challenges, animals have evolved subtle, complex mechanisms to regulate cell volume in response to osmotic stress (*3*). In the case of cells bathed in hypotonic media, the response is called regulatory volume decrease, during which solutes are released into the medium to offset the influx of water as it moves down its concentration gradient (see the figure). The mechanisms of regulatory volume decrease include the opening of ion channels that are activated by changes in osmolarity. This involves anion and cation channels, allowing cells to move salts either in or out, thereby reducing the osmolarity differences that drive cell volume changes. Among these channels is the volume-regulated anion channel (VRAC). Its activity was identified more than 20 years ago (*4*), but its identity has been a mystery. Many candidate proteins have been proposed, but none possesses the required spectrum of functional features (*3*).

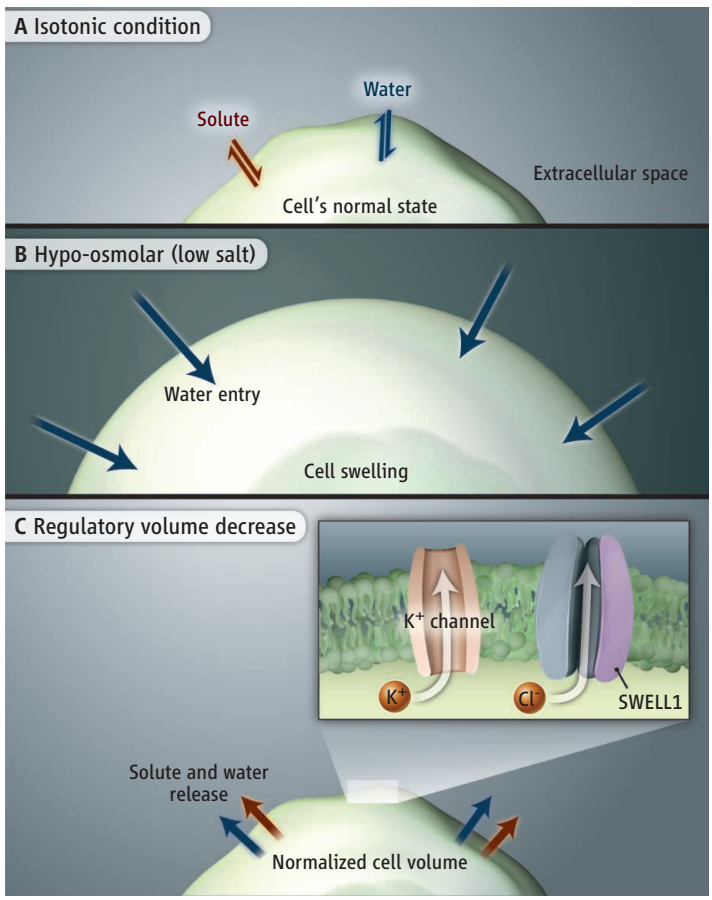

All is SWELL. (**A**) Under isotonic conditions, solute concentration is the same inside and outside of an animal cell. (**B**) When a cell is exposed to hypo-osmolar (low salt) media, a gradient of water forms across the cell membrane so that water flows into the cell, leading to swelling. (**C**) Swelling activates the regulatory volume decrease response to release solutes, thereby balancing the osmotic gradient and normalizing cell volume. The ion channels that open including a potassium (K^+) channel and the SWELL1 anion channel.

Qiu *et al*. and Voss *et al*. have identified a constituent of the VRAC channel by designing a fluorescent protein–based cellular assay for anion flux. Both groups used this test to screen whole-genome human libraries in which small interfering RNAs targeted more than 20,000 known and predicted human genes to reduce their expression. Each group identified a single (identical) gene of previously unknown function called *Leucine-Rich Repeat–Containing 8A* (*LRRC8A*) (*2*), but perhaps more aptly named *SWELL1* (*1*). Both groups show that reducing *SWELL1* expression decreases VRAC activity in multiple cell types, including human T lymphocytes in which swelling-activated electrical currents were originally reported (*4*). Thus, lack of SWELL1 disrupts electrical properties of the membrane that VRAC would otherwise impart.

These findings alone do not prove that SWELL1 is VRAC (or part of it) because SWELL1 could be a regulator of the actual swelling-activated channel. However, several lines of evidence strongly support the idea that SWELL1 is an integral component of VRAC. Using a mutagenic scan of *SWELL1*, Qiu *et al*. found that altering the charge of a single amino acid in SWELL1 changes the relative preference of VRAC for two anions (chloride and iodide) that go through the channel. The authors also found that chemical modifications of SWELL1 subtly change VRAC properties. Thus, the altered residue is likely close to the actual pore traversed by ions and, consequently, that this part of the protein is situated close to that hole. Similarly, Voss *et al*. found that altering the mix of LRRC8 subunits (there are five members of the *LRRC8* gene family) could subtly change the timing of VRAC opening and closing, indicating that the LRRC8 proteins are probably intimately associated with the channel. Moreover, the SWELL1 protein sequence is distantly related to that of a family of proteins called pannexins, which form hexameric ion channels, hinting that SWELL1 might have a sim-

Membrane Transport Biophysics Section, Porter Neuroscience Research Center, National Institute of Neurological Disorders and Stroke, National Institutes of Health, Bethesda, MD 20892, USA. E-mail: mindellj@ninds.nih.gov

CREDIT: V. ALTOUNIAN/SCIENCE

Published by AAAS

ilar function. These findings together suggest that SWELL1 is an integral part of VRAC.

The contention that SWELL1 is part of VRAC invites questions about the other parts of this channel. Voss *et al*. suspected that the four other members of the *LRRC8* gene family might play a role in VRAC activity. Analysis of cell lines constructed to disrupt different combinations of single and multiple *LRRC8* genes revealed that although cells lacking *SWELL1* (*LRRC8A*) lacked VRAC activity, individual deletion of each of the other *LRRC8* genes was tolerated (albeit with subtle changes in VRAC activity). However, even with *SWELL1* (*LRRC8A*) preserved, no VRAC activity appeared in cells lacking the other four *LRRC8* isoforms. Furthermore, in a cell line with all five *LRRC8* genes deleted (and no remaining measurable VRAC activity), adding a combination of *SWELL1* and any one of *LRRC8C*, *D*, or *E* genes restored some form of VRAC behavior. Hence, a functional VRAC complex probably includes SWELL1 and at least one other LRRC8 isomer.

The identification of the SWELL protein family as an integral part of VRAC provides a powerful tool to analyze other parts of the cell's regulatory volume decrease pathway, from possible additional components of the VRAC complex that directly sense volume (if not SWELL itself) to other regulators of the cellular volume response. Structural and functional analyses of VRAC should yield insights into its basic mechanisms of action and may help in the development of drugs to manipulate VRAC in disease.

References

1. Z. Qiu *et al*., *Cell* **157**, 447 (2014).
2. F. K. Voss *et al*., *Science* **344**, 634 (2014); 10.1126/science.1252826.
3. E. K. Hoffmann *et al*., *Physiol. Rev.* **89**, 193 (2009).
4. M. D. Cahalan, R. S. Lewis, *Soc. Gen. Physiol. Ser.* **43**, 281 (1988).

10.1126/science.1254591

ASTRONOMY

Next Steps for Cosmology

Recent observations from Planck and BICEP2 reveal key signatures of the Big Bang—what are the next questions for CMB cosmology in space?

Joseph Silk[1,2] and Jens Chluba[2]

Experiments on the ground, balloons, and satellites have revolutionized our knowledge of the Big Bang by measuring the fossil glow from the first instants of the universe, the cosmic microwave background (CMB) radiation. Infinitesimal fluctuations in the photon temperature have been found, revealing the seeds of all large-scale structures, from galaxies to clusters of galaxies and superclusters. The detected wiggles in the distribution of the temperature fluctuations measure the gravitational coupling between dark matter, baryons, and radiation as the universe emerged from its opaque fireball phase. These measurements, pioneered by the Cosmic Background Explorer (COBE) (*1*) and then greatly refined by its successors, the Wilkinson Microwave Anisotropy Probe (WMAP) (*2*) and Planck (*3*) satellites, have allowed precise determinations of the key parameters of our universe—age, dark matter, dark energy content, and even the number of different types of neutrinos, as well as the strength and distribution of the primordial density fluctuations. Less than two decades ago, it was debated whether the major constituent of the universe, dark energy, even existed. Now its contribution is measured to an accuracy of a few percent.

One of the goals of cosmology is to probe early epochs of the Big Bang. The ultimate target is the epoch of cosmological inflation, a brief period of ultrarapid expansion some 10^{-35} s after the Big Bang, when the seed density fluctuations are thought to have been created. It is believed that inflation also explains the size of the observable universe and the near Euclidean geometry of space.

Inflation has a remarkable implication. When it occurred, there was an immense explosion of space accompanied by the creation of a background of gravitational waves. These waves propagate freely to us, unimpeded by the intervening matter, and carry a very weak degree of polarization that is imprinted on the CMB radiation (*4*, *5*). Polarization can be generated either by compressional modes or by shearing modes. The former make the seed fluctuations; the latter are a unique signature of the shaking induced by the passage of gravity waves.

Cosmologists call the shear effects tensor mode polarization, as opposed to the compressional scalar modes. Scalar modes are generated by the gravity-induced motions of free electrons scattering CMB photons. This was seen by WMAP, but the much smaller tensor polarization modes from inflation are harder to detect. The pursuit of tensor mode polarization from inflation is considered to be one of the final frontiers in CMB cosmology, and several experiments—in the Atacama Desert, at the South Pole, and from balloons—are already searching or preparing for the challenge. These future CMB missions will target tensor-to-scalar ratios as low as 1 in 10,000.

The scientific landscape changed dramatically a few weeks ago, when the BICEP2 (Background Imaging of Cosmic Extragalactic Polarization) collaboration announced (*6*) a first detection of tensor mode polarization at degree angular scales. That measurement transformed CMB science overnight. Previously, the precise level of tensor modes was uncertain, but now a definite target has been identified, and larger than even the optimists had expected.

We now have a unique signal, one that only gravitational waves provide, from very near the beginning of the universe. Within the next decade, terrestrial experiments should be able to characterize the tensor mode contributions to high precision, developing a new perspective on early-universe physics. The key question now, apart from the confirmation that many experiments are rushing to provide, is: What next? It is unclear how much a future CMB space mission dedicated to tensor modes could add to our understanding of inflation, given the long lead time needed to prepare for such an endeavor. Is there any additional goal for a future CMB mission?

One option would be a space-borne spectrometer (possibly with imaging capabilities) that targets tiny deviations of the CMB energy spectrum from the blackbody shape characterizing the thermal history of our universe. Space gives a decisive advantage for spectroscopy over ground-based observations. Absolute spectrometric measurement of the CMB with high sensitivity could improve on the COBE limit by at least three orders of magnitude and reach down to tens of nanokelvin, a sensitivity already achieved over broad frequency bands at low angular resolution by BICEP2.

[1]Institut d'Astrophysique de Paris, 75014 Paris, France. [2]Department of Physics and Astronomy, Johns Hopkins University, Baltimore, MD 21218, USA. E-mail: silk@iap.fr; jchluba@pha.jhu.edu

Published by AAAS

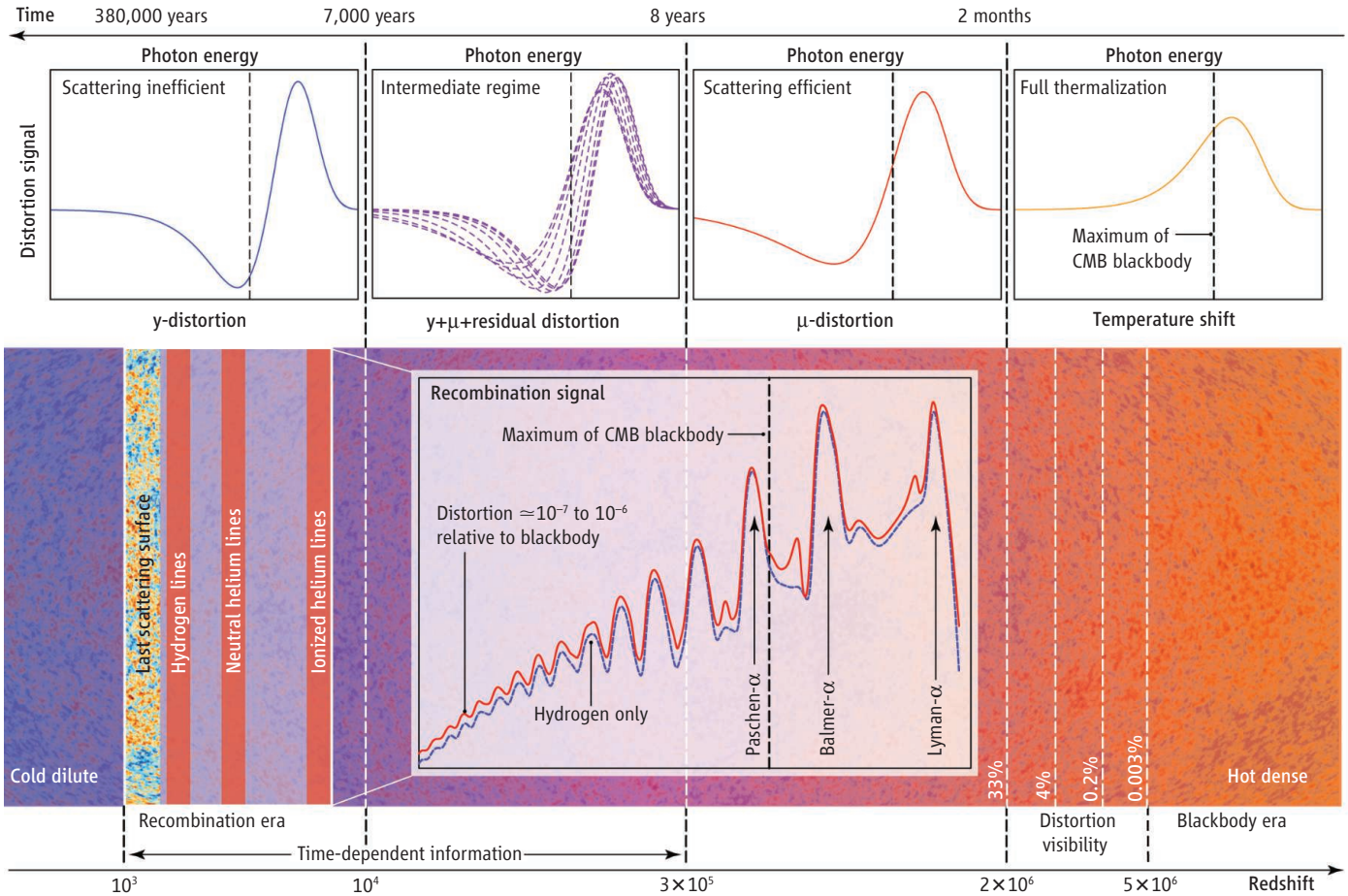

Different distortion signals. The "fingerprint" from the recombination era is produced some 260,000 years (hydrogen), 130,000 years (neutral helium), and 18,000 years (ionized helium) after the Big Bang (*11*). Today these lines are redshifted by more than a factor of 1000 and are visible in the CMB. The primordial μ, y, and residual (non-μ/non-y) distortions arose through interactions of photons and electrons after energy release 2 months after the beginning of the universe.

The optimists would say that with such a huge improvement in sensitivity, one is bound to discover new physics, thereby opening an unexplored window to the early universe, peeking beyond the CMB anisotropies and deep into the predecoupling era. A polarization-sensitive absolute spectrometer with two 55-cm apertures, dubbed PIXIE, was proposed to NASA in 2011, and in Europe, PRISM, an improved Planck-like imager and PIXIE-like spectrometer, was put forward last year (*7*). But are these missions sensitive and scientifically broad enough to capture the imagination of the CMB community in the post-BICEP2 era?

Cosmologists believe that there should be deviations from a blackbody spectrum. One could test energy release by exotic processes such as evaporating black holes or decaying particles back to a few months after the beginning of the universe; before that, all emission rapidly turns into blackbody radiation.

But is there a definite goal beyond searching for signs of new physics? Indeed there is, because the very growth of galaxies from primordial fluctuations leaves an early imprint as the fluctuations struggle to grow against the viscous-like drag of the radiation. Gravitational instability predicts inevitable distortions, and a future spectrometer could see them, opening an independent path toward understanding the early universe.

The search will be difficult, however, as the opaque fog created as photons scatter off electrons means that information reaching our telescopes is scrambled. Primordial distortions are of two main types: one due to the late transfer of photons from low to high energies by contact with hot electrons (the y-distortion), and one due to early photon emission and scattering (the μ-distortion) with peaks at slightly lower frequencies (*8*, *9*). But there is even more information to be had, as in the intermediate regime a more complex and epoch-dependent signal is generated (*10*, *11*) (see the figure).

A revolutionary experiment with guaranteed return would do even more. It could target the recombination spectrum of hydrogen and helium from the last scattering epoch, when matter and radiation decoupled from one another 380,000 years after the Big Bang. With a large aperture [e.g., (*7*, *12*)], one could remove dirty patches of sky, combat source confusion, and push to higher sensitivity, opening up a new window for exploration of the primeval plasma from which all structure originated.

For astronomers, recombination lines are the ultimate exploration tool for gaseous nebulae throughout the observable universe. Detecting the recombination radiation would provide the ultimate proof that the universe cooled down from a hot primeval plasma, testing a fundamental aspect of the Big Bang model and providing a gold standard for measuring distortions produced by the earliest forming structure.

A more exotic goal would be to seek spectroscopically deviant patches in the CMB sky, as traces of the formation of other universes. These are predicted in eternal inflation, whereby vast numbers of other universes are envisaged to have peeled off from ours in

CREDIT: JENS CHLUBA

Published by AAAS

the past in order to explain why we inhabit just one favorable patch of a vast and mostly inhospitable multiverse.

The goals are immensely challenging for a future cosmology space mission, whether toward transformative polarization measurements, or to innovative spectral studies, or even to both, ideally via an imaging absolute spectropolarimeter, to arrive at the ultimate source and noise confusion limits of the cosmic microwave background. Such a mission should have some combination of angular resolution, spectral resolution, sensitivity, and polarimetry to probe unexplored physics and help anchor the Big Bang theory. Innovative design concepts are needed to point us in the optimal direction for the post-Planck and post-BICEP2 future of the CMB community.

References

1. C. Bennett *et al.*, *Astrophys. J.* **508**, 123F (1998).
2. C. Bennett *et al.*, *Astrophys. J.* **208** (suppl.), 20B (2013).
3. P. Ade *et al.*, http://arxiv.org/abs/1303.5076 (2013).
4. M. Kamionkowski, A. Kosowsky, *Phys. Rev. D Part. Fields* **57**, 685 (1998).
5. U. Seljak, M. Zaldarriaga, *Phys. Rev. Lett.* **78**, 2054 (1997).
6. P. Ade *et al.*, http://arxiv.org/abs/1403.3985 (2014).
7. P. Andre *et al.*, *J. Cosmol. Astrophys.* **2**, 006 (2014).
8. R. Sunyaev, Y. Zeldovich, *J. Astrophys. Space Sci.* **4**, 301 (1970).
9. W. Hu, J. Silk, *Phys. Rev. D Part. Fields* **48**, 485 (1993).
10. J. Chluba, R. Sunyaev, *Mon. Not. R. Astron. Soc.* **419**, 1294 (2012).
11. R. Sunyaev, J. Chluba, *Astron. Nachr.* **330**, 657 (2009).
12. A. V. Smirnov *et al.*, *Proc. SPIE* 8442, Space Telescopes and Instrumentation 2012, Optical, Infrared, and Millimeter Wave 84424C (2012).

10.1126/science.1252724

AIDS/HIV

Host Controls of HIV Neutralizing Antibodies

The unusual traits of broadly neutralizing antibodies for HIV-1 are stimulating new strategies to induce their production through vaccination.

Barton F. Haynes and Laurent Verkoczy

A key goal of developing a vaccine for human immunodeficiency virus–1 (HIV-1) is that it should stimulate the production of broadly neutralizing antibodies (bnAbs) that recognize conserved regions of the viral envelope. Unfortunately, no candidate vaccine has proved capable of eliciting such antibodies, possibly because conserved epitopes are obscured by dense glycan "shields" on the viral surface, or because of a failure to produce HIV-1 envelope immunogens that retain their native structure. After 20 years of immunization studies and three HIV-1 vaccine efficacy trials, the induction of bnAb responses by HIV vaccines remains elusive. However, progress in circumventing host factors that limit bnAb induction is now leading to new concepts in vaccinology and immunogen design that hopefully can be applied not only to HIV-1, but also to other vaccines in need of bnAb induction such as for hepatitis C and influenza viral infections.

A minority of HIV-1-infected individuals generate the amounts of bnAbs needed to neutralize a high percentage of virus, but this amount of antibody is present in the plasma only after months to years of infection. The advent of new technologies has allowed the isolation of bnAbs from such patients, the expression of bnAbs, and the reconstruction of bnAb lineages through computational methods. Consequently, much progress has been made in identifying new viral envelope epitopes that are recognized by bnAbs, elucidating the structure of these epitopes, and defining the developmental pathways of B cells that produce bnAbs. We now know that bnAbs bind to at least four regions of the HIV-1 envelope: the binding site on the viral envelope protein gp120 for T cells (CD4 co-receptor for HIV-1); the membrane-proximal region of envelope protein gp41; and two overlapping, glycan-rich regions around the first, second and third variable (V1, V2, V3) regions of gp120 (*1*).

HIV-1 bnAbs have one or more unusual traits: high amounts of somatic hypermutation; poly- or autoreactivity with host or environmental antigens; and a long variable heavy-chain (V_H) complementarity-determining region 3 (HCDR3s) (*2*), the most diverse component of the antibody's antigen-binding site. Unfortunately, the production of antibodies with these traits is generally disfavored by the immune system.

High-affinity antibody results from the somatic hypermutation and affinity-driven selection of B cells in germinal centers of lymphoid tissues. B cell receptors (BCRs), which recognize antigen, possess an immunoglobulin moiety that is identical to the antibodies that these lymphocytes manufacture once stimulated. Whereas pathogens such as influenza virus induce high-affinity, protective, neutralizing antibodies with ~5% V_H mutations, HIV-1 bnAbs have from ~15% to ~30% V_H mutations (*2*). In general, a ceiling exists for affinity maturation such that the dissociation constant (K_d) for binding of antigen to the BCR is ≈0.1 nM (*3*). With the exception of HIV-1 bnAbs, far fewer than 30% mutations are needed in most antibodies to attain nanomolar affinities for antigen. Indeed, the accumulation of antibody mutations eventually decreases binding of the BCR to antigen and reduces cell survival. It is not known what drives mutation rates in the evolution of bnAbs to HIV-1 above those found in neutralizing antibodies to other pathogens. To acquire structurally disfavored antibodies necessary for broad neutralization, it may be that somatic hypermutations must recur over prolonged periods. The high frequency of mutations in bnAbs may reflect the difficulty of acquiring atypical genetic changes necessary for bnAb activity. Insight into the functional importance of bnAb somatic mutations has come from the observation that some mutations that accumulate in antibody framework regions are required for broad neutralization (*4*).

Polyreactivity (antibody binding to multiple, dissimilar antigens) and autoreactivity (binding to one or more self-antigens) are common traits of bnAbs (*5*–*8*). In some cases, the poly- or autoreactivity of BCRs is the result of the viral mimicry of host antigen; this reactivity is sufficient to activate central and peripheral tolerance (*7*–*10*). Hope for eliciting bnAbs that may be affected by immune tolerance comes from the observation that in mice genetically engineered to produce bnAbs, a minority of B cell clones enter the peripheral lymphoid tissue as anergic, or functionally silenced, that can be activated by appropriately designed immunogens (*10*).

Duke Human Vaccine Institute, Departments of Medicine, Immunology and Pathology, Duke University School of Medicine, Durham, NC 27710, USA. E-mail: barton.haynes@duke.edu.

Published by AAAS

Is bnAb poly- or autoreactivity necessary for antiviral activity? One possibility is that bnAb polyreactivity is required for binding to sparse "spikes" of gp120 on the surface of HIV-1 virions, with effective bnAb binding dependent on interaction with both gp120 and associated host membrane epitopes (*6*). The neutralizing activity of bnAbs that react with membrane-proximal gp41 envelope protein and lipids is abrogated by mutations that eliminate antibody binding to the viral membrane.

Many bnAbs have unsually long HCDR3 regions. HCDR3 lengths in bnAbs specific for glycan epitopes in the V1 and V2 regions of gp120 range from 24 to 37 amino acids compared to a median of ~15 in other antibodies (*11*). Newly generated human B cells that express BCRs with long HCDR3 regions are frequently counterselected in the bone marrow, presumably because long HCDR3 regions tend to confer self-reactivity that invokes clonal deletion or interfere with the pairing of heavy and light chains as antibody architecture is forged during B cell development (*12*). Thus, the pool of B cells bearing receptors with long HCDR3 is reduced before their stimulation with antigen, thereby contributing to their rarity in response to HIV-1.

Other examples of viral mimicry of host are glycans on HIV-1 virions that are host-derived and are key targets of bnAbs. The presence of self-glycans on virions also has been proposed to limit the induction of glycan-targeting bnAbs by immune tolerance mechanisms (*13*). Modified glycans have been synthesized to not resemble self-glycans, but as yet have not induced glycan-specific antibodies that bind virions (*13*).

All B cell lineages are initiated by antigen binding to unmutated BCRs on naïve B cells, and lineages that produce bnAbs to HIV-1 are initiated by autologous virus or possibly cross-reactive host antigens (*2*, *8*, *14*). A strategy being tested is to design immunogens that bind to naïve BCRs and/or to later members of bnAb clonal lineages, so as to drive selectively disfavored or subdominant lineages (*2*) (see the figure). One of several new crystal structures of the gp120 trimer should guide the design of native HIV-1 envelope immunogens (*15*). Recent success in mapping coevolution of the viral envelope and bnAbs in HIV-1–infected individuals has identified epitopes as vaccine candidates that actually induced bnAbs in the setting of infection (*11*, *14*). However, because bnAbs are not made soon after HIV-1 infection but rather take months to years to develop, vaccination may also require repetitive immunizations over longer periods of time.

Both immunologic tolerance and difficulty in designing native viral envelope immunogens have conspired against eliciting the production of bnAbs to HIV-1 through vaccination. Now that these factors are better appreciated, we can hopefully accelerate the development of this much needed vaccine, as HIV-1 still infects more than 2 million people and kills more than 1 million people every year, worldwide.

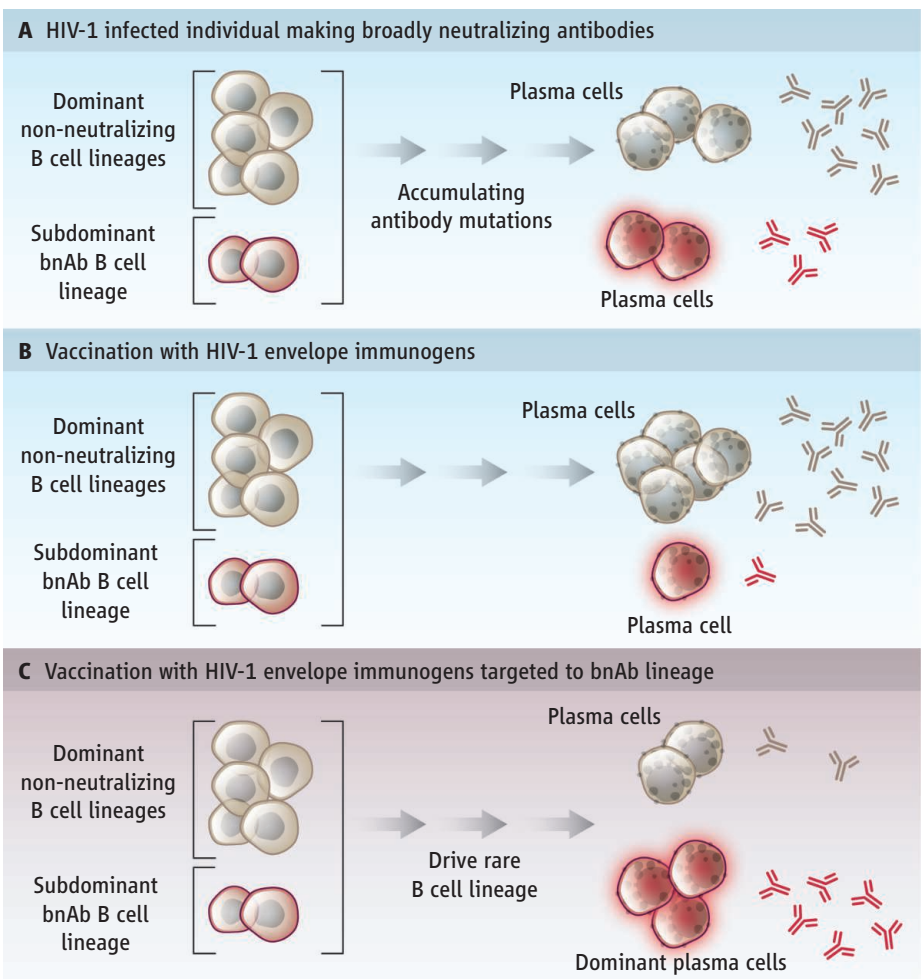

Eliciting broadly neutralizing antibodies to HIV-1. (A) During chronic HIV-1 infection of an individual, a rare B cell clonal lineage that produces a bnAb can emerge and survive after a long antibody maturation process in which large numbers of somatic mutations have accumulated. (**B**) In the setting of vaccination, B cells capable of generating bnAbs may be present at low frequency, along with higher-frequency non-bnAb B cells. Upon immunization, responding B cells differentiate into plasma cells, but non–bnAb-producing B cells are dominant. (**C**) The goal of successful immunization for bnAb induction is to use immunogens that specifically and selectively target the rare bnAb-producing B cell precursors and drive those lineages to become sufficiently dominant to produce protective plasma and tissue fluid bnAbs.

References and Notes

1. D. R. Burton, P. Poignard, R. L. Stanfield, I. A. Wilson, *Science* **337**, 183 (2012).
2. B. F. Haynes, G. Kelsoe, S. C. Harrison, T. B. Kepler, *Nat. Biotechnol.* **30**, 423 (2012).
3. F. D. Batista, M. S. Neuberger, *Immunity* **8**, 751 (1998).
4. F. Klein *et al.*, *Cell* **153**, 126 (2013).
5. B. F. Haynes *et al.*, *Science* **308**, 1906 (2005).
6. H. Mouquet *et al.*, *Nature* **467**, 591 (2010).
7. L. Verkoczy *et al.*, *Proc. Natl. Acad. Sci. U.S.A.* **107**, 181 (2010).
8. G. Yang *et al.*, *J. Exp. Med.* **210**, 241 (2013).
9. C. Doyle-Cooper *et al.*, *J. Immunol.* **191**, 3186 (2013).
10. L. Verkoczy *et al.*, *J. Immunol.* **191**, 2538 (2013).
11. N. A. Doria-Rose *et al.*, *Nature* 10.1038/nature13036 (2014).
12. E. Meffre *et al.*, *J. Clin. Invest.* **108**, 879 (2001).
13. K. J. Doores *et al.*, *Proc. Natl. Acad. Sci. U.S.A.* **107**, 17107 (2010).
14. H. X. Liao *et al.*, *Nature* **496**, 469 (2013).
15. J. P. Julien *et al.*, *Science* **342**, 1477 (2013).

Acknowledgments: Supported by a Center for HIV/AIDS Vaccine Immunology-Immunogen Design grant (UM1-AI00645), grant R01-AI87202 from the National Institute of Allergy and Infectious Disease, Division of AIDS, and a Collaboration for AIDS Vaccine Development Grant from the Bill and Melinda Gates Foundation. We thank G. Kelsoe for comments and collaboration.

10.1126/science.1254990

BIOCHEMISTRY

Trigger Factor Flexibility

A nuclear magnetic resonance study shows how the bacterial chaperone trigger factor can dynamically bind and release many different substrates.

Martin Gamerdinger and Elke Deuerling

Molecular chaperones are found in all cells and are essential for maintaining a functional proteome. The main function of chaperones is to promote correct protein folding by protecting nonnative proteins from folding along pathways that lead to protein misfolding and aggregation. To fulfill this task, chaperones must recognize a non-native protein, transiently bind to it, and then release it at precisely the right time to allow the substrate to proceed with its folding course. Many but not all chaperones use adenosine 5′-triphosphate (ATP) to control the dynamic substrate binding and release cycle (*1*). On page 597 of this issue, Saio *et al*. (*2*) unravel the structural basis and underlying mechanism of action of the ATP-independent chaperone trigger factor (TF).

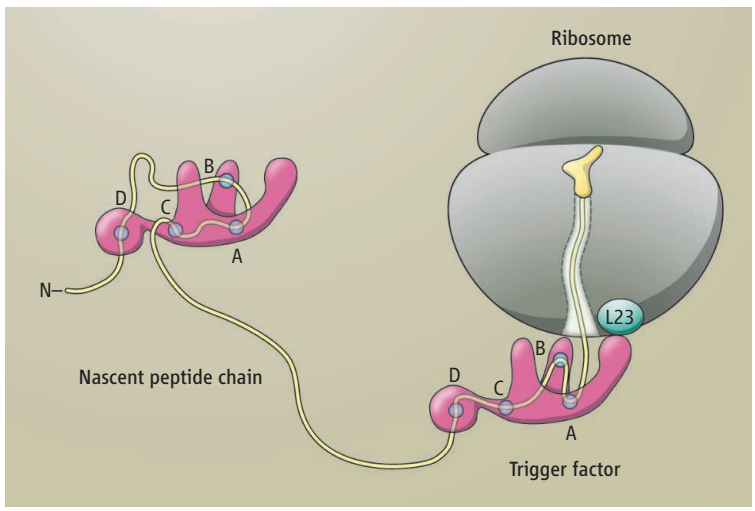

Plasticity in substrate binding. TF contacts the ribosome via ribosomal protein L23 and interacts with the nascent polypeptide that exits the ribosomal tunnel (dashed lines). As synthesis proceeds, TF may depart from the ribosome, remaining bound to the nascent polypeptide. A second TF molecule can then dock to the ribosome and interact with the same nascent chain. Saio *et al*. now show that TF interacts with the unfolded polypeptides through four different hydrophobic binding sites (blue, A to D) in its inner surface. The four binding sites show a high flexibility in their local architecture that allows binding to a large and diverse pool of substrates. Also, the order of engagement of these four sites may vary, as indicated in the two TF molecules.

TF is an abundant bacterial chaperone that associates transiently with ribosomes and binds to nascent polypeptide chains. It has an extended, dragon-like structure with a central body, two protruding arms, a head, and a tail region. Bound to the ribosome as a monomer by its amino-terminal tail, TF leans over the ribosomal exit tunnel, thereby exposing its large interior surface speckled with multiple hydrophobic patches to the exiting nascent peptide chain (*3*) (see the figure). Eukaryotes use structurally different ribosome-associated chaperones, but bacterial TF is by far the best-studied one and is regarded as a paradigm for ribosome-bound chaperones that support the folding of newly synthesized proteins (*4*).

The first evidence that TF acts as a chaperone came from experiments showing that combined loss of TF and another chaperone led to synergistic defects in protein folding, resulting in global protein aggregation and decreased viability (*5*, *6*). Ribosome-bound TF interacts with most newly synthesized polypeptides (*7*) and prevents their premature folding, thereby laying the groundwork for subsequent productive folding that involves additional chaperones (*8*). Recent data suggest that TF is much more versatile than initially thought. It can reshape and improve the folding pathway of a protein by protecting partially folded intermediates (*9*). Even more intriguing, TF can reverse premature folding by facilitating unfolding of preformed structures in nascent polypeptides, allowing the nascent peptide to reenter the productive folding path (*10*).

Despite comprehensive analyses of TF over many years, the molecular details of its versatile chaperone activity were not understood. Using sophisticated nuclear magnetic resonance techniques, Saio *et al*. have now determined the structure and dynamics of purified TF as it interacts with unfolded model substrates in solution, thereby disclosing its mechanism of action in great detail.

The authors show that TF forms a binding scaffold with four distinct substrate-binding sites that are distributed along its inner surface (see the figure). The four binding sites can be used in a variable order, and not all sites are always occupied by substrates. The binding sites contain nonpolar residues forming hydrophobic pockets that bind to hydrophobic peptide stretches of 6 to 10 residues in substrate proteins. The binding sites have a flexible local architecture that allows interaction with a large and diverse population of peptide stretches with unrelated primary sequences. Furthermore, polar residues next to the hydrophobic binding sites can form hydrogen bonds with the substrate, probably to enhance affinity and navigate binding. This high degree of plasticity of its binding surfaces explains how TF can serve a large pool of nascent substrates.

How does TF affect folding of substrates using this highly flexible binding scaffold? Using all of its four binding sites, TF can directly bind up to 50 substrate residues. The hydrophobic peptide stretches bound by TF are separated by linker regions that remain unbound and may even loop outward (see the figure). Moreover, supporting earlier findings (*11*), Saio *et al*. show that multiple TF molecules can bind simultaneously to a substrate. This multistage chaperone mechanism enables TF to retain large polypeptides in an unfolded state and protect them from aggregation by shielding their exposed hydrophobic regions. The multivalent binding of TF to its substrate may even provide enough binding energy to unfold misfolded peptide structures of low thermodynamic stability.

TF binds with low affinity to individual substrate-binding sites, but the affinity gradually increases with the number of bound segments. Substrate binding to the binding sites is highly dynamic and the residence time is short (1 ms at 25°C). Even when TF fully engages its unfolded protein substrate by using all of its available binding sites, the complex remains dynamic, with fast association and dissociation rates. This

Department of Biology, University of Konstanz, 78457 Konstanz, Germany. E-mail: elke.deuerling@uni-konstanz.de

CREDIT: P. HUEY/*SCIENCE*

Published by AAAS

highly dynamic substrate engagement is very important during protein synthesis, allowing TF to accommodate the permanently changing composition of binding sites in the nascent polypeptide that grows by up to 20 amino acid residues per second.

Saio *et al*.'s study provides a milestone in understanding how TF performs its dynamic and multifaceted functions in the cell. The work will pave the way for further exciting advances in understanding the plasticity of this and other ATP-independent chaperones. However, several important questions remain to be answered about the activity of the TF chaperone. For example, Saio *et al*. investigated purified TF, which was not in complex with the ribosome, and it thus remains to be shown whether the binding sites of ribosome-tethered TF are similar. Three binding sites are located in the central body and one in the head domain, but no binding site is found in the amino-terminal tail that tethers TF to the ribosome (see the figure). TF undergoes some structural changes upon binding to ribosomes (*11*) and may thus expose other or additional binding sites.

Another open question is how the dynamic association of one or perhaps more TF molecules with nascent polypeptides is coordinated with the activity of other chaperones that bind to nascent proteins in later stages of protein synthesis (*3*). And finally, TF that is not bound to ribosomes can form dimers that can encapsulate small native-like proteins using primarily polar contacts. This TF activity may promote the assembly of substrates into large complexes (*12*). Further analyses are required to understand how TF can switch between hydrophobic and hydrophilic binding modes for substrates.

References

1. Y. E. Kim *et al*., *Annu. Rev. Biochem.* **82**, 323 (2013).
2. T. Saio *et al.*, *Science* **344**, 1250494 (2014); 10.1126/science.1250494.
3. L. Ferbitz *et al*., *Nature* **431**, 590 (2004).
4. A. Hoffmann, B. Bukau, G. Kramer, *Biochim. Biophys. Acta* **1803**, 650 (2010).
5. E. Deuerling *et al*., *Nature* **400**, 693 (1999).
6. S. A. Teter *et al*., *Cell* **97**, 755 (1999).
7. E. Oh *et al*., *Cell* **147**, 1295 (2011).
8. V. R. Agashe *et al*., *Cell* **117**, 199 (2004).
9. A. Mashaghi *et al*., *Nature* **500**, 98 (2013).
10. A. Hoffmann *et al*., *Mol. Cell* **48**, 63 (2012).
11. C. M. Kaiser *et al*., *Nature* **444**, 455 (2006).
12. E. Martinez-Hackert, W. A. Hendrickson, *Cell* **138**, 923 (2009).

10.1126/science.1254064

MATERIALS SCIENCE

An Internal Cure for Damaged Polymers

A vascular system of microchannels delivers polymer-forming reagents that seal and repair large damaged regions.

Zhouzhou Zhao and Ellen M. Arruda

Design strategies for structural polymers and polymer matrix composites that opt for damage management in lieu of damage prevention may greatly improve materials longevity and reduce repair costs. Nature has evolved many elegant examples of self-healing. Bone continuously remodels via the resorption and replacement of damaged tissue, latex "gasket" excretion in plants self-seals wounds (*1*), and dynamic, sacrificial metalloprotein complexes form the adhesive of the mussel byssus (*2*). Scientists have drawn inspiration from nature to develop self-healing strategies in structural polymeric systems. On page 620 of this issue, White *et al*. (*3*) show how to heal a large volumetric loss in a synthetic polymer autonomously. Their innovative approach enables restoration of mechanical integrity to a damage volume that is roughly 100 times the largest defect previously healed in this manner (*4*).

White *et al*. developed a vascular repair system that can fill and polymerize a defect 10 mm in diameter and 3 mm thick. This defect is "full thickness"—it creates an opening that extends through the sample. Complex and rapid gelation chemistry had to be developed that could plug the hole quickly and prevent bleed-out of the healing agent. Fluids containing healing agents in microchannels wet the surface of the defect, mix, and rapidly and completely fill the defect with gel (see the figure, panel A) as long as surface tension and cohesive and adhesive forces dominate over gravity flow. Polymerization progresses over time scales that are long compared to the gelation time scale. The lost volume is replaced by new structural polymer that forms a viable interface with the matrix polymer and restores mechanical integrity (see the figure, panel B). White *et al*. did not restore the original polymer composition, so, like scar tissue, the repair is functional but not completely regenerative. Nevertheless, the elastic modulus, strength, and impact resistance of the repair site are all restored to structural polymer values; specifically, 62% of native epoxy impact energy is achieved upon self-healing.

Earlier approaches to damage management in polymer design used external stimuli (thermal, electrical, and others) to trigger a healing response [see, for example (*5*, *6*)]. Wudl and co-workers used Diels-Alder–based polymer networks with reversible covalent bonds to mend cracks and fractures upon thermal activation (*6*) in a strategy replicating the sacrificial bonds of byssus threads. Multiple healing cycles were achieved with mechanical performance restorations of up to 60%. Subsequent research moved this approach from stimuli-responsive to autonomous healing by designing dynamic noncovalent bonding or reversible covalent bonding at room temperature (*7*, *8*). Reversible interactions allow repeated healing cycles but are limited to defects in which the surfaces are in intimate contact (*4*).

The work of White *et al*. highlights self-healing strategies that transport mass—a healing agent in liquid form—to local defects. Capsular strategies embed reparative materials within compartments dispersed throughout a polymer matrix that rupture at a proximal damage site. Vascular strategies embed the healing agent within channels or reinforcing fibers (*9*) to be released when damage occurs. Refillable microvascular networks for storage and transport of healing agent have also been developed (*10*). Vascular systems offer multiple healing cycles through the perfusion of fresh healing agent fluids to a damage site until channels are ultimately segmented by multiple damage events.

Recent strategies to improve healing efficiency combine one or more self-healing approaches with stimuli-responsive polymers. For example, Kirkby *et al*. incorporated shape-memory alloy (SMA) wires into the matrix of a polymer that also contained a capsular self-healing system (*11*)

Department of Mechanical Engineering, University of Michigan, Ann Arbor, MI, USA. E-mail: arruda@umich.edu

Published by AAAS

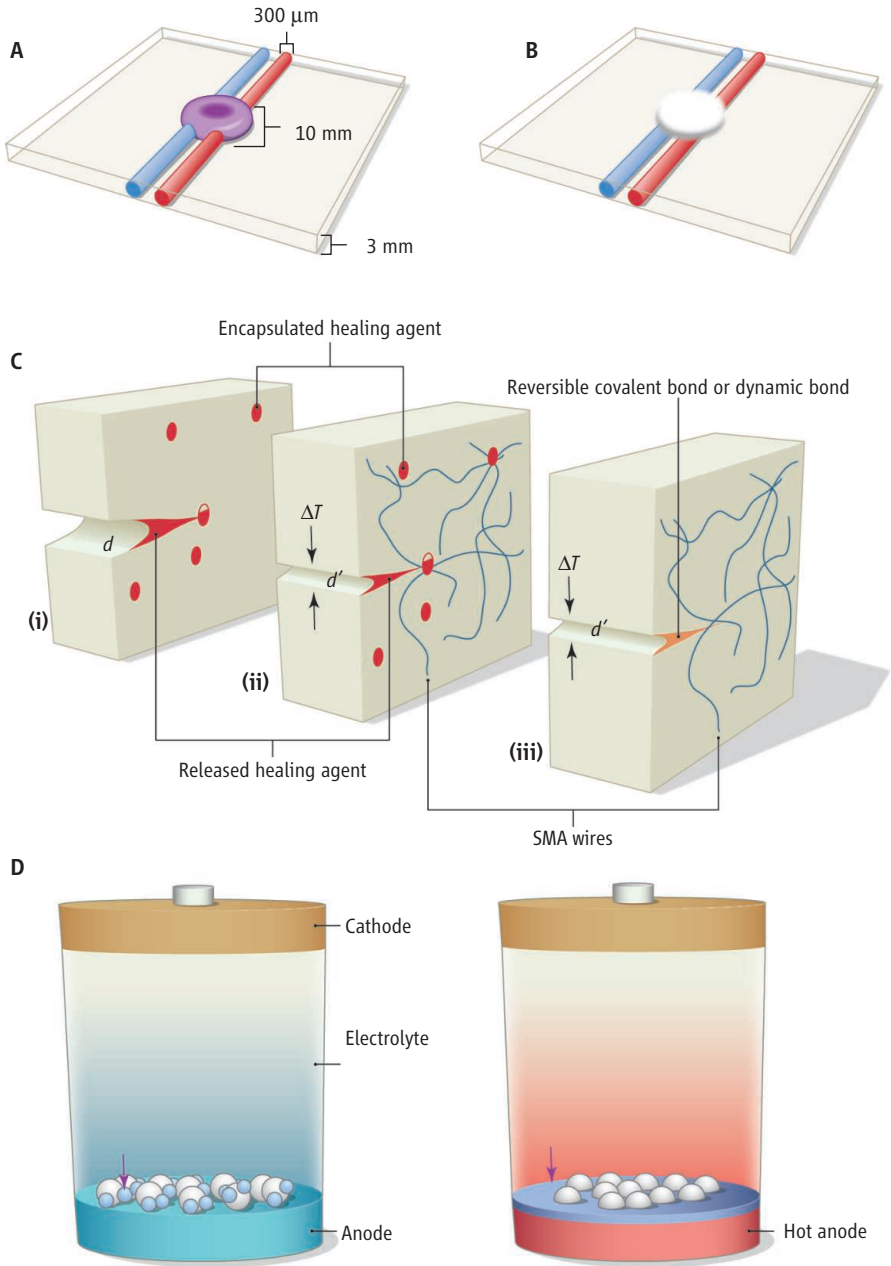

Autonomous strategies in polymer systems. In the approach of White *et al.*, (**A**) healing agents in two independent chambers mix and fill a large, through-thickness defect to seal the hole quickly and (**B**) polymerization of the healing agents restores structural integrity. (**C**) Combining healing strategies can improve healing efficiency. Adding temperature change–triggered (ΔT) shape-memory alloy (SMA) wires to capsular (ii) or (iii) intrinsic self-healing strategies improves contact of the defect surfaces (d') compared to the self-healing strategy alone (d) in (i). (**D**) Multifunctional autonomous polymer microspheres (purple arrow, left) function as part of the shutdown separator in a battery during normal operation but melt (purple arrow, right) if the battery begins to overheat to seal the anode and shut down operation.

(see the figure, panel C). Tee *et al.* combined supramolecular reversible bonds with conductive nanoparticles to develop an electronic sensor skin that demonstrated rapid restoration of mechanical and electrical properties (*12*).

Although numerous efforts are being made to tackle healing of ever-increasing defect sizes, there is an appreciation for the detrimental effects of microscale cracks on the structural integrity of polymer composites. The development of smaller capsular and vascular systems (*13*) can potentially eliminate fracture in these materials by preventing small, noncritical cracks from propagating to critical sizes.

Damage management can compromise performance if a substantial fraction of the polymer mass is engaged only in repair rather than the primary structural functions. One solution is to incorporate multifunctionality into the healing components. An example is solid-state microvascular channels that structurally reinforce the polymer matrix and melt upon application of a temperature rise to repair a defect (*14*). The multifunctional approach has recently been demonstrated in a nonstructural polymer application in which the shutdown separator in a battery is comprised of polymer microspheres that melt before a catastrophic temperature rise and prohibit further ionic conduction (*15*) (see the figure, panel D).

Although these recent advances are exciting, the long-term performance of autonomously healed polymers has largely remained unexamined. Repaired performance efficiencies typically measured are short-term mechanical properties under ambient conditions, so the effects of cyclic loading, aging, and various hostile environmental conditions on the healing efficiency and the integrity of repaired defects are not known. In most self-healing approaches, the repaired sites are not the same composition as the native polymer, so testing of the materials under more realistic conditions, both pre- and post repair, is needed. Methods are also needed to assess and monitor the potential healing ability after multiple repair events. Here again, elegant examples that have evolved in nature can inspire solutions for the next generation of structural polymer designs.

References

1. T. Speck, R. Mulhaupt, O. Speck, in *Self-Healing Polymers: From Principles to Applications*, W. H. Binder, Ed. (Wiley, Weinheim, Germany, 2013), pp. 61–89.
2. M. J. Harrington, A. Masic, N. Holten-Andersen, J. H. Waite, P. Fratzl, *Science* **328**, 216 (2010).
3. S. R. White *et al.*, *Science* **344**, 620 (2014).
4. B. J. Blaiszik *et al.*, *Annu. Rev. Mater. Res.* **40**, 179 (2010).
5. S. R. White *et al.*, *Nature* **409**, 794 (2001).
6. X. Chen *et al.*, *Science* **295**, 1698 (2002).
7. P. Cordier, F. Tournilhac, C. Soulié-Ziakovic, L. Leibler, *Nature* **451**, 977 (2008).
8. K. Imato *et al.*, *Angew. Chem. Int. Ed.* **51**, 1138 (2012).
9. R. Trask, I. Bond, *Smart Mater. Struct.* **15**, 704 (2006).
10. K. S. Toohey, N. R. Sottos, J. A. Lewis, J. S. Moore, S. R. White, *Nat. Mater.* **6**, 581 (2007).
11. E. L. Kirkby *et al.*, *Adv. Funct. Mater.* **18**, 2253 (2008).
12. B. C. K. Tee, C. Wang, R. Allen, Z. Bao, *Nat. Nanotechnol.* **7**, 825 (2012).
13. Y. Zhao, J. Fickert, K. Landfester, D. Crespy, *Small* **8**, 2954 (2012).
14. S. A. Hayes, F. R. Jones, K. Marshiya, W. Zhang, *Appl. Sci. Manuf.* **38**, 1116 (2007).
15. M. Baginska *et al.*, *Adv. Energetic Mater.* **2**, 583 (2012).

10.1126/science.1254317

CREDIT: P. HUEY/*SCIENCE*

Published by AAAS

PSYCHOLOGY

Rice, Psychology, and Innovation

People in wheat-cultivating areas of China are more individualistic and analytical than those in rice-cultivating areas.

Joseph Henrich

By the late 18th century, the earliest tremors of the industrial revolution were beginning to shake England. Fueled by a stream of innovations related to textiles, transportation, and steel manufacturing, this eruption of economic growth would soon engulf northern Europe, spread to Britain's former colonies, and eventually transform the globe. For the first time, humanity would be sprung from the Malthusian trap. The question of why this revolution first emerged in northern Europe remains one of history's great questions. If you stood overlooking the globe in 1000 CE, the most obvious candidates for igniting this engine were perhaps in China or the Middle East, but certainly not in Europe. Addressing this question, researchers have pointed to differences in geography, institutions, religions, and even genes (*1*, *2*). On page 603 of this issue, Talhelm *et al*. (*3*) take an important step forward by fingering psychological differences in analytical thinking and individualism as an explanation for differences in innovation, and then linking these differences to culturally transmitted institutions, and ultimately to environmental differences that influence the feasibility of rice agriculture.

Decades of experimental research show that, compared to most populations in the world, people from societies that are Western, Educated, Industrialized, Rich, and Democratic (WEIRD) (*4*) are psychologically unusual, being both highly individualistic and analytically minded. High levels of individualism mean that people see themselves as independent from others and as characterized by a set of largely positive attributes. They willingly invest in new relationships even outside their kin, tribal, or religious groups. By contrast, in most other societies, people are enmeshed in dense, enduring networks of kith and kin on which they depend for cooperation, security, and personal identity. In such collectivistic societies, property is often corporately owned by kinship units such as clans; inherited relationships are enduring and people invest heavily in them, often at the expense of outsiders, strangers, or abstract principles (*4*).

Psychologically, growing up in an individualistic social world biases one toward the use of analytical reasoning, whereas exposure to more collectivistic environments favors holistic approaches. Thinking analytically means breaking things down into their constituent parts and assigning properties to those parts. Similarities are judged according to rule-based categories, and current trends are expected to continue. Holistic thinking, by contrast, focuses on relationships between objects or people anchored in their concrete contexts. Similarity is judged overall, not on the basis of logical rules. Trends are expected to be cyclical.

Various lines of evidence suggest that greater individualism and more analytical thinking are linked to innovation, novelty, and creativity (*5*). But why would northern Europe have had greater individualism and more analytical thinking in the first place? China, for example, was technologically advanced, institutionally complex, and relatively educated by the end of the first millennium. Why would Europe have been more individualist and analytically oriented than China?

Talhelm *et al*. hypothesized that different combinations of environments and technologies influence the cultural evolution of different forms of social organization. Under

Measuring analytical thinking and individualism. To investigate the individualism and analytical thinking in participants from different agricultural regions in China, Talhelm *et al*. used three tests. They measured analytical thinking with a series of triads. Participants were given a target object, such as a rabbit, and asked which of two other objects it goes with. Analytic thinkers tend to match on categories, so rabbits and dogs go together. Holistic thinkers tend to match on relationships, so rabbits eat carrots. The authors also measured individualism in two ways. First, they asked participants to draw a sociogram, with labeled circles representing themselves and their friends. In this test, individualism is measured implicitly by how much bigger the "self" circle is relative to the average "friends" circle. Second, they assessed the nepotism (in-group loyalty) of participants by asking them about hypothetical scenarios in which they could reward or punish friends and strangers for helpful or harmful action.

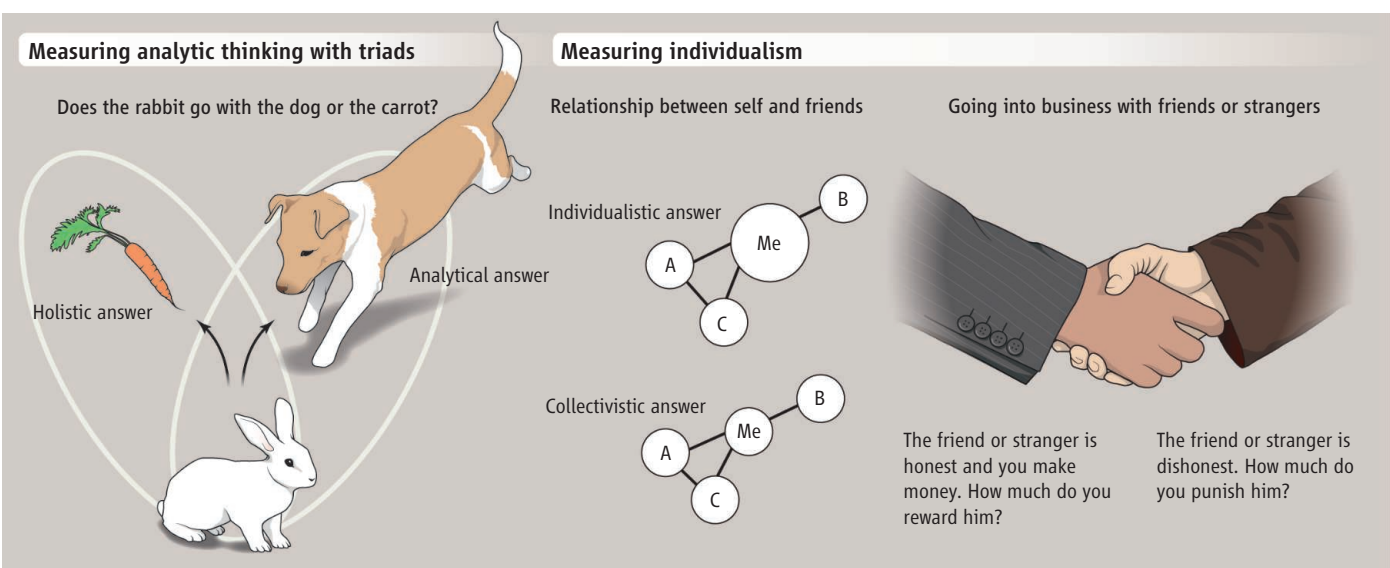

CREDIT: P. HUEY/*SCIENCE*

Departments of Psychology and Economics, University of British Columbia, Vancouver, Canada V6T 1N5. E-mail: henrich@psych.ubc.ca

Published by AAAS

some techno-environmental conditions, only intensely cooperative social groups can endure, prosper, and spread. Although potentially applicable to many situations, including territorial defense and whale hunting, Talhelm *et al.* focus on the different labor requirements of paddy rice and wheat cultivation. By demanding intense cooperation, paddy rice cultivation fosters and reinforces the social norms that govern patrilineal clans. Growing up in strong clans creates a particular kind of collectivistic psychology. In contrast, wheat cultivation permits independent nuclear households and fosters more individualistic psychologies.

To test these ideas, Talhelm *et al*. used standard psychological tools (see the figure) to measure analytical thinking and individualism among university students sampled from Chinese provinces that vary in wheat versus rice cultivation. Focusing on China removes many of the confounding variables such as religion, heritage, and government that would bedevil any direct comparison between Europe and East Asia. The prediction is straightforward: Han Chinese from provinces cultivating relatively more wheat should tend to be more individualistic and analytically oriented.

Sure enough, participants from provinces more dependent on paddy rice cultivation were less analytically minded. The effects were big: The average number of analytical matches increased by about 56% in going from all-rice to no-rice cultivation. The results hold both nationwide and for the counties in the central provinces along the rice-wheat (north-south) border, where other differences are minimized.

Participants from rice-growing provinces were also less individualistic, drawing themselves roughly the same size as their friends, whereas those from wheat provinces drew themselves 1.5 mm larger. [This moves them only part of the way toward WEIRD people: Americans draw themselves 6 mm bigger than they draw others, and Europeans draw themselves 3.5 mm bigger (*6*).] People from rice provinces were also more likely to reward their friends and less likely to punish them, showing the in-group favoritism characteristic of collectivistic populations.

So, patterns of crop cultivation appear linked to psychological differences, but can these patterns really explain differences in innovation? Talhelm *et al.* provide some evidence for this by showing that less dependence on rice is associated with more successful patents for new inventions. This doesn't nail it, but is consistent with the broader idea and will no doubt drive much future inquiry. For example, these insights may help explain why the embers of an 11th century industrial revolution in China were smothered as northern invasions and climate change drove people into the southern rice paddy regions, where clans had an ecological edge, and by the emergence of state-level political and legal institutions that reinforced the power of clans (*7*).

Cultural evolution arises from a rich interplay of ecology, social learning, institutions, and psychology. Environmental factors favor some types of family structures or forms of social organization over others. Honed and refined over generations, these institutions create the conditions to which children adapt developmentally, shaping their psychologies and brains. Long after their ecological causes have become irrelevant, these cultural psychologies and institutions continue to influence rates of innovation, the formation of new institutions, and the success of immigrants in new lands. As such, wheat farming may contribute to explaining the origins of WEIRD psychology and the industrial revolution.

References

1. G. Clark, *A Farewell to Alms: A Brief Economic History of the World* (Princeton Univ. Press, Princeton, NJ, 2007).
2. J. Mokyr, *The Lever of Riches* (Oxford Univ. Press, New York, 1990).
3. T. Talhelm *et al*., *Science* **344**, 603 (2014).
4. J. Henrich, S. J. Heine, A. Norenzayan, *Behav. Brain Sci.* **33**, 61 (2010).
5. Y. Gorodnichenko, G. Roland, *Proc. Natl. Acad. Sci. U.S.A.* **108** (suppl. 4), 21316 (2011).
6. S. Kitayama, H. Park, A. T. Sevincer, M. Karasawa, A. K. Uskul, *J. Pers. Soc. Psychol.* **97**, 236 (2009).
7. A. Greif, G. Tabellini, *Am. Econ. Rev.* **100**, 135 (2010).

10.1126/science.1253815

NEUROSCIENCE

A Price to Pay for Adult Neurogenesis

Newly formed hippocampal neurons participate in the encoding of new memories in adult rodents, but too much neurogenesis may jeopardize memory retention.

Lucas A. Mongiat[1] and Alejandro F. Schinder[2]

We tend to believe that plasticity is what makes brain circuits adaptable to continuous changes in environmental demands and that greater brain plasticity should result in a better ability to cope with the surrounding world. To adapt to everyday life, animals explore, learn, and remember, and these tasks make use of various cortical structures, including the hippocampus. The dentate gyrus, part of the hippocampus, is a remarkable structure in that it is one of two areas of the adult mammalian brain, including the human brain, that continue to generate new neurons throughout postnatal life (*1*). It is well established that adult-born neurons integrate into preexisting neuronal networks and participate in information processing (*2*). Much evidence accumulated over the past decade supports the hypothesis that adult neurogenesis itself is a type of circuit plasticity required for hippocampus-dependent learning and memory recall. The work by Akers *et al*. on page 598 of this issue (*3*) now shows that adult hippocampal neurogenesis may also promote forgetting.

In the adult hippocampus, new-born granule neurons develop and establish synaptic connections within preexisting neuronal networks very slowly. Input and output connections are refined during several weeks as neurons acquire a meaningful functional integration. The specific functional role of these new cells is not clear. Nor is it clear why the dentate gyrus requires freshly assembled neurons to perform its function. It has been proposed, based on its architecture, that the dentate gyrus may play a critical role in performing "pattern separation" of incoming inputs. Pattern separation is the process whereby similar pieces of information are represented by distinct (orthogonal) sets of neurons in the output network. It has been proposed that in a behavioral context pattern separation underlies the capacity to extract the subtle differences among environments or cues that are otherwise

[1]Research Institute for Biodiversity and Environment (INIBIOMA, CONICET), Bariloche, Río Negro, Argentina. [2]Laboratory of Neuronal Plasticity, Leloir Institute (IIBBA, CONICET), Buenos Aires, Argentina. E-mail: aschinder@leloir.org.ar

Published by AAAS

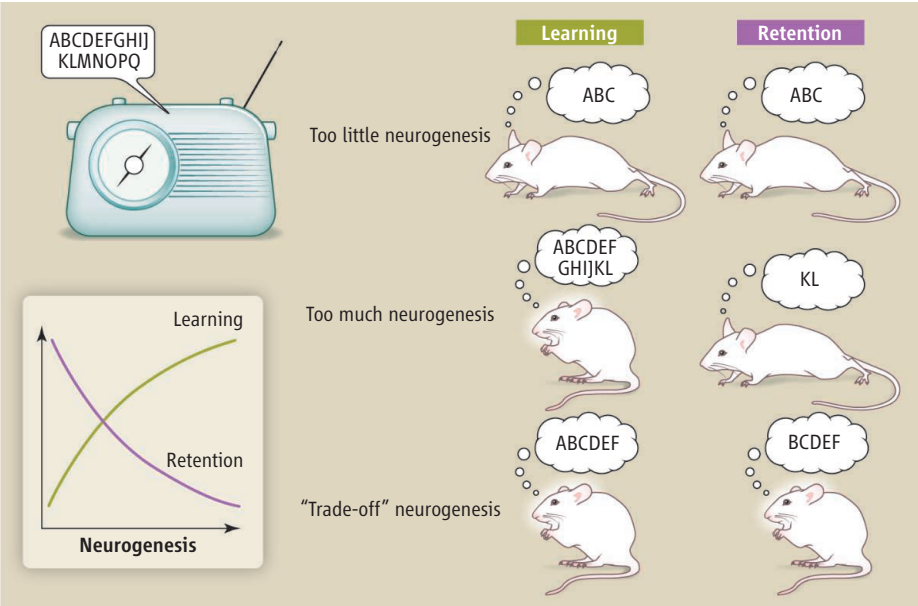

Making new neurons, but not too many. In the cartoon, the mouse must encode environmental cues depicted as characters coming out of the radio. A mouse with little hippocampal neurogenesis exhibits difficulties in learning the task, but information can be stored entirely (left on the graph). A mouse with too much neurogenesis displays excellent learning performance but poor retention due to ongoing circuit remodeling that labilizes memories (right on the graph). A "trade-off" level of neurogenesis allows good performance for both memory acquisition and retention (point of intersection on the graph).

very similar. Hence, much effort has been devoted recently to test the hypothesis that adult neurogenesis may be required for what is now called behavioral pattern separation, with experiments that have been primarily centered on the acquisition of new contextual memories.

An experiment that typifies the approach is the contextual fear discrimination paradigm. Following a randomized order, mice are placed in two very similar but not identical contexts, A or B; in A, they receive brief foot shocks, whereas in B, they receive no stimulus. This scenario is repeated once a day over a period of several days. Because they learn to associate the context with the shock, mice freeze when placed in either context, but with time they learn to identify the small differences that discriminate the safe place from the dangerous one (behavioral pattern separation) and make that learning explicit by keeping calm in the nonshock (B) context. It has been shown that manipulations that decrease the number of functional adult-born neurons impair behavioral pattern separation (*4*, *5*). Consistent with those data, increasing the number of adult-born neurons seems to improve memory encoding (*6*, *7*). In light of these results, one could infer that more adult neurogenesis improves hippocampus-dependent memory. However, theoretical models have led to the suggestion that the network remodeling required to encode new information could also contribute to loss of previously stored memories (*8*), much like palimpsests from the middle ages—manuscripts written on top of older washed-off texts. Indeed, morphological studies have shown that when adult-born neurons integrate into the local dentate networks, they compete for established synapses, thus altering preexisting connections (*9*, *10*).

Akers *et al*. tested the idea that hippocampal neurogenesis will lead to competitive circuit modification and thus contribute to forgetting. The authors approached this problem from different angles using various behavioral paradigms. In an attempt to correlate the rate of neurogenesis with the extent of forgetting, they took advantage of the natural ontogenic decline in postnatal neurogenesis to compare memory retention in early postnatal (17-day-old) pups versus adult mice. Mice were exposed to a novel context where they received brief foot shocks and were tested in the same context at different times (up to 6 weeks) without the foot shocks. Whereas adult mice displayed good memory retention throughout the experimental time span, pups forgot the association within a week. Remarkably, increasing neurogenesis after contextual learning accelerated forgetting in adult mice, whereas reducing neurogenesis after learning improved memory retention in pups. To determine whether the correlation between neurogenesis and forgetting can be generalized, the authors tested memory retention in guinea pigs and degus (brush-tailed rodents), both of which species have extended gestation periods and thus lower levels of postnatal neurogenesis compared with mice. They found that guinea pig pups and degu pups display high levels of retention that are worsened by manipulations that increase neurogenesis. Altogether, the results clearly demonstrated that a substantial correlation exists between neurogenesis and forgetting.

The most straightforward explanation of these experimental observations is that enhanced neurogenesis results in more neurons actively integrating into the neuronal circuitry of the dentate gyrus. If newly generated neurons incorporate in a manner that destabilizes preexisting synaptic connections, neurogenesis would labilize previously encoded memories, as proposed by theoretical models (*11*). A prediction emerging from this mechanistic interpretation is that increasing neurogenesis should not result in an immediate change in memory retention. Instead, forgetting should develop after a certain delay, as the new neurons begin to interconnect within the existing dentate network.

Finally, if encoding novel memories involves remodeling of preexistent synaptic connections with the concomitant loss of stored information, adding new neurons does seem like an efficient strategy for minimizing interference with the preexisting network, where the alternative scenario would require modifying synaptic weights within such networks. Certainly, adult hippocampal neurogenesis does contribute to memory encoding in situations where fine discrimination is needed, such as contextual discrimination. But adding new neurons will still impose a cost to network stability. Therefore, encoding novel memories requires just the right amount of dentate gyrus neurogenesis—neither too little nor too much.

References

1. C. Zhao, W. Deng, F. H. Gage, *Cell* **132**, 645 (2008).
2. L. J. Drew, S. Fusi, R. Hen, *Learn. Mem.* **20**, 710 (2013).
3. K. G. Akers *et al*., *Science* **344**, 598 (2014).
4. C. D. Clelland *et al*., *Science* **325**, 210 (2009).
5. T. Nakashiba *et al*., *Cell* **149**, 188 (2012).
6. D. J. Creer, C. Romberg, L. M. Saksida, H. van Praag, T. J. Bussey, *Proc. Natl. Acad. Sci. U.S.A.* **107**, 2367 (2010).
7. A. Sahay *et al*., *Nature* **472**, 466 (2011).
8. S. Fusi, P. J. Drew, L. F. Abbott, *Neuron* **45**, 599 (2005).
9. N. Toni *et al*., *Nat. Neurosci.* **10**, 727 (2007).
10. N. Toni *et al*., *Nat. Neurosci.* **11**, 901 (2008).
11. V. I. Weisz, P. F. Argibay, *Cognition* **125**, 13 (2012).

10.1126/science.1254236

CREDIT: P. HUEY/*SCIENCE*

Published by AAAS

READ THE FULL ARTICLE ONLINE
http://dx.doi.org/10.1126/science.1242592

Recent developments in molecular, gene, and stem-cell therapies have potential to restore inner-ear function in deaf patients.

Sound Strategies for Hearing Restoration

Gwenaëlle S. G. Géléoc and Jeffrey R. Holt*

Background: Sensorineural hearing loss is the most common sensory deficit in the world, with nearly 300 million affected individuals. The problem is multifactorial and can arise from damage or death of the primary sensory cells or the inner-ear neurons that relay auditory information to the brain. The inner-ear sensory cells and neurons can be damaged by environmental insult (such as exposure to infectious agents, drugs such as aminoglycoside antibiotics or chemotherapeutics, or overexposure to loud sounds) or by a host of genetic factors. Because mature inner ears lack the capacity for self-repair, the cellular damage is permanent. In addition to acquired hearing loss, more than 300 genetic loci have been linked to hereditary hearing loss, with about 70 of the causative genes identified. Eighty percent of genetic hearing loss is recessive, with the rest inherited as a dominant trait. More subtle genetic defects that cause a predisposition toward age-related hearing loss are poorly understood. Unfortunately, there is no cure for acquired, inherited, or age-related hearing loss.

Advances: Efforts to restore and repair damaged inner-ear cells have intensified over the past 10 years. Thus far, a major thrust has been to adapt three biological strategies for use in the inner ear: gene therapy, stem-cell therapy, and molecular therapy. Using these approaches, researchers have restored sensory function at the cellular level in animal models of human hearing loss. A few reports suggest functional recovery at the systems and behavioral levels, although caveats remain.

Outlook: As the population continues to age and expand, so will the number of patients who suffer from clinically serious hearing loss. As such, the need for a deeper and comprehensive understanding of hearing-loss therapies is more pressing than ever. Although the pace of progress is accelerating and clinical trials are on the horizon, it is clear that there are still a number of hurdles to overcome. Overall, there are reasons to be both cautious and optimistic as we attempt to repair and regenerate one of nature's most exquisite mechanosensory devices: the human inner ear.

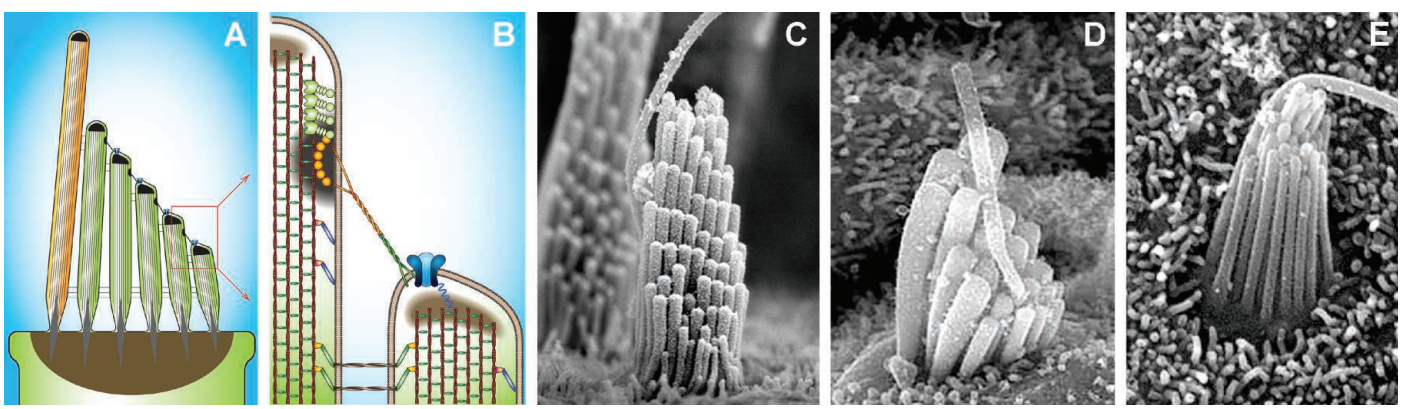

Native and engineered mechanosensory hair cells of the mammalian inner ear. Airborne sound vibrations, funneled through the external ear, are relayed through the middle ear to the inner ear, where they propagate as sound pressure waves in the fluid-filled spaces of the cochlea. The human cochlea contains ~16,000 sensory hair cells that convert sound pressure into electrical signals. (**A**) Hair cells are crowned with mechanosensory organelles composed of 50 to 100 actin-filled microvilli, organized into staircase arrays known as hair bundles. Extracellular linkages couple microvilli and ensure that the entire bundle responds to sound stimulation with coherent motion. (**B**) Bundle motion focuses sound energy onto the mechanotransduction apparatus, which includes one or two mechanically gated ion channels (50 to 100 per cell). According to the prevailing model, the channel complex is anchored to the actin core on the intracellular side at the tip of the shorter microvillus. On the extracellular side, there is a tip-link that extends to the side of the adjacent taller neighbor. At the top end, the tip-link is tethered to intracellular motor molecules that regulate tension within the apparatus. Sound-induced changes in tip-link tension modulate the open probability of the mechanosensitive channels, which in turn modulate the flow of electric current into the cell. Disruption of the sensory hair bundle by genetic mutation, loud sounds, or ototoxic drugs can lead to hair-cell dysfunction and deafness. Strategies to restore hair cells and mechanosensory function are being developed to treat patients with neurosensory hearing loss. [Illustrated by B. Pan] (**C**) Scanning electron microscopy image of a native hair bundle from the mouse inner ear. [Reprinted from]. R. Holt *et al., Cell* **108**, 371–381 (2002) by permission from Elsevier] (**D**) A hair-cell–like cell generated via a gene-therapy strategy and viral-mediated delivery of the transcription factor *Atoh1* into the inner ear of a deaf guinea pig. [Reprinted from Kawamoto *et al.,*]. *Neurosci.* **23**, 4395–4400 (2003) by permission of the Society for Neuroscience] (**E**) A hair-cell–like cell generated from embryonic stem cells and a stepwise differentiation protocol. Similar cells generate functional mechanosensitive responses to microvilli deflection. [Reprinted from Oshima *et al., Cell* **141**, 704–716 (2010) by permission from Elsevier]

Department of Otolaryngology, F. M. Kirby Neurobiology Center, Boston Children's Hospital, Harvard Medical School, Boston, MA 02114, USA.
*Corresponding author. E-mail: jeffrey.holt@childrens.harvard.edu
Cite this article as Géléoc and Holt, *Science* **344**, 1241062 (2014). DOI: 10.1126/science.1241062

Sound Strategies for Hearing Restoration

Gwenaëlle S. G. Géléoc and Jeffrey R. Holt*

Hearing loss is the most common sensory deficit in humans, with some estimates suggesting up to 300 million affected individuals worldwide. Both environmental and genetic factors contribute to hearing loss and can cause death of sensory cells and neurons. Because these cells do not regenerate, the damage tends to accumulate, leading to profound deafness. Several biological strategies to restore auditory function are currently under investigation. Owing to the success of cochlear implants, which offer partial recovery of auditory function for some profoundly deaf patients, potential biological therapies must extend hearing restoration to include greater auditory acuity and larger patient populations. Here, we review the latest gene, stem-cell, and molecular strategies for restoring auditory function in animal models and the prospects for translating these approaches into viable clinical therapies.

The remarkable extension of human life span over the past century has come at a price: It has also expanded our vulnerability to neurodegenerative disorders, including sensorineural hearing loss. Over the course of an average human lifetime, the incidence of hearing loss increases from one in a thousand at birth to one in three by 80 years of age. This dramatic rise in the incidence of hearing loss is due to overexposure to environmental toxins, including toxic noise, genetic predisposition to age-related hearing loss, or both. The problem is further compounded as the human population continues to age; estimates suggest that the number of Americans who suffer substantial hearing impairment will rise from the current level of ~29 million to as many as 65 million by the year 2030 (*1*). This will undoubtedly have enormous socioeconomic impact, with implications for patients, health care providers, and policymakers.

Although the epidemiology numbers are alarming, the consequences for the individual hearing loss patient can be devastating and very personal. As humans, we rely heavily on the richness of spoken language; therefore, loss of auditory function for the individual often leads to social isolation, depression, and in extreme cases, suicide. Indeed, as Helen Keller famously noted in a 1910 letter to Dr. James Love: "The problems of deafness are deeper and more complex, if not more important, than those of blindness. Deafness is a much worse misfortune. For it means the loss of the most vital stimulus—the sound of the voice that brings language, sets thoughts astir and keeps us in the intellectual company of man."

Restoration of auditory function remains a lofty but achievable goal for deaf patients and for scientists. Because hearing loss is a multifactorial problem, arising from many possible causes, it is unlikely that any single strategy will be an effective cure-all. Rather, multiple strategies may ultimately be required, tailored to target the underlying cause of the problem for each individual. Here, we review recent progress toward development of strategies to treat hearing loss, with particular focus on four general approaches: cochlear implants, gene therapy, stem-cell therapy, and molecular therapy. These treatment strategies are at various stages of development and implementation, and each carries its own particular set of advantages, risks, and future promise.

Hair Cells, Spiral Ganglion Neurons, and Auditory Transduction

The perception of sound in the human inner ear begins in the sensory hair cells of the snail-shaped cochlea. Hair cells convert sound vibration into electrical signals, which are transmitted via spiral ganglion neurons through the eighth cranial nerve to the brain (Fig. 1). A number of problems can affect the physical transmission of airborne sound vibrations from the external ear, through the middle ear into the inner ear. These middle-ear problems can give rise to several forms of conductive hearing loss, which are often treatable through surgical intervention, placement of tubes to drain middle ear fluids, or antibiotics. Problems that affect the conversion of sound signals into electrical signals or transmission of those signals to the brain are collectively known as sensorineural hearing loss, for which there is no cure.

There are ~16,000 sensory hair cells in the cochlea of a newborn. Hair cells are interdigitated with supporting cells that together form an epithelial layer. At the hair-cell basal pole are synaptic contacts with spiral ganglion neurons. There are 30,000 to 40,000 afferent neurons (those that relay information toward the central nervous system) in each auditory organ. Hair-cells, supporting cells, and spiral ganglion neurons are critically important for normal auditory function, and because these cells do not spontaneously regenerate, those present at birth must last a lifetime. Unfortunately, because of the fragile cytoarchitecture of the mechanosensory organelle—the hair bundle—hair cells are particularly susceptible to damage and death. Hair-cell loss often begins at the basal, high-frequency end of the cochlea and progresses toward the apical low-frequency end. At birth, the sensitive range of the human auditory organ spans frequencies from 50 to 20,000 Hz. With age, the high frequency end of the auditory spectrum creeps lower, even under the best conditions. Genetic factors, exposure to excessive noise, or ototoxic drugs can accelerate the shift of the high frequency end. If the progressive hearing loss eventually reaches frequencies within the range of human speech—1000 to 4000 Hz—it can interfere with normal speech comprehension in older adults and lead to misunderstanding, frustration, and isolation for both the affected listener and the speaker. Hearing aids offer sound amplification and can help but must rely on the hair cells and neurons that remain.

Auditory afferent neurons, known as spiral ganglion neurons, can also be damaged through genetic and environmental insult. A growing body of evidence suggests that loss of these neurons and damage to the tonically active hair-cell–afferent synapse is a major source of sensorineural hearing loss (*2*). Ninety-five percent of the afferent sensory information is transmitted to spiral ganglion neurons from a subset of hair cells known as inner hair cells. Each inner hair cell is contacted by up to 20 afferent neurons. This diversity of synaptic contacts is hypothesized to encode different aspects of the sound stimulus such as frequency and intensity, as well as temporal qualities such as the beginning and ending of a sound. Efferent feedback from the brain to the inner ear modulates the sensitivity of hair cells and afferent neurons. Both afferent and efferent fibers travel along the eighth cranial nerve. Loss of subsets of these neurons may render a patient insensitive to certain aspects of an auditory stimulus. For example, middle-aged individuals may have near-normal auditory thresholds but have difficulty distinguishing the voice of a speaker amid background noise, such as the cacophony of a crowded cocktail party. Here again, the hearing aid is woefully inadequate because it amplifies all sound and does little to boost the signal-to-noise ratio.

Development of hearing restoration strategies must confront the anatomy and physiology of the inner ear, which present both advantages and disadvantages. Among the advantages is the relatively easy access. Like the eye, the inner-ear sensory organ is bathed by accessible fluid-filled spaces. The inner-ear fluids are separated from the systemic vasculature by the blood-labyrinthine barrier, which provides some protection from immune responses that might interfere with exogenous cells and vectors (*3*). The barrier may also prevent

Department of Otolaryngology, F. M. Kirby Neurobiology Center, Boston Children's Hospital, Harvard Medical School, Boston, MA 02114, USA.

*Corresponding author. E-mail: jeffrey.holt@childrens.harvard.edu

systemic dispersal of inner-ear–targeted therapeutic agents, thus limiting potential side effects in off-target tissues at remote locations. Access to the inner ear, although not as straightforward as to the eye, is possible via injection pipettes that penetrate the round window, a thin membrane that separates the middle- and inner-ear spaces. Injections via the round window allow entry to the inner-ear fluids that bathe hair-cell cell bodies. For strategies that target the fluids that bathe hair bundles, a cochleostomy approach may be required, which necessitates drilling through the bony labyrinth near the cochlear apex (*4*). The fluids of the inner ear also present a substantial challenge. There are two separate fluid-filled compartments: one that contains perilymph and another that contains endolymph. Perilymph is similar in ionic composition to cerebrospinal fluid and other standard extracellular fluids, whereas endolymph has high extracellular potassium, low sodium, and low calcium. Disruption of the tight junctions that separate perilymph and endolymph can cause mixing of low- and high-potassium solutions and a decay of the endolymphatic potential, leading to hair-cell death (*5*). Therefore, accessing the endolymphatic fluids without causing additional damage must be part of any strategy that targets those fluids. Furthermore, vectors and cells introduced into the endolymphatic fluids must be able to tolerate the high K^+ environment (*6*).

The inner ear also includes a multitude of other highly specialized cell types. Regeneration of missing cell types or designing vectors that target specific cell types will be required to address specific deficits that result from many forms of deafness. On the other hand, the limited number of inner-ear sensory cells—16,000 versus ~2 million in the eye—may prove advantageous because only a limited therapeutic load may be required.

Because defects in hair cells, spiral ganglion neurons, or supporting cells can cause deafness, they are all possible targets of emerging technologies designed to treat auditory dysfunction. Indeed, all cell types must be present and functional for normal auditory perception. Although restoration of sound perception across the entire human auditory spectrum is a worthy goal, lessons learned from cochlear implants suggest that even partial restoration may be sufficient to restore some aspects of sound perception.

Cochlear Implants

The cochlear implant is, arguably, the most successful device at the machine-brain interface (*7*). The device was recently acknowledged with the 2013 Lasker-DeBakey Award for Clinical Medical Research, awarded to developers Graeme Clark, Ingeborg Hockmair, and Blake Wilson. Cochlear implants have restored at least partial auditory function for more than 300,000 patients worldwide [the joys of cochlear implant technology can be seen at (*8*)]. The implants bypass the nonfunctional or absent hair cells and directly stimulate spiral ganglion neurons. The technology takes advantage of the tonotopic arrangement of the human auditory organ, which allows for discrete stimulation of auditory neurons that encode different ranges of sound frequencies (Fig. 2). Current implant technology provides stimulation at 8 to 22 discrete sites along the organ, signaling an equal number of auditory frequencies. Remarkably, this minimal auditory input (compared with the thousands of inputs in a healthy cochlea) is sufficient to enable speech comprehension, in some cases restoring the ability to communicate by cellphone.

Unfortunately, for many patients cochlear implants offer little hope (*9*). Patients who lack spiral ganglion neurons are not candidates for cochlear implants because functional implants require these neurons to be present to convey the auditory information from the periphery to brainstem nuclei. For these patients, restoration of spiral ganglion neurons will be required either alone, if hair cells remain intact, or perhaps together with cochlear implants, if hair cells are also absent. Regardless, the success of the cochlear implant has been remarkable and has raised the bar for scientists focused on hearing restoration through biological interventions. Any alternative therapy will need to exceed the implant success rate, reduce the risks, or provide hearing restoration at lower cost if it is to be a competitive therapeutic alternative.

Gene Therapy for Genetic Deafness

With more than 300 genetic loci implicated in hearing loss and the causative genes identified for about 70 of them, gene therapy is poised for development as a powerful hearing-loss remedy (*10*–*12*). Many deafness mutations affect hair-cell genes, whereas some affect neurons or supporting cells. Genetic deafness can be subdivided into two broad categories: syndromic and nonsyndromic. Syndromic mutations cause deafness and some other dysfunction (such as cardiac arrhythmia, as in the case of Jervell and Lange Nielsen Syndrome). Another prominent example of syndromic deafness is Usher Syndrome, which causes profound congenital deafness and progressive visual impairment. There are at least 15 genes associated with Usher Syndrome when mutated, 11 of which have been identified. Gene therapy trials for treatment of retinitis pigmentosa, a form of progressive blindness, are currently underway for Usher Syndrome 1B. Usher 1B is caused by

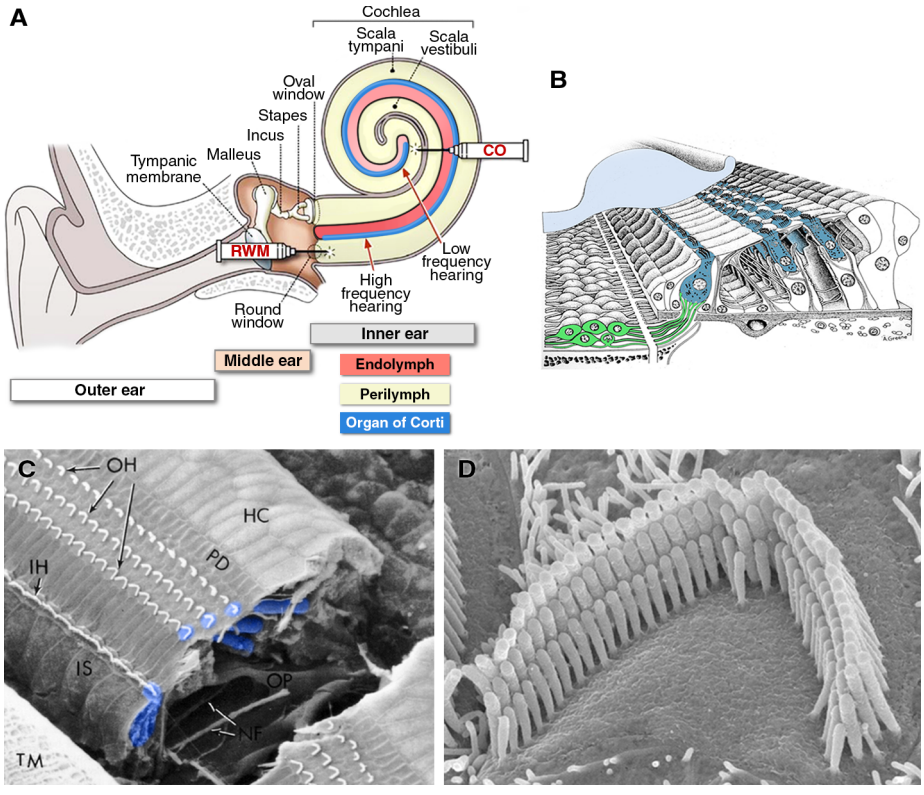

Fig. 1. Anatomy of the inner ear. (**A**) Schematic diagram of the human inner ear. The spiral-shaped cochlea is shown with endolymph and perilymph fluids indicated in red and yellow, respectively. The auditory organ known as the Organ of Corti is shown in blue. Potential routes of entry for therapeutics are indicated: round window membrane (RWM) and cochleostomy (CO). [Credit: (*24*)] (**B**) Schematic diagram of a cross section of the Organ of Corti. The three rows of outer hair cells and the one row of inner hair cells are colored in blue, and the auditory neurons or spiral ganglion neurons are shown in green. [Reproduced by permission of the American Physiological Society from (*81*)] (**C**) Scanning electron micrograph of the Organ of Corti. The hair-cell cell bodies are pseudo-colored blue. [Reproduced by permission of Informa Healthcare from (*82*)] (**D**) Scanning electron micrograph of the hair bundle of a single outer hair cell. [Credit: David N. Furness]

mutations in *MYO7A*, which encodes an unconventional myosin that is expressed in the sensory cells of eyes and ears. The human trial was approved on the basis of successful lentiviral gene transfer of wild-type *MYO7A* into the eyes of mice with Usher 1B phenotype (*13*). This approach could be tested in mouse ears to treat auditory dysfunction in mouse models of Usher 1B. If successful in mouse ears, the approach could be adapted for human trials in the ears of Usher 1B patients.

Nonsyndromic hearing loss affects the ear alone and includes 43 genes that carry autosomal recessive mutations, designated DFNB1-DFNB93, and 25 genes with dominant mutations, designated DFNA1-DFNA64, with some overlap in the affected genes. The most common hereditary hearing loss, DFNB1, affects supporting cells in the inner ear and is responsible for deafness in 40% of patients with genetic hearing loss. Several DFNB1 mutations have been identified in the *GJB2* gene, which encodes connexin-26, a component of inner-ear gap-junction channels. Connexin-26 channels are expressed in a network of supporting cells that connect the Organ of Corti through the basilar membrane to the cells of the stria vascularis. This network is critical for recycling potassium ions released from the hair-cell basolateral membrane back to the potassium-rich endolymph that bathes hair bundles. Disruption of the K^+ recirculation network leads to a decline in endolymph K^+ concentration and a decay of the endolymph potential (~+100 mV), which together result in profound deafness. Several hearing-loss genes, both syndromic and nonsyndromic, have been identified that affect K^+ recirculation, including three gap-junction genes and the Jervell and Lange Nielsen Syndrome gene, *KCNQ1*, which encodes a potassium channel. Gene restoration studies that target the K^+ recirculation network are currently under way, with several focused on connexin-26 in a mouse model of DFNB1. A recent in vitro study presented compelling proof-of-concept evidence that gene transfer of *GJB2* can restore functional gap-junction channels in the supporting cell network required for K^+ recirculation (*14*). In a more recent study, Yu *et al.* (*15*) used a similar adeno-associated viral (AAV) vector approach in vivo in mice in which *Gjb2* was knocked out and reported widespread expression of connexin-26 in the supporting cell network. Although there was no significant hearing improvement, the potential to move this line of investigation forward in animal studies and—if successful—in human studies is tantalizing. Because mutation of *GJB2* is the most common cause of genetic deafness (up to 50% in some populations) (*16*), effective strategies to restore gap-junction function in the cochlear supporting cell network could benefit a substantial percentage of patients with genetic hearing loss.

A number of other mutations affect hair-cell genes, the largest group of these affecting development, maintenance, and function of the mechanosensory hair bundle. For genes that affect hair bundles, the design of effective therapeutic strategies faces several substantial challenges. First, gene delivery systems must be capable of targeting hair cells. Second, because hair cells undergo a precise developmental sequence, it may be necessary to provide the correct gene within the correct developmental time frame. For some genes required early in development (prenatally), this may limit the therapeutic window. Last, current expression systems provide little control over expression level. Even within the right cells and at the right time, achieving the optimal expression level while minimizing toxic overexpression will add to the challenges of hair-cell gene therapy. Nonetheless, a number of studies have reported successful use of viral transfection of mouse cochlear hair cells in vivo at both neonatal (*17*, *18*) and adult stages (Fig. 3) (*19*).

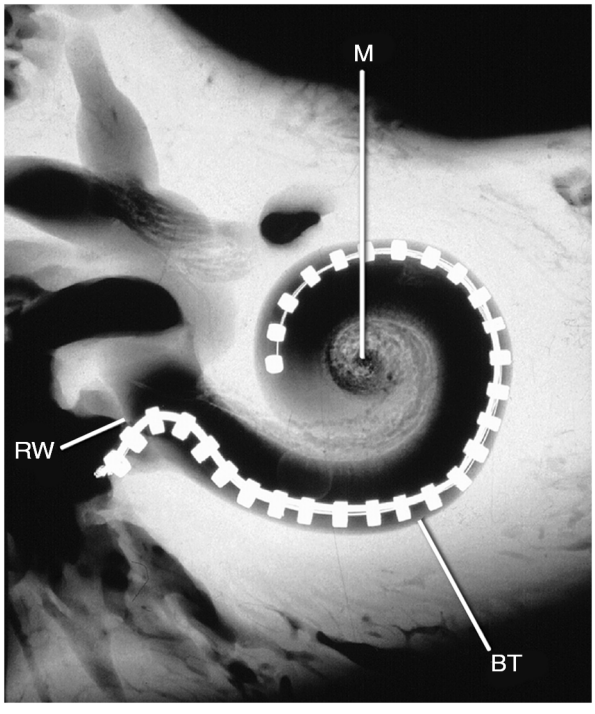

Fig. 2. X-ray image of a cochlear implant in a human cochlea. This implant includes 29 stimulating electrodes. M, modiolus; RW, round window or entry point to the basal turn of the cochlea; BT, basal turn of the cochlea. [Reproduced by permission of the Royal Society from (*83*)]

Moreover, numerous studies have demonstrated adenoviral and AAV vector transfection of rodent hair cells in vitro. For example, Kawashima *et al.* (*20*) used adenoviral vectors with reduced toxicity to replace wild-type *Tmc1* or *Tmc2*, driven by a *MYO7A* hair-cell promoter. The strategy successfully restored hair-cell mechanotransduction in nonfunctional hair cells that lacked endogenous *Tmc1* and *Tmc2*. Although the precise molecular function of TMC1 and TMC2 is controversial (*21*), it is clear that mutations in *TMC1* cause deafness in mice and humans (*22*). As such, gene augmentation in this and other mouse models of human deafness may provide powerful experimental paradigms for investigating gene-therapy strategies to restore auditory function in vivo.

In an in vivo model system, Akil *et al.* (*23*) demonstrated successful replacement of vesicular glutamate transporter 3 (VGLUT3) in a *Vglut3* knockout model [commentaries by Holt and Vandenberghe (*24*) and Martin and Raphael (*25*)]. In this case, AAV vectors, serotype 1, were used to deliver the *Vglut3* sequence to the inner ear. The investigators achieved a high level of transfection efficiency, 100% of the targeted cells, and restored some auditory function as measured with auditory brainstem responses and auditory startle reflexes. Although the vectors carried a promoter with broad activity, chicken β-actin, the *Vglut3* transgene was only expressed in the targeted auditory inner hair cells. The authors suggested that endogenous regulatory mechanisms may govern expression level and thus may help limit off-target expression. If similar mechanisms regulate expression of other hair-cell genes, they may help minimize concern over the need to develop exogenous systems with precise control over expression level. Although the Akil *et al.* (*23*) study presented some of the first data showing gene-therapy–mediated recovery of auditory function in a knockout mouse model, deafness-causing mutations in human *VGLUT3* are not common and when present are dominant (DFNA25), suggesting that the utility of gene augmentation strategies for *VGLUT3* mutations in humans may be limited.

Other mutations, such as those causing the recessive nonsyndromic DFNB9 (*26*), affect neurotransmission at the hair-cell afferent synapse. The mutated gene in DFNB9 encodes otoferlin, which functions as a calcium sensor required for fusion of synaptic vesicles and release of neurotransmitter (*27*). Reisinger *et al.* (*28*) investigated the possibility that synaptotagmin1 might replace otoferlin and used AAV-mediated gene transfer of the synaptotagmin1 gene into mouse hair cells deficient in otoferlin. Although the strategy failed to restore synaptic transmission, the possibility remains that gene transfer of the wild-type otoferlin sequence may restore function for DFNB9 patients. AAV-mediated gene transfer of otoferlin was not attempted because the coding sequence was too large to be packaged into AAV vectors, which further highlights the need for development of larger-capacity vectors.

Gene Therapy for Acquired Deafness

Gene therapy strategies may also prove useful for acquired hearing loss that results from death of

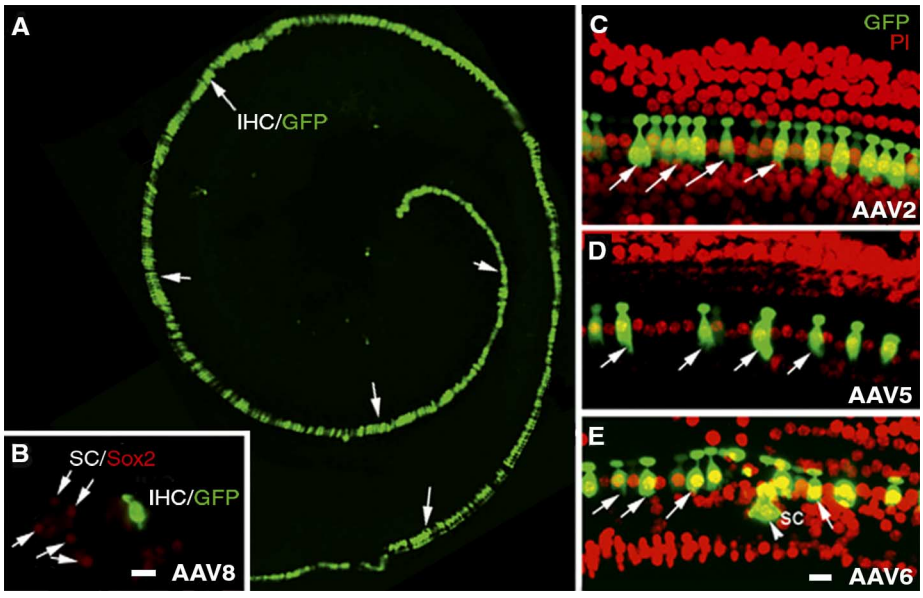

Fig. 3. Confocal images of adult mouse cochlea transfected with AAV vectors of various serotypes. (**A**) Inner hair cells (arrows) were positive for the transgene, GFP, 7 days after transfection with AAV2. (**B**) Cross section of the Organ of Corti transfected with AAV8, counterstained for Sox2 (red), which marks supporting cells. (**C** to **E**) High-magnification view of hair cells transfected with (C) AAV2, (D) AAV5, or (E) AAV6, counterstained with the nuclear marker, propidium iodide (red). Scale bars, 20 μm. [Reprinted from (*19*) by permission of the Nature Publishing Group]

hair cells or spiral ganglion neurons. Hair cells are fragile and can easily be damaged by overexposure to loud sounds, bacterial and viral infections, and an array of ototoxic drugs, including aminoglycoside antibiotics and the anticancer drug, cisplatin. Although lower vertebrates retain the ability to generate new hair cells, this capacity has been lost in mammals, including humans. Therefore, generation of new mammalian hair cells is an active area of research. In addition to stem-cell therapies for hair-cell replacement (below), it may also be possible to convert the phenotype of endogenous supporting cells into hair cells by using key regulatory elements, such as the hair-cell transcription factor ATOH1 [reviewed by Rubel *et al.* (*29*)]. ATOH1 is a basic helix-loop-helix transcription factor that is necessary for proper hair cell differentiation (*30*). Several groups have used transfection of *Atoh1* into inner-ear–supporting cells to drive generation of new hair cells, either in deafened guinea pig inner ears (*31*) or in embryonic mouse inner ears (*32*). In the latter case, the cells were found to be functional, with hair bundles that supported mechanosensory function. In both studies, exogenous *Atoh1* expression was targeted to the supporting cells of the cochlea. However, *Atoh1* may also offer therapeutic benefits in surviving hair cells that have lost their mechanosensory hair bundles. Yang *et al.* (*33*) suggested that forced expression of *Atoh1* in noise-damaged hair cells can induce repair and recovery of sensory hair bundles. If so, such an approach may offer hope for patients who suffer acute noise damage, such as battlefield troops or victims of the Boston Marathon bombing, many of whom suffered hearing loss and are involved in an ongoing clinical study. The therapeutic window may be short, however, because hair cells must be targeted shortly after the injury, before they die. Although additional data will be required to map out the temporal window of opportunity for this potential therapeutic approach, human clinical trials have recently been approved for use of adenoviral delivery of *Atoh1* into the supporting cells of the inner ear to treat auditory and balance dysfunction in an industry collaboration between Novartis and GenVec. The team filed an Investigational New Drug (IND) application with the U.S. Food and Drug Administration (FDA) for the clinical development of the approach and received approval in early 2014.

Gene Therapy for Spiral Ganglion Neurons

Loss of spiral ganglion neurons (SGNs) may occur either as a secondary consequence after loss of trophic support or can occur directly through damage to the afferent synapse or spiral ganglion cell bodies (*34*). Inner-ear cells, including hair cells, release at least two neurotrophins: brain-derived neurotrophic factor (BDNF) and neurotrophin-3 (NT3) (*35*). Although the source of BDNF and NT3 is dynamically regulated during development (*36*, *37*), it has been suggested that hair-cell death leads to loss of trophic support and progressive loss of SGNs. This model has been challenged by Zilberstein *et al.* (*38*), who suggested that inner hair cells are not necessary for SGN survival and that the source of the trophic support may be cochlear supporting cells. Regardless of the cause, loss of SGNs reduces the number of information channels to the brain, impairing speech perception and limiting the therapeutic utility of cochlear implants. Because cochlear implants stimulate SGNs directly with electrical impulses, survival of SGNs is a prerequisite for implant success. Thus, a number of studies have focused on methods for providing exogenous trophic support capable of promoting SGN survival. Several viral vectors have been used successfully to mediate gene transfer of the coding sequence for BDNF into the supporting cells of the inner ear in animal models (*11*, *39*–*41*). The strategy has generally proven successful for promoting SGN survival, at least over the short term. However, several important questions remain. Can the strategy be extended to promote long-term SGN survival, and if so, can it be adapted for use in conjunction with cochlear implant technology in humans? Recent animal studies demonstrated that cochlear implant electrodes can be used to electroporate plasmids that encode BDNF into cochlear tissues and promote SGN neurite outgrowth and survival (*42*). Whether viral-mediated expression of neurotrophins, electroporation, or direct perfusion of exogenous growth factors is better suited for clinical application will be worthy of further investigation.

Stem-Cell Therapies for Generation of Hair Cells

Stem-cell therapy for treating deafness has received considerable attention over the past decade, with major advances in generating hair-cell–like cells and auditory neurons in vitro from fetal auditory stem cells, embryonic stem cells, or induced pluripotent stem cells (*43*). Identification of a renewable source of sensory progenitor cells is an important first step in the quest to develop stem-cell therapy for deafness.

Li *et al.* (*44*) demonstrated the feasibility of using stepwise differentiation for the generation of inner-ear progenitor cells and hair cells from embryonic stem cells. Nestin-positive progenitor cells that expressed markers of the otic placode and otic vesicle were successfully obtained from embryoid-body–derived cell populations with an epidermal growth factor (EGF)/insulin-like growth factor 1 (IGF-1) treatment followed by basic fibroblast growth factor (bFGF). Differentiation was induced by removal of growth factor for 10 to 14 days, after which the presence of inner-ear cell types was indicated by expression of various hair-cell markers, including ATOH1 and MYO7A.

Stepwise differentiation protocols have been further refined to successfully lead to the generation of hair-cell–like cells. Oshima *et al.* (*45*) identified conditions that enabled differentiation of otic progenitors into hair-cell–like cells (Fig. 4, A to C). These cells expressed numerous hair-cell genes, developed actin-based hair-bundle–like protrusions on their apical surfaces, and displayed interciliary links that resembled tip links. Mechanical deflection of the apical bundles evoked mechanosensitive transduction currents; however, the amplitudes were small, and they appeared to lack directional sensitivity. The currents were inhibited

by a mechanotransduction channel blocker, dihydrostreptomycin, suggesting that the currents were carried by bona fide mechanotransduction channels. Oshima *et al.* (*45*) also analyzed voltage-dependent currents that varied in amplitude and kinetics but resembled those of immature vestibular hair cells (*46*). Although an important advance, the generation of hair-cell–like cells required coculture with a feeder layer of stromal cells derived from embryonic chicken utricles. The feeder layer provided required trophic support for a short time, but the specific factors needed remain unknown. The approach was also limited by its low yield, with only very few cells adopting hair-cell–like phenotypes.

More recently, Koehler *et al.* (*47*) used a precise temporal sequence of signaling molecules to recapitulate in vivo development in a three-dimensional culture (Fig. 4, D to H). Preplacodal induction was successful with an interplay of bone morphogenetic protein (BMP) activation and transforming growth factor–β (TGF-β) inhibition. Induction resulted in self-guided formation of sensory epithelia, with hair cells that possessed functional and structural properties of native hair cells. The number of cells generated by this method was astonishing, with more than 1500 cells per aggregate. This tour de force is a giant step forward in the inner-ear stem-cell field. Demonstration that these cells display normal hair-cell functions, including mechanotransduction, will help validate this approach.

Stem-Cell Therapies for Generation of Auditory Neurons

Although generation of sensory hair cells from stem cells has been an important focus of the field, it is only part of the picture. Because damage or loss of SGNs can be a primary cause of deafness (*34*, *48*), development of strategies to generate new auditory neurons has become a major focus. Replacement of auditory neurons could serve two potential clinical needs. For auditory neuropathy patients who retain intact hair cells, generation of new SGNs capable of reinnervating hair-cell epithelia has the potential to restore function. For patients with auditory neuron and hair-cell loss, generation of new SGNs could provide a conduit for cochlear implants to communicate with auditory brainstem nuclei. Of course, both strategies will require that the new SGNs make appropriate and functional contact with the preexisting neuronal circuitry of the auditory brainstem.

Neural progenitors have been successfully derived from cochlear stem cells (*43*, *49*), neural stems of the lateral ventricle (*50*), and human embryonic stem cells (*51*, *52*). Several groups have identified factors capable of promoting stem-cell differentiation into glutamatergic neurons with otic-like, SGN phenotypes (*53*, *54*). To investigate integration of neural progenitors into the damaged inner ear, Corrales *et al.* (*55*) deafened gerbils with ouabain, which selectively killed type I spiral ganglion neurons yet preserved the sensory hair cells. After 10 weeks, transplanted otic-like neural progenitors (ONPs) successfully engrafted into the modiolus-forming ectopic ganglia with differentiated neuronal-type cells that projected to the sensory cells within the organ of Corti. Some fibers were observed at the point they exited the modiolus and projected toward the brainstem. To assess whether such progenitors could restore function, Chen *et al.* (*52*) adopted a similar approach and found that transplanted ONPs not only survived and differentiated, but also grew neurite projections and improved auditory-evoked responses. Otic epithelia progenitors (OEPs) and ONPs were obtained from human embryonic stem cells treated with FGF3 and FGF10, signaling factors necessary for placode

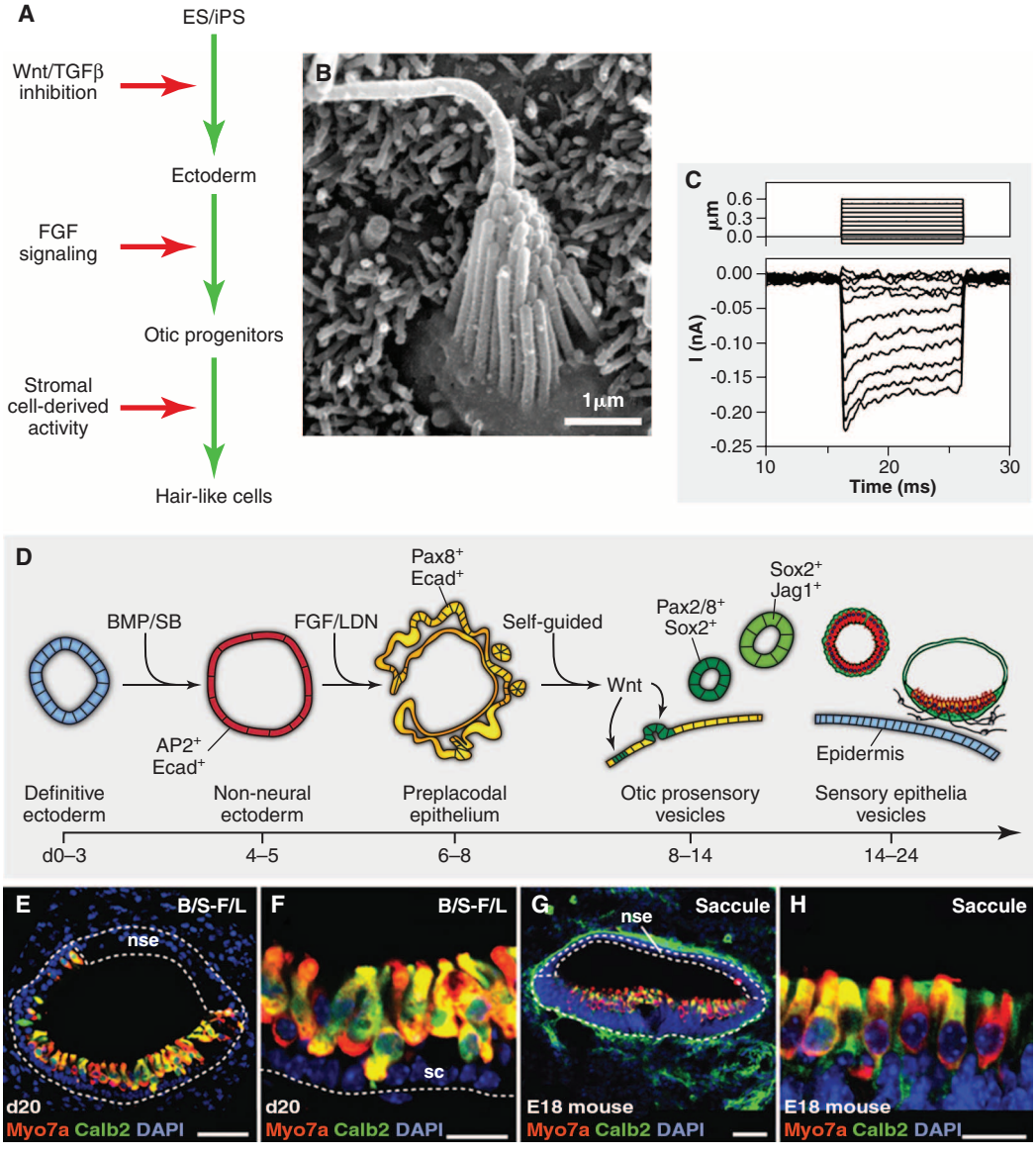

Fig. 4. Examples of stem-cell–derived hair-cell–like cells. (**A**) Strategy used by Oshima *et al.* (*45*). (**B**) Hair bundle generated from strategy shown in (A). (**C**) A family of mechanotransduction currents recorded from a stem-cell–derived hair-cell–like cell. The hair bundle deflection protocol is shown above. [(A) to (C) are reproduced by permission of Elsevier from (*45*)] (**D**) Strategy used by Koehler *et al.* (*49*). (**E** and **F**) Stem-cell–derived otic vesicles and hair cells. (**G** and **H**) Embryonic vestibular organ and hair cells. Immunomakers are color-coded at the bottom. Scale bar, 50 μm (E) and (G); 25 μm (F) and (H). [(D) to (H) are reproduced by permission of the Nature Publishing Group from (*47*)].

induction. ONPs were further differentiated into otic-like neurons by use of a stepwise approach that included several growth and differentiation factors. As early as 4 weeks after transplantation, improvement of hearing thresholds was evident, and by 10 weeks, transplanted animals had recovered ~46% of their auditory function. Although the restoration of proper anatomical connections by using ONPs was observed by both Corrales *et al.* (*55*) and Chen *et al.* (*52*), the functional recovery has yet to be replicated. Validation of these remarkable results will bode well for the development of stem-cell–based restoration strategies for the generation of new auditory neurons in humans (*56*).

Molecular Therapies for Generation of New Hair Cells

Pharmacological compounds that could induce formation of new hair cells would be particularly attractive for treating patients with hearing loss that results from hair-cell death. When hair cells die, the capacity for normal hearing fades. Unfortunately, mammalian cochlear hair cells do not grow back. However, a handful of studies have now reported generation of new hair cells by manipulating endogenous signaling pathways in supporting cells. The possibility that these pathways could be targeted by pharmacological agents is enticing.

White *et al.* (*57*) collected cochlear supporting cells that expressed the cell-cycle inhibitor $P27^{Kip1}$ and grew the cells on a mesenchymal feeder layer in vitro. The supporting cells down-regulated $P27^{Kip1}$ expression and reentered the cell cycle generating new cells, some of which became hair cells. This finding suggests that pharmacologic manipulation of cell-cycle genes may be a viable strategy for generation of new inner supporting cells and new hair cells.

In another line of investigation, a population of cochlear cells was identified that expressed LGR5, a marker associated with stem cells (*49*, *58*–*60*). The LGR5-positive cells were capable of generating new hair cells, confirming that LGR5-positive cells can act as sensory progenitors in vivo (*61*, *62*). Because the cells were responsive to small-molecule Wnt agonists and antagonists, it is plausible that manipulation of the Wnt pathway in the mature cochlea may hold the potential for generation of new hair cells in the human inner ear.

Although these studies have helped define important inner-ear signaling pathways, the work has not yet been developed for in vivo application. Recently, Jeon *et al.* (*63*) used a γ-secretase inhibitor that blocks Notch signaling and removes lateral inhibition between hair cells and supporting cells. The team found that inner-ear progenitor cells can be directed toward a hair-cell phenotype by manipulating γ-secretase activity. The investigators introduced the inhibitor into cochlear explants in vitro and found a large number of new hair cells generated from supporting cells. This observation was confirmed and extended by another group, who used γ-secretase inhibitors to generate hair-cell–like cells from supporting cells in cochleas damaged with ototoxic drugs (*64*). When Mizutari *et al.* (*65*) introduced γ-secretase inhibitors via round-window injection into mature noise-damaged mouse cochleas in vivo, they found that organ of Corti supporting cells were converted into outer hair cells in the mid- to low-frequency regions. The conversion of supporting cells to hair cells was confirmed by using lineage tracers and antibodies to the outer-hair-cell–specific protein, prestin. Generation of new hair cells in vivo was sufficient to restore partial auditory function, as determined by lower sound thresholds in auditory brainstem recordings. Although systemic application of the γ-secretase inhibitor caused severe side effects, local delivery to the inner ear appeared to overcome those effects. The Mizutari *et al.* (*65*) results will likely motivate the search for compounds or delivery methods that can selectively inhibit the Notch signaling pathway in cochlear supporting cells.

Hair cells themselves may also be targets of pharmacologic manipulation for generation of new hair cells. For example, Sage *et al.* (*66*) identified retinoblastoma (Rb) protein as a signaling molecule that prevents mature postmitotic hair cells from reentering the cell cycle. Genetic deletion of Rb was shown to promote mitosis in mature hair cells and formation of new functional hair cells. Unfortunately, the therapeutic utility of this strategy may be limited because Rb is a tumor-suppressor gene and because the newly generated hair cells tended to undergo p53-mediated apoptosis (*67*). Nonetheless, the findings raise the possibility that cell-cycle regulators may be suitable pharmacological or gene-therapy targets for control of hair-cell proliferation and restoration of auditory function. Of course, such strategies will depend on survival of at least some endogenous hair cells and the ability of the new hair cells to resist apoptosis.

Molecular Therapies for Genetic Hearing Loss

To target a specific gene defect, Lentz *et al.* (*68*) provided a startling example of treatment of a genetic deafness using systemic application of antisense oligonucleotides (ASO). The authors used a mouse model of human Usher Syndrome 1C, which affects harmonin (*69*, *70*), a component of the hair-cell transduction complex (*71*). The mouse model was generated so as to mimic a recessive mutation in French-Acadian USH1C patients that introduces a cryptic splice site and results in a severely truncated protein (*68*, *72*). Lentz *et al.* (*68*) screened 47 different ASO sequences for those that could block cryptic splicing and promote correct splicing of the harmonin mRNA transcript. An ASO was identified that provided >20% correct splicing and increased expression of wild-type harmonin protein. Remarkably, homozygous mutant mice treated with a single ASO intraperitoneal injection recovered normal vestibular function and some auditory function, particularly at lower frequencies (8 to 16 kHz in the mouse). The authors went on to show that the ASO treatment restored harmonin protein levels in vivo and restored normal cochlear hair-cell morphology, but they were cautious to point out that the strategy was only effective at very early developmental stages, which may limit the utility of the approach in humans. Although a number of mechanistic questions remain, including the route of ASO entry from intraperitoneal injection into cochlear hair cells, the study presents a stimulating new strategy for the potential treatment of genetic hearing loss by using systemic injection of antisense oligonucleotides.

Future Directions

Despite the remarkable progress outlined above, a number of important questions and challenges remain. Generation of new hair cells or neurons will require proper integration of the new cells into an existing, mature organ. The new hair cells will also need to be properly oriented within the sensory epithelium if they are to be functional. To transduce functionally relevant stimuli, new hair bundles must be sensitive to the appropriate sound-evoked stimulus, which means that their bundles must be oriented with the same polarity as that of native cells. Furthermore, because auditory hair cells come in different varieties (inner and outer) and their biophysical properties vary along the tonotopic axis of the cochlea, newly generated hair cells must mimic the location-dependent properties of native cells if they are to replicate the fully functional auditory system. Likewise, new neurons must be capable of innervating existing hair-cell epithelia within the tonotopic arrangement if they are to convey frequency-specific information. The new neurons must also be capable of projecting to the brainstem and making appropriate, functional contacts that preserve the tonotopic map of the cochlear nucleus. Alternatively, if the auditory system retains the capacity for plastic rearrangement of tonotopic maps, precise connectivity may not be an absolute requirement. As successful cochlear implants and the aging auditory periphery have demonstrated, the central auditory pathways are capable of learning how to deal with imperfect or incomplete sensory information.

For strategies that aim to repair hair cells or other inner-ear cells with gene therapy, there is still a great need to develop better control over exogenous gene targeting and expression. The technical capacity for gene transfer of wild-type sequences into the supporting cells (*17*) and hair cells of the inner ear currently exists. Yet, there is still substantial need for better understanding of the temporal window of therapeutic opportunity, which may vary depending on the specifics of the genetic defect. Also needed are better control over expression level and studies of possible detrimental effects in off-target cell types.

Thus far, most inner-ear gene-therapy strategies have focused on gene replacement or augmentation approaches. These approaches may be well suited for recessive deafness but offer little hope for overcoming the consequences of dominant forms of genetic deafness. Several novel alternatives for

treating dominant deafness are on the horizon. One such approach would involve viral delivery of small interfering RNA (siRNA) sequences designed to suppress expression of the mutant sequence but not the correct, wild-type sequence (*73*). Because many forms of dominant deafness result in single-point mutations, the design of effective and specific siRNAs, with only one nucleotide mismatch, will be challenging.

Another exciting approach would be the use of genome-editing strategies. These cutting-edge approaches have not yet been investigated in the inner ear but could offer hope of a single treatment for restoration of the wild-type sequence in native DNA. Zinc-finger nucleases (ZFNs) or transcriptional activator-like effector nucleases [TALENs; reviewed by Gaj *et al*. (*74*, *75*)] could be designed and packaged into viral vectors that target inner-ear supporting cells or hair cells. RNA-guided DNA endonucleases based on clustered regulatory interspaced short palindromic repeats (CRISPR/Cas) have also recently emerged and hold enormous potential for genome editing in humans (*74*, *76*, *77*). It seems plausible that any of these genome-editing strategies could be adopted for use in hair cells and supporting cells of the inner ear.

In some cases, combinations of the approaches discussed above may be warranted. For example, in cases of genetic deafness hair-cell death may follow as a secondary consequence. If so, these patients may require stem-cell or gene-therapy approaches to restore hair cells. If autologous stem cells are used or if *Atoh1* is used to generate new hair cells from endogenous cells, there may also be need to repair or replace mutant genes in the new hair cells.

Another example of a dual approach might be the use of gene or stem-cell therapies in combination with next-generation cochlear implants (*78*). One potential strategy is the use of optogenetics and the expression of channelrhodopsin in spiral ganglion neurons introduced with gene-therapy vectors (*79*). Cochlear implants could then be designed by using fiber optics and focused stimulation of small numbers of SGNs at perhaps hundreds of locations along the cochlea. This approach could circumvent a problem imposed by electrical stimulation: the spread of electrical current to neighboring off-target neurons, which severely limits the number of positions that can be stimulated along the tonotopic axis of the cochlea.

Last, as a platform to translate potential therapeutic approaches from animal models into human tissue, Kesser *et al*. (*80*) developed a novel experimental paradigm using human inner-ear tissue maintained in organotypic culture. Live vestibular tissue was excised from the inner ears of human patients undergoing resection of tumors growing on the eighth cranial nerve. The sensory epithelia were kept alive in culture dishes and exposed to adenoviral vectors that carried the wild-type coding sequence for green fluorescent protein (GFP) and the potassium channel protein KCNQ4. Both supporting cells and hair cells were transfected, and KCNQ4 was properly localized along the hair-cell basolateral membrane. Because mutations of KCNQ4 cause the dominant-progressive hearing loss, DFNA2, the strategy may require substantial overexpression of the wild-type protein. The study demonstrated that vectors and strategies developed in mice can be adapted for use in human tissue. Furthermore, the in vitro model system may provide a platform to help validate other treatment strategies before initiation of human clinical trials.

Complete restoration of auditory function is a vexing problem. Perception of the rich auditory soundscape that humans encounter daily—which includes speech, music, and a plethora of natural and man-made sounds—demands a system capable of exquisite sensitivity, broad dynamic range, precise frequency discrimination, and high temporal fidelity. This is a tall order for any biological or mechanical system, and restoration of such a system in adult humans only adds to the challenge. Yet with the commitment of government funding agencies, private foundations, and teams of dedicated scientists, it is an achievable goal with a sound future.

References and Notes

1. W. Zhan *et al*., Generational differences in the prevalence of hearing impairment in older adults. *Am. J. Epidemiol.* **171**, 260–266 (2010). doi: 10.1093/aje/kwp370; pmid: 20008889
2. Y. Sergeyenko, K. Lall, M. C. Liberman, S. G. Kujawa, Age-related cochlear synaptopathy: An early-onset contributor to auditory functional decline. *J. Neurosci.* **33**, 13686–13694 (2013). doi: 10.1523/JNEUROSCI.1783-13.2013; pmid: 23966690
3. J. P. Harris, A. F. Ryan, Fundamental immune mechanisms of the brain and inner ear. *Otolaryngol. Head Neck Surg.* **112**, 639–653 (1995). doi: 10.1016/S0194-5998(95)70170-2; pmid: 7777346
4. T. Rivera, L. Sanz, G. Camarero, I. Varela-Nieto, Drug delivery to the inner ear: strategies and their therapeutic implications for sensorineural hearing loss. *Curr. Drug Deliv.* **9**, 231–242 (2012). doi: 10.2174/156720112800389098; pmid: 22283653
5. P. Wangemann, K+ cycling and the endocochlear potential. *Hear. Res.* **165**, 1–9 (2002). doi: 10.1016/S0378-5955(02)00279-4; pmid: 12031509
6. Y. H. Park *et al*., Conditioning the cochlea to facilitate survival and integration of exogenous cells into the auditory epithelium. *Mol. Ther.* **22**, 873–880 (2014).
7. A. A. Eshraghi *et al*., The cochlear implant: Historical aspects and future prospects. *Anat. Rec. (Hoboken)* **295**, 1967–1980 (2012). doi: 10.1002/ar.22580; pmid: 23044644
8. "29 years old and hearing myself for the 1st time!" (2011); www.youtube.com/watch?v=LsOo3jzkhYA.
9. B. E. Pfingst *et al*., Cochlear infrastructure for electrical hearing. *Hear. Res.* **281**, 65–73 (2011). doi: 10.1016/j.heares.2011.05.002; pmid: 21605648
10. M. Di Domenico *et al*., Towards gene therapy for deafness. *J. Cell. Physiol.* **226**, 2494–2499 (2011). doi: 10.1002/jcp.22617; pmid: 21792906
11. H. Fukui, Y. Raphael, Gene therapy for the inner ear. *Hear. Res.* **297**, 99–105 (2013). doi: 10.1016/j.heares.2012.11.017; pmid: 23265411
12. R. Sacheli, L. Delacroix, P. Vandenackerveken, L. Nguyen, B. Malgrange, Gene transfer in inner ear cells: A challenging race. *Gene Ther.* **20**, 237–247 (2013). doi: 10.1038/gt.2012.51; pmid: 22739386
13. T. Hashimoto *et al*., Lentiviral gene replacement therapy of retinas in a mouse model for Usher syndrome type 1B. *Gene Ther.* **14**, 584–594 (2007). doi: 10.1038/sj.gt.3302897; pmid: 17268537
14. G. Crispino *et al*., BAAV mediated GJB2 gene transfer restores gap junction coupling in cochlear organotypic cultures from deaf Cx26Sox10Cre mice. *PLOS ONE* **6**, e23279 (2011). doi: 10.1371/journal.pone.0023279; pmid: 21876744
15. Q. Yu *et al*., Virally expressed connexin26 restores gap junction function in the cochlea of conditional Gjb2 knockout mice. *Gene Ther.* **21**, 71–80 (2013). pmid: 24225640
16. W. E. Nance, X. Z. Liu, A. Pandya, Relation between choice of partner and high frequency of connexin-26 deafness. *Lancet* **356**, 500–501 (2000). doi: 10.1016/S0140-6736(00)02565-4; pmid: 10981905
17. A. M. Sheffield *et al*., Viral vector tropism for supporting cells in the developing murine cochlea. *Hear. Res.* **277**, 28–36 (2011). doi: 10.1016/j.heares.2011.03.016; pmid: 21530627
18. L. Xia, S. Yin, J. Wang, Inner ear gene transfection in neonatal mice using adeno-associated viral vector: A comparison of two approaches. *PLOS ONE* **7**, e43218 (2012). doi: 10.1371/journal.pone.0043218; pmid: 22912830
19. L. A. Kilpatrick *et al*., Adeno-associated virus-mediated gene delivery into the scala media of the normal and deafened adult mouse ear. *Gene Ther.* **18**, 569–578 (2011). doi: 10.1038/gt.2010.175; pmid: 21209625
20. Y. Kawashima *et al*., Mechanotransduction in mouse inner ear hair cells requires transmembrane channel-like genes. *J. Clin. Invest.* **121**, 4796–4809 (2011). doi: 10.1172/JCI60405; pmid: 22105175
21. J. R. Holt, B. Pan, M. A. Koussa, Y. Asai, TMC function in hair cell transduction. *Hear. Res.* (2014). doi: 10.1016/j.heares.2014.01.001; pmid: 24423408
22. K. Kurima *et al*., Dominant and recessive deafness caused by mutations of a novel gene, TMC1, required for cochlear hair-cell function. *Nat. Genet.* **30**, 277–284 (2002). doi: 10.1038/ng842; pmid: 11850618
23. O. Akil *et al*., Restoration of hearing in the VGLUT3 knockout mouse using virally mediated gene therapy. *Neuron* **75**, 283–293 (2012). doi: 10.1016/j.neuron.2012.05.019; pmid: 22841313
24. J. R. Holt, L. H. Vandenberghe, Gene therapy for deaf mice goes viral. *Mol. Ther.* **20**, 1836–1837 (2012). doi: 10.1038/mt.2012.196; pmid: 23023054
25. D. M. Martin, Y. Raphael, Have you heard? Viral-mediated gene therapy restores hearing. *Neuron* **75**, 188–190 (2012). doi: 10.1016/j.neuron.2012.06.008; pmid: 22841304
26. S. Yasunaga *et al*., A mutation in OTOF, encoding otoferlin, a FER-1-like protein, causes DFNB9, a nonsyndromic form of deafness. *Nat. Genet.* **21**, 363–369 (1999). doi: 10.1038/7693; pmid: 10192385
27. I. Roux *et al*., Otoferlin, defective in a human deafness form, is essential for exocytosis at the auditory ribbon synapse. *Cell* **127**, 277–289 (2006). doi: 10.1016/j.cell.2006.08.040; pmid: 17055430
28. E. Reisinger *et al*., Probing the functional equivalence of otoferlin and synaptotagmin 1 in exocytosis. *J. Neurosci.* **31**, 4886–4895 (2011). doi: 10.1523/JNEUROSCI.5122-10.2011; pmid: 21451027
29. E. W. Rubel, S. A. Furrer, J. S. Stone, A brief history of hair cell regeneration research and speculations on the future. *Hear. Res.* **297**, 42–51 (2013). doi: 10.1016/j.heares.2012.12.014; pmid: 23321648
30. N. A. Bermingham *et al*., Math1: an essential gene for the generation of inner ear hair cells. *Science* **284**, 1837–1841 (1999).doi: 10.1126/science.284.5421.1837; pmid: 10364557
31. M. Izumikawa *et al*., Auditory hair cell replacement and hearing improvement by Atoh1 gene therapy in deaf mammals. *Nat. Med.* **11**, 271–276 (2005). doi: 10.1038/nm1193; pmid: 15711559
32. S. P. Gubbels, D. W. Woessner, J. C. Mitchell, A. J. Ricci, J. V. Brigande, Functional auditory hair cells produced in the mammalian cochlea by in utero gene transfer. *Nature* **455**, 537–541 (2008). doi: 10.1038/nature07265; pmid: 18754012

33. S. M. Yang *et al.*, Regeneration of stereocilia of hair cells by forced Atoh1 expression in the adult mammalian cochlea. *PLOS ONE* **7**, e46355 (2012). doi: 10.1371/journal.pone.0046355; pmid: 23029493
34. S. G. Kujawa, M. C. Liberman, Adding insult to injury: Cochlear nerve degeneration after "temporary" noise-induced hearing loss. *J. Neurosci.* **29**, 14077–14085 (2009). doi: 10.1523/JNEUROSCI.2845-09.2009; pmid: 19906956
35. P. Ernfors, T. Van De Water, J. Loring, R. Jaenisch, Complementary roles of BDNF and NT-3 in vestibular and auditory development. *Neuron* **14**, 1153–1164 (1995). doi: 10.1016/0896-6273(95)90263-5; pmid: 7605630
36. U. Pirvola *et al.*, Expression of neurotrophins and Trk receptors in the developing, adult, and regenerating avian cochlea. *J. Neurobiol.* **33**, 1019–1033 (1997). doi: 10.1002/(SICI)1097-4695(199712)33:7<1019::AID-NEU11>3.0.CO;2-A; pmid: 9407020
37. M. Sugawara, J. C. Murtie, K. M. Stankovic, M. C. Liberman, G. Corfas, Dynamic patterns of neurotrophin 3 expression in the postnatal mouse inner ear. *J. Comp. Neurol.* **501**, 30–37 (2007). doi: 10.1002/cne.21227; pmid: 17206617
38. Y. Zilberstein, M. C. Liberman, G. Corfas, Inner hair cells are not required for survival of spiral ganglion neurons in the adult cochlea. *J. Neurosci.* **32**, 405–410 (2012). doi: 10.1523/JNEUROSCI.4678-11.2012; pmid: 22238076
39. M. D. Geschwind *et al.*, Defective HSV-1 vector expressing BDNF in auditory ganglia elicits neurite outgrowth: model for treatment of neuron loss following cochlear degeneration. *Hum. Gene Ther.* **7**, 173–182 (1996). doi: 10.1089/hum.1996.7.2-173; pmid: 8788168
40. A. K. Wise *et al.*, Effects of localized neurotrophin gene expression on spiral ganglion neuron resprouting in the deafened cochlea. *Mol. Ther.* **18**, 1111–1122 (2010). doi: 10.1038/mt.2010.28; pmid: 20216530
41. P. J. Atkinson *et al.*, Neurotrophin gene therapy for sustained neural preservation after deafness. *PLOS ONE* **7**, e52338 (2012). doi: 10.1371/journal.pone.0052338; pmid: 23284995
42. Jeremy L. Pinyon *et al.*, Close-field electroporation gene delivery using the cochlear implant electrode array enhances the bionic ear. *Sci. Transl. Med.* **6**, 233ra54 (2014).
43. W. Chen *et al.*, Human fetal auditory stem cells can be expanded in vitro and differentiate into functional auditory neurons and hair cell-like cells. *Stem Cells* **27**, 1196–1204 (2009). doi: 10.1002/stem.62; pmid: 19418454
44. H. Li, G. Roblin, H. Liu, S. Heller, Generation of hair cells by stepwise differentiation of embryonic stem cells. *Proc. Natl. Acad. Sci. U.S.A.* **100**, 13495–13500 (2003). doi: 10.1073/pnas.2334503100; pmid: 14593207
45. K. Oshima *et al.*, Mechanosensitive hair cell-like cells from embryonic and induced pluripotent stem cells. *Cell* **141**, 704–716 (2010). doi: 10.1016/j.cell.2010.03.035; pmid: 20478259
46. G. S. Géléoc, J. R. Risner, J. R. Holt, Developmental acquisition of voltage-dependent conductances and sensory signaling in hair cells of the embryonic mouse inner ear. *J. Neurosci.* **24**, 11148–11159 (2004). doi: 10.1523/JNEUROSCI.2662-04.2004; pmid: 15590931
47. K. R. Koehler, A. M. Mikosz, A. I. Molosh, D. Patel, E. Hashino, Generation of inner ear sensory epithelia from pluripotent stem cells in 3D culture. *Nature* **500**, 217–221 (2013). doi: 10.1038/nature12298; pmid: 23842490
48. C. A. Makary, J. Shin, S. G. Kujawa, M. C. Liberman, S. N. Merchant, Age-related primary cochlear neuronal degeneration in human temporal bones. *J. Assoc. Res. Otolaryngol.* **12**, 711–717 (2011). doi: 10.1007/s10162-011-0283-2; pmid: 21748533
49. F. Shi, J. S. Kempfle, A. S. Edge, Wnt-responsive Lgr5-expressing stem cells are hair cell progenitors in the cochlea. *J. Neurosci.* **32**, 9639–9648 (2012). doi: 10.1523/JNEUROSCI.1064-12.2012; pmid: 22787049
50. D. Wei *et al.*, Cells of adult brain germinal zone have properties akin to hair cells and can be used to replace inner ear sensory cells after damage. *Proc. Natl. Acad. Sci. U.S.A.* **105**, 21000–21005 (2008). doi: 10.1073/pnas.0808044105; pmid: 19064919
51. F. Shi, C. E. Corrales, M. C. Liberman, A. S. Edge, BMP4 induction of sensory neurons from human embryonic stem cells and reinnervation of sensory epithelium. *Eur. J. Neurosci.* **26**, 3016–3023 (2007). doi: 10.1111/j.1460-9568.2007.05909.x; pmid: 18005071
52. W. Chen *et al.*, Restoration of auditory evoked responses by human ES-cell-derived otic progenitors. *Nature* **490**, 278–282 (2012). doi: 10.1038/nature11415; pmid: 22972191
53. T. Kondo *et al.*, Tlx3 exerts context-dependent transcriptional regulation and promotes neuronal differentiation from embryonic stem cells. *Proc. Natl. Acad. Sci. U.S.A.* **105**, 5780–5785 (2008). doi: 10.1073/pnas.0708704105; pmid: 18391221
54. J. H. Reyes *et al.*, Glutamatergic neuronal differentiation of mouse embryonic stem cells after transient expression of neurogenin 1 and treatment with BDNF and GDNF: in vitro and in vivo studies. *J. Neurosci.* **28**, 12622–12631 (2008). doi: 10.1523/JNEUROSCI.0563-08.2008; pmid: 19036956
55. C. E. Corrales *et al.*, Engraftment and differentiation of embryonic stem cell-derived neural progenitor cells in the cochlear nerve trunk: Growth of processes into the organ of Corti. *J. Neurobiol.* **66**, 1489–1500 (2006). doi: 10.1002/neu.20310; pmid: 17013931
56. F. Shi, A. S. Edge, Prospects for replacement of auditory neurons by stem cells. *Hear. Res.* **297**, 106–112 (2013). doi: 10.1016/j.heares.2013.01.017; pmid: 23370457
57. P. M. White, A. Doetzlhofer, Y. S. Lee, A. K. Groves, N. Segil, Mammalian cochlear supporting cells can divide and trans-differentiate into hair cells. *Nature* **441**, 984–987 (2006). doi: 10.1038/nature04849; pmid: 16791196
58. R. Chai *et al.*, Wnt signaling induces proliferation of sensory precursors in the postnatal mouse cochlea. *Proc. Natl. Acad. Sci. U.S.A.* **109**, 8167–8172 (2012). doi: 10.1073/pnas.1202774109; pmid: 22562792
59. R. Chai *et al.*, Dynamic expression of Lgr5, a Wnt target gene, in the developing and mature mouse cochlea. *J. Assoc. Res. Otolaryngol.* **12**, 455–469 (2011). doi: 10.1007/s10162-011-0267-2; pmid: 21472479
60. F. Shi, L. Hu, A. S. Edge, Generation of hair cells in neonatal mice by β-catenin overexpression in Lgr5-positive cochlear progenitors. *Proc. Natl. Acad. Sci. U.S.A.* **110**, 13851–13856 (2013). doi: 10.1073/pnas.1219952110; pmid: 23918377
61. N. F. Bramhall, F. Shi, K. Arnold, K. Hochedlinger, A. S. Edge, Lgr5-positive supporting cells generate new hair cells in the postnatal cochlea. *Stem Cell Rev.* **2**, 311–322 (2014). doi: 10.1016/j.stemcr.2014.01.008; pmid: 24672754
62. B. C. Cox *et al.*, Spontaneous hair cell regeneration in the neonatal mouse cochlea in vivo. *Development* **141**, 816–829 (2014). doi: 10.1242/dev.103036; pmid: 24496619
63. S. J. Jeon, M. Fujioka, S. C. Kim, A. S. Edge, Notch signaling alters sensory or neuronal cell fate specification of inner ear stem cells. *J. Neurosci.* **31**, 8351–8358 (2011). doi: 10.1523/JNEUROSCI.6366-10.2011; pmid: 21653840
64. S. Korrapati, I. Roux, E. Glowatzki, A. Doetzlhofer, Notch signaling limits supporting cell plasticity in the hair cell-damaged early postnatal murine cochlea. *PLOS ONE* **8**, e73276 (2013). doi: 10.1371/journal.pone.0073276; pmid: 24023676
65. K. Mizutari *et al.*, Notch inhibition induces cochlear hair cell regeneration and recovery of hearing after acoustic trauma. *Neuron* **77**, 58–69 (2013). doi: 10.1016/j.neuron.2012.10.032; pmid: 23312516
66. C. Sage *et al.*, Proliferation of functional hair cells in vivo in the absence of the retinoblastoma protein. *Science* **307**, 1114–1118 (2005).doi: 10.1126/science.1106642; pmid: 15653467
67. H. Laine *et al.*, p19(Ink4d) and p21(Cip1) collaborate to maintain the postmitotic state of auditory hair cells, their codeletion leading to DNA damage and p53-mediated apoptosis. *J. Neurosci.* **27**, 1434–1444 (2007). doi: 10.1523/JNEUROSCI.4956-06.2007; pmid: 17287518
68. J. J. Lentz *et al.*, Rescue of hearing and vestibular function by antisense oligonucleotides in a mouse model of human deafness. *Nat. Med.* **19**, 345–350 (2013). doi: 10.1038/nm.3106; pmid: 23380860
69. E. Verpy *et al.*, A defect in harmonin, a PDZ domain-containing protein expressed in the inner ear sensory hair cells, underlies Usher syndrome type 1C. *Nat. Genet.* **26**, 51–55 (2000). doi: 10.1038/79171; pmid: 10973247
70. M. Bitner-Glindzicz *et al.*, A recessive contiguous gene deletion causing infantile hyperinsulinism, enteropathy and deafness identifies the Usher type 1C gene. *Nat. Genet.* **26**, 56–60 (2000). doi: 10.1038/79178; pmid: 10973248
71. N. Michalski *et al.*, Harmonin-b, an actin-binding scaffold protein, is involved in the adaptation of mechanoelectrical transduction by sensory hair cells. *Pflugers Arch.* **459**, 115–130 (2009). doi: 10.1007/s00424-009-0711-x; pmid: 19756723
72. J. J. Lentz *et al.*, Deafness and retinal degeneration in a novel USH1C knock-in mouse model. *Dev. Neurobiol.* **70**, 253–267 (2010). doi: 10.1002/dneu.20771; pmid: 20095043
73. Y. Maeda, A. M. Sheffield, R. J. Smith, Therapeutic regulation of gene expression in the inner ear using RNA interference. *Adv. Otorhinolaryngol.* **66**, 13–36 (2009). doi: 10.1159/000218205; pmid: 19494570
74. T. Gaj, C. A. Gersbach, C. F. Barbas 3rd, ZFN, TALEN, and CRISPR/Cas-based methods for genome engineering. *Trends Biotechnol.* **31**, 397–405 (2013). doi: 10.1016/j.tibtech.2013.04.004; pmid: 23664777
75. T. Gaj, J. Guo, Y. Kato, S. J. Sirk, C. F. Barbas 3rd, Targeted gene knockout by direct delivery of zinc-finger nuclease proteins. *Nat. Methods* **9**, 805–807 (2012). doi: 10.1038/nmeth.2030; pmid: 22751204
76. P. Mali, K. M. Esvelt, G. M. Church, Cas9 as a versatile tool for engineering biology. *Nat. Methods* **10**, 957–963 (2013). doi: 10.1038/nmeth.2649; pmid: 24076990
77. P. Mali *et al.*, RNA-guided human genome engineering via Cas9. *Science* **339**, 823–826 (2013).doi: 10.1126/science.1232033; pmid: 23287722
78. N. Gunewardene, M. Dottori, B. A. Nayagam, The convergence of cochlear implantation with induced pluripotent stem cell therapy. *Stem Cell Rev.* **8**, 741–754 (2012). doi: 10.1007/s12015-011-9320-0; pmid: 21956409
79. V. H. Hernandez *et al.*, Optogenetic stimulation of the auditory pathway. *J. Clin. Invest.* **124**, 1114–1129 (2014). doi: 10.1172/JCI69050; pmid: 24509078
80. B. W. Kesser, G. T. Hashisaki, K. Fletcher, H. Eppard, J. R. Holt, An in vitro model system to study gene therapy in the human inner ear. *Gene Ther.* **14**, 1121–1131 (2007). doi: 10.1038/sj.gt.3302980; pmid: 17568767
81. Y. Nelson, S. Kang, in *Handbook of Physiology, The Nervous System, Sensory Processes* (Oxford Univ. Press, New York, 1984), vol. 3, pp. 639–674.
82. I. M. Hunter-Duvar, A technique for preparation of cochlear specimens for assessment with the scanning electron microscope. *Acta Otolaryngol. Suppl.* **351**, 3–23 (1978). doi: 10.3109/00016487809122718; pmid: 352089
83. G. M. Clark, The multiple-channel cochlear implant: the interface between sound and the central nervous system for hearing, speech, and language in deaf people-a personal perspective. *Philos. Trans. R. Soc. London B Biol. Sci.* **361**, 791–810 (2006). doi: 10.1098/rstb.2005.1782; pmid: 16627295

Acknowledgments: Inner-ear gene-therapy research in the Holt/Géléoc lab is supported by the Bertarelli Foundation Program in Translational Neuroscience and Neuroengineering. This review was support by grants from the National Institutes of Health/National Institute on Deafness and Other Communication Disorders: RO1DC008853 (G.S.G.G) and R01DC005439 (J.R.H). We thank A. Cheng, D. Corey, and A. Edge for critical comments on the manuscript.

10.1126/science.1241062

READ THE FULL ARTICLE ONLINE
http://dx.doi.org/10.1126/science.1250494

Structural and dynamic data show how molecular chaperones prevent aggregation and misfolding of unfolded proteins.

RELATED ITEMS IN *SCIENCE*

M. Gamerdinger, E. Deuerling, Trigger factor flexibility. *Science* **344**, 590 (2014). DOI: 10.1126/science.1254064

Structural Basis for Protein Antiaggregation Activity of the Trigger Factor Chaperone

Tomohide Saio, Xiao Guan, Paolo Rossi, Anastassios Economou, Charalampos G. Kalodimos*

Introduction: Molecular chaperones prevent aggregation and misfolding of proteins in the cellular environment and are thus central to maintaining protein homeostasis. Molecular chaperones are thought to recognize and bind to exposed hydrophobic regions of the unfolded proteins, thereby shielding these regions from the solvent. If unprotected, the proteins would likely aggregate or misfold to bury the hydrophobic residues. Despite the central importance of the binding of chaperones to unfolded proteins, the structural basis of their interaction remains poorly understood. The scarcity of structural data on complexes between chaperones and unfolded proteins is primarily due to technical challenges originating in the size and dynamic nature of these complexes.

Rationale: Recent advances in nuclear magnetic resonance (NMR) and isotope labeling approaches make it possible to study large, dynamic complexes. We used NMR spectroscopy to characterize the binding of the 48-kD unfolded alkaline phosphatase (PhoA) to the 50-kD trigger factor (TF) chaperone. We obtained atomic insight into the dynamic binding and determined the solution structure of PhoA captured in an extended, unfolded state by three TF molecules. Based on our NMR studies, we gained insight into how TF rescues an aggregation-prone protein and how it exerts its unfoldase activity.

Results: We show that TF uses multiple sites, which are located in two different domains and extend over a distance of ~90 Å, to bind to several regions of the unfolded PhoA that are dispersed throughout its entire length. Three TF molecules are required to interact with the entire length of PhoA, giving rise to a ~200-kD complex in solution. The TF-PhoA interactions are mediated primarily by hydrophobic contacts. TF interacts with PhoA in a highly dynamic fashion, giving rise to a rugged landscape for the free energy of interaction. As the number and length of the PhoA regions engaged by TF increases, a more stable complex gradually emerges. The multivalent binding keeps PhoA in an extended, unfolded conformation. Crucially, even the lowest-energy TF-PhoA complex remains rather dynamic with a lifetime of ~20 ms. The structural data of the three TF molecules in complex with different regions of PhoA reveal how the same binding sites within a molecular chaperone can recognize and interact with a large number of substrates with unrelated primary sequences. This promiscuous recognition is further enabled by the notable plasticity of the substrate-binding sites in TF. We finally show that TF in the cytosol prevents aggregation by interacting transiently with the low-populated, aggregation-prone unfolded state of the substrate but acts as a powerful unfoldase when it is bound at the ribosome and thus is colocalized with translating substrate.

Conclusion: The structural data reveal a multivalent binding mechanism between the chaperone and its protein substrate. This mechanism of binding presents several advantages as it enables chaperones to function as holdases and unfoldases by exerting forces to retain proteins in the unfolded state and at the same time protect them from aggregation by shielding their exposed hydrophobic regions. Given the existence of multiple binding sites in other molecular chaperones, this may present a general mechanism for the action of molecular chaperones. The fast kinetics of substrate binding enables chaperones to interact with transiently exposed, aggregation-prone regions of unstable proteins in the cytosol, thereby preventing their aggregation and increasing their solubility.

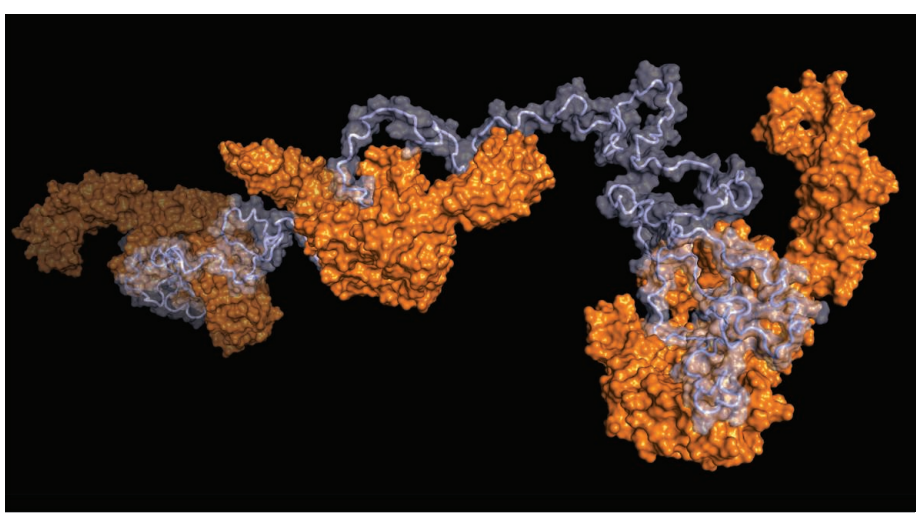

Structural basis of PhoA binding by TF. PhoA (blue/gray) is captured in an unfolded state by three TF chaperone molecules (orange). Complex formation is mediated by multivalent binding of hydrophobic surfaces, which are shielded from water, thereby preventing folding and, at the same time, aggregation of the substrate protein.

The list of author affiliations is available in the full article online.
*Corresponding author. E-mail: babis@rutgers.edu
Cite this article as T. Saio *et al.*, *Science* **344**, 1250494 (2014). DOI: 10.1126/science.1250494

Structural Basis for Protein Antiaggregation Activity of the Trigger Factor Chaperone

Tomohide Saio,[1]* Xiao Guan,[1]* Paolo Rossi,[1] Anastassios Economou,[2,3] Charalampos G. Kalodimos[1]†

Molecular chaperones prevent aggregation and misfolding of proteins, but scarcity of structural data has impeded an understanding of the recognition and antiaggregation mechanisms. We report the solution structure, dynamics, and energetics of three trigger factor (TF) chaperone molecules in complex with alkaline phosphatase (PhoA) captured in the unfolded state. Our data show that TF uses multiple sites to bind to several regions of the PhoA substrate protein primarily through hydrophobic contacts. Nuclear magnetic resonance (NMR) relaxation experiments show that TF interacts with PhoA in a highly dynamic fashion, but as the number and length of the PhoA regions engaged by TF increase, a more stable complex gradually emerges. Multivalent binding keeps the substrate protein in an extended, unfolded conformation. The results show how molecular chaperones recognize unfolded polypeptides and, by acting as unfoldases and holdases, prevent the aggregation and premature (mis)folding of unfolded proteins.

Molecular chaperones maintain a functional proteome in the cell by preventing the aggregation of unfolded proteins, assisting with their folding or disassembling aggregates (*1*–*6*). Nascent polypeptide chains emerging from the exit channel of the ribosome expose long hydrophobic regions that are particularly prone to misfolding and aggregation (*7*–*9*). The bacterial trigger factor (TF) (*10*) binds next to the exit channel of the ribosome (*11*–*15*) and directly interacts with the emerging nascent polypeptide (*16*–*19*). With an estimated cellular concentration of ~50 μM (*20*), TF is one of the most abundant proteins in bacteria. TF prevents the aggregation and premature folding of nascent polypeptides and unfolded proteins in vivo and in vitro, likely by interacting with exposed hydrophobic regions, thereby shielding them from the solvent (*18*, *21*–*23*). Long polypeptides (>20 kD), which are the preferred clients for TF in vivo (*24*, *25*), require multiple TF molecules for their protection. TF remains bound to the unfolded polypeptide even after having departed the ribosome (*18*, *21*, *22*, *26*). TF reduces the speed of folding, thereby increasing the yield of biologically active proteins (*21*, *27*–*29*). TF was shown to have both a weak holdase and an unfoldase activity (*30*). Deletion of the TF gene results in the aggregation of many proteins (*25*) and the stimulation of heat shock response (*31*–*33*). Following its interaction with TF, the unfolded polypeptide folds by dissociating, interacting with foldase chaperones such as Hsp70 and GroEL, or enters the posttranslational secretory pathway to interact with the Sec machinery (*2*, *3*, *5*, *34*–*36*).

Despite the importance of chaperone binding to unfolded proteins, the structural basis of this interaction remains poorly understood. The scarcity of structural data on complexes between chaperones and unfolded proteins is primarily due to technical challenges associated with the size and dynamic nature of these complexes (*37*–*42*). We have exploited recent advances in nuclear magnetic resonance (NMR) and isotope labeling approaches (*43*–*48*) to characterize the dynamic binding of unfolded PhoA to TF and to determine the solution structure of the PhoA captured in an extended, unfolded state by three TF molecules.

NMR of TF Chaperone and Unfolded PhoA

Escherichia coli TF consists of 432 amino acids, comprising the ribosome-binding domain (RBD; residues 1 to 112), the peptidyl prolyl isomerase domain (PPD; residues 150 to 246), and a discontinuous C-terminal domain, positioned structurally between the RBD and PPD (*12*), which, on the basis of the current and previous findings (*49*, *50*), we refer to as the substrate-binding domain (SBD; residues 113 to 149 and 247 to 432) (Fig. 1A and fig. S1, A and B). Unliganded TF in solution forms a dimer (*27*) of ~100 kD (fig. S1C) [dissociation constant (K_d) of dimerization is ~18 μM (*51*)]. The quality of the ^{1}H-^{15}N–correlated NMR spectra (figs. S2A and S3) and the ^{1}H-^{13}C–correlated NMR spectra of methyl-bearing (Ala, Ile, Met, Leu, Thr, and Val) and aromatic (Phe, Trp, and Tyr) residues of TF is high (figs. S2B and S4). By exploiting the modular structural architecture of TF (*52*, *53*), we have obtained near-complete assignment of TF (see the Materials and Methods section).

E. coli alkaline phosphatase (PhoA) is an ~50-kD (471 amino acid residues) periplasmic enzyme that requires oxidizing conditions for folding, as do several other periplasmic proteins (*54*). PhoA was shown biochemically to be in an unfolded and thus degradation-prone state in the reducing environment of the cytosol (*54*–*56*) and to interact extensively with TF (*57*, *58*). The NMR spectra of PhoA, as well as relaxation experiments, confirmed that PhoA is unfolded under reducing conditions (figs. S5, B and C, and S6). Assessment of the presence of secondary structure by NMR (*59*) revealed pervasive random-coil and extended-like conformations, although several of the regions that formed a stable secondary structure in the folded PhoA retained a fraction of their fold in unfolded PhoA (Fig. 2, A and B).

The NMR spectra of unfolded proteins typically show very narrow chemical shift dispersion (*60*). To simplify NMR characterization of unfolded PhoA, which is a large protein by NMR standards, we generated a number of PhoA fragments of varying length that spanned its entire sequence (see Materials and Methods). Superposition of the NMR spectra of any of the PhoA fragments with the NMR spectra of the full-length PhoA demonstrated excellent resonance correspondence (fig. S5D). This is expected because each of these fragments is unfolded, as is the full-length PhoA, and thus, the conformational properties of the isolated fragments recapitulate those of the full-length PhoA. Near-complete assignment has been obtained for full-length PhoA.

Interaction Between TF and PhoA

To determine the residues of unfolded PhoA that are recognized and bound by TF, we monitored by NMR the binding of isotopically labeled PhoA by unlabeled TF (fig. S7). In addition to full-length PhoA, several PhoA fragments were used to enhance spectral resolution (fig. S7A). Differential line broadening analysis (*61*) showed that only a relatively small number of residues (~130 of the 471) in PhoA are recognized and bound by TF (Fig. 2C). There are in total seven distinct TF-binding regions in PhoA (labeled using lowercase letters a through g), with lengths ranging from ~8 to ~40 residues (Fig. 2C and fig. S8A). Analysis of the primary sequence of the TF-binding sites showed that they are enriched in hydrophobic and especially aromatic residues (figs. S8, B and C, and S9), in agreement with previous studies (*18*, *62*). Notably, there seems to be a correlation between the hydrophobicity of the PhoA sequence and the binding preference by TF (Fig. 2C).

To identify the sites that TF uses to interact with PhoA, we monitored by NMR the binding of full-length PhoA as well as select PhoA fragments comprising TF-binding sites to labeled TF (figs. S2, C and D, and S10). The combined data demonstrated that TF uses four distinct sites to interact with PhoA (labeled using uppercase letters; A through D). Three of these sites (A, B, and C) are located in the SBD (Fig. 1A), in agreement

[1]Center for Integrative Proteomics Research and Department of Chemistry and Chemical Biology, Rutgers University, Piscataway, NJ 08854, USA. [2]Laboratory of Molecular Bacteriology, Rega Institute, Department of Microbiology and Immunology, KU Leuven, Minderbroedersstraat 10, B-3000 Leuven, Belgium. [3]Institute of Molecular Biology and Biotechnology-FORTH and Department of Biology, University of Crete, P.O. Box 1385, GR-71110, Iraklio, Crete, Greece.

*These authors contributed equally to this work.
†Corresponding author. E-mail: babis@rutgers.edu

with previous data indicating this domain as being the central chaperone module (*49*, *50*). The fourth binding site (labeled D) is located in the PPD and overlaps with its catalytic site (Fig. 1B). All sites are composed primarily of hydrophobic residues (Fig. 1, B and C). NMR titration of additional protein substrates [such as the maltose binding protein (MBP) and the outer membrane protein A (OmpA)] to TF demonstrated that the same sites are used by TF to interact with these substrates (fig. S11). The substrate-binding sites are the best-conserved regions in TF, along with the region in the RBD that binds to the ribosome (Fig. 1D and fig. S12). Residues located in the identified substrate-binding sites were previously reported to cross-link to the emerging nascent chain when TF is bound to the ribosome (*49*, *50*). Although the RBD surface is very hydrophobic, our data show that this domain does not interact with the protein substrates (Fig. 1A and fig. S11). In contrast, the RBD was seen to cross-link to nascent chains in ribosome-bound TF (*49*, *50*). This discrepancy may be due to the physical proximity of the RBD to the exit channel of the ribosome, or RBD may undergo conformational change upon interacting with the ribosome that enables its interaction with the nascent polypeptide (*13*, *18*).

The crystal structure of free TF (*12*) shows that the identified substrate-binding sites (A to D) consist almost exclusively of nonpolar residues (Fig. 1C). Sites A, B, and C are enriched with methyl-bearing residues, and site D is enriched with aromatic residues (Fig. 1B). Thus, the use of hydrophobic sites to interact with unfolded client proteins is shared among several molecular chaperones, such as GroEL, Skp, Hsp40, and Hsp90 (*63*, *64*). Sites A and B are located inside the cradle-like structure formed by the RBD and SBD, with A located at the base of the cradle and B located at the tip of arm 2 (Fig. 1A). Site C forms a rather elongated ridge near the β sheet that connects the SBD and PPD. Sites A, B, C, and D expose ~530, ~680, ~460, and ~650 Å^2, respectively, of hydrophobic surface, thus providing combined up to ~2300 Å^2 of solvent-exposed nonpolar surface available for binding of protein substrates. The four TF sites extend over a distance of more than 90 Å.

Mode of Binding Between TF and PhoA

We characterized by NMR and isothermal titration calorimetry (ITC) the binding and energetics of each of the PhoA sites, individually and in combination to TF. Both chemical shift and intermolecular TF-PhoA nuclear Overhauser effect (NOE) measurements were used to monitor the interaction at the residue level. Starting from the N terminus, the first PhoA region to interact with TF is site *a* (Figs. 2C and 3A). Chemical shift perturbation as well as intermolecular TF-PhoA NOEs (fig. S13) clearly indicated that PhoA site *a* can interact with all four of the binding sites in TF with a moderate affinity (K_d ~25 μM; Fig. 3B). Similarly, PhoA site *b* can interact with any of the four binding sites in TF but with lower affinity (K_d ~200 μM; Fig. 3C). In contrast, PhoA subsite c^1 (the N-terminal region of site *c*; Fig. 3A) binds exclusively to the SBD and preferably to TF sites A and B (on the basis of chemical shift perturbation, subsite c^1 appears to bind to TF site C, but no intermolecular NOEs were detected, indicating a rather transient interaction; Fig. 3D). PhoA subsite c^2 (the middle region of site *c*; Fig. 3A) interacts exclusively with TF site A (Fig. 3E). The binding to TF of a PhoA fragment consisting of subsites c^1 and c^2 is determined by the combined binding preferences of the subsites (Fig. 3F). The PhoA c^1-c^2 fragment binds to TF with higher affinity than the subsites c^1 and c^2 individually because of avidity (Fig. 3, D to F). Notably, the complete PhoA site *c* (consisting of subsites c^1, c^2, and c^3) binds to TF in a specific orientation and arrangement: PhoA subsite c^1 binds to TF site B, subsite c^2 binds to TF site A, and subsite c^3 binds to TF site C, as demonstrated by the measurement of a unique set of characteristic intermolecular NOEs between the TF sites and the PhoA subsites (Fig. 3G). PhoA site *c* binds only to TF sites A, B, and C in the SBD, and with higher affinity (K_d ~10 μM) than PhoA site *a* or *b*. Thus, PhoA sites *a* and *b* can only interact with TF site D in the context of the PhoA$^{a\text{-}c}$ fragment (superscript denotes the TF-binding sites that the PhoA fragment contains). Because PhoA site *a* binds with much higher affinity to TF than PhoA site *b* (Fig. 3, B and C), in the TF–PhoA$^{a\text{-}c}$ complex, PhoA site *a* binds to TF site D, whereas PhoA site *b* does not interact at all with TF (Fig. 3H). The affinity of PhoA$^{a\text{-}c}$ for TF (K_d ~2 μM; fig. S14) is higher than any of the other PhoA sites.

The results clearly show that although some PhoA sites (for example, sites *a* and *b*) bind

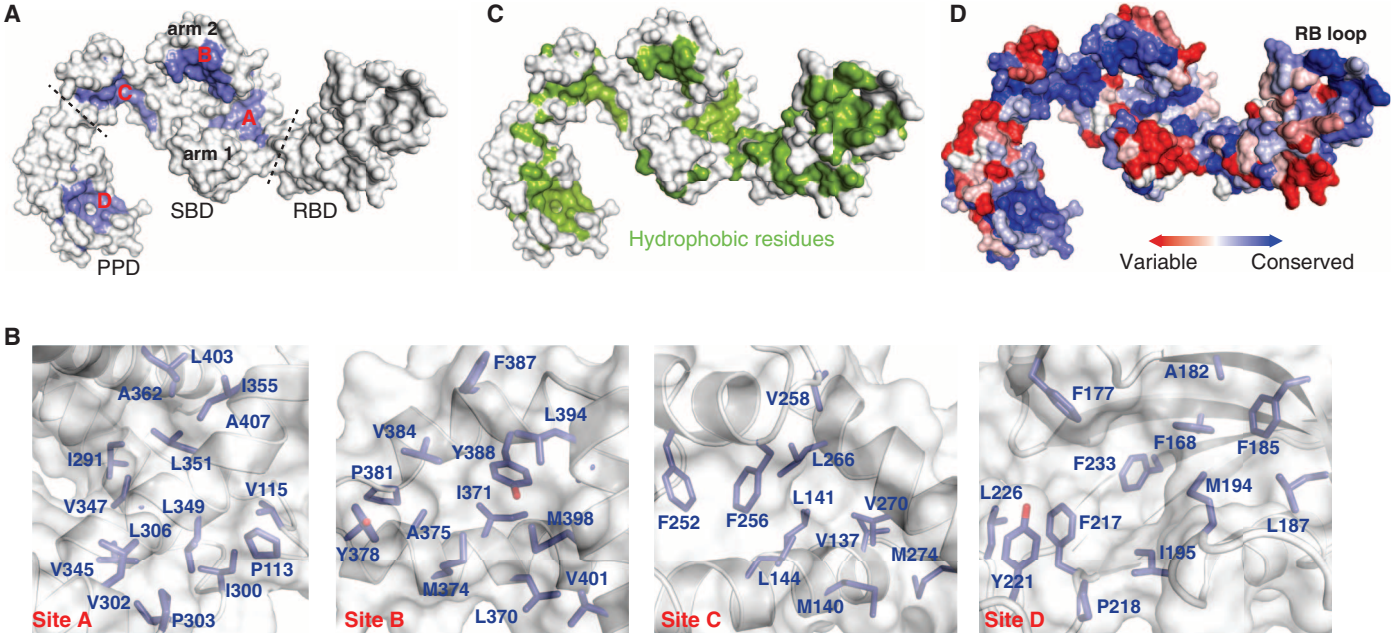

Fig. 1. Substrate-binding sites in TF. (**A**) The TF residues identified by NMR to interact with unfolded protein substrates are colored blue on the crystal structure of free *E. coli* TF [Protein Data Bank (PDB) ID 1W26]. The four main binding sites are labeled A, B, C, and D (in red). The dashed lines indicate the domain boundaries. The two structural protrusions in the SBD are labeled arm 1 and arm 2. An additional binding site, located in arm 1, is used by TF to interact with some of the substrates (see Fig. 7A and fig. S11). (**B**) Expanded view of the four substrate-binding sites in TF identified by the NMR titration experiments. The hydrophobic residues that make up the substrate-binding sites are shown as sticks. (**C**) The hydrophobic residues in TF are colored green, whereas all other residues are colored white. (**D**) TF sequence conservation is color-mapped on the TF structure. The residues that make up the substrate-binding sites are the best-conserved along with the ribosome-binding loop (RB loop) (see fig. S12).

promiscuously to all TF sites, other PhoA sites (for example, subsite c^1) are more selective and some sites (for example, subsite c^2) appear to interact exclusively with specific sites in TF. Therefore, the binding mode of a multisite PhoA fragment to TF will be determined by the combined preferences of the sites (Fig. 3H). Together, the data demonstrate that the interaction of TF and PhoA is dynamic and is best described by a rugged free energy landscape: the various binding interactions shown in panels (B) to (G) of Fig. 3 do not maximize the binding interface and correspond to the higher-energy wells, whereas the maximum-contact arrangement shown in Fig. 3H corresponds to the ground-state, lowest-energy conformation of the complex in which a unique arrangement of the chaperone and the substrate is observed experimentally (Fig. 3H).

The NMR data showed that one TF molecule can accommodate a PhoA fragment encompassing TF-binding sites *a* to *c* ($PhoA^{a-c}$) (Fig. 3 and figs. S14 and S15). Under stoichiometric conditions, the use of a longer PhoA fragment that included site *d* ($PhoA^{a-d}$) resulted in this site not being bound by TF (fig. S16A). Site *d* was bound only when excess TF was added (fig. S16A). Using the experimental approach described in Fig. 3 for

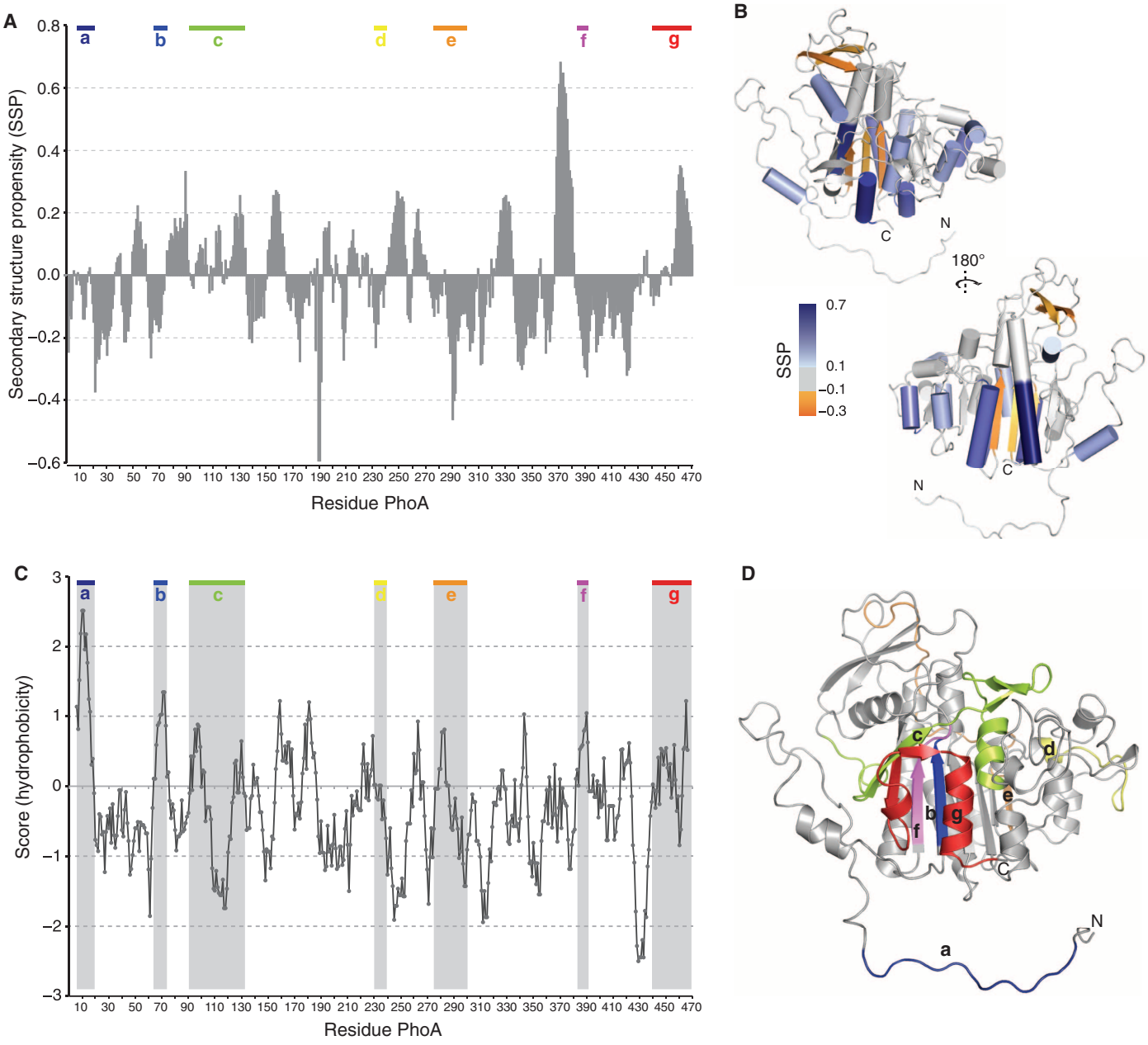

Fig. 2. TF-binding sites and secondary structure in unfolded PhoA. (**A**) Secondary structure propensity (SSP) values (*59*) of unfolded PhoA plotted as a function of the amino acid sequence. A SSP score at a given residue of 1 or −1 reflects a fully formed α-helical or β-structure (extended), respectively, whereas a score of, for example, 0.5 indicates that 50% of the conformers in the native-state ensemble of the protein are helical at that position. The data show that several of the secondary structure elements in the folded PhoA retain some transient structure in the unfolded PhoA. The TF-binding sites (a to g) are indicated. (**B**) The SSP values of unfolded PhoA that correspond to secondary structure elements present in folded PhoA are mapped on the structure of folded *E. coli* PhoA. The signal sequence region (residues 1 to 22) was modeled into the crystal structure of the mature form (PDB ID 1Y6V). Only one subunit of the dimeric PhoA is shown. (**C**) Plot of the hydrophobicity of PhoA as a function of its primary sequence. A hydrophobicity score (Roseman algorithm, window = 9) higher than zero denotes increased hydrophobicity. The seven PhoA regions (labeled a through g) identified by NMR to interact with TF are highlighted in gray. (**D**) Mapping of the TF-binding sites (a to g) on the folded PhoA structure.

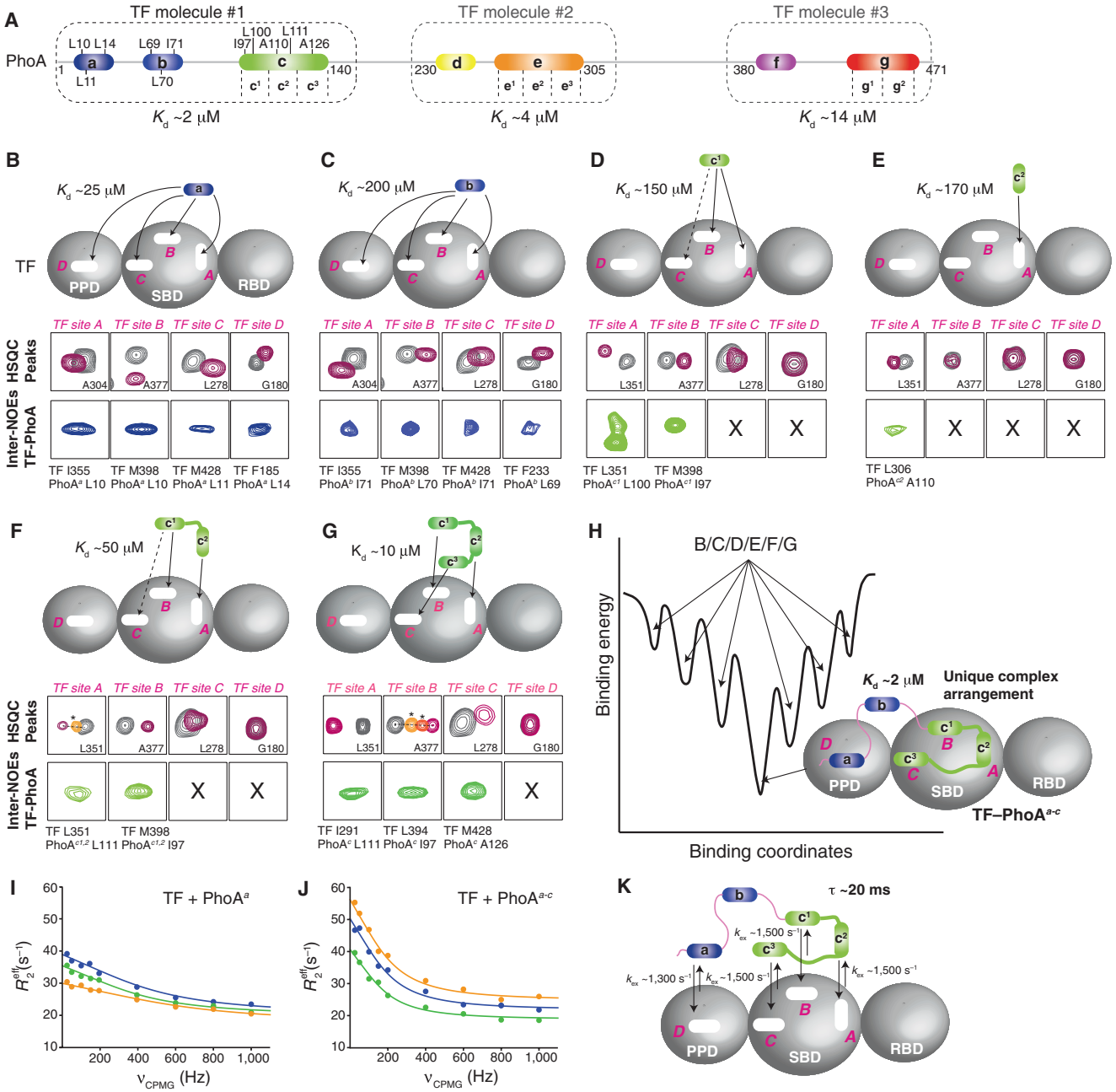

Fig. 3. Dynamic binding and energetics of PhoA by TF. (A) TF-binding sites in PhoA colored as in Fig. 2A. Three TF molecules are required for the simultaneous engagement of the entire PhoA. The K_d for each complex is shown. PhoA residues of sites *a*, *b*, and *c* whose intermolecular NOEs to TF residues are depicted in panels (B) to (G) are indicated. (**B** to **G**) The interaction of the independent PhoA site *a* (B), site *b* (C), subsite c^1 (D), subsite c^2 (E), subsites c^1-c^2 (F), and subsites c^1-c^2-c^3 (site *c*) (G) with TF has been characterized by NMR and ITC. The four PhoA-binding sites in TF (A to D) are labeled in pink. In the rectangles labeled "HSQC peaks," representative peaks from ^{1}H-^{15}N–correlated spectra of labeled TF (TF$^{SBD-PPD}$) free (gray) and in complex (magenta) with the indicated PhoA site are shown. In the rectangles labeled "Inter-NOEs TF-PhoA," representative intermolecular NOEs between the TF and PhoA residues are shown. The full NOESY strips are shown in fig. S13. The symbol X indicates the absence of such NOEs. The K_d values were determined by ITC and NMR. Solid arrows indicate experimentally observed binding of the PhoA site to the designated TF site. Broken arrows indicate transient interaction observed by chemical shift perturbation but for which no intermolecular NOEs were detected. The orange cross peak (marked with an asterisk) for TF site A in panel (F) corresponds to the chemical shift observed for the binding of the individual subsite c^2 to TF site A shown in panel (E). Similarly, the orange and dark-orange cross peaks marked with asterisks in panel (G) for TF site B correspond to the chemical shifts for the binding of the individual subsite c^1 (panel D) and the fragment c^1-c^2 (panel F), respectively. All these resonances fall on the same line connecting the free and PhoA site *c*–bound TF peaks (*93*), further supporting the observed synergistic binding between the PhoA sites as the length of PhoA increases, as well as the selectivity of certain PhoA sites for specific TF sites. (**H**) The progressive increase in PhoA length results in increased affinity for PhoA interaction with TF, and when PhoA is sufficiently long to engage all four of the TF sites simultaneously, as is the case with PhoA^{a-c}, a unique binding mode between PhoA and TF is observed as shown. The binding of PhoA to TF can be described by a rugged free energy landscape, with the conformational arrangement of the TF–PhoA^{a-c} complex depicted in this panel corresponding to the lowest-energy, ground-state structure. The binding interactions shown in panels (B) to (G) correspond to higher-energy states. The results for the interaction of PhoA sites *d* to *g* with TF are shown in fig. S17. (**I** and **J**) Representative relaxation dispersion profiles of three TF residues in complex with PhoA site *a* (I) and PhoA^{a-c} (J). R_2^{eff} is the effective transverse relaxation rate, and ν_{CPMG} is the refocusing frequency of the CPMG train pulse. (**K**) Exchange rate constants (k_{ex}) determined experimentally for the complex between TF and PhoA^{a-c}. The residence time of PhoA^{a-c} bound to TF is ~20 ms at 22°C.

the N-terminal region of PhoA, we found that a second TF molecule is required to fully engage PhoA sites *d* and *e* (fragment PhoA$^{d\text{-}e}$) and a third TF molecule to fully interact with PhoA sites *f* and *g* (fragment PhoA$^{f\text{-}g}$) (Fig. 3A and fig. S17). PhoA sites *d* and *f* bound exclusively to the TF PPD (fig. S17, B and E), whereas sites *e* and *g* bound exclusively to the TF SBD in the binding arrangement shown in Fig. 4A and fig. S17, C and F. Similarly to the TF–PhoA$^{a\text{-}c}$ complex, a unique arrangement was observed for the TF–PhoA$^{d\text{-}e}$ complex, as demonstrated by the measurement of a unique set of characteristic intermolecular NOEs between TF and PhoA (fig. S17D). In contrast, two binding arrangements were observed for the TF–PhoA$^{f\text{-}g}$ complex as shown in fig. S17G, but with one of them being the preferred one (populated by more than 70% of the time) (Fig. 4A).

NMR titration experiments showed that three TF molecules are required to bind to all of the seven TF-binding sites in full-length PhoA (Fig. 4A). The stoichiometry of the TF-PhoA complexes was further corroborated by ITC experiments (fig. S14). Thermodynamic characterization showed that TF formed complexes with the three PhoA fragments (PhoA$^{a\text{-}c}$, PhoA$^{d\text{-}e}$, and PhoA$^{f\text{-}g}$) with K_d values of ~2, ~4, and ~14 μM, respectively (Fig. 3A and fig. S14). The binding arrangement shown for the three TF molecules bound to PhoA sites *a* through *g* depicted collectively in Fig. 4A represents the lowest-energy conformational states for the three complexes. The binding avidity among the proximal PhoA sites and subsites, enhanced by the proximity of the A, B, and C sites in TF, further accounts for the higher stability of the observed ground-state conformations. This observation is confirmed by additional NMR titration experiments (fig. S16B).

Dynamic Engagement of PhoA by TF

Rapid binding and release of unfolded proteins by molecular chaperones is likely important for a productive assisted-folding process (*5*). To determine the kinetics of PhoA binding to TF, we used NMR relaxation dispersion (*65*, *66*). This powerful technique allows characterization of the dynamic interaction of protein complexes at the residue level. In the case of the interaction between TF and PhoA, the kinetics are as follows:

$$\mathrm{TF} + \mathrm{PhoA} \underset{k_{off}}{\overset{k_{on}}{\rightleftharpoons}} \mathrm{TF} - \mathrm{PhoA}$$

where k_{on} and k_{off} are the association and dissociation rate constants, respectively. The exchange rate constant, k_{ex}, of complex formation is given by $k_{ex} = k_{on}[\mathrm{PhoA}] + k_{off}$, where [PhoA] is the concentration of unbound PhoA. We have used ^{15}N relaxation dispersion experiments (*67*, *68*) to determine the k_{ex}, and thus k_{on}, k_{off}, and the residence time τ (=1/k_{off}) (*69*, *70*), of PhoA binding to TF (Fig. 3I). The data show that individual PhoA sites, such as *a* and *d*, interact rapidly with TF, and they stay bound to TF only for a very limited time (τ ~1 ms). As expected, the binding of larger PhoA fragments such as PhoA$^{a\text{-}c}$ or PhoA$^{d\text{-}e}$, which bind to TF with much higher affinity (Fig. 3A), results in increased complex lifetimes. However, even in these cases, the kinetics remain fast with the residence time being only ~20 ms at 22°C (Fig. 3K). The data are consistent with previous findings reporting similar rapid kinetics for the binding of TF to protein substrates (*71*). Thus, even when TF fully engages its unfolded protein substrate by using all of its available binding sites, the complex is still quite dynamic with fast association (k_{on} ~2×10^7 M^{-1} s^{-1}) and dissociation (k_{off} ~50 s^{-1}) rates, as determined by relaxation dispersion.

Structural Basis for the Formation of the TF-PhoA Complex

The three TF molecules in complex with PhoA (Fig. 4A) are linked by long (~80 to 90 amino acids), flexible regions of PhoA that are not bound by TF. Thus, the three PhoA-bound TF molecules tumble and behave as independent entities, corroborated by NMR data of the full-length PhoA in complex with three TF molecules (figs. S7A and S15). We thus determined the high-resolution structure of each of the three complexes (TF–PhoA$^{a\text{-}c}$, TF–PhoA$^{d\text{-}e}$, and TF–PhoA$^{f\text{-}g}$; Fig. 4A) separately. In each case, the structure determined by NMR corresponded to the ground-state, lowest-energy structure. A large number of intermolecular NOEs were collected because of the large interacting surface between TF and PhoA and the high sensitivity provided by the methyl-bearing and aromatic residues of the NMR spectra. The structure and NMR statistics are listed in table S1. Resonance dispersion of PhoA increases markedly in its complexes with TF (fig. S10, A and B) owing to the intimate contacts between the two proteins, thus enabling complete resonance assignment and structure characterization of PhoA.

PhoA binding to TF results in TF monomerization, as demonstrated by multiangle light scattering (MALS) and NMR experiments (figs. S1, C to E, and S18). The data further showed that the putative dimeric interface in TF is dynamic and suggested that substrate-binding regions are partially buried at the dimeric interface (figs. S18A and S19), in agreement with biochemical data (*49*). Thus, full engagement of the unfolded substrate by TF requires monomerization of the chaperone.

Structure determination of the TF–PhoA$^{a\text{-}c}$ complex shows that PhoA$^{a\text{-}c}$ binds simultaneously to all four substrate-binding sites, A to D, in TF (Fig. 4, A and B), confirming the initial binding experiments (Fig. 3H). Specifically, PhoA site *a*, which is ~10 residues long, binds to TF site D located in the PPD, whereas the much longer PhoA site *c* (~40 residues long) binds to all three TF sites located in the SBD (A, B, and C) (Fig. 4, A and B). Other than the regions encompassing the binding sites *a* and *c*, all other regions in PhoA$^{a\text{-}c}$ remain flexible in the complex (fig. S15).

PhoA site *a* uses exclusively nonpolar residues consisting primarily of a cluster of Leu residues to interact through intimate van der Waals contacts with a hydrophobic cluster in TF site D consisting primarily of aromatic residues (Fig. 4B, left). Formation of this subcomplex buries a total of ~1340 Å^2 of nonpolar surface and ~410 Å^2 of polar surface. Following T16 in PhoA site *a*, the next to contact TF is F94, the first residue of PhoA site *c*. PhoA site *c* spans ~40 residues (F94-W131) and binds to all three TF sites in the SBD (Fig. 4, A and B). PhoA site *c* traverses the entire SBD and binds to TF sites B, A, and C using its subsites c^1, c^2, and c^3, respectively (Fig. 4, A and B, right). Thus, each one of the binding sites in TF engages about 6 to 10 PhoA residues. Complex formation between the TF SBD and PhoA site *c* buries a total of ~3820 Å^2 of surface. The majority of the surface (~2580 Å^2) consists of nonpolar residues, whereas ~1240 Å^2 consists of polar residues.

PhoA site *c* (via subsite c^1) is anchored at the tip of arm 2 of the SBD by docking two of its hydrophobic residues, F94 and I97, deep into a hydrophobic pocket formed by TF residues of site B (Fig. 4B, right). Then, using both nonpolar and polar contacts, PhoA twists around the SBD arm 2 to interact with TF site A (via subsite c^2) through contacts involving several aromatic residues. Whereas TF sites A and B are located next to each other, TF site C is located on the other end of the SBD (Fig. 1A). PhoA reaches site C by stretching an ~10-residue-long region (G116-A125) that appears to interact only transiently with TF. The interaction between PhoA site *c* (via subsite c^3) and TF site C is again mediated primarily by nonpolar contacts, with the most prominent being the docking of PhoA W131 into a hydrophobic pocket formed by several residues of TF site C (Fig. 4B). Although the vast majority of the contacts between the TF SBD and PhoA site *c* are mediated by hydrophobic residues, several key hydrogen bonds are also present throughout the complex (Fig. 4B and fig. S20). The structure of the TF–PhoA$^{a\text{-}c}$ complex shows that a total of about 40 to 50 residues of an unfolded client protein can directly interact with the four sites of TF.

A second TF molecule binds to the middle region of PhoA, consisting of sites *d* and *e* (Fig. 4A and fig. S17D). The K_d of the TF–PhoA$^{d\text{-}e}$ complex is ~4 μM (Fig. 3A and fig. S14), similar to that of the TF–PhoA$^{a\text{-}c}$ complex. Structure determination of the TF–PhoA$^{d\text{-}e}$ complex showed that TF recognizes and interacts with the PhoA$^{d\text{-}e}$ region in a similar way as with the PhoA$^{a\text{-}c}$ region. The PPD (site D) binds PhoA site *d* (residues K231-W242) through predominantly nonpolar contacts (Fig. 4C). When compared to PPD-PhoA^{a} (Fig. 4B), two distinct features of the PPD-PhoA^{d} subcomplex are, first, that PhoA site *d* extends over a larger surface, thereby engaging additional PPD residues (for example, T165 and V186), and, second, that recognition of PhoA site *d* is enhanced by three favorable hydrogen bonds (Fig. 4C). Formation of the PPD-PhoA^{d} complex buries a total surface of ~1350 Å^2, with ~880 Å^2 being nonpolar and ~470 Å^2 polar.

PhoA site *e* (residues Leu^{277}-Ile^{301}), like PhoA site *c*, engages all three TF sites of the SBD (Fig. 4A), but the overall architecture is distinct in the two complexes. Whereas PhoA site *c* traverses the SBD

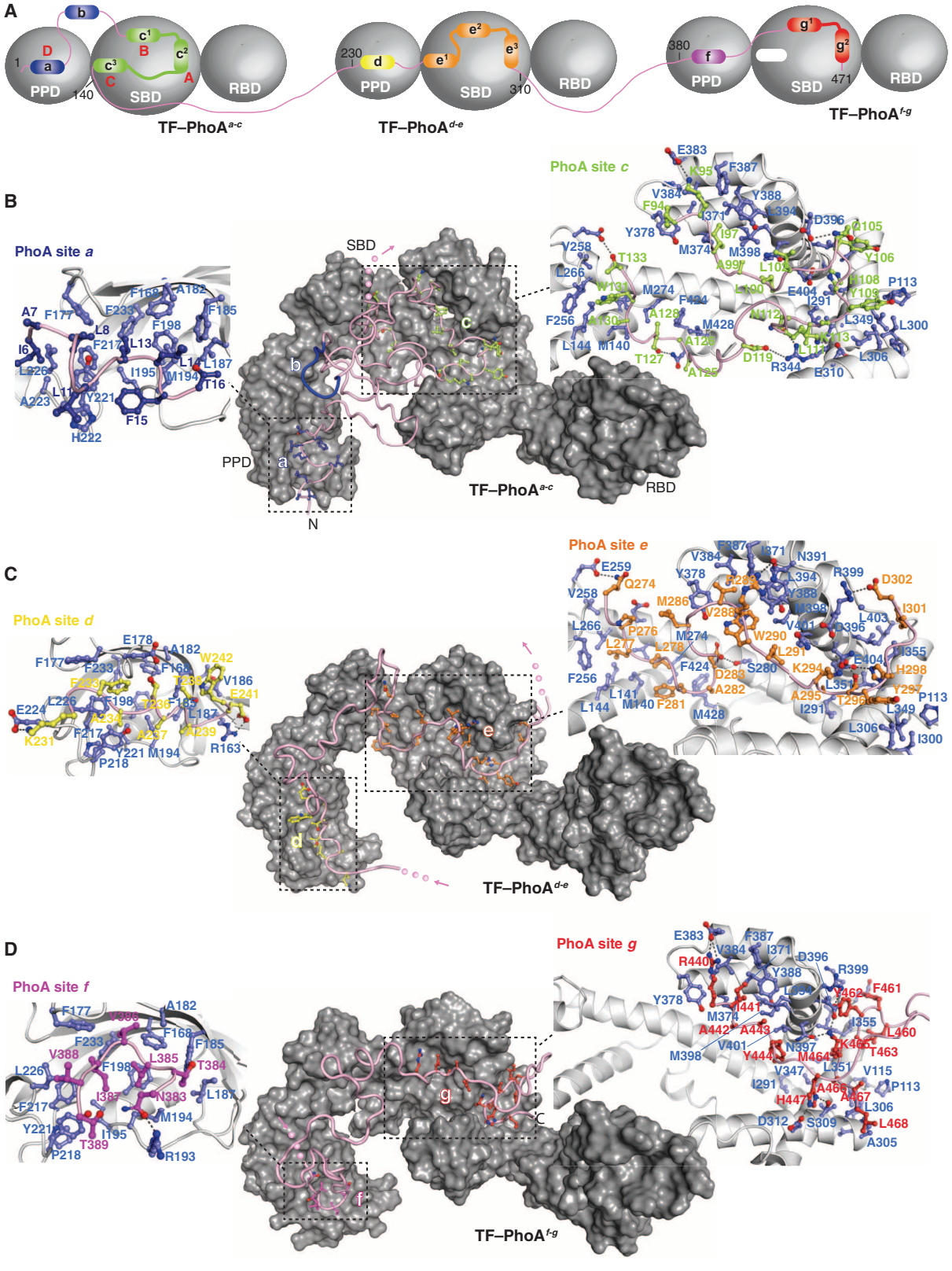

Fig. 4. Structural basis for the formation of the TF-PhoA complexes. (**A**) Schematic for the interaction of PhoA with TF based on the current structural data. The TF-binding sites in PhoA are colored as in Figs. 2 and 3A. (**B** to **D**) Lowest-energy structure of the three TF molecules in complex with the corresponding PhoA regions. TF is shown as a solvent-exposed surface and PhoA as a pink ribbon. The PhoA residues that directly interact with TF are drawn in a ball-and-stick representation, colored as in panel (A). The pink arrows denote the direction of the PhoA chain, from the N to the C terminus. Close-up views of the structures are shown on the left for the PPD (site D) and on the right for the SBD (sites A, B, and C) bound to the corresponding PhoA sites. In the expanded views, the TF backbone is shown as a white cartoon and the PhoA backbone as a pink cartoon. The side chains of TF are colored blue, whereas the side chains of PhoA are colored using the color code for each site. The black broken lines denote hydrogen bonds (present in at least 70% of the conformers of the ensemble).

by interacting first with TF site B, followed by A and C, PhoA site *e* interacts first with TF site C (via subsite e^1), followed by TF site B (via subsite e^2) and TF site A (via subsite e^3) (Fig. 4, A and C, right). Recognition of PhoA site *e* by the TF SBD is mediated predominantly by nonpolar contacts, but several key hydrogen bonds are also present (Fig. 4C and fig. S21). Complex formation between the TF SBD and PhoA site *e* buries a total surface of ~3460 Å^2, with ~2410 Å^2 consisting of nonpolar residues and ~1050 Å^2 consisting of polar residues.

The third TF molecule binds to the C-terminal region of PhoA, consisting of sites *f* and *g* (Fig. 4A and fig. S17G). The K_d of the TF–PhoA$^{f\text{-}g}$ complex is ~14 μM (Fig. 3A and fig. S14), the weakest among the three complexes. Structure determination of the TF–PhoA$^{f\text{-}g}$ complex (the structure of the major conformation out of the possible two was determined; fig. S17G) confirmed that the PPD interacts with PhoA region *f*, and the SBD with PhoA region *g* (Fig. 4, A and D, and fig. S22). PhoA region *f* (residues N383-V388) consisting of only seven residues is the shortest region within PhoA that is recognized and bound by TF (Fig. 2C and fig. S8A). Despite its short length, the nonpolar surfaces between PhoA site *f* and PPD are well juxtaposed, further enhanced by a hydrogen bond, thereby providing sufficient affinity for the formation of a stable complex (Fig. 4D), which buries a total surface of ~1230 Å^2 (~940 Å^2 of nonpolar and ~290 Å^2 of polar surface).

PhoA region *g* (residues Arg^{440}-Leu^{468}) is recognized by the TF SBD. In contrast to PhoA sites *c* and *e*, which both interact with all three TF sites in the SBD (Fig. 4, B and C), PhoA site *g* interacts primarily with TF sites A and B (Fig. 4, A and D, and fig. S17G). PhoA residues Arg^{440}-Tyr^{444} (subsite g^1) interact with TF site B, and PhoA residues L460-L468 (subsite g^2) bind to TF site A (Fig. 4D and fig. S17G). Other than PhoA H447, which forms a bifurcated hydrogen bond with two TF residues (D312 and S309) located in arm 1 of the SBD, none of the other residues of the PhoA region (G445-D459) connecting the g^1 and g^2 subsites appear to interact with TF (Fig. 4D). Complex formation between the SBD and PhoA site *g* buries ~2670 Å^2 of surface (~1840 Å^2 nonpolar and ~830 Å^2 polar), substantially less than the SBD complexes with PhoA sites *c* and *e*, which likely explains the lower affinity of the TF–PhoA$^{f\text{-}g}$ complex (fig. S14).

Amino acid substitutions at the substrate-binding sites in TF resulted in a significant decrease in the affinity for PhoA and a marked decrease of its antiaggregation activity (Fig. 5 and fig. S23).

Recognition of Unfolded PhoA by TF

An important question that remains largely unaddressed is how molecular chaperones recognize unfolded proteins. A common feature shared among molecular chaperones appears to be their interaction with exposed hydrophobic segments of the substrate proteins (*5*). The structural data of TF in complex with PhoA show that TF has a preference for stretches of residues with increased hydrophobicity (Fig. 2C), especially for aromatic residues (Trp, Phe, and Tyr), as well as for large hydrophobic amino acids such as Ile and Leu (fig. S8C). His and Thr residues are also favored (fig. S8C), presumably because they can form both nonpolar and polar contacts. Although there seems to be a good correlation between the sequence hydrophobicity of the substrate protein and its binding preference by TF (Fig. 2C), there are long stretches of hydrophobic residues in PhoA (for example, residues 155 to 185) that are not recognized by TF. This may be due to the complete absence of aromatic residues in this region. The strong preference of TF for aromatic residues may also explain the stronger association of TF with outer membrane proteins (*25*), which are typically enriched in aromatic residues.

The structural data of the three TF molecules in complex with different regions of PhoA (Fig. 4) provide insight into how the same binding sites within a molecular chaperone can recognize and interact with a large number of substrates with unrelated primary sequences. Superposition of the three structures of the TF SBD shows that the binding mode is distinct in the three complexes (Fig. 6 and fig. S24A). The structural data suggest that the two arms of TF are rather dynamic, giving rise to a variable width of the binding crevice in the SBD (fig. S24B), in agreement with NMR dynamic analysis (*53*). In addition, there is notable conformational rearrangement of the side chains in the SBD substrate-binding sites among the three TF complexes with PhoA (Fig. 6E and fig. S24, C and D). Structural analysis of the complexes of the TF SBD with PhoA sites *c*, *e*, and *g* indicated some common binding and recognition patterns (Fig. 6, A to C). For example, TF site B recognizes bulky hydrophobic residues in PhoA that appear to bind to two hydrophobic pockets in TF site B (Fig. 6B). Similarly, there seems to be a pattern, albeit weaker, of bulky and small hydrophobic PhoA residues binding in TF sites A and C (Fig. 6, A and C). A great degree of plasticity is also present in the PPD. For example, PhoA site *f* forms a hairpin-like structure when bound to the PPD, whereas PhoA site *d* binds in an extended conformation (fig. S24, A and F). To accommodate the different PhoA sequences, the residues that make up the PPD binding site appear to undergo significant conformational rearrangement upon complex formation (Fig. 6F).

Structural Basis for the Antiaggregation and Unfoldase Activity of TF

To understand how TF prevents the aggregation of unfolded proteins, we used an aggregation-prone MBP variant as a substrate (Fig. 7A). Such MBP variants have been extensively used as model systems for studying the effect of chaperones on protein aggregation (*72*–*74*). The G32D/I33P double substitution in MBP destabilizes the protein by ~4 kcal mol^{-1} compared to wild-type MBP (MBP^{WT}) (*75*). MBP$^{G32D/I33P}$ (MBP^{mut}) is produced in inclusion bodies in the cell (*75*) and has a high tendency to aggregate in solution (*76*). NMR spectra show that purified MBP^{mut} is folded (Fig. 7B, right, and fig. S25A), in agreement with biochemical (*75*) and crystallographic (*77*) data. However, MBP^{mut} suffers heavy aggregation and precipitation at higher temperatures (above 30°C). Notably, in the presence of TF, MBP^{mut} remains soluble and folded even at temperatures as high as 50°C (fig. S25B).

How does TF prevent aggregation of MBP^{mut}? NMR titration experiments performed at 22°C (Fig. 7B, right, and fig. S25, A and C) show that TF does not interact with the folded state of MBP^{mut}. However, titration of MBP^{mut} to labeled TF at temperatures where MBP^{mut} is prone to aggregation (for example, 38°C) resulted in substantial chemical shift perturbation, indicating complex formation (Fig. 7B, left, and fig. S25, D and E). Thus, unfolded MBP^{mut} is recognized and engaged by TF. In support of this conclusion, titration of

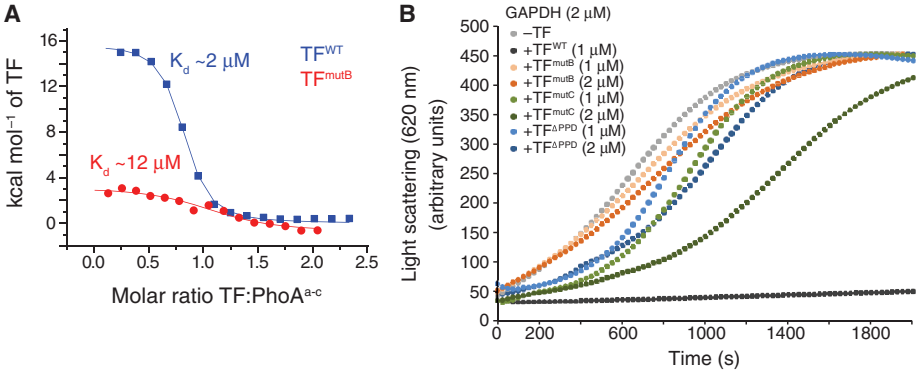

Fig. 5. Effect of mutations in substrate-binding sites on TF activity. (**A**) Binding affinity determined by ITC for PhoA$^{a\text{-}c}$ to TF^{WT} and TF^{mutB}. TF^{mutB} is a mutant in which four hydrophobic amino acids of TF site B were substituted (fig. S23). The mutations result in a sixfold decrease in the affinity. (**B**) Aggregation of chemically denatured glyceraldehyde-3-phosphate dehydrogenase (GAPDH) monitored by light scattering at 620 nm, in the absence or presence of TF^{WT} and its variants. In contrast to TF^{WT}, TF^{mutB} has very poor antiaggregation activity. The antiaggregation activity is also compromised in TF^{mutC}, a mutant in which a single hydrophobic amino acid of TF site C was substituted (fig. S23), as well as in a TF construct wherein the PPD has been deleted (TF$^{\Delta PPD}$).

MBP^{WT} to TF showed no sign of complex formation even at 38°C (fig. S25F). Because of the large difference in their free energy of folding ($\Delta\Delta G_f$ ~4 kcal mol^{-1}, Fig. 7A), the unfolded state will be significantly more populated in MBP^{mut} than in MBP^{WT} at elevated temperatures. NMR analysis (fig. S25, D and E) showed that TF uses all of the possible substrate binding sites to interact with the unfolded state of MBP^{mut} (Fig. 7A and fig. S11C). Together, the results show that multivalent binding between TF and the unfolded state of MBP^{mut} shields and protects the unfolded state from the solvent and results in the prevention of its aggregation (Fig. 7A).

Although TF binds to the unfolded state of MBP^{mut}, the NMR spectra show that TF cannot unfold the protein even at temperatures as high as 50°C (fig. S25B). Because TF lacks adenosine triphosphatase activity, it could, in principle, unfold protein substrates only if the free energy of binding (ΔG_b) of the substrate's unfolded state for TF is much larger than the substrate's intrinsic energy for folding (Fig. 7A). The intrinsic affinity of TF for unfolded substrates is relatively low (ΔG_b ~–7.5 kcal mol^{-1}; fig. S14), and thus, it is expected to unfold only marginally stable proteins. However, the interaction of ribosome-bound TF with the nascent polypeptide is very strong because of their colocalization (*78*). When MBP^{mut} was fused to TF, it was completely unfolded as demonstrated by the disappearance of resonances corresponding to residues located in folded regions and the appearance of resonances in the so-called random-coil region (Fig. 7C). NMR analysis showed that TF makes use of all of its substrate-binding sites to interact and unfold MBP^{mut} (Fig. 7A). Of particular note, maltose binding to MBP^{mut} confers stability (*79*) and prevents its unfolding by TF (Fig. 7C, right). These results are in excellent agreement with elegant biochemical data indicating that TF has a negligible unfoldase activity when free in solution but a strong unfoldase activity when bound to the ribosome (*30*).

Discussion

The TF molecular chaperone engages its unfolded substrate (PhoA) in a highly dynamic manner, giving rise to a rugged free energy landscape (Fig. 3H). It is expected that the features of the binding energy landscape will vary among the various molecular chaperones and even among different substrates binding to the same chaperone. In the case of PhoA binding to TF, we observed a gradual increase in binding affinity as the length of the engaged PhoA increased until all four of the binding sites in TF were fully occupied (Fig. 3 and fig. S17). Because of the topology of the TF-binding sites in PhoA, the selectivity of some of the PhoA sites for specific TF sites (Fig. 3 and fig. S17), and the observed synergistic binding among PhoA sites close to each other (Fig. 3 and fig. S16), the lowest-energy complexes between TF and the three PhoA regions were experimentally observed to exist in one predominant conformation (Fig. 4A and fig. S17, D and G). Notably, the observed binding avidity of the PhoA sites and subsites is relatively weak (Fig. 3 and fig. S17). This is probably because the linker tethering the (sub)sites remains dynamic even in complex with TF, thus allowing for somewhat independent binding of the PhoA sites. The observed weak synergistic binding may be crucial in enabling a dynamic binding and release of the unfolded protein substrate from the chaperone (Fig. 3K).

The excellent quality of the NMR spectra enabled the high-resolution structure determination for each one of the three TF molecules in complex with different regions of PhoA (Fig. 4). Analysis of

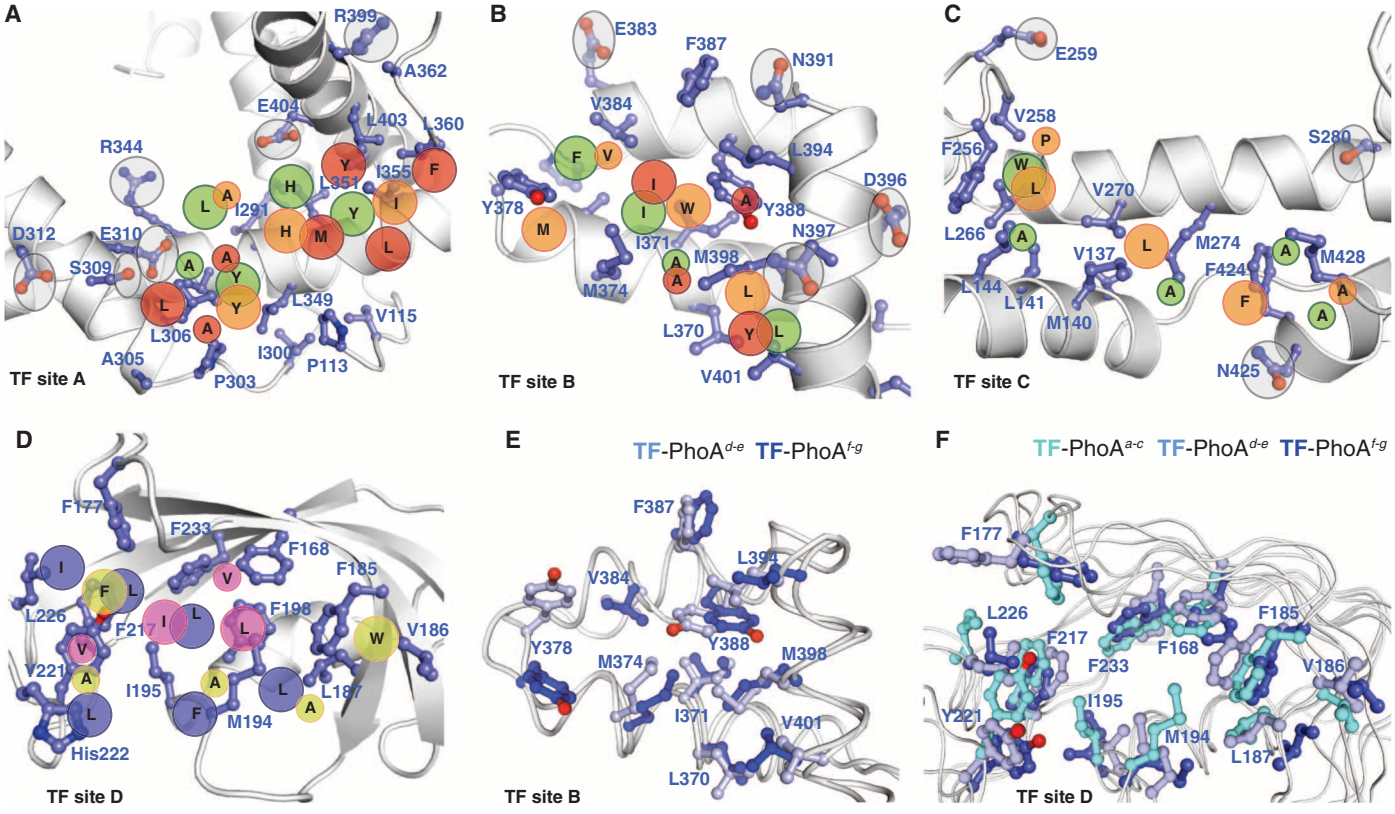

Fig. 6. Substrate recognition conformational plasticity by TF. (**A** to **D**) Interaction and recognition patterns of the PhoA sites in the complexes with the three TF molecules. A close-up view of each one of the four substrate-binding sites in TF (labeled TF site A, B, C, and D) is shown, with the backbone in white ribbon and the interacting residues in blue sticks. The position of hydrophobic residues from PhoA sites interacting with TF is projected on the TF structure and denoted as large (for aromatic or Ile/Leu residues) or small (for Ala/Val residues) circles. For clarity, only one TF molecule is shown. The substrate-binding sites A, B, and C in TF are decorated with polar residues (highlighted with gray circles) that form hydrogen bonds with PhoA. Only PhoA residues involved in nonpolar contacts are shown. The color code of the PhoA residues (in circles) is as follows: site *a*, blue; site *c*, green; site *d*, yellow; site *e*, orange; site *f*, magenta; site *g*, red. (**E** and **F**) Superposition of the TF substrate-binding sites [site B in (E), site D in (F)] in the indicated PhoA-bound complexes. PhoA is not shown for clarity. The TF side chains undergo significant rearrangement to interact with the different PhoA regions.

the structures suggests that the plasticity of the substrate-binding sites in TF, combined with the presence of numerous small hydrophobic pockets on the binding surface and the decoration of these sites by polar residues that can form hydrogen bonds (Fig. 6), is important for the promiscuous recognition of multiple substrate sequences by TF. TF presents a multivalent binding surface to its protein substrate, which binds to TF using several distinct regions. This mechanism of binding presents several advantages because it enables chaperones to function as holdases and unfoldases by exerting forces to retain proteins in the unfolded state, and at the same time protect them from aggregation by shielding their exposed hydrophobic regions. Impairment of the substrate-binding sites in TF results in significant reduction in TF's antiaggregation activity (Fig. 5). Given the existence of multiple binding sites in other molecular chaperones (such as the GroEL), this may present a general mechanism for the action of molecular chaperones (*80*–*82*).

TF appears to have a weak holdase and unfoldase activity in the cytosol but a very strong activity when colocalized with the protein substrate. Thus, in the cytosol, TF is apparently capable of rescuing folded proteins by transiently interacting with the aggregation-prone unfolded population of the substrate, without destabilizing the protein substrate (as seen with MBP^{mut}; Fig. 7, A and B, and fig. S25B). In contrast, when TF is bound to the ribosome, its strong holdase and unfoldase activity (Fig. 7C) will mean that TF can retain the nascent polypeptide in an unfolded state and even actively unfold transiently formed structures. Although PhoA has some fraction of secondary structure present in its unfolded state (Fig. 2, A and B), these regions are devoid of any secondary structure when they are bound to TF (Fig. 4). Together, the data demonstrate that binding of substrate proteins to TF may result not only in global unfolding of the substrate protein but also in melting of secondary structural elements.

The present structural data explain the observation that multiple TF molecules are required to bind to long nascent chains (*18*, *19*, *25*) because a single TF molecule can only accommodate a stretch of about 40 to 50 binding residues of the substrate protein. Moreover, the weak affinity of the first ~70 residues of PhoA for TF, as well as the fact that the predicted TF-binding sites in a number of proteins known to bind strongly to TF (*25*) are located past the first ~70 residues (fig. S26), is in agreement with ribosome profiling data (*25*) that nascent chains with more than ~70 residues protruded from the ribosome exit channel are required for a stable complex with TF. Another interesting aspect of TF is its ability to bind and protect small folded proteins as a dimer (*27*) (fig. S27). The ability of TF to act as a holdase and an unfoldase with unfolded proteins and to encapsulate folded proteins in its dimeric state highlights the versatility of this particular molecular chaperone and the multiple roles it may play in protein folding (*83*).

Materials and Methods

Expression and Preparation of Proteins

The *E. coli* TF was cloned into the pCold vector (Takara Bio). The following TF constructs were prepared: the RBD (residues 1 to 117) and the SBD (residues 113–432Δ150–246) were cloned into pET16b vector (Novagen) and fused to His_6-MBP, including a tobacco etch virus (TEV) protease cleavage site. The PPD (residues 148 to 249), SBD-PPD (residues 113 to 246), and RBD-SBD (1–432Δ150–243) were cloned into pCold vector (Takara Bio). TF mutants were constructed by site-directed mutagenesis using PfuTurbo High Fidelity DNA polymerase (Agilent). All constructs were transformed into BL21(DE3) cells. The following *E. coli* PhoA constructs were prepared (residue numbers of the boundaries are in superscript): $PhoA^{1–471}$ (full length), $PhoA^{1–62}$, $PhoA^{1–82}$, $PhoA^{1–122}$, $PhoA^{1–140}$, $PhoA^{1–150}$, $PhoA^{1–250}$, $PhoA^{23–78}$, $PhoA^{76–150}$, $PhoA^{119–243}$, $PhoA^{1–232}$, $PhoA^{234–349}$, $PhoA^{228–471}$, $PhoA^{349–471}$, $PhoA^{220–310}$, $PhoA^{365–471}$, $PhoA^{228–245}$, $PhoA^{272–327}$, $PhoA^{381–438}$, and $PhoA^{425–471}$. All PhoA fragments were cloned into a pET16b vector and fused to His_6-MBP, including a TEV protease cleavage site. *E. coli* MBP, $MBP^{29–132}$, and $MBP^{G32D/I33P}$ (*75*) were cloned into

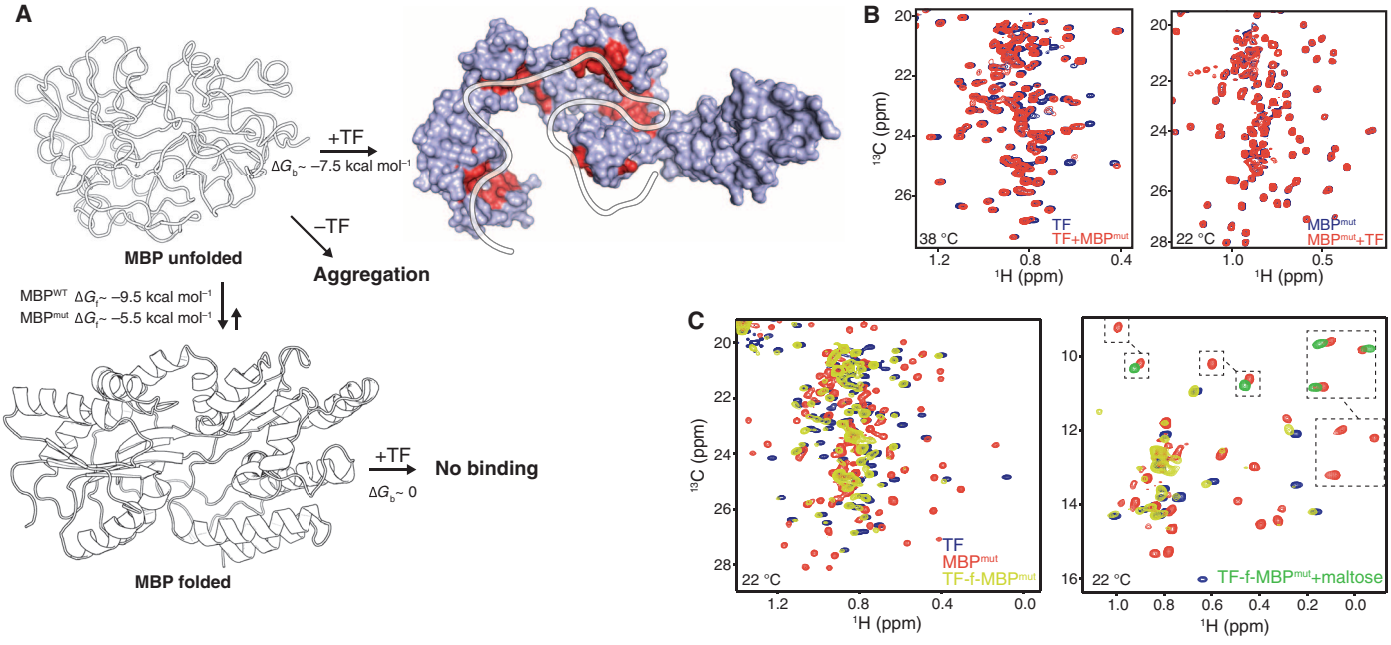

Fig. 7. Antiaggregation and unfoldase activity of TF. (**A**) Schematic of MBP unfolding and binding reactions between TF and MBP^{mut}. ΔG_f is the free energy of folding and ΔG_b is the free energy of binding. The sites that TF uses to interact with the unfolded state of MBP^{mut}, as determined by NMR, are colored red. (**B**) ^1H-^{13}C–correlated methyl NMR spectra of the interaction between TF and MBP^{mut}. The spectrum shown on the left was recorded at 38°C using labeled TF and unlabeled MBP^{mut}, whereas the spectrum shown on the right was recorded at 22°C using the reverse labeling scheme. No interaction was observed at 22°C, where the unfolded population of MBP^{mut} was negligible, whereas binding was observed at 38°C, where the unfolded population of MBP^{mut} was appreciable. For clarity, only the region of the Leu and Val methyl resonances is shown. The full-range spectra are shown in fig. S25. (**C**) ^1H-^{13}C–correlated methyl NMR spectra of the fusion construct between TF and MBP^{mut} (TF-f-MBP^{mut}, yellow). The spectra of free TF (blue) and free MBP^{mut} (orange) are also shown for comparison. The spectrum on the left depicts the region of the Leu and Val methyl resonances, whereas the one on the right depicts the region of the Ile methyl resonances. The disappearance of the peaks belonging to MBP^{mut} residues residing in folded regions and the appearance of peaks in the random-coil region indicates that MBP^{mut} is unfolded when fused to TF. Addition of maltose (green resonances on the Ile spectrum) stabilizes MBP^{mut} and prevents its unfolding by TF.

pET 16b vector (Novagen). The TF-MBP$^{I32D/G33P}$ fusion protein was cloned into pCold vector (Takara Bio) to be fused to TF or TF$^{SBD\text{-}PPD}$ separated by a 25-residue linker. The transmembrane region of OmpA (OmpA^{t}; residues 1 to 192) fused with N-terminal His-tag was cloned into pET16b vector (Novagen). For the unlabeled samples, cells were grown in Luria-Bertani (LB) medium at 37°C in the presence of ampicillin (100 μg ml^{-1}). Protein expression was induced by the addition of 0.1 to 0.8 mM isopropyl-β-D-1-thiogalactopyranoside (IPTG) at OD_{600} ~0.5, followed by 12 to 16 hours of incubation at 18°C. Expression of MBP$^{G32D/I33P}$ was induced by the addition of 0.01 mM IPTG at OD_{600} ~0.5, followed by 48 hours of incubation at 16°C. Cells were harvested at OD_{600} ~1.5 and resuspended in lysis buffer containing 50 mM tris-HCl (pH 8.0), 50 to 500 mM NaCl, 5 mM imidazole, and 1 mM β-mercaptoethanol (βME) (and 8 M urea in the case of PhoA fragments followed by 20-fold rapid dilution in lysis buffer). For OmpA, the cell pellet was resuspended in buffer containing 50 mM tris-HCl (pH 8.0), 500 mM NaCl, 5 mM imidazole, and 6 M guanidine hydrochloride and incubated for 1 hour at room temperature. Cells were disrupted by a high-pressure homogenizer or sonicator and centrifuged at 50,000*g*. Proteins were purified using Ni Sepharose 6 Fast Flow resin (GE Healthcare), followed by tag removal by TEV protease at 4°C (incubation for 16 hours) and gel filtration using Superdex 75 16/60 or 200 16/60 columns (GE Healthcare). OmpA was eluted with a solution containing 50 mM tris-HCl (pH 8.0), 500 mM NaCl, 400 mM imidazole, and 6 M guanidine hydrochloride. The eluted protein was concentrated and diluted 20-fold by rapid dilution in the presence of TF or TF$^{PPD\text{-}SBD}$ in 20 mM potassium phosphate (pH 7.0), 100 mM KCl, 4 mM βME, 0.5 mM EDTA, 0.05% NaN_3. Protein concentration was determined spectrophotometrically at 280 nm using the corresponding extinction coefficient.

MALS Experiments

Multiangle light scattering was measured using DAWN HELEOS-II (Wyatt Technology Corporation) downstream of a Shimadzu liquid chromatography system connected to a Superdex 200 10/300 GL (GE Healthcare) gel filtration column. The typical running buffer was 20 mM KPi (pH 7.0), 100 mM KCl, 4 mM βME, and 0.5 mM EDTA. Two hundred microliters of the sample with a concentration of 100 to 400 μM was injected. The data were analyzed with ASTRA version 6.0.5 (Wyatt Technology Corporation).

GAPDH Aggregation Assay

Aggregation of denatured GAPDH from rabbit muscle (Sigma, G-2267) was measured are described previously (*84*). GAPDH (125 μM) was denatured by 3 M guanidine-HCl in 20 mM KPi (pH 7.0), 100 mM KCl, 4 mM βME, 0.5 mM EDTA, and 0.05% NaN_3 for 12 hours at 4°C. The denatured enzyme was diluted 50-fold in a buffer that does not contain guanidine-HCl, and aggregation was monitored by 90° light scattering at 620 nm on a spectrofluorometer (FluoroMax-4, Horiba) in the presence or absence of TF. The experiment was carried out at 20°C.

Substrate Binding Site Mutations in TF

To assess the effect of reducing the hydrophobicity of the substrate-binding sites of TF on its binding and antiaggregation activity, we sought to mutate the most prominent residues in each one of the binding sites located in the SBD (that is, sites A, B, and C). The following mutants were prepared: L306A, G348E, G352E, I355A (site A); M374A, Y378A, V384A, F387A (site B); M140E, L144A, F256A L266A, M274A, M428A (site C) as single or combined mutants. Although all of the mutants were expressed and purified in a soluble form, NMR characterization indicated that mutations other than the ones shown in fig. S23 are not well tolerated, with the mutated TF proteins showing signs of misfolding and aggregation.

ITC Experiments

Calorimetric titrations were carried out on an iTC200 microcalorimeter (GE Healthcare) at temperatures ranging from 8° to 25°C. All protein samples were extensively dialyzed against ITC buffer containing 20 mM potassium phosphate (pH 7.0), 100 mM KCl, and 1 mM tris(2-carboxyethyl)phosphine. All solutions were filtered using membrane filters (pore size, 0.45 μm) and thoroughly degassed for 20 min before the titrations. For the experiments performed on iTC200, the 200-μl sample cell was filled with ~40 to 100 μM protein (TF or PhoA), and the 40-μl injection syringe was filled with 0.5 to 1 mM solution of protein (PhoA or TF). The titrations were carried out with a preliminary 0.2-μl injection, followed by 15 injections of 2.5 μl each with time intervals of 3 min. The solution was stirred at 1000 rpm. For the experiments performed on VP-ITC, the 1200-μl sample cell was filled with ~40 to 100 μM protein (TF or PhoA), and the 250-μl injection syringe was filled with 0.5 to 1 mM solution of protein (PhoA or TF). The titrations were carried out with 30 injections of 10 μl each with time intervals of 5 min. The solution was stirred at 270 rpm. Data for the preliminary injection, which are affected by diffusion of the solution from and into the injection syringe during the initial equilibration period, were discarded. Binding isotherms were generated by plotting heats of reaction normalized by the modes of injectant versus the ratio of total injectant to total protein per injection. The data were fitted with Origin 7.0 (OriginLab Corporation).

NMR Spectroscopy

NMR samples are prepared in 20 mM KPi (pH 7.0), 100 mM KCl, 4 mM βME, 0.5 mM EDTA, 0.05% NaN_3, and 7% ^2H_2O. Protein concentration was 0.1 to 0.8 mM. NMR experiments were recorded on Agilent UNITY Inova 800 and 600 MHz NMR spectrometers and Bruker Avance III 600 and 700 MHz NMR spectrometers equipped with cryogenic probes. The experiments were run at 10°C for isolated PhoA samples, and at temperatures ranging from 18° to 50°C for the other samples. NMR spectra for the assignment and structure determination of the TF-PhoA complexes were recorded at 22°C. Spectra were processed using the NMRPipe program (*85*), and data analysis was performed with Olivia (fermi.pharm.hokudai.ac.jp/olivia) and SPARKY software.

Binding affinities between TF and PhoA fragments were estimated using ^1H-^{15}N heteronuclear single-quantum coherence (HSQC) titration experiments, where unlabeled PhoA was titrated into labeled TF. Titration curves were obtained by plotting chemical shift perturbations ($\Delta\delta_{ppm}$) against the molar ratio of PhoA and TF. Nonlinear least square fitting calculations were performed in GraphPad Prism (GraphPad Software), using the following equation:

$$\Delta\delta_{ppm} = \Delta\delta_{ppm}^{bound} \times \frac{[P]+[L]+K_d-\sqrt{([P]+[L]+K_d)^2-4[P][L]}}{2[P]}$$

where $[L]$ and $[P]$ are the concentrations of the peptide ligand (PhoA) and protein (TF), respectively, and K_d is the dissociation constant.

Protein Isotope Labeling for NMR Studies

Isotopically labeled samples for NMR studies were prepared by growing the cells in minimal (M9) medium. Cells were typically harvested at OD_{600} ~1.0. U-[^2H,^{13}C,^{15}N]–labeled samples were prepared for the backbone assignment by supplementing the growing medium with $^{15}NH_4Cl$ (1 g liter^{-1}) and $^2H_7$,$^{13}C_6$-glucose (2 g liter^{-1}) in 99.9% ^2H_2O (CIL and Isotec). The methyl-protonated samples (*86*) were prepared as described (*44*, *47*). α-Ketobutyric acid (50 mg liter^{-1}) and α-ketoisovaleric acid (85 mg liter^{-1}) were added to the culture 1 hour before the addition of IPTG. Met-[$^{13}CH_3$]– and Ala-[$^{13}CH_3$]–labeled samples were produced by supplementing the medium with [$^{13}CH_3$]methionine (50 mg liter^{-1}) and [^2H,$^{13}CH_3$]alanine (50 mg liter^{-1}). For Thr labeling, a Thr-auxotrophic cell strain was used, and the medium was supplemented with [^2H,$^{13}CH_3$]threonine (25 mg liter^{-1}) prepared as described (*87*). For Phe, Tyr, and Trp labeling, U-[^1H,^{13}C]–labeled amino acids were used. All precursors and amino acids were added to the culture 1 hour before the addition of IPTG, except Ala, which was added 30 min before induction (*47*).

NMR Assignment of TF

The resonances of the full-length dimeric TF (~100 kD) were assigned by following a domain-parsing approach enabled by the modular architecture of TF. The RBD (*52*), SBD (*53*), and PPD are folded when isolated (fig. S3B). Overlay of the NMR spectra for each one of the domains with the spectra of the full-length TF indicated very good resonance correspondence for the SBD and PPD (figs. S2 to S4) but more significant chemical shift

differences for the RBD (fig. S19). About 70 to 80% of the assignment performed on the isolated domains could be transferred to the full-length TF. Near-complete assignment of TF was achieved by recording nuclear Overhauser effect spectroscopy (NOESY) in full-length TF to resolve ambiguities. In addition, $TF^{SBD\text{-}PPD}$ was prepared and fully characterized by NMR because this fragment is monomeric and contains all of the substrate binding sites. Backbone and side-chain resonances for the domains were assigned using standard triple-resonance NMR pulse sequences. Methyl side-chain and amide resonances for TF and large fragments were confirmed by recording the following NMR experiments [the standard version was used for isolated RBD and PPD and the TROSY (transverse relaxation optimized spectroscopy) version, where applicable, for $TF^{SBD\text{-}PPD}$ and TF]: three-dimensional (3D) (^{1}H)-^{13}C heteronuclear multiple-quantum coherence (HMQC)–NOESY–^{1}H-^{13}C HMQC, ^{13}C-edited NOESY-HSQC, ^{13}C-edited HSQC-NOESY, ^{15}N-edited NOESY-HSQC, 3D (^{1}H)-^{13}C HSQC-NOESY–^{1}H-^{15}N HSQC, and 3D (^{1}H)-^{15}N HSQC-NOESY–^{1}H-^{13}C HSQC.

NMR Assignment of PhoA

Resonance assignment of full-length PhoA was accomplished by first assigning short PhoA fragments followed by assignment transfer. The backbone and side-chain resonances of the following PhoA fragments were fully assigned using standard triple-resonance experiments: $PhoA^{1–122}$, $PhoA^{119–243}$, $PhoA^{234–349}$, and $PhoA^{349–471}$ (the superscript denotes the amino acid residue boundaries of the fragment). Overlay of the spectra of these fragments with the spectra of full-length PhoA indicated excellent resonance correspondence (fig. S5D). This is expected because all of the fragments as well as the full-length PhoA are unfolded. Resonance assignment obtained for the various fragments was transferred to the full-length PhoA, and ambiguities were resolved by the use of 3D NMR spectra. Resonance assignment of PhoA in complex with TF was achieved by tracing the PhoA NMR signals as increasing amounts of unlabeled TF was titrated. Complex formation was on the fast time scale regime, allowing the monitoring of the chemical shift changes in a straightforward manner. Ambiguities were resolved by recording 3D NMR spectra. It should be noted that although resonance dispersion in unliganded PhoA is poor, complex formation with TF alleviates this problem (for the PhoA residues in the TF-binding regions) with the spectra being of high resolution (figs. S2, C and D, and S10).

Structure Determination

In the first step, we used a U-^{12}C,^{15}N–labeled sample that contained specifically protonated methyl groups of Ala, Val, Leu, Met, Thr, and Ile (δ1) and protonated aromatic residues Phe, Tyr, and Trp in an otherwise deuterated background (fig. S4). The high sensitivity and resolution of the methyl region, combined with the high abundance of these eight amino acids in TF (~50% of TF residues), provided a large number of intra- and intermolecular TF-PhoA NOEs sufficient to yield an initial well-defined structure. The initial structure was used to guide the subsequent collection of a much larger number of NOEs, using ^{1}H,^{13}C–labeled samples that resulted in further refinement to precise and accurate coordinates. In the second step, additional NMR restraints were collected for complexes between isolated SBD and PPD, as well as the entire chaperone module $TF^{SBD\text{-}PPD}$, in complex with the corresponding PhoA regions (fig. S10). NMR analysis demonstrated that the structures of the individual SBD and PPD in complex with PhoA are essentially identical to the structure of the full-length TF in complex with PhoA.

The initial structures of TF in complex with PhoA were calculated with CYANA 3.0 (*88*), using NOE peak lists from 3D (^{1}H)-^{13}C HMQC-NOESY–^{1}H-^{13}C HMQC, 3D (^{1}H)-^{15}N HSQC-NOESY–^{1}H-^{13}C HSQC, ^{13}C-edited NOESY-HSQC, and ^{15}N-edited NOESY-HSQC. The ^{13}Cα, ^{13}Cβ, ^{13}C′, Hα, ^{15}N, and NH chemical shifts served as input for the TALOS+ program (*89*) to extract dihedral angles (φ and ψ). Assigned NOE restraints were then used in the second round of calculations using Xplor-NIH (*90*) consisting of two steps. In the first step, the orientation and coordinates of PhoA polypeptide were randomized and then annealed to TF using intermolecular NOEs. TF was kept rigid but PhoA was set as flexible. The best 200 structures were selected and further refined in the second step, where both TF and PhoA were set flexible. Because the RBD does not interact with PhoA, or any other tested unfolded substrate, the coordinates from the *E. coli* TF structure (PDB ID 1W26) were used to model RBD in the current structures. The RBD was held rigid during the entire structure calculation protocol. The structure of the main chaperone module, $TF^{SBD\text{-}PPD}$, was determined using the NMR restraints in each one of the three complexes with $PhoA^{a\text{-}c}$, $PhoA^{d\text{-}e}$, and $PhoA^{f\text{-}g}$. The structures were calculated and refined using all of the restraints, including intra- and intermolecular NOEs, dihedral restraints derived from TALOS+, and hydrogen bond restraints for amides located in helices as determined via NOEs and chemical shift information. Hydrogen bonds between TF and PhoA were assigned when satisfactory geometry was present in at least 70% of the conformers. The 20 lowest-energy structures were finally refined in explicit water with CNS (*91*).

NMR Relaxation Experiments

Three relaxation parameters were measured for backbone amides of full-length PhoA, as well as for $PhoA^{1–232}$ and $PhoA^{228–471}$ for enhanced resolution: the {^{1}H}-^{15}N NOE, the longitudinal relaxation rate R_1, and the transverse relaxation rate R_2. ^{15}N R_1 values were measured from 2D spectra recorded with relaxation delays of 20, 40, 80, 160, 320, 640, 1200, 2500, and 5000 ms; ^{15}N R_2 values were measured from 2D spectra recorded with relaxation delays of 31.7, 47.5, 63.4, 79.2, 95.0, 110.9, 126.7, 158.4, 237.6, 316.8, and 475.2 ms. Data sets were acquired as 100 × 1024 complex points in the $t_1 \times t_2$ time-domain dimensions. Data points were fitted as a function of the length of the parametric relaxation delay to two-parameter decay curves of the form $I(t) = I^0 e^{-Rt}$, where I is the peak intensity. To measure the exchange rate and the kinetics ($k_{ex} = k_{on}[\text{PhoA}] + k_{off}$) of complex formation between TF and PhoA, we used NMR relaxation dispersion experiments (*65*, *66*). An ^{15}N-Carr-Purcell-Meiboom-Gill (CPMG) pulse sequence (*67*, *68*) was used. Two-dimensional data sets were acquired as 100 × 1024 complex points in the $t_1 \times t_2$ time-domain dimensions with a constant relaxation delay of 40 ms. Experiments were recorded at spectrometer frequencies of 600 and 700 MHz. NMR titration experiments showed that formation of all of the TF-PhoA complexes is fast on the NMR chemical shift time scale. k_{ex} was measured by using the Carver-Richards equation (*92*) as applied for fast exchange processes between two sites. Exchange rates were first extracted independently for each residue with appreciable exchange contribution (R_{ex} >5 Hz) for each one of the four binding sites in TF. The similarity of exchange rates extracted from fits of dispersion profiles on a per-residue basis for the four binding sites in TF indeed supports a two-site model of exchange (binding) even for the binding of the larger PhoA sites such as *c* and *e*. k_{on} and k_{off} rates were measured by fitting the relaxation dispersion data obtained for a set of experiments recorded using different PhoA concentrations. Data were analyzed using the programs CPMGFit (palmer.hs.columbia.edu/software/cpmgfit.html) and CPMG_fit provided by L. Kay (University of Toronto). $TF^{SBD\text{-}PPD}$ concentration for the relaxation dispersion experiments was ~0.4 to 0.8 mM in the presence of substoichiometric (~5 to 15%) amount of the corresponding PhoA fragment. It should be noted that the exchange process detected and measured is the binding and release of PhoA from TF as opposed to conformational heterogeneity of PhoA while bound to TF. This is supported by the PhoA concentration–dependent k_{ex} values we measured.

References and Notes

1. B. Bukau, J. Weissman, A. Horwich, Molecular chaperones and protein quality control. *Cell* **125**, 443–451 (2006). doi: 10.1016/j.cell.2006.04.014; pmid: 16678092
2. G. Kramer, D. Boehringer, N. Ban, B. Bukau, The ribosome as a platform for co-translational processing, folding and targeting of newly synthesized proteins. *Nat. Struct. Mol. Biol.* **16**, 589–597 (2009). doi: 10.1038/nsmb.1614; pmid: 19491936
3. F. U. Hartl, M. Hayer-Hartl, Converging concepts of protein folding in vitro and in vivo. *Nat. Struct. Mol. Biol.* **16**, 574–581 (2009). doi: 10.1038/nsmb.1591; pmid: 19491934
4. A. L. Horwich, Protein folding in the cell: An inside story. *Nat. Med.* **17**, 1211–1216 (2011). doi: 10.1038/nm.2468; pmid: 21989012
5. F. U. Hartl, A. Bracher, M. Hayer-Hartl, Molecular chaperones in protein folding and proteostasis. *Nature* **475**, 324–332 (2011). doi: 10.1038/nature10317; pmid: 21776078
6. H. Saibil, Chaperone machines for protein folding, unfolding and disaggregation. *Nat. Rev. Cancer* **13**, 630–642 (2013). doi: 10.1038/nrm3658; pmid: 24026055

7. F. Hartl, M. Hayer-Hartl, Molecular chaperones in the cytosol: From nascent chain to folded protein. *Science* **295**, 1852–1858 (2002). doi: 10.1126/science.1068408; pmid: 11884745
8. J. Young, V. Agashe, K. Siegers, F. Hartl, Pathways of chaperone-mediated protein folding in the cytosol. *Nat. Rev. Mol. Cell Biol.* **5**, 781–791 (2004). doi: 10.1038/nrm1492; pmid: 15459659
9. S. Preissler, E. Deuerling, Ribosome-associated chaperones as key players in proteostasis. *Trends Biochem. Sci.* **37**, 274–283 (2012). doi: 10.1016/j.tibs.2012.03.002; pmid: 22503700
10. A. Hoffmann, B. Bukau, G. Kramer, Structure and function of the molecular chaperone Trigger Factor. *Biochim. Biophys. Acta* **1803**, 650–661 (2010). doi: 10.1016/j.bbamcr.2010.01.017; pmid: 20132842
11. G. Kramer *et al.*, L23 protein functions as a chaperone docking site on the ribosome. *Nature* **419**, 171–174 (2002). doi: 10.1038/nature01047; pmid: 12226666
12. L. Ferbitz *et al.*, Trigger factor in complex with the ribosome forms a molecular cradle for nascent proteins. *Nature* **431**, 590–596 (2004). doi: 10.1038/nature02899; pmid: 15334087
13. D. Baram *et al.*, Structure of trigger factor binding domain in biologically homologous complex with eubacterial ribosome reveals its chaperone action. *Proc. Natl. Acad. Sci. U.S.A.* **102**, 12017–12022 (2005). doi: 10.1073/pnas.0505581102; pmid: 16091460
14. F. Schlünzen *et al.*, The binding mode of the trigger factor on the ribosome: Implications for protein folding and SRP interaction. *Structure* **13**, 1685–1694 (2005). doi: 10.1016/j.str.2005.08.007; pmid: 16271892
15. F. Merz *et al.*, Molecular mechanism and structure of Trigger Factor bound to the translating ribosome. *EMBO J.* **27**, 1622–1632 (2008). doi: 10.1038/emboj.2008.89; pmid: 18497744
16. B. Bukau, E. Deuerling, C. Pfund, E. A. Craig, Getting newly synthesized proteins into shape. *Cell* **101**, 119–122 (2000). doi: 10.1016/S0092-8674(00)80806-5; pmid: 10786831
17. R. Maier, B. Eckert, C. Scholz, H. Lilie, F.-X. Schmid, Interaction of trigger factor with the ribosome. *J. Mol. Biol.* **326**, 585–592 (2003). doi: 10.1016/S0022-2836(02)01427-4; pmid: 12559924
18. C. M. Kaiser *et al.*, Real-time observation of trigger factor function on translating ribosomes. *Nature* **444**, 455–460 (2006). doi: 10.1038/nature05225; pmid: 17051157
19. A. Rutkowska *et al.*, Dynamics of trigger factor interaction with translating ribosomes. *J. Biol. Chem.* **283**, 4124–4132 (2008). doi: 10.1074/jbc.M708294200; pmid: 18045873
20. R. Lill, E. Crooke, B. Guthrie, W. Wickner, The "trigger factor cycle" includes ribosomes, presecretory proteins, and the plasma membrane. *Cell* **54**, 1013–1018 (1988). doi: 10.1016/0092-8674(88)90116-X; pmid: 3046750
21. V. R. Agashe *et al.*, Function of trigger factor and DnaK in multidomain protein folding: Increase in yield at the expense of folding speed. *Cell* **117**, 199–209 (2004). doi: 10.1016/S0092-8674(04)00299-5; pmid: 15084258
22. A. Hoffmann *et al.*, Trigger factor forms a protective shield for nascent polypeptides at the ribosome. *J. Biol. Chem.* **281**, 6539–6545 (2006). doi: 10.1074/jbc.M512345200; pmid: 16407311
23. S. Tomic, A. E. Johnson, F. U. Hartl, S. A. Etchells, Exploring the capacity of trigger factor to function as a shield for ribosome bound polypeptide chains. *FEBS Lett.* **580**, 72–76 (2006). doi: 10.1016/j.febslet.2005.11.050; pmid: 16359675
24. E. Deuerling *et al.*, Trigger Factor and DnaK possess overlapping substrate pools and binding specificities. *Mol. Microbiol.* **47**, 1317–1328 (2003). doi: 10.1046/j.1365-2958.2003.03370.x; pmid: 12603737
25. E. Oh *et al.*, Selective ribosome profiling reveals the cotranslational chaperone action of trigger factor in vivo. *Cell* **147**, 1295–1308 (2011). doi: 10.1016/j.cell.2011.10.044; pmid: 22153074
26. S. K. Lakshmipathy, R. Gupta, S. Pinkert, S. A. Etchells, F. U. Hartl, Versatility of trigger factor interactions with ribosome-nascent chain complexes. *J. Biol. Chem.* **285**, 27911–27923 (2010). doi: 10.1074/jbc.M110.134163; pmid: 20595383
27. E. Martinez-Hackert, W. A. Hendrickson, Promiscuous substrate recognition in folding and assembly activities of the trigger factor chaperone. *Cell* **138**, 923–934 (2009). doi: 10.1016/j.cell.2009.07.044; pmid: 19737520
28. E. P. O'Brien, J. Christodoulou, M. Vendruscolo, C. M. Dobson, Trigger factor slows co-translational folding through kinetic trapping while sterically protecting the nascent chain from aberrant cytosolic interactions. *J. Am. Chem. Soc.* **134**, 10920–10932 (2012). doi: 10.1021/ja302305u; pmid: 22680285
29. A. Mashaghi *et al.*, Reshaping of the conformational search of a protein by the chaperone trigger factor. *Nature* **500**, 98–101 (2013). doi: 10.1038/nature12293; pmid: 23831649
30. A. Hoffmann *et al.*, Concerted action of the ribosome and the associated chaperone Trigger Factor confines nascent polypeptide folding. *Mol. Cell* **48**, 63–74 (2012). doi: 10.1016/j.molcel.2012.07.018; pmid: 22921937
31. P. Genevaux *et al.*, In vivo analysis of the overlapping functions of DnaK and trigger factor. *EMBO Rep.* **5**, 195–200 (2004). doi: 10.1038/sj.embor.7400067; pmid: 14726952
32. E. Deuerling, A. Schulze-Specking, T. Tomoyasu, A. Mogk, B. Bukau, Trigger factor and DnaK cooperate in folding of newly synthesized proteins. *Nature* **400**, 693–696 (1999). doi: 10.1038/23301; pmid: 10458167
33. S. A. Teter *et al.*, Polypeptide flux through bacterial Hsp70: DnaK cooperates with trigger factor in chaperoning nascent chains. *Cell* **97**, 755–765 (1999). doi: 10.1016/S0092-8674(00)80787-4; pmid: 10380927
34. G. Calloni *et al.*, DnaK functions as a central hub in the *E. coli* chaperone network. *Cell Rep.* **1**, 251–264 (2012). doi: 10.1016/j.celrep.2011.12.007; pmid: 22832197
35. P. Bechtluft *et al.*, Direct observation of chaperone-induced changes in a protein folding pathway. *Science* **318**, 1458–1461 (2007). doi: 10.1126/science.1144972; pmid: 18048690
36. R. S. Ullers, D. Ang, F. Schwager, C. Georgopoulos, P. Genevaux, Trigger Factor can antagonize both SecB and DnaK/DnaJ chaperone functions in *Escherichia coli*. *Proc. Natl. Acad. Sci. U.S.A.* **104**, 3101–3106 (2007). doi: 10.1073/pnas.0608232104; pmid: 17360615
37. S. Rudiger, S. M. V. Freund, D. B. Veprintsev, A. R. Fersht, CRINEPT-TROSY NMR reveals p53 core domain bound in an unfolded form to the chaperone Hsp90. *Proc. Natl. Acad. Sci. U.S.A.* **99**, 11085–11090 (2002). doi: 10.1073/pnas.132393699; pmid: 12163643
38. R. Horst *et al.*, Direct NMR observation of a substrate protein bound to the chaperonin GroEL. *Proc. Natl. Acad. Sci. U.S.A.* **102**, 12748–12753 (2005). doi: 10.1073/pnas.0505642102; pmid: 16116078
39. T. A. Walton, C. M. Sandoval, C. A. Fowler, A. Pardi, M. C. Sousa, The cavity-chaperone Skp protects its substrate from aggregation but allows independent folding of substrate domains. *Proc. Natl. Acad. Sci. U.S.A.* **106**, 1772–1777 (2009). doi: 10.1073/pnas.0809275106; pmid: 19181847
40. S. J. Park, B. N. Borin, M. A. Martinez-Yamout, H. J. Dyson, The client protein p53 adopts a molten globule–like state in the presence of Hsp90. *Nat. Struct. Mol. Biol.* **18**, 537–541 (2011). doi: 10.1038/nsmb.2045; pmid: 21460846
41. A. Zhuravleva, E. M. Clérico, L. M. Gierasch, An interdomain energetic tug-of-war creates the allosterically active state in Hsp70 molecular chaperones. *Cell* **151**, 1296–1307 (2012). doi: 10.1016/j.cell.2012.11.002; pmid: 23217711
42. B. M. Burmann, C. Wang, S. Hiller, Conformation and dynamics of the periplasmic membrane-protein–chaperone complexes OmpX–Skp and tOmpA–Skp. *Nat. Struct. Mol. Biol.* **20**, 1265–1272 (2013). doi: 10.1038/nsmb.2677; pmid: 24077225
43. R. Sprangers, L. E. Kay, Quantitative dynamics and binding studies of the 20S proteasome by NMR. *Nature* **445**, 618–622 (2007). doi: 10.1038/nature05512; pmid: 17237764
44. I. Gelis *et al.*, Structural basis for signal-sequence recognition by the translocase motor SecA as determined by NMR. *Cell* **131**, 756–769 (2007). doi: 10.1016/j.cell.2007.09.039; pmid: 18022369
45. T. L. Religa, R. Sprangers, L. E. Kay, Dynamic regulation of archaeal proteasome gate opening as studied by TROSY NMR. *Science* **328**, 98–102 (2010). doi: 10.1126/science.1184991; pmid: 20360109
46. R. Rosenzweig, S. Moradi, A. Zarrine-Afsar, J. R. Glover, L. E. Kay, Unraveling the mechanism of protein disaggregation through a ClpB-DnaK interaction. *Science* **339**, 1080–1083 (2013). doi: 10.1126/science.1233066; pmid: 23393091
47. N. Popovych, S.-R. Tzeng, M. Tonelli, R. H. Ebright, C. G. Kalodimos, Structural basis for cAMP-mediated allosteric control of the catabolite activator protein. *Proc. Natl. Acad. Sci. U.S.A.* **106**, 6927–6932 (2009). doi: 10.1073/pnas.0900595106; pmid: 19359484
48. L. Chen *et al.*, Structural instability tuning as a regulatory mechanism in protein-protein interactions. *Mol. Cell* **44**, 734–744 (2011). doi: 10.1016/j.molcel.2011.09.022; pmid: 22152477
49. S. K. Lakshmipathy *et al.*, Identification of nascent chain interaction sites on trigger factor. *J. Biol. Chem.* **282**, 12186–12193 (2007). doi: 10.1074/jbc.M609871200; pmid: 17296610
50. F. Merz *et al.*, The C-terminal domain of *Escherichia coli* trigger factor represents the central module of its chaperone activity. *J. Biol. Chem.* **281**, 31963–31971 (2006). doi: 10.1074/jbc.M605164200; pmid: 16926148
51. H. Patzelt *et al.*, Three-state equilibrium of *Escherichia coli* trigger factor. *Biol. Chem.* **383**, 1611–1619 (2002). doi: 10.1515/BC.2002.182; pmid: 12452438
52. S.-T. D. Hsu, C. M. Dobson, ^{1}H, ^{15}N and ^{13}C assignments of the dimeric ribosome binding domain of trigger factor from *Escherichia coli*. *Biomol. NMR Assign.* **3**, 17–20 (2009). doi: 10.1007/s12104-008-9130-8; pmid: 19636937
53. Y. Yao, G. Bhabha, G. Kroon, M. Landes, H. J. Dyson, Structure discrimination for the C-terminal domain of *Escherichia coli* trigger factor in solution. *J. Biomol. NMR* **40**, 23–30 (2008). doi: 10.1007/s10858-007-9207-1; pmid: 18043871
54. J. C. Bardwell, K. McGovern, J. Beckwith, Identification of a protein required for disulfide bond formation in vivo. *Cell* **67**, 581–589 (1991). doi: 10.1016/0092-8674(91)90532-4; pmid: 1934062
55. Y. Akiyama, K. Ito, Export of *Escherichia coli* alkaline phosphatase attached to an integral membrane protein, SecY. *J. Biol. Chem.* **264**, 437–442 (1989). pmid: 2535843
56. S. Kamitani, Y. Akiyama, K. Ito, Identification and characterization of an *Escherichia coli* gene required for the formation of correctly folded alkaline phosphatase, a periplasmic enzyme. *EMBO J.* **11**, 57–62 (1992). pmid: 1740115
57. Q. A. Valent *et al.*, Early events in preprotein recognition in *E. coli*: Interaction of SRP and trigger factor with nascent polypeptides. *EMBO J.* **14**, 5494–5505 (1995). pmid: 8521806
58. H. C. Lee, H. D. Bernstein, Trigger factor retards protein export in *Escherichia coli*. *J. Biol. Chem.* **277**, 43527–43535 (2002). doi: 10.1074/jbc.M205950200; pmid: 12205085
59. J. A. Marsh, V. K. Singh, Z. Jia, J. D. Forman-Kay, Sensitivity of secondary structure propensities to sequence differences between α- and γ-synuclein: Implications for fibrillation. *Protein Sci.* **15**, 2795–2804 (2006). doi: 10.1110/ps.062465306; pmid: 17088319
60. H. J. Dyson, P. E. Wright, Elucidation of the protein folding landscape by NMR. *Methods Enzymol.* **394**, 299–321 (2005). doi: 10.1016/S0076-6879(05)94011-1; pmid: 15808225
61. K. Takeuchi, G. Wagner, NMR studies of protein interactions. *Curr. Opin. Struct. Biol.* **16**, 109–117 (2006). doi: 10.1016/j.sbi.2006.01.006; pmid: 16427776
62. H. Patzelt *et al.*, Binding specificity of *Escherichia coli* trigger factor. *Proc. Natl. Acad. Sci. U.S.A.* **98**, 14244–14249 (2001). doi: 10.1073/pnas.261432298; pmid: 11724963
63. W. A. Fenton, Y. Kashi, K. Furtak, A. L. Horwich, Residues in chaperonin GroEL required for polypeptide binding and release. *Nature* **371**, 614–619 (1994). doi: 10.1038/371614a0; pmid: 7935796

64. P. C. Stirling, S. F. Bakhoum, A. B. Feigl, M. R. Leroux, Convergent evolution of clamp-like binding sites in diverse chaperones. *Nat. Struct. Mol. Biol.* **13**, 865–870 (2006). doi: 10.1038/nsmb1153; pmid: 17021621
65. A. Mittermaier, L. E. Kay, New tools provide new insights in NMR studies of protein dynamics. *Science* **312**, 224–228 (2006). doi: 10.1126/science.1124964; pmid: 16614210
66. A. Palmer, NMR characterization of the dynamics of biomacromolecules. *Chem. Rev.* **104**, 3623–3640 (2004). doi: 10.1021/cr030413t; pmid: 15303831
67. J. P. Loria, M. Rance, A. G. Palmer, A TROSY CPMG sequence for characterizing chemical exchange in large proteins. *J. Biomol. NMR* **15**, 151–155 (1999). doi: 10.1023/A:1008355631073; pmid: 10605088
68. F. A. Mulder, A. Mittermaier, B. Hon, F. W. Dahlquist, L. E. Kay, Studying excited states of proteins by NMR spectroscopy. *Nat. Struct. Biol.* **8**, 932–935 (2001). doi: 10.1038/nsb1101-932; pmid: 11685237
69. P. Vallurupalli, D. F. Hansen, E. Stollar, E. Meirovitch, L. E. Kay, Measurement of bond vector orientations in invisible excited states of proteins. *Proc. Natl. Acad. Sci. U.S.A.* **104**, 18473–18477 (2007). doi: 10.1073/pnas.0708296104; pmid: 18006656
70. K. Sugase, J. C. Lansing, H. J. Dyson, P. E. Wright, Tailoring relaxation dispersion experiments for fast-associating protein complexes. *J. Am. Chem. Soc.* **129**, 13406–13407 (2007). doi: 10.1021/ja0762238; pmid: 17935336
71. R. Maier, C. Scholz, F. Schmid, Dynamic association of trigger factor with protein substrates. *J. Mol. Biol.* **314**, 1181–1190 (2001). doi: 10.1006/jmbi.2000.5192; pmid: 11743733
72. D. Tomkiewicz, N. Nouwen, A. J. M. Driessen, Kinetics and energetics of the translocation of maltose binding protein folding mutants. *J. Mol. Biol.* **377**, 83–90 (2008). doi: 10.1016/j.jmb.2008.01.014; pmid: 18241889
73. N. K. Tyagi, W. A. Fenton, A. L. Horwich, GroEL/GroES cycling: ATP binds to an open ring before substrate protein favoring protein binding and production of the native state. *Proc. Natl. Acad. Sci. U.S.A.* **106**, 20264–20269 (2009). doi: 10.1073/pnas.0911556106; pmid: 19915138
74. K. Chakraborty *et al*., Chaperonin-catalyzed rescue of kinetically trapped states in protein folding. *Cell* **142**, 112–122 (2010). doi: 10.1016/j.cell.2010.05.027; pmid: 20603018
75. J. M. Betton, M. Hofnung, Folding of a mutant maltose-binding protein of *Escherichia coli* which forms inclusion bodies. *J. Biol. Chem.* **271**, 8046–8052 (1996). doi: 10.1074/jbc.271.14.8046; pmid: 8626487
76. S. Raffy, N. Sassoon, M. Hofnung, J. M. Betton, Tertiary structure-dependence of misfolding substitutions in loops of the maltose-binding protein. *Protein Sci.* **7**, 2136–2142 (1998). doi: 10.1002/pro.5560071010; pmid: 9792100
77. F. A. Saul *et al*., Crystal structure of a defective folding protein. *Protein Sci.* **12**, 577–585 (2003). doi: 10.1110/ps.0235103; pmid: 12592028
78. J. Kuriyan, D. Eisenberg, The origin of protein interactions and allostery in colocalization. *Nature* **450**, 983–990 (2007). doi: 10.1038/nature06524; pmid: 18075577
79. V. Novokhatny, K. Ingham, Thermodynamics of maltose binding protein unfolding. *Protein Sci.* **6**, 141–146 (1997). doi: 10.1002/pro.5560060116; pmid: 9007986
80. S. Sharma *et al*., Monitoring protein conformation along the pathway of chaperonin-assisted folding. *Cell* **133**, 142–153 (2008). doi: 10.1016/j.cell.2008.01.048; pmid: 18394994
81. G. W. Farr *et al*., Multivalent binding of nonnative substrate proteins by the chaperonin GroEL. *Cell* **100**, 561–573 (2000). doi: 10.1016/S0092-8674(00)80692-3; pmid: 10721993
82. M. Shtilerman, G. H. Lorimer, S. W. Englander, Chaperonin function: Folding by forced unfolding. *Science* **284**, 822–825 (1999). doi: 10.1126/science.284.5415.822; pmid: 10221918
83. A. Hoffmann, B. Bukau, Trigger factor finds new jobs and contacts. *Nat. Struct. Mol. Biol.* **16**, 1006–1008 (2009). doi: 10.1038/nsmb1009-1006; pmid: 19809489
84. G. Kramer *et al*., Functional dissection of *Escherichia coli* trigger factor: Unraveling the function of individual domains. *J. Bacteriol.* **186**, 3777–3784 (2004). doi: 10.1128/JB.186.12.3777-3784.2004; pmid: 15175291
85. F. Delaglio *et al*., NMRPipe: A multidimensional spectral processing system based on UNIX pipes. *J. Biomol. NMR* **6**, 277–293 (1995). doi: 10.1007/BF00197809; pmid: 8520220
86. R. Sprangers, A. Velyvis, L. Kay, Solution NMR of supramolecular complexes: Providing new insights into function. *Nat. Methods* **4**, 697–703 (2007). doi: 10.1038/nmeth1080; pmid: 17762877
87. A. Velyvis, A. M. Ruschak, L. E. Kay, An economical method for production of ^{2}H,$^{13}CH_3$-threonine for solution NMR studies of large protein complexes: Application to the 670 kDa proteasome. *PLOS One* **7**, e43725 (2012). doi: 10.1371/journal.pone.0043725; pmid: 22984438
88. P. Güntert, Automated NMR structure calculation with CYANA. *Methods Mol. Biol.* **278**, 353–378 (2004). pmid: 15318003
89. Y. Shen, F. Delaglio, G. Cornilescu, A. Bax, TALOS+: A hybrid method for predicting protein backbone torsion angles from NMR chemical shifts. *J. Biomol. NMR* **44**, 213–223 (2009). doi: 10.1007/s10858-009-9333-z; pmid: 19548092
90. C. Schwieters, J. Kuszewski, G.M. Clore, Using Xplor-NIH for NMR molecular structure determination. *Prog. Nucl. Magn. Res. Spect.* **48**, 47–62 (2006). doi: 10.1016/j.pnmrs.2005.10.001
91. A. T. Brunger, Version 1.2 of the Crystallography and NMR system. *Nat. Protoc.* **2**, 2728–2733 (2007). doi: 10.1038/nprot.2007.406; pmid: 18007608
92. J. P. Carver, R. E. Richards, A general two-site solution for the chemical exchange produced dependence of T_2 on the Carr-Purcell pulse separation. *J. Magn. Reson.* **6**, 89–105 (1972). doi: 10.1016/0022-2364(72)90090-X
93. S.-R. Tzeng, C. G. Kalodimos, Protein activity regulation by conformational entropy. *Nature* **488**, 236–240 (2012). doi: 10.1038/nature11271; pmid: 22801505

Acknowledgments: C.G.K. thanks L. E. Kay and B. Bukau for fruitful discussions and comments. We thank M. T. Pai and A. Bhattacharya for contributions during the early phase of the project, S. Patel for the use of a spectrofluorometer, and S. Kim and Y. Xia (University of Minnesota) for their help with setting up NMR experiments. This work is supported by NIH grant GM073854 (C.G.K.), Nonaco (Aristeia-Excellence, #1473), KUL-Spa, RiMembR, and StrepSynth (A.E.). T.S. is the recipient of postdoctoral fellowships from the Japanese Society for the Promotion of Science and the American Heart Association (14POST18600039). We thank Bruker Biospin for the use of the 700-MHz instrument. Coordinates and structural restraints have been deposited with the Protein Data Bank under accession codes 2MLY, 2MLX, and 2MLZ, for TF–PhoA$^{a\text{-}c}$, TF–PhoA$^{d\text{-}e}$, and TF–PhoA$^{f\text{-}g}$, respectively.

Supplementary Materials

www.sciencemag.org/content/344/6184/1250494/suppl/DC1
Figs. S1 to S27
Table S1

10.1126/science.1250494

Hippocampal Neurogenesis Regulates Forgetting During Adulthood and Infancy

Katherine G. Akers,[1*] Alonso Martinez-Canabal,[1,2*] Leonardo Restivo,[1*] Adelaide P. Yiu,[1] Antonietta De Cristofaro,[1] Hwa-Lin (Liz) Hsiang,[1,2] Anne L. Wheeler,[1,2] Axel Guskjolen,[1,3] Yosuke Niibori,[1] Hirotaka Shoji,[4] Koji Ohira,[4] Blake A. Richards,[1] Tsuyoshi Miyakawa,[4] Sheena A. Josselyn,[1,2,3,5]† Paul W. Frankland[1,2,3,5]†

Throughout life, new neurons are continuously added to the dentate gyrus. As this continuous addition remodels hippocampal circuits, computational models predict that neurogenesis leads to degradation or forgetting of established memories. Consistent with this, increasing neurogenesis after the formation of a memory was sufficient to induce forgetting in adult mice. By contrast, during infancy, when hippocampal neurogenesis levels are high and freshly generated memories tend to be rapidly forgotten (infantile amnesia), decreasing neurogenesis after memory formation mitigated forgetting. In precocial species, including guinea pigs and degus, most granule cells are generated prenatally. Consistent with reduced levels of postnatal hippocampal neurogenesis, infant guinea pigs and degus did not exhibit forgetting. However, increasing neurogenesis after memory formation induced infantile amnesia in these species.

In both artificial systems and brain networks there is a trade-off between plasticity—the ability to incorporate new information—and stability—ensuring that the process of incorporating new information does not degrade information already stored in that network (*1*). In the hippocampus, new neurons continue to be generated in the subgranular zone of the dentate gyrus (DG) beyond development and into adulthood (*2*, *3*). These new neurons synaptically integrate into hippocampal circuits (*4*–*9*) and provide potential substrates for new learning. Promoting the production of new neurons in adult mice facilitates the formation of new hippocampal memories (*10*, *11*). However, the continuous integration of new neurons may affect memories already stored in these circuits (*12*). As new neurons integrate into the hippocampus, they compete with existing cells for inputs and outputs, establishing new synaptic connections that may coexist with, or even replace, older synaptic connections (*5*, *6*, *13*). As such remodeling necessarily alters the configuration of DG-CA3 circuits and likely rescales synaptic weights of preexisting connections, computational models predict that high levels of hippocampal neurogenesis will lead to forgetting of information already stored in those circuits (*14*–*16*).

Although hippocampal neurogenesis persists throughout life, rates decline dramatically with age (*17*, *18*). Therefore, this predicted remodeling-induced forgetting should be most pronounced during infancy, when hippocampal neurogenesis is high. Consistent with this, infantile forgetting [or infantile amnesia (*19*)] is observed across a wide range of species (*20*), including humans (*21*). Neurobiological accounts of infantile amnesia previously emphasized that continued brain maturation might interfere with consolidation and/or storage of infant memories, rendering them inaccessible at later time points (*22*). Here, we test whether postnatal hippocampal neurogenesis, in particular, modulates ontogenetic changes in memory persistence.

Inverse Relationship Between Levels of Postnatal Neurogenesis and Memory Persistence

We first characterized levels of hippocampal neurogenesis in infant and adult mice using a retrovirus expressing green fluorescent protein (GFP) to label neural progenitors and their progeny (*11*) and immunohistochemistry. Four weeks after retroviral microinjections in infant (postnatal day 17; P17) and adult (P60) mice, we observed a pronounced age-dependent reduction in neurogenesis (i.e., reduction in the number of GFP^+ DG granule cells and their terminal processes in the CA3 region) (Fig. 1, A and C). From infancy to adulthood, there was also a decrease in the number of proliferating ($Ki67^+$) cells (Fig. 1D and fig. S1) and immature (doublecortin$^+$ [DCX^+]) neurons (Fig. 1, B and E). Postnatally generated DG granule cells project a mossy fiber that reaches the CA3 region after ~2 weeks, contacting 11 to 15 pyramidal cells (*5*, *7*, *23*). We observed a reduction in the number of immature (DCX^+) large mossy fiber terminals (LMTs) in the CA3 region of adult mice (Fig. 1, B and F), consistent with a predicted reduction in synaptic rearrangements in the CA3 with age (fig. S2).

Next, we evaluated how age-dependent changes in neurogenesis influence the ability to form enduring hippocampus-dependent memories using the contextual fear conditioning paradigm (*24*). Infant and adult mice were placed in a novel context and presented with a series of foot shocks. One to 28 days later, separate groups of mice were returned to the context, and memory retention was evaluated by measuring freezing behavior (Fig. 1G). Mice trained as adults froze robustly regardless of retention delay. By contrast, mice trained as infants only exhibited high levels of freezing when tested 1 day after training. If infant mice were tested at longer retention delays, less freezing was observed (Fig. 1H) (*25*). Infant mice trained similarly but not shocked showed little freezing when tested 1 day after training (fig. S3), indicating that the freezing observed in shocked infant mice reflects conditioned fear. There were no age-related differences in reaction to the foot shock (Fig. 1I), indicating that forgetting in infant mice was not due to diminished nociception. This pattern of accelerated forgetting in infant mice was replicated using an incidental context learning paradigm (fig. S4).

Increasing Neurogenesis Promotes Forgetting in Adult Mice

To determine if levels of neurogenesis and memory persistence are causally related, we tested whether increasing hippocampal neurogenesis after learning promotes forgetting in adult mice (Fig. 1J) (*26*). We initially used voluntary running, a naturalistic intervention that robustly increases neurogenesis (*27*) (Fig. 2A). Relative to sedentary controls, running increased the number of proliferating ($Ki67^+$) cells (Fig. 2B) and immature (DCX^+) neurons in the DG (Fig. 2C), as well as DCX^+ LMTs in the CA3 of adult mice (Fig. 2D). These increases were evident within 7 days of commencing running, sustained for the duration of exercise, and not associated with increased death of developmentally generated granule cells (fig. S5). We next injected retrovirus expressing GFP into the DG of adult mice. Four weeks later, we observed many GFP^+ neurons in the innermost layers of the DG and GFP^+ LMTs in the stratum lucidum of the CA3. Counterstaining with a marker of mature presynaptic terminals, zinc transporter-3 (ZnT3) (*28*), revealed many new (GFP^+/$ZnT3^+$) LMTs in close apposition to preexisting (GFP^-/$ZnT3^+$) LMTs (Fig. 2E), suggesting that new contacts coexist with established connections (*5*). Running increased the ratio of new-to-established LMTs, indicating that running increases remodeling of DG-CA3 circuits (fig. S6).

To determine whether running-induced increases in hippocampal remodeling induce forgetting of an established hippocampus-dependent memory, we trained adult mice in contextual fear conditioning. After training, mice were given

[1]Program in Neurosciences and Mental Health, The Hospital for Sick Children, Toronto, M5G 1X8, Canada. [2]Institute of Medical Science, University of Toronto, Toronto, M5S 1A8, Canada. [3]Department of Physiology, University of Toronto, Toronto, M5S 1A8, Canada. [4]Division of Systems Medical Science, Institute for Comprehensive Medical Science, Fujita Health University, Toyoake, Aichi, 470-1192, Japan. [5]Department of Psychology, University of Toronto, Toronto, M5S 3GM, Canada.

*These authors contributed equally to this work.
†Corresponding author. E-mail: paul.frankland@sickkids.ca (P.W.F.), sheena.josselyn@sickkids.ca (S.A.J.)

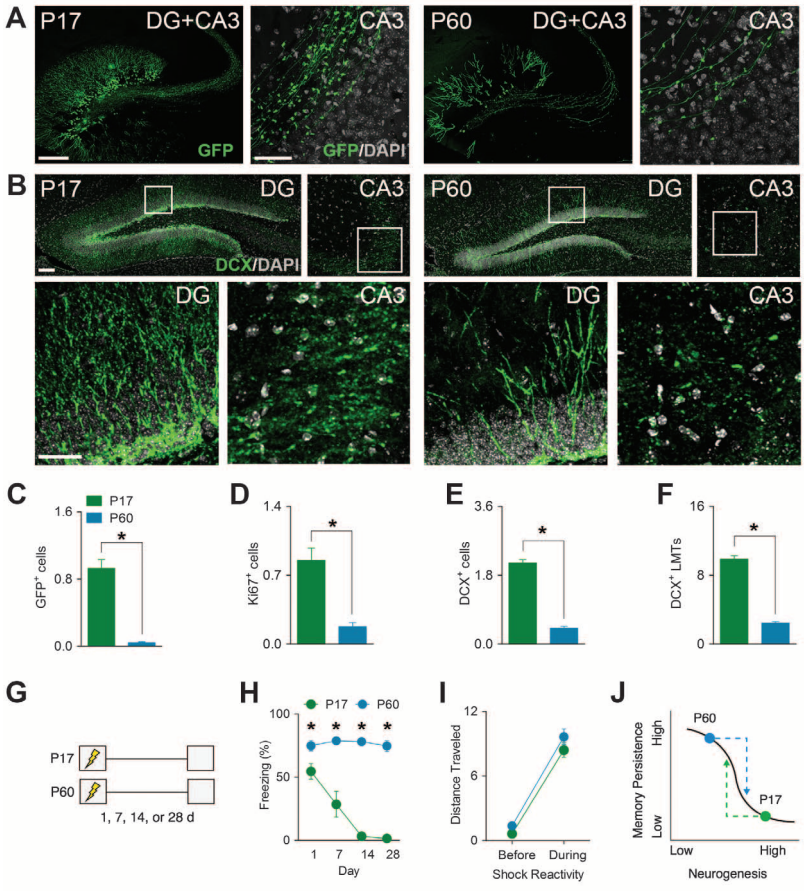

Fig. 1. Age-dependent levels of hippocampal neurogenesis and memory stability are inversely related in mice. (**A**) GFP labeling of granule cells in the DG and CA3 1 month after retroviral infection shows that infant (P17) mice had higher levels of neurogenesis than adult (P60) mice. (Left) Low magnification of DG and CA3 regions. Scale bar, 200 μm. (Right) High magnification of CA3 region showing GFP^+ mossy fibers and LMTs. Scale bar, 50 μm. (**B**) Top row: Infants had more DCX^+ cells in the DG and CA3 than adults. Scale bar, 100 μm. Bottom row: High magnification of DG and CA3. Scale bar, 50 μm. (**C** to **F**) Infants showed more (C) GFP^+ neurons ($t_6 = 8.57$, $P < 0.001$), (D) proliferating ($Ki67^+$) cells ($t_7 = 4.53$, $P < 0.01$), and (E) immature (DCX^+) neurons in the DG ($t_6 = 18.65$, $P < 0.001$), as well as more (F) DCX^+ LMTs in the CA3 ($t_6 = 15.03$, $P < 0.001$) than adults ($n = 4$ to 5 per group). (**G**) Separate groups of infant and adult mice were trained in contextual fear conditioning and tested 1, 7, 14, or 28 days later ($n = 8$ to 9 per group). (**H**) Context fear memory persisted for at least 28 days in adult mice, whereas infants showed intact memory shortly after training but forgetting after longer delays (*age* × *day*, $F_{3,62} = 13.07$, $P < 0.001$; post-hoc *t* tests, 1 day, $P < 0.05$; 7 days, $P < 0.001$; 14 days, $P < 0.001$; 28 days, $P < 0.001$). (**I**) Infants and adults showed equivalent shock reactivity during training (P17 $n = 9$, P60 $n = 8$; arbitrary units, $P > 0.05$). (**J**) Inverse relationship between neurogenesis and memory persistence predicts that increasing neurogenesis in adults will induce forgetting, whereas decreasing neurogenesis in infants will mitigate forgetting. In all panels, cells/LMTs are expressed as number of cells/LMTs per 1000 μm^2. *$P < 0.05$. For all figures, error bars represent standard error of the mean (SEM). DAPI, 4′,6-diamidino-2-phenylindole.

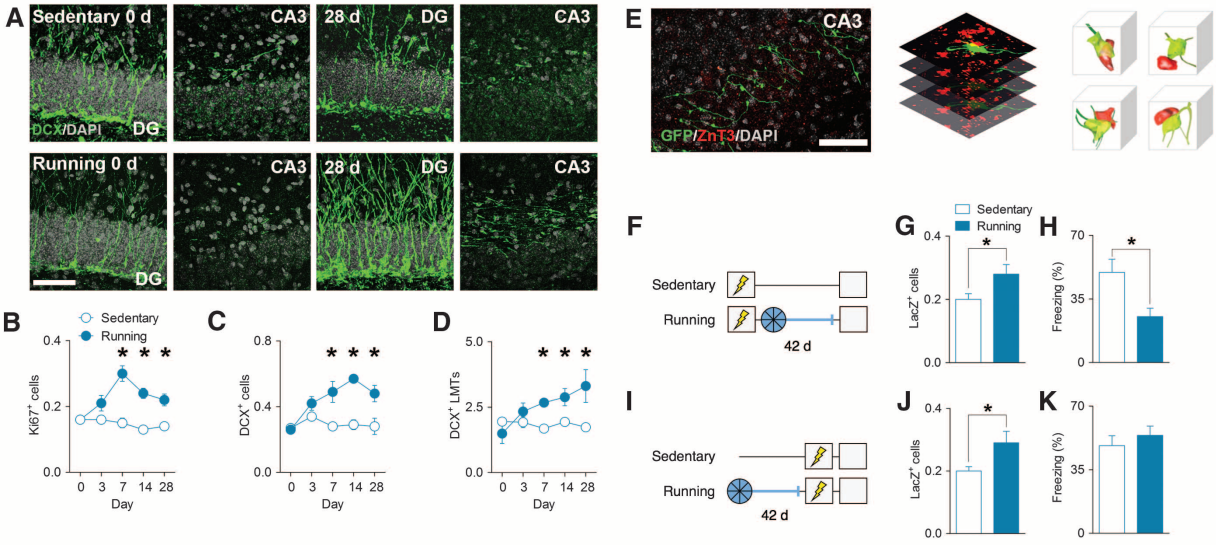

Fig. 2. Voluntary running increases neurogenesis and promotes forgetting in adult mice. (**A**) Adult (P60) mice given access to a running wheel for 28 days showed more immature (DCX^+) neurons in the DG and LMTs in the CA3 than sedentary mice. Scale bar, 50 μm. (**B** to **D**) Adult mice were given access to a running wheel for 0, 3, 7, 14, or 28 days. Running increased the number of (B) proliferating ($Ki67^+$) cells ($n = 8$ per group; *running* × *day*, $F_{4,70} = 7.71$, $P < 0.001$; post hoc *t* tests, 7 days, $P < 0.001$; 14 days, $P < 0.001$; 28 days, $P = 0.001$), and (C) immature (DCX^+) neurons in the DG ($n = 4$ to 8 per group; *running* × *day*, $F_{4,34} = 3.17$, $P < 0.05$; 7 days, $P < 0.05$; 14 days, $P < 0.001$; 28 days, $P < 0.05$), as well as more (D) DCX^+ LMTs in the CA3 ($n = 4$ per group; *running* × *day*, $F_{4,30} = 3.45$, $P < 0.05$; 7 days, $P = 0.001$; 14 days, $P < 0.05$; 28 days, $P < 0.05$) compared with sedentary controls. (**E**) Neurogenesis remodels DG-CA3 circuits. Retrovirus-labeled presynaptic LMTs from new neurons (GFP^+) in close apposition to existing presynaptic LMTs from mature neurons ($ZnT3^+$). Scale bar, 50 μm. Confocal stacks used to reconstruct representative three-dimensional images of new LMTs (green) in close contact with existing LMTs (red) in the CA3. (**F**) Adult mice ran or remained sedentary after contextual fear conditioning. (**G** and **H**) Running increased neurogenesis (sedentary $n = 8$, running $n = 8$; $LacZ^+$ cells; $t_{14} = 2.81$, $P < 0.05$) and induced forgetting (sedentary $n = 9$, running $n = 8$; $t_{15} = 2.75$, $P < 0.05$). (**I**) Adult mice ran or remained sedentary before contextual fear conditioning. (**J** and **K**) Running increased neurogenesis (sedentary $n = 7$, running $n = 8$; $t_{13} = 2.96$, $P < 0.05$) but did not affect formation of a context fear memory (sedentary $n = 10$, running $n = 9$; $P > 0.05$). In all panels, cells/LMTs are expressed as number of cells/LMTs per 1000 μm^2. *$P < 0.05$.

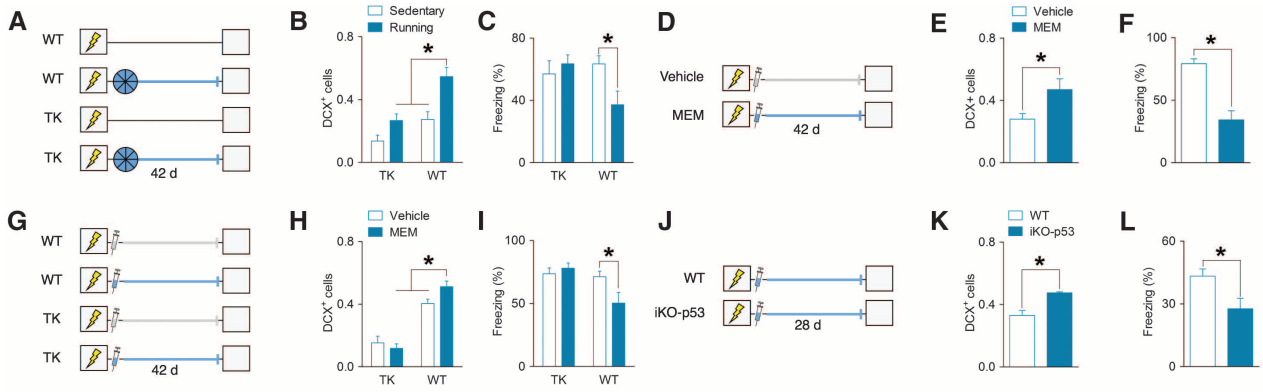

Fig. 3. Forgetting depends on increased neurogenesis. (**A**) Adult GAN-treated WT and TK$^+$ mice remained sedentary or ran after contextual fear conditioning. Running (**B**) increased neurogenesis (sedentary $n = 6$, running $n = 14$; $t_{18} = 2.81$, $P < 0.05$) and (**C**) induced forgetting of a context fear memory in WT mice (sedentary $n = 16$, running $n = 14$; $t_{28} = 2.63$, $P < 0.05$). By contrast, in TK$^+$ mice, both (B) the running-induced increase in neurogenesis (sedentary $n = 8$, running $n = 9$; TK$^+$ running versus WT sedentary, $P > 0.05$; WT running versus TK$^+$ running, $t_{21} = 3.43$, $P < 0.01$) and (C) forgetting (TK$^+$ sedentary $n = 12$, TK$^+$ running $n = 10$; $P > 0.05$; *genotype* × *running* interaction, $F_{1,48} = 4.88$, $P < 0.05$) were blunted. (**D**) Adult WT mice treated with MEM after contextual fear conditioning showed (**E**) increased neurogenesis (vehicle $n = 7$, MEM $n = 6$; $t_{11} = 2.55$, $P < 0.05$) and (**F**) forgetting of a context fear memory (vehicle $n = 8$, MEM $n = 8$; $t_{14} = 5.47$, $P < 0.001$) relative to vehicle-treated controls. (**G**) Adult GAN-treated WT and TK$^+$ mice were treated with vehicle or MEM after contextual fear conditioning. MEM (**H**) increased neurogenesis (vehicle $n = 8$, MEM $n = 8$; $t_{14} = 2.25$, $P < 0.05$) and (**I**) induced forgetting of a context fear memory in WT mice (vehicle $n = 11$, MEM $n = 11$; $t_{20} = 2.23$, $P < 0.05$). By contrast, in TK$^+$ mice, both (H) the MEM-induced increase in neurogenesis (vehicle $n = 8$, MEM $n = 8$; TK$^+$ vehicle versus TK$^+$ MEM, $P > 0.05$; WT MEM versus TK$^+$ MEM, $t_{14} = 8.53$, $P < 0.001$; *genotype* × *drug* interaction, $F_{1,28} = 4.69$, $P < 0.05$) and (I) forgetting (vehicle $n = 13$, MEM $n = 14$; TK$^+$ vehicle versus TK$^+$ MEM, $P > 0.05$; *genotype* × *drug* interaction, $F_{1,45} = 5.41$, $P < 0.05$) were attenuated. (**J**) Post-training tamoxifen treatment (**K**) increased neurogenesis (WT $n = 4$, iKO-p53 $n = 4$; $t_6 = 4.39$, $P < 0.01$) and (**L**) induced forgetting of a context fear memory (WT $n = 14$, iKO-p53 $n = 9$; $t_{21} = 2.68$, $P < 0.05$) in iKO-p53 mice relative to WT controls. In all panels, cell counts are expressed as number of cells per 1000 μm^2. *$P < 0.05$.

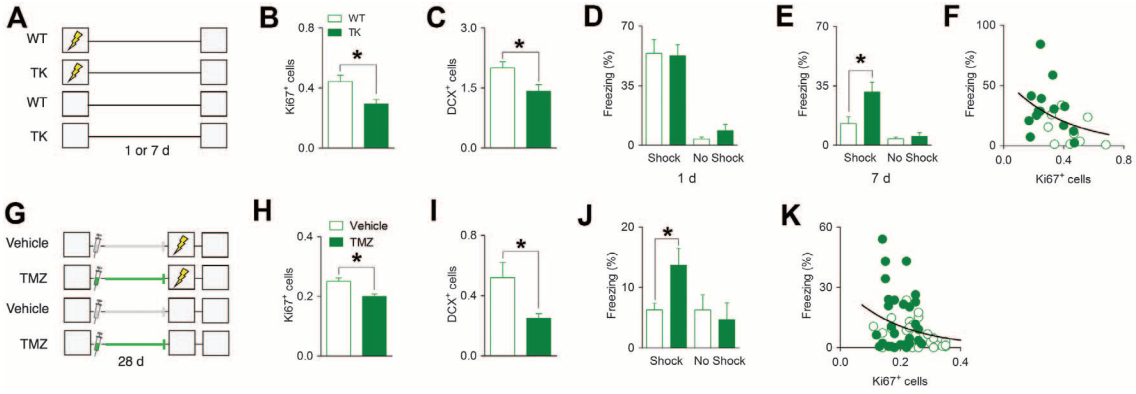

Fig. 4. Genetic and pharmacological decreases in neurogenesis mitigate forgetting in infant mice. (**A**) Infant GAN-treated WT or TK$^+$ mice were trained in contextual fear conditioning or placed in conditioning chambers without foot shocks. TK$^+$ mice had fewer (**B**) proliferating (Ki67$^+$) cells (WT $n = 9$, TK$^+$ $n = 14$; $t_{21} = 3.08$, $P < 0.01$) and (**C**) immature (DCX$^+$) neurons (WT $n = 6$, TK$^+$ $n = 6$; $t_{10} = 2.57$, $P < 0.05$) in the DG than WT mice. (**D**) Shocked WT and TK$^+$ mice showed equivalent context fear memory 1 day after training (WT $n = 9$, TK $n = 13$; $P > 0.05$), and nonshocked mice showed low freezing (WT $n = 7$, TK $n = 9$). (**E**) A separate group of shocked WT mice showed forgetting of a context fear memory 7 days after training, whereas this forgetting was reduced in a separate group of TK$^+$ mice (WT $n = 9$, TK$^+$ $n = 14$; $t_{21} = 2.26$, $P < 0.05$). Separate groups of nonshocked mice again showed low freezing (WT $n = 6$, TK $n = 7$). (**F**) Inverse relationship between proliferation and memory persistence among shocked mice 7 days after training ($r = -0.46$, $P < 0.05$). (**G**) Infant mice were treated with vehicle or TMZ after training in the incidental context learning paradigm (or were similarly treated without foot shocks). TMZ-treated mice had fewer (**H**) proliferating (Ki67$^+$) cells (vehicle $n = 30$, TMZ $n = 29$; $t_{57} = 3.57$, $P = 0.001$) and (**I**) immature (DCX$^+$) neurons (vehicle $n = 5$, TMZ $n = 6$; $t_9 = 2.29$, $P < 0.05$) in the DG. (**J**) Shocked TMZ-treated mice showed less forgetting of a context-only memory (vehicle $n = 30$, TMZ $n = 29$; $t_{57} = 2.47$, $P < 0.05$). Nonshocked mice showed low freezing (vehicle $n = 9$, TMZ $n = 9$). (**K**) Inverse relationship between proliferation and memory persistence among shocked mice ($r = -0.31$, $P < 0.05$). In all panels, cells are expressed as number of cells per 1000 μm^2. *$P < 0.05$.

continuous access to a running wheel in their home cage or housed conventionally (i.e., sedentary; Fig. 2F). Running increased neurogenesis in the DG (Fig. 2G) and reduced context fear memory when mice were tested 6 weeks later (Fig. 2H and fig. S7). Access to a locked running wheel did not induce forgetting (fig. S8), indicating that forgetting was associated with running rather than exposure to a novel object in the home cage. Furthermore, running-induced forgetting of a context fear memory was reduced after a stronger training protocol (i.e., additional foot shocks; fig. S9), suggesting that the degree of forgetting depends, in part, on initial memory strength.

As voluntary running induces several neural and physiological changes apart from increasing hippocampal neurogenesis (*29*), forgetting might alternatively be mediated by these non-neurogenic changes. Therefore, we first examined the impact of running before (rather than after) training (Fig. 2I). Running before training similarly increased neurogenesis (Fig. 2J) but did not affect acquisition of a context fear memory (Fig. 2K), indicating that running does not nonspecifically alter freezing (e.g., by reducing anxiety).

Second, we tested whether preventing the running-induced increase in neurogenesis would prevent forgetting using transgenic mice in which a nestin promoter/enhancer drives expression of a modified herpes simplex virus (HSV) gene

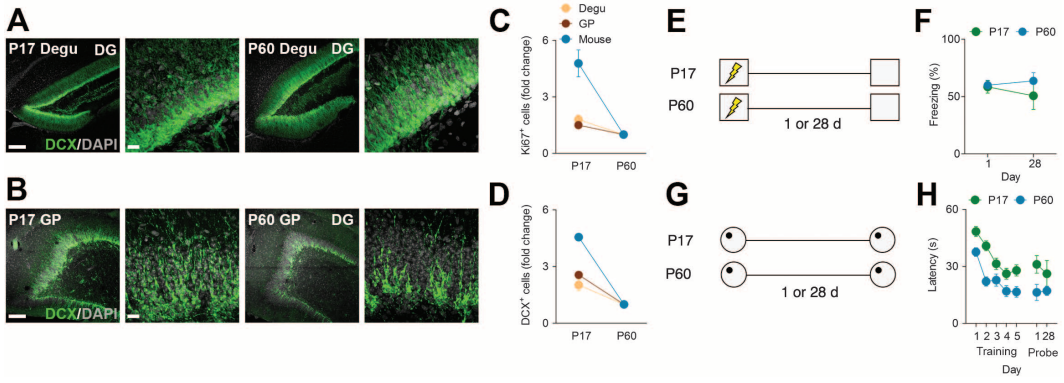

Fig. 5. Precocial degus and guinea pigs show low postnatal neurogenesis and persistent infantile memories. (**A**) DCX$^+$ cells in the DG of infant and adult degus. (Left) Low magnification. Scale bar, 200 μm. (Right) High magnification. Scale bar, 25 μm. (**B**) DCX$^+$ cells in the DG of infant and adult guinea pigs. (Left) Low magnification. Scale bar, 200 μm. (Right) High magnification. Scale bar, 25 μm. Compared with mice (P17 n = 4 to 5, P60 n = 4), degus (P17 n = 3, P60 n = 4 to 6) and guinea pigs (GP; P17 n = 4, P60 n = 4) showed reduced age-related declines in (**C**) proliferating (Ki67$^+$) cells and (**D**) immature (DCX$^+$) neurons in the DG. (**E**) Infant and adult degus were trained in contextual fear conditioning and tested 1 and 28 days later (P17 n = 7, P60 n = 10). (**F**) Both infant and adult degus showed persistent context fear memory (*age* × *delay* interaction and *age* main effect, Ps > 0.05). (**G**) Separate groups of infant and adult guinea pigs were trained in a water maze and tested 1 (P17 n = 8, P60 n = 8) or 28 days later (P17 n = 8, P60 n = 8). (**H**) Both infant and adult guinea pigs showed persistent spatial memory during probe tests (*age* × *delay* interaction, $P > 0.05$; *age* main effect, $F_{1,28} = 6.05$, $P < 0.05$).

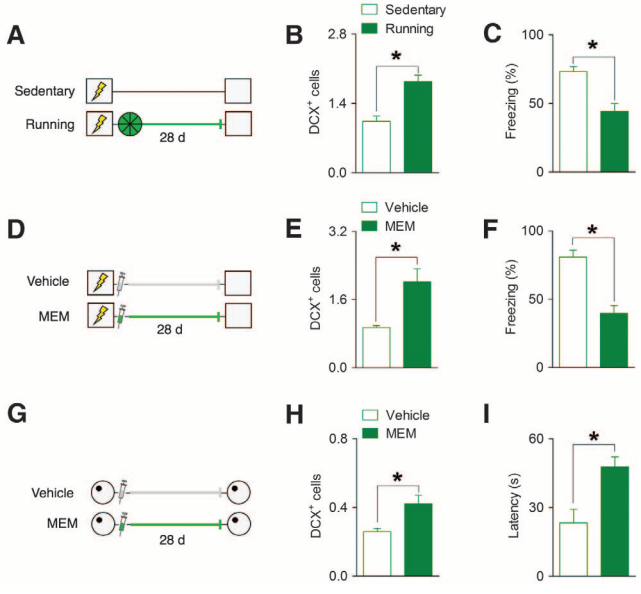

Fig. 6. Increasing neurogenesis promotes forgetting in infant degus and guinea pigs. (**A**) Infant degus were trained in contextual fear conditioning and then remained sedentary or given access to a running wheel for 28 days. Running (**B**) increased neurogenesis (sedentary n = 4, running n = 4; $t_6 = 4.74$, $P < 0.01$) and (**C**) induced forgetting of a context fear memory (sedentary n = 21, running n = 16; $t_{35} = 4.59$, $P < 0.001$). (**D**) Infant degus were trained in contextual fear conditioning and then treated with vehicle or MEM for 28 days. MEM treatment (**E**) increased neurogenesis (vehicle n = 8, MEM n = 5; $t_{11} = 4.41$, $P = 0.001$) and (**F**) induced forgetting of a context fear memory (vehicle n = 12, MEM n = 11; $t_{21} = 5.35$, $P < 0.001$). (**G**) Infant guinea pigs were treated with vehicle or MEM after training in the water maze. MEM treatment (**H**) increased neurogenesis (vehicle n = 3, MEM n = 3; $t_4 = 3.11$, $P < 0.05$) and (**I**) induced forgetting of a spatial memory (vehicle n = 11, MEM n = 12; $t_{21} = 3.32$, $P < 0.01$). In all panels, cells are expressed as number of cells per 1000 μm^2. *$P < 0.05$.

encoding thymidine kinase (HSV-tk) (TK$^+$ mice) (*30*). In TK$^+$ mice, administration of ganciclovir (GAN) ablates only dividing cells expressing the tk transgene. TK$^+$ mice and their wild-type (WT) littermates were trained in contextual fear conditioning and then given access to a running wheel or housed conventionally for 6 weeks. During this period, mice were treated with GAN to suppress neurogenesis (Fig. 3A). GAN treatment in TK$^+$ mice limited the running-induced increase in neurogenesis to WT sedentary levels (Fig. 3B) and prevented forgetting (Fig. 3C).

Third, nonrunning interventions that increase neurogenesis might similarly induce forgetting of established memories. Administering the proneurogenic drugs memantine (MEM) (*31*) (Fig. 3, D to F, and fig. S10) or fluoxetine (*32*) (fig. S11) after training induced forgetting [see also (*33*)]. Both the increase in neurogenesis and forgetting induced by MEM were blocked by activation of the tk transgene in TK$^+$ mice (Fig. 3, G to I). We also generated transgenic mice in which the tumor suppressor gene *p53* was inducibly deleted from neural progenitor cells and their progeny during adulthood (iKO-p53 mice) (Fig. 3J). Similar to previous studies examining global deletion of *p53* (*34*), conditional deletion of *p53* increased the number of proliferating (Ki67$^+$) cells (fig. S12) and immature (DCX$^+$) neurons (Fig. 3K) in the DG. Furthermore, post-training deletion of *p53* induced forgetting of context fear memory in adult mice (Fig. 3L).

Finally, running also induced forgetting of other hippocampus-dependent memories (incidental context learning, fig. S13; water maze, fig. S14). However, running did not induce forgetting of a conditioned taste aversion memory (fig. S15), which does not depend on the hippocampus (*35*).

Reducing Neurogenesis Increases Memory Persistence in Infant Mice

Using genetic and pharmacological strategies, we next examined whether decreasing neurogenesis mitigates forgetting normally observed in infant mice (Fig. 1J). To genetically suppress neurogenesis, we administered GAN to infant TK$^+$ and WT mice (Fig. 4A). GAN treatment reduced the number of proliferating (Ki67$^+$) cells and immature (DCX$^+$) neurons in the DG of TK$^+$ mice compared with WT littermates (Fig. 4, B and C). When tested 1 day after contextual fear conditioning, WT and TK$^+$ mice exhibited equivalent levels of freezing (Fig. 4D), indicating normal memory at this short retention delay. However, when separate groups of mice were tested 7 days after training, TK$^+$ mice froze more than WT mice (Fig. 4E), and freezing levels were inversely correlated with levels of neurogenesis (Fig. 4F). GAN-treated WT and TK$^+$ mice trained without foot shocks showed little freezing when tested 7 days after training (Fig. 4E). These low levels of freezing were similar to those observed in shocked WT mice, indicating substantial forgetting in WT but not TK$^+$ mice. Furthermore, the absence of freezing in nonshocked TK$^+$ mice suggests that suppressing neurogenesis (or GAN treatment) does not simply increase the propensity to freeze.

Using temozolomide (TMZ), a DNA alkylating agent (*36*), to pharmacologically reduce hippocampal neurogenesis in infant WT mice, we observed a similar attenuation of forgetting in an incidental context learning paradigm. Infant mice were preexposed to a context and then treated with TMZ or vehicle for 4 weeks (Fig. 4G). TMZ treatment suppressed neurogenesis (Fig. 4, H

and I) and improved retention of the context-only memory (Fig. 4J), and there was an inverse relationship between hippocampal neurogenesis and freezing (Fig. 4K). TMZ treatment did not decrease the threshold for freezing, however, as similar TMZ treatment before learning did not alter freezing levels (fig. S16). During infancy, high levels of proliferation are associated with high levels of apoptotic cell death in the subgranular zone (*37*). However, post-training pharmacological inhibition of cell death alone failed to attenuate forgetting (fig. S17).

Infantile Forgetting Is Absent in Precocial Guinea Pigs and Degus

As guinea pigs have a longer (~65 days) gestation than mice (~21 days), they are more neurologically mature at birth and have reduced postnatal hippocampal neurogenesis (*38*). This led us to predict that guinea pigs (and possibly other rodents with similarly extended gestation) will not exhibit infantile forgetting. To test this, we examined hippocampal neurogenesis and memory retention in guinea pigs [in which postnatal hippocampal neurogenesis has been described (*38*)] and degus, another precocial rodent (in which postnatal neurogenesis has not previously been studied). Whereas there is a considerable reduction in proliferating ($Ki67^+$) cells and immature (DCX^+) neurons from P17 to P60 in mice, this reduction was much more modest in degus and guinea pigs (Fig. 5, A to D). Unlike infant mice that showed rapid forgetting, infant degus showed normal retention of a context fear memory for up to 1 month (Fig. 5, E and F), and infant guinea pigs showed no change in spatial memory as a function of retention delay (Fig. 5, G and H), indicating that memories are persistent in infant rodent species with low postnatal hippocampal neurogenesis.

Increasing Hippocampal Neurogenesis Is Sufficient to Induce Forgetting in Infant Guinea Pigs and Degus

If levels of hippocampal neurogenesis and forgetting are causally related, then increasing hippocampal neurogenesis in degus and guinea pigs should be sufficient to induce infantile amnesia in these precocial species. To test this, infant (P17) degus were trained in contextual fear conditioning and then either housed conventionally, given access to a running wheel, or treated with MEM or vehicle for 4 weeks (Fig. 6, A and D). Both running and MEM treatment increased neurogenesis (Fig. 6, B and E) and induced forgetting (Fig. 6, C and F). Similarly, forgetting of a spatial memory was observed after MEM treatment in infant guinea pigs (Fig. 6, G to I). These results indicate that increasing hippocampal neurogenesis using mechanistically distinct interventions induces forgetting in precocial rodent species.

Discussion

The hippocampus encodes memories for places and events (*39*). The observation that hippocampal neurogenesis persists into adulthood led to the idea that neurogenesis modulates hippocampal memory function (*40*). To our knowledge, all previous studies examining the relationship between hippocampal neurogenesis and memory have used essentially the same design; they manipulated hippocampal neurogenesis before training and examined the impact of this manipulation on subsequent memory formation (i.e., they investigated the anterograde effects of manipulating neurogenesis on memory) (*40*). The view that emerged from these studies is that, once sufficiently mature, new neurons positively contribute to encoding of new hippocampus-dependent memories, perhaps by providing new substrates for memory storage (*40*). Here, we examined the retrograde impact of similar manipulations of neurogenesis on memory. Through a series of studies, we showed that high levels of neurogenesis disrupt established hippocampus-dependent memories. As such, our findings reveal a novel role for neurogenesis in forgetting or memory clearance, in line with theoretical predictions (*12*, *14*–*16*).

The hippocampus is thought to rapidly and automatically encode experiences (*41*). Because not all experiences are ultimately remembered, it is likely that forgetting processes continuously degrade or clear stored information from the hippocampus. Our results identify neurogenesis as one such process that promotes degradation of hippocampus-dependent memories, most likely by reconfiguring DG-CA3 circuits. Successful memory retrieval may result from the reactivation of patterns of neural activity present at the time of memory encoding (i.e., pattern completion) [e.g., (*42*–*45*)]. Because neurogenesis reconfigures hippocampal circuits, this may reduce the ability of a given set of cues (or inputs) to reinvoke the same pattern of activity (i.e., pattern completion failure) (*46*). During infancy, when neurogenesis levels are elevated, high rates of decay render hippocampus-dependent memories [that are declarative in nature (*21*)] inaccessible at later time points. Reducing neurogenesis at this developmental stage can increase the persistence of hippocampus-dependent memories. During adulthood, when neurogenesis levels are lower, memories are more resistant to decay. Artificially increasing neurogenesis after learning, however, may be sufficient to induce forgetting.

References and Notes

1. W. C. Abraham, A. Robins, *Trends Neurosci.* **28**, 73–78 (2005).
2. C. Zhao, W. Deng, F. H. Gage, *Cell* **132**, 645–660 (2008).
3. G. L. Ming, H. Song, *Annu. Rev. Neurosci.* **28**, 223–250 (2005).
4. D. A. Laplagne *et al.*, *PLOS Biol.* **4**, e409 (2006).
5. N. Toni *et al.*, *Nat. Neurosci.* **11**, 901–907 (2008).
6. N. Toni *et al.*, *Nat. Neurosci.* **10**, 727–734 (2007).
7. C. Zhao, E. M. Teng, R. G. Summers Jr., G. L. Ming, F. H. Gage, *J. Neurosci.* **26**, 3–11 (2006).
8. S. Ge *et al.*, *Nature* **439**, 589–593 (2006).
9. Y. Gu *et al.*, *Nat. Neurosci.* **15**, 1700–1706 (2012).
10. A. Sahay *et al.*, *Nature* **472**, 466–470 (2011).
11. S. S. Stone *et al.*, *J. Neurosci.* **31**, 13469–13484 (2011).
12. P. W. Frankland, S. Köhler, S. A. Josselyn, *Trends Neurosci.* **36**, 497–503 (2013).
13. M. Yasuda *et al.*, *Neuron* **70**, 1128–1142 (2011).
14. K. Deisseroth *et al.*, *Neuron* **42**, 535–552 (2004).
15. L. A. Meltzer, R. Yabaluri, K. Deisseroth, *Trends Neurosci.* **28**, 653–660 (2005).
16. V. I. Weisz, P. F. Argibay, *Cognition* **125**, 13–25 (2012).
17. H. G. Kuhn, H. Dickinson-Anson, F. H. Gage, *J. Neurosci.* **16**, 2027–2033 (1996).
18. T. Seki, Y. Arai, *Neuroreport* **6**, 2479–2482 (1995).
19. S. Freud, *Childhood and Concealing Memories*, in *The Basic Writings of Sigmund Freud*, A. A. Brill, Ed. (Norton, New York, 1905), pp. 30–36.
20. B. A. Campbell, in *Comparative Perspectives on the Development of Memory,* R. V. Kail, N. E. Spear, Eds. (Routledge, 1984), pp. 23-35.
21. D. C. Rubin, *Memory* **8**, 265–269 (2000).
22. B. A. Campbell, N. E. Spear, *Psychol. Rev.* **79**, 215–236 (1972).
23. L. Acsády, A. Kamondi, A. Sík, T. Freund, G. Buzsáki, *J. Neurosci.* **18**, 3386–3403 (1998).
24. J. J. Kim, M. S. Fanselow, *Science* **256**, 675–677 (1992).
25. K. G. Akers, M. Arruda-Carvalho, S. A. Josselyn, P. W. Frankland, *Learn. Mem.* **19**, 598–604 (2012).
26. S. A. Josselyn, P. W. Frankland, *Learn. Mem.* **19**, 423–433 (2012).
27. H. van Praag, G. Kempermann, F. H. Gage, *Nat. Neurosci.* **2**, 266–270 (1999).
28. R. McGonigal, N. Tabatadze, A. Routtenberg, *Hippocampus* **22**, 1242–1255 (2012).
29. H. van Praag, *Trends Neurosci.* **32**, 283–290 (2009).
30. Y. Niibori *et al.*, *Nat Commun* **3**, 1253 (2012).
31. M. Maekawa *et al.*, *Neurosci. Res.* **63**, 259–266 (2009).
32. J. E. Malberg, A. J. Eisch, E. J. Nestler, R. S. Duman, *J. Neurosci.* **20**, 9104–9110 (2000).
33. N. N. Karpova *et al.*, *Science* **334**, 1731–1734 (2011).
34. K. Meletis *et al.*, *Development* **133**, 363–369 (2006).
35. S. A. Josselyn, S. Kida, A. J. Silva, *Neurobiol. Learn. Mem.* **82**, 159–163 (2004).
36. A. Garthe, J. Behr, G. Kempermann, *PLOS ONE* **4**, e5464 (2009).
37. A. Sierra *et al.*, *Cell Stem Cell* **7**, 483–495 (2010).
38. S. Guidi, E. Ciani, S. Severi, A. Contestabile, R. Bartesaghi, *Hippocampus* **15**, 285–301 (2005).
39. H. Eichenbaum, *Neuron* **44**, 109–120 (2004).
40. W. Deng, J. B. Aimone, F. H. Gage, *Nat. Rev. Neurosci.* **11**, 339–350 (2010).
41. R. L. Redondo, R. G. Morris, *Nat. Rev. Neurosci.* **12**, 17–30 (2011).
42. X. Liu *et al.*, *Nature* **484**, 381–385 (2012).
43. L. G. Reijmers, B. L. Perkins, N. Matsuo, M. Mayford, *Science* **317**, 1230–1233 (2007).
44. B. A. Richards, P. W. Frankland, *Hippocampus* **23**, 207–212 (2013).
45. J. F. Danker, J. R. Anderson, *Psychol. Bull.* **136**, 87–102 (2010).
46. A. Treves, E. T. Rolls, *Hippocampus* **4**, 374–391 (1994).

Acknowledgments: This work was supported by grants from Brain Canada to P.W.F., the Canadian Institutes of Health Research (CIHR) to P.W.F. (MOP86762) and S.A.J. (MOP74650), the Centre for Brain and Behavior at the Hospital for Sick Children to P.W.F. and S.A.J., and the Core Research for Evolutional Science and Technology of Japan Science and Technology Agency (JST-CREST) and Ministry of Education, Culture, Sports, Science and Technology Grants-in-Aid for Scientific Research (KAKENHI) to T.M. K.G.A. and H.-L.H. (CIHR), A.M.-C. (El Consejo Nacional de Ciencia y Tecnología), A.P.Y. (Donald and Doris Milne Alzheimer's Disease Fellowship), A.L.W. (Ontario Mental Health Foundation), and A.G. and B.A.R. (Natural Sciences and Engineering Research Council of Canada) were supported by fellowships. Data are archived in the Dryad repository (doi:10.5061/dryad.s7q3c).

Supplementary Materials

www.sciencemag.org/content/344/6184/598/suppl/DC1
Materials and Methods
Figs. S1 to S17
References (*47*–*58*)

25 November 2013; accepted 1 April 2014
10.1126/science.1248903

Large-Scale Psychological Differences Within China Explained by Rice Versus Wheat Agriculture

T. Talhelm,[1]* X. Zhang,[2,3] S. Oishi,[1] C. Shimin,[4] D. Duan,[2] X. Lan,[5] S. Kitayama[5]

Cross-cultural psychologists have mostly contrasted East Asia with the West. However, this study shows that there are major psychological differences within China. We propose that a history of farming rice makes cultures more interdependent, whereas farming wheat makes cultures more independent, and these agricultural legacies continue to affect people in the modern world. We tested 1162 Han Chinese participants in six sites and found that rice-growing southern China is more interdependent and holistic-thinking than the wheat-growing north. To control for confounds like climate, we tested people from neighboring counties along the rice-wheat border and found differences that were just as large. We also find that modernization and pathogen prevalence theories do not fit the data.

Over the past 20 years, psychologists have cataloged a long list of differences between East and West (*1*–*3*). Western culture is more individualistic and analytic-thinking, whereas East Asian culture is more interdependent and holistic-thinking. Analytic thought uses abstract categories and formal reasoning, such as logical laws of noncontradiction—if A is true, then "not A" is false. Holistic thought is more intuitive and sometimes even embraces contradiction—both A and "not A" can be true.

Even though psychology has cataloged a long list of East-West differences, it still lacks an accepted explanation of what causes these differences. Building on subsistence style theory (*1*, *4*), we offer the rice theory of culture and compare it with the modernization hypothesis (*5*) and the more recent pathogen prevalence theory (*6*).

The modernization hypothesis argues that, as societies become wealthier, more educated, and capitalistic, they become more individualistic and analytical. World Values Surveys (*7*) and studies on indigenous Mayans' transition to a market economy (*5*) have given some support to the modernization hypothesis. But this theory has difficulty explaining why Japan, Korea, and Hong Kong are persistently collectivistic despite per-capita gross domestic products (GDPs) higher than that of the European Union.

The pathogen prevalence theory argues that a high prevalence of communicable diseases in some countries made it more dangerous to deal with strangers, making those cultures more insular and collectivistic (*6*). Studies have found that historical pathogen prevalence correlates with collectivism and lower openness to experience (*6*). However, pathogens are strongly correlated with heat (*8*). Because rice grows in hot areas, pathogens may be confounded with rice—a possibility that prior research did not control for.

The Rice Theory

The rice theory is an extension of subsistence style theory, which argues that some forms of subsistence (such as farming) require more functional interdependence than other forms (such as herding). At the same time, ecology narrows the types of subsistence that are possible. For example, paddy rice requires a significant amount of water. Over time, societies that have to cooperate intensely become more interdependent, whereas societies that do not have to depend on each other as much become more individualistic.

In the past, most subsistence research has compared herders and farmers, arguing that the independence and mobility of herding make herding cultures individualistic and that the stability and high labor demands of farming make farming cultures collectivistic (*1*). We argue that subsistence theory is incomplete because it lumps all farming together. Two of the most common subsistence crops—rice and wheat—are very different, and we argue that they lead to different cultures.

The two biggest differences between farming rice and wheat are irrigation and labor. Because

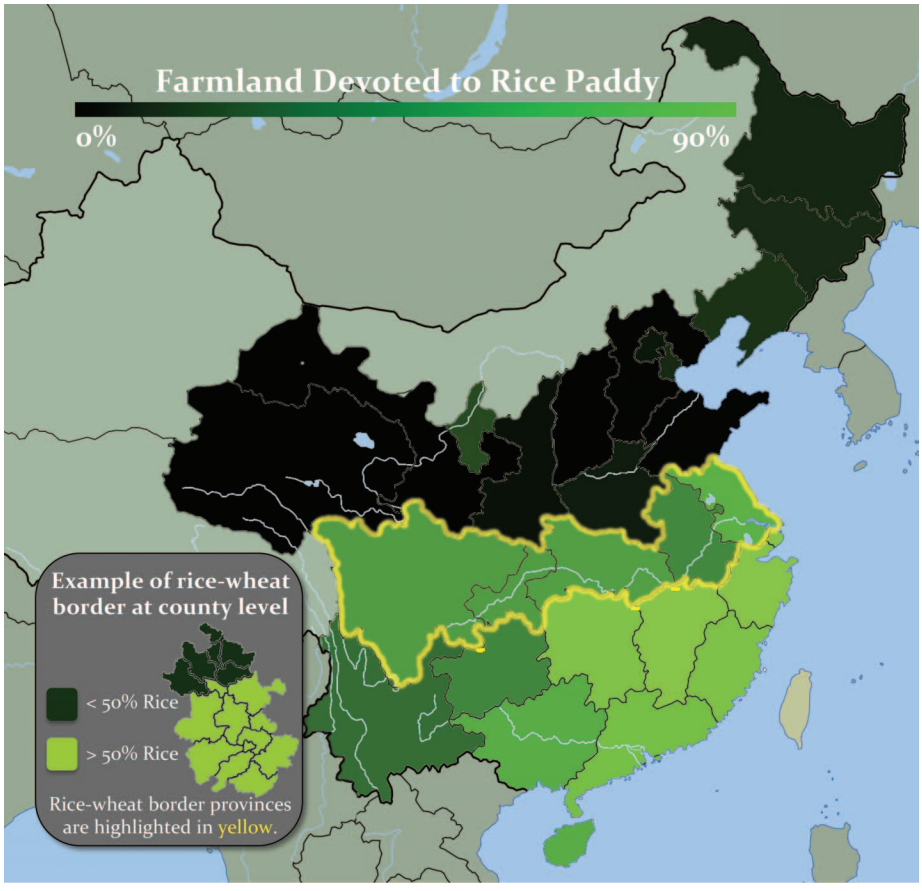

Fig. 1. Percent of cultivated land devoted to rice paddies in 1996. Three major herding provinces are not shaded: Tibet, Xinjiang, and Inner Mongolia. Along the rice-wheat border (highlighted), people from the rice counties thought more holistically than their neighbors in wheat counties.

[1]Department of Psychology, University of Virginia, Charlottesville, VA 22904, USA. [2]Department of Psychology, Beijing Normal University, Beijing, China. [3]State Key Lab of Cognitive Neuroscience and Learning, Beijing Normal University, Beijing 100875, China. [4]Department of Psychology, South China Normal University, Guangzhou, China. [5]Department of Psychology, University of Michigan, Ann Arbor, MI 48109, USA.
*Corresponding author. E-mail: tat8dc@virginia.edu

rice paddies need standing water, people in rice regions build elaborate irrigation systems that require farmers to cooperate. In irrigation networks, one family's water use can affect their neighbors, so rice farmers have to coordinate their water use. Irrigation networks also require many hours each year to build, dredge, and drain—a burden that often falls on villages, not isolated individuals.

Paddy rice also requires an extraordinary amount of work. Agricultural anthropologists visiting premodern China observed the number of hours farmers worked and found that growing paddy rice required at least twice the number of hours as wheat (*9*). The difference in man-hours was not a difference only noticeable to scientists. Medieval Chinese people grew both wheat and rice, and they were aware of the huge labor difference between the two. A Chinese farming guide in the 1600s advised people, "If one is short of labor power, it is best to grow wheat" [quoted in (*10*)]. A Chinese anthropologist in the 1930s concluded that a husband and wife would not be able to farm a large enough plot of rice to support the family if they relied on only their own labor (*11*). Strict self-reliance might have meant starvation.

To deal with the massive labor requirements, farmers in rice villages from India to Malaysia and Japan form cooperative labor exchanges (*12*). Farmers also coordinate their planting dates so that different families harvest at different times, allowing them to help in each others' fields (*12*). These labor exchanges are most common during transplanting and harvesting, which need to be done in a short window of time, creating an urgent need for labor. In economic terms, paddy rice makes cooperation more valuable. This encourages rice farmers to cooperate intensely, form tight relationships based on reciprocity, and avoid behaviors that create conflict.

In comparison, wheat is easier to grow. Wheat does not need to be irrigated, so wheat farmers can rely on rainfall, which they do not coordinate with their neighbors. Planting and harvesting wheat certainly takes work, but only half as much as rice (*9*). The lighter burden means farmers can look after their own plots without relying as much on their neighbors.

One point of clarification about the rice theory is that it applies to rice regions, not just the people farming rice. It is a safe bet that none of our thousand participants have actually farmed rice or wheat for a living. Instead, the theory is that cultures that farm rice and wheat over thousands of years pass on rice or wheat cultures,

Table 1. Holistic thought hierarchical linear models for rice (28 provinces, 1019 participants), GDP per capita (28 provinces, 1019 participants), and pathogens (21 provinces, 725 participants). See supplementary materials for detailed information on site effects and regressions with GDP, rice, and pathogens in a single model. Gender is coded as 0 = male and 1 = female.

	B	SE	*z*	*P*	*B*	SE	*z*	*P*	*B*	SE	*z*	*P*
Gender	0.20	0.06	3.55	<0.001	0.20	0.06	3.53	<0.001	0.13	0.07	1.97	0.05
$Site_{Fujian}$	−0.34	0.11	−3.21	0.001	−0.33	0.11	−3.07	0.002	−0.36	0.12	−3.09	0.002
Rice	0.56	0.21	2.72	0.007								
Per-capita GDP					0.52[1]	0.23[1]	2.24[1]	0.03[1]				
Pathogens									−0.22[1]	0.10[1]	−2.08[1]	0.04[1]

[1]Predictor correlates in the opposite direction from what theory predicts.

Table 2. Implicit individualism and loyalty/nepotism hierarchical linear models for rice, GDP per capita, and pathogens. Implicit individualism *N* equals 28 provinces, 515 participants for rice and GDP. *N* equals 21 provinces and 452 participants for pathogens. Loyalty/nepotism *N* equals 27 provinces, 166 participants for rice and GDP. *N* equals 21 provinces and 146 participants for pathogens.

		SE	*t*	*P*	*B*	SE	*t*	*P*	*B*	SE	*t*	*P*
					Implicit individualism							
Gender	−0.06	0.02	−2.51	0.01	−0.05	0.02	−2.34	0.02	−0.05	0.02	−2.04	0.04
$Site_{BeijingW2011}$	−0.27	0.05	−5.18	<0.001	−0.25	0.06	−4.40	<0.001	−0.18	0.05	−3.44	0.001
Rice	−0.20	0.08	−2.57	0.016								
Per-capita GDP					0.01	0.15	0.07	0.95				
Pathogens									0.01[1]	0.04[1]	0.33[1]	0.74[1]
					Loyalty/Nepotism							
$Site_{Sichuan}$	2.04	0.83	2.47	0.01	1.63	0.87	1.88	0.06	1.91	0.85	2.25	0.03
Rice	2.45	1.16	2.12	0.04								
Per-capita GDP					1.66[1]	1.69[1]	0.98[1]	0.34[1]				
Pathogens									−0.13	0.62	−0.21	0.84

[1]Predictor correlates in the opposite direction from what theory predicts.

Table 3. Divorce and invention regression models for rice, GDP per capita, and pathogens. Divorces are calculated as divorces per marriage, with 27 provinces for rice and per-capita GDP models and 21 provinces for pathogens. Inventions are the log number of successful patents per capita. Inventions *N* equals 27 provinces for rice and GDP; *N* equals 21 for pathogens.

	B	SE	β	*t*	*P*	*B*	SE	β	*t*	*P*	*B*	SE	β	*t*	*P*
								Divorces							
Per-capita GDP	0.10	0.04	0.48	2.71	0.01	0.13	0.03	0.61	3.89	0.001	0.11	0.05	0.52	2.04	0.06
Rice						−0.11	0.04	−0.49	−3.11	0.005					
Pathogens											−0.01	0.03	−0.07	−0.26	0.80
								Inventions							
Per-capita GDP	2.22	0.41	0.73	5.37	<0.001	2.55	0.37	0.84	6.98	<0.001	1.78	0.59	0.60	3.00	0.008
Rice						−1.27	0.39	−0.39	−3.28	0.003					
Pathogens											−0.34	0.31	−0.22	−1.10	0.29

even after most people put down their plows. Simply put, you do not need to farm rice yourself to inherit rice culture.

We propose that the rice theory can partly explain East-West differences. Prior subsistence theory cannot fully explain East-West differences because it focuses on herding versus farming (*1*), which is not the main East-West difference. Several Western regions herd, such as parts of Scotland and Switzerland, but the bulk of Europe historically farmed wheat (and similarly grown crops, such as barley). Instead, rice-wheat is the main East-West difference, and psychologists have not studied it.

The easiest way to test whether rice and wheat lead to different cultures is to show that rice areas (East Asia) are interdependent and that wheat areas (the West) are independent. But that logic is obviously flawed. We cannot just compare East and West because they differ on many factors besides rice and wheat—religion, politics, and technology, to name a few. A more convincing test case would be a country that has a shared history, government, language, and religion, but farms rice in some areas and wheat in other areas.

China as a Natural Test Case

Han China is a fitting natural test case because it has traditionally grown both rice and wheat but is more ethnically and politically unified than, say, Europe or sub-Saharan Africa. China is over 90% Han Chinese, and the same dynasties have ruled over the wheat and rice cores for most of the past few thousands of years, which controls for some of the major variables that confound East-West comparisons.

Within China, the Yangtze River splits the wheat-growing north from the rice-growing south (Fig. 1). For generations, northern China has grown wheat, and southern China has grown rice. Of course, two regions can never be 100% equivalent. There are differences such as climate and spoken dialect between north and south. To rule out these smaller differences, we report additional analyses that compare people from neighboring counties along the rice-wheat border.

Three Predictions

The three theories make different predictions about which parts of China should be the most interdependent. First, the modernization hypothesis predicts that the least-developed provinces should be the most interdependent. Development has been uneven in China partly because in the late 1970s Deng Xiaoping made several areas along the southeast coast "special economic zones" open to foreign trade. This policy has given southeastern provinces like Guangdong a GDP per capita about 3.5 times that of interior provinces like Guizhou (*13*). That is roughly the ratio difference between the United States and Kazakhstan. Thus, modernization would predict the highest collectivism in China's least-developed interior provinces.

Second, pathogen prevalence theory predicts a gradual rise in interdependence from north to south because pathogens rise gradually along with temperatures (*8*). Among Chinese provinces, overall pathogen rates and latitude are correlated: $r(20) = -0.49$, $P = 0.02$ (*14*). Furthermore, pathogen theory would predict the highest interdependence in the southwest, which has the highest rates of infectious disease death.

Third, the rice theory predicts the highest interdependence in the south and east. Unlike pathogens, rice is not the highest in the southernmost provinces. Instead, rice is concentrated in the east around Shanghai, which has flat floodplains ideal for growing rice. The rice theory also predicts a sharp divide along the rice-wheat border, which is different from the gradual rise of pathogens with climate.

To measure the prevalence of rice farming, we used statistical yearbook data on the percentage of cultivated land in each province devoted to rice paddies (*13*). Because some rice is grown with less labor on dry land (without paddies), we used statistics on rice paddies, rather than rice output. Because we wanted to assess the crop that different regions farmed traditionally, rather than figures affected by recent advances in irrigation and mechanization, we used rice statistics from 1996, the earliest available on the Bureau of Statistics Web site.

To test the modernization hypothesis, we collected GDP per capita for each province from the same year. To measure precontemporary disease prevalence, we used the earliest study we could find with disease rates in different provinces, from 1976 (*15*). Because the 1976 study did not cover 10 provinces, we also collected recent statistics (*13*). This increased the sample by four provinces. Both sources gave similar pictures: higher disease in the south and the highest in the southwest.

Samples

We tested 1162 Han Chinese students from six sites: Beijing (north), Fujian (southeast), Guangdong (south), Yunnan (southwest), Sichuan (west central), and Liaoning (northeast). We used three measures: a measure of cultural thought, implicit individualism, and loyalty/nepotism (described below). We chose these tasks because they are not self-report scales, avoiding the documented problems with use of self-report scales to measure cultural differences (*16*).

Results from these different sites show that rice-wheat differences held regardless of testing site (*14*). For all tasks, we analyzed only ethnic Han Chinese and excluded Han participants from the provinces of Tibet, Inner Mongolia, and Xinjiang. These areas are historically herding areas and have different ethnicities, cultures, languages, and religions that would confound our comparisons of rice and wheat.

We tested the hypotheses with multilevel models because participants (level 1) were nested within provinces (level 2). We report correlations as an effect size at the province level that can be compared across variables. We calculated this by comparing the province-level variance of the

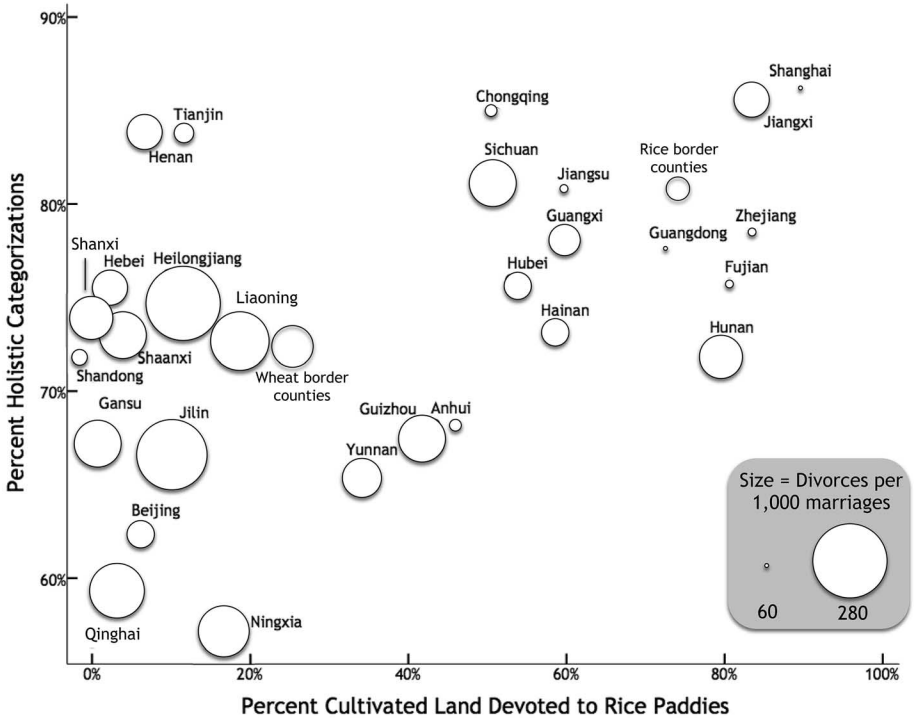

Fig. 2. Cultural thought style by percentage of cultivated area devoted to rice paddies. Each circle represents a province. Circle size represents divorce and controls for effect of GDP. To illustrate cultural differences along the rice-wheat border, circles represent the rice and wheat border counties.

models with and without the key predictor (Tables 1 to 3 report regression output).

Our main dependent variable was a common measure of cultural thought, the triad task (*17*). The triad task shows participants lists of three items, such as train, bus, and tracks. Participants decide which two items should be paired together. Two of the items can be paired because they belong to the same abstract category (train and bus belong to the category vehicles), and two because they share a functional relationship (trains run on tracks). People from Western and individualistic cultures choose more abstract (analytic) pairings, whereas East Asians and people from other collectivistic cultures choose more relational (holistic) pairings (*1*, *17*). We report scores as a percentage of holistic choices, where 100% is completely holistic and 0% is completely analytic.

We first tested the modernization hypothesis by testing whether people from provinces with lower GDP per capita thought more holistically. People from richer provinces actually thought more holistically: $\gamma(25) = 0.52$, $P = 0.03$, $r = 0.46$. (γ represents province-level HLM regression coefficients.)

We then tested the pathogen prevalence theory by testing whether provinces with higher rates of disease thought more holistically. Provinces with higher disease rates actually thought less holistically: $\gamma(18) = -0.22$, $P = 0.04$, $r = -0.44$.

The large-scale disease study from 1976 included statistics for 31 counties across China (*15*), which let us test the pathogen theory more precisely. Thus, we tested whether the 198 people in our sample who came from these 31 counties had different thought styles based on the historical disease prevalence in their county. Even with this finer precision, pathogen prevalence predicted thought style marginally in the wrong direction: $\gamma(28) = -0.43$, $P = 0.08$, $r = -0.33$.

The rice theory was the only model that fit the data (Fig. 2). People from provinces with a higher percentage of farmland devoted to rice paddies thought more holistically: $\gamma(25) = 0.56$, $P = 0.007$, $r = 0.51$. [Controlling for GDP per capita made little difference (table S1).]

Northern and southern China also differ in several factors other than rice, such as climate, dialect, and contact with herding cultures. Therefore, we analyzed differences among neighboring counties along in the five central provinces along the rice-wheat border (Sichuan, Chongqing, Hubei, Anhui, and Jiangsu). Differences between neighboring counties are less likely to be due to climate or other third variables.

We gathered the rice cultivation statistics for each county in these provinces and split counties into rice and wheat counties. We defined rice counties as more than 50% of farmland devoted to rice paddies. Figure 1 depicts an example of the county split in the province of Anhui. The rice-wheat difference between neighboring counties can be stark. For example, in Anhui, Bozhou county farms only 2% rice, whereas neighboring Huainan county farms 67%. We tested for differences in cultural thought style, which had the largest sample, including 224 participants from the rice-wheat border.

People from the rice side of the border thought more holistically than people from the wheat side of the border: $B(221) = 0.54$, $P < 0.001$ (table S5). To compare the border effect size with the effect size for rice and wheat in all of China, we compared effect of a categorical rice-wheat variable. The effect sizes were similar (rice-wheat border, $B = 0.53$; all China, $B = 0.43$). (For group comparisons, wheat provinces are defined throughout as <50% farmland devoted to rice paddies; rice provinces as >50%.)

To test whether the findings generalize beyond thought style, we tested subsamples on two measures previously used for East-West cultural differences. The first was the sociogram task (n = 515), which has participants draw a diagram of their social network, with circles to represent the self and friends (*18*). Researchers measure how large participants draw the self versus how large they draw their friends to get an implicit measure of individualism (or self-inflation). A prior study found that Americans draw themselves about 6 mm bigger than they draw others, Europeans draw themselves 3.5 mm bigger, and Japanese draw themselves slightly smaller (*18*).

People from rice provinces were more likely than people from wheat provinces to draw themselves smaller than they drew their friends: $\gamma(24) = -0.20$, $P = 0.03$, $r = -0.17$ (fig. S2). On average, people from wheat provinces self-inflated 1.5 mm (closer to Europeans), and people from rice provinces self-inflated –0.03 mm (similar to Japanese).

Pathogen prevalence did not predict self-inflation on the sociogram task: $\gamma(17) = 0.003$, $P = 0.95$, $r = 0$. GDP per capita also failed to predict self-inflation: $\gamma(24) = 0.04$, $P = 0.81$, $r = 0$.

The second measure was the loyalty and nepotism task, which measures whether people draw a sharp distinction between how they treat friends versus strangers (n = 166). One defining feature of collectivistic cultures is that they draw a sharp distinction between friends and strangers (*3*). A previous study measured this by having people imagine going into a business deal with (i) an honest friend, (ii) a dishonest friend, (iii) an honest stranger, and (iv) a dishonest stranger (*19*). In the stories, the friend or stranger's lies cause the participant to lose money in a business deal, and the honesty causes the participant to make more money. In each case, the participants have a chance to use their own money to reward or punish the other person.

The original study found that Singaporeans rewarded their friends much more than they punished them, which could be seen positively as loyalty or negatively as nepotism (*19*). Americans were much more likely than Singaporeans to punish their friends for bad behavior. We pre-

Table 4. Instrumental variable regressions. Instrumental variable regressions help test whether reverse causality is a problem in the data set—whether regions that were already more collectivistic chose to grow rice. In the topmost regression, "rice suitability" is a z score of the environmental suitability of each province for growing wetland rice based on the United Nations Food and Agriculture Organization's Global Agro-ecological Zones database (*27*). In the five other regressions, "rice suitability" is the predicted rice from the topmost regression with rice suitability. Dash entries indicate not applicable.

	B	SE	β	*t*/*z*	*P*
	Actual rice farming				
Rice suitability	0.27	0.03	0.85	8.31	<0.001
28 provinces					
	Holistic thought				
Gender	0.20	0.06	–	3.56	<0.001
$Site_{Fujian}$	–0.34	0.11	–	–3.16	0.002
Rice suitability	0.66	0.25	–	2.66	0.008
28 provinces, 1019 participants					
	Implicit individualism				
Gender	–0.05	0.02	–	–2.35	0.02
$Site_{BeijingW2011}$	–0.24	0.05	–	–4.87	<0.001
Rice suitability	–0.24	0.10	–	–2.47	0.02
28 provinces, 510 participants					
	Loyalty/nepotism				
$Site_{Sichuan}$	1.64	0.80	–	2.05	0.04
Rice suitability	3.73	1.40	–	2.67	0.009
27 provinces, 176 participants					
	Divorces				
Per-capita GDP	0.11	0.03	0.51	3.65	0.001
Rice suitability	–0.15	0.04	–0.56	–4.04	<0.001
27 provinces					
	Inventions				
Per-capita GDP	2.30	0.34	0.76	6.68	<0.001
Rice suitability	–1.50	0.43	–0.40	–3.50	<0.002
27 provinces					

dicted that people from rice areas would be less likely to punish their friends than people from wheat areas.

We computed loyalty/nepotism as the amount they rewarded their friend minus the amount they punished their friend. People from rice provinces were more likely to show loyalty/nepotism: $\gamma(25) = 2.45$, $P = 0.04$, $r = 0.49$. In their treatment of strangers, people from rice and wheat provinces did not differ: $\gamma(24) = -0.09$, $P = 0.90$, $r = 0$.

Pathogen prevalence was not related to loyalty/nepotism: $\gamma(19) = -0.13$, $P = 0.84$, $r = -0.08$. GDP per capita did not predict loyalty/nepotism: $\gamma(25) = 1.66$, $P = 0.36$, $r = 0.33$.

In short, the results consistently showed that participants from rice provinces are more holistic-thinking, interdependent, and loyal/nepotistic than participants from the wheat provinces. However, one weakness of these studies is that the participants were all college students. To test whether the cultural differences extend beyond college students, we gathered provincial statistics on variables that have been linked to collectivism and analytic thought: divorce rates and patents for new inventions.

A prior study showed that individualistic countries have higher divorce rates, even controlling for gross national product per capita (*20*). Rice culture's emphasis on avoiding conflict and preserving relationships may make people from rice cultures less willing to get divorced. We collected divorce statistics from the same statistical yearbook as the farming statistics, 1996. We also collected statistics from the 2000 and the 2010 yearbooks to track the differences over the past 15 years.

In China, modernization did predict divorce: wealthier provinces had more divorce: $B(26) = 0.10$, $P = 0.01$, $\beta = 0.48$. Adding rice to the model explained even more variation in divorce rates, with rice provinces having lower divorce rates: $B(25) = -0.11$, $P = 0.005$, $\beta = -0.49$. Pathogen prevalence did not predict divorce: $B(20) = -0.01$, $P = 0.80$, $\beta = -0.07$ (controlling for GDP). In 1996, wheat provinces had a 50% higher divorce rate than rice provinces. Although divorce rates have almost doubled in the past 15 years, the raw divorce rate gap between the wheat and rice provinces remained the same in the 2000 and 2010 statistics.

We also analyzed the number of successful patents for new inventions in each province because research has shown that analytic thinkers are better at measures of creativity and thinking of novel uses for ordinary objects (*21*). Within the United States, immigrants from individualistic cultures hold more patents for inventions (*22*).

We controlled for GDP per capita because wealthier provinces had more patents: $B(26) = 2.22$, $P < 0.001$, $\beta = 0.73$. Rice provinces had fewer successful patents for new inventions than wheat provinces: $B(25) = -1.27$, $P = 0.003$, $\beta = -0.39$. Pathogen prevalence did not predict patents: $B(19) = -0.34$, $P = 0.29$, $\beta = -0.22$. Wheat provinces had 30% more patents for inventions than rice provinces. This difference persisted through the 2000 statistics but not the 2010 statistics.

This study shows that China's wheat and rice regions have different cultures. China's rice regions have several markers of East Asian culture: more holistic thought, more interdependent self-construals, and lower divorce rates. The wheat-growing north looked more culturally similar to the West, with more analytic thought, individualism, and divorce. Furthermore, Table 4 presents an instrumental variable regression showing that climatic suitability for rice significantly predicts all of the cultural variables in this study, which suggests that reverse causality is unlikely.

How large are these differences compared with East-West differences? We compared results on our main task (cultural thought style) in our China sample to a prior U.S. sample. An East-West categorical variable had an effect of $B = 0.78$. In the China data, a categorical rice-wheat variable had an effect of $B = 0.38$ (table S2). This suggests that rice versus wheat can explain a portion of the variance in thought style between East and West but not all of it. It should also be noted that psychologists have found holistic thought in parts of the world beyond East Asia, which suggests holistic thought is not just an East-West difference (*23*).

Modernization predicted divorce and patents, but why did it fail to predict the other differences? In China, modernization seems to have changed customs such as divorce, but perhaps the parts of culture and thought style we measured are more resistant to change. Or perhaps modernization simply takes more generations to change cultural interdependence and thought style. However, most of our participants were born after China's reform and opening, which started in 1978. Furthermore, Japan, South Korea, and Hong Kong modernized much earlier than China, but they still score less individualistic on international studies of culture than their wealth would predict (fig. S2).

The rice theory can explain wealthy East Asia's strangely persistent interdependence. China has a rice-wheat split, but Japan and South Korea are complete rice cultures. Most of China's wheat provinces devote less than 20% of farmland to rice paddies. None of Japan's 9 regions or South Korea's 16 regions has that little rice (except for two outlying islands). Japan and Korea's rice legacies could explain why they are still much less individualistic than similarly wealthy countries.

This study focuses on East Asia, but the rice theory also makes predictions about other parts of the world. For example, India has a large rice-wheat split. Indonesia and parts of West Africa have also traditionally farmed rice. If the rice theory is correct, we should find similar cultural differences there.

There are still unresolved questions with the rice theory. For example, studies can test whether irrigation is central to the effect of rice by comparing paddy rice with dryland rice cultures, which grow rice without irrigation. Studies can also explore how rice differences persist in the modern world, whether through values, institutions, or other mechanisms.

There is also the question of how long rice culture will persist after the majority of people stop farming rice. There is evidence that U.S. regions settled by Scottish and Irish herders have higher rates of violence, even though most locals stopped herding long ago (*24*). This is one example of how subsistence style can shape culture long after people have stopped relying on that subsistence style. In the case of China, only time will tell.

Psychologists, economists, and anthropologists have studied the effects of subsistence style and irrigation (*1*, *4*, *25*, *26*). This study extends that work by using psychological measures to test differences resulting from rice and wheat agriculture. The rice theory provides a theoretical framework that might explain why East Asia is so much less individualistic than it "should be" based on its wealth. Finally, the rice theory can explain the large cultural differences within China, advancing a more nuanced picture of East Asian cultural diversity.

References and Notes

1. R. E. Nisbett, K. Peng, I. Choi, A. Norenzayan, *Psychol. Rev.* **108**, 291–310 (2001).
2. H. R. Markus, S. Kitayama, *Psychol. Rev.* **98**, 224–253 (1991).
3. H. C. Triandis, *Individualism and Collectivism* (Westview, Boulder, CO, 1995).
4. J. W. Berry, *J. Pers. Soc. Psychol.* **7**, 415–418 (1967).
5. P. M. Greenfield, *Dev. Psychol.* **45**, 401–418 (2009).
6. C. L. Fincher, R. Thornhill, D. R. Murray, M. Schaller, *Proc. Biol. Sci.* **275**, 1279–1285 (2008).
7. R. Inglehart, *Wash. Q.* **23**, 215–228 (2000).
8. V. Guernier, M. E. Hochberg, J.-F. Guégan, *PLOS Biol.* **2**, e141 (2004).
9. J. L. Buck, *Land Utilization in China* (Univ. Chicago Press, Chicago, IL, 1935).
10. M. Elvin, in *The Chinese Agricultural Economy*, R. Barker, R. Sinha, B. Rose, Eds. (Westview, Boulder, CO, 1982), pp. 13–35.
11. F. Xiaotong, *Earthbound China: A Study of Rural Economy in Yunnan* (Univ. Chicago Press, Chicago, IL, 1945).
12. F. Bray, *The Rice Economies: Technology and Development in Asian Societies* (Blackwell, New York, 1986).
13. State Statistical Bureau of the People's Republic of China, *China Statistical Yearbook* (1996 and 2005).
14. Materials and methods are available on *Science* Online.
15. C. Junshi, T. C. Campbell, J. Li, R. Peto, *Diet, Life-Style, and Mortality in China: A Study of the Characteristics of 65 Chinese Counties* (Oxford Univ. Press, Oxford, 1990).
16. K. Peng, R. E. Nisbett, N. Y. C. Wong, *Psychol. Methods* **2**, 329–344 (1997).
17. L. J. Ji, Z. Zhang, R. E. Nisbett, *J. Pers. Soc. Psychol.* **87**, 57–65 (2004).
18. S. Kitayama, H. Park, A. T. Sevincer, M. Karasawa, A. K. Uskul, *J. Pers. Soc. Psychol.* **97**, 236–255 (2009).
19. C. S. Wang, A. K.-Y. Leung, Y. H. M. See, X. Y. Gao, *J. Exp. Psychol.* **47**, 1295–1299 (2011).
20. D. Lester, *Psychol. Rep.* **76**, 258 (1995).
21. H. A. Witkin, C. A. Moore, D. R. Goodenough, P. W. Cox, *Rev. Educ. Res.* **47**, 1–64 (1977).
22. S. A. Shane, *J. Bus. Venturing* **7**, 29–46 (1992).
23. J. Henrich, S. J. Heine, A. Norenzayan, *Behav. Brain Sci.* **33**, 61–83, discussion 83–135 (2010).
24. D. Cohen, R. E. Nisbett, *Culture of Honor* (Westview, Boulder, CO, 1997).
25. M. Harris, *Cannibals and Kings* (Random House, New York, 1977).

26. M. Aoki, *Toward a Comparative Institutional Analysis* (MIT Press, Cambridge, MA, 2001).
27. Food and Agricultural Organization (FAO)/International Institute for Applied Systems Analysis (IIASA), Global Agro-ecological Zones (GAEZ v3.0) (2010).

Acknowledgments: We thank Z. Xia, N. Qingyun, Y. Wu, Y. Wang, Y. Ma, and A Jiao for collecting data; A. Leung and C. Wang for making the loyalty/nepotism task available; L. Jun Ji for the Chinese version of the triad task; M. Hunter for statistical guidance; and J. P. Seder, A. Putnam, Y. Wang, T. Wilson, and E. Gilbert for comments on earlier versions of this paper. The data are available at the Inter-University Consortium for Political and Social Research (ICPSR no. 35027) or by request to the first author. This research was supported by a Fulbright Scholarship, a NSF Graduate Research Fellowship, and a NSF East Asian and Pacific Summer Institute Fellowship. The Beijing Key Lab of Applied Experimental Psychology supplied laboratory space for the study.

Supplementary Materials
www.sciencemag.org/content/344/6184/603/suppl/DC1
Materials and Methods
Figs. S1 and S2
Tables S1 to S12
References (*28*–*49*)

4 October 2013; accepted 25 March 2014
10.1126/science.1246850

REPORTS

Fermi Surface and Pseudogap Evolution in a Cuprate Superconductor

Yang He,[1] Yi Yin,[1]* M. Zech,[1] Anjan Soumyanarayanan,[1] Michael M. Yee,[1] Tess Williams,[1] M. C. Boyer,[2]† Kamalesh Chatterjee,[2] W. D. Wise,[2] I. Zeljkovic,[1]‡ Takeshi Kondo,[3]§ T. Takeuchi,[3] H. Ikuta,[3] Peter Mistark,[4] Robert S. Markiewicz,[4] Arun Bansil,[4] Subir Sachdev,[1] E. W. Hudson,[2]‖¶ J. E. Hoffman[1]¶

The unclear relationship between cuprate superconductivity and the pseudogap state remains an impediment to understanding the high transition temperature (T_c) superconducting mechanism. Here, we used magnetic field–dependent scanning tunneling microscopy to provide phase-sensitive proof that *d*-wave superconductivity coexists with the pseudogap on the antinodal Fermi surface of an overdoped cuprate. Furthermore, by tracking the hole-doping (p) dependence of the quasi-particle interference pattern within a single bismuth-based cuprate family, we observed a Fermi surface reconstruction slightly below optimal doping, indicating a zero-field quantum phase transition in notable proximity to the maximum superconducting T_c. Surprisingly, this major reorganization of the system's underlying electronic structure has no effect on the smoothly evolving pseudogap.

Superconductivity is one of several phenomena, including the pseudogap, that arises from interactions of electrons near the Fermi surface (FS) in hole-doped cuprates. The FS topology is therefore crucial to understanding these phenomena and their relationships. High-field quantum oscillation (QO) measurements (*1*–*3*) revealed an unexpectedly small FS in underdoped $YBa_2Cu_3O_{6.5}$ (YBCO), in contrast to the conventional, large FS of overdoped cuprates like $Tl_2Ba_2CuO_{6+x}$ (*4*). Further high-field investigations led to the discovery of a quantum phase transition (QPT) at the low doping edge of this small FS regime, perhaps associated with a metal-insulator transition (*5*) or the formation of density-wave order (*6*). However, the large-to-small FS transition presumed to occur at higher doping has thus far not been observed by QO within a single hole-doped material system. Furthermore, it is unclear whether the small FS is merely revealed by QO or possibly created by their necessarily high magnetic fields.

A zero-field alternative to QO, angle-resolved photoemission spectroscopy (ARPES), has a long history of mapping the FS in $Bi_2Sr_2CaCu_2O_{8+x}$ (Bi2212) (*2*, *7*–*11*). Here, the onset of the pseudogap (PG) is defined by the opening of an antinodal gap and the reduction of the large FS to a "Fermi arc," which may actually be one side of a Fermi pocket, consistent with QO results (*10*). The PG onset may be associated with a QPT just above optimal doping at $p = 0.19$ (*11*). A second QPT to another competing phase is suggested to occur (*11*) at lower doping ($p = 0.076$), similar perhaps to that found by QO (*5*, *6*). However, if the transition near optimal doping is a FS reconstruction to pockets, as suggested in (*10*), why are sharp antinodal quasiparticles seen below this doping, all the way down to $p = 0.08$ (*7*, *9*, *11*)? Further, if the antinodal FS persists down to $p = 0.08$, what impact does the QPT associated with the onset of the PG at $p = 0.19$ have on the FS?

To address these outstanding questions, we used scanning tunneling microscopy (STM) to study $(Bi,Pb)_2(Sr,La)_2CuO_{6+\delta}$ (Bi2201). In this hole-doped cuprate, the absence of bilayer splitting and the suppression of the supermodu-

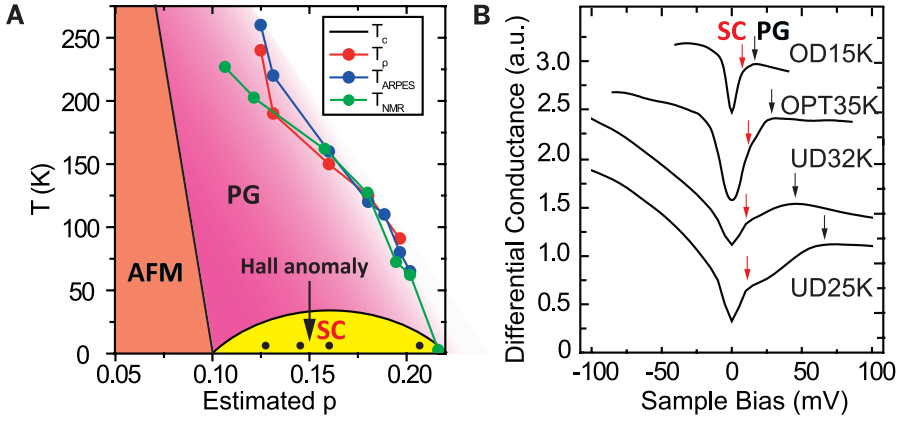

Fig. 1. Phase diagram and spectra. (**A**) Schematic temperature-doping phase diagram of Bi2201, showing antiferromagnetic insulator (AFM), superconductor (SC), and PG phases. Four black points represent the sample batches of this study, namely underdoped UD25K and UD32K, optimal OPT35K, and overdoped OD15K. The PG transition line T^* is plotted as measured by ARPES (*12*), resistivity (*12*) and nuclear magnetic resonance (*13*). Anomaly in the Hall coefficient (*28*) is marked by a black arrow. (**B**) The spatially averaged differential conductance $g(E)$ for each sample. The PG edge is marked with black arrows, whereas the low-energy kink in each spectrum, considered to be related to the superconducting gap (*14*, *15*), is marked with red arrows. a.u., arbitrary units.

[1]Department of Physics, Harvard University, Cambridge, MA 02138, USA. [2]Department of Physics, Massachusetts Institute of Technology (MIT), Cambridge, MA 02139, USA. [3]Department of Crystalline Materials Science, Nagoya University, Nagoya 464-8603, Japan. [4]Department of Physics, Northeastern University, Boston, MA 02115, USA.

*Present address: Department of Physics, Zhejiang University, Hangzhou, China.
†Present address: Department of Physics, Clark University, Worcester, MA 01610, USA.
‡Present address: Department of Physics, Boston College, Chestnut Hill, MA 02467, USA.
§Present address: Institute for Solid State Physics, University of Tokyo, Tokyo, Japan.
‖Present address: Department of Physics, Pennsylvania State University, University Park, PA 16802, USA.
¶Corresponding author. E-mail: jhoffman@physics.harvard.edu (J.E.H.); ehudson@psu.edu (E.W.H.)

lation by Pb doping both simplify momentum space measurements. Additionally, the separation between the expected QPT near optimal doping and the well-characterized PG onset at much higher doping (*12*, *13*) allows a clear investigation of the relationship between these two phenomena. We thus carried out a systematic investigation of Bi2201 at four different dopings (Fig. 1A), all of which display signatures of both the PG and the superconducting gap (*14*, *15*) in their low-temperature spectra (Fig. 1B). To extract FS information, we mapped their differential conductance $g(\boldsymbol{r}, E)$, proportional to the local density of states (DOS) of the sample, as a function of position r and energy E. We used ratio maps, $Z(\boldsymbol{r}, E) = g(\boldsymbol{r}, +E) / g(\boldsymbol{r}, -E)$, to enhance the quasi-particle interference (QPI) signal and cancel the setpoint effect (*16*), then we Fourier-transformed the data. This technique can highlight dominant QPI wave vectors that arise from elastic scattering between momentum space regions of high joint density of states (JDOS), thus enabling a probe of the FS (*17*, *18*).

In our most underdoped samples (UD25K and UD32K), we found a set of energy-dependent wave vectors $\{q_i\}$ following the "octet model" (*17*) (Fig. 2A). From these $\{q_i\}$, we extracted points on the Fermi surface, but we found that they extend only to the antiferromagnetic Brillouin zone (AFBZ) boundary (Fig. 2I), similar to the behavior previously observed in Bi2212 (*18*). At higher doping (in UD32K, OPT35K, and OD15K samples), we found a "triplet" feature (outlined in black in Fig. 2, F to H). This feature exists at multiple sub-PG energies without apparent dispersion (fig. S3). However, its relative prominence at large q and low energies distinguishes it from the static checkerboard (*19*, *20*), charge density wave (*21*), smectic (*22*), or fluctuating stripe (*23*) states that appear near $q \sim (0, \frac{1}{4} \cdot \frac{2\pi}{a_0})$ at low energies or near $q \sim (0, \frac{3}{4} \cdot \frac{2\pi}{a_0})$ around the PG energy.

To understand the momentum space origin of this triplet QPI, we followed (*24*, *25*) and, taking into account reported spectral broadening (*9*, *26*) that is particularly acute in the antinode,

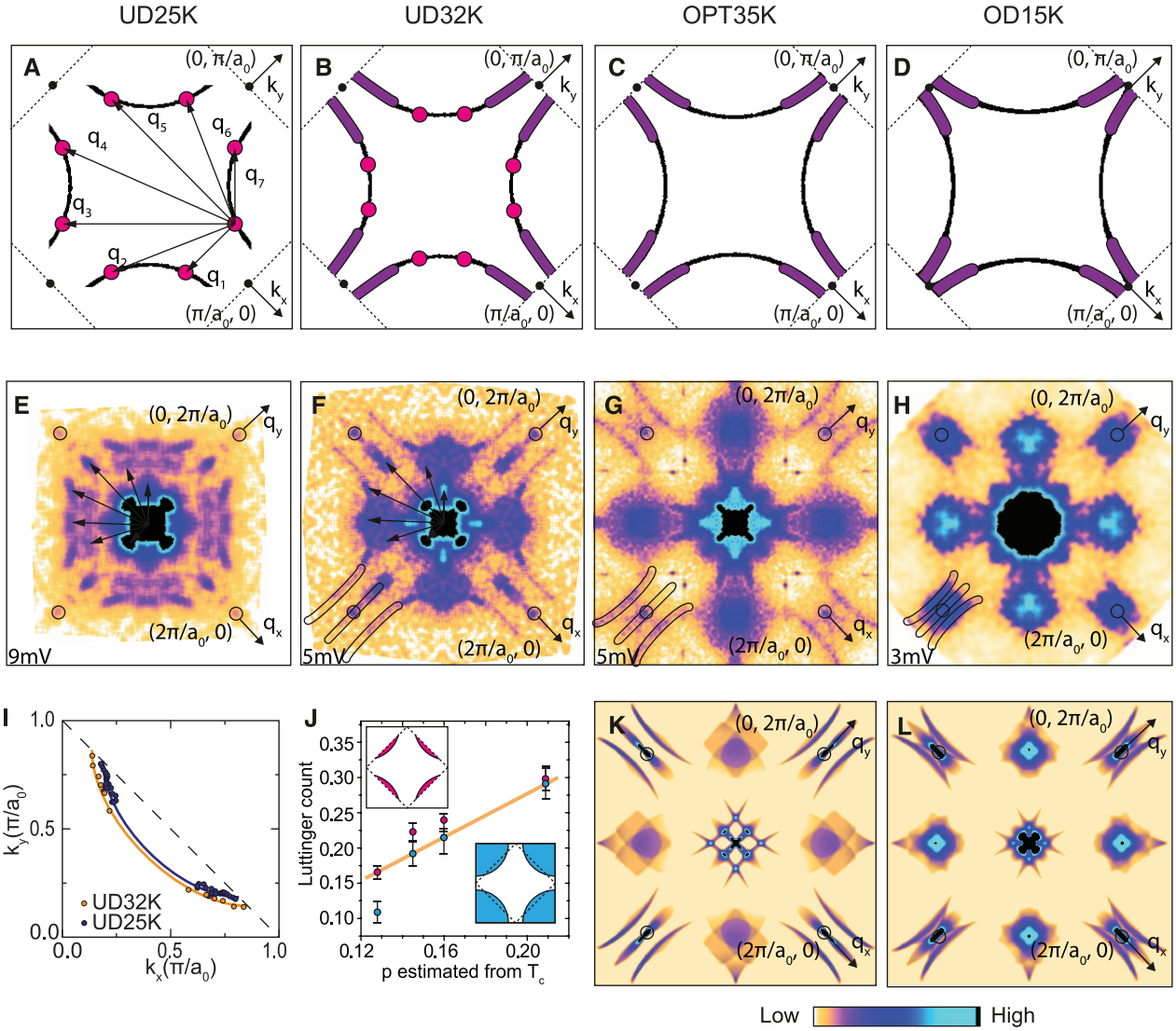

Fig. 2. QPI. (**A** to **D**) Schematic of the high-DOS regions which contribute to QPI, superimposed on the calculated tight-binding FS (*15*) for each doping. Pink circles represent regions contributing to octet QPI. Purple regions represent the FS sections contributing to antinodal QPI. (**E** to **H**) Low-energy $Z(q, E)$ on four samples: UD25K at E = 9 mV (E), UD32K at E = 5 mV (F), OPT35K at E = 5 mV (G), and OD15K at E = 3 mV (H). In UD25K (E) and UD32K (F) samples, conventional octet QPI is observed, dispersing with energy. In UD32K (F), OPT35K (G), and OD15K (H) samples, antinodal QPI appears. The evolution from octet to antinodal QPI shows the transition from small to large FS. (**I**) Locus of maximum DOS in the Bogoliubov band from fitting octet QPI peaks. Orange and blue lines show tight-binding fits. The BQP interference pattern vanishes around the AFBZ boundary (dashed line). (**J**) Luttinger hole counts from small FS (pink dots and upper inset) and large FS (blue dots and lower inset) scenarios versus hole-doping estimated from T_c. Error bars on the y axis come from the 0.01-eV chemical potential uncertainty in the tight-binding parameterization. (**K** to **L**) Autocorrelation of broadened antinodal FS sections marked with purple in (C) and (D). This model of antinodal scattering agrees well with the data (G and H).

computed the autocorrelation of all antinodal states within a small energy window of the high-temperature FS. This autocorrelation corresponds to the low-energy antinodal JDOS in the presence of pair breaking and matches well with the data (compare Fig. 2, K and L to G and H). The triplet feature thus arises from states near the antinodal FS. It could be considered as a continuation of octet QPI, and we refer to it hereafter as the antinodal QPI. We conclude that the extinction of octet QPI at the AFBZ boundary in underdoped Bi2201 (Fig. 2I), followed by the appearance of antinodal QPI at higher doping, reveals the FS reconstruction (*1*–*4*) shown schematically in Fig. 2J.

Our UD32K sample shows both octet and antinodal QPI (Fig. 2F), suggesting that the QPT occurs near $p \sim 0.15$ doping. We support this point by using a modified Luttinger count to compute the hole concentration p in both the large and small FS scenarios according to

$$p_{\text{large}} = \frac{2A_{\text{blue}}}{A_{\text{BZ}}} - 1;\ p_{\text{small}} = \frac{A_{\text{pink}}}{A_{\text{AFBZ}}} = \frac{2A_{\text{pink}}}{A_{\text{BZ}}}$$

where A_{blue} and A_{pink} are the areas schematically indicated in the insets to Fig. 2J and computed according to the tight binding fits in table S2. The x-axis hole concentration is independently estimated from the measured superconducting temperature (T_c) (*27*). In either small or large FS scenario alone, we observed a sudden drop in Luttinger hole count from UD32K to UD25K. However, by using p_{small} in the UD25K sample and p_{large} in the other samples, we found the expected linear relationship between the Luttinger count and the estimated hole concentration, providing further evidence of a small to large FS reconstruction upon increasing doping. These results agree well with high-field Hall measurements of similar Bi2201 samples (*28*), suggesting that high-field measurements in general are revealing rather than creating small Fermi pockets.

Surprisingly, the PG appears to be unaffected by this QPT, with a spectral signature that evolves smoothly through the transition. The PG in Bi2201 is known (*12*–*14*) to exist well into the overdoped region of the phase diagram (Fig. 1A), rather than terminating near optimal doping as in some other cuprates (*29*). Thus, the FS reconstruction we observe is distinct from the onset of the PG.

We now face the question of how complete the coexistence of superconductivity and the PG is, both in momentum- and real space. To address the former, we used the phase-sensitive technique of magnetic field–dependent QPI imaging (Fig. 3). In a superconductor, the QPI participants are Bogoliubov quasi-particles (BQPs), quantum-coherent mixtures of particles and holes. The scattering intensity of BQPs depends on the relative sign of the superconducting order parameter across the scattering wave vector. Furthermore, it is known empirically (*30*) and theoretically (*31*) that sign-preserving scattering

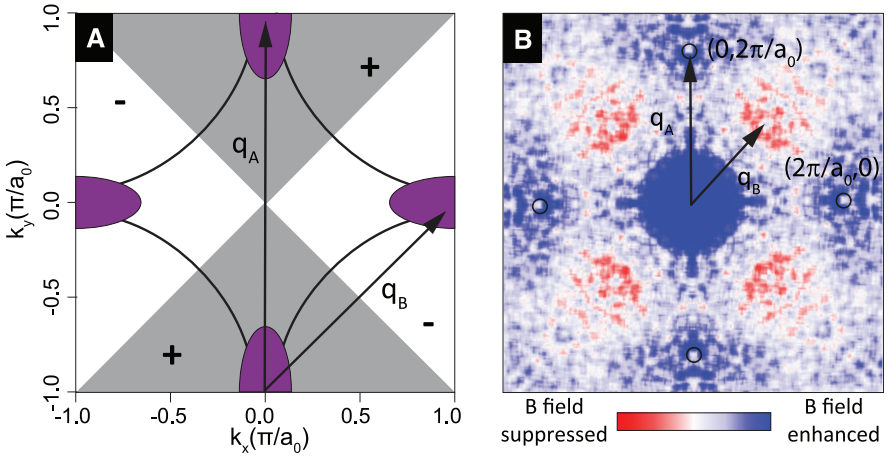

Fig. 3. Antinodal *d*-wave pairing. (**A**) First Brillouin zone of the OD15K sample, with calculated tight-binding FS. White and gray areas represent opposite signs of the *d*-wave superconducting order parameter. The antinodal bands approach each other in overdoped materials and are represented by merged purple regions around *M* points for simplicity. The simplified scattering vectors q_A and q_B are shown as black arrows. (**B**) $Z(q, 6\text{ mV}, 9\text{T}) - Z(q, 6\text{ mV}, 0\text{T})$ showing *B*-suppressed (red) and *B*-enhanced (blue) weights, demonstrating the presence of superconducting BQP at the FS antinode where they coexist with the PG.

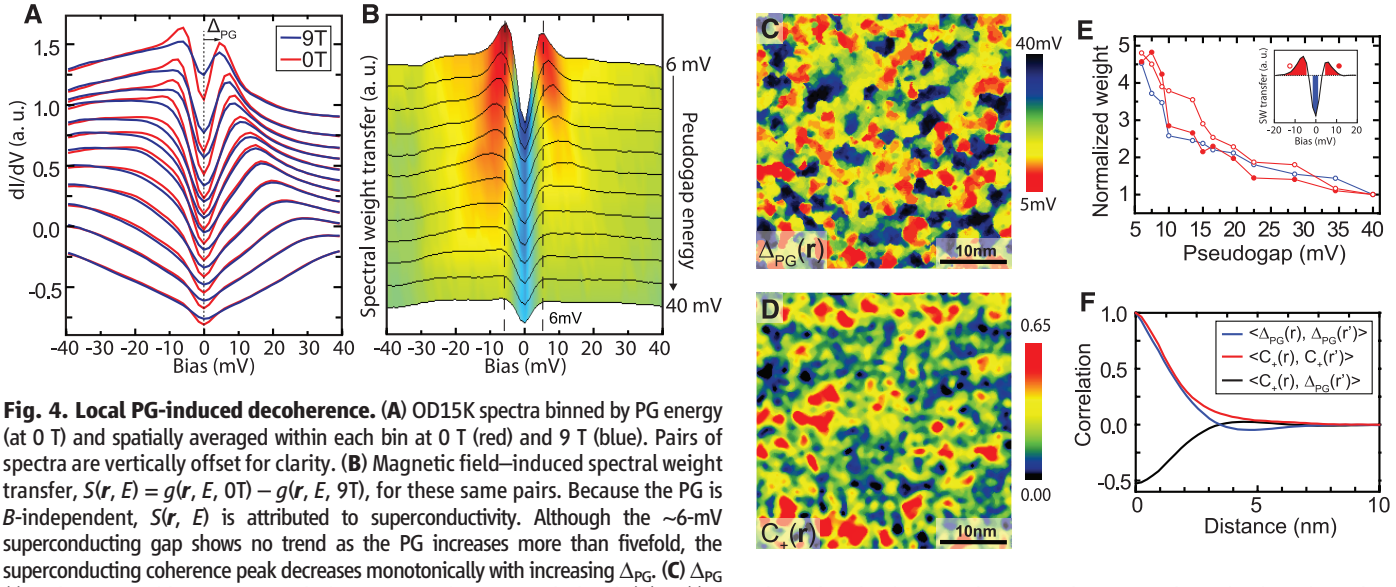

Fig. 4. Local PG-induced decoherence. (**A**) OD15K spectra binned by PG energy (at 0 T) and spatially averaged within each bin at 0 T (red) and 9 T (blue). Pairs of spectra are vertically offset for clarity. (**B**) Magnetic field–induced spectral weight transfer, $S(\boldsymbol{r}, E) = g(\boldsymbol{r}, E, 0\text{T}) - g(\boldsymbol{r}, E, 9\text{T})$, for these same pairs. Because the PG is *B*-independent, $S(\boldsymbol{r}, E)$ is attributed to superconductivity. Although the ~6-mV superconducting gap shows no trend as the PG increases more than fivefold, the superconducting coherence peak decreases monotonically with increasing Δ_{PG}. (**C**) $\Delta_{PG}(\boldsymbol{r})$ in the same field of view from which Figs. 2H and 3B were calculated. (**D**) $C_+(\boldsymbol{r})$ map, defined as the difference between coherence peak amplitude and zero bias conductance [$S(\boldsymbol{r}, 6\text{ mV}) - S(\boldsymbol{r}, 0\text{ mV})$], of the same area as (**C**). The color bar is reversed for better comparison to $\Delta_{PG}(\boldsymbol{r})$. (**E**) Dependence of coherence peak amplitude and gap depth on Δ_{PG}. Coherence peak amplitude is integrated from ±6 to ±12 mV, whereas gap depth is integrated from −1.5 to 1.5 mV. Red solid and hollow dots stand for the positive and negative coherence peak weight, respectively. Blue hollow dots stand for gap depth. All data shown are normalized to their values at Δ_{PG} = 40 mV for better comparison. (**F**) Angle-averaged autocorrelations of $\Delta_{PG}(\boldsymbol{r})$ (blue) and $C_+(\boldsymbol{r})$ (red) and cross-correlation of $\Delta_{PG}(\boldsymbol{r})$ with $C_+(\boldsymbol{r})$ (black).

will be enhanced by a magnetic field, whereas sign-reversing scattering will appear relatively suppressed. A *d*-wave superconducting order parameter changes sign in *k*-space (Fig. 3A); in our OD15K sample, the two branches of the FS around the antinode are close to each other (Fig. 2D) and are shown for simplicity in Fig. 3A as a single merged region at each antinode. Thus for a *d*-wave superconductor with antinodal BQPs, the simplified scattering process q_A would be sign-preserving, whereas q_B would be sign-reversing. We observed that the sign-preserving q_A scattering is enhanced in a magnetic field, whereas the sign-reversing q_B scattering appears relatively suppressed (Fig. 3B; full field dependence in fig. S12). This field-dependent QPI is thus fully consistent with the existence of *d*-wave BQPs in the antinodal FS.

For completeness, we considered several other possible causes of our field-dependent antinodal QPI. First, we ruled out a field-enhanced charge order, such as has been observed in vortex cores in Bi2212 (*19*), because it would not explain the existence of both enhanced and suppressed scattering. Second, we ruled out (π, π) and incommensurate orders such as antiferromagnetism, spin density waves, stripes, or *d*-density waves, which would not explain the features around both (π, π) and $(2\pi, 0)$. Thus, we note that although non–phase-sensitive ARPES and STM (*12*, *32*) postulated a similar scenario, our field-dependent phase-sensitive QPI directly demonstrates the coexistence of *d*-wave BQPs and the PG at the antinode.

Given that the PG and superconductivity (SC) coexist in momentum space at the antinode, we next examine the nature of their spatial coexistence. We turn to a real space study of OD15K, where, among our samples, the PG magnitude (Δ_{PG}) is most comparable to the SC gap (Δ_{SC}). To focus on the superconducting component, we suppress superconductivity with a 9-T field and then remove the field-independent (PG) density of states by computing $S(\boldsymbol{r}, E) = g(\boldsymbol{r}, E, 0\text{ T}) - g(\boldsymbol{r}, E, 9\text{ T})$. Compared with Fig. 4A, where spatially disparate spectra show that Δ_{PG} varies by more than a factor of five across the field of view, $S(\boldsymbol{r}, E)$ shows a relatively homogeneous gap of 6 mV (Fig. 4B), consistent with the homogeneous superconducting gap reported by a previous temperature-dependent STM measurement on samples from the same batch (*14*). Our results thus support the two-gap scenario (*8*, *14*, *32*, *33*) and suggest that $S(\boldsymbol{r}, E)$ is indicative of the local superconducting spectrum.

Although the inhomogeneous PG does not appear to relate to the magnitude Δ_{SC} of the superconducting order parameter (vertical dashed lines in Fig. 4B), the coherence peak amplitude and gap depth, which have been shown to scale with superfluid density (*7*, *33*, *34*), decay markedly in regions of large Δ_{PG} (Fig. 4E). Similar to the ARPES analysis (*33*), we quantified the real space decoherence effect of the pseudogap by defining a local coherent spectral weight, $C_{\pm}(\boldsymbol{r}) = S(\boldsymbol{r}, \pm 6\text{ mV}) - S(\boldsymbol{r}, 0\text{ mV})$, which increases with the height of the coherence peaks and depth of the gap. Visual comparison between maps of $\Delta_{PG}(\boldsymbol{r})$ and $C_{+}(\boldsymbol{r})$ (Fig. 4, C and D), and their cross-correlation in Fig. 4F, demonstrate that stronger PG [larger $\Delta_{PG}(\boldsymbol{r})$] correlates with local suppression of superconducting coherence on a very short (~2 nm) length scale.

Thus, our phase-sensitive momentum-space and normalized real-space measurements demonstrate that at high doping the PG coexists with superconductivity at the antinode but correlates with suppressed superconducting coherence, suggesting a competitive relationship. We also find that the PG transition is well separated from a zero-field FS reconstruction that occurs near optimal doping, where SC is strongest. The existence of a QPT near optimal doping has been long expected and suggested by a variety of other measurements (*29*). However, its differentiation from the PG onset is unexpected and requires explanations of two phenomena rather than one. A number of theories have been proposed to explain the FS QPT. We can rule out the effect of crystal structure on the basis of its observed doping independence (*35*). Our observed FS evolution is partly consistent with the phenomenological Yang-Rice-Zhang model (*36*) but does not show the completion of the arc to a pocket found in the closely related microscopic FL* model (*37*). Other orders such as antiferromagnetic fluctuations, charge order (*38*), *d*-density wave (*39*), quadrupole density wave (*40*, *41*), and vestigial nematicity (*42*) are all consistent with our observation of the FS QPT. With respect to the PG onset, we observe that charge modulations are similarly unaffected by the FS QPT (figs. S17 and S18), suggesting that the PG is associated with fluctuating charge order (*23*), which is pinned in all of our samples. Such charge order has recently been reported to compete with SC in YBCO (*43*), whereas non-superconducting $La_{1.6-x}Nd_{0.4}Sr_xCuO_4$ shows static charge order ("stripes") (*44*), suggesting that such order (or its fluctuations) may be a universal competitor to superconductivity in the cuprates.

References and Notes

1. N. Doiron-Leyraud *et al.*, *Nature* **447**, 565–568 (2007).
2. M. R. Norman, *Physics* **3**, 86 (2010).
3. S. E. Sebastian, N. Harrison, G. G. Lonzarich, *Rep. Prog. Phys.* **75**, 102501 (2012).
4. B. Vignolle *et al.*, *Nature* **455**, 952–955 (2008).
5. S. E. Sebastian *et al.*, *Proc. Natl. Acad. Sci. U.S.A.* **107**, 6175–6179 (2010).
6. D. LeBoeuf *et al.*, *Phys. Rev. B* **83**, 054506 (2011).
7. D. L. Feng *et al.*, *Science* **289**, 277–281 (2000).
8. K. Tanaka *et al.*, *Science* **314**, 1910–1913 (2006).
9. I. M. Vishik *et al.*, *Nat. Phys.* **5**, 718–721 (2009).
10. H.-B. Yang *et al.*, *Phys. Rev. Lett.* **107**, 047003 (2011).
11. I. M. Vishik *et al.*, *Proc. Natl. Acad. Sci. U.S.A.* **109**, 18332–18337 (2012).
12. T. Kondo *et al.*, *Nat. Phys.* **7**, 21–25 (2010).
13. G. Q. Zheng, P. L. Kuhns, A. P. Reyes, B. Liang, C. T. Lin, *Phys. Rev. Lett.* **94**, 047006 (2005).
14. M. C. Boyer *et al.*, *Nat. Phys.* **3**, 802–806 (2007).
15. R.-H. He *et al.*, *Science* **331**, 1579–1583 (2011).
16. T. Hanaguri *et al.*, *Nat. Phys.* **3**, 865–871 (2007).
17. K. McElroy *et al.*, *Nature* **422**, 592–596 (2003).
18. Y. Kohsaka *et al.*, *Nature* **454**, 1072–1078 (2008).
19. J. E. Hoffman *et al.*, *Science* **295**, 466–469 (2002).
20. C. Howald, H. Eisaki, N. Kaneko, A. Kapitulnik, *Proc. Natl. Acad. Sci. U.S.A.* **100**, 9705–9709 (2003).
21. W. D. Wise *et al.*, *Nat. Phys.* **4**, 696–699 (2008).
22. M. J. Lawler *et al.*, *Nature* **466**, 347–351 (2010).
23. C. V. Parker *et al.*, *Nature* **468**, 677–680 (2010).
24. U. Chatterjee *et al.*, *Phys. Rev. Lett.* **96**, 107006 (2006).
25. K. McElroy *et al.*, *Phys. Rev. Lett.* **96**, 067005 (2006).
26. J. W. Alldredge *et al.*, *Nat. Phys.* **4**, 319–326 (2008).
27. Y. Ando *et al.*, *Phys. Rev. B* **61**, R14956–R14959 (2000).
28. F. F. Balakirev *et al.*, *Nature* **424**, 912–915 (2003).
29. J. L. Tallon *et al.*, *Phys. Status Solidi B* **215**, 531–540 (1999).
30. T. Hanaguri *et al.*, *Science* **323**, 923–926 (2009).
31. T. Pereg-Barnea, M. Franz, *Phys. Rev. B* **78**, 020509 (2008).
32. J.-H. Ma *et al.*, *Phys. Rev. Lett.* **101**, 207002 (2008).
33. T. Kondo, R. Khasanov, T. Takeuchi, J. Schmalian, A. Kaminski, *Nature* **457**, 296–300 (2009).
34. B. Sacépé *et al.*, *Nat. Phys.* **7**, 239–244 (2011).
35. I. Zeljkovic *et al.*, *Nat. Mater.* **11**, 585–589 (2012).
36. K.-Y. Yang, T. M. Rice, F.-C. Zhang, *Phys. Rev. B* **73**, 174501 (2006).
37. M. Punk, S. Sachdev, *Phys. Rev. B* **85**, 195123 (2012).
38. N. Harrison, S. E. Sebastian, "On the relationship between charge ordering and the Fermi arcs observed in underdoped high T_c superconductors," http://arxiv.org/abs/1401.6590 (2014).
39. X. Jia, P. Goswami, S. Chakravarty, *Phys. Rev. B* **80**, 134503 (2009).
40. K. B. Efetov, H. Meier, C. Pépin, *Nat. Phys.* **9**, 442–446 (2013).
41. S. Sachdev, R. La Placa, *Phys. Rev. Lett.* **111**, 027202 (2013).
42. L. Nie, G. Tarjus, S. A. Kivelson, "Quenched disorder and vestigial nematicity in the pseudo-gap regime of the cuprates," http://arxiv.org/abs/1311.5580 (2013).
43. J. Chang *et al.*, *Nat. Phys.* **8**, 871–876 (2012).
44. J. M. Tranquada, B. J. Sternlieb, J. D. Axe, Y. Nakamura, S. Uchida, *Nature* **375**, 561–563 (1995).

Acknowledgments: We thank H.-I. Ha for her role in the Harvard STM system construction and E. Dalla Torre, E. Demler, S. Kivelson, L. Taillefer, P. Phillips, F. Zhang, R. He, J. C. Davis, P. Coleman, I. Mazin, L. Benfatto, C. Varma, T. Honma, M. Randeria, and N. Trivedi for helpful discussion. Work at Harvard University was supported by the Air Force Office of Scientific Research under grant FA9550-06-1-0531, the NSF under grants DMR-0847433 and DMR-1103860, and the New York Community Trust–George Merck Fund. Work at MIT was supported by a Cottrell Scholarship awarded by the Research Corporation and by the Materials Research Science and Engineering Center and Early Career Development (CAREER) programs of the NSF. Work at Northeastern University was supported by the U.S. Department of Energy (DOE), Office of Science, Basic Energy Sciences contract number DE-FG02-07ER46352, and benefited from Northeastern University's Advanced Scientific Computation Center, theory support at the Advanced Light Source, Berkeley and the allocation of time at the National Energy Research Scientific Computing supercomputing center through DOE grant number DE-AC02-05CH11231. T.K., T.T., and H.I. synthesized and characterized the samples. M.B., K.C., and D.W. performed the STM measurements on UD25K, UD32K, and OPT35K samples; Y.Y., T.W., and M.Z. performed the magnetic field–dependent STM measurements on OD15K samples. Y.H. analyzed the data and wrote the manuscript, with input from A.S., M.M.Y., and S.S. P.M. and R.S.M. performed theoretical simulations, with advice from A.B. E.W.H. and J.E.H. advised the experiments and analysis, and shaped the manuscript. The authors declare no competing financial interests. Correspondence and requests for materials should be addressed to J.E.H. (jhoffman@physics.harvard.edu) and E.W.H. (ehudson@psu.edu).

Supplementary Materials

www.sciencemag.org/content/344/6184/608/suppl/DC1
Materials and Methods
Figs. S1 to S18
Tables S1 to S4
References (*45*–*73*)

14 May 2013; accepted 4 April 2014
10.1126/science.1248221

Simultaneous Transitions in Cuprate Momentum-Space Topology and Electronic Symmetry Breaking

K. Fujita,[1,2,3]* Chung Koo Kim,[1]* Inhee Lee,[1] Jinho Lee,[1,4,5] M. H. Hamidian,[1,2] I. A. Firmo,[2] S. Mukhopadhyay,[2,6] H. Eisaki,[7] S. Uchida,[3] M. J. Lawler,[2,8] E.-A. Kim,[2] J. C. Davis[1,2,9,10]†

The existence of electronic symmetry breaking in the underdoped cuprates and its disappearance with increased hole density p are now widely reported. However, the relation between this transition and the momentum-space ($\vec{\mathbf{k}}$-space) electronic structure underpinning the superconductivity has not yet been established. Here, we visualize the $\vec{\mathbf{Q}} = 0$ (intra–unit-cell) and $\vec{\mathbf{Q}} \neq 0$ (density-wave) broken-symmetry states, simultaneously with the coherent $\vec{\mathbf{k}}$-space topology, for $Bi_2Sr_2CaCu_2O_{8+\delta}$ samples spanning the phase diagram $0.06 \leq p \leq 0.23$. We show that the electronic symmetry-breaking tendencies weaken with increasing p and disappear close to a critical doping $p_c = 0.19$. Concomitantly, the coherent $\vec{\mathbf{k}}$-space topology undergoes an abrupt transition, from arcs to closed contours, at the same p_c. These data reveal that the $\vec{\mathbf{k}}$-space topology transformation in cuprates is linked intimately with the disappearance of the electronic symmetry breaking at a concealed critical point.

The highest known superconducting critical temperature T_c (*1*–*3*) occurs atop the $T_c(p)$ (where p is hole density) "dome" of hole-doped cuprates (Fig. 1A). In addition to the superconductivity, electronic broken-symmetry states (*4*) have also been reported at low p in many such compounds. Wave vector $\vec{\mathbf{Q}} = 0$ (intra–unit-cell) symmetry breaking, typically of 90°-rotational (C_4) symmetry, is reported in $YBa_2Cu_3O_{6+\delta}$, $Bi_2Sr_2CaCu_2O_{8+\delta}$, and $HgBa_2CuO_{4+x}$ (*5*–*14*). Finite wave vector $\vec{\mathbf{Q}} \neq 0$ (density-wave) modulations breaking translational symmetry, long detected in underdoped $La_{2-x-y}Nd_ySr_xCuO_4$ and $La_{2-x}Ba_xCuO_4$ (*15*, *16*), are now also reported in underdoped $YBa_2Cu_3O_{7-\delta}$, $Bi_2Sr_2CuO_{6+\delta}$, and $Bi_2Sr_2CaCu_2O_{8+\delta}$ (*17*–*25*). Summarizing all such reports in Fig. 1A reveals some stimulating observations. First, although the $\vec{\mathbf{Q}} = 0$ and $\vec{\mathbf{Q}} \neq 0$ states are detected by widely disparate techniques and are distinct in terms of symmetry, they seem to follow approximately the same phase-diagram trajectory (shaded band Fig. 1A), as if facets of a single phenomenon (*26*). The second implication is that a critical point (perhaps a quantum critical point) associated with these broken-symmetry states may be concealed beneath the $T_c(p)$ dome. Numerous earlier studies reported sudden alterations in many electronic and magnetic characteristics near $p = 0.19$ (*2*, *3*, *27*), but whether these phenomena are caused by electronic symmetry changes (*28*) at a critical point was unknown.

In momentum space ($\vec{\mathbf{k}}$-space), the hole-doped cuprates also exhibit an unexplained transition in electronic structure with increasing hole density. Open contours, or "Fermi arcs" (*29*–*32*), are reported at low p in all compounds studied, whereas at high p closed holelike pockets surrounding $\vec{\mathbf{k}} = (\pm 1, \pm 1)\pi/a_0$ (where a_0 is the unit cell dimension) are observed (*33*, *34*). One possibility is that such a transition could occur due to the disappearance of an electronic ordered state, with the resulting modifications to the Brillouin zone geometry altering the topology of the electronic bands (*28*).

Our strategy, therefore, is a simultaneous examination of both the $\vec{\mathbf{k}}$-space electronic structure and the $\vec{\mathbf{Q}} = 0$ and $\vec{\mathbf{Q}} \neq 0$ broken-symmetry states, over a sufficiently wide range of p to include any concealed critical point. The objective is to search for a relation between the broken-symmetry

[1]Condensed Matter Physics and Materials Science Department, Brookhaven National Laboratory, Upton, NY 11973, USA. [2]Laboratory of Atomic and Solid State Physics, Department of Physics, Cornell University, Ithaca, NY 14853, USA. [3]Department of Physics, University of Tokyo, Bunkyo-ku, Tokyo 113-0033, Japan. [4]Institute for Basic Science, Seoul 151-747, Republic of Korea. [5]Department of Physics and Astronomy, Seoul National University, Seoul 151-747, Korea. [6]Cornell Center for Materials Research, Cornell University, Ithaca, NY 14853, USA. [7]Institute of Advanced Industrial Science and Technology, Tsukuba, Ibaraki 305-8568, Japan. [8]Department of Physics and Astronomy, Binghamton University, Binghamton, NY 13902, USA. [9]School of Physics and Astronomy, University of St. Andrews, Fife KY16 9SS, Scotland. [10]Kavli Institute at Cornell for Nanoscale Science, Cornell University, Ithaca, NY 14853, USA.

*These authors contributed equally to this work.
†Corresponding author. E-mail: jcseamusdavis@gmail.com

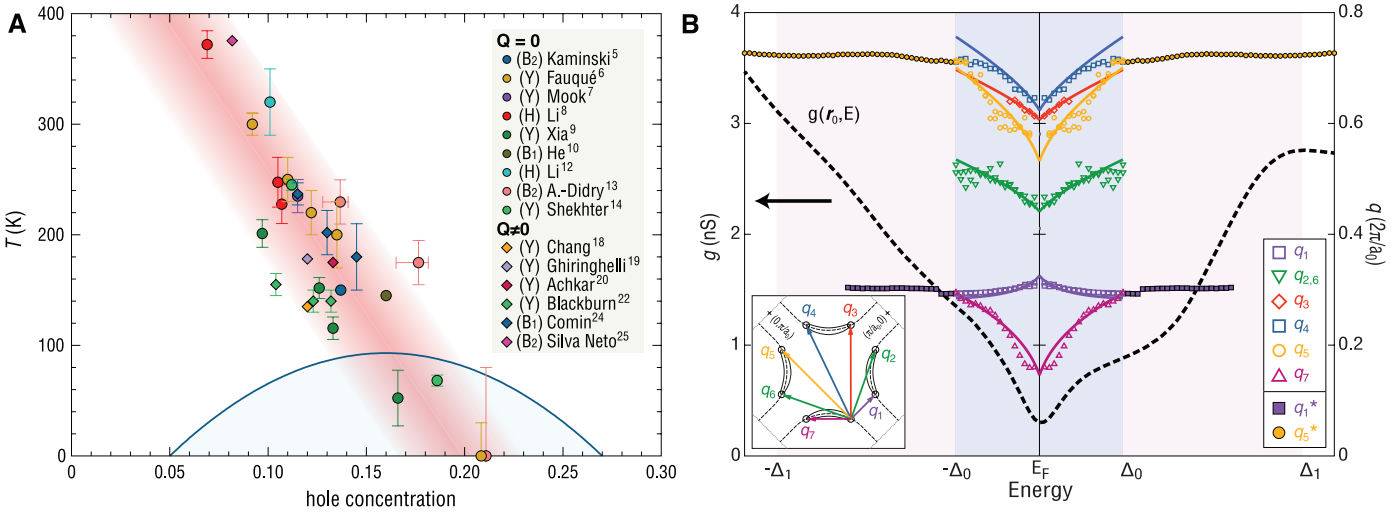

Fig. 1. Hole-density dependence of cuprate broken-symmetry states. (**A**) Phase diagram of hole-doped cuprates showing the $T_c(p)$ "dome" (blue curve). Symbols denote the onset temperature (T) of two types of symmetry breaking reported in $Bi_2Sr_2CuO_{6+\delta}(B_1)$, $Bi_2Sr_2CaCu_2O_{8+\delta}(B_2)$, $YBa_2Cu_3O_{7-\delta}(Y)$, and $HgBa_2CuO_{4+x}(H)$. Circles, $\vec{\mathbf{Q}} = 0$ (intra–unit-cell) symmetry breaking; diamonds, $\vec{\mathbf{Q}} \neq 0$ broken translational symmetry (density waves). Error bars indicate the uncertainties in estimated hole concentration (horizontal) and the onset temperatures (vertical). (**B**) The dashed black curve denotes the typical differential conductance spectrum $g(E)$ of underdoped $Bi_2Sr_2CaCu_2O_{8+\delta}$ here at $p = 0.06$. The pale blue shaded region indicates where the dispersive $\vec{\mathbf{q}}_m(E)$; $m = 1, 2, \ldots, 7$ Bogoliubov QPI wave vectors indicative of Cooper pair breaking exist (color coded in inset); they disappear at energy Δ_0. Solid curves, simulation for QPI in a $d_{x^2-y^2}$ symmetry superconductor; pink shaded regions, quasi-static conductance modulations (density waves) exhibiting wave vectors $\vec{\mathbf{q}}_1^*$ and $\vec{\mathbf{q}}_5^*$.

states (*5*–*25*) and the Fermi surface (FS) topology (*29*–*34*). Fourier transform analysis of spectroscopic imaging scanning tunneling microscopy (SI-STM) is distinctive in that it allows access simultaneously to the $\vec{\mathbf{Q}} = 0$ and $\vec{\mathbf{Q}} \neq 0$ broken-symmetry states (*26*, *35*) and to the $\vec{\mathbf{k}}$-space electronic structure by using quasi-particle scattering interference (QPI) (*35*). The SI-STM tip-sample differential tunneling conductance $g(\vec{\mathbf{r}}, E = eV)$ (e, electron charge; V, tip-sample bias voltage) at location $\vec{\mathbf{r}}$ and energy E relates to density of electronic states $N(\vec{\mathbf{r}}, E)$ as

$$g(\vec{\mathbf{r}}, E) \propto \left[eI_S / \int_0^{eV_S} N(\vec{\mathbf{r}}, E')dE'\right] N(\vec{\mathbf{r}}, E)$$ (I_S and V_S are arbitrary parameters) (*35*). In cuprates, it is necessary to study the ratio of the differential conductances $Z(\vec{\mathbf{r}},|E|) = g(\vec{\mathbf{r}}, E)/g(\vec{\mathbf{r}}, -E)$ because it suppresses the severe systematic errors due to the unknown denominator $\int_0^{eV_S} N(\vec{\mathbf{r}}, E')dE'$ by division, thereby allowing $\vec{\mathbf{q}}$-vectors and symmetries to be measured correctly (*35*).

The $\vec{\mathbf{k}}$-space structure of coherent Bogoliubov quasi-particles is then detectable, because scattering between the eight density-of-states maxima at $\vec{\mathbf{k}}_j(E)$; $j = 1, 2, ...,8$ (circles in inset Fig. 1B) produces interference patterns with wave vectors $\vec{\mathbf{q}}(E) = \vec{\mathbf{k}}_j(E) - \vec{\mathbf{k}}_i(E)$ in $Z(\vec{\mathbf{q}}, E)$, the Fourier transform of $Z(\vec{\mathbf{r}}, E)$. At low p, one finds that the predicted set of seven inequivalent Bogoliubov QPI wave vectors $\vec{\mathbf{q}}_m(E)$; $m = 1, 2, ...,7$ (inset Fig. 1B) exist only below an energy Δ_0 (Fig. 1B), indicating that it is the limiting binding energy of a Cooper pair (*35*). At $|E| > \Delta_0$, the dispersive $\vec{\mathbf{q}}_m$ disappear (Fig. 1B and movie S1) and are replaced by broken-symmetry states consisting of (i) spatial modulations with energetically quasi-static wave vectors $\vec{\mathbf{q}}_1^*$ and $\vec{\mathbf{q}}_5^*$ breaking translational symmetry (*24*, *25*, *35*, *36*) and (ii) $\vec{\mathbf{Q}} = 0$ (intra–unit-cell) breaking of C_4 symmetry detectable either directly in $\vec{\mathbf{r}}$-space (*11*, *36*) or at the Bragg wave vectors (*11*, *26*, *35*). But the complete doping dependence of these broken-symmetry signatures was unknown.

To determine the $\vec{\mathbf{k}}$-space topology of coherent states across the phase diagram of $Bi_2Sr_2CaCu_2O_{8+\delta}$, we use a recently developed approach (*37*) that requires measurement of only a single QPI wave vector, $\vec{\mathbf{q}}_4$ (blue arrow in Fig. 1B, inset). Brillouin zone geometry (Fig. 2A) means that $\vec{\mathbf{q}}_4$ is simply related to the FS states $\vec{\mathbf{k}}_F$ as

$$\vec{\mathbf{q}}_4(E = \Delta(\vec{\mathbf{k}}_F)) = 2\vec{\mathbf{k}}_F \qquad (1)$$

Here $\Delta(\vec{\mathbf{k}})$ is the $d_{x^2-y^2}$ superconducting energy gap whose energy-minimum follows the trajectory of $\vec{\mathbf{k}}_F$. An image of the locations of $\vec{\mathbf{q}}_4(E)/2$ for all $0 < |E| < \Delta_0$ (pale blue region in Fig. 1B) then yields the FS location of coherent states that contribute to Cooper pairing. An efficient way to locate these states is to sum all the $Z(\vec{\mathbf{q}}, E)$ images to the energy Δ_0

$$\Lambda(\vec{\mathbf{q}}) = \sum_{E\geq 0}^{\Delta_0} Z(\vec{\mathbf{q}}, E) \qquad (2)$$

and then to plot the contour of $\vec{\mathbf{q}}_4$ within these $\Lambda(\vec{\mathbf{q}})$ images (see supplementary text section I and figs. S1 and S2) (*38*). The power of this procedure is demonstrated in the determination of the FS in Fig. 2B (supplementary text section II) (*38*). Applying this $\Lambda(\vec{\mathbf{q}})$ approach to determine the doping dependence of $\vec{\mathbf{k}}$-space topology, we find very different results at low and high p. Figure 2C shows $\Lambda(\vec{\mathbf{q}})$ at $p = 0.14$, whereas Fig. 2D shows $\Lambda(\vec{\mathbf{q}})$ at $p = 0.23$. The most prominent difference between the two is that the contour of $\vec{\mathbf{q}}_4$ only spans four arcs in Fig. 2C, whereas it completes four closed curves surrounding $\vec{\mathbf{q}} = (\pm 1, \pm 1)2\pi/a_0$ in Fig. 2D. He *et al.* report similar phenomena in $Bi_2Sr_2CuO_{6+\delta}$ (*37*). In Fig. 2E, we show the complete doping dependence of measured $\vec{\mathbf{q}}_4/2$ over the full range of p (supplementary text section II) (*38*). A notable transition in $\vec{\mathbf{k}}$-space topology is observed within the narrow range $p \approx 0.19 \pm 0.01$, wherein the arc of coherent Bogoliubov states typical of low p suddenly switches to the complete closed contour surrounding $\vec{\mathbf{k}} = (\pm 1, \pm 1)\pi/a_0$ (supplementary text section II, fig. S3, and movie S2) (*38*).

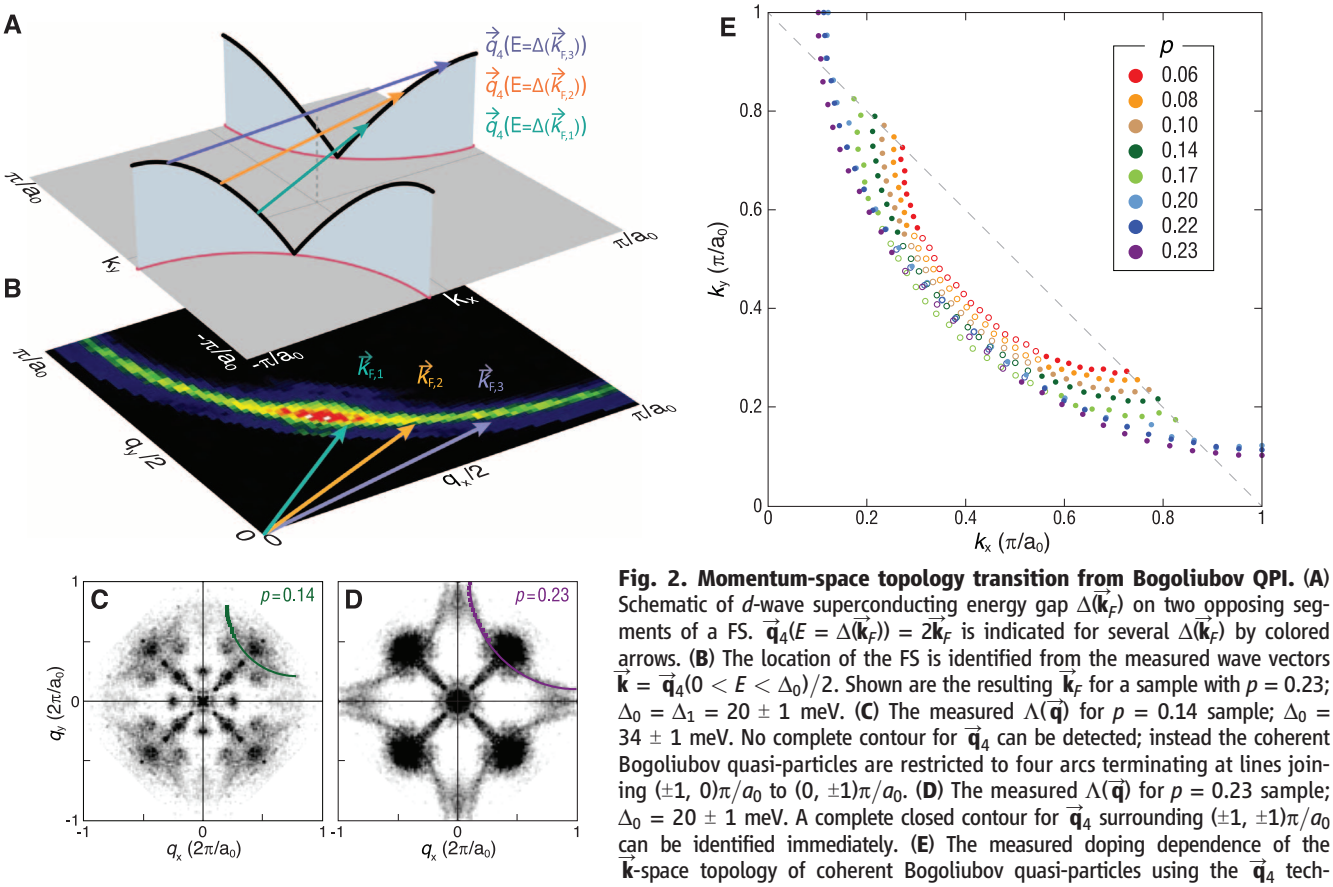

Fig. 2. Momentum-space topology transition from Bogoliubov QPI. (A) Schematic of *d*-wave superconducting energy gap $\Delta(\vec{\mathbf{k}}_F)$ on two opposing segments of a FS. $\vec{\mathbf{q}}_4(E = \Delta(\vec{\mathbf{k}}_F)) = 2\vec{\mathbf{k}}_F$ is indicated for several $\Delta(\vec{\mathbf{k}}_F)$ by colored arrows. **(B)** The location of the FS is identified from the measured wave vectors $\vec{\mathbf{k}} = \vec{\mathbf{q}}_4(0 < E < \Delta_0)/2$. Shown are the resulting $\vec{\mathbf{k}}_F$ for a sample with $p = 0.23$; $\Delta_0 = \Delta_1 = 20 \pm 1$ meV. **(C)** The measured $\Lambda(\vec{\mathbf{q}})$ for $p = 0.14$ sample; $\Delta_0 = 34 \pm 1$ meV. No complete contour for $\vec{\mathbf{q}}_4$ can be detected; instead the coherent Bogoliubov quasi-particles are restricted to four arcs terminating at lines joining $(\pm 1, 0)\pi/a_0$ to $(0, \pm 1)\pi/a_0$. **(D)** The measured $\Lambda(\vec{\mathbf{q}})$ for $p = 0.23$ sample; $\Delta_0 = 20 \pm 1$ meV. A complete closed contour for $\vec{\mathbf{q}}_4$ surrounding $(\pm 1, \pm 1)\pi/a_0$ can be identified immediately. **(E)** The measured doping dependence of the $\vec{\mathbf{k}}$-space topology of coherent Bogoliubov quasi-particles using the $\vec{\mathbf{q}}_4$ technique. The transition from arcs terminating at the lines $(\pm 1, 0)\pi/a_0$ to $(0, \pm 1)\pi/a_0$ to complete hole-pockets surrounding $(\pm 1, \pm 1)\pi/a_0$ at $p \approx 0.19$ is evident.

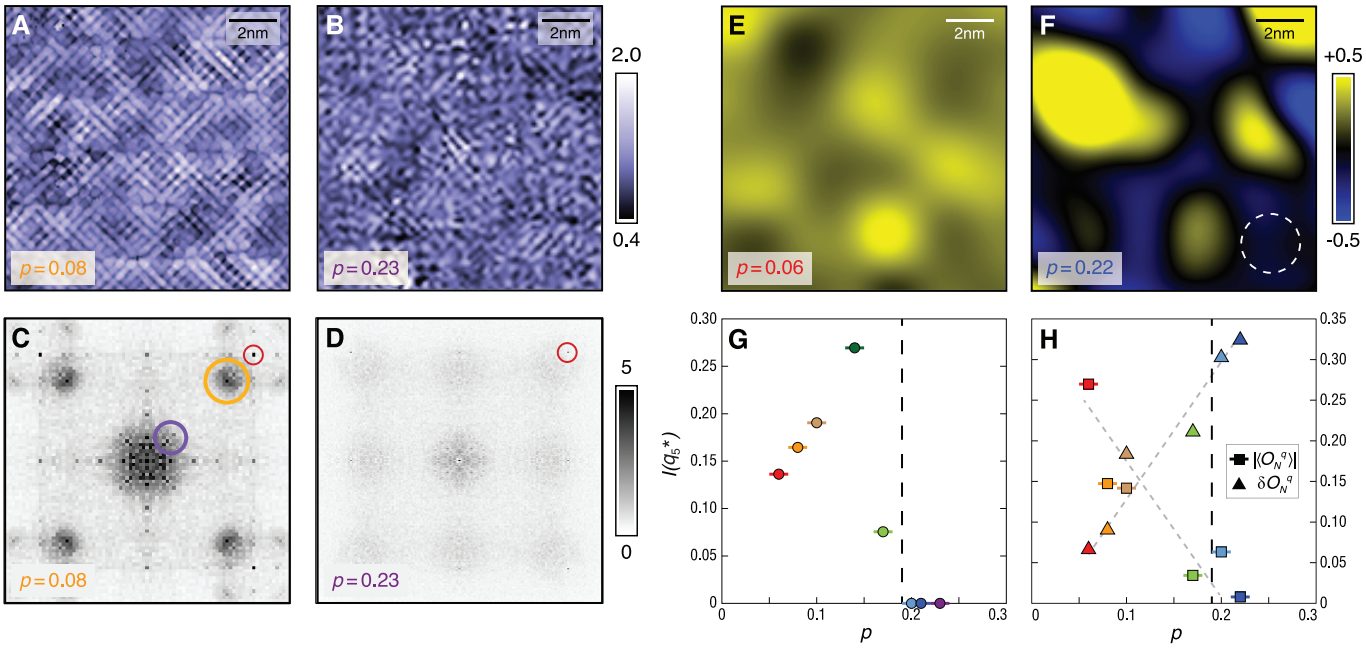

Fig. 3. Measurements of hole-density dependence of $\vec{Q} = 0$ and $\vec{Q} \neq 0$ ordering. (**A**) $Z(\vec{r}, E \sim \Delta_1)$ for $p = 0.08$. Incommensurate conductance modulations are clearly seen; $\Delta_1 = 84 \pm 1$ meV. (**B**) $Z(\vec{r}, E \sim \Delta_1)$ for $p = 0.23$ is shown; $\Delta_1 = 20 \pm 1$ meV. No specific $\vec{q}$-vector for modulations is seen, although the QPI signature of Bogoliubov quasi-particles does produce a jumbled standing wave pattern. (**C**) $Z(\vec{q}, E \sim \Delta_1)$ for $p = 0.08$ from (A); $\vec{q}_1^*$ and $\vec{q}_5^*$ wave vectors are indicated by purple and orange circles, respectively. Bragg peaks in (C) and (D) are denoted by red circles. (**D**) $Z(\vec{q}, E \sim \Delta_1)$ for $p = 0.23$ from (B). No specific broken-symmetry state wave vectors are apparent, whereas the residual dispersive effects of Bogoliubov quasi-particles are seen. (**E**) $\vec{Q} = 0$ broken C_4-symmetry order parameter $O_N^q(\vec{r}, E \sim \Delta_1)$ for $p = 0.06$; $\Delta_1 = 124 \pm 1$ meV. This whole field of view is a single color, indicating that long-range $\vec{Q} = 0$ intra–unit-cell C_4 symmetry breaking exists. (**F**) Intra–unit-cell broken C_4 symmetry $O_N^q(\vec{r}, E \sim \Delta_1)$ for $p = 0.22$; $\Delta_1 = 28 \pm 1$ meV. Long-range order has been lost, but nanoscale domains of opposite nematicity persist. The dashed circle represents the spatial resolution of the analysis. (**G**) Intensity of incommensurate modulations with wave vector $\vec{q}_5^*$, $I(\vec{q}_5^*)$ initially increases upon doping peaking near $p \sim 1/8$, and then diminishes to reach zero at $p \approx 0.19$. (**H**) Squares indicate measured spatial average value of the $\vec{Q} = 0$ broken C_4 symmetry $|< O_N^q(\vec{r}, E \sim \Delta_1) >|$, which diminishes steadily with increasing p, to reach zero near $p = 0.19$. Triangles indicate measured standard deviation of O_N^q : $\delta O_N^q(\vec{r}, E \sim \Delta_1)$.

Next we study the broken-symmetry states by examining $Z(\vec{r}, E)$ measured simultaneously with the $\vec{k}$-space data in Fig. 2, but now for $\Delta_0 < |E| < \Delta_1$ (pink regions in Fig. 1B), where Δ_1 is the maximum detectable gap [pseudogap at low p and maximum superconducting gap at high p (*35*)]. These images exhibit several distinct broken spatial symmetries whose evolution with p we explore. Figure 3A shows $Z(\vec{r}, E \sim \Delta_1)$ for $p = 0.08$, whereas Fig. 3B shows $Z(\vec{r}, E \sim \Delta_1)$ for $p = 0.23$, with their Fourier transforms $Z(\vec{q}, E \sim \Delta_1)$ shown in Fig. 3, C and D, respectively. The former exhibits the widely reported (*24*–*26*, *35*, *36*) quasi-static wave vectors $\vec{q}_1^*$ and $\vec{q}_5^*$ of states with local symmetry breaking along with the Bragg peaks (red circle), whereas in the latter, the quasi-static wave vectors $\vec{q}_1^*$ and $\vec{q}_5^*$ have disappeared. The $\vec{Q} = 0$ broken C_4-symmetry states can be detected by using the lattice-phase–resolved nematic order parameter (*11*)

$$O_N^q(E) = ReZ(\vec{Q}_y, E) - ReZ(\vec{Q}_x, E) \quad (3)$$

The $\vec{Q}_x$ and $\vec{Q}_y$ are the Bragg vectors after the necessary transformation to nearly perfect lattice periodicity in $Z(\vec{r}, E)$ so that real and imaginary components of the Bragg amplitudes, $ReZ(\vec{Q}, E)$ and $ImZ(\vec{Q}, E)$, are well defined (*11*, *35*). The measured $O_N^q(\vec{r}, E \sim \Delta_1)$ for $p = 0.06$ and $O_N^q(\vec{r}, E \sim \Delta_1)$ for $p = 0.23$ are shown in Fig. 3, E and F, respectively (supplementary text section IV) (*38*). Here we see that the extensive order in $O_N^q(\vec{r}, E \sim \Delta_1)$ observed at low p (*11*) has disappeared at high p, leaving nanoscale domains of opposite nematicity (*26*) probably nucleated by disorder. The doping dependence of $I(\vec{q}_5^*)$, the intensity of the $\vec{q}_5^*$ modulations in $Z(\vec{q}, E)$, is shown in Fig. 3G (supplementary text section III and figs. S4 and S5) (*38*), whereas the dependence of the spatially averaged magnitude $|< O_N^q(\vec{r}, E \sim \Delta_1) >|$ of the $\vec{Q} = 0$ C_4 breaking is shown in Fig. 3H (supplementary text section IV and figs. S7 and S8) (*38*). These plots reveal that the more extended $\vec{Q} = 0$ broken symmetry and the shorter-range ordering tendencies in $\vec{Q} \neq 0$ modulations (*11*, *26*, *35*) disappear near a critical doping $p_c \approx 0.19$.

Figure 4A is a schematic summary of our findings, from Bogoliubov QPI techniques (*32*, *35*, *37*), on the dependence of $\vec{k}$-space electronic structure with increasing p. Fig. 4B shows that the wave vectors $\vec{k} = \vec{q}_E/2$ of states at which Bogoliubov QPI disappears (circles) evolve along the $\vec{k}$-space lines $(\pm 1, 0)\pi/a_0 \rightarrow (0, \pm 1)\pi/a_0$ with increasing p. Concomitantly, the quasi-static wave vectors $\vec{q}_1^*/2$ and $(2\pi - \vec{q}_5^*)/2$ of broken-symmetry states also evolve on the same trajectory (squares). Thus, the $\vec{q}_1^*$ and $\vec{q}_5^*$ wave vectors of incommensurate (density-wave) modulations evolve with doping, as shown in Fig. 4C (*35*). Figure 4D shows the area of $\vec{k}$-space between the arc and the line $(1, 0)\pi/a_0 \rightarrow (0, 1)\pi/a_0$ (left inset) increasing proportional to hole density p (*32*, *35*); at $p = 0.19$, there is a transition to a diminishing area of electron count as $1\text{-}p$ for the closed-contour FS topology. Finally, we show in Fig. 4, E to G, that the critical point $p_c \approx 0.19$ is associated microscopically with a transition to conventional d-wave Bogoliubov QPI on a complete FS (simulated in Fig. 4E and measured at $p > p_c$ in 4G) from a highly distinct form of scattering (Fig. 4F) of unknown cause (*39*).

To recapitulate: With increasing hole density, the $\vec{Q} \neq 0$ modulations (density waves) weaken and disappear at $p_c \approx 0.19$ (Fig. 1A and Fig. 3, A to D and G). Concurrently, the $\vec{Q} = 0$ broken-symmetry (intra–unit-cell nematic) states become progressively more disordered (*13*) and reach a zero average value at approximately the same p_c (Fig. 1A and Fig. 3, E to F and H). Simultaneously, the $\vec{k}$-space topology of coherent Bogoliubov quasi-particles (or the FS supporting their superconducting gap) undergoes an abrupt transition from arcs to closed contours (Figs. 2 and 4 and movie S2) (*38*). This key transformation of cuprate electronic structure is therefore linked directly with disappearance of electronic symmetry breaking. However, this phenomenology

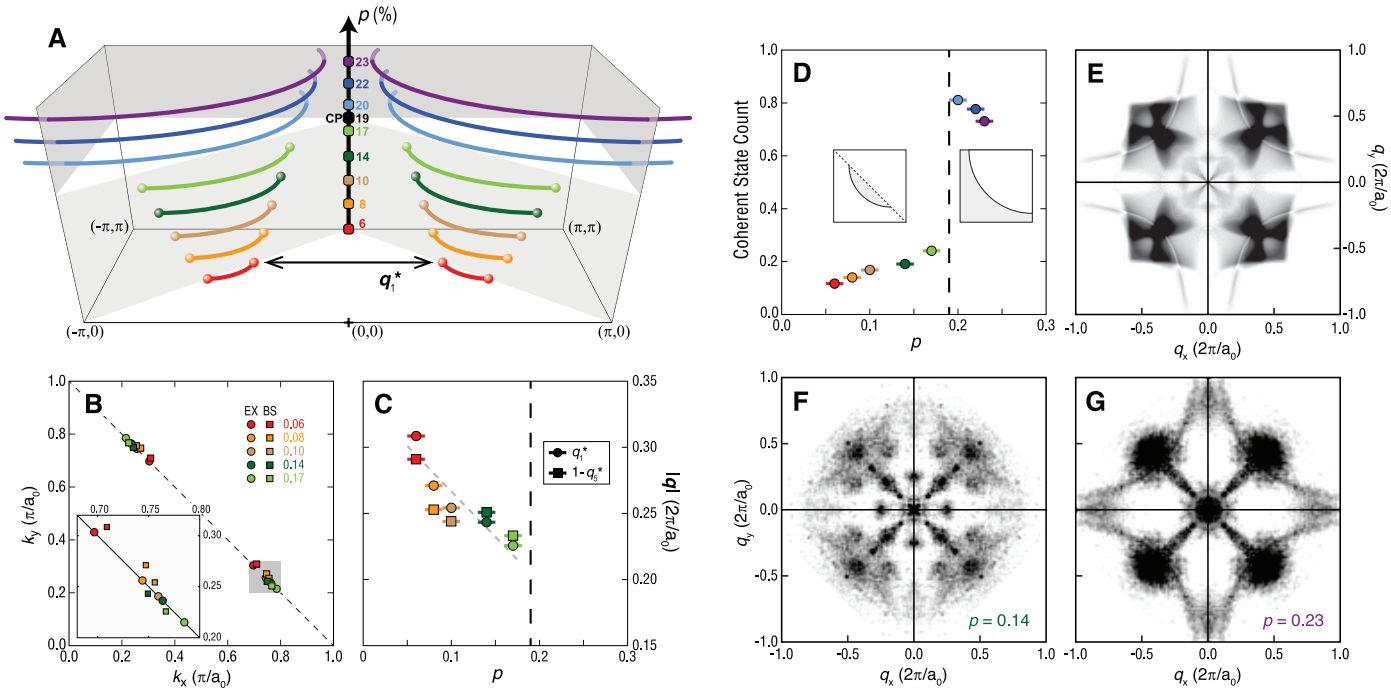

Fig. 4. Interlinked $\vec{k}$-space structure of Bogoliubov QPI and $\vec{Q} \neq 0$ symmetry breaking at lines joining $(\pm1,0)\pi/a_0$ to $(0,\pm1)\pi/a_0$. (**A**) Schematic of $\vec{k}$-space locus of states generating Bogoliubov QPI with increasing hole density in $Bi_2Sr_2CaCu_2O_{8+\delta}$. An abrupt transition occurs at $p \approx 0.19$. (**B**) Measured wave vectors $\vec{k}$ of states at which Bogoliubov QPI disappears $\vec{q}_E/2$ (circles), and those of the quasi-static broken-symmetry modulations with $\vec{q}_1^*/2$ and $(2\pi-\vec{q}_5^*)/2$ (squares). (**C**) Measured doping dependence of wave vectors of incommensurate conductance modulations (density waves) $\vec{q}_1^*$ and $\vec{q}_5^*$ derived from (B) (*35*). The vertical dashed line indicates p_c. (**D**) The $\vec{k}$-space area between the arc and the line joining $(\pm1, 0)\pi/a_0$ to $(0, \pm1)\pi/a_0$ is proportional to p. With the appearance of the closed FS at $p \approx 0.19$, there is a transition to a diminishing area of electron count 1-p. Insets, $\vec{k}$-space areas used. (**E**) T-matrix scattering interference simulation for $\Lambda(\vec{q})$ for a complete FS and *d*-wave gap with conventional (time-reversal preserving) scattering. (**F**) Measured $\Lambda(\vec{q})$ for $p = 0.14$ ($\Delta_0 = 34\pm1$meV) is in sharp contrast to the simulation result in (E). (**G**) For $p = 0.23$, $\Lambda(\vec{q})$ conforms closely to the conventional *d*-wave Bogoliubov scattering scheme, as anticipated in (E).

also exhibits many peculiar components unexpected within a simple FS reconstruction scenario. First, the coevolution and contiguous disappearance at p_c of the signatures of two distinct broken symmetries (Figs. 1A and 3) reinforce the deductions that they are microscopically closely related (*11*, *26*, *35*, *36*, *40*). Second, because the $\vec{Q} \neq 0$ modulations exhibit wave vectors generated by scattering regions (hot spots) moving along the $\vec{k}$-space lines $(\pm1, 0)\pi/a_0 \rightarrow (0, \pm1)\pi/a_0$ (Fig. 4, A to C) (*32*, *35*), FS nesting provides an inadequate explanation for the cuprate density waves. Third, the abrupt $\vec{k}$-space topology change at p_c (Fig. 2E and Fig. 4, A, F, and G) exhibits characteristics more reminiscent of an antinodal coherence recovery transition (*41*) than of a conventional band reorganization. Fourth, because the disappearance of the pseudogap is associated axiomatically with the reappearance of coherent antinodal states, and because the latter is precisely what occurs at p_c (Figs. 2E and 4A), the pseudogap (*1*–*3*) and the electronic symmetry breaking (*5*–*25*) must be intimately linked (Fig. 1A). Finally, as neither long-range $\vec{Q} \neq 0$ order nor any associated quantum critical point can exist with quenched disorder (*40*), a nematic critical point, at which the electronic symmetry breaking between the two oxygen sites within the CuO_2 unit cell (*11*, *26*, *35*, *36*) disappears, seems most consistent with our observations.

References and Notes

1. J. Orenstein, A. J. Millis, *Science* **288**, 468–474 (2000).
2. M. R. Norman, D. Pines, C. Kallin, *Adv. Phys.* **54**, 715–733 (2005).
3. T. Timusk, B. Statt, *Rep. Prog. Phys.* **62**, 61–122 (1999).
4. S. A. Kivelson, E. Fradkin, V. J. Emery, *Nature* **393**, 550–553 (1998).
5. A. Kaminski *et al.*, *Nature* **416**, 610–613 (2002).
6. B. Fauqué *et al.*, *Phys. Rev. Lett.* **96**, 197001 (2006).
7. H. A. Mook, Y. Sidis, B. Fauqué, V. Balédent, P. Bourges, *Phys. Rev. B* **78**, 020506 (2008).
8. Y. Li *et al.*, *Nature* **455**, 372–375 (2008).
9. J. Xia *et al.*, *Phys. Rev. Lett.* **100**, 127002 (2008).
10. R.-H. He *et al.*, *Science* **331**, 1579–1583 (2011).
11. M. J. Lawler *et al.*, *Nature* **466**, 347–351 (2010).
12. Y. Li *et al.*, *Phys. Rev. B* **84**, 224508 (2011).
13. S. De Almeida-Didry *et al.*, *Phys. Rev. B* **86**, 020504(R) (2012).
14. A. Shekhter *et al.*, *Nature* **498**, 75–77 (2013).
15. J. M. Tranquada, B. J. Sternlieb, J. D. Axe, Y. Nakamura, S. Uchida, *Nature* **375**, 561–563 (1995).
16. M. Hücker *et al.*, *Phys. Rev. B* **83**, 104506 (2011).
17. Y.-J. Kim, G. Gu, T. Gog, D. Casa, *Phys. Rev. B* **77**, 064520 (2008).
18. J. Chang *et al.*, *Nat. Phys.* **8**, 871–876 (2012).
19. G. Ghiringhelli *et al.*, *Science* **337**, 821–825 (2012).
20. A. J. Achkar *et al.*, *Phys. Rev. Lett.* **109**, 167001 (2012).
21. D. H. Torchinsky, F. Mahmood, A. T. Bollinger, I. Božović, N. Gedik, *Nat. Mater.* **12**, 387–391 (2013).
22. E. Blackburn *et al.*, *Phys. Rev. Lett.* **110**, 137004 (2013).
23. J. P. Hinton *et al.*, *Phys. Rev. B* **88**, 060508(R) (2013).
24. R. Comin *et al.*, *Science* **343**, 390–392 (2014).
25. E. H. da Silva Neto *et al.*, *Science* **343**, 393–396 (2014).
26. A. Mesaros *et al.*, *Science* **333**, 426–430 (2011).
27. J. L. Tallon, J. W. Loram, *Physica C* **349**, 53–68 (2001).
28. A. J. Millis, M. R. Norman, *Phys. Rev. B* **76**, 220503(R) (2007).
29. A. G. Loeser *et al.*, *Science* **273**, 325–329 (1996).
30. M. R. Norman *et al.*, *Nature* **392**, 157–160 (1998).
31. K. M. Shen *et al.*, *Science* **307**, 901–904 (2005).
32. Y. Kohsaka *et al.*, *Nature* **454**, 1072–1078 (2008).
33. M. Platé *et al.*, *Phys. Rev. Lett.* **95**, 077001 (2005).
34. B. Vignolle *et al.*, *Nature* **455**, 952–955 (2008).
35. K. Fujita *et al.*, *J. Phys. Soc. Jpn.* **81**, 011005 (2012).
36. Y. Kohsaka *et al.*, *Science* **315**, 1380–1385 (2007).
37. Y. He *et al.*, *Science* **344**, 608–611 (2014).
38. Materials and methods are available as supplementary materials on *Science* Online.
39. E.-A. Kim, M. J. Lawler, *Phys. Rev. B* **81**, 132501 (2010).
40. L. Nie, G. Tarjus, S. A. Kivelson, http://arxiv.org/abs/1311.5580
41. U. Chatterjee *et al.*, *Proc. Natl. Acad. Sci. U.S.A.* **108**, 9346–9349 (2011).

Acknowledgments: We are particularly grateful to S. Billinge, J. E. Hoffman, S. A. Kivelson, D.-H. Lee, and A. P. Mackenzie for key scientific advice. We thank K. Efetov, E. Fradkin, P. D. Johnson, J. W. Orenstein, C. Pepin, S. Sachdev, and

K. M. Shen for helpful discussions and communications. Experimental studies were supported by the Center for Emergent Superconductivity, an Energy Frontier Research Center, headquartered at Brookhaven National Laboratory (BNL) and funded by the U.S. Department of Energy under grant DE-2009-BNL-PM015, as well as by a Grant-in-Aid for Scientific Research from the Ministry of Science and Education (Japan) and the Global Centers of Excellence Program for Japan Society for the Promotion of Science. C.K.K. acknowledges support from the FlucTeam program at BNL under contract DE-AC02-98CH10886. J.L. acknowledges support from the Institute for Basic Science, Korea. I.A.F. acknowledges support from Fundação para a Ciência e a Tecnologia, Portugal, under fellowship number SFRH/BD/60952/2009. S.M. acknowledges support from NSF grant DMR-1120296 to the Cornell Center for Materials Research. Theoretical studies at Cornell University were supported by NSF grant DMR-1120296 to Cornell Center for Materials Research and by NSF grant DMR-0955822. The original data are archived by Davis Group, BNL, and Cornell University.

Supplementary Materials
www.sciencemag.org/content/344/6184/612/suppl/DC1
Materials and Methods
Supplementary Text
Figs. S1 to S9
References (*42*–*45*)
Movies S1 and S2

21 November 2013; accepted 20 March 2014
10.1126/science.1248783

Direct, Nonoxidative Conversion of Methane to Ethylene, Aromatics, and Hydrogen

Xiaoguang Guo,[1] Guangzong Fang,[1] Gang Li,[2,3] Hao Ma,[1] Hongjun Fan,[2] Liang Yu,[1] Chao Ma,[4] Xing Wu,[5] Dehui Deng,[1] Mingming Wei,[1] Dali Tan,[1] Rui Si,[6] Shuo Zhang,[6] Jianqi Li,[4] Litao Sun,[5] Zichao Tang,[2] Xiulian Pan,[1] Xinhe Bao[1]*

The efficient use of natural gas will require catalysts that can activate the first C–H bond of methane while suppressing complete dehydrogenation and avoiding overoxidation. We report that single iron sites embedded in a silica matrix enable direct, nonoxidative conversion of methane, exclusively to ethylene and aromatics. The reaction is initiated by catalytic generation of methyl radicals, followed by a series of gas-phase reactions. The absence of adjacent iron sites prevents catalytic C-C coupling, further oligomerization, and hence, coke deposition. At 1363 kelvin, methane conversion reached a maximum at 48.1% and ethylene selectivity peaked at 48.4%, whereas the total hydrocarbon selectivity exceeded 99%, representing an atom-economical transformation process of methane. The lattice-confined single iron sites delivered stable performance, with no deactivation observed during a 60-hour test.

The challenge of converting natural gas into transportable fuels and chemicals (*1*) has been spurred by several emerging industrial trends, including rapidly rising demand for H_2 (for upgrading lower-quality oils) and a global shortage of aromatics caused by shifting refinery targets toward gasoline. Light olefins, which are key chemical feedstocks, are currently made from methanol, which itself is made through multistage catalytic transformations via syngas (a mixture of H_2 and CO) (*2*, *3*), although there is also ongoing research to convert syngas directly to light olefins (*4*, *5*). However, in all such approaches, either CO or H_2 is needed to remove oxygen from CO, resulting in a carbon-atom utilization efficiency below 50%. Despite their low efficiency, high capital and production costs, and enormous CO_2 emissions, syngas routes dominate current and near-term industrial practices for natural gas conversion (*6*, *7*).

Direct conversion of CH_4 is potentially more economical and environmentally friendly but is challenging because CH_4 exhibits high C–H bond strength (434 kJ/mol), negligible electron affinity, large ionization energy, and low polarizability (*8*). In the pioneering work of Keller and Bhasin in the early 1980s, CH_4 was activated with the assistance of oxygen (*9*). This finding initiated a worldwide research surge to explore the high-temperature (>1073 K) oxidative coupling of methane (OCM) to C_2 hydrocarbons (*10*, *11*). Hundreds of catalytic materials have since been synthesized and tested, principally during the 1990s, as well as in recent years. Unfortunately, the presence of O_2 leads irreversibly to overoxidation, resulting in a large amount of the thermodynamically stable end-products CO_2 and H_2O. Thus, the carbon utilization efficiency of OCM remains relatively low (*12*, *13*). Slow progress in discovering new catalysts to circumvent this problem has hindered further development, and no economically viable process has been put into practice so far.

In a recent report, elemental sulfur was used as a softer oxidant than O_2 (*14*): For a 5% CH_4/Ar mixture at 1323 K, the best catalyst, PdS/ZrO_2, gave a CH_4 conversion of ~16% and ethylene selectivity near 20%, albeit at the expense of the by-products CS_2 and H_2S (*14*). In contrast, the bifunctional catalysts based on Mo/zeolites catalyze CH_4 conversion to aromatics (benzene and naphthalene) nonoxidatively, thereby avoiding CO_2 formation (*15*–*18*). CH_4 is activated on the metal sites forming CH_x species, which dimerize to C_2H_y. Subsequent oligomerization on the acidic sites located inside the zeolite pores yields benzene and naphthalene, as well as copious amounts of coke (*19*–*21*). Commercial prospects for this process are further hampered by the instability of zeolites at the very high reaction temperatures.

To achieve direct conversion of CH_4 efficiently, the challenges lie in cleaving the first C–H bond while suppressing further catalytic dehydrogenation, avoiding both CO_2 generation and coke deposition. We report that these conditions can be met using lattice-confined single iron sites embedded in a silica matrix. These sites activate CH_4 in the absence of oxidants, generating methyl radicals, which desorb from the catalyst surface and then undergo a series of gas-phase reactions to yield ethylene, benzene, and naphthalene as the only products (with ethylene dominating at short space-times for a selectivity of ~52.7% at 1293 K). A methane conversion as high as 48.1% is achieved at 1363 K.

The catalysts were obtained by fusing ferrous metasilicate with SiO_2 at 1973 K in air and from commercial quartz, followed by leaching with aqueous HNO_3 and drying at 353 K (*22*). The resulting catalyst was designated 0.5% Fe©SiO_2 (© denotes confinement and here represents a catalyst characterized by the lattice-confined single iron sites embedded within a silica matrix). It contained 0.5 weight percent (wt %) Fe and had a Brunauer–Emmett–Teller surface area of <1 m^2/g. The catalyst was activated in a fixed-bed microreactor in the reaction atmosphere [90 volume percent (vol %) CH_4/N_2] at 1173 K. The effluent was analyzed by online gas chromatography (GC). At 1223 K, CH_4 conversion was 8.1% (Fig. 1A) and increased with temperature, exceeding 48.1% at 1363 K (Fig. 1B). Only ethylene, benzene, and naphthalene were produced; neither coke nor CO_2 was detected, despite the relatively high reaction temperature. A single-pass yield of 48% hydrocarbons is achieved at 1363 K and 21.4 liters per gram of catalyst (gcat) per hour. Selectivities vary from 40.9 to 52.1% for ethylene, 21.0 to 29.1 for benzene, and 23.6 to 38.2% for naphthalene, over the investigated temperature range (1223 to 1363 K).

By comparison, a blank experiment (an empty reactor with no catalyst) under the same conditions showed a CH_4 conversion of only 2.5%, and 95% of the product was coke (Fig. 1A). A test with unmodified SiO_2 as the catalyst yielded virtually

[1]State Key Laboratory of Catalysis, Dalian Institute of Chemical Physics, Chinese Academy of Sciences, Dalian 116023, People's Republic of China. [2]State Key Laboratory of Molecular Reaction Dynamics, Dalian Institute of Chemical Physics, Chinese Academy of Sciences, Dalian 116023, People's Republic of China. [3]State Key Laboratory of Fine Chemicals, Institute of Coal Chemical Engineering, School of Chemical Engineering, Dalian University of Technology, Dalian 116012, People's Republic of China. [4]Beijing National Laboratory for Condensed Matter Physics, Institute of Physics, Chinese Academy of Sciences, Beijing 100190, People's Republic of China. [5]Nano-Pico Center, Key Laboratory of Micro-Electro-Mechanical System (MEMS) of Ministry of Education, Southeast University, Nanjing 210096, People's Republic of China. [6]Shanghai Synchrotron Radiation Facility, Shanghai Institute of Applied Physics, Chinese Academy of Sciences, Shanghai 201204, People's Republic of China.
*Corresponding author. E-mail: xhbao@dicp.ac.cn

the same result (table S1) (*22*). Most notably, the use of 0.5 wt % Fe/SiO_2 as the catalyst (prepared with wet impregnation on amorphous SiO_2 with a high surface area, 348 m^2/g) (*22*) also led to high coke formation (>98%). We have varied the iron loadings, support materials, and preparation methods, which unfortunately do not preclude coke on iron nanoparticles (NPs). For example, coke remained the principal product (>50%) over 0.5% Fe/ZSM. 0.8% Fe/SiO_2 prepared by sol-gel method and 0.2% Fe/SiC (*22*) enhanced selective formation of hydrocarbons to some extent, but still with a considerable amount of coke (Fig. 1A).

Figure S1 (*22*) demonstrates that the reactivity of 0.5% Fe©SiO_2 was very reproducible. All mass balances are above 99%. At 1363 K, the space-time yields for ethylene, benzene, and naphthalene were 91, 18, and 9 mol $kgcat^{-1}$ $hour^{-1}$, respectively. Moreover, the process represents a new and sustainable approach to H_2 production because the by-products are high–value-added hydrocarbons (ethylene and aromatics) instead of coke and CO_2 (*23*, *24*). The yield of H_2 varies with the reaction conditions, and the concentrations in the effluent range from 10.9 to 51.2% (fig. 1D) (*22*).

Furthermore, the 0.5% Fe©SiO_2 catalyst was very stable, and no deactivation was observed during a 60-hour test at 1293 K (Fig. 1C). Methane conversion remained at ~32% throughout this long run. Selectivities to ethylene (52.7%), benzene (21.5%), and naphthalene (25.8%) were constant, and the total selectivity to these products remained >99%. The combination of atom-economy, high selectivity, and high conversion is notable, considering the rather low loading of Fe (0.5 wt %) and very low surface area (<1 m^2/g) of the SiO_2. Although noncatalytic pyrolysis of CH_4 has been extensively studied for light hydrocarbon synthesis, the product is dominated with acetylene accompanied by high coke formation (*25*–*27*). By comparison, the catalytically initiated reaction described here compares very favorably with other reported direct-conversion processes, including pyrolysis, OCM (*13*), and nonoxidative aromatization (*21*). Finally, because natural gas usually contains some ethane, we added 1 and 5 vol % ethane to the reactant stream. The presence of ethane substantially enhanced methane conversion (fig. S2) (*22*), and ethane is almost completely converted, although a small amount of coke is formed at 1173 K and a space velocity of 4.84 liter $gcat^{-1}$ h^{-1}.

The unprecedented efficiency of the catalytically initiated CH_4 conversion process is attributed to the high activity of the coordinatively unsaturated iron sites toward the C-H bond of CH_4 (*28*, *29*). The isolated nature of these sites, as evidenced by sub-angstrom–resolution high-angle annular-dark field (HAADF) scanning transmission electron microscopy (STEM) and in situ x-ray absorption near-edge spectroscopy (XANES), precludes surface C-C coupling and, hence, coke formation. Transmission electron microscopy indicates that in the fresh 0.5% Fe©SiO_2 catalyst, iron oxide NPs with a size of ~3 to 4 nm are distributed homogeneously throughout the SiO_2 matrix (fig. S3) (*22*). A STEM-HAADF image of the catalyst after reaction reveals many bright dots of atomic size scattered across the SiO_2 matrix, highlighted by the red circles in Fig. 2A. Each dot represents an individual Fe atom, considering the much lower contrast of Si and O in the HAADF image. This result suggests that the iron species are redistributed from the original oxide NPs to isolated atoms during catalyst activation.

This hypothesis is validated by the in situ XANES during activation. The near-edge spectrum of the catalyst is similar to that of Fe foil (Fig. 2B). In Fig. 2C, the Fourier-transformed k^3-weighted $\chi(k)$ function (where k is wave number) (*30*) shows that, after activation, the Fe-O scattering paths apparent in the spectrum of the fresh catalyst (line 1) have disappeared,

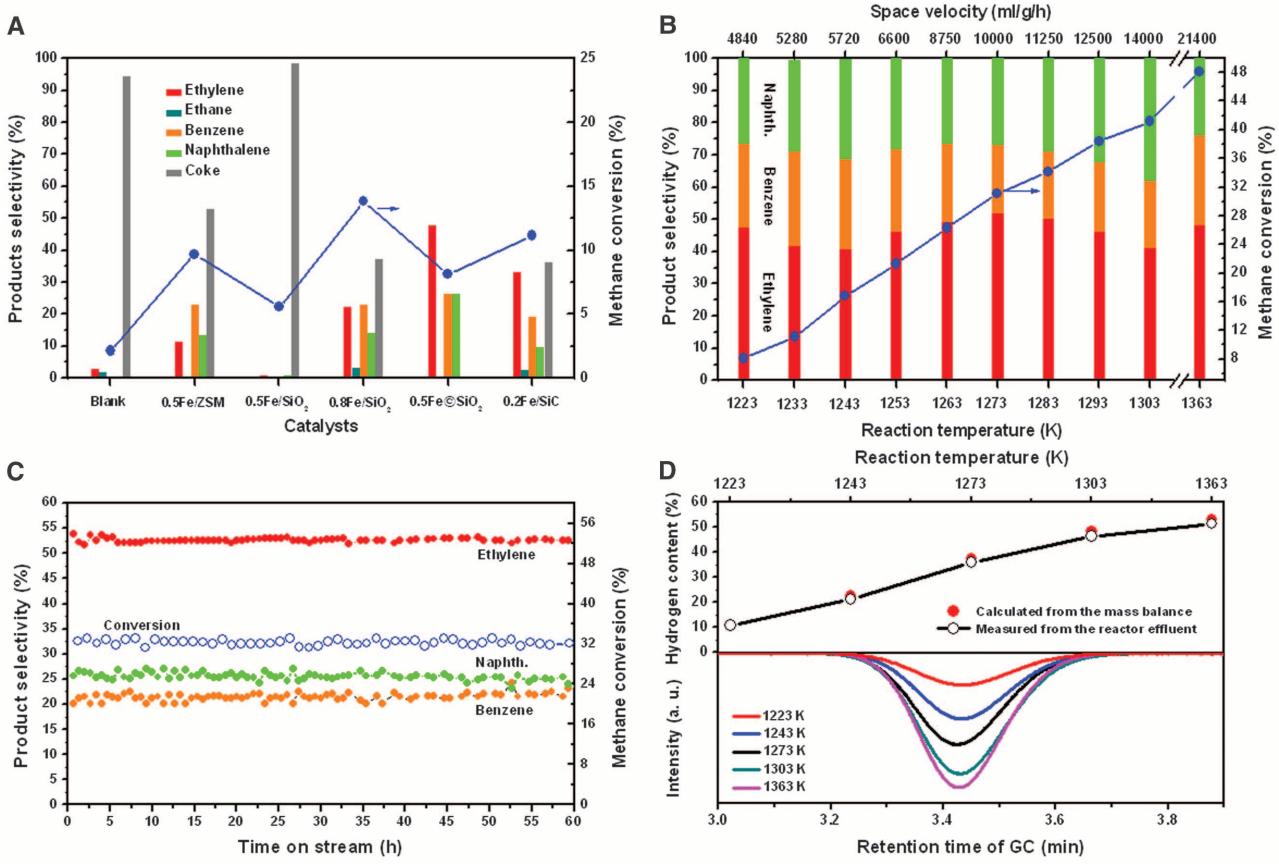

Fig. 1. Reaction performance. (**A**) Comparison of different catalysts at 1223 K and 4.84 liter $gcat^{-1}$ $hour^{-1}$. (**B**) Effect of reaction temperatures and space velocities on the 0.5% Fe©SiO_2 catalyst. Blue circles denote CH_4 conversion, whereas bars represent product selectivities. (**C**) Long-term stability test of 0.5% Fe©SiO_2 at 1293 K and 14.5 liter $gcat^{-1}$ $hour^{-1}$. (**D**) (Top) Hydrogen contents of the reactor effluent (open circles) and the calculated values (solid circles); (bottom) H_2 peaks in GC analysis normalized by the internal standard N_2 (*22*). a. u., arbitrary units.

whereas new scattering paths appear (line 2). They are assigned to Fe-C and Fe-Si paths, by comparison to the spectra of reference materials such as Fe_2O_3, $FeSi_2$, and iron carbides (*31*). In the presence of CH_4 above 1173 K, iron oxide species in the fresh 0.5% Fe©SiO_2 interact extensively with the support, becoming embedded in the silica matrix through bonding to Si and C atoms. Thus, these otherwise extremely reactive, coordinatively unsaturated iron atoms are stabilized and persist under the very harsh reaction conditions. No aggregation was observed, even after prolonged reaction for 60 hours.

In contrast, the 2- to 5-nm-sized iron NPs in 0.5% Fe/SiO_2 (fig. S5a) (*22*) after activation under the same conditions exhibit only a Fe–Fe bond (line 3 in Fig. 2, B and C). This result explains the extensive carbon deposition observed for 0.5% Fe/SiO_2, considering that iron NPs are widely used for the synthesis of carbon nanotubes (*32*). That process involves catalytic cleavage of C–H bonds and dissolution of carbon species into the iron lattice. Subsequent C-C coupling on an iron NP surface and crystallization from the supersaturated carbide solid solution drive the growth of nanotubes (*33*). However, under the harsh reaction conditions in the current reaction, 0.5% Fe/SiO_2 deactivates very rapidly, and iron NPs aggregated and grew to 20 to 30 nm after reaction (fig. S4b) (*22*). These results again highlight the crucial role played by the site isolation of the iron species in 0.5% Fe©SiO_2 in achieving high selectivity toward hydrocarbons and preventing coke formation.

Furthermore, density functional theory (DFT) calculations suggest that the most stable structure in the reactive atmosphere is an iron atom coordinated by one Si and two C atoms and is thus embedded within the SiO_2 matrix, as depicted in Fig. 3A and fig. S5. The calculated Fe–C and Fe–Si bond lengths are 1.6 and 2.4 Å, respectively, which are consistent with those estimated from extended x-ray absorption fine structure (EXAFS) (table S2) (*22*). This lattice-confined single iron site initiates CH_4 dehydrogenation by generating a •CH_3 radical, which subsequently releases from the surface with an energy barrier of 2.32 eV instead of undergoing further dehydrogenation or C-C coupling (fig. S5) (*22*). The Fe site is then exposed and becomes active for adsorption of a second methane molecule and release of another methyl radical, with energy barriers of 3.07 and 2.19 eV, respectively (Fig. 3A). Migration of H from C in Fe-C-Si sites to Fe involves a barrier of 0.58 eV. The resulting surface H species desorbs as H_2 with an energy barrier of 1.61 eV.

The intermediacy of methyl radicals was verified by online vacuum ultraviolet soft photoionization molecular-beam mass spectrometry (VUV-SPI-MBMS) (fig. S6) (*22*). Molecules were ionized with a 10.6-eV VUV lamp, which has an energy lower than the CH_4 ionization energy (12.6 eV). This allows detection of intermediate radicals and products (*34*, *35*). Figure 3B and its inset display all species detected at 1193 K. Methyl radicals,

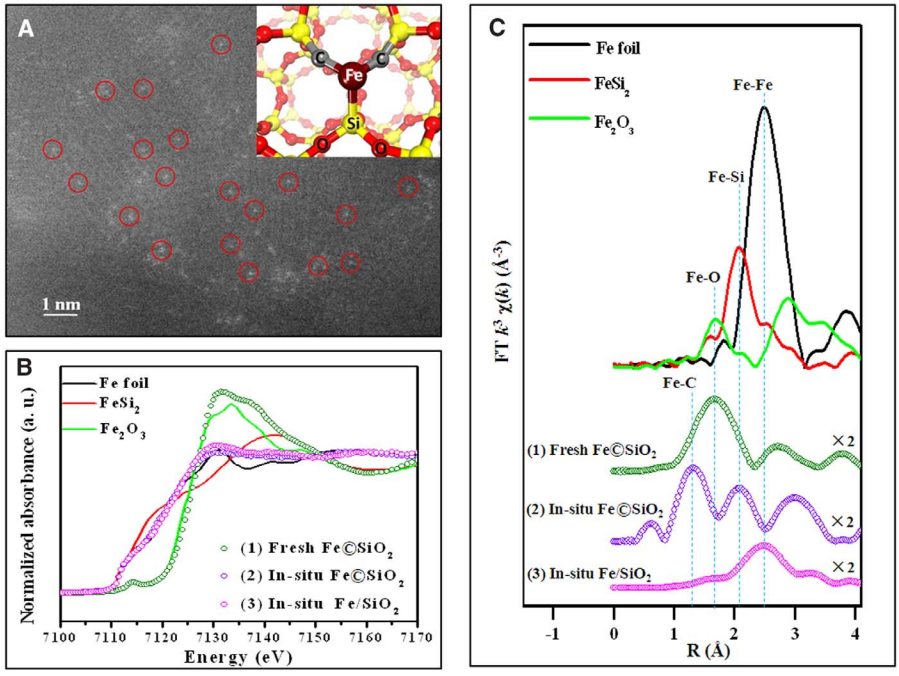

Fig. 2. Structural features of 0.5% Fe©SiO_2. (**A**) STEM-HAADF image of the catalyst after reaction, with the inset showing the computational model of the single iron atom bonded to two C atoms and one Si atom within silica matrix. (**B**) In situ XANES upon activation and (**C**) Fourier transformed (FT) k^3-weighted $\chi(k)$-function of the EXAFS spectra. Solid lines denote reference samples of Fe foil, $FeSi_2$, and Fe_2O_3. Line 1 denotes the fresh 0.5% Fe©SiO_2. Line 2 stands for 0.5% Fe©SiO_2 and line 3 for 0.5% Fe/SiO_2 upon activation in 10% CH_4/N_2 at 1173 K for 2 hours, respectively. R(Å), distance in angstroms.

represented by the signal at mass/charge ratio (m/z) = 15, are clearly observed. Additional signals at m/z = 28, 40, 42, 78, 92, and 128 are assigned to ethylene (C_2H_4), propyne or propadiene (C_3H_4), propylene (C_3H_6), benzene (C_6H_6), toluene (C_7H_8), and naphthalene ($C_{10}H_8$), respectively.

To further elucidate the mechanism, the reaction profile of methyl radicals at 1225 K was simulated with DFT (Fig. 3C and fig. S7) (*22*). Two •CH_3 radicals combine to form C_2H_6 via a strongly exothermic process. C_2H_6 undergoes dehydrogenation readily, giving C_2H_4 and H atoms with an energy barrier of 1.58 eV. By abstraction of H from C_2H_4, the resulting •C_2H_3 radical tends to react with additional C_2H_4 molecules. Further dehydrogenation and cyclization leads to benzene, with an energy barrier of 2.85 eV. C_6H_6 is also readily dehydrogenated by •H and, after further chain growth and cyclization, yields the thermodynamically more stable naphthalene. The low barrier for transformation of C_2H_6 to C_2H_4 explains the absence of C_2H_6 among the experimentally observed products under steady-state reaction conditions, whereas the thermodynamically more stable hydrocarbons C_2H_4, C_6H_6, and $C_{10}H_8$ accumulated and were detected.

At equilibrium at 1225 K and atmospheric pressure, the yields of C_2H_4, C_6H_6, and $C_{10}H_8$ from CH_4 were estimated to be 9.0, 34.0, and 57.0% (*22*), respectively. The relative ratios of these products could be manipulated by changing the reaction conditions. For example, increasing the CH_4 flow rate in the VUV-SPI-MBMS reactor favors formation of C_2H_4 (Fig. 3D), whereas lower flow rates (corresponding to longer residence times) promote cyclization of intermediates leading to aromatics, which are consistent with the GC analysis obtained in the microreactor. These results lend further support to the hypothesis that the reaction is initiated by the catalytic generation of methyl radicals, which subsequently undergo a series of gas-phase reactions. Thus, the conversion efficiency is high, despite the very limited number of surface iron sites and the extremely low surface area of the catalyst.

Heterogeneous systems for CH_4 activation generally still suffer from poor carbon utilization, caused in part by low selectivity. Here, we demonstrate an atom-economical direct CH_4 conversion process, enabled by the lattice-confined single iron sites embedded within a silica matrix, which activate CH_4 and generate methyl radicals. A conversion as high as 48.1% was obtained at 1363 K and a space velocity of 21.4 liter $gcat^{-1}$ $hour^{-1}$, with a selectivity to C_2H_4 of >48.4% (the remainder being aromatics). No deactivation was observed even after reaction for 60 hours, and the total carbon selectivity to the three products remained >99%. Although the dehydrogenation itself is endothermic, high selectivity to ethylene in this process substantially reduces the heat input (estimated to be about half that of a typical thermal pyrolysis process with dominating acetylene in product), as shown in table S3 (*22*). These findings open up new possibilities for fundamental studies of direct, nonoxidative activation of CH_4.

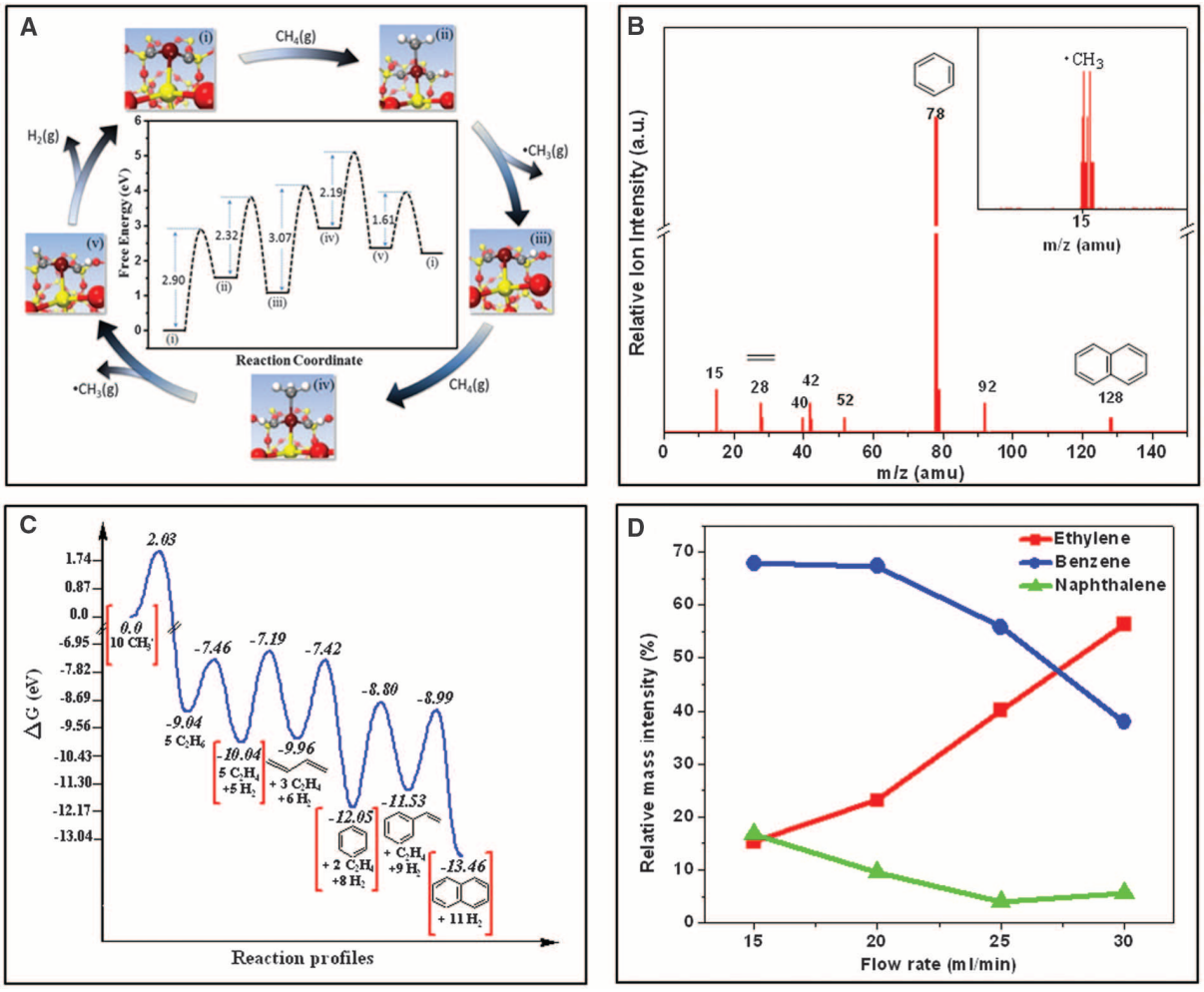

Fig. 3. Investigation of the reaction mechanism over 0.5% Fe©SiO_2. (**A**) DFT calculations on catalytic generation of methyl radicals at 1223 K. (**B**) Species in the reactor effluent at 1193 K, detected by VUV-SPI-MBMS. amu, atomic mass units. (**C**) DFT simulated reaction profile of methyl radicals in the gas phase at 1225 K. ΔG, Gibbs free energy. (**D**) Relative intensity of VUV-SPI-MBMS signals of major products as a function of CH_4 flow rate at 1223 K.

It is anticipated that combining a catalyst such as this one with an efficient reactor technology may enable the development of non–syngas-based routes to transform light hydrocarbons into high–value-added chemicals.

References and Notes

1. www.chemweek.com/lab/ACC-US-chemical-investment-linked-to-shale-gas-reaches-$100-billion_58946.html.
2. J. Li *et al.*, *J. Am. Chem. Soc.* **134**, 836–839 (2012).
3. F. Diederich, *Angew. Chem. Int. Ed.* **52**, 6–7 (2013).
4. H. M. T. Galvis *et al.*, *J. Am. Chem. Soc.* **134**, 16207–16215 (2012).
5. H. M. Torres Galvis *et al.*, *Science* **335**, 835–838 (2012).
6. Note that the construction of two megascale methanol plants in the U.S. Pacific Northwest was recently announced to supply olefin feedstocks to Dalian, China.
7. www.chemweek.com/lab/Chinese-group-plans-two-mega-methanol-plants-in-USPacific-Northwest-to-supply-olefins-feedstock_58289.html.
8. F. P. Larkins, A. Z. Khan, *Aust. J. Chem.* **42**, 1655–1670 (1989).
9. G. E. Keller, M. M. Bhasin, *J. Catal.* **73**, 9–19 (1982).
10. H. Arakawa *et al.*, *Chem. Rev.* **101**, 953–996 (2001).
11. J. H. Lunsford, *Angew. Chem. Int. Ed. Engl.* **34**, 970–980 (1995).
12. S. Arndt *et al.*, *Catal. Rev. Sci. Eng.* **53**, 424–514 (2011).
13. U. Zavyalova, M. Holena, R. Schlögl, M. Baerns, *ChemCatChem* **3**, 1935–1947 (2011).
14. Q. Zhu *et al.*, *Nat. Chem.* **5**, 104–109 (2013).
15. L. S. Wang *et al.*, *Catal. Lett.* **21**, 35–41 (1993).
16. B. M. Weckhuysen, D. J. Wang, M. P. Rosynek, J. H. Lunsford, *J. Catal.* **175**, 338–346 (1998).
17. R. W. Borry, Y. H. Kim, A. Huffsmith, J. A. Reimer, E. Iglesia, *J. Phys. Chem. B* **103**, 5787–5796 (1999).
18. D. J. Wang, J. H. Lunsford, M. P. Rosynek, *J. Catal.* **169**, 347–358 (1997).
19. D. Ma *et al.*, *J. Catal.* **208**, 260–269 (2002).
20. R. Ohnishi, S. T. Liu, Q. Dong, L. Wang, M. Ichikawa, *J. Catal.* **182**, 92–103 (1999).
21. S. Ma, X. Guo, L. Zhao, S. Scott, X. Bao, *J. Energy Chem.* **22**, 1–20 (2013).
22. Supplementary materials are available on *Science* Online.
23. T. V. Choudhary, C. Sivadinarayana, C. C. Chusuei, A. Klinghoffer, D. W. Goodman, *J. Catal.* **199**, 9–18 (2001).
24. M. A. Ermakova, D. Y. Ermakov, A. L. Chuvilin, G. G. Kuvshinov, *J. Catal.* **201**, 183–197 (2001).
25. A. Beloqui Redondo, E. Troussard, J. A. van Bokhoven, *Fuel Process. Technol.* **104**, 265–270 (2012).
26. A. Holmen, O. Olsvik, O. A. Rokstad, *Fuel Process. Technol.* **42**, 249–267 (1995).
27. G. P. Van Der Zwet, P. A. J. M. Hendriks, R. A. Van Santen, *Catal. Today* **4**, 365–369 (1989).
28. H. Schwarz, *Angew. Chem. Int. Ed.* **50**, 10096–10115 (2011).
29. E. W. McFarland, H. Metiu, *Chem. Rev.* **113**, 4391–4427 (2013).
30. B. Qiao *et al.*, *Nat. Chem.* **3**, 634–641 (2011).
31. E. de Smit, A. M. Beale, S. Nikitenko, B. M. Weckhuysen, *J. Catal.* **262**, 244–256 (2009).
32. R. C. Che, L. M. Peng, X. F. Duan, Q. Chen, X. L. Liang, *Adv. Mater.* **16**, 401–405 (2004).
33. X. Pan *et al.*, *Nat. Mater.* **6**, 507–511 (2007).
34. Z. Zhou, H. Guo, F. Qi, *Trends Analyt. Chem.* **30**, 1400–1409 (2011).
35. L. Luo *et al.*, *Sci. Rep.* **3**, 1625 (2013).

Acknowledgments: This work was financially supported by the "Strategic Priority Research Program" of the Chinese Academy of Sciences (grant XDA09030101), the National Natural Science Foundation of China (grants 21321002, 11079005, 21033009, and 21103181), and the Ministry of Science and Technology of China (grants 2011CBA00503 and 2013CB933100). We thank S. L. Scott and H. Metiu for fruitful discussion. An international patent application under the Patent Cooperation Treaty is pending (PCT/CN2013/079977).

Supplementary Materials

www.sciencemag.org/content/344/6184/616/suppl/DC1
Materials and Methods
Figs. S1 to S7
Tables S1 to S3
References (*36*–*66*)

10 March 2014; accepted 15 April 2014
10.1126/science.1253150

Restoration of Large Damage Volumes in Polymers

S. R. White,[1,2]* J. S. Moore,[2,3] N. R. Sottos,[2,4] B. P. Krull,[2,4] W. A. Santa Cruz,[2,3] R. C. R. Gergely[2,5]

The regenerative power of tissues and organs in biology has no analog in synthetic materials. Although self-healing of microscopic defects has been demonstrated, the regrowth of material lost through catastrophic damage requires a regenerative-like approach. We demonstrate a vascular synthetic system that restores mechanical performance in response to large-scale damage. Gap-filling scaffolds are created through a two-stage polymer chemistry that initially forms a shape-conforming dynamic gel but later polymerizes to a solid structural polymer with robust mechanical properties. Through the control of reaction kinetics and vascular delivery rate, we filled impacted regions that exceed 35 mm in diameter within 20 min and restored mechanical function within 3 hours. After restoration of impact damage, 62% of the total absorbed energy was recovered in comparison with that in initial impact tests.

Whereas biology achieves regeneration through vascularization and recruitment of stem cells (*1*–*3*), engineering materials are generally avascular, with a limited ability to self-heal (*4*, *5*). A variety of repair strategies exist for microscopic defects and cracks (*6*–*10*), but autonomic restoration of materials that suffer large-scale damage and associated mass loss has not been realized. Restoration requires overcoming the interplay of mass transport, environmental factors, intrinsic forces (such as surface tension), and extrinsic forces (such as gravity) that act on liquid reagents and the chemical reactions associated with damage repair.

Our restoration concept for structural materials is illustrated in Fig. 1. The strategy is predicated on the delivery of reactive fluids through two independent vascular networks to the site of damage. Events that lead to substantial mass loss (such as ballistic impact) trigger release of fluids, subsequent mixing, and initiation of the restoration process. A reactive system that progresses from liquid to gel (gel stage) and gel to polymer (polymer stage) is hypothesized to deliver low-viscosity fluids to the site of damage, initially resulting in a shape-conforming yet self-supporting viscoelastic scaffold. Addition of new material proceeds until the damaged region is fully filled and complete replacement of lost mass is achieved. Transformation of the gel into a stiff polymer then allows for recovery of the mechanical properties of the original material.

We developed a two-stage polymer chemistry in which catalyzed gelation of liquid monomer is followed by bulk polymerization to a structural solid (Fig. 1). The reactive monomer solutions begin as stable, low-viscosity (time t_0), until damage-triggered release initiates the chemical processes. A relatively fast gel stage (time t_1, from 30 s to a few minutes) creates a semisolid scaffold on which additional solution is accreted. Gelators A, a bis-acylhydrazine–terminated poly (ethylene glycol), and B, a tris[(4-formylphenoxy) methyl]ethane, form a cross-linked network of dynamic acylhydrazone bonds through acid-catalyzed condensation (synthesis is provided in fig. S1) (*11*). This chemistry is capable of gelling a wide range of organic liquids, including acrylic and thiol-ene monomers. Monomer gelation accomplishes the need to fill gaps stemming from mass loss, and conversion to polymer completes the restoration process. Polymerization kinetics on a time scale > t_1 (hours) avoids premature stiffening of the restored material. Room-temperature polymerization is achieved with judicious choice of radical initiators, promoters, and inhibitors. Although biological systems require a complex and highly regulated system of biochemical processes to achieve regeneration (*12*–*19*), our strategy produces reliable performance with relatively simple synthetic reagents.

The properties of the structural polymer are tailored by selection of the monomer, as demonstrated below with two examples. In one example, a thermoplastic was polymerized by using 2-hydroxyethyl methacrylate (HEMA) initiated by a radical redox reaction between methyl ethyl ketone peroxide (MEKP) initiator and cobalt naphthenate (CoNp) promoter (*20*); in a second example, liquid thiol-ene agents 1,3-glyceryl dimethacrylate and trimethylolpropane tris(3-mercaptopropionate) react to form a thermosetting material (fig. S2). Monomers were selected to fulfill a stringent set of requirements, including high boiling point, nonwetting properties, low viscosity, favorable cure kinetics, and the ability to dissolve gelators. The reagents required for each example are mutually compatible with the reagents for gelation chemistry. Independently tunable chemical triggers selectively control the rates of both gelation and polymerization. The components for both examples are strategically divided into two stable solutions and loaded into separate microchannels (Fig. 1, left, and table S6).

Oscillatory rheology confirmed the separate occurrence of gelation and polymerization stages as well as the ability to regulate the reaction kinetics of each stage (Fig. 2, A to C). A representative reaction shown in Fig. 2A shows the evolution of storage (G') and loss (G") moduli of a 12 weight percent (wt %) gelator solution in HEMA. The first plateau of G' reflects monomer gelation to a ~10^4 to 10^5 Pa semi-solid. Onset of the gel stage (t_1) was defined as the crossover of G' and G". The second modulus plateau, several orders of magnitude higher, reflects a slower transformation from gel to structural polymer.

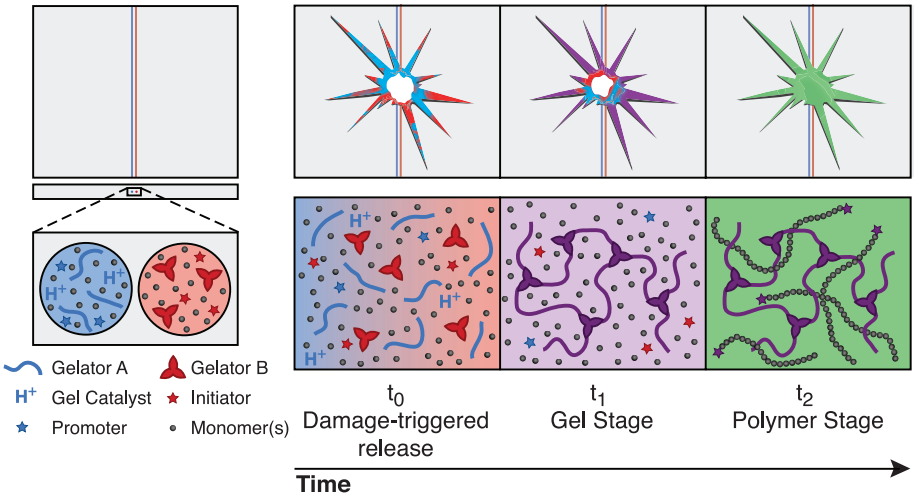

Fig. 1. Two-stage restoration strategy. Reactive monomer solutions are incorporated into a vascularized specimen (blue and red channels). Time t_0, impact damage initiates fluid release into the damage region. Time t_1, gel stage (purple) occurs by covalent cross-linking of gelators A and B with an acid catalyst. Deposition of fluid and subsequent gelation continues until the void is filled. Time t_2, the polymer stage (green) follows by using a two-component initiation for monomer polymerization, resulting in recovery of structural performance. Chemical structures of the two-stage polymer system are given in fig. S2.

[1]Department of Aerospace Engineering, University of Illinois at Urbana-Champaign, Urbana, IL 61801, USA. [2]The Beckman Institute, University of Illinois at Urbana-Champaign, Urbana, IL 61801, USA. [3]Department of Chemistry, University of Illinois at Urbana-Champaign, Urbana, IL 61801, USA. [4]Department of Materials Science and Engineering, University of Illinois at Urbana-Champaign, Urbana, IL 61801, USA. [5]Department of Mechanical Science and Engineering, University of Illinois at Urbana-Champaign, Urbana, IL 61801, USA.

*Corresponding author. E-mail: swhite@illinois.edu

Polymerization onset (t_2) was designated as the peak of the loss factor (tan δ = G"/G') (fig. S3A). Rates of gelation and polymerization are largely independent (fig. S4), which enables precise control of t_1 and t_2 by varying the concentrations of catalyst for the gelation reaction and initiators for the polymerization reaction. Plots of the time scales of staged transitions for the HEMA example are shown in Fig. 2, B and C. Gelation rate is dependent on catalyst concentration and determines the scaffold-forming ability (Fig. 2B). Control of polymerization was achieved by varying promoter concentration in an inert environment (Fig. 2C). However, free-radical polymerizations of acrylates are sensitive to atmospheric oxygen. In contrast, the thiol-ene thermoset chemistry is oxygen-tolerant and cures in aerobic environments. Thiol-ene polymerizations are fast and have been known to cure without the use of initiators (*21*). To allow sufficient time for gel formation, the radical inhibitor cupferron was used to slow the polymerization rate (fig. S3B) (*22*, *23*). The ability to tune the rates of our two-stage restorative system enables adaptation to a wide variety of damage geometries.

Gelation allows deposition of material beyond that which is dictated by surface tension alone. When damage size exceeds a certain threshold, surface tension is insufficient to retain unreacted fluid, and gravity pulls it out of the damage zone. The boundary between surface tension and gravity-dominated regimes (described by Tate's Law and the drop-weight method of analysis) (fig. S5) (*24*–*26*) was validated for our experimental setup with standard test fluids (Fig. 2D). In contrast to these nonreactive fluids, the gel deposition volume exceeds that expected from Tate's Law by over an order of magnitude. Two formulations containing different gel fractions are plotted in Fig. 2D, with the greater gel fraction producing a larger deposition volume. The increase in volume retained over nonreactive fluids is due to the mechanical support of the in situ–formed gel. If gelation and deposition occur on the same time scale, the growing material is no longer retained by the surface tension of the fluid alone; it is also retained by the cohesion of the restored material and its adhesion to the deposition surface.

In our model experiments, the restorative reagents span gaps and fill large damage volumes by forming a free-standing, dynamic gel scaffold on which continued material growth occurs. We used an open cylinder (sample dimensions are 52 by 52 by 3 mm thick, 330-μm-diameter parallel channels) (fig. S6A) as a model geometry to test the filling of large-scale damage in thin epoxy sheets. Solutions of HEMA-containing gelators, acid catalyst, and fluorescent dye (Nile Red and perylene) were delivered to the damage area via separate microchannels (Fig. 3A). A computer-controlled, pressurized system ensures reagents were delivered at 1:1 volume ratios (supplementary materials, materials and methods). Upon entering the damaged region, the components mix and quickly wet the inner surface of the sample owing to low viscosity and a low fluid-substrate contact angle (table S1). Rapid gelation forms a scaffold on which additional fluid from the microvascular channels was deposited. The faceted appearance of the recovering damage region (Fig. 3A) reflects the mechanical stiffness of the developing gel because an ideal liquid would assume a smooth circular shape to minimize surface energy. Gelled material grows inward, and the entire damage region is filled as the process of deposition and gelation continues. The dynamic nature (*27*) of the gelator chemistry enables continuous (defect-free) gel interfaces and the formation of a monolithic plug in place of the original void.

Restoration to full mechanical function was accomplished by replenishing lost mass and transforming the gelled monomer to a fully polymerized solid. The filling performance of gelling and nongelling controls is compared for increasing damage area in Fig. 3B. The area fill ratio (AFR) is calculated for each damage area as the ratio A_{fill}:A_0, where A_{fill} is the area filled by the restorative solutions and A_0 is the total damage area. The control solutions achieve an AFR of 1 only for diameters up to 6.3 mm. For larger diameters, the effect of gravity dominates surface tension and causes the controls to drip out of the damaged region, which results in incomplete filling. In contrast, gelling solutions fill to capacity (AFR = 1) for damage diameters up to 9.0 mm by overcoming gravity and circumventing failure by dripping. Damage sizes exceeding 8.0 mm do not reliably fill for all replicates because gravity causes gel material to grow downward rather than toward the damage center; however, the AFR remains substantially higher than that of control solutions because of superior material retention.

A pressure cell was used to verify mechanical recovery of our system by applying 345 kPa of nitrogen to one side of a damage sample and monitoring leakage on the opposite side (fig. S6B) (*28*). Because only a completely filled damage region will withstand pressurization, we tested the maximum damage areas at which each restorative system attained complete filling for each of five replicates (Fig. 3C). All gelling systems are able to fill larger damage areas than can nongelling solutions but do not provide mechanical recovery without a second transition to polymer.

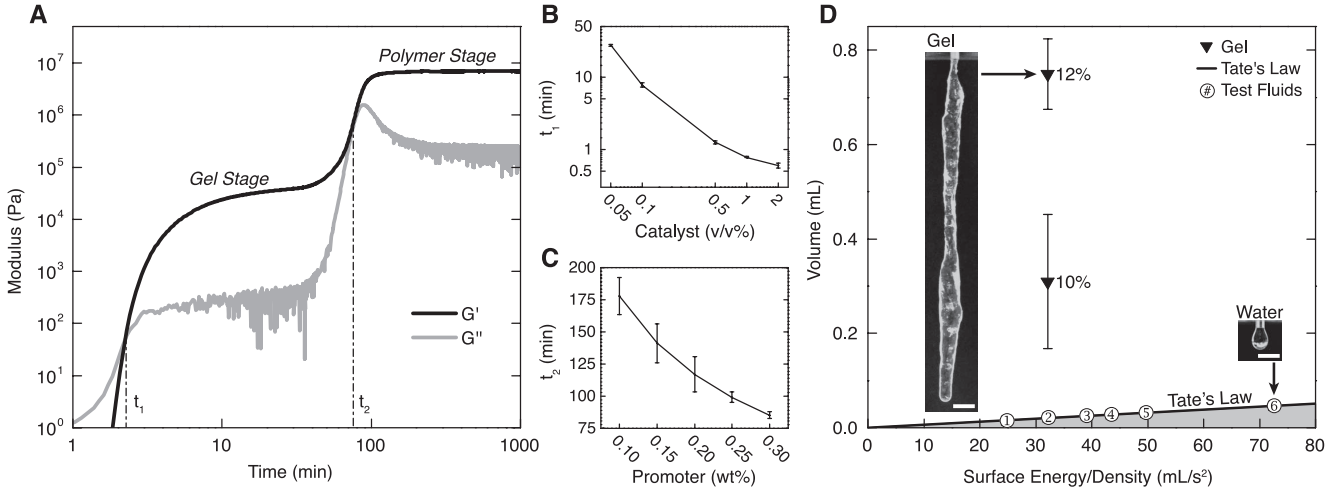

Fig. 2. Characterization of the two-stage process. Solutions contain gelators in HEMA (monomer) with dichloroacetic acid (catalyst), methyl ethyl ketone peroxide (initiator), and cobalt naphthenate (promoter). (**A**) Rheological properties of the restorative reagents over time display both the fast formation of the organogel (t_1, seconds to minutes), and slower reaction rate to polymer (t_2, hours) controlled by the concentrations of chemical triggers. (**B**) Control of gel-stage kinetics by varying catalyst concentration (1.5 wt % initiator, 0.1 wt % promoter). (**C**) Control of polymer stage kinetics by varying promoter (2 v/v % catalyst, 1.5 wt % initiator). (**D**) Volume deposited by using restorative gel chemistry (HEMA gel, 2 v/v % catalyst, no initiator or promoter). Tate's Law describes the limiting volume of a nonreactive fluid that can be retained with surface tension; standard test fluids confirm this relationship (1, pentane; 2, HEMA; 3, dimethyl sulfoxide; 4, ethylene glycol; 5, glycerol; and 6, water). Two-stage chemistry far exceeds this limit, but deposition is dependent on the concentration of gelators. The inset optical image on the left shows the volume deposited by 12 wt % gelators, whereas the inset optical image on the right shows water test fluid. Scale bars, 5 mm.

Only the thermoplastic and thermoset two-stage polymers combine filling performance with mechanical recovery. A standard two-part epoxy resin is presented for comparison, and neither fills a substantial damage area nor seals after a 24-hour room-temperature cure. As demonstrated with larger-area fill ratios and higher seal rates, two-stage polymers provide restoration performance superior to traditional healing chemistries (*29*). The final mechanical properties of the two-stage polymer systems are comparable with commercial poly(methyl methacrylate) (PMMA) polymers (*30*). Quasistatic tensile testing of the two-stage thermoplastic (HEMA) system yields an elastic modulus of 1.8 GPa and a tensile strength of 45 MPa (fig. S7 and table S2).

To test more realistic damage modes, we impacted and punctured specimens using a drop tower apparatus. The multiscale damage present in impact specimens represents a substantial challenge and requires chemistry that can both regrow the lost mass as well as penetrate into microcracks to create a pressure-tight seal. Dropping a striker with a hemispherically shaped tip at 6.26 J (Fig. 4A)

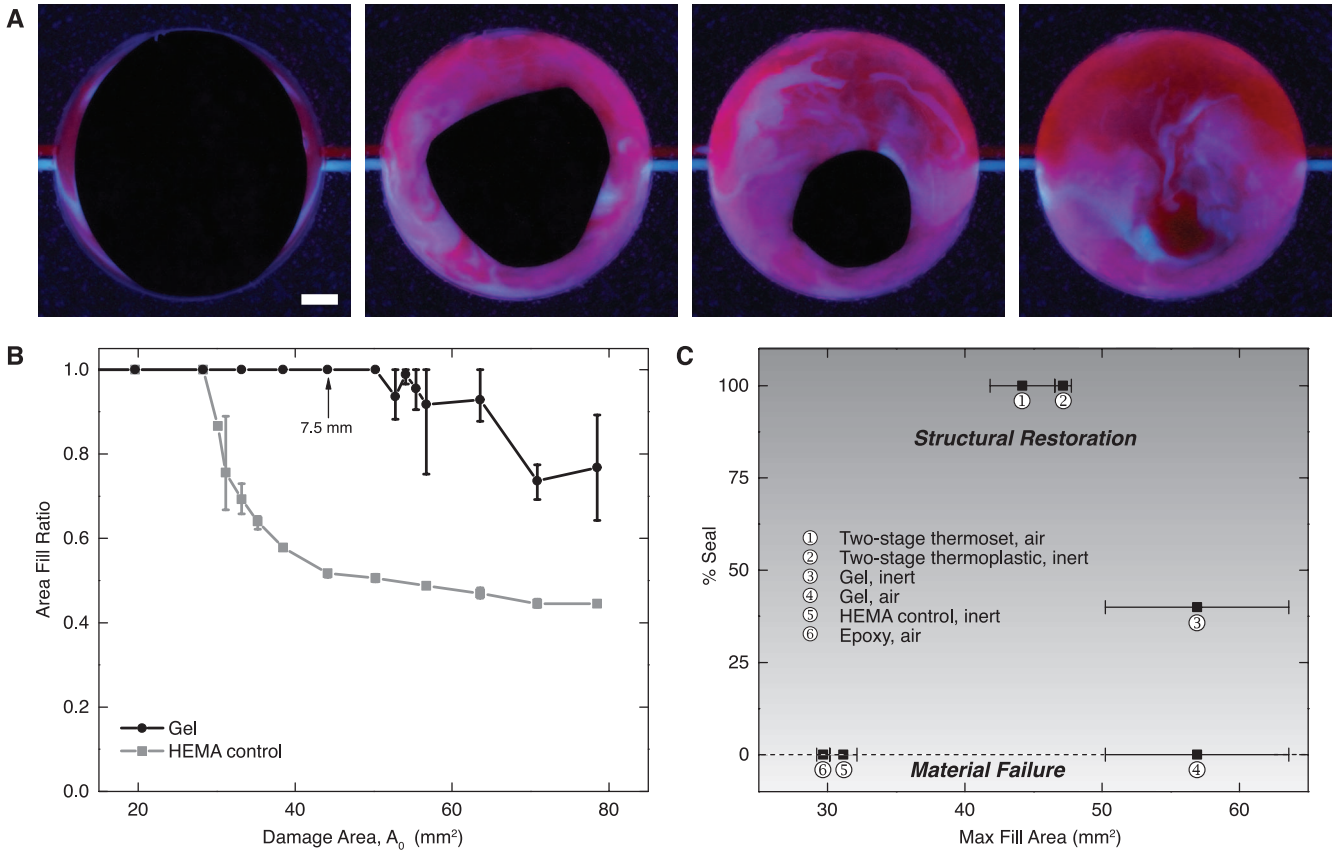

Fig. 3. Cylinder damage geometry to test restoration performance. (**A**) Optical images of 7.5-mm-diameter open-cylinder damage geometry after 1, 3, 7, and 13 min (left to right) pressurized delivery of HEMA gel solutions (2 v/v % catalyst, no initiator or promoter). Blue liquid is part A [HEMA, gelator A (56% of total gel A), DCA catalyst] dyed with perylene, and red liquid is part B [HEMA, gelator A (44% of total gel A), gelator B] dyed with Nile Red. Scale bar, 1 mm. (**B**) Fill performance achieved for cylindrical holes of increasing size for HEMA gel and a nongelling neat HEMA control. AFR = A_{fill}/A_0. (**C**) Restoration performance of various healing systems after a 24-hour room-temperature cure, with the curing atmosphere indicated in the legend. Samples are subjected to 345 kPa N_2 pressure loading. Restoration requires both a complete fill and recovery of full mechanical function.

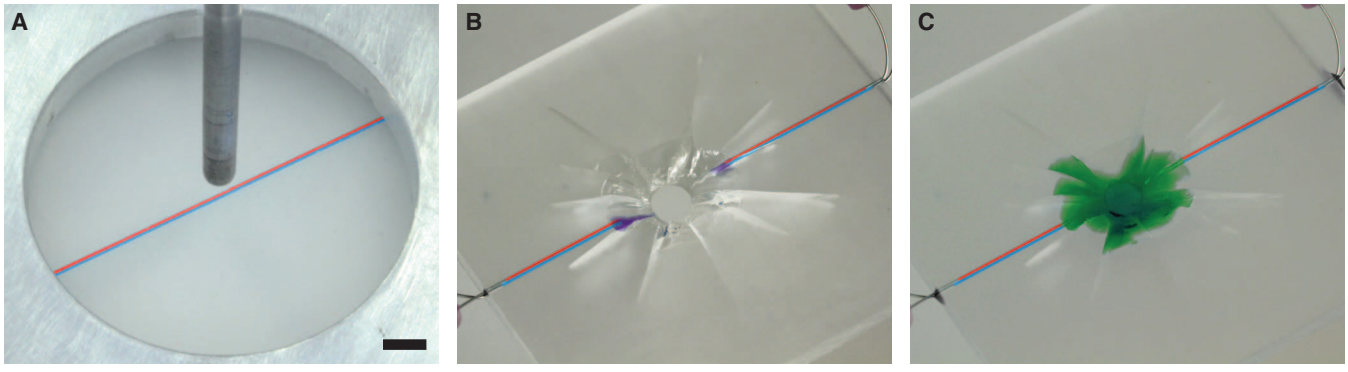

Fig. 4. Restoration of impact damage. Perspective views of impact specimen restored with two-stage thermoplastic (HEMA) system (0.1 v/v % catalyst, 1.5 wt % initiator, 0.1 wt % promoter). Both components of two-part solutions are dyed and recolored in images for visualization. (**A**) Specimen mounted into impact test fixture; 4-mm striker with a hemispherically shaped tip suspended over specimen. (**B** and **C**) Impact damage with central puncture and radiating cracks (B) before filling and (C) after filling. Scale bar, 5 mm.

creates a central puncture and radiating cracks, with damage spanning ~35 mm in diameter. We implemented the same pressurized delivery scheme to fill the damage post-impact. A dye (Oil Blue N) was used to observe the deposition process, which included wicking into the radiating cracks (Fig. 4, B and C). Although fast gelation chemistry is advantageous for the regrowth of lost mass, it may not provide sufficient time for the reagents to fully penetrate into radiating microcracks. By tuning (slowing) the gelation kinetics, we were able to achieve gap-filling and partial penetration of radial microcracks emanating from the central hole. Pressure testing of impact samples yielded ~60% sealing success, with most failures attributed to the lack of sealing of the dense network of radiating microcracks. After restoration of impact damage, we reimpacted specimens using the same testing protocol and measured 62% recovery of total absorbed energy in comparison with the initial impact test. The restored material performed on par (76%) with control specimens in which the native substrate material was injected into the damage and cured at a high temperature (table S3).

We have demonstrated a vascular approach to damage restoration using a polymer that replaces lost mass and recovers structural performance. Our two-stage chemistry makes use of both a rapid gelation (gel stage) for gap-filling scaffolds and a slower polymerization (polymer stage) for restoration of structural performance. When damage is unpredictable and uncontrolled, more complex and interconnected vascular networks (*31*) will be necessary to provide sufficient vascular coverage and redundancy to circumvent channel blockage. Truly regenerative polymers may be possible in the future via on-demand delivery of the chemical components of the native substrate polymer coupled with tunable gel and polymer transitions.

References and Notes

1. K. D. Birnbaum, A. Sánchez Alvarado, *Cell* **132**, 697–710 (2008).
2. M. D. C. Carnevali, F. Bonasoro, E. Lucca, M. C. Thorndyke, *J. Exp. Zool.* **272**, 464–474 (1995).
3. R. J. Lauzon, K. J. Ishizuka, I. L. Weissman, *Dev. Biol.* **249**, 333–348 (2002).
4. E. B. Murphy, F. Wudl, *Prog. Polym. Sci.* **35**, 223–251 (2010).
5. R. P. Wool, *Soft Matter* **4**, 400–418 (2008).
6. B. J. Blaiszik *et al.*, *Annu. Rev. Mater. Res.* **40**, 179–211 (2010).
7. X. Chen *et al.*, *Science* **295**, 1698–1702 (2002).
8. P. Cordier, F. Tournilhac, C. Soulié-Ziakovic, L. Leibler, *Nature* **451**, 977–980 (2008).
9. A. C. Balazs, T. Emrick, T. P. Russell, *Science* **314**, 1107–1110 (2006).
10. S. R. White *et al.*, *Nature* **409**, 794–797 (2001).
11. G. H. Deng, C. M. Tang, F. Y. Li, H. F. Jiang, Y. M. Chen, *Macromolecules* **43**, 1191–1194 (2010).
12. E. Nacu, E. M. Tanaka, *Annu. Rev. Cell Dev. Biol.* **27**, 409–440 (2011).
13. K. Echeverri, E. M. Tanaka, *Semin. Cell Dev. Biol.* **13**, 353–360 (2002).
14. J. I. Morrison, S. Lööf, P. He, A. Simon, *J. Cell Biol.* **172**, 433–440 (2006).
15. J. P. Brockes, A. Kumar, *Nat. Rev. Mol. Cell Biol.* **3**, 566–574 (2002).
16. C. Jopling, S. Boue, J. C. Izpisua Belmonte, *Nat. Rev. Mol. Cell Biol.* **12**, 79–89 (2011).
17. S. J. Odelberg, *Anat. Rec. B New Anat.* **287**, 25–35 (2005).
18. J. M. W. Slack, *Trends Cell Biol.* **16**, 273–275 (2006).
19. A. Kumar, C. P. Velloso, Y. Imokawa, J. P. Brockes, *PLOS Biol.* **2**, E218 (2004).
20. C. S. Sheppard, V. R. Kamath, *Polym. Eng. Sci.* **19**, 597–606 (1979).
21. C. E. Hoyle, T. Y. Lee, T. Roper, *J. Polym. Sci. A Polym. Chem.* **42**, 5301–5338 (2004).
22. Y. B. Kim, H. K. Kim, H. C. Choi, J. W. Hong, *J. Appl. Polym. Sci.* **95**, 342–350 (2005).
23. P. Esfandiari *et al.*, *J. Polym. Sci. A Polym. Chem.* **51**, 4261–4266 (2013).
24. T. Tate, *Philos. Mag. Ser. 4* **27**, 176–180 (1864).
25. W. D. Harkins, F. E. Brown, *J. Am. Chem. Soc.* **41**, 499–524 (1919).
26. J. L. Lando, H. T. Oakley, *J. Colloid Interface Sci.* **25**, 526–530 (1967).
27. R. J. Wojtecki, M. A. Meador, S. J. Rowan, *Nat. Mater.* **10**, 14–27 (2011).
28. B. A. Beiermann, M. W. Keller, N. R. Sottos, *Smart Mater. Struct.* **18**, 085001 (2009).
29. K. S. Toohey, C. J. Hansen, J. A. Lewis, S. R. White, N. R. Sottos, *Adv. Funct. Mater.* **19**, 1399–1405 (2009).
30. J. E. Mark, Ed., *Polymer Data Handbook* (Oxford Univ. Press, New York, 1999), pp. 656.
31. J. F. Patrick *et al.*, *Adv. Mater.* 10.1002/adma.201400248 (2014).

Acknowledgments: This research has been financially supported by the Air Force Office of Scientific Research (grant FA9550-10-1-0255). We extend our gratitude to the Mechanical Testing Instructional Laboratory (MTIL) and the Beckman Institute for facilities; Y. Fedonina, J. Carlson, A. Komnick, and C. Kirk for assistance with sample fabrication and material synthesis; and G. Milner for test fixture construction.

Supplementary Materials

www.sciencemag.org/content/344/6184/620/suppl/DC1
Materials and Methods
Figs. S1 to S15
Tables S1 to S7
References (*32*–*38*)
Movie S1

21 January 2014; accepted 7 April 2014
10.1126/science.1251135

In Situ TEM Observation of a Microcrucible Mechanism of Nanowire Growth

Rebecca Boston,[1,2] Zoe Schnepp,[3] Yoshihiro Nemoto,[4] Yoshio Sakka,[4] Simon R. Hall[1]*

The growth of metal oxide nanowires can proceed via a number of mechanisms such as screw dislocation, vapor-liquid-solid process, or seeded growth. Transmission electron microscopy (TEM) can resolve nanowires but invariably lacks the facility for direct observation of how nanowires form. We used a transmission electron microscope equipped with an in situ heating stage to follow the growth of quaternary metal oxide nanowires. Video-rate imaging revealed barium carbonate nanoparticles diffusing through a porous matrix containing copper and yttrium oxides to subsequently act as catalytic sites for the outgrowth of Y_2BaCuO_5 nanowires on reaching the surface. The results suggest that sites on the rough surface of the porous matrix act as microcrucibles and thus provide insights into the mechanisms that drive metal oxide nanowire growth at high temperatures.

The fabrication of nanowires of functional materials has become an important goal for their application in miniaturized circuits as diodes and transistors, coaxial gates and sensors (*1*). Fabrication methods such as soft lithography have yielded ternary or more complex metal oxide nanowires (*2*); however, these types of techniques rely on an underlying substrate that may have a detrimental effect on the properties of the material. Simple metal oxide nanowires such as ZnO (*3*) or TiO_2 (*4*) have been grown with a variety of methods, although the unsupported crystallization of more complex quaternary and quinternary oxide functional materials such as magnetoresistive $La_{0.67}Ca_{0.33}MnO_3$, piezoelectric $PbZr_{0.52}Ti_{0.48}O_3$, and the superconductors $YBa_2Cu_3O_{7-\delta}$ (Y123) and $Bi_2Sr_2Ca_{n-1}Cu_nO_{2n+4+x}$ (BSCCO) is difficult at the nanoscale, owing to the formation of stable impurity phases and/or the lack of a suitable nanoparticulate catalytic seed (*1*). Wires and whiskers of BSCCO have previously been grown on the macroscale (*5*, *6*), using a rapidly cooled glassy Bi-rich BSCCO precursor seeded with Al_2O_3 powder to provide sites of nucleation and outgrowth. The mechanism for this growth, however, has yet to be fully characterized, and although several processes have been proposed, the microcrucible mechanism is generally the favored one (*7*).

The microcrucible mechanism is a two-phase growth process that relies on the presence of a liquid and a solid phase. The liquid phase dissolves ions out of a solid matrix, and once supersaturated, growth occurs at the exposed surface of the droplet with the nanowire being extruded from the bulk (*5*). The microcrucible itself is composed of the solid underlying substrate, which

[1]Complex Functional Materials Group, School of Chemistry, University of Bristol, Bristol BS8 1TS, UK. [2]Bristol Centre for Functional Nanomaterials, Centre for Nanoscience and Quantum Information, Tyndall Avenue, Bristol BS8 1FD, UK. [3]School of Chemistry, University of Birmingham, Birmingham B15 2TT, UK. [4]National Institute for Materials Science, 1-2-1 Sengen, Tsukuba, Ibaraki 305-0047, Japan.

*Corresponding author. E-mail: simon.hall@bristol.ac.uk

forms a crucible-like structure to contain and concentrate the molten precursor and act as a conduit for the provision of more precursor materials as the nanowire forms. Crystals produced by this mechanism would, therefore, have well-defined faceted leading edges, rather than the commonly observed tapered crystals grown via the vapor-liquid-solid (VLS) mechanism, which typically have a catalytic nanoparticle at the tip that is consumed during the course of nanowire growth (*7*). For use in an application (for example, in a microcircuit), a nanowire that tapers is invariably undesirable, as the functionality would vary along the length or perhaps even vanish once a critical size was reached (*8*, *9*).

In this work, we used a transmission electron microscope fitted with an in situ heating stage to present direct observation of the microcrucible growth mechanism in quaternary metal oxide Y_2BaCuO_5 (Y211) nanowires. Full details on the materials and methods are available as supplementary materials (*10*), but to briefly summarize, the samples were prepared from stoichiometric mixtures of yttrium and barium and copper nitrates with sodium alginate in deionized water. The resulting composite was dried for 12 hours at 60°C, then calcined in a chamber furnace for 6 hours at 500°C with a ramp rate of 1°C min^{-1} before being heated a second time to 800°C for 2 hours at the same ramp rate. Once cool, these samples were then dispersed onto transmission electron microscopy (TEM) grids and introduced into either a JEM-2100F or a JEOL ARM200F transmission electron microscope, each fitted with an AHA-21 Aduro Protochips heating stage.

To assess which growth mechanism occurred, we first determined the crystallochemical nature of the system prior to in situ TEM heating. Figure S1 shows powder x-ray diffraction (XRD) confirming the complex mix of phases present immediately before nanowire growth (*10*). $BaCO_3$ is a major crystalline phase at this point, along with various crystalline copper and yttrium phases. The XRD background is flat, particularly between 20° and 30° 2θ, thereby suggesting only a minor amorphous contribution to the matrix. The crystalline matrix is porous (fig. S2), and the chemical composition of the system was confirmed by energy dispersive x-ray analysis (EDXA), which shows the presence of only yttrium, barium, copper, and oxygen (fig. S3) (*10*).

The results of the in situ TEM heating experiments are shown in Fig. 1. Nanowires were observed to grow with sharply faceted ends (fig. S4A) and a uniform cross section (fig. S4B), indicative of a microcrucible mechanism (*7*). The uniformity of the cross section of the wire throughout the initial stages of the growth indicates that crystallization is occurring within a region of fixed diameter corresponding to the diameter of the microcrucible.

To determine the direction of growth and ascertain whether the nanowires are stoichiometrically Y211, we conducted crystallographic analyses of the nanowires. Figure 1A shows a typical nanowire, in the early stages of growth, that has a single crystalline region along the length, with the zone axis determined as the $[7\bar{8}5]$ direction and the direction of growth perpendicular to the $(\bar{1}13)$ crystal planes of Y211 (Fig. 1B). Lattice fringes due to the $(\bar{1}13)$ crystal planes can be observed along the entire length of the nanowire (Fig. 1C).

For nanowire growth to proceed via the microcrucible mechanism, continuous crystallization of a molten phase must occur with support from an underlying matrix. In this work, we have identified that this molten phase comes from $BaCO_3$ nanoparticles, which melt and diffuse to

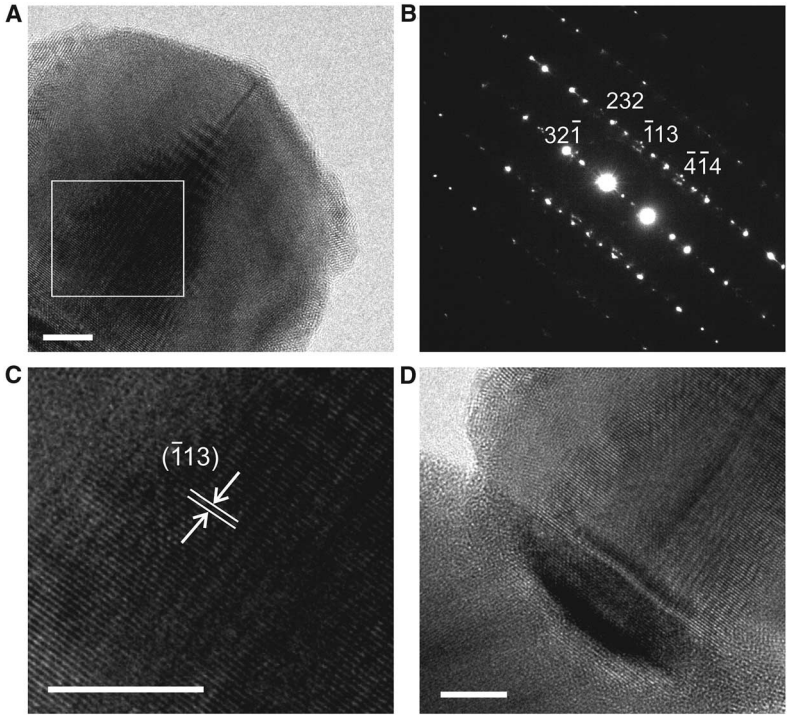

Fig. 1. TEM images showing crystallographic detail of a Y211 nanowire and underlying microcrucible. (**A**) Image showing the tip of a Y211 nanowire, with the region highlighted by the white square corresponding to the high-resolution TEM image in (C) showing the uniformity of the crystal lattice fringes in the center of the nanowire. The electron diffraction image in (**B**) corresponds to the region in (**C**) and is indexed to the Y_2BaCuO_5 phase [Joint Committee on Powder Diffraction Standards (JCPDS) card no. 01-078-2214]. The TEM image in (**D**) shows detail of the base of this nanowire, with the nonuniformity of the lattice fringes at the extremities of the nanowire suggestive of the physical breakdown and creep of the microcrucible. Scale bars in (A), (C), and (D): 5 nm.

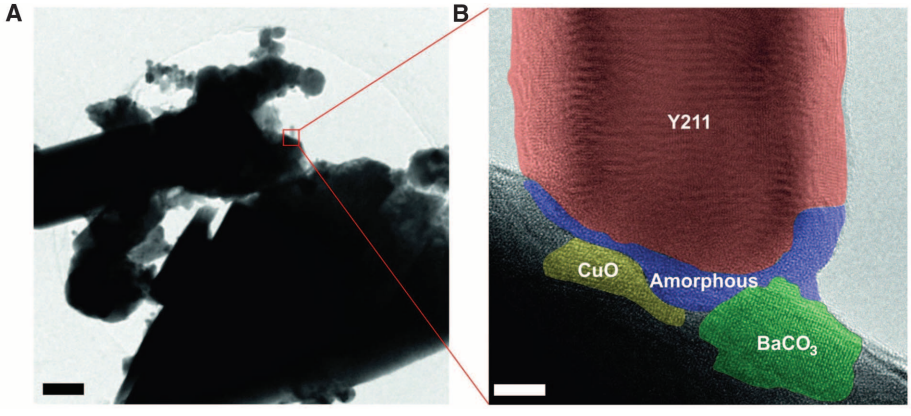

Fig. 2. TEM images of a Y211 nanowire quenched during growth. (**A**) Image of an in situ heating experiment, rapidly cooled during the initial stages of nanowire growth. (**B**) Image of the region highlighted by the red square in (A), with the composition of different phases identified using the lattice fringes observed. In (B), red corresponds to the Y_2BaCuO_5 phase (JCPDS card no. 01-078-2214), green to $BaCO_3$ (JCPDS card no. 00-041-0373), and yellow to CuO (JCPDS card no. 01-074-1021). The blue region is amorphous and contains a mixture of yttrium, copper, and barium, as determined by EDXA (fig. S6). Scale bars: 200 nm in (A); 5 nm in (B).

the surface of the precursor matrix (Fig. 2, fig. S5, and movie S1) (*10*). On the heating stage of the TEM, $BaCO_3$ nanoparticles became molten at an applied temperature of 450°C, so the ramp rate was slowed from 20°C min^{-1} to 4°C min^{-1} to ensure time for adequate heat transfer from the grid to the sample. On reaching the surface of the porous matrix, the molten $BaCO_3$ nanoparticle initiates nanowire outgrowth, and no molten drop is observed at the growing tip of the nanowire.

Figure 2A shows a partially grown nanowire that was rapidly cooled just after the start of outgrowth, when the nanoparticle at the base of the nanowire was still molten. Figure 2B is a high-resolution image of the base of this nanowire and illustrates the chemical composition of the component parts of the microcrucible, which were identified crystallographically from the lattice fringes. The nanowire itself was determined to be Y211, with regions that indexed to $BaCO_3$ and CuO being found in the underlying material. Crucially, the majority of the material separating the crystalline porous matrix from the nanowire was found to be amorphous. This finding confirms that, at the onset of rapid cooling, this material was a liquid, thereby providing further support for the microcrucible mechanism. EDX analysis (fig. S6) of this amorphous region showed that it was composed of Y, Ba, and Cu. By diffusing through regions containing the other two precursor ions, $BaCO_3$ nanoparticles are able to solubilize the Y and Cu cations required for Y211 formation, thereby increasing ionic concentration at the eventual outgrowth site at the surface of the matrix. There is precedent for this, as it has been shown that using

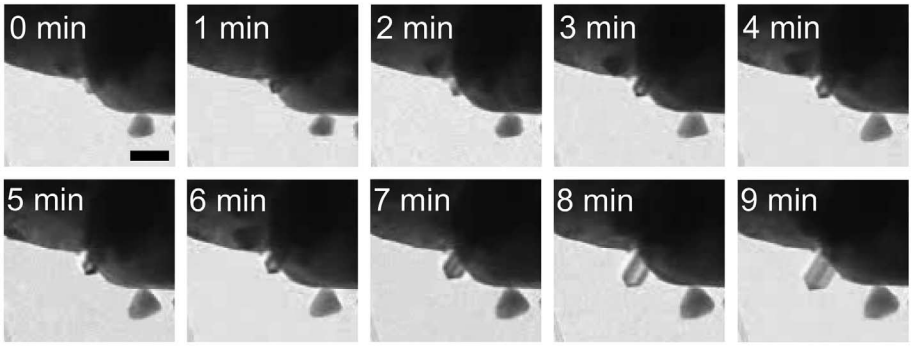

Fig. 3. TEM images taken from movie S2 showing nanowire growth. Each frame represents a 1-min interval showing the initial stages of growth of a Y211 nanowire at 500°C. Scale bar: 100 nm.

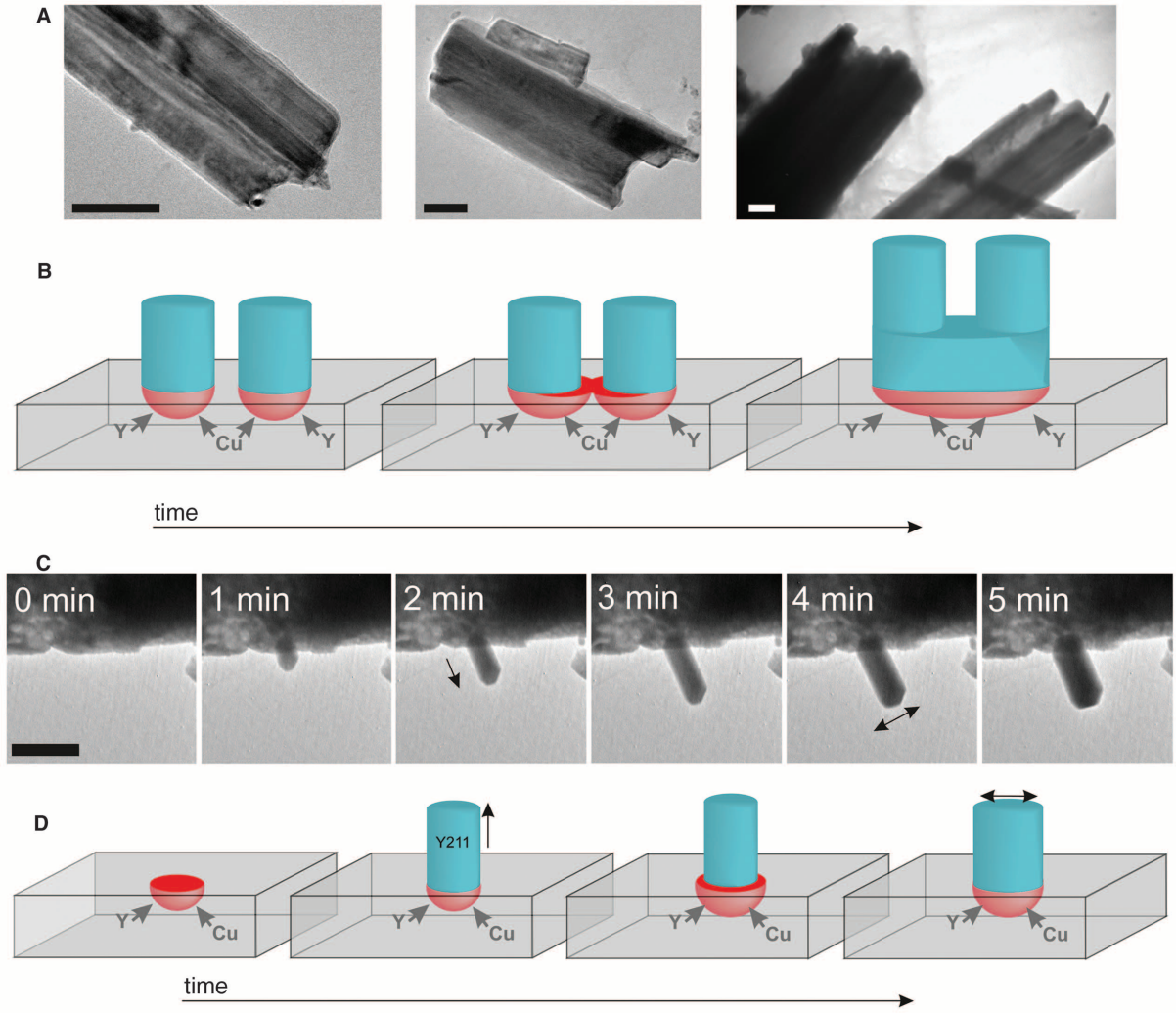

Fig. 4. Images showing mechanisms of nanowire expansion due to creep in the microcrucible system. (**A**) TEM images with (**B**) schematic showing microcrucible intergrowth producing wider, stepped nanowires. (**C**) TEM images with (**D**) schematic of a nanowire spontaneously broadening as a result of microcrucible creep and expansion on continuing heating at 500°C. Scale bars: 100 nm in (A); 200 nm in (C).

the high affinity of carbon for certain metals (*11*), molten metal nanoparticles are able to act as catalytic sites for the uptake of carbon with subsequent carbon nanotube outgrowth (*12*).

Under continuing heating, we observed nanowire growth over the course of 10 min (Fig. 3). Movie S2, taken at a higher resolution, better shows the initial stages of growth at high temperature (*10*). The faceted end of the emerging wire indicates that the free end of the wire is solid during the growth process.

Because the walls of the microcrucible contain the ions that are consumed in the formation of the nanowire, as the nanowire grows it would be expected that the dimensions of the microcrucible itself would change, leading to alteration of the nanowire morphology. The continual evolution of the liquid-solid interface of the microcrucible is a dynamic process that leads to creep of the interface and the concomitant morphogenesis of nonclassical crystal structures. Changes in the structure of the microcrucible have been observed previously in the growth of BSCCO and Y123 whiskers at the microscale, with the resultant creation of single-crystal morphologies as unorthodox as bows and rings (*13*, *14*). In this work, microcrucible creep resulted in two distinct nanowire morphologies: (i) those that underwent growth in both length and width and (ii) those for which two nearby microcrucibles joined together to form wires with "stepped" ends. Figure 4 shows nanowires with stepped ends as a result of two microcrucibles joining together (Fig. 4, A and B), as well as the progression of a growing wire over the course of 5 min, which shows the walls of the microcrucible breaking down (Fig. 4, C and D). Because the nanowire in Fig. 4C is short and at high temperature, the molten material is able to wet the side edge of the nanowire as the microcrucible supporting it breaks down (allowing for a droplet of greater diameter), causing a rapid and uniform increase in width. Evidence of creep can also be seen in Fig. 1D, where the regions of the nanowire at the edges of the microcrucible are crystallographically distinct from those in the center. A degree of control of the liquid-solid interface is exhibited here, as the $BaCO_3$ nanoparticles are of low-size polydispersity (*15*) and therefore limit the type and amount of creep in the system and, consequently, the diversity of structural features in the nanowires.

In previous studies on the synthesis of quaternary oxide nanowires (*15*, *16*), nanowires grew with a tapered morphology and a VLS-like catalytic drop. The key difference in those studies was that carbon-rich precursors such as citrate and acetate were used in the syntheses; these substances tend to persist for longer under calcination (*17*, *18*) than do the nitrates used here (fig. S7). In turn, this leads to a lower-density matrix, enabling nanoparticles to leave the surface and act as catalytic sites on the leading edges of the outgrowing nanowires. This is followed by tapered growth as the nanoparticle is consumed, producing morphologies more reminiscent of a VLS process. The loss of nitrates at a lower calcination temperature means that in this work, the matrix is denser at the point at which nanowire growth begins. We deduce that here the matrix is still porous and reticulated, but the higher density will therefore tend to entrap Ba-rich nanoparticles at the surface and lead to the microcrucible growth observed. It is likely that in previous reports where nitrate precursors were used to form the complex oxides of $La_3Ga_5SiO_{14}$ (*19*) and $La_{0.67}Sr_{0.33}MnO_3$ (*20*) via a porous matrix, the faceted-ended nanowires produced were also the result of a microcrucible mechanism.

Through judicious design of the synthetic protocol, we have demonstrated the direct observation of a microcrucible growth mechanism and confirmed that it is a viable method for the growth of complex oxide nanowires. The successful formation of nanowires is predicated on the presence of a catalytic nanoparticle and a porous matrix that enables migration of the former through the latter, leading to nanowire outgrowth at the surface. The uniform cross section arising from the microcrucible mechanism means that the nanowires produced in this way will have the same physical properties along their entire length, leading to more uniform current-carrying ability, ferroic behavior, and tensile strength for the future use of complex functional oxide nanowires in applications.

References and Notes

1. G. A. Ozin, *Nanochemistry—A Chemical Approach to Nanomaterials* (Royal Society of Chemistry, Cambridge, 2005).
2. K. Xu, J. R. Heath, *Nano Lett.* **8**, 3845–3849 (2008).
3. Z. L. Wang, *J. Phys. Condens. Matter* **16**, R829–R858 (2004).
4. J. D. Berrigan *et al*., *Adv. Funct. Mater.* **21**, 1693–1700 (2011).
5. I. Matsubara *et al*., *J. Cryst. Growth* **141**, 131–140 (1994).
6. P. Badica, K. Togano, *J. Mater. Res.* **20**, 3358–3367 (2005).
7. P. Badica, K. Togano, S. Awaji, K. Watanabe, H. Kumakura, *Supercond. Sci. Tech.* **19**, R81–R99 (2006).
8. C. Yang, Z. Zhong, C. M. Lieber, *Science* **310**, 1304–1307 (2005).
9. K. Nagashima, T. Yanagida, K. Oka, H. Tanaka, T. Kawai, *Appl. Phys. Lett.* **93**, 153103 (2008).
10. See supplementary materials on *Science* Online.
11. Y. Cao *et al*., *Nano Lett.* **12**, 3783–3787 (2012).
12. A. Gorbunov, O. Jost, W. Pompe, A. Graff, *Carbon* **40**, 113–118 (2002).
13. P. Badica *et al*., *Supercond. Sci. Tech.* **25**, 105003 (2012).
14. S. Cagliero *et al*., *Supercond. Sci. Tech.* **25**, 125002 (2012).
15. Z. A. Schnepp, S. C. Wimbush, S. Mann, S. R. Hall, *Adv. Mater.* **20**, 1782–1786 (2008).
16. S. R. Hall, *Adv. Mater.* **18**, 487–490 (2006).
17. L. A. Chick *et al*., *Mater. Lett.* **10**, 6–12 (1990).
18. H. C. Zeng, S. K. Tung, *Chem. Mater.* **8**, 2667–2672 (1996).
19. Z. Schnepp, J. Mitchells, S. Mann, S. R. Hall, *Chem. Commun.* **46**, 4887–4889 (2010).
20. Z. Schnepp, S. C. Wimbush, S. Mann, S. R. Hall, *CrystEngComm* **12**, 1410–1415 (2010).

Acknowledgments: S.R.H. and R.B. acknowledge the Engineering and Physical Sciences Research Council (EPSRC), UK (grant EP/G036780/1), and the Bristol Centre for Functional Nanomaterials for project funding. S.R.H. and R.B. also acknowledge the support of the EPSRC under their "Building Global Engagements in Research" scheme (grant EP/K004581/1) and the Electron and Scanning Probe Microscopy Facility and Electron Microscopy Group in the Schools of Chemistry and Physics, University of Bristol, respectively. Z.S. would like to thank the National Institute for Materials Science (NIMS) in Japan for the award of an International Center for Young Scientists Postdoctoral Fellowship. All authors would like to thank M. Takeguchi for his help with all aspects of TEM operation at NIMS. A part of this work was supported by the NIMS microstructural characterization platform as a program of the "Nanotechnology Platform" of the Ministry of Education, Culture, Sports, Science and Technology, Japan.

Supplementary Materials

www.sciencemag.org/content/344/6184/623/suppl/DC1
Materials and Methods
Figs. S1 to S7
Reference (*21*)
Movies S1 and S2

31 January 2014; accepted 11 April 2014
10.1126/science.1251594

Spatially Distributed Local Fields in the Hippocampus Encode Rat Position

Gautam Agarwal,[1] Ian H. Stevenson,[1]* Antal Berényi,[2,3] Kenji Mizuseki,[2]† György Buzsáki,[2]†† Friedrich T. Sommer[1]††

Although neuronal spikes can be readily detected from extracellular recordings, synaptic and subthreshold activity remains undifferentiated within the local field potential (LFP). In the hippocampus, neurons discharge selectively when the rat is at certain locations, while LFPs at single anatomical sites exhibit no such place-tuning. Nonetheless, because the representation of position is sparse and distributed, we hypothesized that spatial information can be recovered from multiple-site LFP recordings. Using high-density sampling of LFP and computational methods, we show that the spatiotemporal structure of the theta rhythm can encode position as robustly as neuronal spiking populations. Because our approach exploits the rhythmicity and sparse structure of neural activity, features found in many brain regions, it is useful as a general tool for discovering distributed LFP codes.

Two qualitatively different types of electric signals can be detected extracellularly, action potentials (spikes) and local field potentials (LFPs) (*1*–*5*), and these signals are regarded as complementary readouts of information about neuronal computation (*5*, *6*). As a rat moves through its environment, hippocampal pyramidal cells spike at specific locations (place cells) (*7*). In contrast, the LFP maintains rhythmic (8 to 9 Hz) theta oscillations, independent of the rat's position (*8*, *9*). We hypothesized that the theta rhythm also contains information about the rat's position, since it is

primarily the place cell population whose membrane potential fluctuations give rise to the LFP (*10*).

Rats were implanted with 32-, 64-, or 256-site silicon probes in the hippocampus to monitor both LFP and unit firing (Fig. 1A) while they traversed a linear track (Fig. 1B), open field, or a T maze (*11*). When mapped onto electrode space, the theta rhythm showed spatiotemporal variations (Fig. 1A) that changed gradually over multiple cycles (movie S1). By analogy to radio communication, we defined the theta oscillation to be a carrier wave whose modulation contains information. This information was extracted from the theta rhythm using a demodulation operation (fig. S1). First, the theta-band-filtered oscillatory activity of each electrode was converted to a complex-valued signal, representing its instantaneous phase and amplitude (Fig. 1D). The carrier signal, identified by principal component analysis, was highly coherent across electrodes (Fig. 1D, lower trace). The demodulation operation then removed the phase of the theta carrier from each electrode, resulting in a spatiotemporal pattern of relative phase and amplitude that covaried smoothly (Fig. 1, E and F) with the rat's position.

The position of the rat during navigation was estimated from the demodulated LFP (Fig. 2 and fig. S2) and compared to spike-based decoding (*1*, *7*, *12*, *13*). Although the cross-validated accuracy of the two decoders was comparable [optimal linear estimator (OLE) median error 6.7 ± 0.2 cm (LFP) and 9.2 ± 0.2 cm (spiking)] (Fig. 2G and fig. S2), they had distinct velocity and position dependence (Fig. 2, B and D). Accurate decoding of the theta rhythm depended on demodulation, as well as preserving the high dimensionality of the signal, even though the variance of the multielectrode signal was largely concentrated in a low-dimensional subspace (Fig. 2C), visible in the strong correlations in the LFP recorded at different electrodes (Fig. 1, C and D). Whitening and Bayesian decoding methods further improved accuracy, especially in the open field (120 by 120 or 180 by 180 cm^2) (Fig. 2G).

Because position encoding is sparse, a theoretical result (*14*) based on compressed sensing (*15*) suggests that unsupervised learning can discover position-dependent sparse structure in the LFP without explicit knowledge of the rat's position. We tested this prediction by examining the evolving spatiotemporal distribution of the theta-filtered LFP using independent component analysis (ICA) (*16*, *17*). A subset of the components [termed feature-tuned field potentials (FFPs)] showed selective activation at specific positions along one direction of motion (Fig. 3A and figs. S3 and S4) and comprised the major portion of the signal variance (53%, 69%, and 79% of total variance for $n = 3$ rats). When FFPs were projected back onto the anatomical space, they were distributed across the entire surface of the electrode array (Fig. 3B and movie S2).

We next asked whether the sparse structure of the broadband LFP (4 to 80 Hz) is also position dependent by training a convolutional sparse coding algorithm (*18*), which models signals as

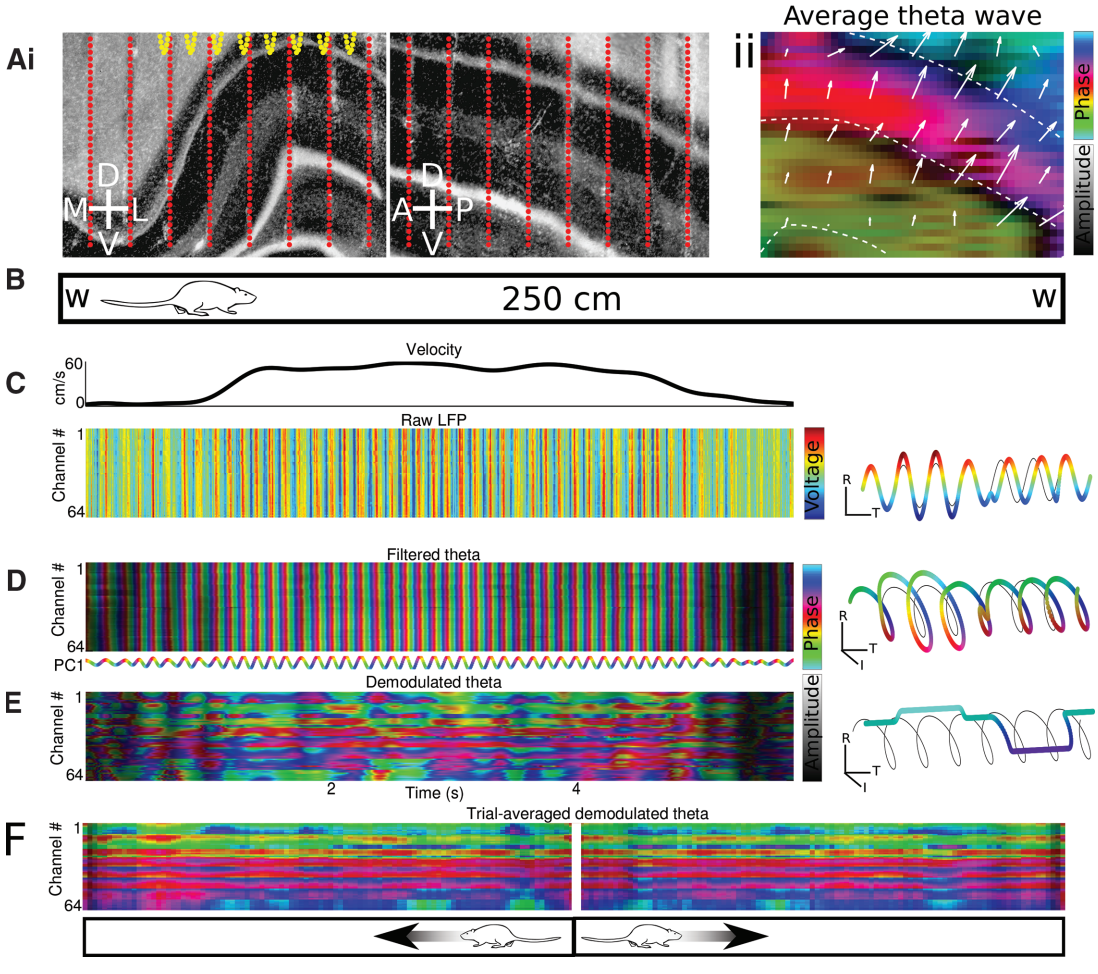

Fig. 1. Recording space- and time-dependent variations in theta rhythm. (**Ai**) Arrangement of 64 (yellow) and 2 by 256 (red) electrode arrays implanted in the hippocampi of different rats. Left and right panels depict recordings along orthogonal axes: D/V, dorsoventral; A/P, anteroposterior; M/L, mediolateral. (**Aii**) Average spatial distribution of theta recorded by the electrode array in the right panel of (Ai) reveals systematic differences in the anatomical distribution of the theta rhythm. Arrows depict local phase gradients. (**B**) A rat runs across a 250-cm track to receive a water reward (w) at both ends. (**C** to **E**) (Left) LFP recorded during one run across the track. (Right) schematic of signal representation. Axes: T, time; R, real; I, imaginary. (C) Velocity of the rat (top) and the original, broadband signal (bottom), which shows a strong theta rhythm during running. (D) (Top) Filtering the signal with Morlet wavelet (5 to 11 Hz half-power cutoff) results in a complex-valued waveform with time-varying amplitude and phase. (Bottom) The first principal component (PC1) of the complex-valued signal, which tracks the global theta oscillation. (E) Demodulating the signal using PC1 as a carrier identifies modulations in amplitude and phase. (**F**) Averaging the demodulated signal over multiple runs reveals that its variations depend systematically on the rat's position. For (E) and (F), phase is scaled by a factor of 16 to emphasize time-varying structure.

[1]Redwood Center for Theoretical Neuroscience, University of California, Berkeley, Berkeley, CA 94720, USA. [2]The Neuroscience Institute, Center for Neural Science, New York University, School of Medicine, New York, NY 10016, USA. [3]Magyar Tudományos Akadémia-Szegedi Tudományegyetem (MTA-SZTE) Momentum Oscillatory Neuronal Networks Research Group, University of Szeged, Department of Physiology, Szeged, H-6720, Hungary.

*Present address: University of Connecticut, Department of Psychology, Storrs, CT 06269, USA.
†Present address: Allen Institute for Brain Science, Seattle, WA 98103, USA.
††Corresponding author. E-mail: fsommer@berkeley.edu (F.T.S.); gyorgy.buzsaki@nyumc.org (G.B.)

a sparse superposition of spatiotemporal features. Despite differences in the analysis method and training data, the broadband components activated at single positions were spaced along the whole track, similar to the theta-band components (Fig. 3D and fig. S5). Each broadband feature exhibited the sawtooth waveform characteristic of hippocampal theta, with unique spatial variations in attributes such as onset and peak time (Fig 3C). Broadband features, similar to theta-band FFPs, remained largely silent outside a small range of preferred positions, each activating briefly at theta frequency (Fig. 3D).

The entire population of FFPs in a given session uniformly tiled the linear track (Fig. 4A). The phase of each demodulated FFP showed progressive advancement as the rat traversed the corresponding place field (Fig. 4A), reminiscent of the theta-phase precession of place cell spikes (*19*), and suggesting that the theta-rhythm arises largely from a population of phase-precessing neurons (*10*). The distribution of the place fields of pyramidal cells was more irregular than that of the FFPs (Fig. 4B and fig. S6), consistent with the performance of the corresponding decoders (Fig. 2). Unlike FFPs, pyramidal cells had multiple place fields in one or both directions of travel, leading to distinct pairwise activity profiles of the populations (Fig. 4C and fig. S6). We also examined FFPs as the rat performed a spatial alternation memory task (*20*) in a T maze with a 10-s delay period in a large waiting area (Fig. 4D). Recordings from two 256-electrode arrays (*11*) contained ~50 FFPs that together covered the entire maze (Fig. 4D). About half of all FFPs densely tiled the two-dimensional (2D) waiting area (Fig. 4D). Most 2D place fields occupied largely similar positions independent of whether the rat came from a leftward or rightward journey (fig. S7). Accurate LFP decoding and identification of FFPs could also be performed on recording sites within the dendritic layers (fig. S8), excluding somatic layers where spikes were detected.

To understand how properties of FFPs relate to the activity of the underlying neuronal population, a simulation was constructed in which the LFP was modeled as the superimposed activity generated by numerous place-modulated synaptic inputs (fig. S9). Although individual electrodes showed weak place-tuning, their collective activity could nonetheless be decoded. Furthermore, ICA identified a large number of learned FFPs tuned to very specific locations of the track, consistent with theory (fig. S10) (*14*). However, as the trial-by-trial variability of neuronal activity was increased, ICA identified a decreasing number of FFPs. For noisy populations, FFP width increased in proportion to, but never exceeded, the tuning width of the underlying population's place fields.

We demonstrated that the rat's location is encoded by spatial variations of the hippocampal LFP. An often-assumed limitation of the LFP is that each electrode subsamples (pools) the activity of a large population of neurons. In topographically

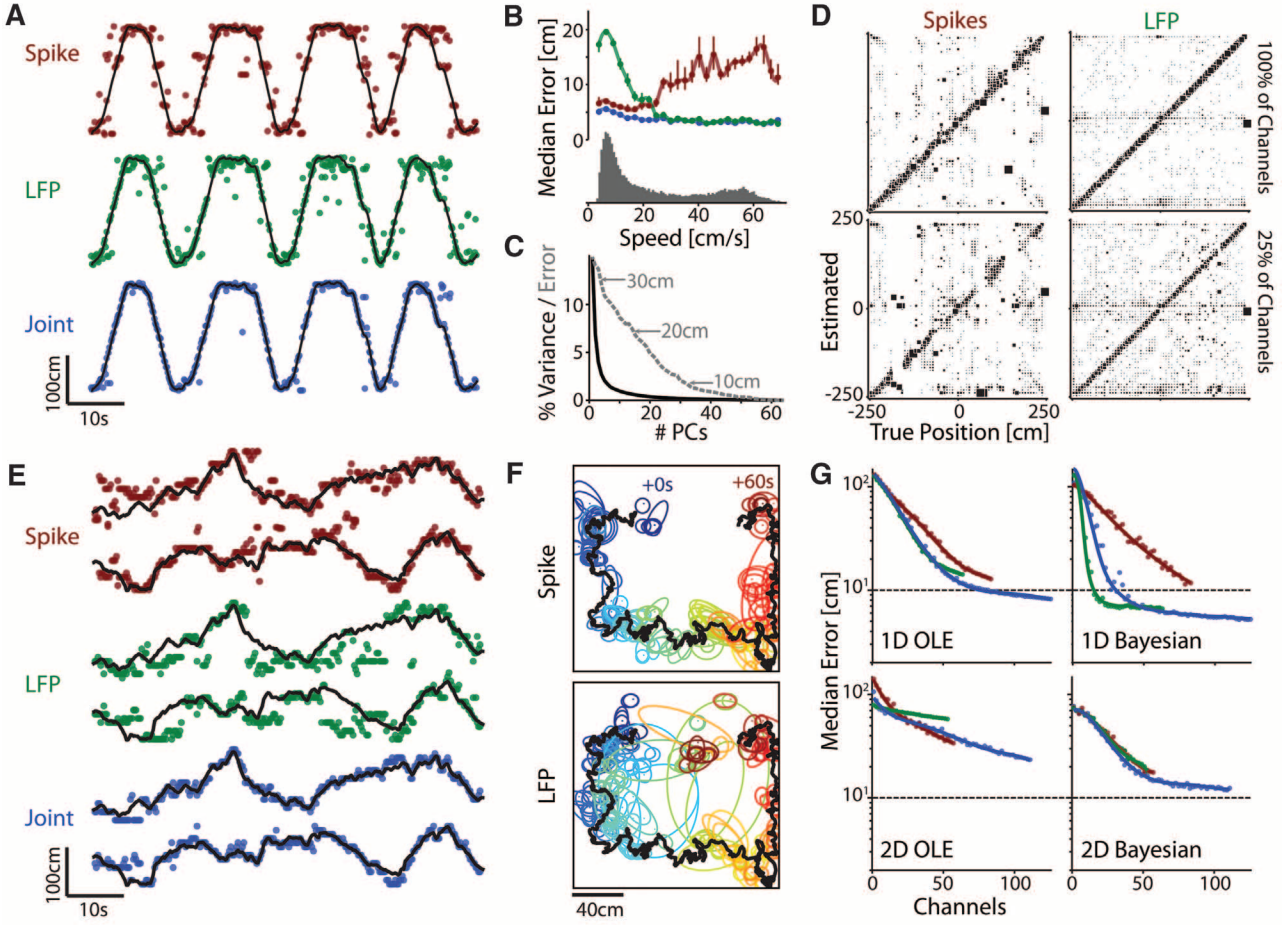

Fig. 2. Decoding of position by demodulated LFP and spikes. (**A**) Decoding of rat position on a linear track by LFP and spikes. Lines indicate actual trajectory, while dots indicate OLE estimate of position (*y* axis) at each time point (*x* axis). (**B**) LFP-based decoder performs best at high velocities, unlike spike-based decoder. The lower histogram shows the time spent at different speeds. (**C**) Variance is largely explained by PC1 (~85% of total variance, falling outside of plotted range), and accurate, cross-validated decoding depends on a large number of PC dimensions. (**D**) Histogram of decoder predictions; dark squares indicate high-probability events. Decoders trained on subsets of LFP channels (right) degrade uniformly, whereas those trained on spikes from subsets of neurons (left) degrade in a patchy manner. (**E**) Decoding of rat position in a 2D open field using a Bayesian filter-based decoder. Lines indicate actual trajectory in *x* and *y* coordinates; dots indicate decoder estimates. (**F**) Bird's eye view of actual (black) and estimated (color) position at different time points. Ellipses indicate ~1 SD confidence regions. (**G**) Median error of decoders as a function of the number of (random) channels used. Data is from rat ec014, with 64 electrodes straddling the cornu ammonis 1 (CA1) pyramidal layer. Identical color codes are used for (A), (B), (E), and (G).

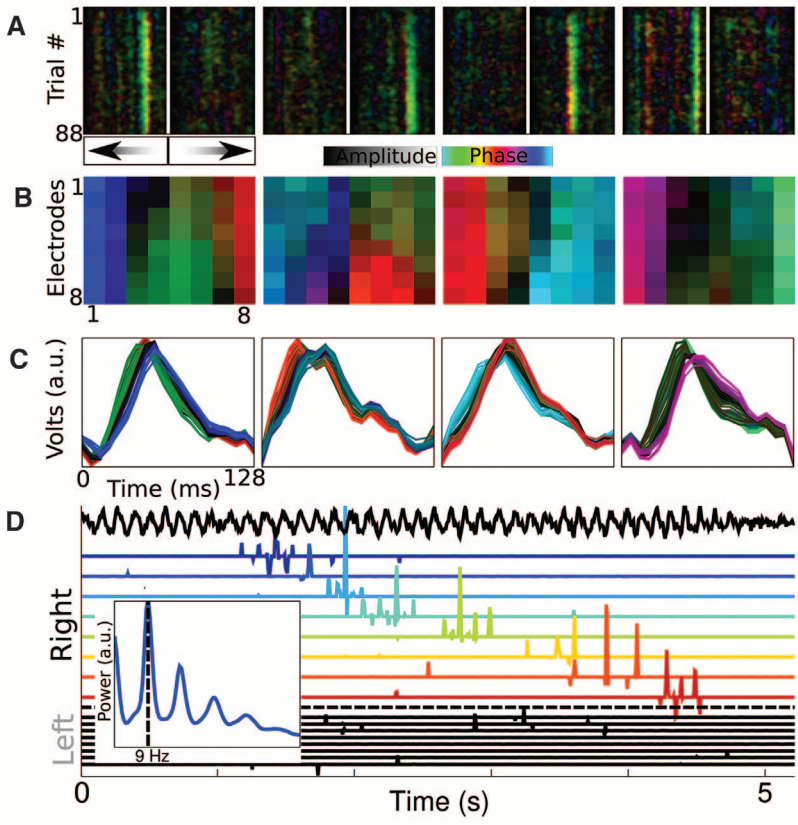

Fig. 3. Sparse decompositions of oscillatory features in multielectrode data. (**A**) ICA of the signal reveals components, termed FFPs, that activate selectively at particular locations. (**B**) Each FFP exhibits a unique phase-amplitude relationship across the recorded area. For display purposes, FFPs are mean-subtracted to reveal differences (see supplementary materials). (**C**) Sparse decomposition of the broadband signal (4 to 80 Hz) reveals components that activate at corresponding locations and have distinctive broadband structure, consisting of diverse onsets and peaks. Individual traces are colored according to their corresponding electrodes in (B). (**D**) Broadband sparse components activate sequentially on the track, also exhibiting theta periodicity; components that activate in the reverse direction (black lines) remain silent. (Inset) Mean power spectrum of component activations. Data was recorded by a 64-electrode array implanted in CA1.

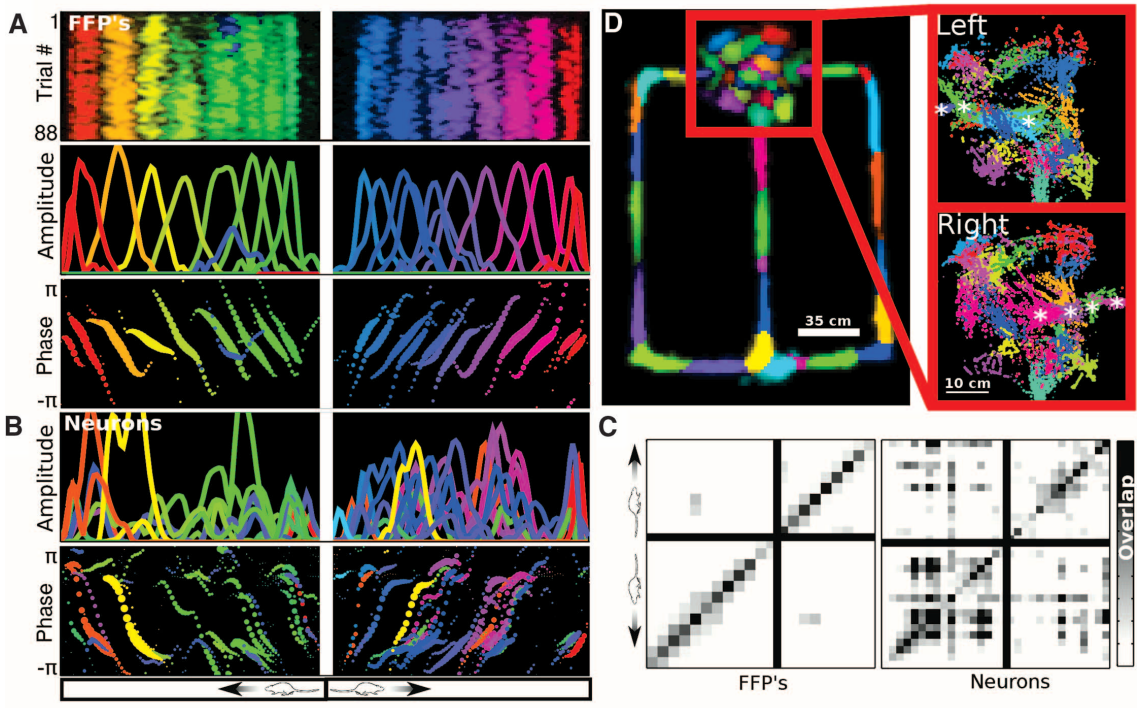

Fig. 4. Population properties of FFPs and neuronal spikes during a single session. (**A**) FFPs uniformly tile the length of the track. The spatial extent and spacing of different FFPs is largely homogeneous across the track (middle). FFPs exhibit phase precession with respect to PC1 (bottom). (**B**) Pyramidal cells have place fields that are more variable in extent and distribution. (**C**) The overlap of FFP activations is largely restricted to neighbors, unlike that for pyramidal cells [grayscale range of *P*(Overlap) = 0 to 0.1]. (**D**) Activation of FFPs in a T maze. Waiting area is enclosed in a red box. Right panels show close-up of activations in waiting area, separated by direction of entry. Asterisks mark activations that are entry-direction selective. Each point represents a time bin where FFP activation exceeds a threshold, its size indicating the magnitude of activation. In (A) and (B), place-field hues are assigned based on location of maximal activation; in (D), hues are assigned to distinguish neighbors. Data for (A), (B), and (C) are collected by a 64-electrode array; (D) was from 2- by 256-electrode arrays.

organized brain regions, this limitation is less hampering, because the electrode conveys the activity of similarly tuned neurons (*21*, *22*). In contrast, because place cells in the hippocampus are distributed without topographic ordering (*23*), the LFP measured at any single location exhibits only weak place-modulation (fig. S9). However, compressed sensing methods can recover sparse signals even from mixed and subsampled measurements (*15*). During movement, population activity in the hippocampus is largely determined by a single (i.e., highly sparse) cause: the rat's current position. Therefore, distributed messages can be discovered by unsupervised learning methods such as ICA (*14*). Our experimental and simulation results show that the ICA-derived FFPs exhibit several properties reminiscent of place cells: They have smooth, localized place fields, exhibit phase precession, and show considerable trial-by-trial variability (*24*). Building on earlier work [e.g., (*25*)], these findings show how large-scale recordings of LFP can help in understanding the organization of activity in other brain regions, as well as developing robust decoders for brain-computer interfaces.

References and Notes

1. M. A. Wilson, B. L. McNaughton, *Science* **261**, 1055–1058 (1993).
2. W. J. Freeman, *Clin. Neurophysiol.* **115**, 2077–2088 (2004).
3. G. Buzsáki, C. A. Anastassiou, C. Koch, *Nat. Rev. Neurosci.* **13**, 407–420 (2012).
4. S. Łęski, H. Lindén, T. Tetzlaff, K. H. Pettersen, G. T. Einevoll, *PLOS Comput. Biol.* **9**, e1003137 (2013).
5. N. K. Logothetis, *J. Neurosci.* **23**, 3963–3971 (2003).
6. E. R. John, *Science* **177**, 850–864 (1972).
7. J. O'Keefe, L. Nadel, *The Hippocampus as a Cognitive Map* (Clarendon Press, Oxford Univ. Press, Oxford and New York, 1978).
8. C. H. Vanderwolf, *Electroencephalogr. Clin. Neurophysiol.* **26**, 407–418 (1969).
9. G. Buzsáki, E. I. Moser, *Nat. Neurosci.* **16**, 130–138 (2013).
10. C. Geisler *et al.*, *Proc. Natl. Acad. Sci. U.S.A.* **107**, 7957–7962 (2010).
11. A. Berényi *et al.*, *J. Neurophysiol.* **111**, 1132–1149 (2014).
12. O. Jensen, J. E. Lisman, *J. Neurophysiol.* **83**, 2602–2609 (2000).
13. K. Zhang, I. Ginzburg, B. L. McNaughton, T. J. Sejnowski, *J. Neurophysiol.* **79**, 1017–1044 (1998).
14. C. Hillar, F. T. Sommer, When can dictionary learning uniquely recover sparse data from subsamples? (2011); http://arxiv.org/abs/1106.3616).
15. D. L. Donoho, *Inf. Theory IEEE Trans. On* **52**, 1289–1306 (2006).
16. A. Hyvärinen, E. Oja, *Neural Netw.* **13**, 411–430 (2000).
17. M. Novey, T. Adali, *Proc. IEEE Workshop Mach. Learn. Signal Process* (Arlington, VA, 6 to 8 September, 2006), pp. 79–84.
18. A. Khosrowshahi *et al.*, *Exploring the Statistical Structure of Large-Scale Neural Recordings Using a Sparse Coding Model* (Cosyne, Salt Lake City, UT, 2010).
19. J. O'Keefe, M. L. Recce, *Hippocampus* **3**, 317–330 (1993).
20. E. Pastalkova, V. Itskov, A. Amarasingham, G. Buzsáki, *Science* **321**, 1322–1327 (2008).
21. C. Mehring *et al.*, *Nat. Neurosci.* **6**, 1253–1254 (2003).
22. A. de Cheveigné, J.-M. Edeline, Q. Gaucher, B. Gourévitch, *J. Neurophysiol.* **109**, 261–272 (2013).
23. A. D. Redish *et al.*, *J. Neurosci.* **21**, RC134 (2001).
24. R. Schmidt *et al.*, *J. Neurosci.* **29**, 13232–13241 (2009).
25. W. J. Freeman, B. Baird, *Behav. Neurosci.* **101**, 393–408 (1987).
26. K. Mizuseki, A. Sirota, E. Pastalkova, K. Diba, G. Buzsaki, Multiple single unit recordings from different rat hippocampal and entorhinal regions while the animals were performing multiple behavioral tasks (2013); available at http://crcns.org/data-sets/hc/hc-3.

Acknowledgments: This work was supported by NIH National Research Service Award fellowship no. 1F32MH093048 (G.A.); NSF CIF-D-018 no. 0937060 (I.H.S.); Marie Curie FP7-PEOPLE-2009-IOF grant no. 254780, EU-FP7-ERC-2013-Starting grant no. 337075, and the Lendület program of the Hungarian Academy of Sciences (A.B.); Japan Society for the Promotion of Science's Research Fellowship for Research Abroad (K.M.); NIH nos. NS-034994, MH-54671, and NS074015, NSF SBE no. 0542013, and the J. D. McDonnell Foundation (G.B.); NSF nos. 0855272 and 1219212 (F.S.). We thank D. Kaufman and J. Wolfe for advice on movies; C. Thanapirom for suggesting the Kuramoto model for rendering; K. D. Harris for suggestions about modeling; A. Khosrowshahi, J. Culpepper, C. Cadieu, and B. Olshausen for convolutional sparse coding; Walter Freeman for feedback; and members of the Buzsaki laboratory and the Redwood Center for discussions. All data collected from 32- to 64-electrode arrays is available in the hc-3 data set at crcns.org (*26*).

Supplementary Materials

www.sciencemag.org/content/344/6184/626/suppl/DC1
Materials and Methods
Figs. S1 to S10
Movies S1 and S2
References (*27*, *28*)

6 January 2014; accepted 14 April 2014
10.1126/science.1250444

Vascular and Neurogenic Rejuvenation of the Aging Mouse Brain by Young Systemic Factors

Lida Katsimpardi,[1,2]* Nadia K. Litterman,[1,2] Pamela A. Schein,[1,2] Christine M. Miller,[1,2,3] Francesco S. Loffredo,[1,2,4] Gregory R. Wojtkiewicz,[5] John W. Chen,[5] Richard T. Lee,[1,2,4] Amy J. Wagers,[1,2,3] Lee L. Rubin[1,2]*

In the adult central nervous system, the vasculature of the neurogenic niche regulates neural stem cell behavior by providing circulating and secreted factors. Age-related decline of neurogenesis and cognitive function is associated with reduced blood flow and decreased numbers of neural stem cells. Therefore, restoring the functionality of the niche should counteract some of the negative effects of aging. We show that factors found in young blood induce vascular remodeling, culminating in increased neurogenesis and improved olfactory discrimination in aging mice. Further, we show that GDF11 alone can improve the cerebral vasculature and enhance neurogenesis. The identification of factors that slow the age-dependent deterioration of the neurogenic niche in mice may constitute the basis for new methods of treating age-related neurodegenerative and neurovascular diseases.

In the adult brain, neural stem cells reside in a three-dimensional (3D) heterogeneous niche, where they are in direct contact with blood vessels and the cerebrospinal fluid. The vasculature can influence neural stem cell proliferation and differentiation by providing a local source of signaling molecules secreted from endothelial cells (*1*) as well as by delivering systemic regulatory factors (*2*). The hormone prolactin (*3*), dietary restriction (*4*), and an exercise/enriched environment (*5*) positively modulate neurogenesis, whereas increased levels of glucocorticoids associated with stress have the opposite effect (*6*). In the aging niche, the vasculature deteriorates with a consequent reduction in blood flow (*7*), and the neurogenic potential of neural stem cells declines, leading to reduced neuroplasticity and cognition (*8*–*10*). Systemic factors can also affect these aging-associated events, either positively in which circulating monocytes enhance remyelination in aged mice (*11*, *12*) or negatively in which the accumulation of chemokines in old blood can reduce neurogenesis and cognition in young mice (*10*).

To test whether the age-related decline of the neurogenic niche can be restored by extrinsic young signals, we used a mouse heterochronic parabiosis model. Our experiments reveal a remodeling of the aged cerebral vasculature in response to young systemic factors, producing noticeably greater blood flow, as well as activation of subventricular zone (SVZ) neural stem cell proliferation and enhanced olfactory neurogenesis, leading to an improvement in olfactory function. Furthermore, we tested GDF11, a circulating transforming growth factor–β (TGF-β) family member that reverses cardiac hypertrophy in aged mice (*13*), and found that it can also stimulate vascular remodeling and increase neurogenesis in aging mice. Thus, we have observed that age-dependent remodeling of this niche is reversible by means of systemic intervention.

[1]Department of Stem Cell and Regenerative Biology, Harvard University, Cambridge, MA 02138, USA. [2]Harvard Stem Cell Institute, Cambridge, MA 02138, USA. [3]Howard Hughes Medical Institute, Joslin Diabetes Center and the Paul F. Glenn Laboratories for the Biological Mechanisms of Aging, Harvard Medical School, Boston, MA 02115, USA. [4]Cardiovascular Division, Department of Medicine, Brigham and Women's Hospital, Boston, MA 02115, USA. [5]Center for Systems Biology and Department of Radiology, Massachusetts General Hospital, Harvard Medical School, Boston, MA 02115, USA.

*Corresponding author. E-mail: lee_rubin@harvard.edu (L.L.R.); lida_katsimpardi@harvard.edu (L.K.)

To test our hypothesis, we generated heterochronic parabiotic pairs between 15-month-old (Het-O) and 2-month-old (Het-Y) male mice, as well as control groups of age-matched pairs, namely isochronic young (Iso-Y) and isochronic old (Iso-O) pairs (fig. S1). The average lifespan of this strain of mice in the National Institute of Aging's growth conditions is 27 months. All parabiotic pairs remained surgically joined for 5 weeks (*14*). Because aging leads to a reduced number of progenitor cells (*15*–*17*), we assessed how heterochronic parabiosis can affect the SVZ neural stem cell populations by analyzing coronal SVZ sections (fig. S2A) of heterochronic and isochronic brains for different SVZ stem/progenitor cell types, such as proliferative Ki67$^+$ cells, Sox2$^+$ stem cells, and Olig2$^+$ transit amplifying progenitors (Fig. 1, A, B, and C, respectively). Quantification of these sections revealed an increase of 26.9% for Ki67$^+$ cells (fig. S2B), 112% for Sox2$^+$ cells (Fig. 1D), and 57% for Olig2$^+$ cells (Fig. 1E) in the Het-O compared with the Iso-O SVZ. However, these cell populations were unaffected in the Het-Y mice (Fig. 1, D and E, and fig.S2C). Systemic factors in old blood can have detrimental effects on hippocampal neurogenesis in young animals (*10*); however, we saw no decrease in neural stem/progenitor cell numbers in the SVZ of young mice joined to 15-month-old partners. We wondered whether this discrepancy was related to differences between the SVZ and the hippocampus or to the fact that our old animals were younger than the old animals used in the previous study. We therefore joined 2-month-old mice with 21-month-old mice (fig. S3A) and found that the older blood negatively affected young SVZ neurogenesis because Het-Y21 mice showed decreased proliferative Ki67$^+$ (fig. S3, B and D) and Sox2$^+$ cell populations (fig. S3, C and E) in the SVZ as compared with those of Iso-Y mice. These data are consistent with the previously reported negative effect of older blood on hippocampal neurogenesis (*10*) and indicate an age-dependent accumulation of factors in the blood of older mice that affect neurogenic zones in both the hippocampus and SVZ.

Aging results in longer cell-cycle times in precursor cells isolated from the SVZ (*18*). To assess the effect of heterochronic parabiosis on neural stem cell proliferation, we cultured neural stem cells from parabiotic brains as neurospheres (*19*, *20*). After the first passage, neurospheres derived from the Het-O SVZ were 43% larger in diameter than those derived from the Iso-O SVZ (fig. S4), and after removal of growth factors, they generated ~2.5-fold more TuJ1$^+$ neurons than did the Iso-O (fig. S5). This suggests that neural stem cells exposed to young systemic factors increase their ability to proliferate and differentiate into neurons. Collectively, these data demonstrate that youthful circulating factors can restore the self-renewal and differentiation potential of aged SVZ stem cells, and this effect can persist for some time after isolation from the mouse brain.

Adult SVZ neural stem and progenitor cells differentiate into neuroblasts and migrate through the rostral migratory stream to the olfactory bulb, where they mature into interneurons (*21*). We asked whether the increase in neural stem and progenitor cells could produce a subsequent change in olfactory neurogenesis in the Het-O mice. We pulsed parabiotic pairs with BrdU to label newborn neurons, and after 3 weeks, the mice were analyzed for BrdU$^+$/NeuN$^+$ cells to quantify newborn neurons (Fig. 2A). As expected from our in vitro studies, we observed increased olfactory neurogenesis in vivo. Het-O newborn neuron populations were enriched by 92% as compared with Iso-O populations (Fig. 2B). In accordance with our above results, the number of new neurons in Het-Y mice was only slightly negatively affected, although the decrease was not statistically significant (Fig. 2C).

To test the functional implication of these findings, we performed an olfaction assay in which naïve single parabionts, separated from their parabiotic partners after 5 weeks, were exposed to different concentrations of an odorant (*22*). After a short habituation period, each parabiont was presented with different concentrations of an odorant, and the total time that each parabiont spent exploring the odorant for each concentration was measured. In this assay, Het-O (Fig. 2D) and young control (Fig. 2D) mice both spent more time exploring a low concentration of odorant (diluted 10^5 times), whereas a high concentration (diluted 10 times) produced a negative response. In comparison, Iso-O mice spent roughly the same amount of time exploring the odorant regardless of its concentration (Fig. 2D). These results suggest that Het-O mice have a higher olfactory discrimination than do the Iso-O mice. Therefore, exposure of the neurogenic niche to young systemic factors enhances functional neurogenesis, culminating in improved olfactory behavior.

Cerebrovascular architecture, capillary density, and cerebral blood flow have been reported to decline with aging (*23*–*25*). Given the interconnection between the vasculature and neural stem cells, we asked whether young blood factors can also rejuvenate blood vessel architecture and function. To test this, we created "angiograms," 3D reconstructions of the blood vessels (fig. S6A). Volumetric analysis of these angiograms showed that aging causes a decrease in blood vessel volume, as expected (Fig. 3, A and B). However, heterochronic parabiosis reversed this decline, increasing blood vessel volume by 87% in the Het-O compared with the Iso-O group (Fig. 3, A and B). Furthermore, we

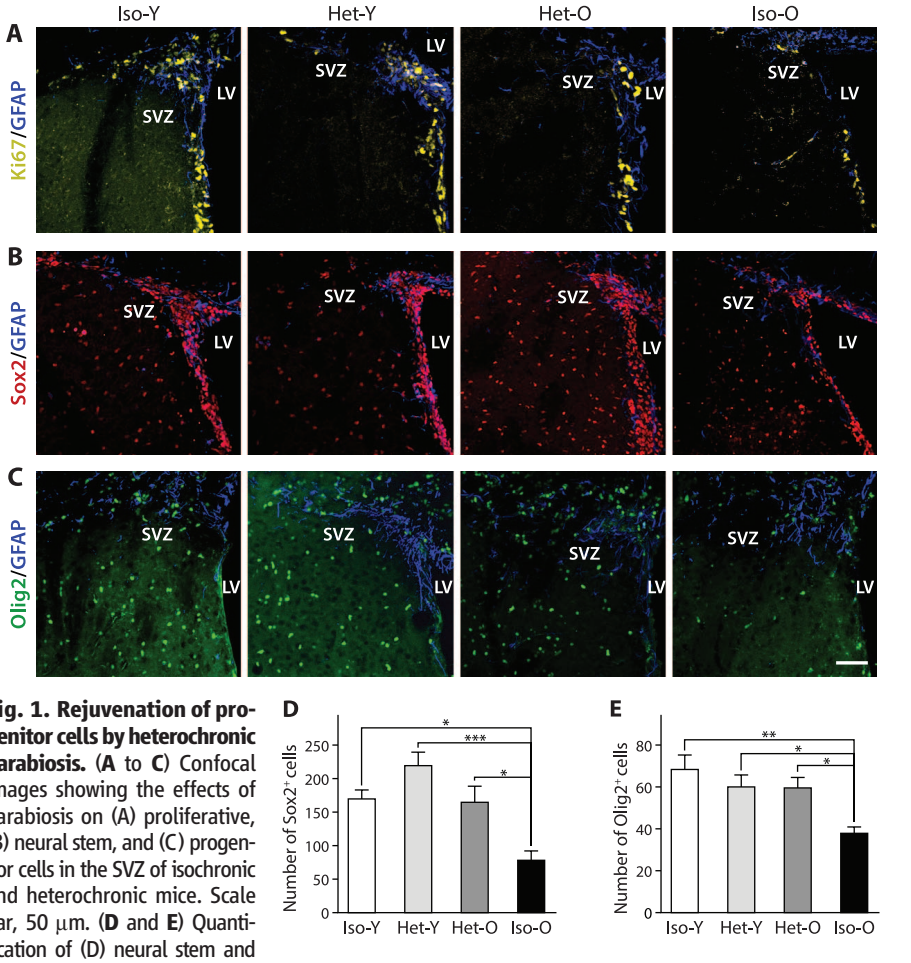

Fig. 1. Rejuvenation of progenitor cells by heterochronic parabiosis. (**A** to **C**) Confocal images showing the effects of parabiosis on (A) proliferative, (B) neural stem, and (C) progenitor cells in the SVZ of isochronic and heterochronic mice. Scale bar, 50 μm. (**D** and **E**) Quantification of (D) neural stem and (E) progenitor cell populations of the above images ($n = 9$ animals for each experimental group, $^*P < 0.05$, $^{**}P < 0.01$, $^{***}P < 0.001$). Data shown as mean ± SEM; statistical analysis was performed with analysis of variance (ANOVA).

observed that blood vessel branching increased by 21% in Het-O versus Iso-O mice (fig. S6B). Some blood vessels in the Het-O mice were not associated with AQP4$^+$ astrocytic endfeet, suggesting that these vessels are newly formed and potentially leaky, thus providing NSCs with enhanced nutritive support (fig. S6E). This phenomenon of vascular remodeling in the Het-O mice extended to other neurogenic areas such as the hippocampus (fig. S7, A and B) and also to non-neurogenic areas such as the cortex (Fig. S7C). To test whether the increased blood vessel volume led to functional improvement, we measured cerebral blood flow (CBF) with magnetic resonance imaging (MRI) in the parabiotic mice (Fig. 3E) because CBF is known to decrease with aging (*26*). We found that heterochronic parabiosis indeed restored CBF to the levels seen in young animals (Fig. 3, C, D, and E), indicating that the vascular remodeling observed in Het-O mice changes the hemodynamics of the vascular system in the central nervous system. Young vasculature, on the contrary, retained the same volumetric (Fig. 3, A and B), blood flow (fig. S6D), and branching (fig. S6C) characteristics in both isochronic and heterochronic parabiosis.

New vessels can form either by sprouting from existing capillaries or de novo from circulating

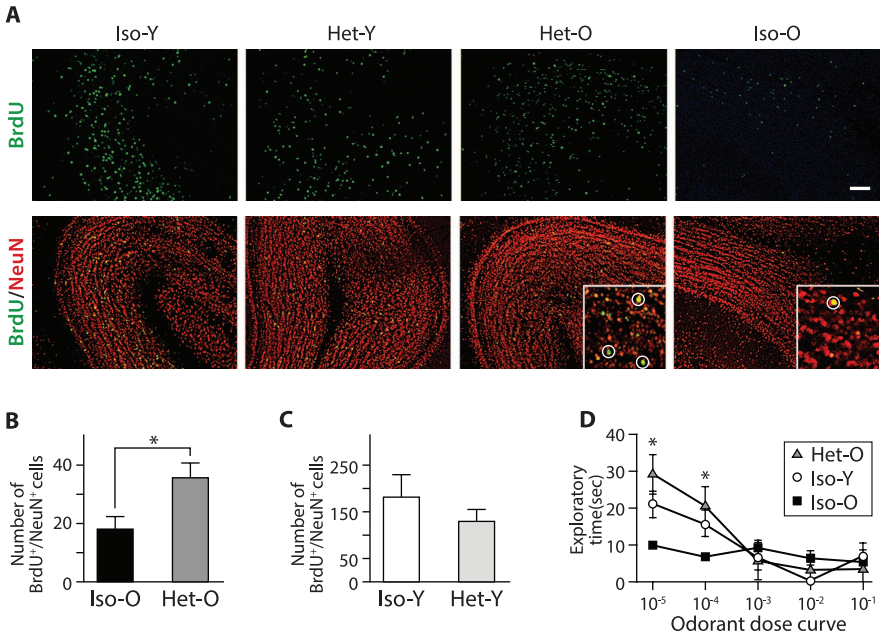

Fig. 2. Heterochronic parabiosis enhances neurogenesis and cognitive functions in the aging mouse. (**A**) Representative images of olfactory bulbs showing newborn neurons in isochronic and heterochronic parabionts. Scale bar, 100 μm. Circles in higher-magnification inserts indicate BrdU$^+$/NeuN$^+$ double-positive cells. (**B** and **C**) Quantification of neurogenesis in the olfactory bulbs of (B) old and (C) young parabionts (n = 4, *P < 0.05). (**D**) Measurement of the exploratory time during the olfactory sensitivity assay (n = 3). Data are shown as mean ± SEM; statistical analysis was performed with t test. "n" indicates the number of animals for each experimental group.

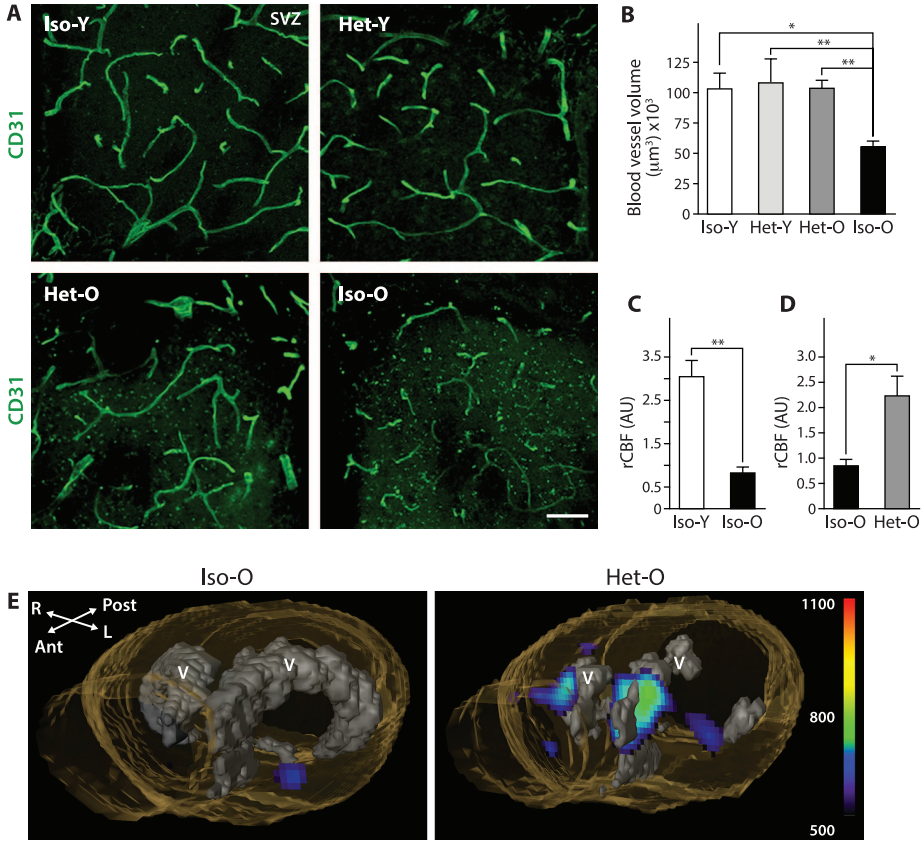

Fig. 3. Young blood induces vascular remodeling and increases blood flow in old mice. (**A**) Confocal images of the SVZ area showing the changes in vasculature after heterochronic parabiosis. Scale bar, 50 μm. (**B**) Measurement of blood vessel volume in isochronic and heterochronic parabionts (n_{old} = 9, n_{young} = 6). (**C** and **D**) Measurements of cerebral blood flow in the SVZ region of the parabionts: Iso-O versus (C) Iso-Y or (D) Het-O mice (n = 4). (**E**) Perfusion MRI images of the brain. "V" indicates the ventricles. Data are shown as mean ± SEM; statistical analysis was performed with ANOVA in (B) and t test in (C) and (D); *P < 0.05, **P < 0.01, ***P < 0.001. "n" indicates the number of animals for each experimental group.

endothelial progenitors. To test which of these mechanisms is taking place, we parabiotically joined young green fluorescent protein (GFP) mice with old non-GFP mice for 5 weeks. Analysis of these brains excluded any detectable contribution of young circulating endothelial progenitors to the vascular remodeling in Het-O animals (fig. S8). Because pericytes play a role in vasoconstriction in capillaries (*27*), we sought to investigate whether their numbers were altered by heterochronic parabiosis. The number of pericytes associated with blood vessels was unaffected by parabiosis (fig. S9). The likelihood that systemic factors can act directly on endothelial cells was further supported when we cultured primary mouse brain capillary endothelial cells and treated them with serum isolated from either young or old mice. Young serum stimulated endothelial cell proliferation by 88% as compared with old serum (fig. S10).

Several factors—including Sonic Hedgehog, erythropoietin, nitric oxide, Notch ligands, Fibroblast Growth Factor, and Vascular Endothelial Growth Factor (*28*–*31*)—that affect neurogenesis are also involved in blood vessel maintenance and proliferation. Of most relevance to our study are those factors that decrease with aging. Recently, one such factor—GDF11/BMP11, a circulating member of the BMP/TGF-β family—was found to be present in higher concentrations in young and heterochronic old than in old mouse serum. GDF11 administration to older mice reproduces many of the beneficial effects of parabiosis on aging hypertrophic cardiac muscle (*13*). This prompted us to test whether GDF11 could also restore the age-related decline in neurogenesis and participate in vascular remodeling. For that purpose, 21- to 23-month-old mice were treated with daily injections of either recombinant GDF11 (rGDF11, 0.1 mg/kg mouse body weight), a dosing regimen that increases GDF11 levels in old mice toward youthful levels (*13*), or phosphate-buffered saline (PBS) (vehicle) for 4 weeks, and their blood vessels were subsequently analyzed by using the volumetric assay described above. The volume of blood vessels in GDF11-treated old mice increased by 50% compared with the PBS-treated mice (Fig. 4, A and C). Moreover, the population of $Sox2^+$ cells in GDF11-treated old mice increased by 29% compared with the control (Fig. 4, B and D).

In vitro experiments confirmed that GDF11 acts, at least in part, on brain capillary endothelial cells. First, treating endothelial cells with rGDF11 (40 ng/ml) activates the well-known TGF-β signaling pathway in these cells, revealed by an increase in SMAD phosphorylation cascade (Fig. 4, E and F). Second, a 6-day treatment of primary brain capillary endothelial cells with rGDF11 (40 ng/ml) increased their proliferation by 22.9% as compared with that of controls (fig. S11), but not in the presence of a TGF-β inhibitor (fig. S12), confirming that GDF11 has a direct biological effect on these cells through the p-SMAD pathway.

The physiology of the brain is intimately dependent on its vasculature during aging. In the normal brain, there is a close association between stimulation of neural stem cells and blood vessels in the SVZ (*4*–*6*) and in the dentate gyrus. Here, we show that heterochronic parabiosis increases neurogenesis and improves vascularity and blood flow of the neurogenic niche. GDF11, a factor that also rejuvenates heart and skeletal muscle in aged mice (*32*), also was able to increase blood flow and neurogenesis in aged mice. Its effects were not as large as those of parabiosis itself, although that may relate to using suboptimal doses of this factor. In addition, some of its actions may be direct, and others may be indirect. Additional experiments will be needed to address this issue.

A question that arises from our work relates to aging-associated changes in the balance of positively and negatively acting circulating factors. We show here that blood from 15-month-old mice does not have a detrimental effect on young mice, whereas older blood (21 months old) dramatically decreases neural stem-cell populations in the young brain, an effect also observed in the hippocampus (*10*). This observation suggests that there is an age at which deleterious systemic factors accumulate and/or young factors are reduced. However, regardless of the age of the old brain, we and others (*10*, *11*) have shown that young blood is still able to rejuvenate the aged brain.

In conclusion, circulating factors, specifically including GDF11, have diverse positive effects in aging mice, including enhancing neurogenesis. Aging also affects the microvascular network in non-neurogenic regions of the brain (*7*). Circulating factors improved the vasculature in the cortex, as well as in other parts of the aging mouse brain. It is possible that increased blood flow might result in increased neural activity and function, opening new therapeutic strategies for treating age-related neurodegenerative conditions.

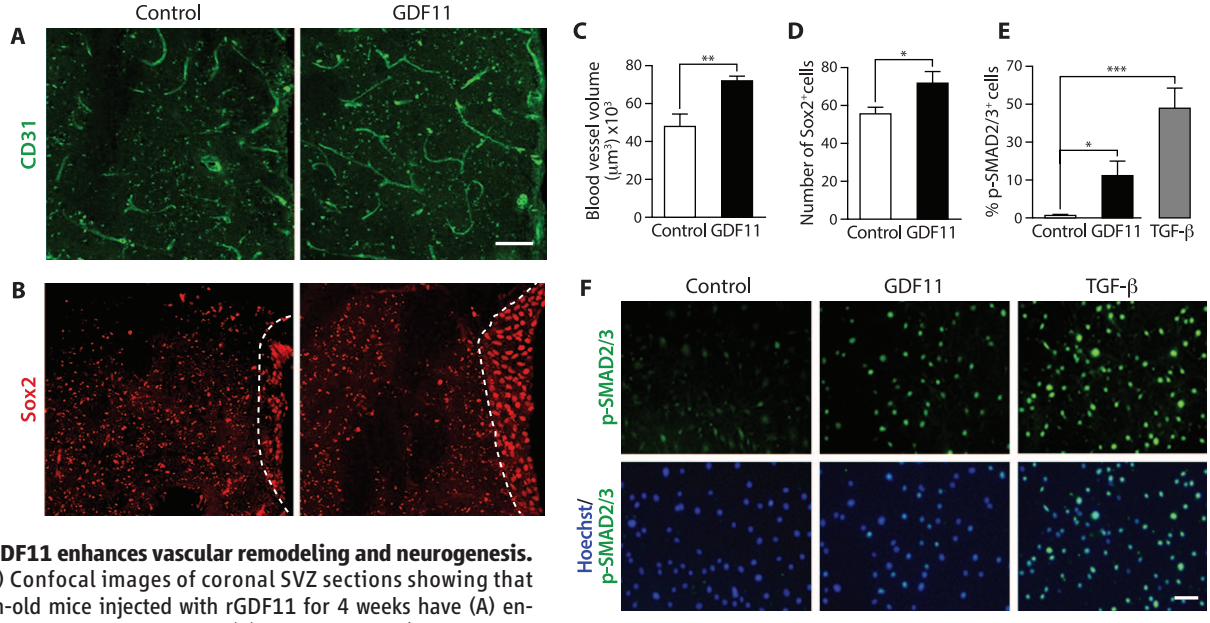

Fig. 4. GDF11 enhances vascular remodeling and neurogenesis. (**A** and **B**) Confocal images of coronal SVZ sections showing that 22-month-old mice injected with rGDF11 for 4 weeks have (A) enhanced vascularization as well as (B) increased $Sox2^+$ neural stem cell populations compared with those of control. (**C**) Measurement of blood vessel volume in rGDF11-treated and control mice ($n = 9$). (**D**) Quantification of $Sox2^+$ cells in the SVZ area ($n = 6$); "n" indicates the number of animals for each experimental group. (**E**) Quantification and (**F**) representative images of the percentage of phospho-$SMAD2/3^+$ cells in primary brain capillary endothelial cell cultures treated with either GDF11 (40ng/ml) or TFG-β (10ng/ml) in the presence of sodium orthovanadate used to inhibit phosphatase activity for 30 min ($n = 7$). Scale bar, 100 μm. Data are shown as mean ± SEM; statistical analysis was performed with t test, between each experimental condition and the untreated control; $^*P < 0.05$, $^{**}P < 0.01$, $^{***}P < 0.001$.

References and Notes

1. Q. Shen *et al.*, *Science* **304**, 1338–1340 (2004).
2. M. Tavazoie *et al.*, *Cell Stem Cell* **3**, 279–288 (2008).
3. T. Shingo *et al.*, *Science* **299**, 117–120 (2003).
4. P. Wu *et al.*, *Neurobiol. Aging* **29**, 1502–1511 (2008).
5. H. van Praag, G. Kempermann, F. H. Gage, *Nat. Neurosci.* **2**, 266–270 (1999).
6. J. S. Snyder, A. Soumier, M. Brewer, J. Pickel, H. A. Cameron, *Nature* **476**, 458 (2011).
7. E. Farkas, P. G. Luiten, *Prog. Neurobiol.* **64**, 575–611 (2001).
8. H. G. Kuhn, H. Dickinson-Anson, F. H. Gage, *J. Neurosci.* **16**, 2027–2033 (1996).
9. T. Seki, Y. Arai, *Neuroreport* **6**, 2479–2482 (1995).
10. S. A. Villeda *et al.*, *Nature* **477**, 90–94 (2011).
11. J. M. Ruckh *et al.*, *Cell Stem Cell* **10**, 96–103 (2012).
12. V. E. Miron *et al.*, *Nat. Neurosci.* **16**, 1211–1218 (2013).
13. F. S. Loffredo *et al.*, *Cell* **153**, 828–839 (2013).
14. D. E. Wright, A. J. Wagers, A. P. Gulati, F. L. Johnson, I. L. Weissman, *Science* **294**, 1933–1936 (2001).
15. T. Seki, *J. Neurosci. Res.* **70**, 327–334 (2002).
16. A. Garcia, B. Steiner, G. Kronenberg, A. Bick-Sander, G. Kempermann, *Aging Cell* **3**, 363–371 (2004).
17. J. Luo, S. B. Daniels, J. B. Lennington, R. Q. Notti, J. C. Conover, *Aging Cell* **5**, 139–152 (2006).
18. V. Tropepe, C. G. Craig, C. M. Morshead, D. van der Kooy, *J. Neurosci.* **17**, 7850–7859 (1997).
19. B. A. Reynolds, S. Weiss, *Science* **255**, 1707–1710 (1992).
20. L. Katsimpardi *et al.*, *Stem Cells* **26**, 1796–1807 (2008).
21. A. Carleton, L. T. Petreanu, R. Lansford, A. Alvarez-Buylla, P. M. Lledo, *Nat. Neurosci.* **6**, 507–518 (2003).
22. R. M. Witt, M. M. Galligan, J. R. Despinoy, R. Segal, *J. Vis. Exp.* **28**, 949 (2009).
23. M. J. Reed, J. M. Edelberg, *Sci. SAGE KE* **2004**, pe7 (2004).
24. A. Rivard *et al.*, *Circulation* **99**, 111–120 (1999).
25. D. R. Riddle, W. E. Sonntag, R. J. Lichtenwalner, *Ageing Res. Rev.* **2**, 149–168 (2003).
26. C. L. Grady *et al.*, *Neuroimage* **8**, 409–425 (1998).
27. R. Balabanov, P. Dore-Duffy, *J. Neurosci. Res.* **53**, 637–644 (1998).
28. P. Carmeliet, *Nat. Rev. Genet.* **4**, 710–720 (2003).
29. A. Alvarez-Buylla, D. A. Lim, *Neuron* **41**, 683–686 (2004).
30. M. Brines, A. Cerami, *Nat. Rev. Neurosci.* **6**, 484–494 (2005).
31. E. R. Matarredona, M. Murillo-Carretero, B. Moreno-López, C. Estrada, *Brain Res. Brain Res. Rev.* **49**, 355–366 (2005).
32. M. Sinha *et al.*, *Science* **344**, 649–652 (2014).

Acknowledgments: We thank C. McGillivray and D. Faria at the HSCRB Histology Core for providing help with sectioning and D. Smith and B. Götze at the HCBI for providing microscope facilities. We also thank W. Stallcup for providing the anti-NG2 antibody, C. Bonal for technical help and J. LaLonde for editorial assistance. This work was supported by a Senior Scholar in Aging Award from The Ellison Medical Foundation to L.L.R.; awards from GlaxoSmithKline and the Harvard Stem Cell Institute to L.L.R.; NIH (R01 AG032977 1R01 AG040019) to R.T.L.; and the Paul F. Glenn Foundation for Medical Research, NIH (1R01 AG033053, 1DP2 OD004345, and 5U01 HL100402), and Harvard Stem Cell Institute to A.J.W. Additional data are in the Supplement. J.C. was funded by NIH R01NS070835 and R01NS072167. L.L.R., A.J.W., R.T.L., and L.K. are inventors on a U.S. patent application filed by Harvard University and Brigham and Women's Hospital entitled "Methods and Compositions for Increasing Neurogenesis and Angiogenesis" (61/833,813).

Supplementary Materials

www.sciencemag.org/content/344/6184/630/suppl/DC1
Materials and Methods
Figs. S1 to S12
References (*33*–*34*)

22 January 2014; accepted 10 April 2014
10.1126/science.1251141

Identification of LRRC8 Heteromers as an Essential Component of the Volume-Regulated Anion Channel VRAC

Felizia K. Voss,[1,2,3] Florian Ullrich,[1,2,3] Jonas Münch,[1,2,3] Katina Lazarow,[1] Darius Lutter,[1,2,3] Nancy Mah,[2] Miguel A. Andrade-Navarro,[2] Jens P. von Kries,[1] Tobias Stauber,[1,2]* Thomas J. Jentsch[1,2,4]*

Regulation of cell volume is critical for many cellular and organismal functions, yet the molecular identity of a key player, the volume-regulated anion channel VRAC, has remained unknown. A genome-wide small interfering RNA screen in mammalian cells identified LRRC8A as a VRAC component. LRRC8A formed heteromers with other LRRC8 multispan membrane proteins. Genomic disruption of *LRRC8A* ablated VRAC currents. Cells with disruption of all five *LRRC8* genes required LRRC8A cotransfection with other LRRC8 isoforms to reconstitute VRAC currents. The isoform combination determined VRAC inactivation kinetics. Taurine flux and regulatory volume decrease also depended on LRRC8 proteins. Our work shows that VRAC defines a class of anion channels, suggests that VRAC is identical to the volume-sensitive organic osmolyte/anion channel VSOAC, and explains the heterogeneity of native VRAC currents.

Cells regulate their volume to counteract swelling or shrinkage caused by osmotic challenges and during processes such as cell growth, division, and migration. As water transport across cellular membranes is driven by osmotic gradients, cell volume regulation requires appropriate changes of intracellular concentrations of ions or organic osmolytes such as taurine (*1*, *2*). Regulatory volume decrease (RVD) follows the extrusion of intracellular Cl^- and K^+ and other osmolytes across the plasma membrane. A key player is the volume-regulated anion channel VRAC that mediates characteristic swelling-activated Cl^- currents [$I_{Cl(swell)}$] and is ubiquitously expressed in vertebrate cells (*3*–*5*). Nearly inactive under resting conditions, VRAC slowly opens upon hypotonic swelling. The mechanism behind VRAC opening remains enigmatic. VRAC currents are outwardly rectifying [hence the alternative name VSOR for volume-stimulated outward rectifier (*4*, *5*)] and show variable inactivation at inside-positive voltages. VRAC conducts iodide (I^-) better than chloride (Cl^-) and might also conduct organic osmolytes such as taurine (*6*) [hence VSOAC, volume-stimulated organic osmolyte/anion channel (*7*)], but this notion is controversial (*8*–*10*). VRAC is believed to be important for cell volume regulation and swelling-induced exocytosis (*11*) and also for cell cycle regulation, proliferation, and migration (*1*, *3*, *4*). It may play a role in apoptosis and various pathological states, including ischemic brain edema and cancer (*4*, *12*). Progress in the characterization of VRAC and its biological roles has been limited by the failure to identify the underlying protein(s) despite decades of efforts (*1*, *5*). ClC-2 Cl^- channels activate upon cell swelling, but their inward rectification and Cl^- over I^- selectivity deviate from VRAC (*13*). *Drosophila* dBest1, a member of a family of Ca^{2+}-activated Cl^- channels, mediates swelling-activated Cl^- currents in insect cells (*14*, *15*), but their characteristics differ from those of VRAC currents, and the mammalian homolog of dBest1 is swelling-insensitive (*16*). We show that VRAC represents a distinct class of anion channels that also conduct organic osmolytes.

To identify VRAC, we used a genome-wide RNA interference screen that could identify nonredundant VRAC components. Swelling-induced I^- influx into human embryonic kidney (HEK) cells expressing the I^--sensitive yellow fluorescent protein YFP(H148Q/I152L) (*17*) was used as readout in a fluorometric imaging plate reader (Fig. 1A). Exposure to saline containing 50 mM I^- yielded a slow fluorescence decay under isotonic conditions, whereas hypotonicity induced a delayed increase in YFP quenching (Fig. 1B) that could be reduced by VRAC inhibitors such as carbenoxolone (*18*) (fig. S1). In a prescreen targeting 21 anion transporters (table S1), only small interfering RNAs (siRNAs) against the Cl^-/HCO_3^- exchanger AE2 gave significant effects (Fig. 1B). They decreased I^- influx under both isotonic and hypotonic conditions.

Our genome-wide screen used three separately transfected siRNAs per gene (fig. S2). Offline data analysis (fig. S3, A and B) yielded the maximal slope of fluorescence quenching that was used to define hits. Further criteria included the presence of predicted transmembrane domains and a wide expression pattern. Eighty-seven genes (table S2) were taken into a secondary screen with independent siRNAs. Of these, only sup-

[1]Leibniz-Institut für Molekulare Pharmakologie (FMP), Berlin. [2]Max-Delbrück-Centrum für Molekulare Medizin (MDC), Berlin. [3]Graduate Program of the Freie Universität Berlin. [4]Neurocure, Charité Universitätsmedizin, Berlin.

*Corresponding author. E-mail: jentsch@fmp-berlin.de (T.J.J.); tstauber@fmp-berlin.de (T.S.)

pression of leucine-rich repeat–containing 8A (LRRC8A) robustly slowed hypotonicity-induced YFP quenching (Fig. 1C). *LRRC8A* knockdown also strongly suppressed $I_{Cl(swell)}$ in patch-clamp experiments (Fig. 1, D to F), suggesting that the multispan membrane protein LRRC8A is an indispensable component of VRAC or is needed for its activation.

Although LRRC8A reached the plasma membrane (Fig. 1G, and fig. S4A for HeLa cells), its transfection into HEK cells rather decreased $I_{Cl(swell)}$ (Fig. 1F). We hypothesized that VRAC contains LRRC8A as part of a heteromer and that LRRC8A overexpression led to a subunit stoichiometry that was incompatible with channel activity. LRRC8A has four closely related homologs (LRRC8B to LRRC8E), which all have four predicted transmembrane domains (*19*, *20*). Expressed sequence tag (EST) databases suggested that all homologs were widely expressed. Immunocytochemistry of transfected HeLa cells (fig. S4A) and of native HEK cells (Fig. 1, G and H) detected LRRC8A at the plasma membrane. Truncation of its C terminus, as in a patient with agammaglobulinemia (*21*), led to cytoplasmic retention (fig. S4B). LRRC8B through LRRC8E remained intracellular when transfected alone, but reached the plasma membrane when cotransfected with LRRC8A (Fig. 1, I and J, and fig. S4, C to H). Unlike LRRC8A transfection, LRRC8A and LRRC8C coexpression did not suppress $I_{Cl(swell)}$ (Fig. 1F). However, neither this coexpression, nor any other combination tested, significantly increased current amplitudes above wild-type (WT) values.

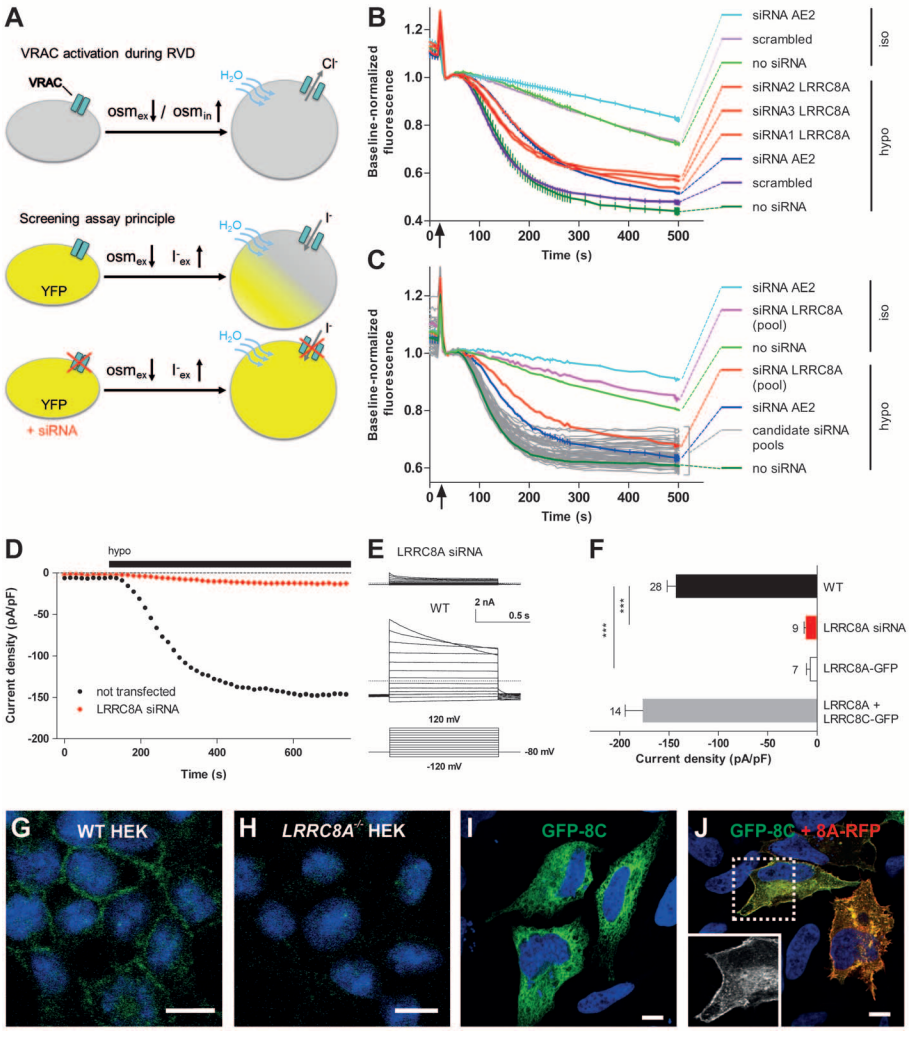

Fig. 1. siRNA screen for volume-regulated anion channel VRAC identifies LRRC8A. (**A**) Principle of screen. Top: In regulatory volume decrease (RVD), VRAC releases Cl^-. Bottom: Quenching of YFP fluorescence by I^- entering through VRAC used as readout. (**B**) Example traces, normalized to fluorescence at ~30 to 50 s. Traces averaged from wells treated with control siRNAs (scrambled, AE2, both $n = 3$) and no siRNA ($n = 2$) (error bars, SEM), and individual traces from wells singly transfected with the three siRNAs against LRRC8A. Except for LRRC8A siRNA2 and 3, all traces are from the same plate. Arrow indicates addition of I^--containing hypotonic (hypo; 229 mOsm) or isotonic (iso; 329 mOsm) saline. (**C**) Secondary screen using siRNA pools against candidate genes. Averaged control traces as in (B). (**D**) Typical time course of VRAC activation in WT or LRRC8A siRNA-treated HEK cells. Current densities at −80 mV are shown. Bar, application of hypotonic (240 mOsm) saline (hypo). (**E**) Current traces of fully activated $I_{Cl(swell)}$ measured with the protocol shown below. Dotted lines indicate zero current. (**F**) $I_{Cl(swell)}$ amplitudes (at −80 mV) of WT HEK cells, cells treated with LRRC8A siRNA, or transfected with indicated LRRC8 cDNAs. Error bars, SEM; number of experiments is indicated; ***$P < 0.001$. (**G**) Plasma membrane localization of endogenous LRRC8A in HEK cells. (**H**) No LRRC8 labeling in *LRRC8A*$^{-/-}$ HEK cells. (**I**) LRRC8C is intracellular when transfected into HeLa cells, but (**J**) reaches the plasma membrane when cotransfected with LRRC8A. (Inset) Magnification of boxed area showing only GFP fluorescence. Scale bars, 10 μm.

We used zinc-finger nuclease and clustered regularly interspaced short palindromic repeats (CRISPR)–Cas (*22*) technologies to constitutively disrupt *LRRC8* genes. In addition to polyploid HEK cells, we used stably diploid human HCT116 cells for increased disruption efficiency. Gene disruption was confirmed by sequencing and Western blots (Fig. 2A and table S3). To exclude off-target effects, we generated two HEK and three HCT116 lines in which *LRRC8A* was disrupted at different positions (tables S3 and S4). $I_{Cl(swell)}$ was abolished in all five lines and could be rescued by LRRC8A transfection (Fig. 2, B and C, and fig. S5), demonstrating that LRRC8A is essential for $I_{Cl(swell)}$. We also produced HCT116 cells in which other *LRRC8* genes were disrupted singly or in combinations, including a line with disruption of all five *LRRC8* genes (henceforth called *LRRC8*$^{-/-}$ cells). Except for *LRRC8A*, disruption of single *LRRC8* genes did not abolish VRAC currents (Fig. 2, B and C). However, $I_{Cl(swell)}$ amplitudes were robustly reduced in *LRRC8E*$^{-/-}$ and in *LRRC8(C/E)*$^{-/-}$ double and *LRRC8(C/D/E)*$^{-/-}$ triple knockout (KO) cells. $I_{Cl(swell)}$ was abolished in *LRRC8(B/C/D/E)*$^{-/-}$ cells (Fig. 2, B and C). $I_{Cl(swell)}$ inactivated faster and at less positive potentials in *LRRC8C*$^{-/-}$ and *LRRC8(C/E)*$^{-/-}$ cells compared to WT HCT116, *LRRC8B*$^{-/-}$, *LRRC8D*$^{-/-}$, or *LRRC8E*$^{-/-}$ cells. By contrast, $I_{Cl(swell)}$ inactivated more slowly and at more positive voltages in *LRRC8(D/E)*$^{-/-}$ HTC116 cells (Fig. 2, B and D, and fig. S6D) and in WT HEK cells (Figs. 1E and 2D). $I_{Cl(swell)}$ of these mutant cell lines retained the ion selectivity of WT VRAC with the characteristic $I^- > NO_3^- > Cl^- >> Glc^-$ (gluconate) permeability sequence (fig. S6A).

LRRC8A transfection into quintuple KO *LRRC8*$^{-/-}$ cells failed to rescue $I_{Cl(swell)}$ (Fig. 2, E and F), agreeing with the absence of $I_{Cl(swell)}$ in *LRRC8(B/C/D/E)*$^{-/-}$ cells (Fig. 2, B and C). Cotransfecting *LRRC8*$^{-/-}$ cells with LRRC8A and either LRRC8C or LRRC8E yielded $I_{Cl(swell)}$ with current densities similar to those of native cells (Fig. 2F). Coexpressing LRRC8A with LRRC8D yielded lower currents (Fig. 2, E and F). No current was observed upon coexpression of LRRC8A and LRRC8B, which may relate to the poor expression of LRRC8B (Fig. 3, D and F). These findings are consistent with the low currents observed in *LRRC8(C/E)*$^{-/-}$ cells (Fig. 2C), where LRRC8A can only interact with poorly expressed LRRC8B and/or LRRC8D. Reconstituted $I_{Cl(swell)}$ activated similarly to WT VRAC

upon swelling (Fig. 2E) and displayed its typical anion permeability sequence (fig. S6, B and C).

$I_{Cl(swell)}$ inactivated more slowly and at more positive voltages when LRRC8A was coexpressed with LRRC8C in *LRRC8*$^{-/-}$ cells compared to cells coexpressing LRRC8A with LRRC8E or LRRC8D (Fig. 2, E and G, and fig. S6E). This observation was in agreement with the faster $I_{Cl(swell)}$ inactivation in *LRRC8C*$^{-/-}$ cells (Fig. 2, B and D, and fig. S6D) in which the "decelerating" LRRC8C subunit may be replaced by LRRC8E or other "accelerating" subunits.

Native $I_{Cl(swell)}$ currents display different inactivation kinetics (*3*). Whereas $I_{Cl(swell)}$ shows prominent inactivation at positive potentials in HEK cells (*23*, *24*) (Fig. 1E, Fig. 2D, and fig. S6D) and even more inactivation in HCT116 cells (Fig. 2, B and D, and fig. S6D), it inactivates much less in blood cells such as promyelocytic HL-60 cells and in vascular smooth muscle and neurons (*24*–*26*). EST databases suggest that these cells express the "decelerating" subunit LRRC8C, but lack LRRC8E that potently induces inactivation (Fig. 2, E and G, and fig. S6E). Quantitative reverse transcription–polymerase chain reaction confirmed that HEK and HCT116 cells expressed LRRC8A through LRRC8E, whereas LRRC8E was almost absent from HL-60 cells (fig. S7). Moreover, HCT116 cells, whose $I_{Cl(swell)}$ inactivates to a greater extent than that of HEK cells (Fig. 1E, Fig. 2, B and D, and fig. S6D), express less "decelerating" LRRC8C than HEK (fig. S7).

LRRC8 proteins have four predicted transmembrane domains (TMDs) followed by hydrophilic C termini with up to 17 leucine-rich repeats (*27*) (Fig. 3A). Their C termini were originally thought to be extracellular (*19*, *21*), but proteome databases revealed (*20*) that the TMD2-TMD3 linker can be phosphorylated and suggested that LRRC8 N and C termini are cytoplasmic (Fig. 3A). LRRC8 proteins display weak homology (*20*) to pannexins, pore-forming proteins (*28*) with

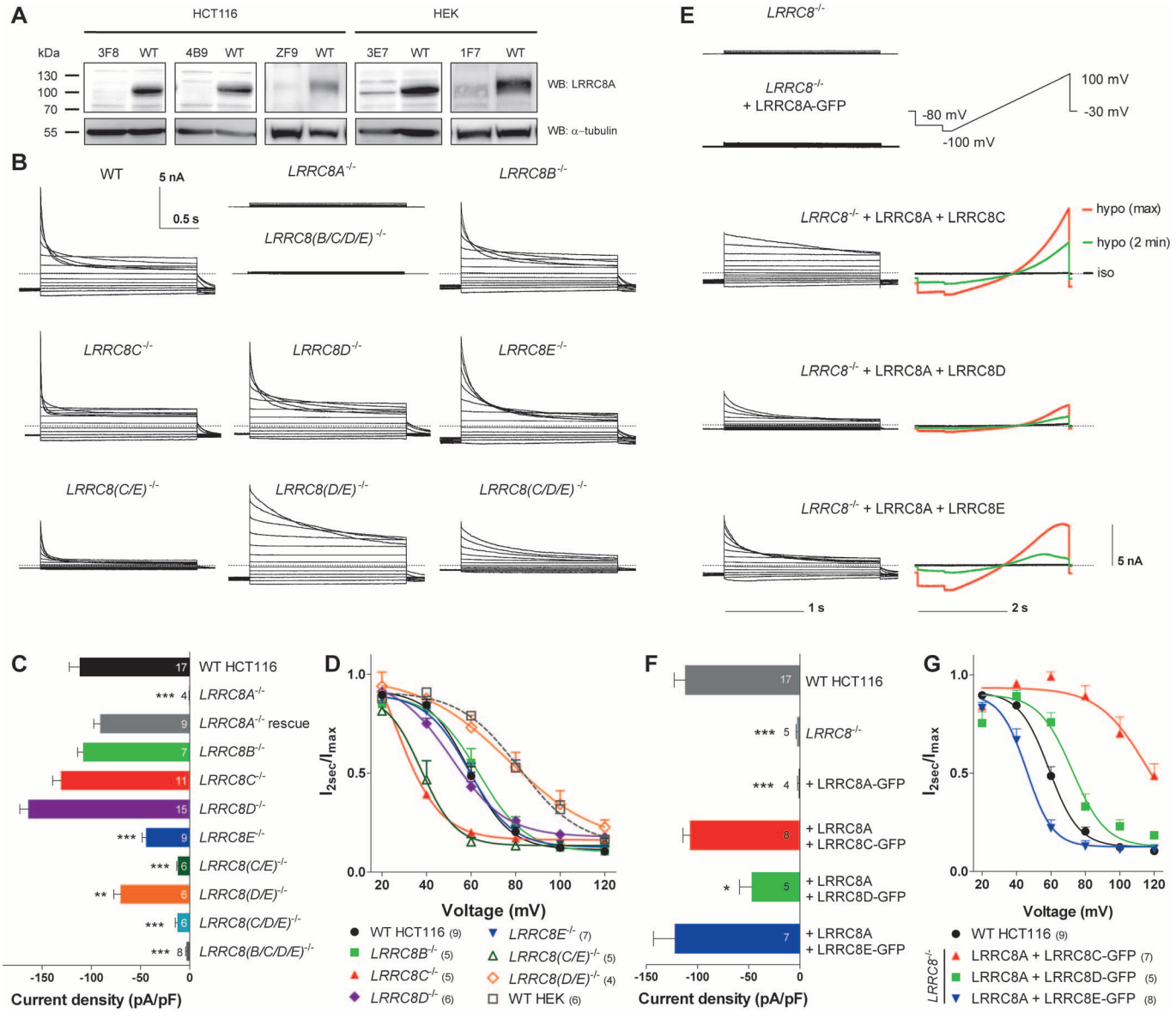

Fig. 2. Characterization of *LRRC8* KO cells and of reconstituted $I_{Cl(swell)}$. (**A**) Western blots confirm *LRRC8A* disruption in mutant cell lines (table S3). α-Tubulin, loading control. (**B**) Example $I_{Cl(swell)}$ traces (as in Fig. 1E, but 2-s pulses) of WT and mutant HCT116 cells. (**C**) Current densities (at –80 mV) of maximally activated $I_{Cl(swell)}$ of WT and mutant HCT116 cells. (**D**) $I_{Cl(swell)}$ inactivation assessed by ratio of current at end and beginning of pulse. (**E**) When transfected into HCT116 *LRRC8*$^{-/-}$ cells (with all *LRRC8* genes disrupted), LRRC8A rescues $I_{Cl(swell)}$ only with LRRC8C, D, or E [left panels; example traces measured as in (B)]. Right panels, example ramp current traces from reconstituted $I_{Cl(swell)}$ at isotonicity (black), 2 min after switching to hypotonicity (green) and with maximal activation (red). Ramp protocol shown at top. (**F**) $I_{Cl(swell)}$ current densities at –80 mV for indicated combinations. (**G**) Voltage-dependent inactivation of $I_{Cl(swell)}$. Error bars, SEM. Number of cells is shown in parentheses. *P < 0.05, **P < 0.01, and ***P < 0.001 versus WT.

connexin-like topology. Connexins form hexameric hemichannels and gap junctions (*29*). This similarity suggested (*20*) that LRRC8 proteins form hexameric channels for as yet unknown substrates. Like VRAC currents (*14*, *15*, *30*), LRRC8 proteins are found in vertebrates but not in other phyla such as arthropoda (*20*).

We ascertained the pannexin- and connexin-like transmembrane topology of LRRC8A. Mutating potential N-linked glycosylation sites between TMD1 and TMD2 abolished the size shift upon PNGaseF treatment (Fig. 3B), demonstrating that this loop is extracellular. Immunofluorescence of cells transfected with hemagglutinin (HA)–tagged LRRC8A constructs showed that the TMD3-4 segment is extracellular and the C terminus cytoplasmic (Fig. 3C).

The formation of LRRC8 heteromers was confirmed by coimmunoprecipitation from HEK cells transfected with LRRC8A and epitope-tagged versions of either LRRC8B, C, D, or E. LRRC8A coprecipitated each of the other isoforms, but not the Cl^- channel ClC-1 used as a control (Fig. 3, D and E). Conversely, precipitation of epitope-tagged versions of LRRC8B through LRRC8E coprecipitated LRRC8A (Fig. 3F). Coprecipitation of LRRC8 isoforms was also observed for native HEK cells (fig. S8).

Hypotonicity induced a robust taurine efflux from HEK and HCT116 cell lines, but not from their *LRRC8A*$^{-/-}$ derivates (Fig. 4A and fig. S9A), where taurine efflux could be rescued by LRRC8A and LRRC8C cotransfection (fig. S9B for HEK cells). Taurine efflux was also abolished in *LRRC8(B/C/D/E)*$^{-/-}$ HCT116 cells (Fig. 4A). Because both $I_{Cl(swell)}$ and swelling-induced taurine efflux similarly depended on LRRC8 heteromers, VRAC is most likely identical to VSOAC, the volume-sensitive organic osmolyte/anion channel (*7*). Accordingly, *LRRC8A*$^{-/-}$ HEK cells showed severely impaired volume regulation. After initial swelling, WT, but not *LRRC8A*$^{-/-}$, cells slowly reduced their volume in the continuous presence of extracellular hypotonicity (Fig. 4B). Hence, LRRC8-containing VSOAC plays a major role in RVD.

The absence of $I_{Cl(swell)}$ upon genomic disruption of *LRRC8A* and its rescue by transient reexpression identified LRRC8A as an indispensable component of VRAC, or alternatively, as being crucial for its activation. The wide expression pattern of *LRRC8* genes and the plasma membrane residency of LRRC8A-containing heteromers fulfill the prerequisites for LRRC8 proteins forming the channel. The dependence of current properties on LRRC8 isoform combinations indicated that LRRC8 heteromers are integral components

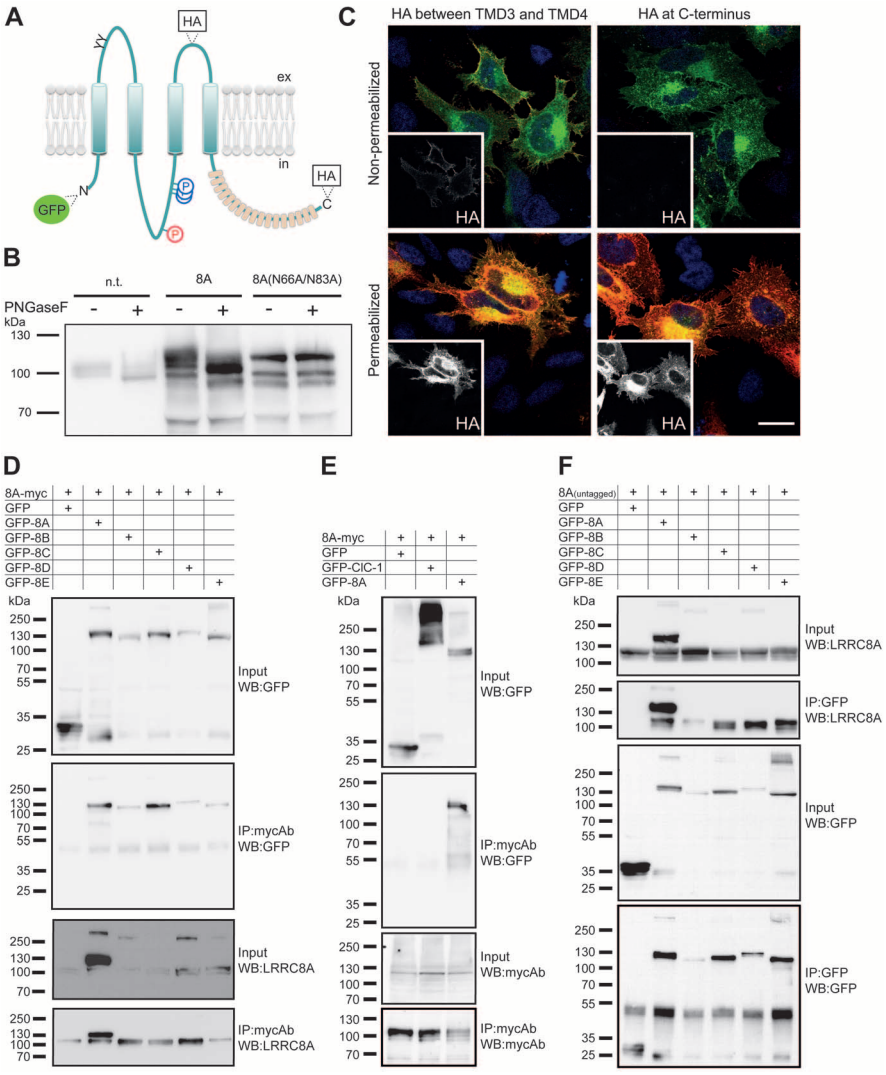

Fig. 3. Transmembrane topology and heteromerization of LRRC8A. (**A**) LRRC8 model [modified from (*20*)]. Four transmembrane domains precede a C terminus with up to 17 leucine-rich repeats (*27*) (orange). Phosphoserines in LRRC8A (red P) and LRRC8D (blue P), according to Uniprot (*32*), predicted N-linked glycosylation sites (Y), and added epitopes are indicated. (**B**) PNGaseF treatment of endogenous LRRC8A, transfected LRRC8A, but not of LRRC8A(N66A,N83A) with disrupted glycosylation sites, decreased LRRC8A size in Western blots. The changed banding pattern of LRRC8A(N66A,N83A) suggests altered posttranslational modifications. n.t., nontransfected. (**C**) Immunofluorescence of nonpermeabilized and permeabilized HeLa cells transfected with HA-tagged GFP-LRRC8A. Overlays of GFP (green) and HA (red) labeling. Insets show exclusively HA staining. Scale bar, 20 μm. (**D**) LRRC8A coprecipitated epitope-tagged LRRC8B through LRRC8E in double-transfected HEK cells. LRRC8B and LRRC8D were poorly expressed. (**E**) LRRC8A did not coprecipitate the ClC-1 Cl^- channel. (**F**) Epitope-tagged LRRC8B through LRRC8E coprecipitated LRRC8A.

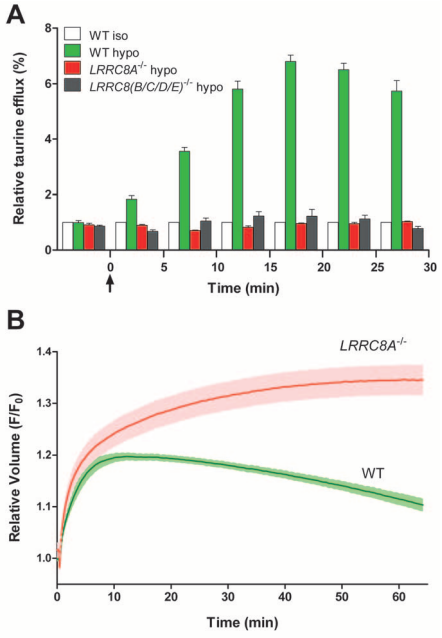

Fig. 4. LRRC8 proteins are crucial for swelling-induced taurine efflux and RVD. (**A**) ^{3}[H]-Taurine efflux from HCT116 cells of indicated genotypes. Cells were either in isotonic solution throughout (WT, white bars) or exposed to hypotonic solution starting at $t = 0$ (arrows). Bars, means of six measurements; error bars, SEM. (**B**) WT and *LRRC8A*$^{-/-}$ HEK cells were shifted to hypotonic saline (96 mOsm) at $t = 30$s, and cell volume was monitored by calcein fluorescence. Mean of six measurements; error range, SEM. Similar results were obtained in three experiments.

of VRAC, a notion buttressed by the homology of LRRC8 proteins to pannexins. Because cotransfection of LRRC8 isoforms did not significantly increase $I_{Cl(swell)}$ amplitude over that of the WT, other factors limit VRAC activity; for example, an auxiliary subunit of VRAC or part of the signaling cascade leading to its activation. Indeed, VRAC currents seem to be highly regulated, with amplitudes differing by a factor of only 2 to 3 across cell types (*3*, *30*).

The homology between LRRC8 proteins and pannexins suggested that LRRC8 proteins form hexameric channels (*20*). We confirmed the pannexin-like topology of LRRC8A and propose that VRAC is formed by LRRC8 hexamers of LRRC8A and at least one other family member. In this model, VRAC may contain two to five different LRRC8 isoforms, creating a potentially large variety of VRAC channels with different properties. The variation of $I_{Cl(swell)}$ inactivation kinetics between different tissues and cells (*3*) can be ascribed to different expression ratios of LRRC8 isoforms. LRRC8-dependent Cl^- and taurine fluxes indicated that VRAC is identical to VSOAC (*6*) and fit to a pore formed by LRRC8 hexamers, because hexameric pannexin channels likewise display poor substrate specificity (*28*).

Our results provide the basis to explore the structure-function relationship of VRAC/VSOAC, to clarify the signaling pathway that couples cell volume increase to channel opening, and to investigate the role of the channel in basic cellular processes such as cell division, growth, and migration and in various pathological states. Interestingly, a truncating *LRRC8A* mutation has been described in a patient with agammaglobulinemia (*21*), and *LRRC8C* may have a role in fat metabolism (*31*).

References and Notes

1. E. K. Hoffmann, I. H. Lambert, S. F. Pedersen, *Physiol. Rev.* **89**, 193–277 (2009).
2. H. Pasantes-Morales, R. A. Lezama, G. Ramos-Mandujano, K. L. Tuz, *Am. J. Med.* **119** (suppl. 1), S4–S11 (2006).
3. B. Nilius *et al.*, *Prog. Biophys. Mol. Biol.* **68**, 69–119 (1997).
4. Y. Okada, K. Sato, T. Numata, *J. Physiol.* **587**, 2141–2149 (2009).
5. Y. Okada, *Am. J. Physiol.* **273**, C755–C789 (1997).
6. P. S. Jackson, K. Strange, *Am. J. Physiol.* **265**, C1489–C1500 (1993).
7. K. Strange, P. S. Jackson, *Kidney Int.* **48**, 994–1003 (1995).
8. I. H. Lambert, E. K. Hoffmann, *J. Membr. Biol.* **142**, 289–298 (1994).
9. D. B. Shennan, *Cell. Physiol. Biochem.* **21**, 15–28 (2008).
10. A. Stutzin *et al.*, *Am. J. Physiol.* **277**, C392–C402 (1999).
11. T. Moser, R. H. Chow, E. Neher, *Pflugers Arch.* **431**, 196–203 (1995).
12. Y. Okada *et al.*, *J. Membr. Biol.* **209**, 21–29 (2006).
13. S. Gründer, A. Thiemann, M. Pusch, T. J. Jentsch, *Nature* **360**, 759–762 (1992).
14. S. C. Stotz, D. E. Clapham, *PLOS ONE* **7**, e46865 (2012).
15. L. T. Chien, H. C. Hartzell, *J. Gen. Physiol.* **132**, 537–546 (2008).
16. R. Fischmeister, H. C. Hartzell, *J. Physiol.* **562**, 477–491 (2005).
17. L. J. Galietta, P. M. Haggie, A. S. Verkman, *FEBS Lett.* **499**, 220–224 (2001).
18. V. Benfenati *et al.*, *Channels* **3**, 323–336 (2009).
19. K. Kubota *et al.*, *FEBS Lett.* **564**, 147–152 (2004).
20. F. Abascal, R. Zardoya, *Bioessays* **34**, 551–560 (2012).
21. A. Sawada *et al.*, *J. Clin. Invest.* **112**, 1707–1713 (2003).
22. L. Cong *et al.*, *Science* **339**, 819–823 (2013).
23. B. Nilius, J. Prenen, U. Wissenbach, M. Bödding, G. Droogmans, *Pflugers Arch.* **443**, 227–233 (2001).
24. C. Y. Hernández-Carballo, J. A. De Santiago-Castillo, T. Rosales-Saavedra, P. Pérez-Cornejo, J. Arreola, *Pflugers Arch.* **460**, 633–644 (2010).
25. G. X. Wang *et al.*, *Am. J. Physiol. Heart Circ. Physiol.* **287**, H533–H544 (2004).
26. J. L. Leaney, S. J. Marsh, D. A. Brown, *J. Physiol.* **501**, 555–564 (1997).
27. G. Smits, A. V. Kajava, *Mol. Immunol.* **41**, 561–562 (2004).
28. S. Penuela, R. Gehi, D. W. Laird, *Biochim. Biophys. Acta* **1828**, 15–22 (2013).
29. S. Maeda *et al.*, *Nature* **458**, 597–602 (2009).
30. B. Nilius *et al.*, *Pflugers Arch.* **428**, 364–371 (1994).
31. T. Hayashi *et al.*, *Biol. Pharm. Bull.* **34**, 1257–1263 (2011).
32. M. Magrane, U. Consortium, *Database (Oxford)* **2011**, bar009 (2011).

Acknowledgments: We thank M. Neuenschwander for technical advice concerning the assay; H.-P. Rahn for help with fluorescence-activated cell sorting; A. Brockhoff and W. Meyerhof for use of their Fluorometric Image Plate Reader in a pilot experiment; and J. Liebold, N. Krönke, J. Jedamzick, and S. Kleissle for technical assistance. Supported by the European Research Council Advanced Grant (FP/2007-2013) 294435 "Cytovolion" and the Deutsche Forschungsgemeinschaft (Exc 257 "Neurocure") to T.J.J.

Supplementary Materials

www.sciencemag.org/content/344/6184/634/suppl/DC1
Materials and Methods
Author Contributions
Figs. S1 to S10
Tables S1 to S4
References (*33*–*38*)

3 March 2014; accepted 2 April 2014
Published online 10 April 2014;
10.1126/science.1252826

Gibberellin Acts Positively Then Negatively to Control Onset of Flower Formation in *Arabidopsis*

Nobutoshi Yamaguchi,[1] Cara M. Winter,[1]* Miin-Feng Wu,[1] Yuri Kanno,[2] Ayako Yamaguchi,[1] Mitsunori Seo,[2] Doris Wagner[1]†

The switch to reproductive development is biphasic in many plants, a feature important for optimal pollination and yield. We show that dual opposite roles of the phytohormone gibberellin underpin this phenomenon in *Arabidopsis*. Although gibberellin promotes termination of vegetative development, it inhibits flower formation. To overcome this effect, the transcription factor LEAFY induces expression of a gibberellin catabolism gene; consequently, increased LEAFY activity causes reduced gibberellin levels. This allows accumulation of gibberellin-sensitive DELLA proteins. The DELLA proteins are recruited by SQUAMOSA PROMOTER BINDING PROTEIN–LIKE transcription factors to regulatory regions of the floral commitment gene *APETALA1* and promote *APETALA1* up-regulation and floral fate synergistically with LEAFY. The two opposing functions of gibberellin may facilitate evolutionary and environmental modulation of plant inflorescence architecture.

Synchronization of the developmental transitions that lead to reproductive competence is important for species survival. Plants form new lateral organs iteratively throughout their life from the flanks of the shoot apical meristem (fig. S1) (*1*, *2*). The type of the lateral organ produced depends on the phase of the life cycle. In *Arabidopsis*, rosette leaves are produced during the vegetative phase. During the reproductive phase, an inflorescence forms. Not all lateral organ primordia of the inflorescence are competent to become flowers. Those that are not instead give rise to branches subtended by cauline leaves during the first inflorescence phase (*3*, *4*). The duration of the branch-producing first inflorescence phase determines inflorescence architecture and is critical for optimal seed set.

To gain insight into the regulation of the transition from branch to floral fate in the lateral primordia of the inflorescence, we analyzed public genome-wide binding and expression data and identified genes that are direct targets of the LEAFY (LFY) transcription factor (*5*–*7*) (table S1). LFY promotes flower formation (*8*, *9*). We identified for further study the *EUI-LIKE P450 A1* (*ELA1*) gene (fig. S2), which encodes a cytochrome P450 (*10*). *ELA1* expression was very low in vegetative tissues but increased when flowers formed (fig. S3). On the basis of in situ hybridization and reporter studies, *ELA1* was initially expressed on the abaxial side of incipient flower primordia and later along their entire circumference (Fig. 1A and fig. S3). *ELA1* expression was dependent on the

[1]Department of Biology, University of Pennsylvania, 415 South University Avenue, Philadelphia, PA 19104–6018, USA. [2]RIKEN Center for Sustainable Resource Science, Yokohama, Kanagawa, 230-0045, Japan.

*Present address: Department of Biology, Duke University, Box 90338, Durham, NC 27708, USA.
†Corresponding author. E-mail: wagnerdo@sas.upenn.edu

presence of functional LFY and on the presence of LFY-bound cis elements in the *ELA1* regulatory region (Fig. 1B and fig. S4). To determine whether ELA1 is required for the switch to flower formation in long-day photoperiods, we obtained three mutant alleles (fig. S5). Consistent with its very low expression in vegetative tissues, *ela1* mutants did not alter the duration of the vegetative phase (fig. S5) (*11*). By contrast, loss of *ELA1* function significantly delayed flower formation (Fig. 1C and fig. S5). Thus, ELA1 promotes floral fate in lateral organ primordia of the inflorescence.

ELA1 functions in catabolism of bioactive gibberellins that are not hydroxylated at the carbon 13 position, such as gibberellin A4 (GA_4) (*10*, *11*) (fig. S6). Through up-regulation of *ELA1*, LFY may reduce the levels of GA_4 during flower formation. Indeed, analysis of GA_4 levels by mass spectrometry after liquid chromatography revealed that this hormone is elevated in *lfy* null mutants and reduced in transgenic plants overexpressing LFY (Fig. 2A and fig. S7). Presence of bioactive gibberellin leads to degradation of DELLA proteins and triggers transcriptional repression of gibberellin biosynthesis genes, including *GIBBERELLIN 20 OXIDASE 2* (*GA20ox2*) (*12*, *13*). Consistent with their elevated levels of GA_4, *lfy* inflorescences had reduced levels of the DELLA protein REPRESSOR OF GA1-3 (RGA) and of *GA20ox2* mRNA. In contrast, LFY-overexpressing inflorescences had elevated levels of RGA protein and *GA20ox2* mRNA, relative to wild-type plants (Fig. 2, B and C, and fig. S7). Moreover, removal of ELA1 activity from 35S:LFY plants restored *GA20ox2* mRNA to wild-type levels (fig. S7). In agreement with their altered gibberellin levels, the Gene Ontology term "response to gibberellin stimulus" was significantly enriched (adjusted $P < 0.0005$) among genes differentially expressed in *lfy* mutants or LFY-overexpressing plants (fig. S7). Finally, LFY-overexpressing plants displayed phenotypes characteristic of gibberellin-deficient mutants, such as reduced height and increased chlorophyll content (*14*), that were partly rescued by application of exogenous gibberellin (fig. S7). The data indicate that LFY directs a reduction of gibberellin levels in inflorescences.

In *Arabidopsis*, gibberellin promotes the transition from vegetative development to the first inflorescence phase of reproductive development (*15*–*19*). However, our observations suggest that gibberellin may actually inhibit the transition to flower formation. This result was unexpected because, in general, mutants that delay onset of the first inflorescence phase also delay flower formation, whereas those that accelerate onset of the first inflorescence phase also accelerate flower formation (*20*) (Fig. 3A and fig. S8). We therefore examined the effect of altered gibberellin levels or response on these two transitions. Under long-day conditions, mutants deficient in gibberellin biosynthesis or gibberellin response produced more rosette leaves (delayed onset of the first inflorescence phase) (*19*) but fewer branches and cauline leaves (accelerated flower formation) (Fig. 3B, and fig. S8). Likewise, plants treated with the gibberellin biosynthesis inhibitor paclobutrazol (*21*) had more rosette leaves but fewer branches and cauline leaves (fig. S8). By contrast, plants treated with exogenous gibberellin formed fewer rosette leaves (*15*) and more branches and cauline leaves (Fig. 3C and fig. S8). We then decreased the gibberellin response selectively in lateral organ primordia of the inflorescence, by expressing a negative gibberellin-response regulator (the stabilized DELLA protein rgl1) from the *LFY* promoter. This had no effect on the duration of the vegetative phase but significantly accelerated flower formation (Fig. 3D and fig. S9). These results demonstrate that, whereas gibberellin promotes the transition from vegetative to inflorescence development, it inhibits flower formation.

Reduced gibberellin may increase the competence of lateral organ primordia to adopt a floral fate by enhancing their responsiveness to LFY. To test this hypothesis, we used a constitutively expressed version of LFY fused to the rat glucocorticoid receptor hormone–binding domain (GR), which enables control of LFY activity by dexamethasone (*5*). We also took advantage of the observation that the direct LFY target *APETALA1* (*AP1*) is only expressed in flower primordia (*3*), which makes *AP1* expression a good proxy for floral competence. Simultaneous treatment of plants expressing LFY-GR with dexamethasone and the gibberellin biosynthesis inhibitor paclobutrazol caused increased production of *AP1* in young flower primordia (Fig. 4A and fig. S9), relative to treatment with either paclobutrazol or dexamethasone alone. Via its inhibition of gibberellin biosynthesis, paclobutrazol promotes accumulation of DELLA proteins (*21*, *22*). In agreement with this, dexamethasone treatment of plants expressing both a constitutively expressed DELLA protein fused to GR (RGA-GR) (*23*) and LFY-GR also caused an increase in *AP1* expression (Fig. 4A and fig. S9). The slightly lower expression of *AP1* in RGA-GR LFY-GR plants treated with dexamethasone compared with LFY-GR plants treated with dexamethasone and paclobutrazol may be explained by the ability of paclobutrazol to stabilize multiple DELLA proteins or by degradation of RGA-GR due to the presence of endogenous gibberellin. Although DELLA proteins are best known for their roles in transcriptional repression, they can also activate transcription (*13*, *22*, *24*). Using chromatin immunoprecipitation followed by quantitative polymerase chain reaction (ChIP-qPCR), we found that a tagged version of RGA expressed from its own promoter (*12*) associated with several regulatory regions in the *AP1* locus (Fig. 4B and fig. S9). Moreover, dexamethasone activation of RGA-GR LFY-GR plants in the presence of protein synthesis inhibitor also caused increased *AP1* induction (fig. S9). We conclude that the DELLA

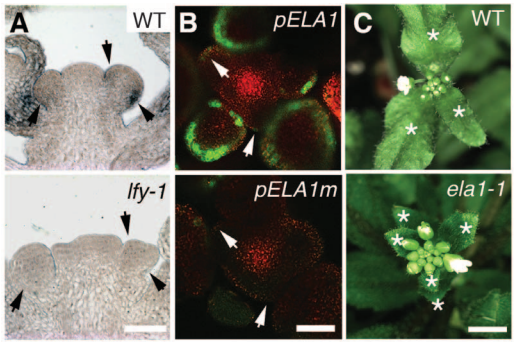

Fig. 1. *ELA1* is a direct LFY-regulated target and promotes flower formation. (**A**) *ELA1* in situ hybridization in wild-type (top) and *lfy-1* (bottom) inflorescences. (**B**) GFP reporter expression driven from wild-type (top) or LFY binding site–mutated (bottom) *ELA1* promoter. (A and B) Arrows: young floral primordia. (**C**) Top view of wild-type (top) and *ela1-1* mutant (bottom) inflorescences. The average number of cauline leaves and branches formed was significantly ($P < 10^{-5}$, two-sided Student's *t* test) higher in *ela1-1* (4.6 ± 0.1) than in the wild type (2.8 ± 0.1). Means ± SEM. Asterisks: cauline leaves subtending branches. Scale bars: 50 μm (A) and (B), 5 mm (C).

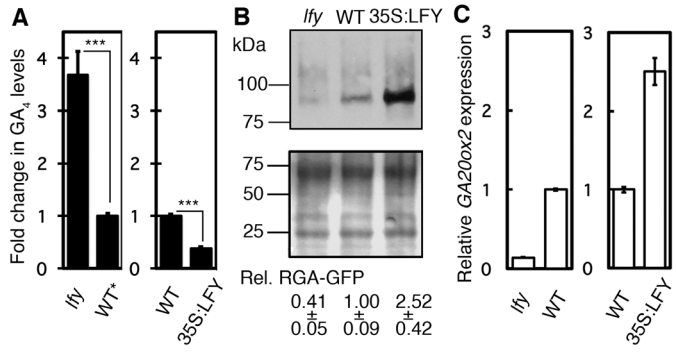

Fig. 2. LFY causes a reduction of gibberellin levels in the inflorescence. (**A**) The amount of GA_4 in *lfy* null mutant and in 35S:LFY-overexpressing relative to control inflorescences was determined by liquid chromatography–tandem mass spectrometry. ***$P < 10^{-3}$ based on two-sided Student's *t* test. (**B**) (Top) Antibody against GFP in a Western blot of *lfy* null mutant, wild-type (WT), or 35S:LFY inflorescences expressing pRGA:RGA-GFP. (Center) Ponceau S–stained membrane. (Bottom) Band intensity in three biological replicates ($P = 0.007$ for *lfy* versus WT, $P = 0.008$ for 35S:LFY versus WT; two-sided Student's *t* test). (**C**) mRNA abundance of the GA biosynthesis gene *GA20ox2* in *lfy*, wild-type, and 35S:LFY inflorescences. Means ± SEM.

protein RGA potentiates LFY activity and directly promotes the transcription of *AP1*.

DELLA proteins lack DNA binding domains and are thought to be recruited to target loci by sequence-specific transcription factors (*22*). The regulatory regions of the *AP1* locus occupied by RGA were similar to those occupied by a known transcriptional activator of *AP1*, the microRNA miR156 target SQUAMOSA PROMOTER BINDING PROTEIN–LIKE 9 (SPL9) (*25*) (Fig. 4B). SPL9 can physically interact with DELLA proteins (*18*). We therefore next examined the possibility that RGA promotes *AP1* transcription in association with SPL proteins. The *AP1* induction by dexamethasone plus paclobutrazol treatment of LFY-GR was reduced when we simultaneously depleted SPL proteins with an ethanol-inducible version of *MIR156* (*26*) (Fig. 4C), which suggested that SPL proteins contribute to this effect. In agreement with this interpretation, concurrent activation of constitutively expressed SPL9 fused to GR (SPL9-GR) and LFY-GR also led to increased *AP1* induction (Fig. 4C). The synergistic effect of SPL9-GR and LFY-GR on *AP1* induction most likely requires the presence of DELLA proteins, because it was strongly reduced after application of exogenous gibberellin (Fig. 4C). In addition, SPL proteins were necessary for recruitment of RGA to the *AP1* regulatory region both in plants and in yeast one-hybrid assays (Fig. 4D and fig. S9). Finally, increased activity of LFY, SPL9, and DELLA proteins caused flower formation immediately after termination of the vegetative phase (Fig. 4E and fig. S9). We conclude that SPL9 recruits DELLA proteins such as RGA to the *AP1* locus, where they induce *AP1* expression and promote the transformation of lateral primordia into flowers (Fig. 4F).

We reveal a mechanism for sequential coupling of the biphasic transition to reproductive competence in *Arabidopsis thaliana*. This mechanism is based on an increase and a subsequent decrease in hormone levels. Elevated gibberellin promotes termination of the vegetative phase and increases expression of genes encoding transcription factors such as the SPLs and LFY (*16*–*18*, *27*, *28*) (fig. S9). The subsequent reduction in gibberellin levels allows reaccumulation of transcriptional

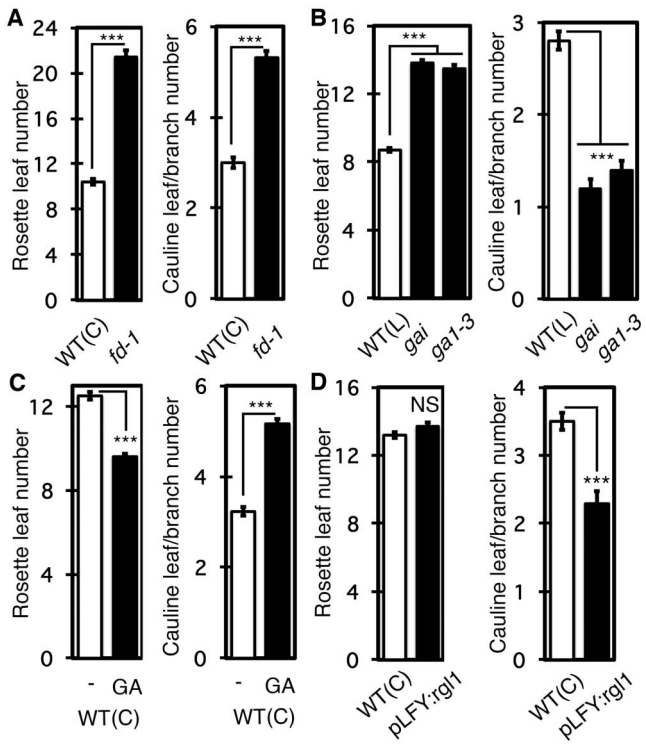

Fig. 3. Gibberellin inhibits the switch to flower formation. Duration of the vegetative phase (number of rosette leaves formed) and of the first inflorescence phase (number of cauline leaves and associated branches formed) in long-day photoperiods. White bar (control) and black bar (experimental) genotype or treatment. Means ± SEM. ***$P < 10^{-6}$ based on two-sided Student's *t* test. NS: not significant ($P = 0.25$, two-sided Student's *t* test) (**A**) Typical effect of a mutant [*fd-1* (*20*)] that prolongs both phases. (**B**) Mutants with decreased gibberellin (GA) response (*gai*) or levels (*ga1-3*). (**C**) Treatment with exogenous GA. (**D**) Reduction of the GA response specifically in incipient flower primordia (pLFY:rgl1). Throughout, matched WT genotypes were used [WT (L), wild type in the L*er* accession; WT (C); wild type in the Columbia accession].

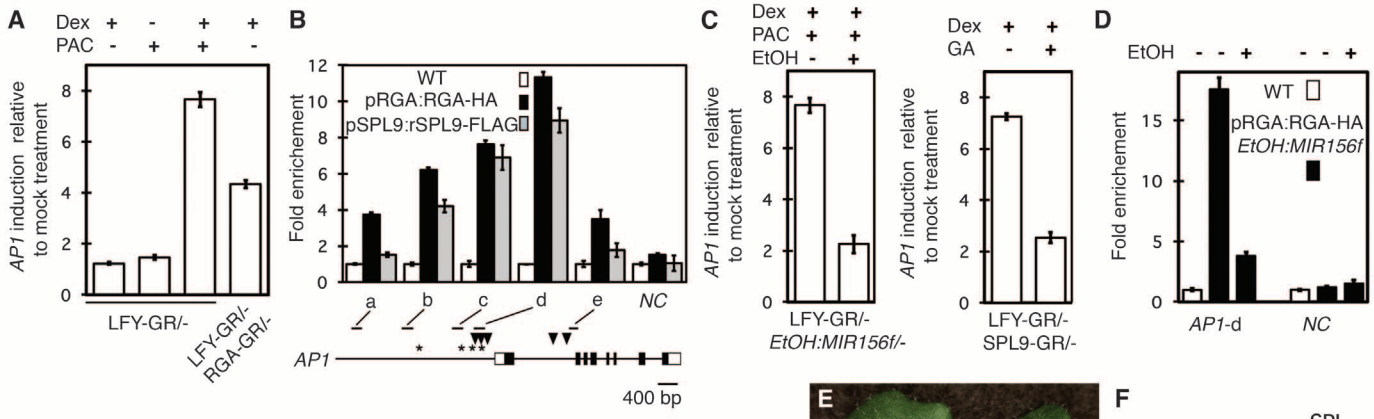

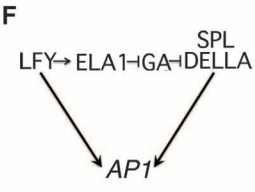

Fig. 4. Gibberellin-sensitive DELLA transcriptional co-regulators promote floral fate. (**A**) qRT-PCR determination of *AP1* induction relative to mock treated plants. Treatments: dexamethasone (Dex), gibberellin biosynthesis inhibitor paclobutrazol (PAC). (**B**) ChIP-qPCR of pRGA:RGA-HA and pSPL9:rSPL9-FLAG inflorescences using antibodies against hemagglutinin (HA) and FLAG. WT: ChIP in nontransgenic wild-type plants. NC: negative control locus. (Bottom) *AP1* promoter with PCR fragments amplified. Asterisks, SPL binding motifs; triangles, LFY binding motifs. (**C**) qRT-PCR determination of *AP1* induction relative to mock treated plants. Treatments: Dex, PAC, ethanol vapor induction of ETOH:*MIR156f* (*26*) to deplete miR156-sensitive SPL proteins, or GA to deplete DELLA proteins (*12*). (**D**) pRGA:RGA-HA association with the *AP1* locus "d" region in the presence (-ETOH) or absence (+ETOH) of miR156-sensitive SPL proteins. ChIP controls were as in (B). (A) to (D) Means ± SEM. (**E**) Immediate switch to flower formation in plants with increased LFY (35S:LFY), SPL9 (miR156 resistant pSPL9:rSPL9-FLAG) and DELLA (PAC treatment) levels. The number of cauline leaves formed in 35S:LFY pSPL9:rSPL9-FLAG PAC plants (0.3 ± 0.1) was significantly less ($P < 10^{-16}$, two-sided Student's *t*-test) than that of 35S:LFY plants (2.5 ± 0.2). (**F**) LFY and SPL9/DELLA synergistically induce *AP1*.

co-regulators, the DELLA proteins (*12*), which potentiate the ability of SPL9 (directly) and LFY (indirectly) to induce *AP1* and to trigger the onset of flower formation (fig. S9). LFY initiates the reduction in gibberellin levels—which results in increased DELLA accumulation—at least in part by inducing expression of the gibberellin catabolism enzyme ELA1.

Our findings may help explain the previously paradoxical observation that gibberellin acts positively in the switch to reproductive development in most plants but negatively in some woody plant species, such as grapevine (*29*). In addition, our data make gibberellin a prime candidate for a "branching" factor predicted by mathematical modeling of inflorescence architectures (*30*). Finally, our results suggest that the degree of inflorescence branching, which determines seed yield and, thus, reproductive success, could be adjusted by altering gibberellin accumulation before the inflorescence forms or the rate of gibberellin catabolism thereafter.

References and Notes

1. T. A. Steeves, I. Sussex, *Pattern in Plant Development* (Cambridge Univ. Press, Cambridge, 1989).
2. R. S. Poethig, *Science* **250**, 923–930 (1990).
3. O. J. Ratcliffe, D. J. Bradley, E. S. Coen, *Development* **126**, 1109–1120 (1999).
4. F. D. Hempel *et al.*, *Development* **124**, 3845–3853 (1997).
5. C. M. Winter *et al.*, *Dev. Cell* **20**, 430–443 (2011).
6. M. Schmid *et al.*, *Nat. Genet.* **37**, 501–506 (2005).
7. M. Schmid *et al.*, *Development* **130**, 6001–6012 (2003).
8. D. Weigel, J. Alvarez, D. R. Smyth, M. F. Yanofsky, E. M. Meyerowitz, *Cell* **69**, 843–859 (1992).
9. D. Weigel, O. Nilsson, *Nature* **377**, 495–500 (1995).
10. Y. Zhang *et al.*, *Plant J.* **67**, 342–353 (2011).
11. T. Nomura *et al.*, *Plant Cell Physiol.* **54**, 1837–1851 (2013).
12. A. Dill, H. S. Jung, T. P. Sun, *Proc. Natl. Acad. Sci. U.S.A.* **98**, 14162–14167 (2001).
13. R. Zentella *et al.*, *Plant Cell* **19**, 3037–3057 (2007).
14. M. Koornneef, J. H. van der Veen, *Theor. Appl. Genet.* **58**, 257–263 (1980).
15. J. Langridge, *Nature* **180**, 36–37 (1957).
16. V. C. Galvão, D. Horrer, F. Küttner, M. Schmid, *Development* **139**, 4072–4082 (2012).
17. A. Porri, S. Torti, M. Romera-Branchat, G. Coupland, *Development* **139**, 2198–2209 (2012).
18. S. Yu *et al.*, *Plant Cell* **24**, 3320–3332 (2012).
19. R. N. Wilson, J. W. Heckman, C. R. Somerville, *Plant Physiol.* **100**, 403–408 (1992).
20. M. Koornneef, C. J. Hanhart, J. H. van der Veen, *Mol. Gen. Genet.* **229**, 57–66 (1991).
21. W. Rademacher, *Annu. Rev. Plant Physiol. Plant Mol. Biol.* **51**, 501–531 (2000).
22. J. M. Davière, P. Achard, *Development* **140**, 1147–1151 (2013).
23. X. Hou, L. Y. Lee, K. Xia, Y. Yan, H. Yu, *Dev. Cell* **19**, 884–894 (2010).
24. K. Hirano *et al.*, *Plant J.* **71**, 443–453 (2012).
25. J. W. Wang, B. Czech, D. Weigel, *Cell* **138**, 738–749 (2009).
26. N. Yu *et al.*, *Plant Cell* **22**, 2322–2335 (2010).
27. M. A. Blázquez, D. Weigel, *Nature* **404**, 889–892 (2000).
28. S. Eriksson, H. Böhlenius, T. Moritz, O. Nilsson, *Plant Cell* **18**, 2172–2181 (2006).
29. P. K. Boss, M. R. Thomas, *Nature* **416**, 847–850 (2002).
30. P. Prusinkiewicz, Y. Erasmus, B. Lane, L. D. Harder, E. Coen, *Science* **316**, 1452–1456 (2007).

Acknowledgments: We are grateful to Wagner laboratory members and K. Gallagher, R. S. Poethig, and J. D. Wagner for critical comments. We thank R. Austin for the LFY binding motif functional depth analyses, T. Sun for pRGA:RGA-GFP and GA pathway mutant seeds, X. Chen for *35S:AlcR pAlcA:MIR156f* and pRGA:RGA-HA seeds, M. Schmid for RGL1 and rgl1delta17 constructs, S. Poethig for pSPL9:rSPL9-FLAG and 35S:SPL9-GR seeds, H. Yu for *ga1-3 rgl2-1 rga-2* 35S:RGA-GR seeds, G. Angenent for pAP1:AP1-GFP seeds, and the *Arabidopsis* Biological Resource Center for insertion mutant seeds and the F6A4 bacterial artificial chromosome clone. This work was supported by NSF grants IOS 0849298 and 1257111 to D.W. and training grant T32-HD007516 (Developmental Biology) support to C.M.W.

Supplementary Materials

www.sciencemag.org/content/344/6184/638/suppl/DC1
Materials and Methods
Figs. S1 to S9
Tables S1 and S2
References (*31*–*65*)

7 January 2014; accepted 2 April 2014
10.1126/science.1250498

Cancer Immunotherapy Based on Mutation-Specific CD4+ T Cells in a Patient with Epithelial Cancer

Eric Tran,[1] Simon Turcotte,[1]* Alena Gros,[1] Paul F. Robbins,[1] Yong-Chen Lu,[1] Mark E. Dudley,[1]† John R. Wunderlich,[1] Robert P. Somerville,[1] Katherine Hogan,[1] Christian S. Hinrichs,[1] Maria R. Parkhurst,[1] James C. Yang,[1] Steven A. Rosenberg[1]‡

Limited evidence exists that humans mount a mutation-specific T cell response to epithelial cancers. We used a whole-exomic-sequencing-based approach to demonstrate that tumor-infiltrating lymphocytes (TIL) from a patient with metastatic cholangiocarcinoma contained CD4+ T helper 1 (T_H1) cells recognizing a mutation in erbb2 interacting protein (ERBB2IP) expressed by the cancer. After adoptive transfer of TIL containing about 25% mutation-specific polyfunctional T_H1 cells, the patient achieved a decrease in target lesions with prolonged stabilization of disease. Upon disease progression, the patient was retreated with a >95% pure population of mutation-reactive T_H1 cells and again experienced tumor regression. These results provide evidence that a CD4+ T cell response against a mutated antigen can be harnessed to mediate regression of a metastatic epithelial cancer.

The human immune system has evolved to recognize and eliminate cells expressing foreign, nonself antigens. All malignant tumors harbor nonsynonymous mutations or other genetic alterations (*1*), some of which may generate neo-"nonself" epitopes that could potentially trigger an antitumor T cell response. Indeed, mutation-reactive T cells can frequently be found infiltrating human melanomas (*2*) and likely play a critical role in the clinical efficacy of adoptive cell therapy (ACT) and other immunotherapies in melanoma (*3*–*7*). However, limited evidence exists demonstrating that the human immune system can mount an endogenous, mutation-specific T cell response against epithelial cancers that comprise over 80% of all human malignancies (*8*-*11*), and it is unclear whether this response can be harnessed to develop effective personalized cancer immunotherapies (*12*). Moreover, epithelial cancers often contain fewer mutations than melanoma (*1*), which may decrease the probability of eliciting a mutation-specific T cell response. We thus first set out to determine whether tumor-infiltrating lymphocytes (TIL) recognizing patient-specific mutations can be identified in patients with metastatic gastrointestinal (GI) cancers.

To this end, a 43-year-old woman with widely metastatic cholangiocarcinoma (patient 3737, table S1) who progressed through multiple chemotherapy regimens was enrolled in a TIL-based ACT protocol for patients with GI cancers (NCT01174121) (*13*). Lung metastases were resected and used as a source for whole-exomic sequencing and generation of T cells for treatment. Whole-exomic sequencing revealed 26 nonsynonymous mutations (table S2). To test whether the patient's TIL recognized any of these mutations, we used a minigene approach. Briefly, for each mutation we designed a minigene construct that encoded for the mutated amino acid flanked on each side by 12 amino acids from the endogenous protein (fig. S1). Multiple minigenes were synthesized in tandem to generate tandem minigene (TMG) constructs (fig. S1 and table S3), which were then used as templates for the generation of in vitro transcribed (IVT) RNA (*13*). Each of these IVT TMG RNAs was then

[1]Surgery Branch, National Cancer Institute (NCI), National Institutes of Health, Bethesda, MD 20892, USA.

*Present address: Department of Surgery, Université de Montréal, and Institut du Cancer de Montréal, Centre de Recherche du Centre Hospitalier de l'Université de Montréal, Montréal, QC H2X0A9, Canada.

†Present address: Cell and Gene Therapies, Novartis Institutes for BioMedical Research Incorporated, Cambridge, MA 02139, USA.

‡Corresponding author. E-mail: sar@nih.gov

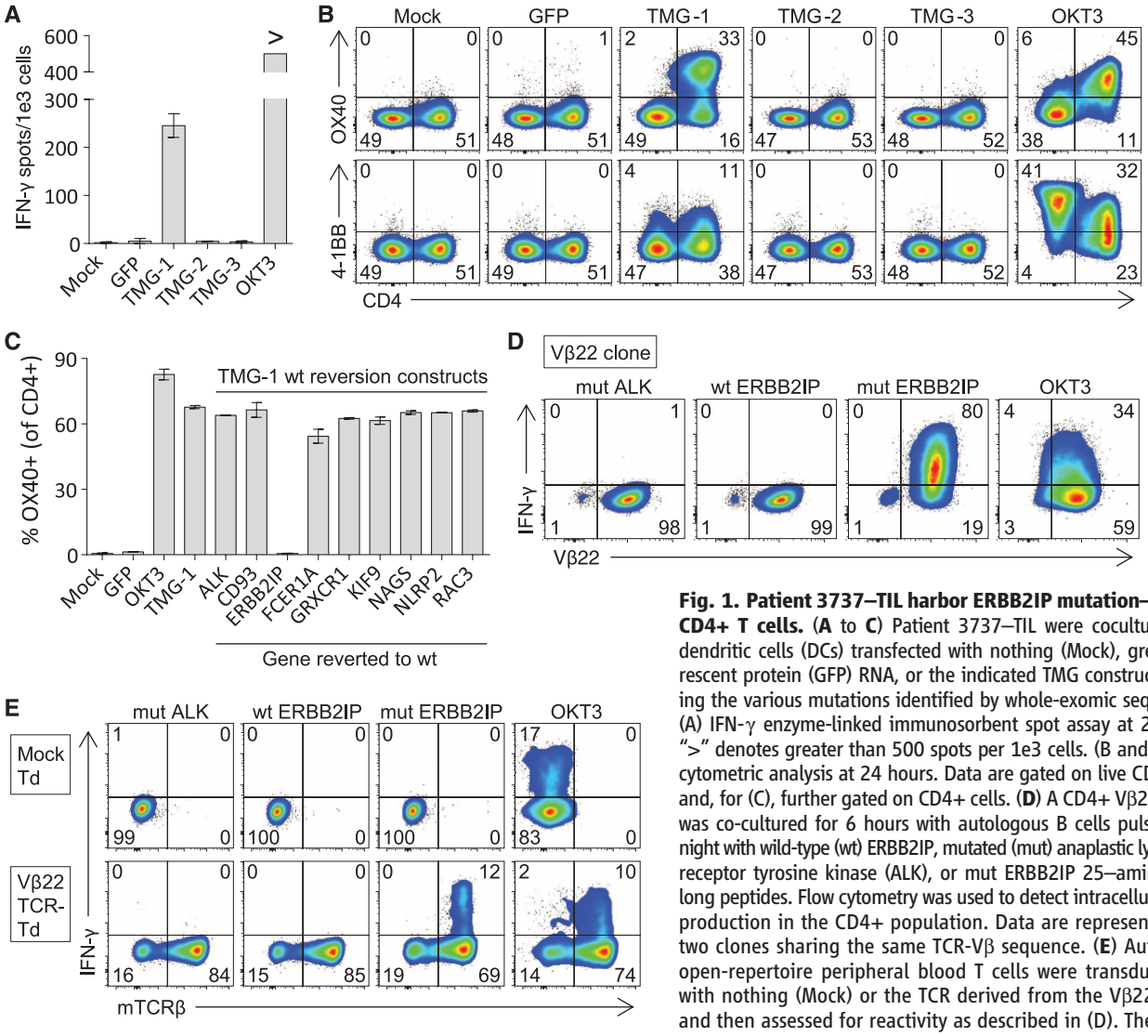

Fig. 1. Patient 3737–TIL harbor ERBB2IP mutation–specific CD4+ T cells. (**A** to **C**) Patient 3737–TIL were cocultured with dendritic cells (DCs) transfected with nothing (Mock), green fluorescent protein (GFP) RNA, or the indicated TMG construct encoding the various mutations identified by whole-exomic sequencing. (A) IFN-γ enzyme-linked immunosorbent spot assay at 20 hours. ">" denotes greater than 500 spots per 1e3 cells. (B and C) Flow-cytometric analysis at 24 hours. Data are gated on live CD3+ cells and, for (C), further gated on CD4+ cells. (**D**) A CD4+ Vβ22+ clone was co-cultured for 6 hours with autologous B cells pulsed overnight with wild-type (wt) ERBB2IP, mutated (mut) anaplastic lymphoma receptor tyrosine kinase (ALK), or mut ERBB2IP 25–amino acid–long peptides. Flow cytometry was used to detect intracellular IFN-γ production in the CD4+ population. Data are representative of two clones sharing the same TCR-Vβ sequence. (**E**) Autologous open-repertoire peripheral blood T cells were transduced (Td) with nothing (Mock) or the TCR derived from the Vβ22+ clone and then assessed for reactivity as described in (D). The endogenous Vβ22+ TCR constant regions were swapped with mouse constant regions, allowing for the detection of the introduced TCR using antibodies against the mouse TCRβ constant region (mTCRβ). Plate-bound OKT3 was used as a control in all assays. All data are representative of at least two independent experiments. Error bars are SD.

individually transfected into autologous antigen-presenting cells, followed by a coculture with TIL to determine whether any of the processed and presented mutated antigens were recognized by TIL. We observed reactivity of 3737-TIL to a mutated antigen present in TMG-1 but not TMG-2 or TMG-3 (Fig. 1A). Moreover, the reactivity predominated in the CD4+ T cell population, as demonstrated by up-regulation of the activation markers OX40 and 4-1BB (Fig. 1B). Although some 4-1BB up-regulation was observed in the CD4-negative (CD8+) T cell population, we sorted these cells and found no reactivity against the TMG. To determine which of the nine mutations in TMG-1 was being recognized by 3737-TIL, we synthesized nine additional TMG-1 constructs, each one containing a reversion of one of the mutations back to the wild-type sequence. Reactivity of 3737-TIL to TMG-1 was abrogated only when the erbb2 interacting protein (*ERBB2IP*) mutation was reverted back to the wild-type sequence, indicating that the TIL specifically recognized the ERBB2IP^{E805G} mutation (Fig. 1C). The response was restricted by HLA-DQB1*0601, and the minimal epitope was located within the 13–amino acid sequence NSKEETGHLENGN (where E is Glu; G, Gly; H, His; K, Lys; L, Leu; N, Asn; S, Ser; and T, Thr) (fig. S2).

We next characterized the clonality of the mutated ERBB2IP-specific CD4+ T cells by sorting them after antigen-specific activation, using OX40 as a marker of activation (fig. S3A). These cells were then bulk-expanded and cloned by limiting dilution. A flow cytometry–based survey of the T cell receptor–Vβ (TCR-Vβ) repertoire demonstrated that the bulk-expanded population was >95% Vβ22+ and that 10/11 clones assessed were purely Vβ22+ (fig. S3, B and C). TCR sequence analysis revealed the same TCRβ variable, diversity, joining (V-D-J) sequence in 6/6 Vβ22+ clones tested (table S4), suggesting that the majority of the ERBB2IP mutation–reactive T cells was composed of a dominant Vβ22+ T cell clone. T cell clones expressing this Vβ22 TCR specifically produced the cytokine interferon (IFN)–γ upon stimulation with the mutated ERBB2IP peptide (Fig. 1D). Moreover, autologous open repertoire peripheral blood T cells genetically modified with this TCR-Vβ22 chain matched with its alpha chain (table S5) conferred specific reactivity to the mutated ERBB2IP peptide (Fig. 1E), demonstrating that this TCR specifically recognized the ERBB2IP^{E805G} mutation.

The patient underwent adoptive transfer of 42.4 billion TIL containing CD4+ ERBB2IP mutation-reactive T cells followed by four doses of interleukin (IL)–2 to enhance T cell proliferation and function (fig. S4). Flow cytometry analysis demonstrated that about 25% of the entire 3737-TIL product administered was composed of the

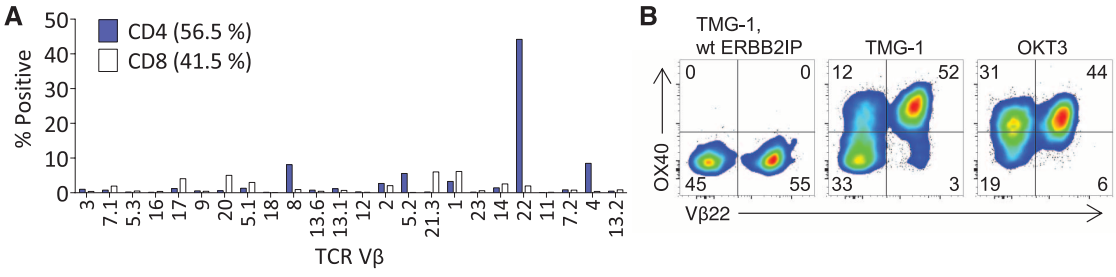

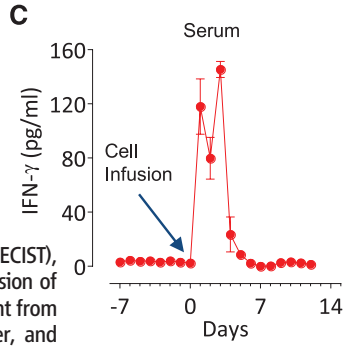

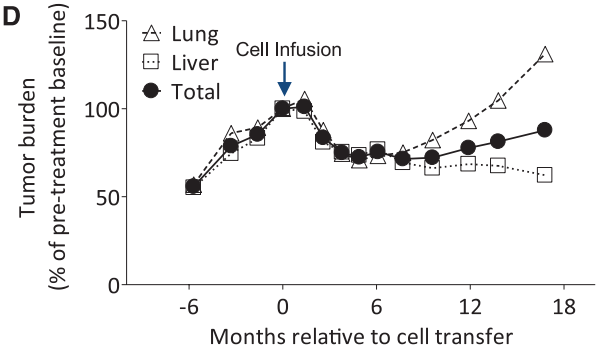

Fig. 2. Adoptive transfer of TIL containing ERBB2IP mutation–reactive T cells. (**A**) Flow-cytometric analysis of the TCR-Vβ repertoire of 3737-TIL, gated on live CD4+ or CD8+ T cells. (**B**) Patient 3737–TIL were cocultured with DCs transfected with TMG-1 or TMG-1 encoding the wt ERBB2IP reversion, and flow cytometry was used to assess OX40 and Vβ22 expression on CD4+ T cells at 24 hours post-stimulation. Plate-bound OKT3 stimulation was used as a positive control. (A) and (B) are representative of at least two independent experiments. (**C**) IFN-γ enzyme-linked immunosorbent assay on patient 3737 serum samples pre– and post–adoptive cell transfer of 3737-TIL. Error bars are SEM. (**D**) Tumor growth curves [Response Evaluation Criteria in Solid Tumors (RECIST), sum of maximum diameters] before and after infusion of 3737-TIL. Data are expressed as a change in percent from pretreatment baseline and stratified on lung, liver, and total tumors.

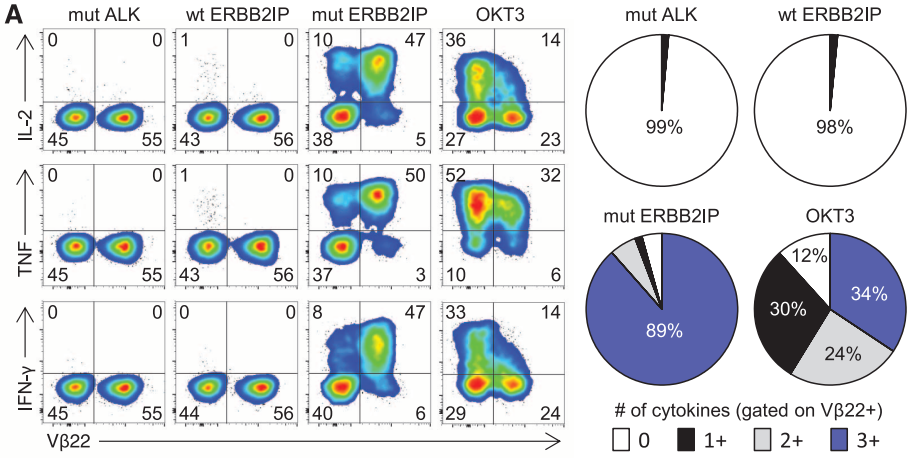

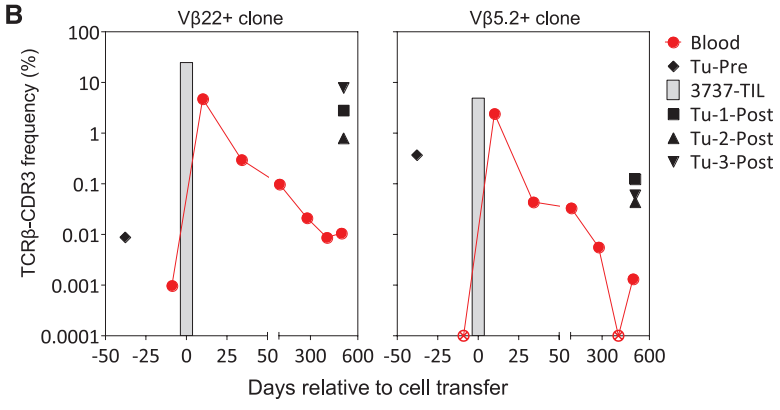

Fig. 3. Functional phenotype and persistence of ERBB2IP mutation–specific CD4+ T cells. (**A**) Patient 3737–TIL were cocultured for 6 hours with autologous B cells pulsed overnight with wt ERBB2IP, mut ALK, or mut ERBB2IP 25–amino acid–long peptides. Flow cytometry was used to assess expression of Vβ22 and to detect intracellular production of IL-2, TNF, and IFN-γ in the CD4+ population. Pie charts display the percentage of Vβ22+ cells that expressed the indicated number of cytokines. Data are representative of at least three independent experiments. (**B**) TCR-Vβ deep sequencing of 3737-TIL and blood and tumors of patient 3737 at various times pre– and post–adoptive cell transfer with 3737-TIL. Data show the frequency of the two ERBB2IP mutation–specific TCRβ-CDR3 clonotypes. ⊗, not detected.

Vβ22+, mutation-reactive T cells (Fig. 2, A and B), equating to the infusion of over 10 billion ERBB2IP mutation–specific CD4+ T cells. Elevated levels of IFN-γ were detected in the patient's serum for the first 5 days after cell infusion (Fig. 2C). Although the patient had clear evidence of progressive disease before the cell infusion, tumor regression was observed by the 2-month follow-up, and all target lung and liver lesions continued to regress, reaching a maximum reduction of 30% at 7 months post-treatment (Fig. 2D). The patient experienced disease stabilization for about 13 months after cell infusion, after which disease progression was observed only in the lungs but not liver.

To determine whether there was evidence that the CD4+ ERBB2IP mutation–reactive T cells played a role in the disease stabilization, we evaluated the in vitro phenotype and function and in vivo persistence of these cells. A number of preclinical studies (*14*–*20*) and one case report in melanoma (*21*) have demonstrated that T helper 1 (T_H1) cells, through a variety of mechanisms including the secretion of the pleiotropic cytokines IFN-γ and tumor necrosis factor (TNF) (*22*, *23*), can mediate tumor regression. Moreover, CD4+ T cells that can simultaneously produce multiple effector cytokines (polyfunctional T cells) have been correlated with effective antitumor T cell responses (*19*, *24*). We found that the Vβ22+ ERBB2IP mutation–reactive CD4+ T cells were polyfunctional T_H1 cells, because stimulation with the mutated ERBB2IP peptide induced the robust coexpression of IFN-γ, TNF, and IL-2 (Fig. 3A) but little to no IL-4 or IL-17. Further phenotypic characterization revealed that these cells were predominantly effector memory CD4+ T cells with cytolytic potential (fig. S5, A and B).

There also appeared to be a minor population of polyfunctional Vβ22-negative, ERBB2IP mutation–reactive CD4+ T cells present in 3737-TIL (Figs. 2B and 3A). Sorting of the Vβ22-negative cells followed by activation of these cells revealed that one or more additional clonotypes reactive to this epitope were present in 3737-TIL (fig. S6, A and B), the most dominant clonotype of which was Vβ5.2 (fig. S6, C and D). The majority of the Vβ5.2+ cells produced multiple cytokines in an antigen-specific manner (fig. S6E and table S6). There also appeared to be a minor population of Vβ5.2-negative (and Vβ22-negative) CD4+ T cells that recognized mutated ERBB2IP (fig. S6E). Thus, the TIL used to treat patient 3737 contained at least three different polyfunctional CD4+ T cell clones that recognized the same mutation in ERBB2IP, suggesting that this mutation was highly immunogenic.

The in vivo persistence of adoptively transferred T cells in the blood at 1 month post–cell transfer is correlated with improved outcomes in melanoma patients treated with ACT (*25*). We thus evaluated the in vivo persistence of the ERBB2IP mutation–reactive CD4+ T cell clones in patient 3737. TCR-Vβ deep sequencing revealed that these clonotypes were rare or not detectable in the peripheral blood before ACT (Fig. 3B). Ten days after ACT, both clones were present at greater than 2% of the total T cells in the peripheral blood, but declined to less than 0.3% by day 34 post–cell infusion (Fig. 3B). Three lung metastases, which were resected nearly a year and a half after ACT, were infiltrated by the ERBB2IP mutation–reactive T cells (Fig. 3B), suggesting that these cells contributed to the cancer regression and disease stabilization. The Vβ22+ ERBB2IP mutation–reactive clone was the most frequent clone detected in tumor nodule–3 (Tu-3-Post) and represented nearly 8% of total T cells in the tumor (Fig. 3B), whereas this clone was the second and twelfth most frequent in tumor nodules–1 and –2, respectively. The Vβ5.2+ ERBB2IP mutation–reactive clone was also enriched compared with its frequency in blood in all three tumor nodules (Fig. 3B). Thus, patient 3737 experienced tumor regression with stabilization of disease for more than 1 year after receiving over 10 billion ERBB2IP mutation–specific polyfunctional T_H1 cells that infiltrated and persisted in the metastatic lesions.

We observed relatively high levels of *ERBB2IP* expression in both the original and the recurrent lung lesions as determined by quantitative reverse transcription polymerase chain reaction (fig. S7A), and Sanger sequencing validated the presence of the ERBB2IP mutation in all tumor lesions (fig. S7B). The T cell infiltrate and major histocompatibility complex expression of the tumors in situ are summarized in tables S7 and S8, respectively. The presence of T cells reactive to the ERBB2IP mutation in progressing tumors that expressed this mutation suggests the presence of immunosuppressive influences at the tumor site that may need to be overcome to increase the anticancer effects of the transferred cells.

To specifically evaluate the contribution of mutation-reactive T_H1 cells to the antitumor response in vivo, we generated and adoptively transferred a TIL product that was comprised of >95% of the Vβ22+ ERBB2IP mutation–reactive T_H1 cells (Fig. 4, A and B) (*13*). Again, the patient experienced a decrease in target lesions, but, unlike the first treatment, tumor regression was observed even at the first-month follow-up and continues as of the last follow-up at 6 months (Fig. 4C).

Mapping of the mutational landscape of human cancers is occurring at a rapid pace, but strategies to exploit this information for clinical benefit remain to be fully realized. Here, we used a whole-exome sequencing approach to demonstrate that the human immune system can mount an endogenous T_H1 response against a mutation expressed by an epithelial cancer, and we provide evidence that this response can be harnessed for therapeutic benefit. Given that a major hurdle for the success of immunotherapies for GI and other cancers is the apparent low frequency of tumor-reactive T cells (*26*), the strategies reported here could be used to generate a T cell product that is highly enriched in mutation-reactive T cells for use in ACT. The ability to immunologically target unique mutations in cancers can potentially extend highly personalized immunotherapies to patients with epithelial cancers, which account for about 90% of cancer deaths in the United States.

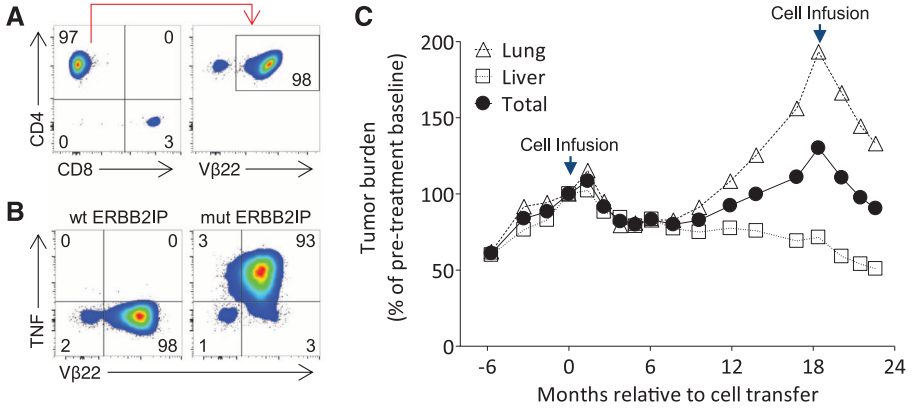

Fig. 4. Evidence of tumor regression after treatment with a highly pure population of Vβ22+ ERBB2IP mutation–reactive CD4+ T cells. (**A**) Flow-cytometric analysis of the TIL product used for retreatment. Data are gated on live CD3+ T cells (left) and further gated on CD4+ cells (right). (**B**) Retreatment TIL were cocultured for 6 hours with autologous B cells pulsed overnight with wt or mut ERBB2IP 25–amino acid–long peptides. Flow cytometry was used to detect intracellular TNF production in the CD4+ population. (A) and (B) are representative of at least two independent experiments. (**C**) Tumor growth curves (sum of maximum diameters) of patient 3737 before and after first and second adoptive cell transfers. The first infusion product consisted of 42.4 billion T cells containing about 25% (10 billion) Vβ22+ ERBB2IP mutation–reactive T_H1 cells. The second infusion product consisted of 126 billion T cells containing over 95% (120 billion) Vβ22+ ERBB2IP mutation–reactive T_H1 cells. Data are expressed as a change from baseline and stratified on lung, liver, and total tumors. Some target lesions selected in (C) differ from Fig. 2D because only lesions that were present throughout both treatments were selected for measurement.

References and Notes

1. B. Vogelstein *et al.*, *Science* **339**, 1546–1558 (2013).
2. P. van der Bruggen, V. Stroobant, N. Vigneron, B. Van den Eynde, "Tumor antigens resulting from mutations," *Cancer Immunity* (2013), http://cancerimmunity.org/peptide/mutations/.
3. P. F. Robbins *et al.*, *Nat. Med.* **19**, 747–752 (2013).
4. N. van Rooij *et al.*, *J. Clin. Oncol.* **31**, e439–e442 (2013).
5. Y. C. Lu *et al.*, *J. Immunol.* **190**, 6034–6042 (2013).
6. V. Corbière *et al.*, *Cancer Res.* **71**, 1253–1262 (2011).
7. J. Huang *et al.*, *J. Immunol.* **172**, 6057–6064 (2004).
8. H. Echchakir *et al.*, *Cancer Res.* **61**, 4078–4083 (2001).
9. S. Mandruzzato, F. Brasseur, G. Andry, T. Boon, P. van der Bruggen, *J. Exp. Med.* **186**, 785–793 (1997).
10. K. T. Hogan *et al.*, *Cancer Res.* **58**, 5144–5150 (1998).
11. V. Karanikas *et al.*, *Cancer Res.* **61**, 3718–3724 (2001).
12. S. Wedén *et al.*, *Int. J. Cancer* **128**, 1120–1128 (2011).
13. Materials and methods are available as supplementary materials on *Science* Online.
14. D. Mumberg *et al.*, *Proc. Natl. Acad. Sci. U.S.A.* **96**, 8633–8638 (1999).
15. A. Corthay *et al.*, *Immunity* **22**, 371–383 (2005).
16. S. A. Quezada *et al.*, *J. Exp. Med.* **207**, 637–650 (2010).
17. Y. Xie *et al.*, *J. Exp. Med.* **207**, 651–667 (2010).
18. P. D. Greenberg, D. E. Kern, M. A. Cheever, *J. Exp. Med.* **161**, 1122–1134 (1985).
19. Z. C. Ding *et al.*, *Blood* **120**, 2229–2239 (2012).
20. K. A. Shafer-Weaver *et al.*, *Cancer Res.* **69**, 6256–6264 (2009).
21. N. N. Hunder *et al.*, *N. Engl. J. Med.* **358**, 2698–2703 (2008).
22. H. Braumüller *et al.*, *Nature* **494**, 361–365 (2013).
23. Z. Qin, T. Blankenstein, *Immunity* **12**, 677–686 (2000).
24. J. Yuan *et al.*, *Proc. Natl. Acad. Sci. U.S.A.* **105**, 20410–20415 (2008).
25. S. A. Rosenberg *et al.*, *Clin. Cancer Res.* **17**, 4550–4557 (2011).
26. S. Turcotte *et al.*, *J. Immunol.* **191**, 2217–2225 (2013).

Acknowledgments: We thank the Milstein Family Foundation for their generous support; C.-C. R. Lee, Y. F. Li, A. Mixon, S. Farid, and J. Gartner for helpful technical support and reagents; and the Surgery Branch clinical team for outstanding patient care. The data presented in this manuscript are tabulated in the main paper and the supplementary materials. The raw whole-exome sequence data are available on the Sequence Read Archive database: Bioproject PRJNA243084. This research was supported by the Intramural Research Program of the NIH and NCI.

Supplementary Materials
www.sciencemag.org/content/344/6184/641/suppl/DC1
Materials and Methods
Figs. S1 to S7
Tables S1 to S8
References (*27*, *28*)

21 January 2014; accepted 9 April 2014
10.1126/science.1251102

The Transcription Factor Gata6 Links Tissue Macrophage Phenotype and Proliferative Renewal

Marcela Rosas,[1]* Luke C. Davies,[1]* Peter J. Giles,[2] Chia-Te Liao,[1] Bashar Kharfan,[1] Timothy C. Stone,[2] Valerie B. O'Donnell,[1] Donald J. Fraser,[3] Simon A. Jones,[1] Philip R. Taylor[1]†

Tissue-resident macrophages are heterogeneous as a consequence of anatomical niche–specific functions. Many populations self-renew independently of bone marrow in the adult, but the molecular mechanisms of this are poorly understood. We determined a transcriptional profile for the major self-renewing population of peritoneal macrophages in mice. These cells specifically expressed the transcription factor Gata6. Selective deficiency of Gata6 in myeloid cells caused substantial alterations in the transcriptome of peritoneal macrophages. Gata6 deficiency also resulted in dysregulated peritoneal macrophage proliferative renewal during homeostasis and in response to inflammation, which was associated with delays in the resolution of inflammation. Our investigations reveal that the tissue macrophage phenotype is under discrete tissue-selective transcriptional control and that this is fundamentally linked to the regulation of their proliferation renewal.

Tissue-resident macrophages play fundamental roles specific to their microanatomical niche, ranging from dedicated homeostatic functions to immune surveillance (*1*). Such heterogeneity predicts that discrete transcriptional controls probably exist in specific macrophage populations that determine both their particular phenotypes and tissue-specific functions.

Many resident macrophages self-renew by local proliferation [(*1*) and references therein]. This is initiated after seeding of macrophages into tissues during development and their expansion during the neonatal period (*1*). Under specific conditions, these tissue-resident macrophages may also be derived from blood monocytes (*1*). Classic F4/80^{high}CD11b^{high} peritoneal-resident macrophages fit this model (*2*–*7*), and they proliferate above homeostatic levels in response to inflammation (*6*). Proliferation of human macrophages has also been observed in several contexts [reviewed in (*1*)]. However, the factors controlling these processes remain ill-defined. We hypothesized that discrete transcriptional controls would govern both the specific phenotype of tissue

[1]Cardiff Institute of Infection and Immunity, Cardiff University School of Medicine, Heath Park, Cardiff CF14 4XN, UK. [2]Central Biotechnology Services, Cardiff University School of Medicine, Heath Park, Cardiff CF14 4XN, UK. [3]Institute of Molecular Medicine, Cardiff University School of Medicine, Heath Park, Cardiff CF14 4XN, UK.

*These authors contributed equally to this work.
†Corresponding author. E-mail: taylorpr@cf.ac.uk

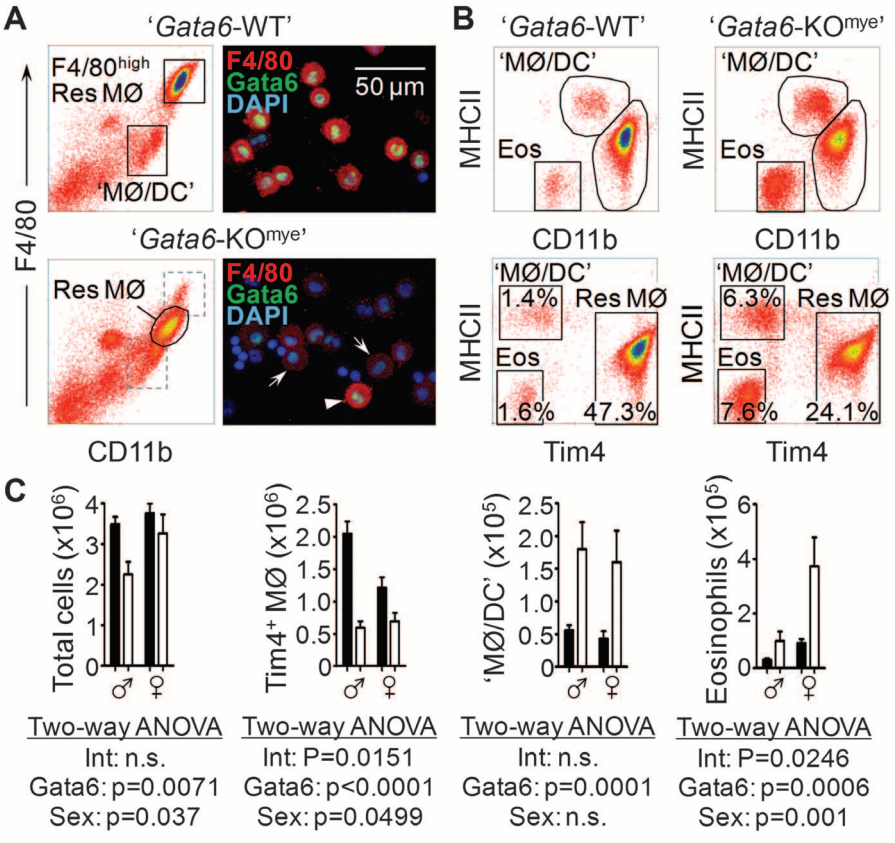

Fig. 1. Selective myeloid cell alterations in the peritoneum of mice with myeloid Gata6 deficiency. (**A**) Representative flow cytometric and immunofluorescent assessment of peritoneal-resident macrophages from WT and Gata6-KO^{mye} mice. F4/80^{high} (arrowhead) and F4/80^{low} (arrows) macrophages are indicated. Fluorescent images were captured with a ×40 objective lens, the scale bar is indicated, and the images are representative of four mice per group (fig. S9). (**B**) Representative flow cytometric analysis of the peritoneal myeloid cell (CD11b^{+}CD19^{-}) composition of the Gata6-WT and Gata6-KO^{mye} mice. Percentages indicate typical proportions of the cell types of all peritoneal cells. (**C**) Quantification of peritoneal myeloid cells in the Gata6-WT (black bars, n = 9♂/7♀) and Gata6-KO^{mye} mice (white bars, n = 5♂/5♀) analyzed by flow cytometry in (A) and (B) above. Data represent the mean ± SEM of mice pooled from two independent experiments and were analyzed by two-way analysis of variance (ANOVA) MØ, macrophage; Res, tissue-resident; Eos, eosinophil; DC, dendritic cell; Int, interaction statistic; Gata6, Gata6 effects; Sex, sex effects.

macrophages and their proliferative renewal in a select tissue microenvironment.

We performed a transcriptional analysis of murine monocyte-like cells during acute peritonitis (figs. S1 to S3 and tables S1 to S3). Our approach analyzed populations specifically enriched in tissue-resident macrophages (*6*), allowing definition of a tissue macrophage–restricted transcriptional profile, which was associated with homeostatic and metabolic processes (cluster 15; fig. S2 and table S3, A to C). *Gata6* was selectively expressed in peritoneal macrophages when compared to both in vitro–generated bone marrow–derived macrophages and, when isolated during inflammation, contemporary monocyte-derived (*8*) macrophages (fig. S1, D, F, and G). Perhaps best known for its essential requirement in the development of the heart, gut, and liver (*9*–*11*), the role of Gata6 in macrophages is unknown.

We crossed conditional knockout (KO) *Gata6*$^{tm2.1Sad/J}$ mice (*12*) with Lysozyme M (*Lyz2*) Cre-recombinase knockin mice (*Lyz2*^{Cre}, official strain name B6.129P2-*Lyz2*$^{tm1(cre)Ifo/J}$) (*13*) to generate mice with a myeloid deficiency of Gata6 (Gata6-KO^{mye} mice) (*14*). *Lyz2*^{Cre} mediates recombination in approximately 95% of peritoneal macrophages (*13*). Flow cytometric analysis of peritoneal cells from Gata6-KO^{mye} mice compared to their wild-type (WT) littermates indicated a gross change in the characteristic F4/80^{high}CD11b^{high} phenotype, with the majority (~95%) of classic peritoneal macrophages exhibiting reduced F4/80 and CD11b expression (Fig. 1A). Further analysis of peritoneal myeloid cells (CD11b^{+}CD19^{-}), indicated that although the F4/80^{low} macrophages exhibited relatively normal expression of Tim4 [a marker expressed by the majority of peritoneal resident macrophages and found in this study to be selectively expressed by these cells during acute peritonitis; fig. S1 and (*6*)], there was a reduction in their numbers and an increase in eosinophils and MHCII^{high}F4/80^{low} macrophages/dendritic cells (Fig. 1, B and C). However, there were no substantive alterations in the numbers of peritoneal lymphocytes (fig. S4A) or peripheral blood cells (fig. S4, B and C).

We established a panel of lentiviral vectors (fig. S5A and table S4) with which we achieved selective high expression of transgenes in peritoneal-resident macrophages in vivo (fig. S5, A and B). Lentiviral delivery of Cre to the peritoneal-resident macrophages of adult *Gata6*$^{tm2.1Sad/J}$ mice resulted in alteration of their phenotype, including lower F4/80 expression (fig. S5C). This confirmed that Gata6 was important for phenotype maintenance in the adult. We also excluded a role for Cre toxicity (*15*) (fig. S5, C to E).

We assessed the importance of Gata6 as a regulator of the characteristic peritoneal macrophage phenotype by microarray analysis of macrophages from WT and Gata6-KO^{mye} mice (*14*) (Fig. 2A and table S5, A and B). Analysis of peritoneal macrophage–specific transcripts indicated that there was a significant overrepresentation of probe sets that were down-regulated in the absence of Gata6 (Fig. 2B). The array data were validated by examination of surface receptors whose mRNA was altered (Fig. 2, C to E). An additional study (*16*) identified genes specific to peritoneal macrophages when compared to other tissues, and there was a similar overrepresentation of genes from this list that were down-regulated in the absence of Gata6 (fig. S6 and table S6). Using both data sets, in addition to Gata6, we identified a gene list that could be considered peritoneal macrophage–specific by both criteria (within and between tissues), of which 60% of genes were down-regulated in the absence of Gata6 (fig. S6). This confirmed Gata6 as a major regulator of the peritoneal macrophage phenotype. Peritoneal macrophage–selective transcripts were not the only transcripts that were altered in the absence of Gata6, however, indicating

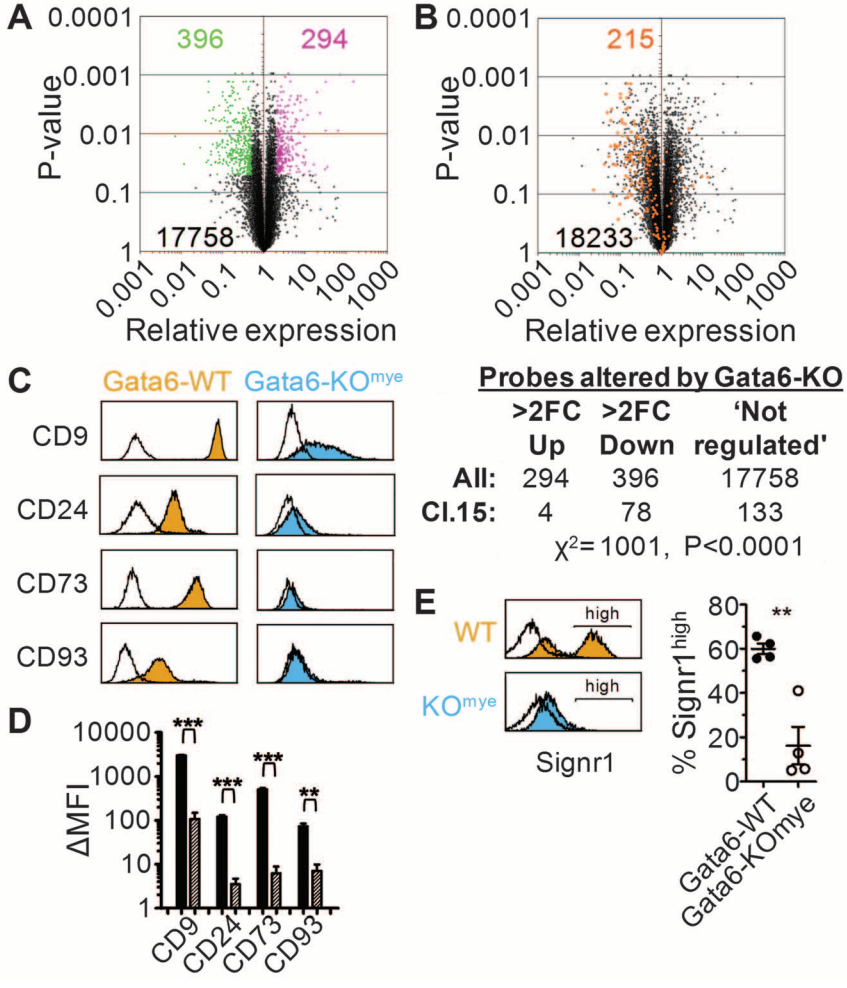

Fig. 2. Gata6 is fundamental to the peritoneal-resident macrophage phenotype. (**A**) Volcano plot showing the differential gene expression between peritoneal macrophages from Gata6-KO^{mye} and WT mice. Significantly two-fold down-regulated (green) and up-regulated (magenta) probe sets are indicated. (**B**) Same volcano plot as (A), overlaid (orange) with the 215 peritoneal macrophage–selective cluster 15 (Cl. 15) probe sets [figs. S1 and S2 (*14*)], which were significantly (below) disproportionately down-regulated in the absence of Gata6. (**C** to **E**) Representation [(C) and (E)] and quantification [(D) and (E)] of flow cytometric validation of the array data from (A). Data (analyzed by *t* test) represent the difference in median fluorescent intensity (ΔMFI) between receptor-specific and isotype-control antibodies (mean ± SEM) of individual mice (n = 4) from one of two experiments (solid bars denote WT and hatched bars denote Gata6-KO^{mye} mice).

a broader impact on phenotype (Fig. 2, A and B). Consistent with a role in peritoneal phenotype specialization, enforced Gata6 expression in bone marrow–derived macrophages promoted their peritoneal retention and altered their phenotype toward that of peritoneal resident macrophages (fig. S7). Although we have not addressed this, we would anticipate that Gata6 would also be up-regulated in bone marrow–derived cells recruited to the peritoneum when replacing the tissue-resident pool; for example, as can occur in irradiation chimeras (*17*). Peritoneal macrophages in WT mice are capable of renewal without monocytic input (*6*, *7*), particularly under homeostatic conditions. In accordance with this, genes associated with the regulation of cell proliferation (Gene Ontology term GO:0042127) were also altered by Gata6 deficiency (table S5A), including *Cdkn2b*, *Csf1*, *Igf1*, *Tgfb2*, *Tgfbr2*, and *Bmpr1a*. Moreover, Gata6-deficient peritoneal macrophages exhibited increased basal proliferation

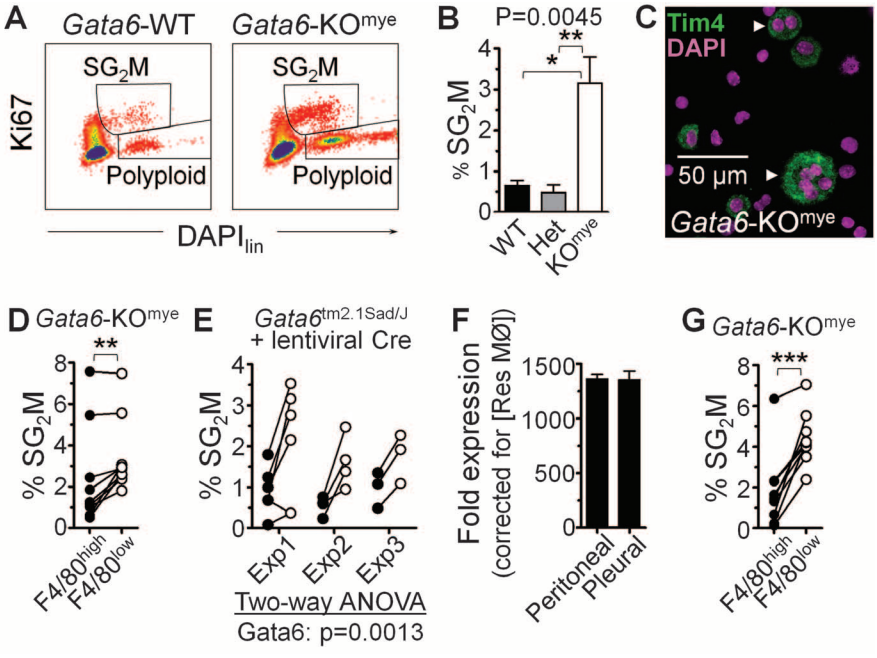

Fig. 3. Dysregulated peritoneal macrophage proliferation in the absence of Gata6. (**A** to **C**) Representative density plots (A) gated on resident peritoneal macrophages (Fig. 1A) showing proliferation (SG_2M) and polyploidy, which were quantified (B) and visualized [arrowheads in (C)], respectively. Data in (A) and (B) are derived from one of two independent experiments [Gata6-KO^{mye}, n = 5 mice; heterozygous Gata6-KO^{mye} (Het), n = 4 mice; WT, n = 3 mice] represented as mean ± SEM and analyzed by one-way ANOVA (P value as indicated) with Bonferroni post tests. Immune fluorescence is representative of five mice. (**D**) Examination of proliferative differences between the majority F4/80^{low} (white circles) KO and the WT F4/80^{high} (black circles) macrophages (fig. S9) within the same Gata6-KO^{mye} mice. Lines denote paired samples from the same mice (n = 9), which were pooled from two similar experiments and analyzed by paired t test. (**E**) The impact of Gata6 deletion on proliferation was examined 7 days after delivery of Cre-expressing lentiviruses to *Gata6*$^{tm2.1Sad/J}$ mice intraperitoneally. The proportion of cells in the SG_2M phases of the cell cycle were compared between F4/80^{low}Cre^{+} (white circles) and F4/80^{high}Cre^{-} (black circles) macrophages. Data are represented as three independent experiments (Exp), with lines denoting paired samples from the same mice and analyzed as indicated. (**F**) Gata6 mRNA expression compared by quantitative polymerase chain reaction between peritoneal and pleural leukocytes. The data show mean ± SEM from one of two independent experiments in 129S6 mice (n = ≥3 per group), normalized to reflect the number of resident macrophages. (**G**) Similar analysis to that in (D), except using pleural macrophages. Data from two similar experiments were pooled and analyzed by a paired t test. *P < 0.05, **P < 0.01, ***P < 0.001.

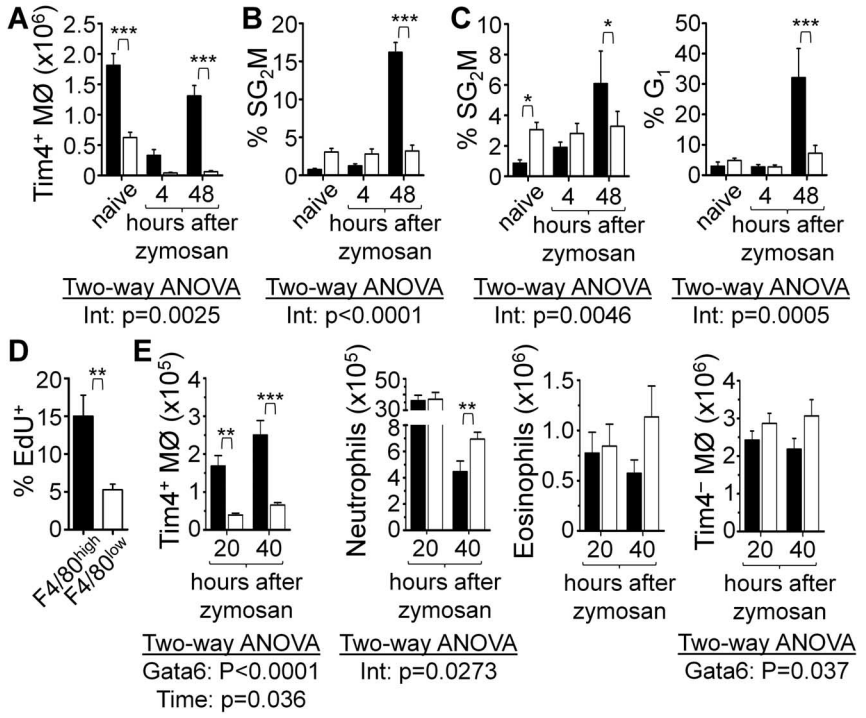

Fig. 4. Impaired proliferative recovery of peritoneal macrophages during inflammation in the absence of Gata6. (**A** and **B**) Quantification of the numbers (A) and proliferation (B) of Tim4^{+} macrophages at the indicated times after intraperitoneal zymosan injection (2×10^6 particles). Data were pooled from two independent experiments with Gata6-WT (black bars) and Gata6-KO^{mye} (white bars) mice (n = 5 to 11 per group). (**C**) Comparison of the SG_2M and G_1 stages of the cell cycle in the Gata6-KO (Tim4^{+}F4/80^{low}, white bars) and WT (Tim4^{+}F4/80^{high}, black bars) macrophages within the Gata6-KO^{mye} mice from (A) and (B). (**D**) Verification of the proliferative alterations shown in (C) by in vivo incorporation of 5-ethynyl-2'-deoxyuridine (EdU) (n = 8 mice, pooled from two independent experiments). (**E**) Analysis of inflammatory parameters in the resolution phase of a higher-dose zymosan (2×10^7 particles) peritonitis model comparing cell counts from WT (black bars) and Gata6-KO^{mye} (white bars) mice [data pooled from three independent experiments (n = 11 to 13 per group)]. All data in this figure represent mean ± SEM of individual mice and were examined by ANOVA (as indicated) with pairing as appropriate and Bonferroni post tests, except (D), which was analyzed by paired t test. *P < 0.05, **P < 0.01, ***P < 0.001.

as compared to macrophages in WT mice (Fig. 3, A and B). As with WT cells (*8*), the proliferation of Gata6-deficient peritoneal macrophages in vivo is dependent on the cytokine macrophage colony-stimulating factor (M-CSF). We observed marked polyploidy in Gata6-deficient cells (Fig. 3, A and C, and fig. S8). Polyploid Gata6-deficient cells were multinucleate, and this could reflect failed cytokinesis (*18*) or the creation of a fusogenic phenotype by the marked alteration in membrane-associated molecules (an enrichment of Gene Ontology term GO:0005886, Benjamini $P = 0.000007$). We took advantage of the existence of F4/80^{high} peritoneal macrophages in the mice (Fig. 1A), which we confirmed had escaped Cre-mediated *Gata6* deletion and were phenotypically normal (fig. S9). Within the Gata6-KO^{mye} mice, we observed a significantly lower level of proliferation of F4/80^{high} WT cells as compared to F4/80^{low} KO macrophages (Fig. 3D), which was comparable to that observed in WT mice. Similar results were obtained by lentiviral-mediated Cre delivery into peritoneal macrophages of adult conditional-KO mice (Fig. 3E). These studies demonstrated a cell-intrinsic role for Gata6 in limiting basal proliferation. Although the mechanisms controlling this response are unclear, it is likely that Gata6 influences proliferation through both direct and indirect impacts on the cellular phenotype of peritoneal macrophages. Given the similarities between tissue-resident peritoneal and pleural macrophages, we examined *Gata6* expression and found it comparable at both sites (Fig. 3F). Similar to peritoneal macrophages, the pleural macrophages of Gata6-KO^{mye} mice were predominantly F4/80^{low} and exhibited a cell-intrinsic increase in proliferation and polyploidy when compared to the contemporary F4/80^{high} pleural macrophages from the same microenvironment (Fig. 3G and fig. S8D).

During acute inflammation, peritoneal macrophage numbers first decrease. This is followed by the M-CSF–dependent (*Il4ra*-independent) proliferation of surviving macrophages (*6*, *8*). We induced acute peritonitis with 2×10^6 zymosan particles and observed increases in the numbers of neutrophils and eosinophils in both WT and Gata6-KO^{mye} mice (fig. S10). The initial decrease in the number of Tim4$^+$ macrophages was seen in both genotypes; however, whereas the Tim4$^+$ macrophages were mostly restored to preinflammation levels in WT mice, this did not occur in the Gata6-KO^{mye} mice 48 hours after challenge (Fig. 4A). In contrast to the inflammation-enhanced proliferative response in WT mice, the proliferation of Gata6-KO^{mye} macrophages remained unaltered (Fig. 4B). Because alterations in inflammation or basal conditions between WT and Gata6-KO^{mye} mice could affect the proliferative recovery of the tissue macrophages, we compared the proliferative state of the Tim4$^+$F4/80^{high} WT macrophages to that of the Tim4$^+$F4/80^{low} KO cells within the same Gata6-KO^{mye} mice (Fig. 4, C and D). Unlike the KO macrophages, the F4/80^{high} WT cells in the same environment responded to inflammation with elevated proliferation, confirming that the role of Gata6 was cell-intrinsic and not a consequence of secondary and/or environmental factors (Fig. 4, C and D). The mechanism underlying these phenotypic alterations is likely to be complex. A bioinformatic analysis indicated a high probability that multiple transcriptional networks were influenced by Gata6 deficiency (table S7). Thus, the altered phenotype imposed by the loss of Gata6 activity may arise from both direct Gata6 signaling and indirect responses mediated downstream of Gata6. Gata6 can therefore alter both cell proliferation and the phenotypic specialization of macrophages within the resident tissue. As validation of our approach, we selected *Map3k8*, which exhibits significantly altered expression in the absence of Gata6 (fig. S11, A and B). We anticipated that Map3k8 may be involved in the proliferation of peritoneal macrophages, because we had found that this process has an absolute requirement for M-CSF (*8*). Lentiviral short hairpin RNA–mediated *Map3k8* knockdown resulted in significantly reduced proliferation during inflammatory resolution (fig. S11, C to E). Alterations in macrophage phenotype and restoration could affect inflammatory resolution; for example, leading to delayed neutrophil clearance, so we initiated inflammation with a higher dose of zymosan (2×10^7 particles), where the initiation of inflammation is less macrophage-dependent (*3*, *19*–*21*) (Fig. 4E). Compared to WT animals, Gata6-KO^{mye} mice had substantially lower numbers of recoverable Tim4$^+$ macrophages, slightly increased levels of Tim4$^-$ macrophages, and increased neutrophil numbers during the resolution of inflammation (Fig. 4E).

Here we have identified Gata6 as a master controller of the peritoneal macrophage–specific phenotype. This phenotype is intrinsically linked to the regulation of proliferation. Our observations demonstrate transcriptional control of tissue-resident macrophage proliferative renewal and have implications for the study of tissue macrophages and tissue physiology in general. They indicate that not only do resident macrophages acquire a specialized phenotype adapted for a specific microenvironment, but that this is integral to the systems that preserve regulated self-renewal. Ex vivo, peritoneal macrophages alter their phenotype (*22*, *23*), including an apparent absence of proliferation (*24*). We also observed a down-regulation of Gata6 in ex vivo cultures, which in itself alludes to the presence of local *Gata6* induction within the tissue. Further afield, these observations dictate that to understand the master controllers and interaction of any resident macrophage population within its tissue, a full context-specific characterization of these cells will be required. It can be anticipated that many of the individual downstream pathways used by tissue-resident macrophages to interact with their environment may be common between different sites. The development of viable Gata6-deficient peritoneal macrophages provides an opportunity to dissect the functional interaction between tissue-resident macrophages and their tissue in a highly tractable system to aid in the identification of approaches to promote tissue homeostasis, the resolution of inflammation, and host defense.

References and Notes

1. L. C. Davies, S. J. Jenkins, J. E. Allen, P. R. Taylor, *Nat. Immunol.* **14**, 986–995 (2013).
2. V. Dioszeghy *et al.*, *J. Immunol.* **181**, 6514–6524 (2008).
3. M. Rosas, S. Gordon, P. R. Taylor, *Eur. J. Immunol.* **37**, 2518–2528 (2007).
4. M. Rosas, B. Thomas, M. Stacey, S. Gordon, P. R. Taylor, *J. Leukoc. Biol.* **88**, 169–180 (2010).
5. P. R. Taylor, G. D. Brown, A. B. Geldhof, L. Martinez-Pomares, S. Gordon, *Eur. J. Immunol.* **33**, 2090–2097 (2003).
6. L. C. Davies *et al.*, *Eur. J. Immunol.* **41**, 2155–2164 (2011).
7. S. Yona *et al.*, *Immunity* **38**, 79–91 (2013).
8. L. C. Davies *et al.*, *Nat Commun* **4**, 1886 (2013).
9. M. Koutsourakis, A. Langeveld, R. Patient, R. Beddington, F. Grosveld, *Development* **126**, 723 (1999).
10. A. C. Laverriere *et al.*, *J. Biol. Chem.* **269**, 23177–23184 (1994).
11. R. Zhao *et al.*, *Mol. Cell. Biol.* **25**, 2622–2631 (2005).
12. C. P. Sodhi, J. Li, S. A. Duncan, *BMC Dev. Biol.* **6**, 19 (2006).
13. B. E. Clausen, C. Burkhardt, W. Reith, R. Renkawitz, I. Förster, *Transgenic Res.* **8**, 265–277 (1999).
14. Information on materials and methods is available as supplementary material on *Science* Online.
15. M. Schmidt-Supprian, K. Rajewsky, *Nat. Immunol.* **8**, 665–668 (2007).
16. E. L. Gautier *et al.*, *Nat. Immunol.* **13**, 1118–1128 (2012).
17. D. Hashimoto *et al.*, *Immunity* **38**, 792–804 (2013).
18. C. D. Capo-chichi, K. Q. Cai, J. R. Testa, A. K. Godwin, X. X. Xu, *Mol. Cell. Biol.* **29**, 4766–4777 (2009).
19. J. U. McDonald, M. Rosas, G. D. Brown, S. A. Jones, P. R. Taylor, *PLOS ONE* **7**, e45781 (2012).
20. M. Rosas *et al.*, *J. Immunol.* **181**, 3549–3557 (2008).
21. S. C. Mullaly, P. Kubes, *Eur. J. Immunol.* **37**, 224–234 (2007).
22. J. C. Pfau *et al.*, *Am. J. Physiol. Lung Cell. Mol. Physiol.* **286**, L354–L362 (2004).
23. P. R. Taylor *et al.*, *J. Immunol.* **169**, 3876–3882 (2002).
24. S. Gordon, Z. Cohn, *J. Exp. Med.* **133**, 321–338 (1971).

Acknowledgments: We thank the staff of our animal facilities for the care of the animals. We also thank C. Pepper, J. Fisher, C. Watkins, and M. Musson for their help with cell purifications and Affymetrix analysis. P.R.T conceived and designed the project and wrote the manuscript; M.R., L.C.D, P.J.G, C.-T.L., B.K., T.C.S., and P.R.T designed and conducted the experiments; and all authors contributed to the analysis and interpretation of the data. The data presented in this manuscript are tabulated in the main paper and in the supplementary materials. Microarray data has been deposited in the Gene Expression Omnibus (accession nos. GSE28621 and GSE47049). P.R.T. is a Medical Research Council (MRC) UK Senior Non-Clinical Fellow (grant G0601617). This work was also supported by an MRC project grant (MR/J002151/1). V.O.D. is supported by a Wellcome Trust Programme Grant. L.C.D. is an MRC Doctoral Training Grant recipient, Cardiff University 125 for 125 scholar, and MRC Centenary Award holder. All animal work was conducted in accordance with institutional and UK Home Office guidelines. The authors declare no conflicts of interest.

Supplementary Materials

www.sciencemag.org/content/344/6184/645/suppl/DC1
Materials and Methods
Figs. S1 to S11
Tables S1 to S7
References (*25*–*37*)

28 January 2014; accepted 11 April 2014
Published online 24 April 2014;
10.1126/science.1251414

Restoring Systemic GDF11 Levels Reverses Age-Related Dysfunction in Mouse Skeletal Muscle

Manisha Sinha,[1,2,3,4]* Young C. Jang,[1,2,4]* Juhyun Oh,[1,2,4] Danika Khong,[1,2,4] Elizabeth Y. Wu,[1,2,4] Rohan Manohar,[1,2,4] Christine Miller,[1,2,4] Samuel G. Regalado,[1,5] Francesco S. Loffredo,[1,6] James R. Pancoast,[1,6] Michael F. Hirshman,[2] Jessica Lebowitz,[1,2,4] Jennifer L. Shadrach,[1,2,3] Massimiliano Cerletti,[1,2]† Mi-Jeong Kim,[2] Thomas Serwold,[2] Laurie J. Goodyear,[2,7] Bernard Rosner,[8] Richard T. Lee,[1,6] Amy J. Wagers[1,2,3,4]‡

Parabiosis experiments indicate that impaired regeneration in aged mice is reversible by exposure to a young circulation, suggesting that young blood contains humoral "rejuvenating" factors that can restore regenerative function. Here, we demonstrate that the circulating protein growth differentiation factor 11 (GDF11) is a rejuvenating factor for skeletal muscle. Supplementation of systemic GDF11 levels, which normally decline with age, by heterochronic parabiosis or systemic delivery of recombinant protein, reversed functional impairments and restored genomic integrity in aged muscle stem cells (satellite cells). Increased GDF11 levels in aged mice also improved muscle structural and functional features and increased strength and endurance exercise capacity. These data indicate that GDF11 systemically regulates muscle aging and may be therapeutically useful for reversing age-related skeletal muscle and stem cell dysfunction.

Skeletal muscle is a highly specialized tissue composed predominantly of contractile, multinucleated fibers whose regeneration after injury depends on the activity of a specialized subset of muscle fiber–associated mononuclear stem cells called satellite cells (*1*, *2*). Satellite cells can be isolated by fluorescence-activated cell sorting based on their unique surface marker profile ($CD45^-Sca\text{-}1^-CD11b^-CXCR4^+\beta1\text{-}integrin^+$), which effectively distinguishes them from non-myogenic cells and more differentiated myoblasts within the muscle (*3*, *4*).

Aged muscle exhibits decreased satellite cell number, impaired satellite cell function, and reduced regenerative potential (*2*, *5*–*9*). To evaluate satellite cell function in aged muscle on a per cell basis, we performed clonal myogenesis assays (*5*, *9*) and found that $CD45^-Sca\text{-}1^-CD11b^-CXCR4^+\beta1\text{-}Integrin^+$ satellite cells (fig. S1) from aged mice formed fewer colonies by up to a factor of 4 compared with young cells (fig. S2A) (*5*, *9*). To investigate the molecular basis of this reduced satellite cell activity in aged muscle, we examined DNA integrity in young and aged satellite cells using single-cell gel electrophoresis assays. Freshly sorted satellite cells showed a marked increase in DNA damage with age (fig. S2, B and C), with ~60% of aged cells exhibiting severely compromised DNA integrity (red bars, fig. S2B). Likewise, nearly 60% of satellite cells sorted from aged muscle (fig. S2, D and E) or identified by Pax7 staining on isolated muscle fibers (fig. S3) showed increased immunoreactivity for the phosphorylated form of histone H2AX (pH2AX), a marker of DNA damage (*10*). In contrast, 40% of freshly isolated young satellite cells were devoid of detectable DNA damage by gel electrophoresis assay (fig. S2, B and C), and young satellite cell nuclei rarely contained more than two pH2AX foci when assayed after cell sorting (fig. S2, D and E) or on single myofibers (fig. S3). Induction of DNA damage by x-irradiation reduced the myogenic function of young satellite cells in transplantation assays (fig. S4), which suggests

[1]Harvard Stem Cell Institute and Department of Stem Cell and Regenerative Biology, Harvard University, Cambridge, MA, USA. [2]Joslin Diabetes Center, Boston, MA 02215, USA. [3]Howard Hughes Medical Institute, Cambridge, MA, USA. [4]Paul F. Glenn Laboratories for the Biological Mechanisms of Aging, Harvard Medical School, Boston, MA, USA. [5]University of California, Berkeley, CA, USA. [6]Cardiovascular Division, Department of Medicine, Brigham and Women's Hospital and the Brigham Regenerative Medicine Center, Boston, MA, USA. [7]Department of Medicine, Brigham and Women's Hospital and Harvard Medical School, Boston, MA, USA. [8]Department of Biostatistics, Harvard School of Public Health, Boston, MA, USA.

*These authors contributed equally to this work.
†Present address: UCL Centre for Nanotechnology and Regenerative Medicine, Division of Surgery and Interventional Science, University College London, London NW3 2QG, UK.
‡Corresponding author. E-mail: amy_wagers@harvard.edu

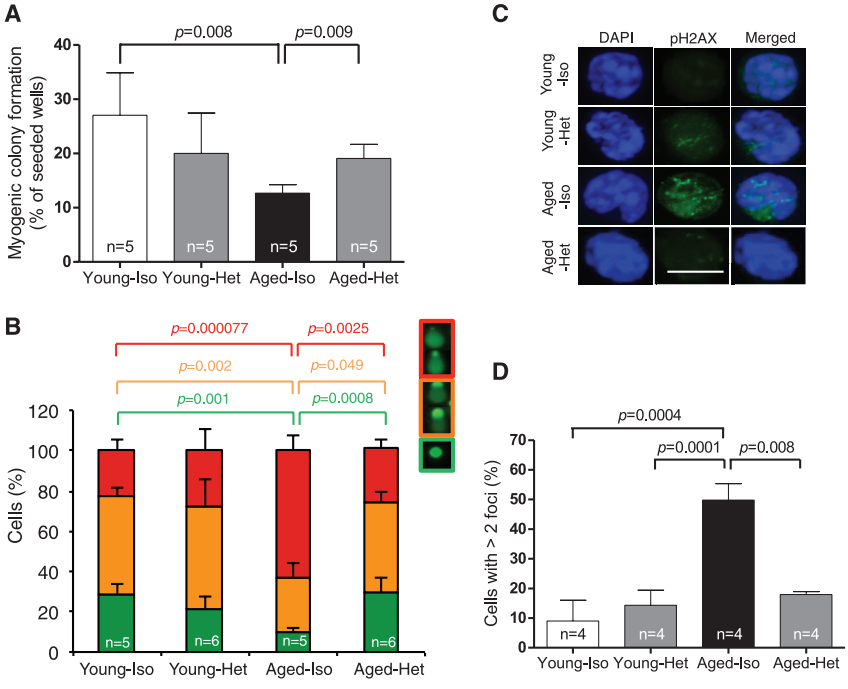

Fig. 1. Rejuvenation of muscle stem cells by heterochronic parabiosis. (**A**) Frequency of clone-sorted satellite cells from isochronic (Iso) or heterochronic (Het) mice forming colonies after 5 days in culture. All colonies showed characteristic morphology of muscle lineage cells. (**B**) DNA damage in freshly sorted satellite cells assessed by single-cell gel electrophoresis under alkaline conditions. Damage was quantified using a visual scoring metric (*25*) (key at top) and represented by color coding: no damage, green; moderate damage, orange; maximal damage, red. (**C**) Representative images (confocal *z* stacks) of freshly sorted satellite cells stained with 4′,6-diamidino-2-phenylindole (DAPI) (blue) and antibody to pH2AX (green). Data are quantified in (**D**). All graphs represent mean ± SD, with *P* values calculated by Mann-Whitney analysis. *n*, number of mice used for each analysis. Scale bar, 10 μm.

that increased DNA damage could cause impaired regeneration in aged muscle.

Previous studies demonstrate that impaired regeneration in aged muscle can be reversed by heterochronic parabiosis, which exposes aged tissues to a youthful systemic environment and restores injury-induced satellite cell activation by up-regulation of Notch signaling (*11*). To determine whether this intervention also restores the function and genomic integrity of aged satellite cells, we generated heterochronic parabionts (fig. S5), joining young C57BL/6 males (2 months of age) with aged partners (22 months of age), and compared these to isochronic (young-young or aged-aged) parabiotic controls. Strikingly, satellite cells sorted from aged mice joined to young partners (referred to hereafter as aged-heterochronic mice) showed improved myogenic colony-forming activity when compared with satellite cells from aged-isochronic controls (Fig. 1A). Satellite cells from aged-heterochronic mice also exhibited restored genomic integrity, with DNA damage scores that were indistinguishable from those of young-isochronic mice (Fig. 1B) and reduced numbers of pH2AX foci as compared with aged-isochronic mice (Fig. 1, C and D). Interestingly, this restoration of genomic integrity was not accompanied by detectable changes in satellite cell proliferation or proliferative history, as assessed by bromodeoxyuridine incorporation (fig. S6A).

Several growth factors and cytokines have been studied as potential regulators of muscle growth and repair, including transforming growth factor-β1 (TGF-β1), myostatin, and Wnt-like molecules (*7*, *11*). We recently reported a decline in aged mice in the systemic levels of growth differentiation factor 11 (GDF11), a member of the TGF-β superfamily with homology to myostatin (MSTN) (*12*). In contrast with GDF11, MSTN levels are unchanged and TGF-β1 increased in the plasma of aged mice (fig. S7, A and B, left panels). GDF11 levels decline in the muscle of aged mice as well (fig. S7C), whereas TGF-β1 and MSTN levels are unaltered (fig. S7, A and B, right panels).

Our previous studies showed that restoration of more youthful levels of systemic GDF11 could reverse age-related cardiac hypertrophy (*13*). To determine whether supplementation of GDF11 from the young partner might similarly underlie changes in skeletal muscle in heterochronic parabionts, we treated aged mice with daily intraperitoneal injections of recombinant GDF11 (rGDF11, 0.1 mg per kg of bodyweight) to increase systemic GDF11 levels. After 4 weeks, satellite cell frequency, determined by flow cytometry (Fig. 2A), and function (Fig. 2B) increased in the muscles of rGDF11-treated mice, whereas other myofiber-associated mononuclear cell populations were unaffected (fig. S8). Aged mice treated with rGDF11 also showed increased numbers of satellite cells with intact DNA (Fig. 2C), as compared with cells from aged mice receiving vehicle alone for the same length of time. Moreover, the percentage of freshly isolated satellite cells with severely damaged DNA was reduced by a factor of 4 upon treatment with rGDF11 (red bars, Fig. 2C). In contrast to results obtained in aged mice, young mice treated with an identical regimen of rGDF11 injections showed no changes in satellite cell frequency, myogenic colony formation, or DNA damage (Fig. 2, A to C).

We next evaluated the effect of rGDF11 supplementation on the in vivo regenerative activity of satellite cells by injuring a cohort of rGDF11-treated and control mice. Treatment was initiated 28 days before cryoinjury to the tibialis anterior muscle (TA) and continued for 7 days thereafter. Supplementation of rGDF11 in aged mice restored more youthful profiles of myofiber caliber in regenerating muscle (Fig. 2, D and E) and increased the mean size of regenerating myofibers in these animals to 92% of the size of regenerating fibers in young control mice (fig. S9A). However, rGDF11 supplementation for 5 weeks did not alter the myofiber caliber of uninjured young or aged muscles (fig. S9, B and C). rGDF11 supplementation in aged mice also enhanced the regenerative capacity of satellite cells

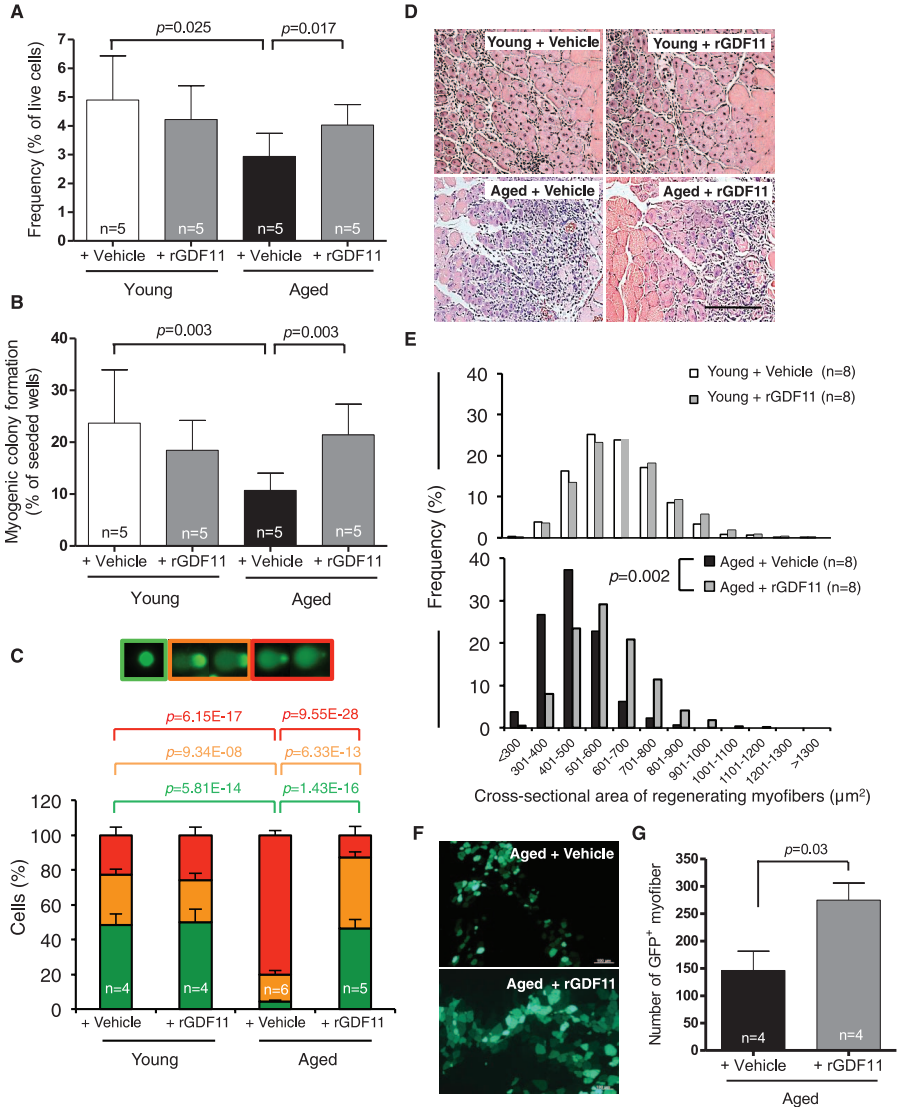

Fig. 2. Rejuvenation of muscle stem cells by rGDF11 supplementation. (**A** and **B**) Frequency (A) and myogenic colony formation (B) of satellite cells from vehicle- or rGDF11-treated mice. (**C**) Quantification of DNA damage assays using freshly sorted satellite cells from vehicle- or rGDF11-treated mice, scored as in Fig. 1B. (**D** and **E**) Hematoxylin and eosin staining (D) and frequency distribution of myofiber size (E) in regenerating TA muscles 7 days after cryoinjury in vehicle- or rGDF11-treated young and aged mice. Scale bar, 100 μm. (**F**) Representative images of transverse cryosections of TA muscles 2 weeks after transplantation. (**G**) Quantification of transplant data as maximal number of GFP^+ myofibers found in each engrafted muscle. Graphs represent mean ± SD [in (A) to (C) and (G)]. *P* values were calculated by Mann-Whitney analysis [(A) to (C)], Wilcoxon Exact analysis (E), or Student's *t* test (G). *n*, number of mice used for each analysis.

in a transplantation model, in which equal numbers of green fluorescent protein (GFP)–marked satellite cells were injected into the injured muscles of aged animals treated with rGDF11 or vehicle alone for 4 weeks before and 2 weeks after transplantation. Recipients treated with rGDF11 showed almost twice as many engrafted (GFP^+) fibers as vehicle-treated recipients (Fig. 2, F and G). Newly regenerated fibers in rGDF11-treated recipients were also larger in caliber (fig. S10), consistent with the effects of rGDF11 on the endogenous repair of muscle injury in aged mice (Fig. 2, D and E).

We next investigated the mechanistic basis for rGDF11's effects on aged muscle. Although we saw no alterations in gross anatomy, body weight, fat mass, or muscle mass (fig. S11), immunofluorescence analysis demonstrated increases in the size of neuromuscular junctions after rGDF11 treatment (fig. S12). In addition, electron microscopy of uninjured muscle revealed striking improvements of myofibrillar and mitochondrial morphology in aged mice treated with rGDF11 (Fig. 3A). Treated muscles showed reduction of atypical and swollen mitochondria, reduced accumulation of vacuoles, and restoration of regular sarcomeric and interfibrillar mitochondrial patterning (Fig. 3A). Consistent with these ultrastructural improvements, levels of peroxisome proliferator–activated receptor gamma coactivator 1α (PGC-1α), a master regulator of mitochondrial biogenesis, were increased in the muscle of aged rGDF11-treated mice (Fig. 3B), which suggests that GDF11 may affect mitochondrial dynamics of fission and fusion to generate new mitochondria. Consistent with this notion, in vitro treatment of differentiating cultures of aged satellite cells with rGDF11 yielded increased numbers of multinucleated myotubes exhibiting greater mitochondrial content and enhanced mitochondrial function (fig. S13). Finally, we observed increased basal levels of autophagosome (macroautophagy) markers (assessed as the ratio of autophagic intermediates LC3-II over LC3-I) in the uninjured skeletal muscle of rGDF11-treated aged animals (Fig. 3C). Collectively, these data suggest enhanced autophagy/mitophagy and mitochondrial biogenesis as likely explanations for the cellular remodeling of muscle fibers in rGDF11-treated aged mice.

We next questioned whether improvements in muscle ultrastructure and mitochondrial turnover in rGDF11-treated aged mice might translate into improved physical function in exercise endurance and grip-strength analyses. Aged mice treated with rGDF11 showed increased average exercise endurance (35 min versus 57 min), despite variation in the responses of individual animals (Fig. 3D). rGDF11-treated animals also exhibited improved clearance of systemic lactate (fig. S14A) and lower levels of glucose (fig. S14B) after 40 min of strenuous running, providing additional evidence indirectly supporting improved mitochondrial function in aged rGDF11-treated animals. Finally, in accord with r GDF11-stimulated remodeling of myofiber ultrastructure, rGDF11-treated animals exhibited increased average grip strength (Fig. 3E and fig. S15) in a standardized testing platform (*14*).

Our studies reported here establish GDF11 as a novel humoral regulator of youthful regenerative potential and demonstrate that restoration of aged satellite cell function by this factor is coincident with reversal of accumulated DNA damage. These data suggest that genome toxicity may constrain stem cell function in aged muscle, as reported previously for the hematopoietic system (*15*). However, accumulating evidence indicates that DNA strand breaks may arise in stem cells not only as a result of genomic insult but also as a conserved and necessary event for nuclear reprogramming to allow for cell differentiation (*16*). Transcriptome profiling of young and aged muscle stem cells indicates that some muscle differentiation genes are upregulated in aged satellite cells (*6*) (fig. S16), despite the fact that aged cells show compromised regenerative capacity (*7*–*9*, *11*) (Fig. 2). In addition, we failed to detect age-related alterations in expression of DNA damage recognition and repair enzymes by immunofluorescence analysis (fig. S17). These data raise the possibility that aged satellite cells display an apparent increase in DNA damage because they are arrested at an early stage of myogenesis, in which differentiation-associated DNA strand breaks have been induced but not resolved. Extending this logic, systemic "rejuvenation" by parabiosis or rGDF11 treatment may release these cells from this age-induced differentiation block. This notion is consistent with our data demonstrating (i) increased detection of DNA damage and an increase in activated cleaved-Caspase-3 in aged satellite cells (figs. S2 and S18) (*16*), (ii) the resolution of these changes upon restoration of myogenic activity in "rejuvenated" muscle (Figs. 1 and 2), and (iii) the ability of in vitro treatment with rGDF11 to increase myogenic cell number and promote myotube formation in cultures of aged satellite cells (figs. S19 and S13A). Given that rGDF11-stimulated rejuvenation of aged satellite cells coincides with remodeling of the aged satellite cell niche (Figs. 2 and 3 and fig. S10), we speculate that supple-

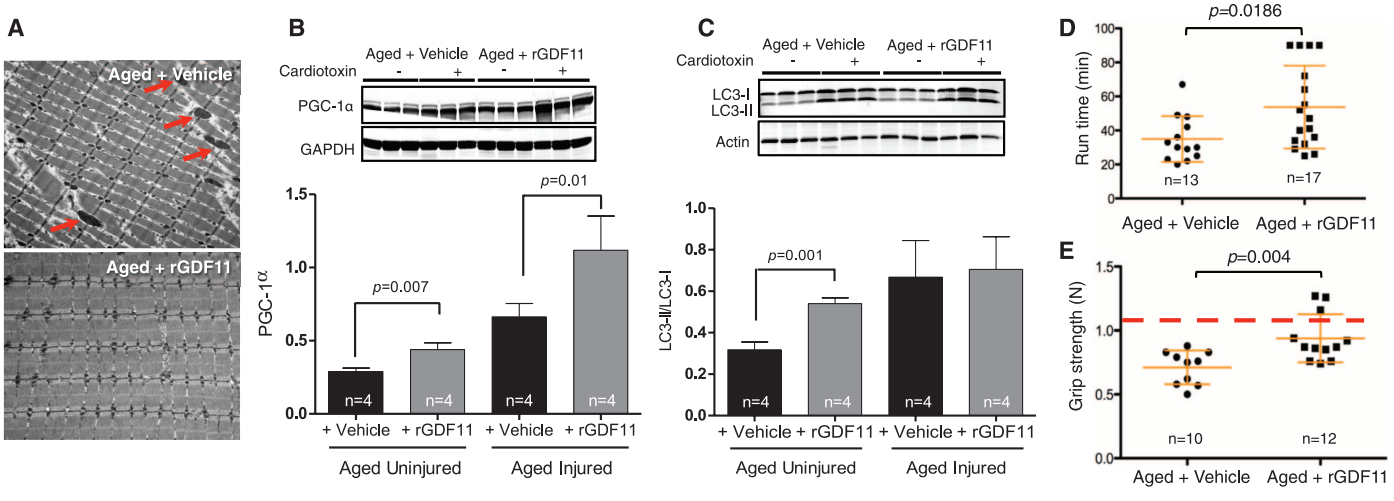

Fig. 3. Improved muscle physiology and physical function after rGDF11 supplementation. (**A**) Electron micrographs of transverse sections of TA muscle from vehicle- or rGDF11-treated aged mice (representative of $n = 4$ mice per group). Arrows indicate swollen mitochondria. (**B** and **C**) Western blot of PGC-1α (B) and LC3 forms I and II (C) in TA muscle extracts from cardiotoxin-injured or uninjured vehicle- or rGDF11-treated aged mice. Three animals are shown for each experimental group. Densitometric quantification of Western data are provided below each blot, normalized to glyceraldehyde phosphate dehydrogenase (GAPDH) (B) or Actin (C). (**D** and **E**) Scatter plots of exercise endurance [(D), maximum treadmill runtime in a 90-min window] or forelimb grip strength (E) of vehicle- or rGDF11-treated aged mice. Grip strength is plotted as maximum force (Newton, N) exerted in triplicate trials. The red line represents the maximum grip strength of 33- to 39-week-old young male mice. Data are presented for individual mice (black symbols) overlaid with mean ± SD (orange lines). *P* values were calculated by Mann-Whitney analysis. *n*, number of mice used for each analysis.

mentation of GDF11 levels in aged mice may act both directly and indirectly to restore satellite cell regenerative function, stimulating intrinsic changes in satellite cell differentiation capacity (fig. S13A) and producing a more "promyogenic" niche that extrinsically supports endogenous regeneration and transplant-associated myogenic engraftment (Figs. 2 and 3).

GDF11 belongs to a conserved family of growth factors that regulate diverse cellular processes (*17*). Genetic deficiency of GDF11 in mice causes profound developmental abnormalities, including agenesis of the kidneys, and perinatal lethality (*12*, *18*, *19*). The mature form of GDF11 shares ~90% sequence identity with MSTN, known for its potent negative influence on skeletal muscle mass (*12*), and binds the same receptors (ACVR1B/ALK4, ACVR1A/ALK5, and ACVR1C/ALK7) (*20*). A previous study reported relatively low levels of ALK4/5 expression by postnatal day 12 satellite cells and failed to detect a difference in proliferation of these cells upon exposure to MSTN (*21*). We found that in vitro exposure of aged satellite cells to rGDF11, but not recombinant MSTN or TGF-β1, produced dose-responsive increases in cell proliferation (fig. S19) and differentiation (fig. S13A), suggesting that GDF11, in contrast to MSTN, can act directly on satellite cells to alter their function. Interestingly, growth promotion may be the primordial role of MSTN/GDF11, because invertebrates possess only a single ortholog of the MSTN/GDF11 family, and down-regulation of this gene results in retarded growth (*22*). In any event, the unique combination of rGDF11's promyogenic effects in skeletal muscle, antihypertrophic effects in the heart (*13*), and beneficial effects on neurogenesis and neuronal function (*23*) in aged mice should encourage further investigation of its therapeutic potential for a variety of age-related diseases and suggests that GDF11 should be regarded as a new molecular regulator of mammalian aging with potentially broad-reaching applications.

References and Notes

1. A. Mauro, *J. Biophys. Biochem. Cytol.* **9**, 493–495 (1961).
2. Y. C. Jang, M. Sinha, M. Cerletti, C. Dall'Osso, A. J. Wagers, *Cold Spring Harb. Symp. Quant. Biol.* **76**, 101–111 (2011).
3. R. I. Sherwood *et al.*, *Cell* **119**, 543–554 (2004).
4. M. Cerletti *et al.*, *Cell* **134**, 37–47 (2008).
5. M. Cerletti, Y. C. Jang, L. W. Finley, M. C. Haigis, A. J. Wagers, *Cell Stem Cell* **10**, 515–519 (2012).
6. J. V. Chakkalakal, K. M. Jones, M. A. Basson, A. S. Brack, *Nature* **490**, 355–360 (2012).
7. A. S. Brack *et al.*, *Science* **317**, 807–810 (2007).
8. G. Shefer, G. Rauner, Z. Yablonka-Reuveni, D. Benayahu, *PLOS ONE* **5**, e13307 (2010).
9. B. D. Cosgrove *et al.*, *Nat. Med.* **20**, 255–264 (2014).
10. L. J. Mah, A. El-Osta, T. C. Karagiannis, *Leukemia* **24**, 679–686 (2010).
11. I. M. Conboy *et al.*, *Nature* **433**, 760–764 (2005).
12. A. C. McPherron, T. V. Huynh, S. J. Lee, *BMC Dev. Biol.* **9**, 24 (2009).
13. F. S. Loffredo *et al.*, *Cell* **153**, 828–839 (2013).
14. C. H. Hakim, D. Li, D. Duan, *Methods Mol. Biol.* **709**, 75–89 (2011).
15. D. J. Rossi *et al.*, *Nature* **447**, 725–729 (2007).
16. B. D. Larsen *et al.*, *Proc. Natl. Acad. Sci. U.S.A.* **107**, 4230–4235 (2010).
17. J. Nickel, W. Sebald, J. C. Groppe, T. D. Mueller, *Cytokine Growth Factor Rev.* **20**, 367–377 (2009).
18. A. C. McPherron, A. M. Lawler, S. J. Lee, *Nat. Genet.* **22**, 260–264 (1999).
19. Y. J. Lee *et al.*, *Dev. Biol.* **347**, 195–203 (2010).
20. J. Kim *et al.*, *Science* **308**, 1927–1930 (2005).
21. H. Amthor *et al.*, *Proc. Natl. Acad. Sci. U.S.A.* **106**, 7479–7484 (2009).
22. C. De Santis *et al.*, *J. Exp. Biol.* **214**, 2671–2677 (2011).
23. L. Katsimpardi *et al.*, *Science* **344**, 630–634 (2014).

Acknowledgments: We thank the Harvard Stem Cell Institute/Department of Stem Cell and Regenerative Biology's Flow Cytometry Core, Harvard's Center for Biological Imaging, and C. Dall'Osso and B. Hunter for technical assistance. This work was funded in part by grants from the American Heart Association to F.S.L. (postdoctoral fellowship); NIH (R01 AR42238) to L.J.G.; Glenn Foundation for Medical Research, Harvard Stem Cell Institute, and NIH (1R01 AG033053, 1DP2 OD004345, and 5U01 HL100402) to A.J.W.; NIH (R01 AG032977 1R01 AG040019) to R.T.L.; and Project Ascelegen to A.J.W. and R.T.L. A.J.W. is an Early Career Scientist of the Howard Hughes Medical Institute. M.F.H. owns shares in Abbott Laboratories, Amgen Inc., Colgate Palmolive Co., Eli Lilly and Co., Medtronic Inc., and Abbvie Inc. A.J.W. and R.T.L. are inventors on patent applications filed by Harvard University and Brigham and Women's Hospital entitled 'Methods and Compositions for Rejuvenating Skeletal Muscle Stem Cells' and 'Methods and Compositions for Rejuvenating Neuromuscular Junctions.'

Supplementary Materials

www.sciencemag.org/content/344/6184/649/suppl/DC1
Materials and Methods
Figs. S1 to S19
References (*24*, *25*)

22 January 2014; accepted 4 April 2014
10.1126/science.1251152

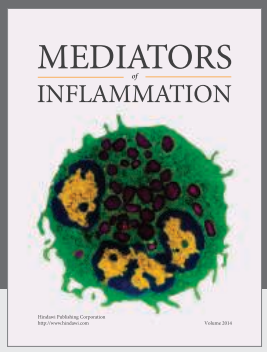

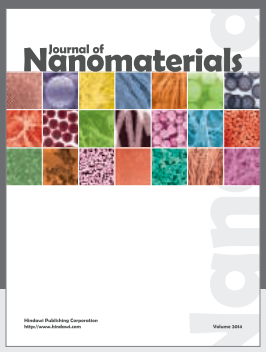

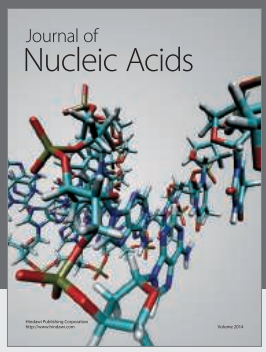

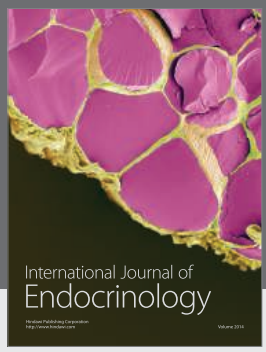

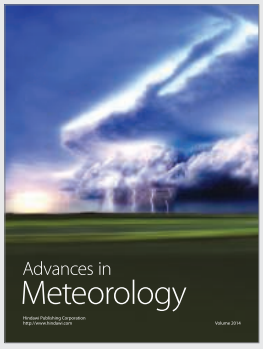

Hindawi

Submit your manuscripts at
http://www.hindawi.com

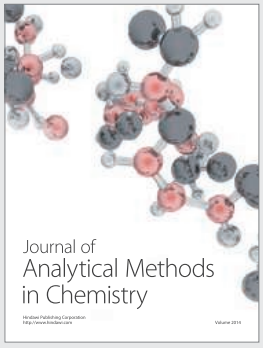

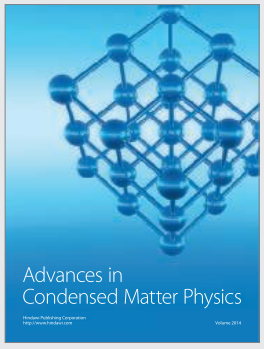

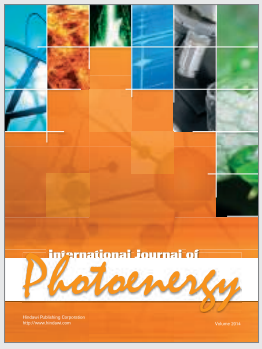

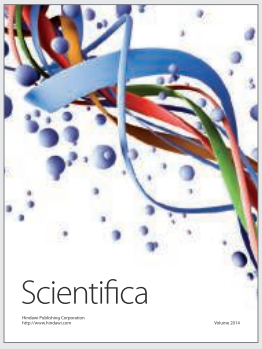

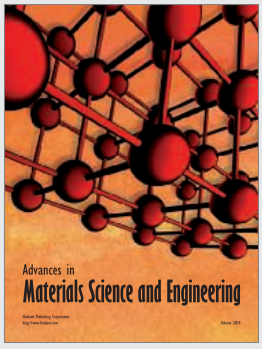

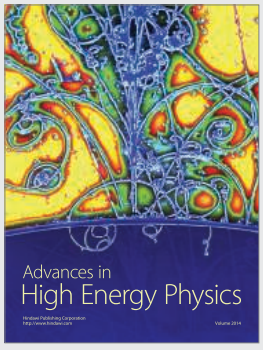

BD Horizon Brilliant™ Ultraviolet and the BD LSRFortessa™ X-20

Ultraviolet laser and reagents expand research capabilities and clarify results.

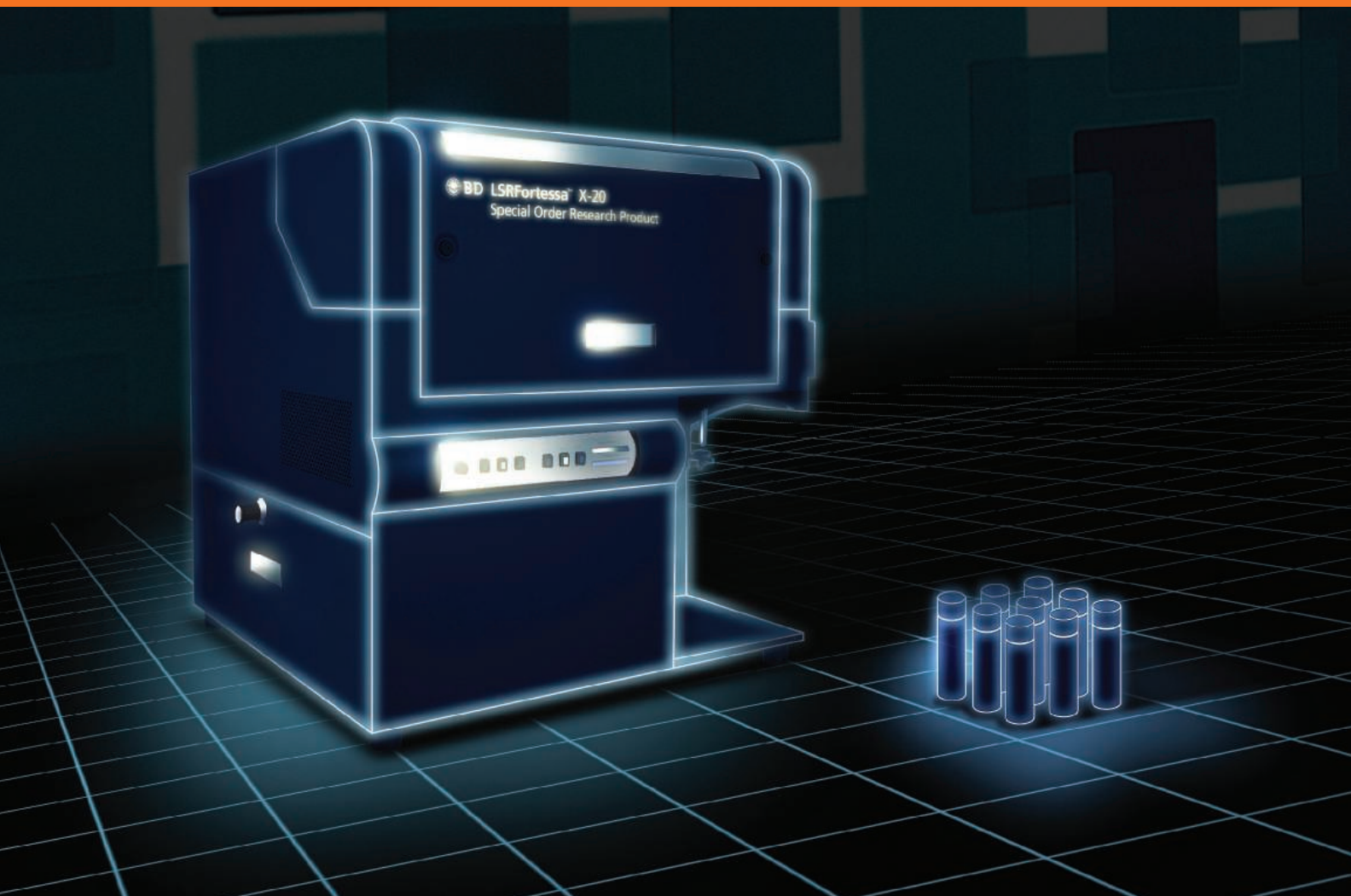

A whole new spectrum of choice.

BD Horizon Brilliant Ultraviolet reagents open a new world of choice and productivity for scientists who use multicolor flow cytometry in their research. By adding the ultraviolet range to panel design, markers can be spread over more lasers, reducing compensation requirements of the experiment.

Use of these new ultraviolet excitable dyes can reduce setup time because there is less need to adjust for compensation.

When the dyes are combined with a dedicated ultraviolet laser position, your options and capabilities are further expanded.

Find out how you can add a whole new spectrum of productivity to your research with BD Horizon Brilliant Ultraviolet dyes and the ultraviolet capable BD LSRFortessa X-20 special order analyzer. Tools and information available at **bdbiosciences.com/go/ultra.**

BD

Helping all people live healthy lives

For Research Use Only. Not for use in diagnostic or therapeutic procedures.
BD, BD Logo and all other trademarks are the property of Becton, Dickinson and Company. © 2014 BD
23-15993-01

BD Biosciences
2350 Qume Drive
San Jose, CA 95131
bdbiosciences.com

NEW ENGLAND BioLabs® Inc.
enabling technologies in the life sciences

Make ends meet.

Gibson Assembly® Cloning Kit

New England Biolabs has revolutionized your laboratory's standard cloning methodology. The Gibson Assembly Cloning Kit combines the power of the Gibson Assembly Master Mix with NEB 5-alpha Competent *E. coli*, enabling fragment assembly and transformation in just under two hours. Save time, without sacrificing efficiency.

Making ends meet is now quicker and easier than ever before, with the Gibson Assembly Cloning Kit from NEB.

NEBuilder™ for Gibson Assembly

Visit **NEBGibson.com** to view the latest tutorials and to try our primer design tool.

Gibson Assembly Cloning Kit provides robust transformation efficiencies

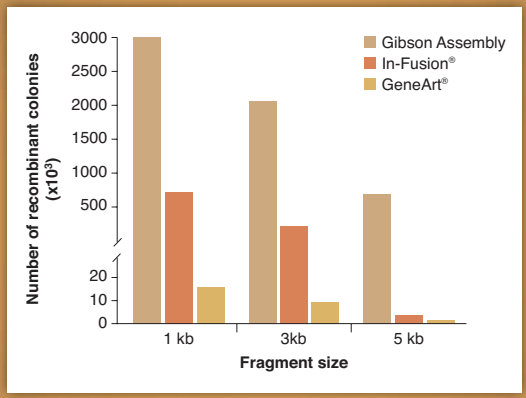

Assembly reactions containing 25 ng of linear pUC19 vector and 0.04 pmol of each fragment were performed following individual suppliers' recommended protocols and using the competent cells provided with the kit. The total number of recombinant colonies was calculated per 25 ng of linear pUC19 vector added to the assembly reaction.

IN-FUSION® is a registered trademark of Clontech Laboratories, Inc.
GENEART® is a registered trademark of Life Technologies, Inc.
GIBSON ASSEMBLY® is a registered trademark of Synthetic Genomics, Inc.

SGIDNA

Some components of this product are manufactured by New England Biolabs, Inc. under license from Synthetic Genomics, Inc.

Science Signaling

The Leading Journal for Cell Signaling

Publishing key findings of broad relevance in the multidisciplinary field of cell signaling

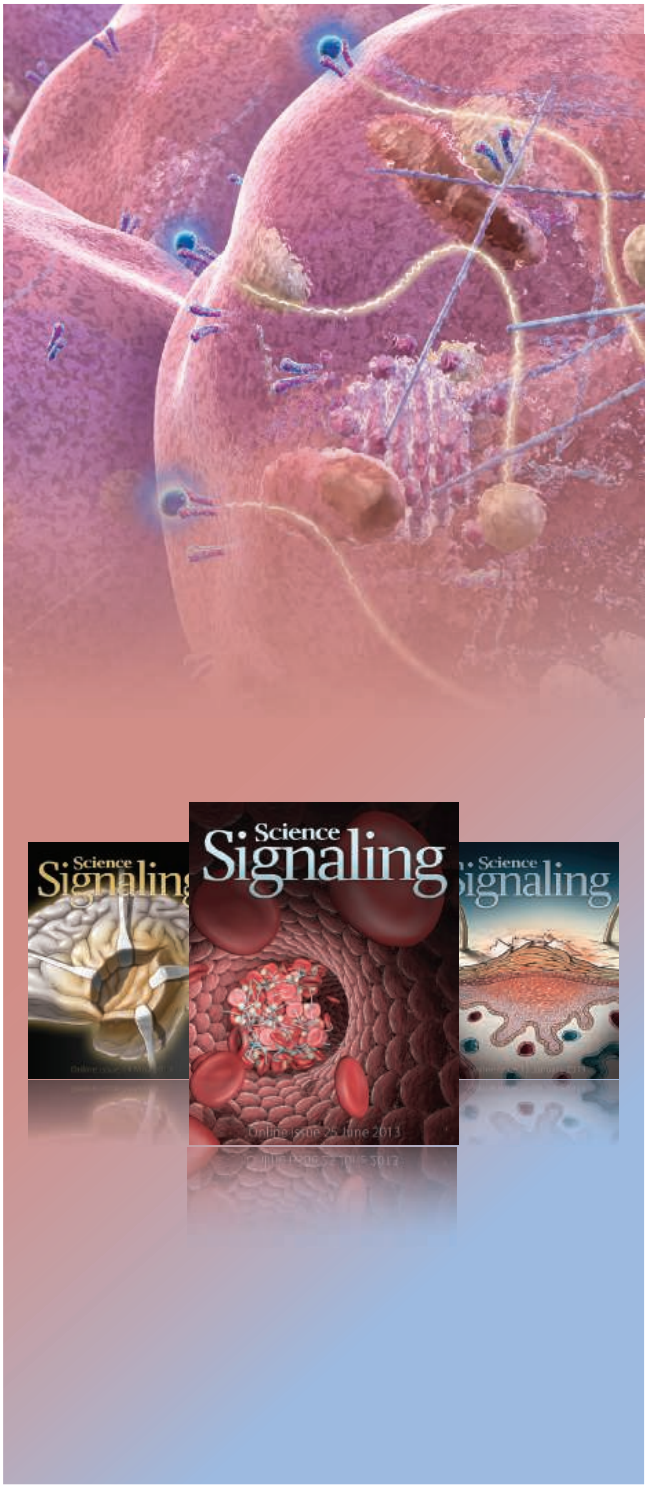

Submit your research

ScienceSignaling.org

Recommend to your library

ScienceOnline.org/recommend

Join the ranks of high-profile papers published in *Science Signaling*:

Cancer Biology
Vemurafenib Potently Induces Endoplasmic Reticulum Stress–Mediated Apoptosis in BRAFV600E Melanoma Cells
D. Beck *et al.* (F. Meier), *Sci. Signal.* **6**, ra7 (2013)

Neuroscience
Requirement for Nuclear Calcium Signaling in *Drosophila* Long-Term Memory
J.-M. Weislogel *et al.* (H. Bading), *Sci. Signal.* **6**, ra33 (2013)

Cell and Molecular Biology
A Nontranscriptional Role for HIF-1α as a Direct Inhibitor of DNA Replication
M. E. Hubbi *et al.* (G. L. Semenza), *Sci. Signal.* **6**, ra10 (2013)

Immunology
Monovalent and Multivalent Ligation of the B Cell Receptor Exhibit Differential Dependence upon Syk and Src Family Kinases
S. Mukherjee *et al.* (A. Weiss), *Sci. Signal.* **6**, ra1 (2013)

Computational and Systems Biology
Cross-Species Protein Interactome Mapping Reveals Species-Specific Wiring of Stress Response Pathways
J. Das *et al.* (H. Yu), *Sci. Signal.* **6**, ra38 (2013)

Chief Scientific Editor
Michael B. Yaffe, M.D., Ph.D.
Massachusetts Institute of Technology

Editor
Nancy R. Gough, Ph.D.
AAAS, Washington, DC

Science Signaling
AAAS

sciencesignalingeditors@aaas.org

WEBINAR

The Many Roads to Cell Death:

Gaining a Practical Understanding of Apoptosis, Necrosis, and Autophagy

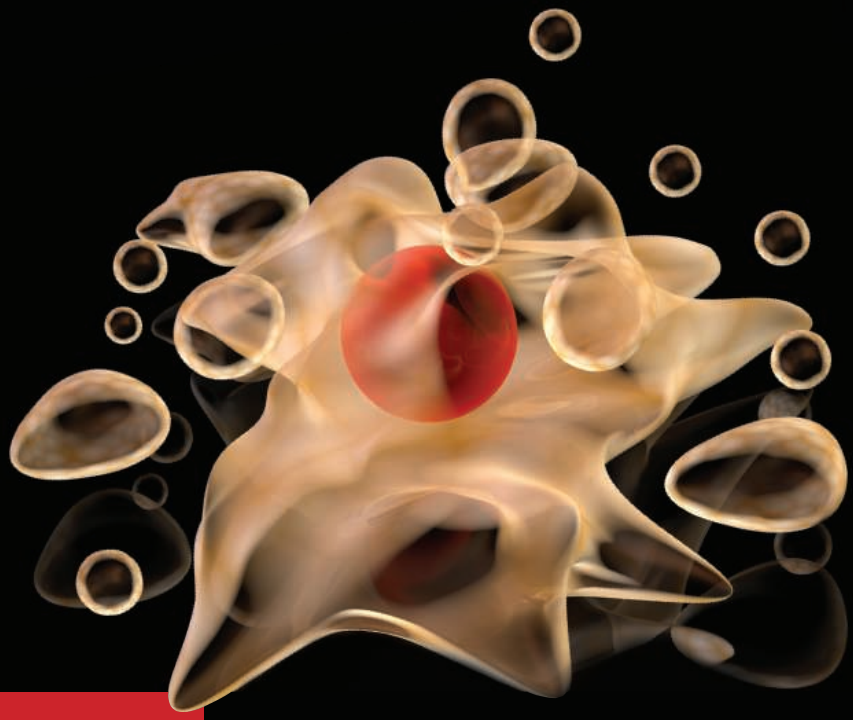

Wednesday, June 4, 2014

12 noon Eastern, 9 a.m. Pacific, 5 p.m. UK, 6 p.m. CEST

Cell death is, ironically, an essential part of life. In recent years, the study and understanding of cell death pathways has been dramatically transformed by the insights gained into non-apoptotic pathways, including necro-apoptosis and autophagy, together with a deeper understanding of the mechanism of the apoptotic cascade. New discoveries have been enabled by cutting-edge technologies, particularly in the realm of cytometry and cell-death–specific markers. In this webinar, the latest insights into cell death pathways will be discussed, including the molecular markers and cellular changes that characterize each pathway. Viewers will also learn practical cytometry-based strategies for dissecting cell death pathways, and how to use the data to better understand the pathophysiology of diseases such as cancer as well as to uncover new targets for drug discovery and development.

During the webinar, the speakers will:

- Review the latest insights into the different cell death pathways
- Present their own recent data and research on cell death mechanisms and impacts
- Describe techniques to detect and dissect cell death pathways
- Answer your questions live and in real time!

Speakers

John Abrams, Ph.D.
University of Texas
Southwestern Medical Center
Dallas, TX

William G. Telford, Ph.D.
National Institutes of Health
Bethesda, MD

REGISTER NOW!
webinar.sciencemag.org

Sponsored by

EMD MILLIPORE

@SciMagWebinars

Brought to you by the *Science*/AAAS Custom Publishing Office

Science
AAAS

Science Translational Medicine

Integrating Science, Engineering, and Medicine

Publishing results that harness the basic sciences to advance human health in all areas of medicine

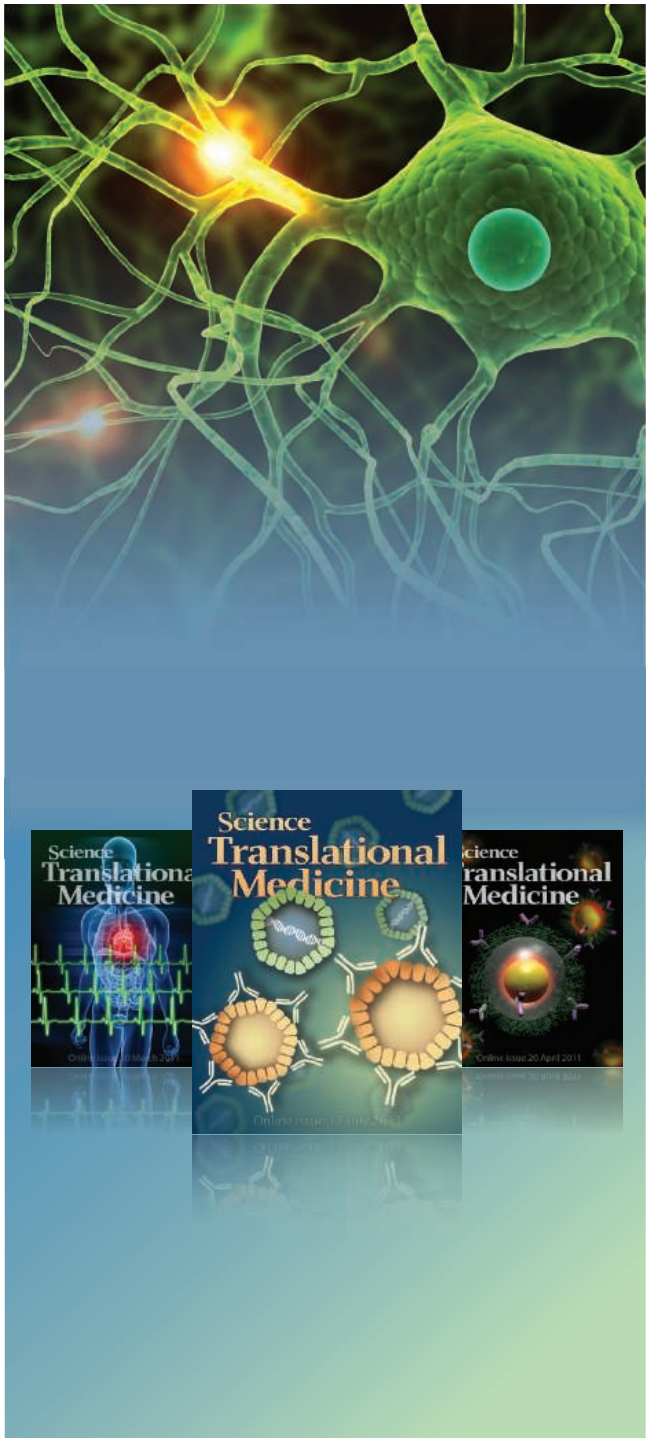

Submit your research

ScienceTranslationalMedicine.org

Recommend to your library

ScienceOnline.org/recommend

Join the ranks of high-profile papers published in *Science Translational Medicine*:

Neurology

A Theoretically Based Index of Consciousness Independent of Sensory Processing and Behavior

A. G. Casali *et al.* (M. Massimini), *Sci. Transl. Med.* **5** 198ra105 (2013)

Immunology

TGFβ Receptor Mutations Impose a Strong Predisposition for Human Allergic Disease

P.A. Frischmeyer-Guerrerio *et al.* (H. Dietz), *Sci. Transl. Med.* **5** 195ra94 (2013)

Bioengineering

A Human Disease Model of Drug Toxicity-Induced Pulmonary Edema in a Lung-on-a-Chip Microdevice

D. Huh *et al.* (D. Ingber), *Sci. Transl. Med.* **5** 159ra147 (2012)

Cancer

Genome-Wide Mutational Signatures of Aristolochic Acid and its Application as a Screening Tool

S.L. Poon *et al.* (B. T. Teh), *Sci. Transl. Med.* **5** 197ra101 (2013)

Tissue Engineering

Human Cartilage Repair with a Photoreactive Adhesive-Hydrogel Composite

B. Sharma *et al.* (J.J. Elisseeff), *Sci. Transl. Med.* **5** 167 ra6 (2013)

Chief Scientific Advisors

Elazer Edelman, M.D., Ph.D.
Massachusetts Institute of Technology

Garret FitzGerald, M.D.
University of Pennsylvania

Editor

Katrina L. Kelner, Ph.D.
AAAS, Washington, DC

Science Translational Medicine AAAS

scitranslmededitors@aaas.org

BARCODE READER

The Tracxer Code Reader RD235 CRYO offers a high-end solution for scanning whole racks with 2-D Data-Matrix or TraXis coded tubes. Featuring a CCD image sensor the new reader provides unmatched high-resolution image quality, ensuring the highest accuracy 2-D code reading. The Tracxer Code Reader RD235 CRYO features an anti-frost system which minimizes condensation on the scanner plate. This way, tube codes from even frozen samples can be read, thereby improving productivity and preserving the integrity of your samples. Just a couple of mouse clicks using the highly intuitive Tracxer Code Reader software allows you to scan a complete rack of 2-D coded tubes in seven seconds and a single tube in less than two seconds. Using the Tracxer Code Reader RD235 CRYO in conjunction with a Tracxer 1D Rack Barcode Reader BC235 accessory the software allows you to read the 1-D rack barcodes and 2-D tube codes together.

Micronic

For info: +31-320-277070 | www.micronic.com

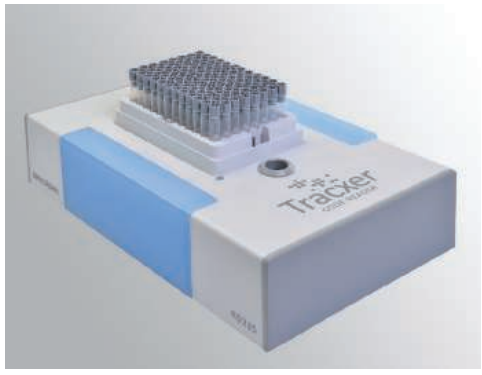

3-D SUPERRESOLUTION MICROSCOPY

With a new module, ELYRA P.1 now enables superresolution photoactivated localization microscopy (PALM) in 3-D for endogenously expressed photo-switchable fluorescent proteins. Users can capture highly resolved structures in 3-D, while treating the sample so gently it stays fit for long-term observation. In PALM, photo-switchable fluorescent molecules are sparsely activated so that only one out of many will be in its on-state within a single point spread function (PSF). In 3-D, the PSF shape codes for the *z*-position. The localizations are plotted in a new image to create the superresolved image. ELYRA P.1 achieves resolutions in the range of 20–30 nm laterally and 50–80 nm axially. With ELYRA, researchers can investigate the structural arrangement of one or multiple proteins and reveal the ultrastructure of cell organelles in 2-D and 3-D as well as map and count molecules within a structure. Sophisticated algorithms relate photon statistics to precision information in all directions, so researchers can display their structures fully rendered in 3-D.

Carl Zeiss

For info: +49-36-4164-3949 | www.zeiss.de

CELL CULTURE MEDIUM

Live-cell fluorescence microscopy is an essential technique for the visualization of fundamentally important and physiologically relevant biological events. A key challenge with this technique is the ability to image weak fluorophors without causing cell damage, photobleaching, or undesirable changes to cell health. Gibco has addressed this problem by developing FluoroBrite DMEM, a media formulation with background fluorescence that is comparable to PBS and 90% lower than that emitted by standard phenol red-free DMEM. The medium is formulated to include the required nutrients for routine cell culture when supplemented with 10% fetal bovine serum and 4 mM L-glutamine or GlutaMAX. FluoroBrite DMEM is designed to enhance the signal-to-noise ratio of fluorophors so that researchers can visualize even the weakest fluorescent events in an environment that promotes optimum cell health.

Life Technologies

For info: 800-955-6288 | www.lifetechnologies.com/fluorobrite

AUTOMATED PERFUSION SYSTEM

The Dynaflow Resolve automated perfusion system uses microfluidics for rapid and efficient solution exchange experiments, enabling the measurement of ion channel current regardless of cell type or compound. The new Temperature Control add-on module has been specifically developed to enable high-performance patch clamp experiments at physiological temperatures, from room temperature up to 45°C. Temperature control during ion channel research is particularly important when investigating ion channel kinetics and toxicity screening applications, and now Cellectricon's Dynaflow Resolve Temperature Control ensures patch clamp experiments can be performed with unsurpassed speed, control, and flexibility at these elevated temperatures for true physiological insight. Developed in response to customer demand, the Dynaflow Resolve Temperature Control guarantees precise, definable temperature control, and complete stability, even for hour-long experiments. Without any risk of temperature fluctuations following solution switch, scientists can be assured of reliable, reproducible results in constant physiological conditions.

Cellectricon

For info: +46-(0)-31-760-35-00 | www.cellectricon.com

SEROLOGICAL PIPETTOR

The new PIPETBOY acu 2 serological pipettor is equipped with the latest technology providing a significant increase in pipetting speed and a sizeable weight reduction, making use of the instrument over extended periods of time even more comfortable. These two new developments help improve your productivity and deliver an enhanced ergonomic pipetting experience. The PIPETBOY acu 2 serological pipettor combines all essential characteristics for productive work with pipettes: precision, speed, ease-of-use, comfort, long operating battery life, and reliability. PIPETBOY acu 2 is designed for use with all commercially available glass and plastic serological pipettes in the volume range 1–100 mL. Pipetting using PIPETBOY acu 2 is controlled by two operating buttons and an adjustment wheel for setting the pipetting speed. Precise drop-by-drop dispensing is easily achieved by applying a slight pressure on the operating button. PIPETBOY acu 2 is available in a range of six attractive colors.

Integra Biosciences

For info: + 41-(0)-81-286-95-30 | www.integra-biosciences.com

Electronically submit your new product description or product literature information! Go to **www.sciencemag.org/products/newproducts.dtl** for more information. Newly offered instrumentation, apparatus, and laboratory materials of interest to researchers in all disciplines in academic, industrial, and governmental organizations are featured in this space. Emphasis is given to purpose, chief characteristics, and availability of products and materials. Endorsement by *Science* or AAAS of any products or materials mentioned is not implied. Additional information may be obtained from the manufacturer or supplier.

Bat man wins young scientist prize in Stockholm. Are you next?

Science & SciLifeLab PRIZE FOR YOUNG SCIENTISTS

Photo: Nancy Evelyn - UGA

The 2014 *Science* and SciLifeLab Prize is now open and we are looking for new bright ideas. Are you like Daniel Streicker? Are you a recent PhD graduate eager to win a prize? Daniel is a true "bat man" having spent many hours in dark caves studying bats, to better understand how infectious diseases emerge and establish in new host species. It is for this work that Daniel was published in the journal *Science*, December 6, 2013, as the Grand Prize winner of the 2013 *Science* & SciLifeLab Prize for Young Scientists.

The journal *Science* and SciLifeLab have come together to recognize and celebrate excellence in PhD Research. The *Science* & SciLifeLab Prize has been established to support young scientists at the start of their career.

The four categories for the 2014 prize are: Cell and Developmental Biology; Genomics and Proteomics; Environment; and Translational Medicine. The Grand Prize winner will receive 25,000USD and the other three Category Prize winners will receive 3,000USD each. The Grand Prize winning essay will be published in *Science* and the Category Prize winners will be published in *Science* online.

The deadline for submissions is August 1, 2014.
For further details and to enter, please visit: www.sciencemag.org/scilifelabprize

For over 130 years the journal Science has been the world's leading journal of original scientific research, global news and commentary.

SciLifeLab is a collaboration among four universities in Stockholm and Uppsala, Sweden, and is a national center for molecular biosciences with focus on health and environmental research.

This prize is made possible with the kind support of the Knut and Alice Wallenberg Foundation.

Science AAAS

SciLifeLab

Knut och Alice Wallenbergs Stiftelse

Get to the Bottom of Your Signal Transduction Research Faster.

Run one ELISA instead of multiple Western blots.
Optimize your experimental parameters with
ELISAs from R&D Systems.

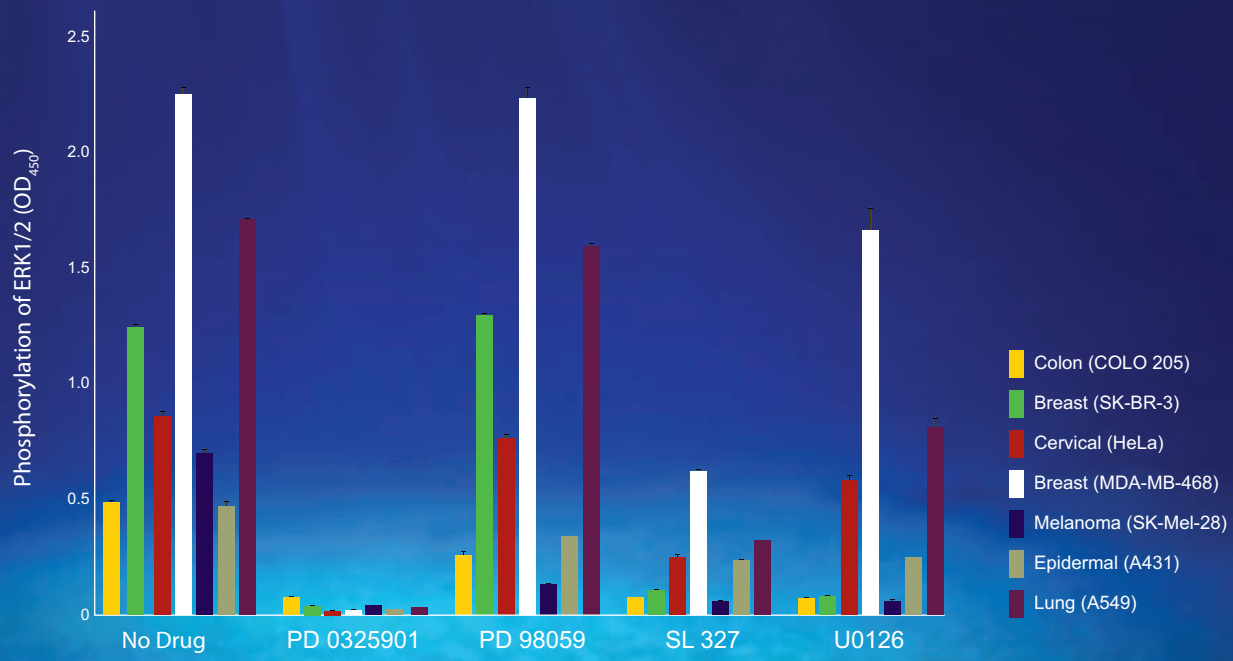

Interact with this data and learn more about our ELISA formats for intracellular targets

RnDSystems.com/Optimize

TOCRIS bioscience

R&D SYSTEMS®

BostonBiochem®

Science Careers Advertising

For full advertising details, go to ScienceCareers.org and click For Employers, or call one of our representatives.

Tracy Holmes
Worldwide Associate Director
Science Careers
Phone: +44 (0) 1223 326525

THE AMERICAS

E-mail: advertise@sciencecareers.org
Fax: 202-289-6742

Tina Burks
Phone: 202-326-6577

Nancy Toema
Phone: 202-326-6578

Marci Gallun
Sales Administrator
Phone: 202-326-6582

Online Job Posting Questions
Phone: 202-312-6375

EUROPE / INDIA / AUSTRALIA / NEW ZEALAND / REST OF WORLD

E-mail: ads@science-int.co.uk
Fax: +44 (0) 1223 326532

Axel Gesatzki
Phone: +44 (0)1223 326529

Sarah Lelarge
Phone: +44 (0) 1223 326527

Kelly Grace
Phone: +44 (0) 1223 326528

JAPAN

Yuri Kobayashi
Phone: +81-(0)90-9110-1719
E-mail: ykobayas@aaas.org

CHINA / KOREA / SINGAPORE / TAIWAN / THAILAND

Ruolei Wu
Phone: +86-1367-1015-294
E-mail: rwu@aaas.org

All ads submitted for publication must comply with applicable U.S. and non-U.S. laws. *Science* reserves the right to refuse any advertisement at its sole discretion for any reason, including without limitation for offensive language or inappropriate content, and all advertising is subject to publisher approval. *Science* encourages our readers to alert us to any ads that they feel may be discriminatory or offensive.

Science Careers
From the journal *Science* AAAS

ScienceCareers.org

DEPARTMENT OF BIOTECHNOLOGY
MINISTRY OF SCIENCE & TECHNOLOGY, GOVERNMENT OF INDIA
NOMINATIONS / APPLICATIONS FOR THE POST OF DIRECTOR, CDFD, HYDERABAD

Nominations / Applications are invited for the post of Director on deputation (including short term contract), Centre for DNA Fingerprinting & Diagnostics (CDFD), Hyderabad, an autonomous institute under the Department of Biotechnology, Government of India, from Indian citizens including those staying abroad and Non - Resident Indians (NRIs).

The Centre uniquely combines two kinds of activities, the first being those of services in the twin areas of DNA profiling for law - enforcement agencies and diagnostics tests and clinical counseling for genetic disorders, and the second that of cutting - edge basic research in various disciplines of modern biology, in such a way that each supports and in turn is enriched by the other.

The applicants should be below 56 years of age. The post carries HAG Scale of Pay of ₹ 67,000 (annual increment @ 3%) - 79,000/- with usual allowances as per the Government of India Rules.

The applicants should be Scientists from Central / State Governments, research institutes, autonomous bodies etc.

(i) Holding analogues post on regular basis in the parent Department.
(ii) 3 years service in PB - IV with Grade Pay of ₹ 10,000/-; or equivalent in the parent cadre; or
(iii) 5 years service in PB - IV with Grade Pay of ₹ 8900/-; or
(iv) 7 years service in PB - IV with Grade Pay of ₹ 8700/-; and possessing the following qualifications & experiences:-

Essential

(i) Ph.D in any life science discipline / M.D. or equivalent
(ii) Experience of research in the area of organismal, cellular, molecular or systems biology, or biotechnology.
(iii) Excellent track record, hand in publications, patent and awards.

Desirable

(i) Experience in successfully running large programme, centre, institution
(ii) Experience of guiding research activities in the area of specialization.

N.B.:- "In case no candidate is found suitable, the Search - cum - Selection Committee is empowered to consider / nominate persons of capability and eminence with lesser experience and younger in age to be appointed as Director, CDFD, Hyderbad on pay scale / emoluments negotiable in the process"

The period of deputation includes period of deputation in other ex-cadre posts, held immediately preceding this appointment in the same or some other organization / Department should ordinarily not exceed 5 years. The maximum age limit for appointment on deputation should not exceed 56 years as on the closing date of receipt of nominations / applications.

The nomination / application along with detailed curriculum vitae including the date of birth, address for correspondence including telephone no., fax and e-mail address, qualifications acquired, professional and research experience, present position and scale of pay with total emoluments, publication details and a 500 words write-up on the candidate's vision of CDFD for the next ten years may be sent to **Smt. Kusum Lata Sharma, Deputy Secretary, Department of Biotechnology, Block - 2, CGO Complex, Lodi Road, New Delhi - 110 003,** superscribing the cover **"Nomination / Application for the Post of Director, CDFD"** so as to reach her within 30 days from the date of publication of this advertisement. The detailed advertisement and format of application is available at DBT website www.dbtindia.nic.in and at the CDFD website www.cdfd.org.in

The Department reserves the right to relax any of the requirements prescribed above.

AAAS is here – helping scientists achieve career success.

Every month, over 400,000 students and scientists visit ScienceCareers.org in search of the information, advice, and opportunities they need to take the next step in their careers.

A complete career resource, free to the public, *Science* Careers offers a suite of tools and services developed specifically for scientists. With hundreds of career development articles, webinars and downloadable booklets filled with practical advice, a community forum providing answers to career questions, and thousands of job listings in academia, government, and industry, *Science* Careers has helped countless individuals prepare themselves for successful careers.

As a AAAS member, your dues help AAAS make this service freely available to the scientific community. If you're not a member, join us. Together we can make a difference.

To learn more, visit
aaas.org/plusyou/sciencecareers

AAAS + U = Δ

TUM is the first university in Germany to reinforce its recruitment policy by a comprehensive tenure track system. Based on best international standards and transparent performance criteria, it offers merit-based academic career options for high-potential early-career scientists as well as for scholars of distinction.

The **Department of Chemistry** invites applications for

Professorships in »Inorganic Chemistry with research emphases on metal-organic chemistry and molecular catalysis«

to be appointed either as one Full Professorship (pay scale grade W3, Chair Position) or as one Associate Professorship (pay scale grade W3) and one Tenure Track Assistant Professorship (pay scale grade W2 plus option for W3), as soon as possible. The appointments are aimed at securing and stabilizing the excellent international reputation of these research areas at TUM on the highest level. Attractive working conditions are available in the laboratories of the newly built TUM Catalysis Research Center (CRC), which will open soon.

Only candidates who can be expected to establish and maintain an internationally recognized research agenda in the field of metal-organic chemistry and molecular catalysis and to further develop TUM's scientific profile will be considered.

Generally, applications from high-potential early-career scientists (as Tenure Track Assistant Professors) are just as welcome as applications from scholars of distinction with advanced research experience and international standing (as Associate or Full Professors). Appointment as Full Professor assumes an excellent international reputation, documented for example by scientific awards.

Appointments as Tenure Track Assistant Professor will initially be for 6 years. After positive evaluation in the final year, the candidate is tenured on an Associate Professor level. In exceptional cases, the tenure evaluation may be initiated after a minimum of three years. Such cases will have to be justified by outstanding achievements of the candidate and the candidate's contributions to strategically shaping the university's profile. Eligible candidates have established a strong track record in the postdoctoral phase and demonstrate pedagogical and personal aptitude to take over a professorship.

As Associate Professor, there is the possibility of being promoted to a Full Professor position (pay scale grade W3, Chair Position). Promotion requires a Post-Tenure Performance Review, with a successful and positive reviewing period of at least 3 years after appointment as a TUM Associate Professor.

Successful candidates are expected to have broadly and competently mastered the core subject of inorganic chemistry during their education and to have oriented their research toward metal-organic chemistry and molecular catalysis. International experience counts among the requirements for appointment. Leading figures are sought who can, with an independent scientific profile, contribute significantly to the continuing sustainable development of inorganic chemistry and homogeneous catalysis at the Technische Universität München, thus helping to shape the content as well as the concept of the new TUM Catalysis Research Center (opening in 2014).

Independent of their career level, successful applicants are expected to demonstrate pedagogical aptitude and to contribute actively to the ongoing development of the department's and the university's teaching program. A moderate level of participation in administrative functions of the TUM Catalysis Research Center and TUM is required. In addition, special emphasis and high value will be placed on the promotion of young scientists, as well as on further development of the research and teaching agenda of TUM.

Prerequisites for this position are a university degree, a doctoral degree, teaching skills at university level, and additional academic achievements (according to Art. 7 and Art. 10 III BayHSchPG).

Candidates for this position should be aged 51 or under at the time of appointment; exceptions to this rule might be possible.

A proven ability to attract competitive national and international funding, collaboration with national and international researchers as well as substantial international experience are expected. The ability to teach in English is a prerequisite for TUM Professors.

The regulations according to "TUM Faculty Recruitment and Career System" (http://www.tum.de/ faculty-tenure-track) apply.

As part of the Excellence Initiative of the German federal and state governments, TUM has been pursuing the strategic goal of substantially increasing the diversity of its faculty. As an equal opportunity and affirmative action employer, TUM explicitly encourages nominations of and applications from women as well as from all others who would bring additional diversity dimensions to the university's research and teaching strategies. Preference will be given to disabled candidates with essentially the same qualifications.

The TUM Munich Dual Career Office provides support for dual career couples and families.

Applications accompanied by supporting documentation in English (CV, certificates, credentials, list of publications, 3 selected reprints and a short statement with a max. of 1,000 characters about their impact on your research profile, presentation of research strategy, list of courses taught, statement on teaching strategy and teaching philosophy, third-party funding, as well as the names and addresses of at least 3 references) should be submitted by **June 15, 2014** to:

Director of CRC, Catalysis Research Center
Prof. Dr. Ueli Heiz
Technische Universität München
Ernst-Otto-Fischer Straße 1, D-85748 Garching
E-Mail: irmgard.groetsch@mytum.de

Science Careers online @sciencecareers.org

Center for Immunology & Microbial Disease
Albany Medical College

Faculty Position

The Center for Immunology & Microbial Disease at Albany Medical College invites applications for a tenure-track, junior or senior faculty position from individuals who have a doctoral degree, postdoctoral experience, and demonstrated research productivity. Those with an interest in host-pathogen interactions are particularly encouraged to apply. The successful candidate will be expected to establish an independent, extramurally-funded research program and participate in the teaching of medical and graduate students. The basic science departments at Albany Medical College are organized as interdisciplinary research centers and the Center for Immunology & Microbial Disease has a focus on microbial pathogenesis and immune defense, particularly as related to biothreat agents and emerging infections. The new faculty recruit will receive a competitive salary, an attractive start-up package, laboratory space in our newly constructed research building, and access to all departmental core services including the Center's fully-staffed Immunology and ABSL-3/BSL-3 Cores. Albany Medical College is located in a mid-sized city within the upstate New York Capital Region, and has easy access to Boston, New York City, and the Adirondack Mountains.

Applicants should send their curriculum vitae, a statement of research plans, and three letters of reference to:

Faculty Search Committee
Center for Immunology & Microbial Disease
Albany Medical College
47 New Scotland Avenue, MC-151
Albany, NY 12208

For further information about the Center, visit **www.amc.edu/Academic/Research/imd.htm**

An Equal Opportunity/Affirmative Action Employer. Women and minorities are encouraged to apply.

Boston, MA

Northeastern

Associate/Full Professor-Pharmacology

Department of Pharmaceutical Sciences

The Northeastern University Bouvé College of Health Sciences' Department of Pharmaceutical Sciences is seeking qualified candidates for a full-time tenured faculty position at the associate or full professor level. Expertise broadly in the field of pharmacology with a background in behavioral, molecular or systems pharmacology is required. The Department has long-standing strengths in neuropharmacology, immunology, medicinal chemistry, pharmaceutics, imaging, drug discovery, development and delivery, and it seeks candidates able to complement, collaborate, and expand these areas of strength. Qualified candidates must hold a Ph.D. in pharmacology or related specialty field such as neuroscience or pharmaceutical science, and will have an established extramurally-funded research program in one of the areas of pharmacology named above. Applicants with current transferable funding will be given priority.

To apply, visit **http://apptrkr.com/465448** Applicants should submit a cover letter of interest, the names and contact information for three references, curriculum vitae, and a 5-year plan for future research plans. For more information, please contact the search committee chair Raymond G. Booth (ra.booth@neu.edu).

Northeastern University is an Equal Opportunity/Affirmative Action, Title IX, and an ADVANCE institution. Minorities, women, and persons with disabilities are strongly encouraged to apply. Northeastern University is an E-Verify employer

---

Department of the Army
US Army Medical Research and Materiel Command
US Army Medical Research Institute of Infectious Diseases

Science Director

The U. S. Army Medical Research Institute of Infectious Diseases (USAMRIID), the Department of Defense's premiere research institute for medical defense against biological threats located at Fort Detrick, Maryland, is seeking to fill the position of Science Director. The USAMRIID is a subordinate unit of the U.S. Army Medical Research and Materiel Command, a subordinate command of the U.S. Army Medical Command. The incumbent will be involved in the development of the scientific strategy and management of the research portfolio. In addition, the incumbent will be responsible for execution of the institute's discovery and early development activities. The Science Director will be responsible for ensuring USAMRIID' s continued leadership role in the field of biodefense through the adoption of state-of-the-art technologies, recruitment of a premier workforce, and improvements in the management and operation of the institute's technical work unit.

Desired Qualifications: A degree in Medicine, Veterinary Medicine, PhD. or related degree in the biological sciences and 10-15 years of relevant experience in leading a world-class research organization. A successful candidate should be a recognized expert or global leader in one core area of biological research, yet have a broad understanding of the biological sciences. They should have strong process orientation with the ability to understand the strategic and tactical link between basic research and early development. The candidate should have strong business and scientific perspective, demonstrated ability to deliver results in a structured organization, and a solid background in the management of a technical organization, preferably in either a pharmaceutical or biotechnology organization. Excellent communication skills, both written and oral, strong project management skills, and the ability to work cooperatively in a collaborative, cross-functional team environment are required.

Fort Detrick is located within the boundaries of the city of Frederick, Maryland, which offers modern housing, schools, recreation areas, excellent utilities, and access to major metropolitan areas. Situated between Baltimore, Maryland and Washington, D.C., Frederick County, Maryland adjoins Virginia, West Virginia, and Pennsylvania. For additional information about USAMRIID, Fort Detrick, and USAMRMC, please visit **http://www.usamriid.army.mil**, **http://www.detrick.army.mil**, and **https://mrmc.amedd.army.mil**. Please apply for this position at: **www.usajobs.gov**

Introducing the new
***Science* Careers Jobs app** from Science

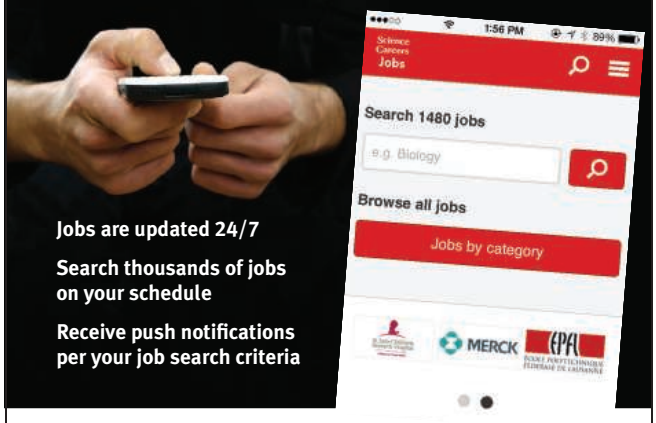

Jobs are updated 24/7

Search thousands of jobs on your schedule

Receive push notifications per your job search criteria

Get a job on the go.
Search worldwide for thousands of scientific jobs in academia, industry, and government. Keep your finger on the pulse of your field—set up an alert for the type of job you are looking for and receive push notifications when jobs are posted that meet your criteria. The application process is seamless, linking you directly to job postings from your customized push notifications.

Scan this code to download app or visit **apps.sciencemag.org** for information.

Science Careers
From the journal *Science* AAAS

ScienceCareers.org

Recruitments of talents abroad by Nanjing University of Science and Technology

南京理工大学 NANJING UNIVERSITY OF SCIENCE & TECHNOLOGY

http://rczp.njust.edu.cn/urp-portal/portal/group/Recruit

Nanjing University of Science and Technology (NUST) is one of the first national "211 Project" universities affiliated with the Ministry of Industry and Information Technology. It has become a multi-disciplinary and coordinated developing engineering-based university along with science, liberal arts, economics, management, law, education, etc. It is an ideal place for research work for its strong scientific research ability, prominent advantages, perfect construction of infrastructural facilities and it's also a pleasant place to live in since the beautiful scenery of Dr. Sun Yat-sen's Mausoleum which is only less than one mile away.

Please refer to the following application guidelines and we welcome your applications.

Majors for recruitment:

Related disciplines of Ordnance Science and Technology, Mechanical Engineering, Instrumentation Science and Technology, Chemical Engineering and Technology, Chemical, Electronic Science and Technology, Information and Communication Engineering, Optics, Optical Engineering, Computer Science and Technology, Control Science and Technology, Electrical Engineering, Transportation Engineering, Aerospace Science and Technology, Power Engineering and Thermal Physics, New Energy, Mechanics, Mathematics, Physics, Civil Engineering, Materials Science and Engineering, Environmental Science and Engineering, Biomedical Engineering, Law, Intellectual Property, Public Administration, Sociology, Economics, Management Science, (Applied) Linguistics and Literature, Art and Design.

Position and requirements:

Recruiting position: "Zijin scholars" distinguished professor, "Young Talents Professors", Professor, Associate Professor, Assistant Professor.

Basic qualities: Overseas talents with a doctorate degree, passion for education, high academic achievement and strong research capability and, good professionalism, academic character and team spirit as well. Among them, the candidates for "Young Talent Professor" staff position should be under 35 years old.

Related treatment:

The full-time employed teachers will be directly categorized into national institution, enjoying free medical care, pensions and other state welfare, and the family issues such as children's nursery and schooling will be addressed. We provide the high-level personnel and young talents with transitional housing, financial relief, research funding and other supports with generous salaries, comfortable working and living conditions. For high-level talents, we help settle down in terms of team building, work, housing, etc. Specific treatment will be determined by personal discussion.

1. For the full-time "Thousands of Plans" and other leading talents, NUST will provide 600 thousand to 1 million RMB annual salary and no less than 8 million RMB research start-up funds.
2. For the "Thousands Youth Talents" and other related talents, we provide no less than 300 thousand RMB annual salary, 1 million RMB financial relief and 2-4 million RMB research start-up funds.
3. For the "Zijin scholars" distinguished professor, we provide 500 thousand to 2 million RMB financial relief, 1 to 5 million RMB research funds and stipulated wages and other benefits along with certain amount of professor allowances per year.
4. For the "Young Talented Professors", we provide 300 thousand RMB annual salary, with certain financial relief and start-up funds.
5. For the professor, associate professor, assistant professor, we will provide salary and financial relief which is competitive in the same region, as well as starter home, and provide appropriate amount of research funds.

Way for recruitment:

The recruitments of talents abroad by NUST is under way regularly, please log in NUST Recruitment Network http://rczp.njust.edu.cn/urp-portal/portal/group/Recruit to have a registration, or contact us directly.

Contact us:

JI Wenchao Meng Yang
Tel: 86-25-84316943
Mail: rcb@njust.edu.cn
NUST website: www.njust.edu.cn

CHONGQING UNIVERSITY OF TECHNOLOGY

Faculty Recruiting

Chongqing University of Technology (CQUT) is a full-time multidisciplinary undergraduate university in China. Founded in 1940, CQUT has gained over seven decades of experience in higher education. Covering an area of 2288 Mu（153 Hectares）, CQUT has grown into a well recognized higher academic institution and research center in southwest China with unique strength and competitiveness in engineering, science and management. CQUT has successfully established "Postdoctoral Workstation" and "Academician Experts Workstation". Now among its 1,000-plus faculty members, more than 600 are full and associate professors and over 100 have been selected as state-level and provincial-level talents. In 2011, our university was listed as a Pilot Zone Talents Cultivation in Chongqing, the first and only academic institution granted with such an honor in Chongqing Municipality.

At present, the campus is home to over 24,000 students, ranging from full-time junior college students, undergraduates, graduate students to overseas students. CQUT presently offers 55 undergraduate programs, and 39 postgraduate programs authorized to confer Master's degree.

In recent years, our university has undertaken over 600 national- or provincial-level research programs; published about 5500 research papers in domestic and international academic journals and symposiums, 1200 of which have been collected by SCI, EI and ISTP; published about 220 textbooks and works; obtained over 450 authorized patents and open patents. It has been awarded four national prizes in scientific research, one national patent gold prize and 91 provincial ones. Our university library boasts a total collection of over 2.3 million books and various other digital materials.

In the era of globalization, CQUT is fully committed to building an even stronger faculty. We highly value integrity, responsibility, creativity and innovation. Now, faculty positions are open for individuals with excellence in teaching and academic research from both home and abroad. Candidates should have at least obtained PhD degree, or gained postdoctoral research experience, with proven track research record in related fields. Those who have conducted research and made distinctive achievements in mechanics, electronics, economics, accountancy and material science are preferred.

Further information is available at http:// www.cqut.edu.cn

Contact us:

Email: xhh@cqut.edu.cn zuojiankang@cqut.edu.cn
Telephone: 0086-23-62563352, 62563354

Faculty Positions available at Hohai University, Nanjing, China

Hohai University invites applications for faculty positions at the assistant, associate, or full professor level in the area of engineering, science, economics, management, liberal arts, and law. Applicants should have a doctoral degree from a prestigious university. For the complete job announcements and directions on how to apply, visit: rsc.hhu.edu.cn or contact the Department of human resource at 86-25-83786205.

Hohai University, founded in 1915, wins its worldwide reputation on the research of Water Science& Civil Engineering&Environment Engineering. It is a National key university of China, and among the universities of the National "*211 Project*" and Innovation Bases of the National "*985 Project*". Hohai University aims to be a research oriented university.

For your career in science, there's only one **Science**

A career plan customized *for* you, *by* you.

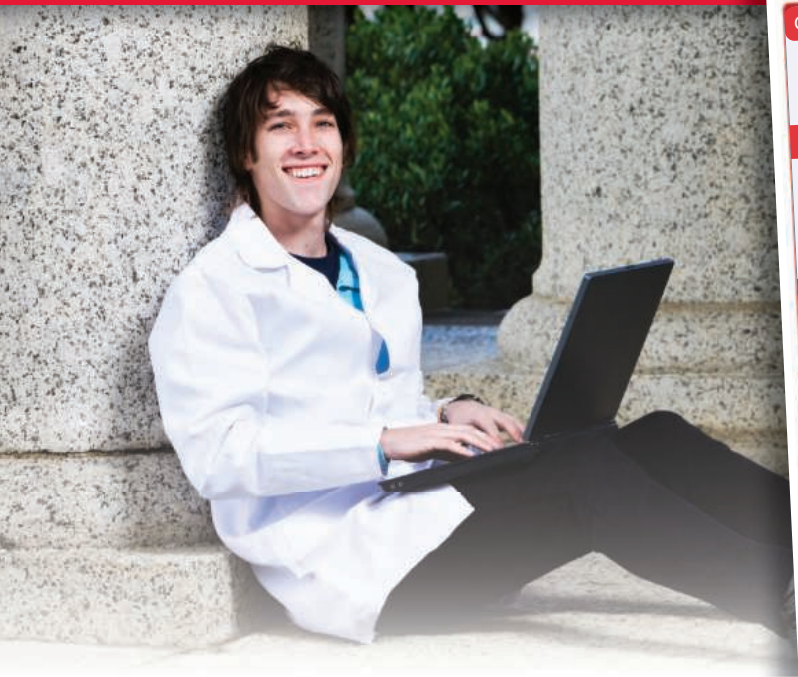

myIDP.sciencecareers.org

Recommended by leading professional societies and endorsed by the National Institutes of Health, an individual development plan will help you prepare for a successful and satisfying scientific career.

my IDP Science Careers

In collaboration with FASEB, UCSF, and the Medical College of Wisconsin and with support from the Burroughs Wellcome Fund, AAAS and *Science* Careers present the first and only online app that helps scientists prepare their very own individual development plan.

Visit the website and start planning today!
myIDP.sciencecareers.org

In partnership with:

advancing the life sciences 1912-2012 FASEB Federation of American Societies for Experimental Biology

UCSF University of California San Francisco

Medical College of Wisconsin

Burroughs Wellcome Fund

2015 Vetlesen Prize

Call for Nominations

Nominations should be sent prior to 30 June 2014 to:

Sean C. Solomon, Director
Lamont-Doherty Earth Observatory
PO Box 1000
61 Route 9W Palisades NY 10964
Tel: 845/365-8729

or via electronic submission to:
vetlesenprize@ldeo.columbia.edu

Lamont-Doherty Earth Observatory
COLUMBIA UNIVERSITY | EARTH INSTITUTE

The Vetlesen Prize, established in 1959 by the G. Unger Vetlesen Foundation, is awarded for scientific achievement that has resulted in a clearer understanding of the Earth, its history, or its relations to the universe. The prize consists of a medal and a cash award of $250,000. Nominations are now open for the next prize, which will be awarded in 2015.

As of 2015, the prize will be awarded to a single individual, who can reside and work anywhere in the world. The prize is administered by Columbia University's Lamont-Doherty Earth Observatory.

Nomination packages should include at least two letters that describe the nominee's contributions to a fuller understanding of the workings of our planet, along with a one-paragraph biographical sketch and the full curriculum vitae of the candidate.

For more information about the Vetlesen Prize:
http://www.ldeo.columbia.edu/vetlesen-prize

Past Vetlesen Laureates

2012 Susan Solomon, Jean Jouzel
2008 Walter Alvarez
2004 W. Richard Peltier, Sir Nicholas J. Shackleton
2000 W. Jason Morgan, Walter C. Pitman III, Lynn R. Sykes
1996 Robert E. Dickinson, John Imbrie
1993 Walter H. Munk
1987 Wallace S. Broecker, Harmon Craig
1981 M. King Hubbert
1978 J. Tuzo Wilson
1974 Chaim L. Pekeris
1973 William A. Fowler
1970 Allan V. Cox, Richard R. Doell, S. Keith Runcorn
1968 Francis Birch, Sir Edward Bullard
1966 Jan Hendrik Oort
1964 Pentti E. Eskola, Arthur Holmes
1962 Sir Harold Jeffreys, Felix Andries Vening Meinesz
1960 W. Maurice Ewing

KOREA UNIVERSITY
Faculty Openings

Korea University, in Seoul, South Korea, seeks candidates to join the faculty in the spring semester of 2015 beginning March 1. We are recruiting enthusiastic, well-trained scholars who wish to refine their teaching experience and research in this part of the world. Korea University, founded in 1905, is ranked one of the top universities in Korea by major global assessment reports. The positions available for the candidates are assistant, associate, or full professors (a two or three year tenure track appointment, OR non-tenure track appointment). All candidates are expected to have ample university-level teaching experience, a strong commitment to excellence in scholarship, and dedication to teaching and research in their fields.

[Online Application] - Applicants are asked to submit their applications electronically by using the website at http://kuweb.korea.ac.kr/faculty
- Application Deadline : May 30, 2014

[Point of Contact] - Phone : +82-2-3290-1072
- Fax : +82-2-929-9164
- E-mail : faculty@korea.ac.kr

KOREA UNIVERSITY

FUNDING OPPORTUNITIES

U.S. Department of Defense
Defense Medical Research and Development Program

Peer Reviewed Medical Research Program

The Peer Reviewed Medical Research Program (PRMRP) funds exceptional research with the goal to improve the health and well-being of all military service members, Veterans, and beneficiaries. The PRMRP received ***$200 million*** in fiscal year 2014 (FY14), and seeks grant applications in the following ***topic areas***:

Acupuncture
Arthritis (other than post-traumatic osteoarthritis and rheumatoid arthritis)
Chronic Migraine and Post-Traumatic Headaches
Congenital Heart Disease
DNA Vaccine Technology for Post-Exposure Prophylaxis
Dystonia
Epilepsy
Food Allergies
Fragile X Syndrome
Hereditary Angioedema
Illnesses Related to Radiation Exposure (excludes cancer)
Inflammatory Bowel Disease
Interstitial Cystitis
Lupus
Malaria
Metabolic Disease
Neuroprosthetics
Pancreatitis
Polycystic Kidney Disease
Post-Traumatic Osteoarthritis
Psychotropic Medications
Respiratory Health (excludes lung cancer and mesothelioma)
Rheumatoid Arthritis
Segmental Bone Defects
Tinnitus

The FY14 PRMRP Program Announcements and General Application Instructions are anticipated to be posted on Grants.gov by ***May 1, 2014:***

- Clinical Trial Award
- Discovery Award
- Focused Program Award
- Investigator-Initiated Research Award
- Technology/Therapeutic Development Award

All applications must conform to the Program Announcements and General Application Instructions that will be available for electronic downloading from the Grants.gov website (all viewable under CFDA number 12.420). Execution management support will be provided by the Congressionally Directed Medical Research Programs.

http://cdmrp.army.mil
http://cdmrp.army.mil/funding/prmrp.shtml

Science Careers online @sciencecareers.org

Science Careers

There's only one

Dr. Shirley Malcom

To Dr. Shirley Malcom, born and raised in the segregated South more than 65 years ago, a career based on her studies in science seemed even less likely than the launch of the Soviet's Sputnik. But with Sputnik's success, the Space Race officially started and, in an instant, brought a laser-like focus to science education and ways to deliver a proper response. Not long after, Dr. Malcom entered the picture.

Although black schools at the time received fewer dollars per student and did not have sufficient resources to maintain their labs at a level equivalent to the white schools, Dr. Malcom found her way to the University of Washington where she succeeded in obtaining a B.S. in spite of the difficulties of being an African American woman in the field of science. From there she went on to earn a Ph.D. in ecology from Penn State and held a faculty position at the University of North Carolina, Wilmington.

Dr. Malcom has served at the AAAS in multiple capacities, and is presently Head of the Directorate for Education and Human Resources Programs. Nominated by President Clinton to the National Science Board, she also held a position on his Committee of Advisors on Science and Technology. She is currently a member of the Caltech Board of Trustees, a Regent of Morgan State University, and co-chair of the Gender Advisory Board of the UN Commission on Science and Technology for Development. She has held numerous other positions of distinction and is the principal author of *The Double Bind: The Price of Being a Minority Woman in Science*.

Of her active career in science, Dr. Malcom says, "I guess I have become a poster child for taking one's science background and using that in many other ways: we ask questions; we try to understand what we find; we consider what evidence we would need to confirm or refute hypotheses. And that happens in whatever setting one finds oneself."

At *Science* we are here to help you in your own scientific career with expert career advice, forums, job postings, and more — all for free. Visit *Science* today at **ScienceCareers.org**.

For your career in science, there's only one Science

AAAS

ScienceCareers.org

Career advice | Job postings | Job Alerts | Career Forum | Crafting resumes/CVs | Preparing for interviews

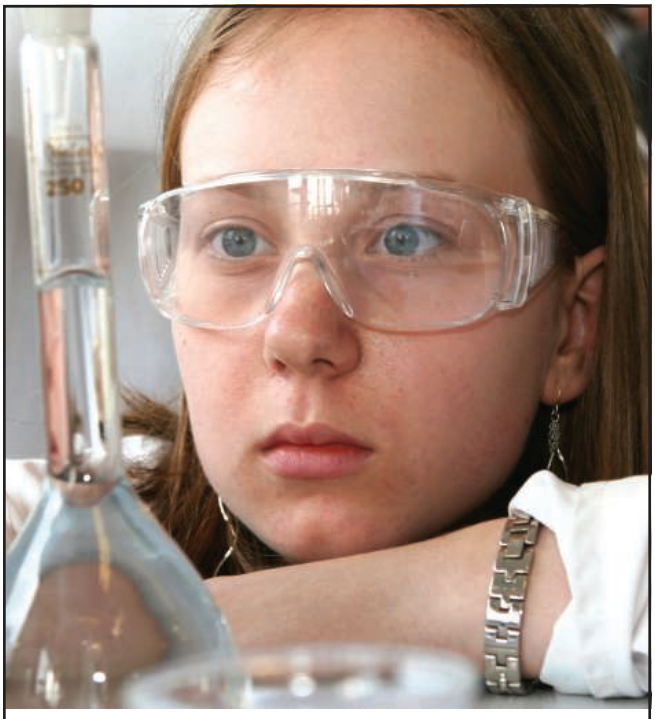

AAAS is here – promoting universal science literacy.

In 1985, AAAS founded Project 2061 with the goal of helping all Americans become literate in science, mathematics, and technology. With its landmark publications *Science for All Americans* and *Benchmarks for Science Literacy*, Project 2061 set out recommendations for what all students should know and be able to do in science, mathematics, and technology by the time they graduate from high school. Today, many of the state standards in the United States have drawn their content from Project 2061.

As a AAAS member, your dues help support Project 2061 as it works to improve science education. If you are not yet a member, join us. Together we can make a difference.

To learn more, visit
aaas.org/plusyou/project2061

AAAS + U = Δ

Unil
UNIL | Université de Lausanne
Faculty of Biology and Medicine

| le savoir vivant |

THE FACULTY OF BIOLOGY AND MEDICINE OF THE UNIVERSITY OF LAUSANNE, SWITZERLAND, INVITES APPLICATIONS FOR A POSITION OF:

FULL PROFESSOR OR ASSOCIATE PROFESSOR AT THE DEPARTMENT OF BIOCHEMISTRY

Envisioned starting date: September, 2014.

The Department of Biochemistry (http://www.unil.ch/ib) wishes to strengthen its activities in the fields of immunology and infectious diseases.

Successful candidates must have a record of outstanding research achievements and are expected to utilize the dynamic research environment in Lausanne in order to develop an internationally recognized research programme funded by external sources.

The Department has excellent experimental facilities and access to state-of-the-art imaging, proteomics and genomics facilities. A start-up package as well as funding for several research positions will be available.

Pre-existing knowledge of French is not required but the selected candidate is expected to learn the language. She(he) will supervise Masters and PhD students, and participate in teaching activities by the Department. Candidates will also share administrative responsibilities in the management of the Department.

The job description is available on the Internet site www.unil.ch/fbm/page64812.html.

Further information may be obtained from the Dean of the Faculty, Prof. Béatrice Desvergne (beatrice.desvergne@unil.ch), chairwoman of the search committee.

Applications must be formulated in English and should include a motivation letter, the curriculum vitae, a list of publications highlighting the five most significant ones, a brief statement of the past and future research programmes, the teaching experience, and the names and contact information of three references. They should be submitted online by July 9th, 2014 as a single pdf file to www.unil.ch/iafbm/application.

Seeking to promote an equitable representation of women and men among its staff, the University encourages applications from women.

POSITIONS OPEN

TENURE-TRACK FACULTY POSITION in Bacteriology

The Department of Pathology, Microbiology, and Immunology at the University of South Carolina's School of Medicine invites applications for a tenure-track **ASSISTANT PROFESSOR** position in Bacteriology. The successful candidate is expected to develop a strong extramurally funded research program, and must participate in the teaching mission of the department. Outstanding applicants working in an area complementing our existing faculty research interests (**website: http://pmi.med.sc.edu/**) will be considered. Candidates must have a Ph.D. or equivalent, and at least three years of postdoctoral research experience. Preference will be given to a candidate who has shown evidence of independence with currently active grant funding. Competitive salary and startup funds are available. Please submit curriculum vitae, teaching philosophy, and statement of research plans to: **Dr. Mitzi Nagarkatti, Chair, Department of Pathology, Microbiology, and Immunology, University of South Carolina School of Medicine, Columbia, SC 29208** or **e-mail: bacteriology@uscmed.sc.edu.** Kindly arrange to submit three letters of recommendation upon request. The search will start immediately and will continue until the position is filled.

University of South Carolina, Columbia is an Equal Opportunity/Affirmative Action Employer and encourages applications from women and minorities and is responsive to the needs of dual career couples.

CHAIRPERSON
Department of Physiology
Kirksville College of Osteopathic Medicine

The Department of Physiology at A.T. Still University (ATSU) invites applications for Chairperson. The successful candidate will report to the Dean of the College and will be responsible for envisioning, developing, and coordinating the implementation of programmatic academic innovations. Applicants must have a Ph.D. or other doctoral degree in physiology or a related biomedical discipline. The successful candidate will have demonstrated breadth of mature academic skills in the discipline of physiology and will have significant physiology teaching experience at the medical and/or graduate school level. The successful candidate will demonstrate consistent scholarly productivity as a biomedical researcher with success in publication and acquisition of extramural research funding. The successful candidate will have been involved in academic governance and leadership. Position details are described at **website: http://jobs.atsu.edu/chairperson-of-the-department-of-physiology-kcom/job/4404029.** Qualified persons should send a current curriculum vitae, a personal statement of teaching and research goals, and contact information for three to four references. Electronic submission of all materials should be directed to **e-mail: hr@atsu.edu.** *ATSU is an Equal Opportunity Employer and does not discriminate on the basis of race, color, religion, national origin, sex, gender, sexual orientation, age or disability.*

TENURE-TRACK ASSISTANT PROFESSOR

Loyola University Chicago, Health Sciences Division, is currently advertising for a tenure-track Assistant Professor to work with the viral hepatitis research group within the division to develop a strong mathematical modeling program. Ph.D. required with an established research program in viral hepatitis dynamics in vivo and in vitro. For full consideration, please apply online at **website: http://www.careers.luc.edu/applicants/Central?quickFind=56966** by June 30, 2014. Direct questions to **Ms. Marie Go, e-mail: mago@lumc.edu.** *Loyola University Chicago is an Equal Opportunity Employer for Minorities, Women, Veterans, and the Disabled.*

POSITIONS OPEN

FACULTY MEMBER
Division of Research
Department of Pathology
Lsu School Health Sciences Center-Shreveport

The Division of Research within the Department of Pathology at Louisiana State University Health Sciences Center-Shreveport (LSUMC) is seeking applicants for a tenure-track appointment at the **ASSISTANT/ASSOCIATE PROFESSOR** level. This position is open to individuals possessing Ph.D., M.D., or M.D.-Ph.D. degrees.

The ideal candidate should have expertise in one or more of the following areas: molecular/cell biology of extracellular matrix molecules, angiogenesis, cell adhesion and signaling, and/or vascular wall pathology. Applicants with expertise in the above areas especially in the context of cardiovascular disease or cancer are particularly encouraged to apply.

The selected candidate will have limited personal teaching/clinical responsibilities, primarily defined by his/her interests and training.

Applicants should submit curriculum vitae, list of at least three references, and a brief description of research interests and direction by June 30 to: **Kevin McCarthy, Ph.D., Professor, Department of Pathology, LSU Health Sciences Center in Shreveport, P.O. Box 33932, Shreveport, LA 71130.**

LSUMC is an Equal Opportunity Employer and all qualified applicants will receive consideration for employment without regard to race, color, religion, sex, national origin, disability status, protected veteran status, or any other characteristic protected by law.

ASSISTANT PROFESSOR OF PHYSIOLOGY
Kirksville College of Osteopathic Medicine

The Department of Physiology at Kirksville College of Osteopathic Medicine invites applications for a tenure-track Assistant Professor position. Ideal candidates will have a Ph.D. or equivalent and a minimum of two years of postdoctoral training and experience in teaching. The successful candidate will be expected to develop an independent research program with potential for attracting extramural funding and will be able to supervise graduate students. This position will include teaching medical, dental, and graduate level students. Evidence of teaching effectiveness using modern teaching technologies is expected. Position details are described at **website: http://jobs.atsu.edu/kcom-assistant-professor-physiology/job/4524094.** Qualified and interested persons should send current curriculum vitae along with a personal statement of teaching and research goals and a list of three to four references. Electronic submission of all materials should be directed to **e-mail: hr@atsu.edu.** *A.T. Still University is an Equal Opportunity Employer and does not discriminate on the basis of race, color, religion, national origin, sex, gender, sexual orientation, age or disability.*

Find your future here.

Science Careers
From the journal *Science* AAAS
www.ScienceCareers.org

Stop searching for a job; start your career.
www.ScienceCareers.org

Nontraditional Careers: Opportunities Away From the Bench
Webinar

Want to learn more about exciting and rewarding careers outside of academic/industrial research? View a roundtable discussion that looks at the various career options open to scientists and strategies you can use to pursue a nonresearch career.

Now Available On Demand
www.sciencecareers.org/webinar

Produced by the *Science*/AAAS Business Office.

Science Careers
From the journal *Science* AAAS